SANDIA REPORT

Sandia Report SAND97-1730 • UC-814
Unlimited Release
Printed September 1997

Yucca Mountain Site Characterization Project

Three-Dimensional Hydrological and Thermal Property Models of Yucca Mountain, Nevada

C. A. Rautman, S.A. McKenna

Prepared by
Sandia National Laboratories
Albuquerque, New Mexico 87185 and Livermore, California 94550
for the United States Department of Energy
under Contract DE-AC04-94AL85000

Issued by Sandia National Laboratories, operated for the United States Department of Energy by Sandia Corporation.

Available to DOE and DOE contractors from
Office of Scientific and Technical Information
PO Box 62
Oak Ridge, TN 37831

Prices available from (615) 576-8401, FTS 626-8401

Available to the public from
National Technical Information Service
US Department of Commerce
5285 Port Royal Rd
Springfield, VA 22161

NTIS price codes
Printed copy: A08
Microfiche copy: A01

SAND97-1730
Unlimited Release
Printed November 1997

Distribution
Category UC-814

Three-Dimensional Hydrological and Thermal Property Models of Yucca Mountain, Nevada

Christopher A. Rautman
Sean A. McKenna
Geohydrology Department
Sandia National Laboratories
P. O. Box 5800
Albuquerque, New Mexico 87185-1324

ABSTRACT

Three-dimensional heterogeneous, yet spatially correlated models of selected rock matrix properties have been created using geostatistical conditional simulation for three major rock units present within the unsaturated and shallow saturated zones in the vicinity of the potential nuclear-waste repository site at Yucca Mountain, Nevada. The three rock units are all of Miocene age, and they include the nonwelded and principally vitric materials of the upper Paintbrush Group below the densely welded portion of the Tiva Canyon Tuff (PTn model unit), the densely welded and principally devitrified rocks of the Topopah Spring Tuff (unit TSw), and the nonwelded to partially welded and variably zeolitized materials of the Calico Hills Formation and Prow Pass Tuff unit (CH–PP). The rock properties modeled include porosity, bulk density, and saturated hydraulic conductivity for each unit, and thermal conductivity for the TSw model unit. These property models synthesize the vertical and lateral variability of porosity measurements obtained through both laboratory measurement of core samples and down-hole petrophysical observations from across the entire Yucca Mountain site area. The models of hydraulic conductivity, bulk density, and thermal conductivity are based on the use of cross-variable correlations with porosity, in which the spatial continuity patterns of the different rock properties are coregionalized. The simulated models are intended principally for use as input to numerical modeling of ground-water flow and radionuclide transport, including coupled thermal and hydrologic processes. The suites of statistically similar simulated models have been summarized as “expected-value” (E-type) models similar to those that would result from application of an interpolation algorithm. This post-processing of replicate simulations has also allowed an assessment of the uncertainty in the prediction of spatially varying rock properties that results from less-than-exhaustive site characterization.

The simulated models indicate substantial material-property heterogeneity, both vertically and laterally and that this geologic heterogeneity exists on several spatial scales. The use of quantitative spatial correlation through the modeling process, combined with the influence of actual measurements of physical properties such as porosity, induces small-scale, “layered” and zonal heterogeneity that is not dependent upon the arbitrary distinction of numerous individual and discrete “stratigraphic” units whose lateral continuity is uncertain. The modeling methodology makes use of the constraining influence of broadly deterministic geologic processes, while at the same time respecting geologic knowledge from both modern and other ancient analogue environments that indicates a complex influence of secondary and tertiary alteration processes on the present-day material properties. The simulated models are constrained to reproduce observed rock property values at the locations of actual samples (subject to discretization limits). Elsewhere, the simulated property values vary stochastically within the statistical bounds of the measured data.

ACKNOWLEDGMENTS

This work was performed for the U.S. Department of Energy, Office of Civilian Radioactive Waste Management, Yucca Mountain Site Characterization Program Office under contract EA9012M5X. Scientific investigations involving three-dimensional rock characteristics modeling are conducted under the descriptions of work contained in the Site Characterization Plan (DOE, 1988) and in Study Plan 8.3.1.4.3.2 ("Three-Dimensional Rock Characteristics Models"); the work-breakdown structure element for this activity is 1.2.3.2.2.2.2. The planning document that directed this work activity is WA-0302, Rev. 2 ("Three-Dimensional Rock Characteristics Models"), and the work has been documented using a scientific notebook filed under this work agreement. The information and models documented in this report were processed under a fully qualified quality assurance program. The authors thank S.J. Altman and B.W. Arnold for critical technical reviews and D.A. Zimmerman for computer assistance. Sandia is a multiprogram laboratory operated by Sandia Corporation, a Lockheed-Martin Company, for the United States Department of Energy under contract DE-AC04-94AL85000.

CONTENTS

FIGURES

TABLES

(This page intentionally left blank.)

Three-Dimensional Hydrological and Thermal Property Models of Yucca Mountain, Nevada

INTRODUCTION

This report describes the creation of three-dimensional numerical models of selected rock-matrix properties for the region of the potential high-level nuclear waste repository site at Yucca Mountain, which is located in southern Nevada (fig. 1). The models have been generated for a majority of the unsaturated and shallow saturated zone within an area referred to within the Yucca Mountain Site Characterization Project as the "site area." They comprise a number of material properties of importance both to detailed process-level modeling activities and to more summary-style performance assessment modeling. The material properties within these models are both spatially variable (heterogeneous) and spatially correlated, as the rocks are understood from data obtained from site-characterization drill holes widely scattered across the site area.

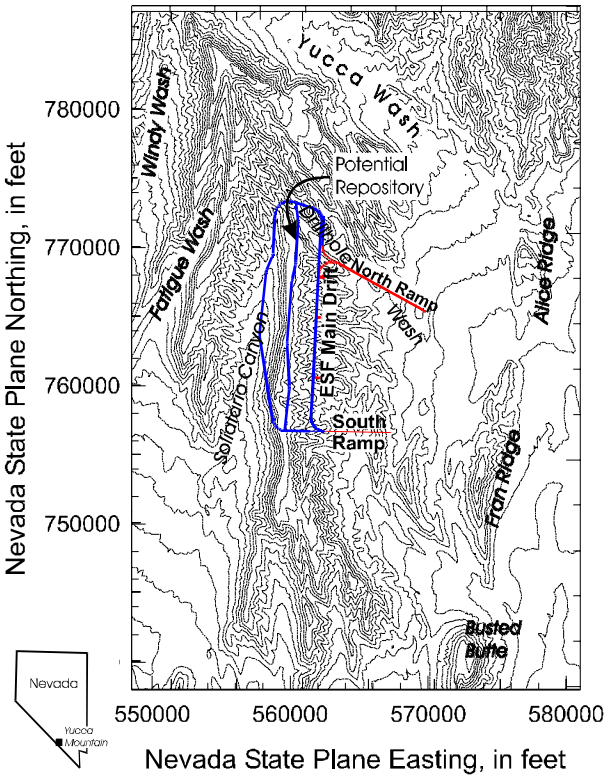

Figure 1. Index map showing the location of the potential repository in southern Nevada.

GEOLOGIC HETEROGENEITY, UNCERTAINTY, AND MODELING OF THE YUCCA MOUNTAIN SITE

Numerical Modeling

Licensing of the Yucca Mountain site as a geologic disposal site for nuclear waste will require quantitative predictions of the waste-isolation performance of the rocks that form Yucca Mountain and of the engineered barrier system for an extended period of time into the future. These predictions will require the use of numerical modeling in an attempt to capture the essence of highly complex physical processes, such as ground-water flow and the transport of potential radionuclide contaminants under both unsaturated and saturated conditions. Additional numerical modeling will be required as part of the licensing process to demonstrate that a mined geologic repository can be constructed within the rocks of Yucca Mountain such that the underground openings will be stable for a period of time sufficient to allow construction of the repository, emplacement of the waste packages, and retrieval of the waste if necessary. Stability of the mined openings in the near term and the performance of the site in the longer term will be influenced both by present-day conditions and by future conditions that must account for perturbation by the thermal pulse of the emplaced waste forms.

A fundamental principle involved in the numerical representation of real-world physical processes is that the properties of the modeled domain that are important to that representation must be known "exhaustively." Standard procedure in virtually all numerical physical-process modeling is to discretize the model volume into a (large) number of individual elements or grid nodes, assign the necessary attributes to each element or

node, and then apply one or more sets of mathematical expressions that are believed to represent the operation of the physical processes under investigation, given some set of external boundary and initial conditions. Because each element or node within the model domain must be assigned a set of properties to represent the variables within the numerical approximation of the process, those properties must be known exhaustively at each relevant point in space.

In contrast, the description or characterization of any site invariably consists of collecting various observations of properties or state variables at a limited number of locations. This is particularly true for the three-dimensional characterization of a geologic site, such as at Yucca Mountain. Because descriptive characterization is limited both by access (particularly to the subsurface) and by the availability of resources, that description is necessarily incomplete. Therefore, the exhaustive description of a site for purposes of numerical physical-process modeling requires the *prior assumption* of some type of conceptual model for the site, which is then implemented to assign the values of the necessary properties and other variables at every point in space.

Many types of conceptual models of varying complexity have been used historically for these purposes. However, just as a more detailed mathematical representation (and/or numerical implementation) of the underlying physical process being modeled will generally yield a more accurate approximation of behavior of a real-world physical system than a less detailed, overly simplified conceptualization, so too, an exhaustive physical description that captures more of the relevant real-world detail will generally yield a better prediction of that behavior than a simplified description that ignores or misrepresents important features of the real-world system. In any actual modeling exercise, however, there are non-trivial limits on the level of detail actually possible, which are imposed by the resources (theoretical, computational, physical, or human) that are available to conduct the modeling. The appropriate level of detail required for both the process and the domain description must be determined in light of the overall modeling situation and the uses to which the model results will be put.

Geologic Heterogeneity

Licensing of the Yucca Mountain site as a geologic repository involves the exhaustive description of a complex geologic environment. The rock properties of that environment, which form the real-world domain for predictive flow-and-transport and other physical-process modeling, are spatially variable and heterogeneous by virtue of the spatially and temporally variable geologic processes of volcanism, tectonism, and post-depositional alteration that produced Yucca Mountain itself. A fundamental concern underlying all performance assessment modeling of actual processes at the Yucca Mountain site is therefore how best to represent this heterogeneous, complex accumulation of volcanogenic rocks, given the types of process modeling exercises and the programmatic and regulatory decisions that are required as part of the viability assessment and licensing procedure.

It is clear that a “truly exhaustive” description of rock material properties is impossible: there would be no physical Yucca Mountain left, were the entire volume to be excavated and processed through some laboratory machine for measuring properties. A “practically” exhaustive description of the site, defined as obtaining and measuring actual samples at a large-but-finite number of spatial locations corresponding to each and every grid node of a numerical computer model is also highly improbable. A “model-based” exhaustive description is thus essential to deal pragmatically with the realities of “undersampling,” or less-than-exhaustive description.

The simplest possible conceptual model of rocks at Yucca Mountain is to assume *a priori* that the material properties needed for numerical process modeling are homogeneous and uniform throughout the site. Although such a model might possess some utility for rough, back-of-the-envelope calculations, even the most cursory inspection of Yucca Mountain indicates that such a model is vastly oversimplified and of limited value in advanced regulatory applications. However, many past performance assessment and other modeling exercises have been conducted for Yucca Mountain (Dudley and others, 1988; Barnard and Dockery, 1991; Barnard and others, 1992; Wilson and others,

1994; Atkins and others, 1995) using an only slightly more sophisticated conceptual model.

This slightly refined but still extremely simplified conceptual model makes use of the fact that at Yucca Mountain (as in many other geologic environments), the lithologic deposits were produced by relatively widespread but temporally variable geologic processes. In particular, the volcanic activity responsible for the formation of Yucca Mountain was episodic in nature, with thick widespread ash deposits produced by near-instantaneous (geologically speaking) eruptions separated by thin inter-eruption deposits that probably represent much longer intervals of time. Such models make use of the observation that the widespread conditions under which the rocks were emplaced and altered appear to have varied vertically within the thick deposits of volcanic tuff. However, these layered models still rely upon the prior assumption that, within each subhorizontal layer, the material properties of interest are uniform and homogeneous. All grid nodes or modeling elements falling within a particular layer are thus assigned a constant value presumed to be "representative" in some manner.

Geologic studies of the volcanogenic rocks at Yucca Mountain (DOE, 1988) and of similar deposits elsewhere in the world (Fisher and Schmincke, 1984; Cas and Wright, 1987) indicate that although the "deterministic geologic processes" (Rautman and Flint, 1992) responsible for deposition of these materials may be quite extensive laterally, those processes (and the resulting deposits) varied both temporally and areally. This variation of process has produced spatial heterogeneity of material properties in all three dimensions. Yet despite the existence of heterogeneity, the spatial distribution of material properties is not "random," and a conceptual framework based simply on random assignment of property values that correspond to some arbitrary univariate prior distribution is likewise a simplification (and possibly an unwarranted distortion) of the real world. In fact, the geologic processes that produced any given volume of real estate were spatially and temporally correlated to a greater or lesser extent. It then follows that the resultant rock properties are spatially correlated in the stratigraphically horizontal and vertical directions ("time" in a progressively accumulating deposit of any type can be considered effectively "frozen" and preserved in some spatial dimension).

A number of mathematical techniques have been developed that provide for the quantitative description and conceptual modeling of material properties that are both spatially variable (heterogeneous) and spatially correlated (e.g., David, 1977; Journel and Huijbregts, 1978; Isaaks and Srivastava, 1989; Cressie, 1991; Deutsch and Journel, 1992). *Spatially correlated* in this context means that the values of a material property at "nearby" locations are more similar than the values of that same property at more "distant" locations, where the proximity descriptions have a specific quantitative meaning (discussed in later sections of this report). The ability to describe rigorously the nature and extent of spatial correlation for any particular material property has significant implications for the conceptual modeling of heterogeneous materials and for the quantitative description of the uncertainty that results from inevitably less-than-complete physical description.

Uncertainty

Despite the existence of a highly heterogeneous and spatially variable rock mass at Yucca Mountain, there is no "uncertainty" in the real world as to what are the true material properties of the rocks at Yucca Mountain. The material properties of the rocks exist and they are essentially static at the present time, although it is quite likely that some of these "static" properties may change, including over human time scales, if heat-generating waste is emplaced in an actual repository at the site. Even then, there is no "uncertainty" in those evolving and changing rock properties. There is only one Yucca Mountain as created by Mother Nature, and the state of those rocks at the site will be determined uniquely at all future times by the combined actions of Mother Nature and — to a much lesser extent — of Humankind.

Uncertainty, given a premise of real-world uniqueness, is thus a knowledge-based concept. Less-than-exhaustive site characterization produces "geologic uncertainty" that impacts the

implementation of both site description and the numerical representation of the real-world physical processes that operate on the rocks provided by Mother Nature. We are *uncertain in our predictions* of the values of material properties at unsampled locations (even though the properties themselves are unique and unchanging over short time scales). Likewise, we are *uncertain of our predictions* of the waste-isolation performance of a potential Yucca Mountain repository because of (1) our uncertain representation of material properties at all points in space and (2) approximations and simplifications in our conceptualization (and numerical representation) of the true physical processes operating at the site (even though those real processes will produce a unique, invariant result at any specified time regardless of our state of knowledge). The implication of this logical framework is that if we add information of the proper type in a physically appropriate conceptual manner to a predictive modeling exercise (all else being equal), the result of that prediction will be less uncertain than it would be in the absence of that additional information.

Implications for Modeling

The implications of knowledge-related uncertainty in general have been recognized in the engineering sciences for almost as many years as humankind has tried to predict the future performance of engineered structures. Many methods, including sensitivity studies, bounding calculations, and Monte Carlo analyses, have been developed in efforts to make more robust engineering predictions of "successful" performance. However, the distinction between, and the interplay of *uncertainty* (as a state of imperfect information, resulting from less-than-complete observation) and spatial *heterogeneity* (as a state of being, unaffected by the availability or lack of information) becomes absolutely critical in the application of predictive engineering methods to the geologic environment. Natural earth materials are, in fact, heterogeneous to a far greater extent than most conventional materials of engineering interest. Property heterogeneity affects the operation of physical processes. The impact of that heterogeneity on the numerical approximation of physical processes is only compounded by our geologic uncertainty. Incomplete information must be accounted for in predictive modeling; so also must be the effects of material properties that are different in different physical locations. Improper conceptualization and treatment of spatial heterogeneity in the predictive modeling of physical processes may produce wholly inappropriate results.

We explicitly acknowledge that there are many other sources of uncertainty relevant to engineering prediction. For example, knowledge of the true material properties of any sample, or more generally of the in-situ rock at any observed location, is uncertain because of issues related to the sampling and/or observation/measurement process itself. However, we also hold that for many rock material properties of interest at the Yucca Mountain site, these non-geologic sources of uncertainty are of lesser importance than the fundamental spatial heterogeneity of a major volcanic pile that was emplaced over millions of years and which has been altered by at least two overlapping geochemical processes, faulted, tilted, submerged in part beneath the water table, and partially altered again over the course of some ten million years and more. Furthermore, there are methods for quantitatively addressing at least some of the uncertainty concerns associated with measurements of the material properties.

This report—which outlines one particular approach to the exhaustive description of material properties for use in modeling coupled physical processes involving ground-water flow, the redistribution of heat from emplaced nuclear waste, and the transport and ultimate fate of potential radionuclide contaminants—is based on the premise that the material properties extant at Yucca Mountain are, to a first-order approximation, controlled by the operation of quasi-deterministic geologic processes related both to the original emplacement of the rocks and to their subsequent alteration in mineralogy, composition, and position. These deterministic geologic processes are only partially understood, and the prediction of the specific properties prevailing at any specified position within the site area is further complicated by incomplete physical sampling and observation. We thus address the resulting geologic uncertainty in our material property predictions through a stochastic,

or Monte Carlo statistical, approach. We provide a number of alternative numerical representations of the material properties at Yucca Mountain, all of which are more or less consistent with the observed measurements at the locations of those measurements, and which vary away from the locations of observations in a manner that is consistent with the overall statistical character (both univariate and spatial) of the data. The net result of this modeling activity is a suite of numerical models that are indistinguishable from reality on an objective, quantitative basis, given the available data.

We acknowledge that other conceptual approaches to providing similar exhaustive descriptions of material properties at the Yucca Mountain site are not only possible, but may be desirable for several reasons. These reasons include: (1) (quasi-)independent confirmation that the general distribution of properties ultimately used in downstream physical-process modeling activities is geologically reasonable, (2) the use of such models in preliminary, bounding, or sensitivity calculations, and — to no small extent — (3) as a matter of computational tractability of those downstream modeling efforts. Also, the specific models created for this report may be inappropriate for a particular physical-process modeling by simple virtue of the fact that these rock property models were generated using a relatively coarse grid spacing.[†] We believe, however, that the models presented in this report, and the underlying descriptions of the spatial variability and geologic uncertainty that these models summarize (albeit in perhaps crude form), arguably represent the most detailed and comprehensive integration of information for these material properties that has been undertaken to-date as part of site characterization activities (DOE, 1988) at the Yucca Mountain site. Furthermore, we believe that the evaluation and incorporation of insights gained from these exhaustively descriptive rock property models into whatever model descriptions are ultimately used in viability and licensing analyses will lead to more geologically accurate, and hopefully more defensible, performance modeling of the potential nuclear waste repository at Yucca Mountain.

[†]A distinction needs to be drawn between the simple modeling of material property values on a coarse grid and the physical-process-dependent upscaling of multiple small-scale material property measurements to represent the "effective" property of a larger-scale 3-dimensional volume. This report presents models of what are essentially small-scale "observations" (core plugs or downhole geophysical-log volumes) distributed at regular locations within the subsurface of the Yucca Mountain site area. The upscaling of these (or any other) property values for Yucca Mountain is beyond the scope of this report. McKenna and Rautman (1996) provide a literature review and a relatively comprehensive evaluation of a number of scaling techniques and approaches.

DEVELOPMENT OF THE MODELS

Conceptual Approach

Construction of the three-dimensional rock properties models described in this report has been guided by the related but philosophically separate concepts of heterogeneity and uncertainty described in the preceding section. The models attempt to make maximum use of "deterministic" genetic processes to constrain the extrapolation, or "expansion" (Journel and Alabert, 1989) of measured property values away from the physical locations of those measurements. The effort to capture genetic processes as they relate to material properties has led to the separation of the geologic column of interest into several discrete geologic units, each of which is internally more "homogenous" in some identifiable manner than subdivisions based on other criteria. An interpretation that the material properties of the rocks are controlled principally by the original genetic geologic processes and that much of the post-depositional alteration that has produced second-order variability in properties occurred before tectonic tilting and faulting suggests that the influence of such deformation should be discounted in the modeling process. We have adopted the concept of using a *stratigraphic coordinate system* during the modeling process, as distinct from a *real-world coordinate system* that describes the present-day location of points within the several geologic units. Because measurements of most material properties of the site are quite limited in number and spatial distribution, we employ the concept of *porosity-as-a-surrogate* in order to use relatively abundant and widely distributed (in three dimensions) porosity/density data as a first approximation of the geologic heterogeneity of the site. Furthermore, we attempt to integrate measurements of porosity from all available sources to provide a unified three-dimensional representation of the entire Yucca Mountain site area. A schematic flow diagram capturing the major steps and intermediate products of this modeling effort is presented in figure 2. Details of the various entities shown in the figure are described at greater length in the sections that follow.

Separate Modeling of Distinctive Geologic Units

Rock properties models have been created for three distinctly different geologic units: the upper Paintbrush nonwelded (PTn) unit, the welded portion of the Topopah Spring Tuff (TSw), and the combined Calico Hills-Prow Pass interval (CH-PP). The relationship of these three geologic units to both the "official" Project conventional stratigraphic nomenclature and selected historically used stratigraphic names is presented graphically in table 1. All of the model units are Miocene in age.

Note that the stratigraphic units selected for separate rock properties modeling efforts do *not* coincide with the breaks between genetic "packages" of rock, which at Yucca Mountain are typically collections of virtually coeval pyroclastic flow deposits associated with a major volcanic event such as a caldera-collapse sequence. However, the available measurements of material properties indicate that the modeling units as defined here are more "homogeneous" (consistent) internally than are the major genetic packages. This internal homogeneity is shown for two well-characterized drillholes in figures 3 and 4. In this respect, we follow the precedent of Ortiz and others (1985), who originally defined the PTn and TSw units based on material property distinctions (table 1). A majority of past performance modeling exercises (Dudley and others, 1988; Barnard and Dockery, 1991; Barnard and others, 1992; Wilson and others, 1994; Atkins and others, 1995) have also subdivided the rock column at Yucca Mountain according to material-property-based classifications.

Specifically, segregation of the welded portion of the Topopah Spring Tuff from the over- and underlying partially to nonwelded portions of the Topopah Spring Tuff as a whole, groups together typically densely welded rocks of low porosity, high bulk density, low saturated hydraulic conductivity, and high thermal conductivity (figs. 3, 4). The overlying partially to nonwelded tuffs at the top of the Topopah Spring Tuff are combined with the equally nonwelded, high-porosity, low density, high hydraulic conductivity and low thermal con-

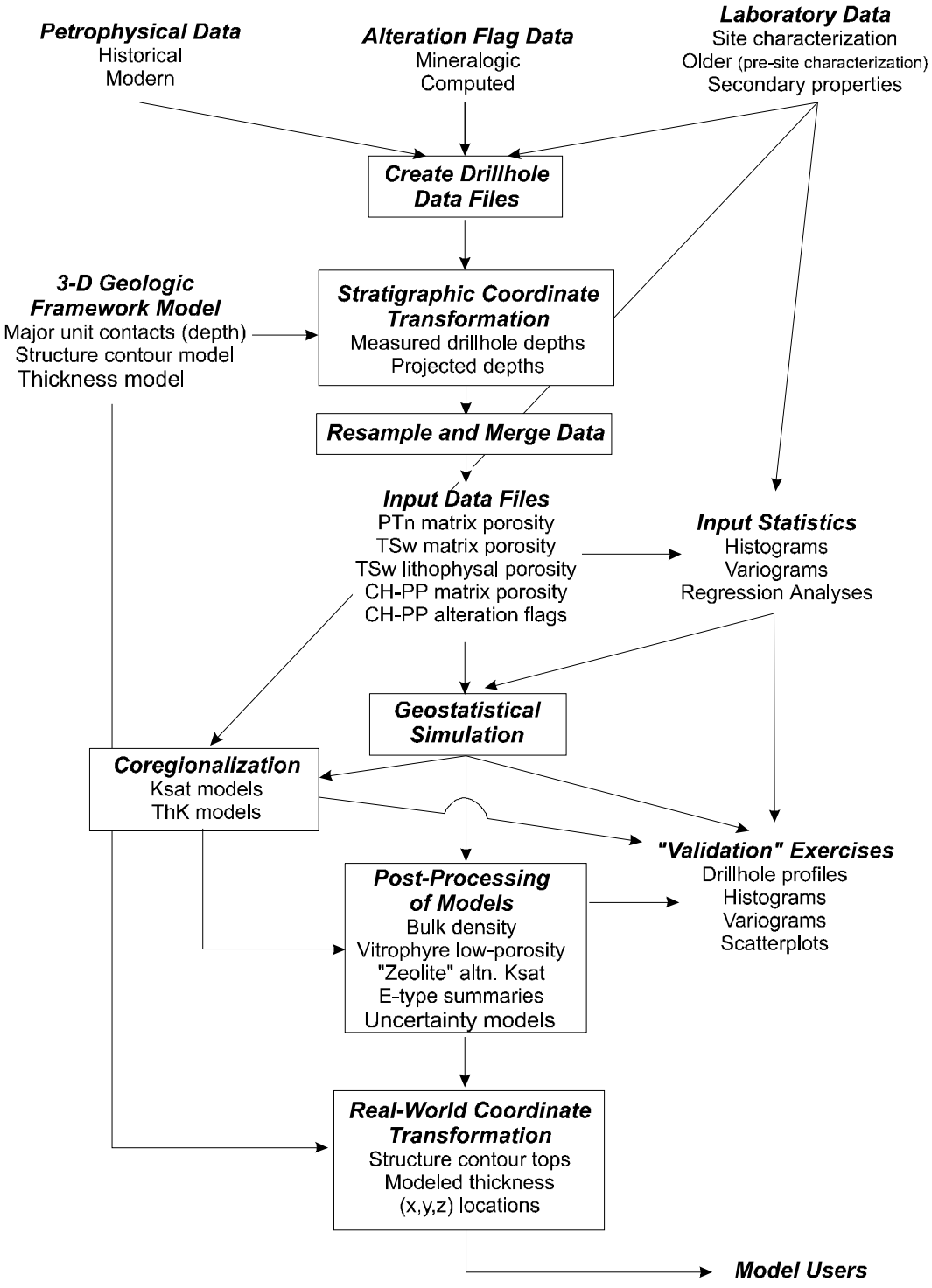

Figure 2. Schematic representation of the modeling process used in this study. Boxed entries are "activities," unboxed entries are input or output "products."

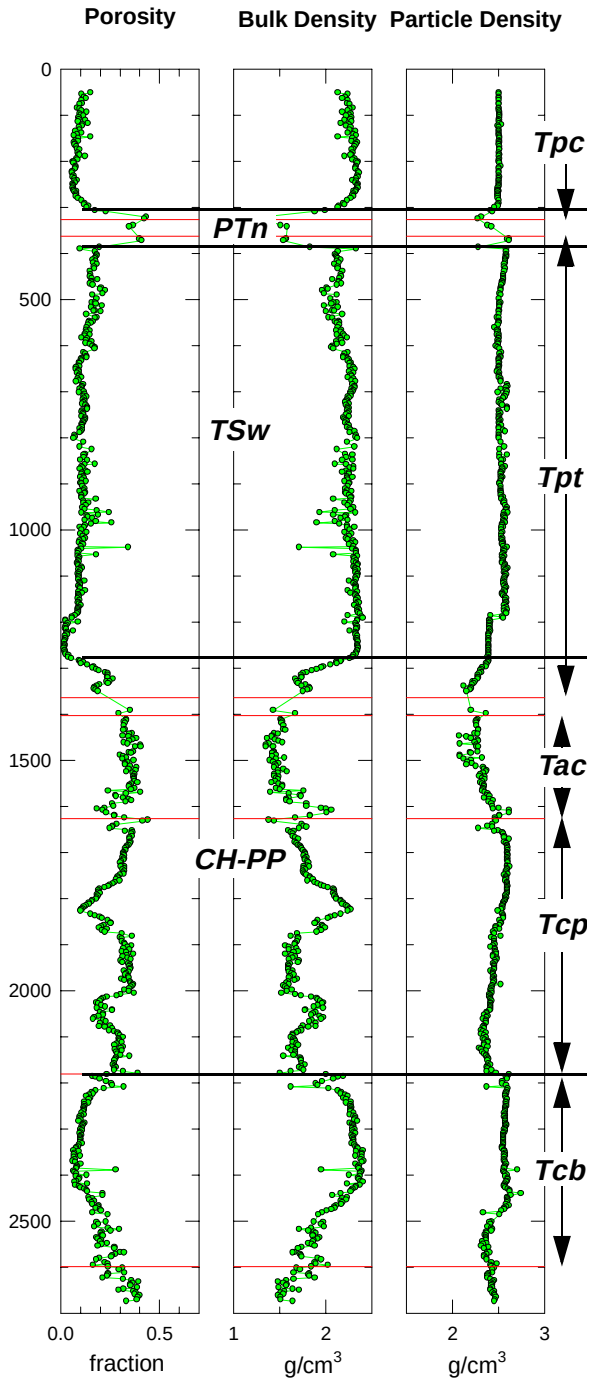

Figure 3. Material property profiles for the USW SD-7 drill hole (from Rautman and Engstrom, 1996b), showing overall variability and definition of modeling units. Unit abbreviations: PTn–upper Paintbrush nonwelded model unit; TSw–Topopah Spring welded model unit; CH-PP–Calico Hills-Prow Pass model unit; Tpc–Tiva Canyon Tuff; Tpt–Topopah Spring Tuff; Tac–Calico Hills Formation; Tcp–Prow Pass Tuff; Tcb–Bullfrog Tuff.

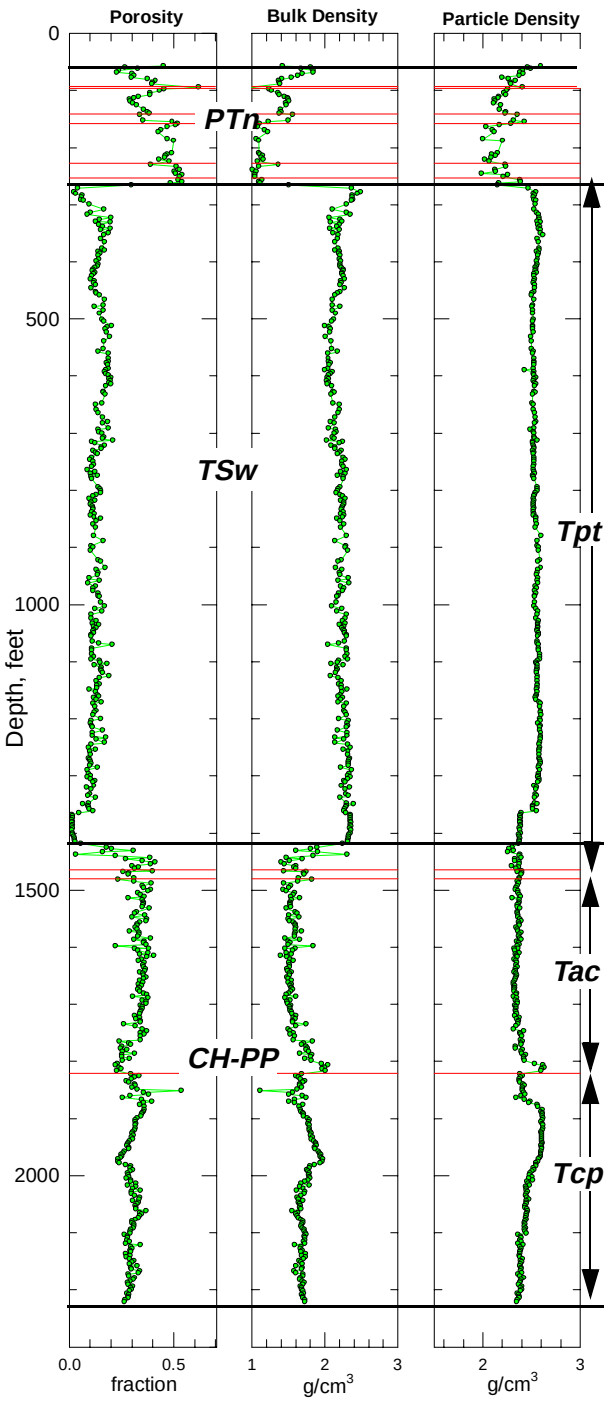

Figure 4. Material property profiles for the USW SD-9 drill hole (from Engstrom and Rautman, 1996), showing overall variability and definition of modeling units. See fig. 3 for unit abbreviations.

ductivity materials conventionally assigned to the Pah Canyon and Yucca Mountain Tuffs and their associated "pre-unit bedded tuff" intervals, to form the upper Paintbrush nonwelded unit. Reworked materials ("bedded tuff") and nonwelded to partially welded rocks formally associated with the lowermost part of the stratigraphically higher Tiva Canyon Tuff (table 1) are also aggregated as part of the PTn model unit.

The welded portion of the Tiva Canyon Tuff (unit TCw of Ortiz and others, 1985; table 1) was not modeled as part of the current study for several reasons. First, the Tiva Canyon welded unit, which forms the vast majority of the surface exposures in the vicinity of the potential repository, is extensively fractured, and infiltrating ground water appears to flow rapidly through these fractures to the general stratigraphic level of the upper Paintbrush nonwelded (PTn) model unit (Flint and others, in review[†]). Because of this dominance of flow by fractures, detailed modeling of matrix properties in the TCw model unit would appear to be of lesser value by comparison. Flint and Flint (1994) and Hudson and Flint (in prep.)[‡] also demonstrated that distinctions between bedrock exposures and areas covered by alluvium/colluvium, when combined with topographic/morphologic categories (ridge crest, sideslope, valley bottom, north-facing slope, south-facing slope, etc.), provided by far the most significant control of infiltration. Second, because the vast majority of deep drillholes at Yucca Mountain have been located in the bottoms of washes for logistical reasons, there are only a handful of holes that provide penetration of meaningful sections of Tiva Canyon Tuff. Attempts to describe spatial variations in much of the Tiva Canyon welded unit consequently would depend on extremely sparse data resulting in very large uncertainties in the modeled values except immediately adjacent to those few drillholes. A third reason for the decision not to model the Tiva Canyon welded unit explicitly involved limits on the resources available for the modeling effort.

The decision to model the lowermost nonwelded to partially welded units of the Topopah Spring Tuff together with the immediately underlying nonwelded Calico Hills Formation is based on material-property similarity. Figures 3 and 4 clearly indicate that the lower contact of the formally defined Topopah Spring Tuff (Tpt), which is stratigraphically below the prominent less-than-5-percent-porosity interval at a depth of approximately1200–1280 feet (SD-7, fig. 3) and 1350–1400 feet (SD-9, fig. 4), respectively, is gradational. Most of the transitional increase in porosity has more affinity to the generally high-but-variable nature of the porosity values that underlie the transition than to the uniformly low porosity values above that transition. The porosity of the ash-flow tuffs (approximately upper two-thirds) of the Calico Hills Formation (Tac) is uniformly high at approximately 30 percent; however, the basal "bedded tuff" and tuffaceous sandstone portions (approximately lower one-third) of the Calico Hills exhibit more variable porosity profiles.

The decision to include rocks of the Prow Pass Tuff in a combined "Calico Hills–Prow Pass" model unit was influenced by a combination of geologic and pragmatic factors. Geologically, as indicated by the porosity profiles of figure 3 and 4, values from within the Prow Pass Tuff (Tcp) are generally high, but most definitely variable. Previous material-property-based stratigraphic classifications of the Prow Pass interval (for example, Ortiz and others, 1985; Schenker and others, 1995) have recognized two separate nonwelded stratigraphic units separated by a partially to moderately welded interval (CFUn–PPw–CFMn; see table 1). However, the variability and segregation of high and low porosity values into a coherent "welded" unit is not consistent from drillhole to drillhole. For example, figure 4 is a porosity profile from drill hole USW SD-9, and the two lower-porosity zones from figure 3 (at about 1820–1850 ft; 2000–2100 ft) simply are not present. The generally-high-but-inconsistently-variable nature of this combined

Depth in feet

[†]Flint, A.L., Hevesi, J.A., and Flint, L.E., in review, Conceptual and numerical model of infiltration for the Yucca Mountain area, Nevada: intended for publication as U.S. Geological Survey Water-Resources Investigations Report.

[‡]Hudson, D.B., and Flint, A.L., in prep., Estimation of shallow infiltration and presence of potential fast pathways for shallow infiltration in the Yucca Mountain area, Nevada: intended for publication as U.S. Geological Survey Water-Resources Investigations Report.

Table 1: Comparison of stratigraphic terminology for volcanic rocks at Yucca Mountain and encountered on the Yucca Mountain Site Characterization Project (no scale) showing modeling units used in this work.

Geologic Unit (from Sawyer and others, 1994)		Older hydrologic zonation (modified after Scott and Bonk, 1984)			Proposed Zonation of Buesch (1996); also Moyer and Geslin (1995)	Newer Hydrologic Zonation (Flint, written comm., 1997)	Thermal/mechanical unit (Ortiz and others, 1985)	Modeling Units Used in this Report
Paintbrush Group	Tiva Canyon Tuff	Paintbrush Tuff	Tiva Canyon Member	ccr - caprock	Tpcrv	CCR	TCw	(not modeled)
				cuc - upper cliff	Tpcrn	CUC		
				cul - upper lithophysal	Tpcrl	CUL		
					Tpcpul	CW		
				cks - clinkstone	Tpcpmn			
				cll - lower lithophysal	Tpcpll			
				ch - hackly	Tpcplnh			
				cc - columnar	Tpcplnc			
					Tpcpv3	CMW		
				ccs - shardy base	Tpcpv2	CNW	PTn	PTn
					Tpcpv1			
	Yucca Mtn. Tuff		Yucca Mtn. Mbr.			BT4 / TPY / BT3		
	Pah Cyn. Tuff		Pah Cyn. Mbr.			TPP		
	Topopah Spring Tuff		Topopah Spring Member	upper nonwelded	Tptrv3	BT2		TSw
					Tptrv2			
				tc - caprock	Tptrv1	TC	TSw1	
				tr - rounded	Tptm	TR		
				tul - upper lithophysal	Tptrl	TUL		
					Tptpul			
				tn - nonlithophysal	Tptpmn	TMN	TSw2	
				tll - lower lithophysal	Tptpll	TLL		
				tm - mottled	Tptpln	TM2		
						TM1		
				tv - basal vitrophyre	Tptpv3	PV3	TSw3	
				nonwelded base	Tptpv2	PV2	CHn1	CH-PP
					Tptpv1	BT1 / BT1a		
Calico Hills Formation		Tuffaceous Beds of Calico Hills		(not subdivided)	Unit 5 Unit 4 Unit 3 Unit 2 Unit 1	CHV / CHZ		
					bedded tuff unit basal sandstone unit	BT	CHn2	
Crater Flat Group	Prow Pass Tuff	Crater Flat Tuff	Prow Pass Member	Not subdivided	Unit 4	PP4	CHn3	
					Unit 3	PP3	PPw	
					Unit 2 Unit 1	? PP2 / PP1	CFUn	
	"bedded tuff"		"bedded tuff"		bedded tuff unit			
	Bullfrog Tuff		Bullfrog Member		Not subdivided (?)	? BF3	BFw	(not modeled)
	"bedded tuff"		"bedded tuff"			BF2 ?	CFMn1	
							CFMn2	
	Tram Tuff		Tram Member				CFMn3	
							TRw	
							Not Recognized	

Calico Hills–Prow Pass stratigraphic interval thus is the defining characteristic of this modeling unit. An additional factor is that as one proceeds deeper into the volcanic pile of Yucca Mountain, the quantity and spatial density of the available data decrease markedly (see, for example, table 4 on page 16). Rather than attempt to deal separately with two generally-high-but-inconsistently-variable porosity units, we have elected to combine the two formal geologic units to achieve larger statistical mass.

Stratigraphic Coordinates

Each of the three major lithologic intervals described in this report has been modeled in a unit-specific *stratigraphic-coordinate system* (fig. 2) that reflects the original, pre-faulting depositional continuity of the involved ash-flow and air-fall tuffaceous deposits, as illustrated schematically in figure 5. Stratigraphic coordinates use the same east-west and north-south coordinates (Nevada state plane coordinate system, defined in feet[†]) as the drill hole from which the relevant data were obtained. However, the "stratigraphically vertical" coordinate of a sample is represented as the relative fractional position of that sample within the thickness of the entire unit at that location (after Gomez-Hernandez and Srivastava, 1990). The logic underlying the development and use of a stratigraphic coordinate system is as follows.

As shown in part (a) of figure 5, regions of varying material properties are presumed to have been emplaced or otherwise formed by various alteration processes in an essentially stratiform manner. At Yucca Mountain, the volumetrically dominant rocks were formed by deposition by pyroclastic flows to form thick ash-flow sheets that thin laterally away from their source. Thus, there is a tendency for these regions of somewhat similar material properties to occupy roughly the same relative vertical position within a unit. Later faulting as part of Basin and Range tectonism disrupted the originally continuous volcanic rocks and tilted the rock units, with their contained material properties, toward the east, as indicated in part (b) of the figure. Modeling of those rock properties is illustrated in part (c) of figure 5. The vertical locations of drill hole samples are specified within the stratigraphic coordinate system as a fractional distance where the base of the unit is assigned a distance of zero and the top of the unit is assigned a distance of one. Stratigraphic coordinates are thus dimensionless.

As also suggested by the mesh of intersecting dotted lines in the right-hand portion of part (c) of figure 5, a regular rectangular modeling grid is defined within each stratigraphic coordinate system. Because the various material property zones have been stretched or compressed vertically so that the overall stratigraphic thickness of the unit is constant, defining the modeling grid within this framework generally positions nodes within similar materials on a stratigraphically "horizontal" plane. This repositioning of similar materials in similar relative locations greatly simplifies the search for data in the neighborhood of an unsampled location, as shown conceptually by the search ellipse in part (c) of figure 5. Although it is possible to rotate the principal direction of the search ellipse to match the overall tectonic dip of the unit [see part (b) of the figure], it is virtually impossible to modify the search strategy to account for offset of the material property zones by discrete faults. For an example of material-property artifacts produced by this type of uncompensated fault displacement, see cross sections published by Rautman and Robey (1994).

At the end of a modeling exercise, the transformation process between parts (b) and (c) in figure 5 is reversed by assigning each grid node a computed vertical position derived from knowledge of the structure contour model for the top of each unit and the spatially varying thickness of each unit. These values are obtained from the independently developed, three-dimensional geologic framework model (Clayton and others, 1997). Although this framework model is necessarily

[†]Nevada state plane coordinates, which are defined in feet, are widely used on the Yucca Mountain Project. These coordinates are for the central zone of Nevada, and they are based on a Transverse Mercator projection. The origin of this projection for the central zone of Nevada is latitude 34°47'N., and the central meridian is at longitude 116°40'W. Note that metric conversions of Nevada state plane coordinates are distinct from metric coordinates obtained using the 10,000 metre Universal Transverse Mercator grid, Zone II. To obtain metric-converted Nevada state plane coordinates, divide feet by 3.281.

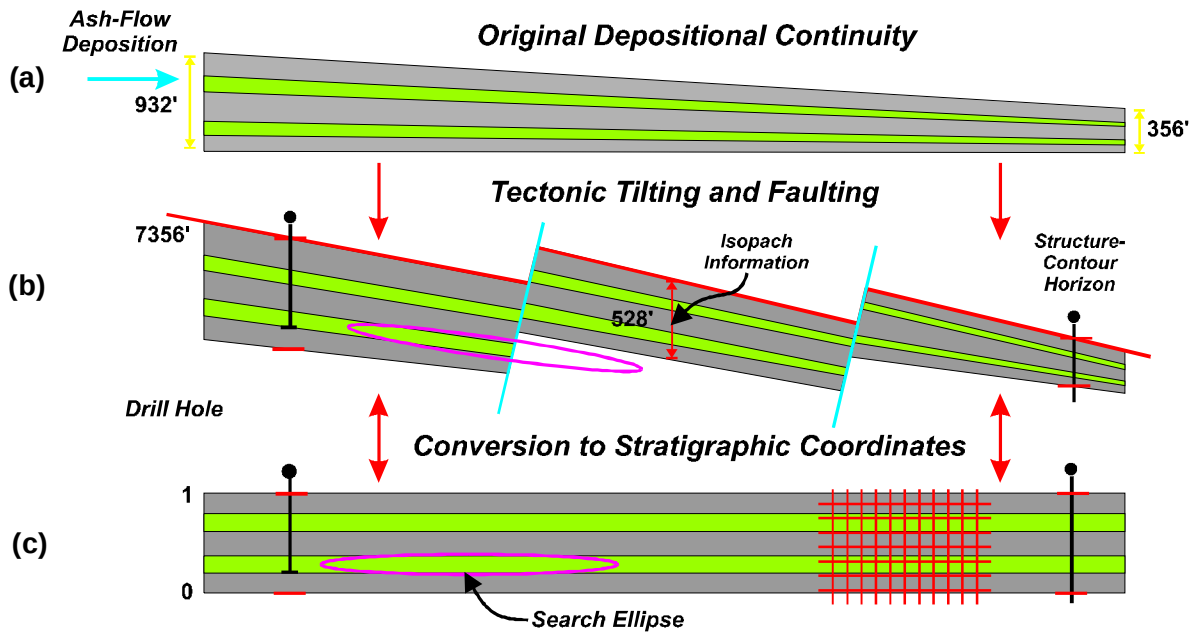

Figure 5. Conceptual illustration of the construction and use of stratigraphic coordinates. (a) Rock unit is formed by areally extensive volcanic (or sedimentary) processes. Zones of differing rock properties (shaded colors) are formed in a stratiform manner. (b) Tectonic deformation tilts and disrupts original stratiform continuity by faulting. (c) Modeling unit is returned to an approximation of original continuity in a rectangular coordinate system in which all vertical distances are measured as a fractional position measured from the top or bottom of the rock unit.

interpretive, the use of all available drillhole information, and the existence of regionally continuous thickness trends within the volcanic rocks at Yucca Mountain, combined with a rigorous volumetric modeling technique, ensures that the three-dimensional representation of the several rock units is geologically plausible and internally consistent.

In practice, implementation of the stratigraphic-coordinate concept is slightly more complicated than the idealized example of figure 5. First, sample locations are typically specified in terms of their depth within a specific drillhole (the drilling procedure measures all locations from the collar of the hole, regardless of the physical elevation of the hole and its contained samples). Thus, the *measured* depths were converted to *stratigraphic depths* initially, and only to stratigraphic *elevations* at the time of modeling. Second, for reasons involving principally numerical precision within the computer programs that implement the actual rock properties modeling algorithm(s), the fractional stratigraphic positions indicated in figure 5(c) are multiplied by an arbitrary unit-specific scaling constant to obtain values that approximate the nominal thickness of the different units in the real world. Additionally, unlike the two-dimensional example shown in figure 5, actual modeling was conducted in full three-dimensional space.

Finally, the issue arises regarding how to treat samples from a drillhole that fails to penetrate

the entire thickness of the geologic unit in question (represented by the drillhole at the left-hand side of figure 5). Clearly it is inappropriate to assign a stratigraphic elevation of zero to a sample obtained from the very bottom of the hole itself, as the materials at this elevation in general are not representative of materials at the very base of the unit here or elsewhere. Yet without drilling deeper, the distance between the foot of the hole and the true base of the unit is unknown. Such situations have been reconciled by inferring the base of the unit in question from the framework geologic model of Clayton and others (1997) and adjusting the fractional position accordingly. The presumption is that the base of the unit projected from the framework model is a reasonable approximation of the unknown true position at that location.

Use of Porosity as a Surrogate

The concept of using abundant porosity data as a surrogate for modeling the spatial variability of other properties, which are by comparison almost universally *undersampled* at Yucca Mountain, is not new. The technique has been reported by Longenbaugh and others (1995), Rautman (1995, 1996), and Altman and others (1996), and the technique was described explicitly by Flint and others (1996a). However, this report provides the first detailed description of porosity-as-a-surrogate in the joint modeling of multiple properties in three dimensions. In this study, we have used porosity to model the spatial distributions of (1) bulk density, (2) saturated hydraulic conductivity, and (3) thermal conductivity.

The concept of porosity-as-a-surrogate is based on empirically observed correlations of secondary material properties, often actually of greater modeling interest than porosity itself, that are less-well sampled. A consequence of such undersampling is that the spatial variability of the undersampled variable cannot be described confidently on a stand-alone basis, let alone such that the *joint spatial continuity patterns* of the two (or more) variables can be reproduced simultaneously. It is important to understand that modeling the spatial distribution of several material properties without properly considering the inter-variable correlations can lead to highly unrealistic input to physical-process modeling codes, which in turn can lead to highly unreasonable estimates of performance parameters. Simply sampling randomly from separate (univariate) probability density functions may easily produce such un-physical combinations as a low porosity–low thermal conductivity–high hydraulic conductivity tuff. The severity of the consequences of neglecting cross-variable correlations in modeling spatially variable domains increases as physical-process modeling attempts to capture multiple coupled processes (for example, Francis and others, 1996[†]).

Using porosity as a surrogate for various other material properties in modeling Yucca Mountain is supported by consideration of the physics involved in the site-specific rock units being modeled. For example, for a given rock type, increasing the volume of pore space must decrease the bulk density of the rock mass. The part of the rock that "isn't there" is available to hold fluids but it contributes nothing to the total mass contained within a unit volume of material: the definition of bulk density. Again for a given rock type, the conduction of heat energy through the material is directly related to the density (or, inversely, the pore space) of the material. All else being equal, a higher porosity–lower density tuff will conduct heat less readily, leading to a lower measured thermal conductivity value. Note here that it is the total amount of void space in a rock that affects thermal conductivity, not simply the amount of pore space that is conducting water within the unsaturated zone.

And finally, although hydraulic conductivity is not generally well correlated with porosity across many classes of soils and/or rock materials, the empirical observation at Yucca Mountain is that this correlation is quite strong within limited groupings of lithologic types. Specifically, both welded and nonwelded lithologies appear to be associated with a continuum of saturated hydraulic conductivity values; see also the section on *Satu-*

[†]Francis, N.D., Mishra, S., Ho, C.K., Arnold, B.W., Bandurraga, M., Wu, Y., Statham, W. H., and Zhang, H., 1996, Thermo-hydrologic modeling of the potential repository at Yucca Mountain using a 3-D site-scale unsaturated-zone model, Level 3 Milestone Report T6533, Yucca Mountain Site Characterization Project.

rated Hydraulic Conductivity beginning on page 35. Evidently, unless affected by some additional physical process (such as zeolitic or other alteration), there is a relatively strong relationship between progressive, overall reduction in porosity and the progressive reduction in the average diameter of the passages between interconnected pores (which is what exerts principal control on the flow of water through the existing pore space) across this continuum of nonwelded to densely welded materials. Conversely, a genetic process that changes the diameter and/or geometry of the pore throats, while not commensurately filling in the total quantity of void space, can reduce the hydraulic conductivity of the rock by orders of magnitude while leaving the porosity essentially unchanged. In fact, both of these cases are observed and modeled for Yucca Mountain.

Geostatistical Methods

We have used selected geostatistical methods (fig. 2) to create the exhaustive material property descriptions described on page 1 using the available data from the Yucca Mountain site. Geostatistical methods in general are one of a variety of methods for distributing attributes in space. A fundamental principle underlying all geostatistical techniques is the quantification and use of some measure of spatial correlation, which may be defined informally as the degree to which samples "close" to one another resemble each other more than do samples "far" away from each other. Because of this emphasis on identifying, quantifying, and using the spatial continuity of rock properties in creation of the exhaustive material property models required for modeling of ground-water flow and radionuclide transport at the Yucca Mountain site, geostatistical methods are broadly compatible with the guiding principles summarized in the section on Geologic Heterogeneity, and more particularly on page 3. Furthermore, unlike many other methods for predicting the material property attributes of a large volume from direct observation of a relatively minuscule fraction of that material, geostatistical methods offer a quantitative and more-or-less rigorous approach to the issues of knowledge-based uncertainty discussed on page 3. Addressing uncertainty issues is particularly important at Yucca Mountain because of the ultimate regulatory decision regarding potential licensing of an actual nuclear-waste repository at the site.

Within the purview of geostatistical methods are two broad classes of algorithms for predicting attributes at unsampled locations constrained by some limited set of actual measurements: estimation and simulation. Geostatistical *estimation* is focused on the prediction of the attribute values *most likely* to be encountered at a given spatial position, and may be thought of as modeling the *expected value* of a variable of interest. Geostatistical estimation is most frequently described using the term, *kriging*, named after one of the early practitioners of this approach. In effect, kriging is simply a weighted-average *interpolation* method using some *neighborhood* of relevant data. What distinguishes kriging (and geostatistical methods in general) from other interpolation algorithms using averages of relevant data is two-fold. First, kriging is the only interpolation method that also provides a quantitative measure of the associated least-squares estimation error (via the kriging variance; see Isaaks and Srivastava, 1989). Second, is that estimates are computed using a data-specific weighting scheme based on the geostatistical (geological) distance of the point being estimated from the surrounding measured values. Note that this "distance" is not necessarily equal to the simple Euclidean distance between two points. In contrast, one non-geostatistical method simply assigns all the weight to the nearest neighboring data point to an estimated location, an approach that results in interlocking irregularly shaped *polygons* of uniform attributes throughout the model domain. Another common method involves arbitrarily weighting nearby data in inverse proportion to their straight-line distance to the point being estimated (i.e., closer points receive more weight as they are "believed" to be more relevant than data located farther away). In some implementations of this class of *inverse-distance techniques*, the weighting function decreases as the square of the distance. A common thread connecting all estimation methodologies is that they are *interpolation* techniques directed toward producing a model in which the estimated values grade progressively and smoothly away from the data locations and away from one another.

The other broad class of geostatistical methods comprises a variety of *simulation* algorithms. These techniques are conceptually equivalent to the Monte Carlo simulation process frequently employed in engineering analyses. In common with other Monte Carlo simulation approaches, the emphasis is less on the specific predicted values, which are in effect simply the products of a random number generator with certain "desirable" properties, and much more on evaluation of the uncertainty associated with some *performance measure* computed to represent the behavior of the modeled system. This process is portrayed schematically in figure 6. Because of the need to capture spatial correlation, geostatistical simulation effectively amounts to drawing entire material property models (as intact objects because of the need to maintain spatial correlation among the values) from some hypothetical "distribution" of alternative "realities." Each of these individual *realizations* or *stochastic images* of reality is then evaluated through some type of relevant *transfer function* (for example, a radionuclide-transport computer code) and the likelihood of various acceptable vs. unacceptable performance responses is evaluated.

Model Domain

The geographic region for which material properties models were created is the "extended site area," as shown in figure 7 (see also fig. 1). This region extends generally from north of Yucca Wash to south of Busted Butte, and from the general vicinity of Fatigue Wash and Windy Wash on the west to east of Alice Ridge, Fran Ridge, and Busted Butte. The modeled domain was selected to coincide as closely as geologically reasonable with the "extended" site-scale unsaturated zone flow model being developed by researchers at Lawrence Berkeley Laboratory ("LBL"; Wittwer and others, 1995; Bodvarsson and Bandurraga, 1996[†]). The outline of the LBL unsaturated flow model domain is also indicated in figure 7, as is the location and extent of the geostatistical modeling grid used in this study.

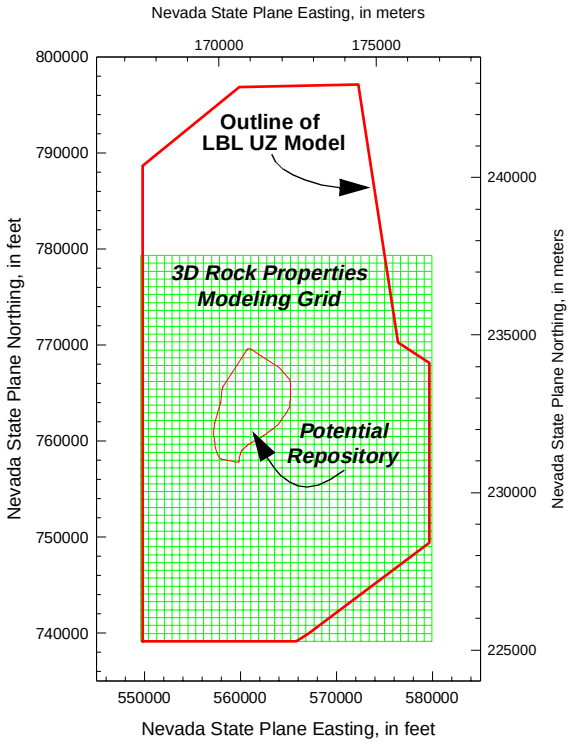

Figure 7. Location of the extended site area at Yucca Mountain, the LBL extended site scale flow model domain, and the model grid for this study.

Definition of the geostatistical modeling grid in this study was closely tied to the location and nominal grid spacing of the LBL numerical process model grid (table 2; T.M. Bandurraga, LBL, written communication, 1996; see also fig. 5.3.1 of Haukwa and Chen, 1996[‡], *in* Bodvarsson and Bandurraga, 1996). Details of the geostatistical grid are presented in table 3.

Available Data

The data used in modeling the spatial variability of material properties in this report were

[†]Bodvarsson, G.S., and Bandurraga, T.M., eds., 1996, Development and calibration of the three-dimensional site-scale unsaturated zone model of Yucca Mountain, Nevada, 1996, Milestone Report OB02, Lawrence Berkeley National Laboratory, Berkeley, Calif.

[‡]Haukwa, C., and Chen, G., Grid generation and analysis, Chapter 5 *in:* Bodvarsson, G.S., and Bandurraga, T.M., eds., 1996, Development and calibration of the three-dimensional site-scale unsaturated zone model of Yucca Mountain, Nevada, 1996, Milestone Report OB02, Lawrence Berkeley National Laboratory, Berkeley, Calif.

Table 2: Nevada state plane coordinates for the origin of the rock properties modeling grid and the LBL site-scale unsaturated zone flow model
[southwestern-most corner of each model]

Easting		Northing	
(m)	(ft)	(m)	(ft)
167,580.0	549,829.98	225,280.0	739,143.68

obtained from a number of sources (Appendix A), including both laboratory measurements of core samples and down-hole petrophysical measurements of in-situ rocks. Only surface-based drill holes have been used in the current modeling exercise, as the large areal extent of the model and the requirement that the vertical position of all data be expressed in stratigraphic coordinates effectively precluded the use of samples from the underground workings of the Exploratory Studies Facility. The location of the various drill holes used in modeling each separate geologic unit are shown in figures 8 through 10. Note that although there is major consistency of the drill hole coverage from unit to unit, the suite of holes that contain data relevant to the rock properties of any particular model unit is unique. The identity and Nevada state-plane coordinates of the specific holes used in each separate modeling exercise are given in table 4. Data-tracking numbers associated with all data values are tabulated in Appendix A.

Table 3: Geostatistical modeling grid-specification parameters
[n/a–not applicable]

Grid Direction		Midpoint (ft/m)	Spacing (ft/m)	N	Total Nodes
Model X (Easting)		550,240.105 167,705.000	820.250 250.000	37	n/a
Model Y (Northing)		739,553.805 225,405.000	820.250 250.000	49	n/a
Model Z (Stratigraphic Vertical)	PTn	3.281 1.000	6.562 2.000	30	54,390
	TSw	16.405 5.000	32.810 10.000	31	56,203
	CH-PP	16.405 5.000	32.810 10.000	25	45,325

Table 4: Drill holes used in modeling rock material properties
[Age Designator (for petrophysical data): O– "older" hole; M–"modern" hole; N–State of Nevada drillhole. Data-availability codes: F–full penetration of unit; P–partial penetration; leaders (--)–no penetration. Location data taken from Clayton and others, 1997]

Drill Hole ID		Nevada State Plane		PTn	TSw	CH-PP
(USW- or UE-25)	Age	Easting (ft)	Northing (ft)			
G-1	O	561000.5	770500.2	F	F	F
G-2	O/M	560503.9	778824.2	P	F	F
G-3	O	558501.0	752690.0	F	F	F
G-4	O	563081.6	765807.1	F	F	F
H-1	O	562388.0	770254.3	--	F	F
H-3	O	558451.7	756542.1	F	F	F

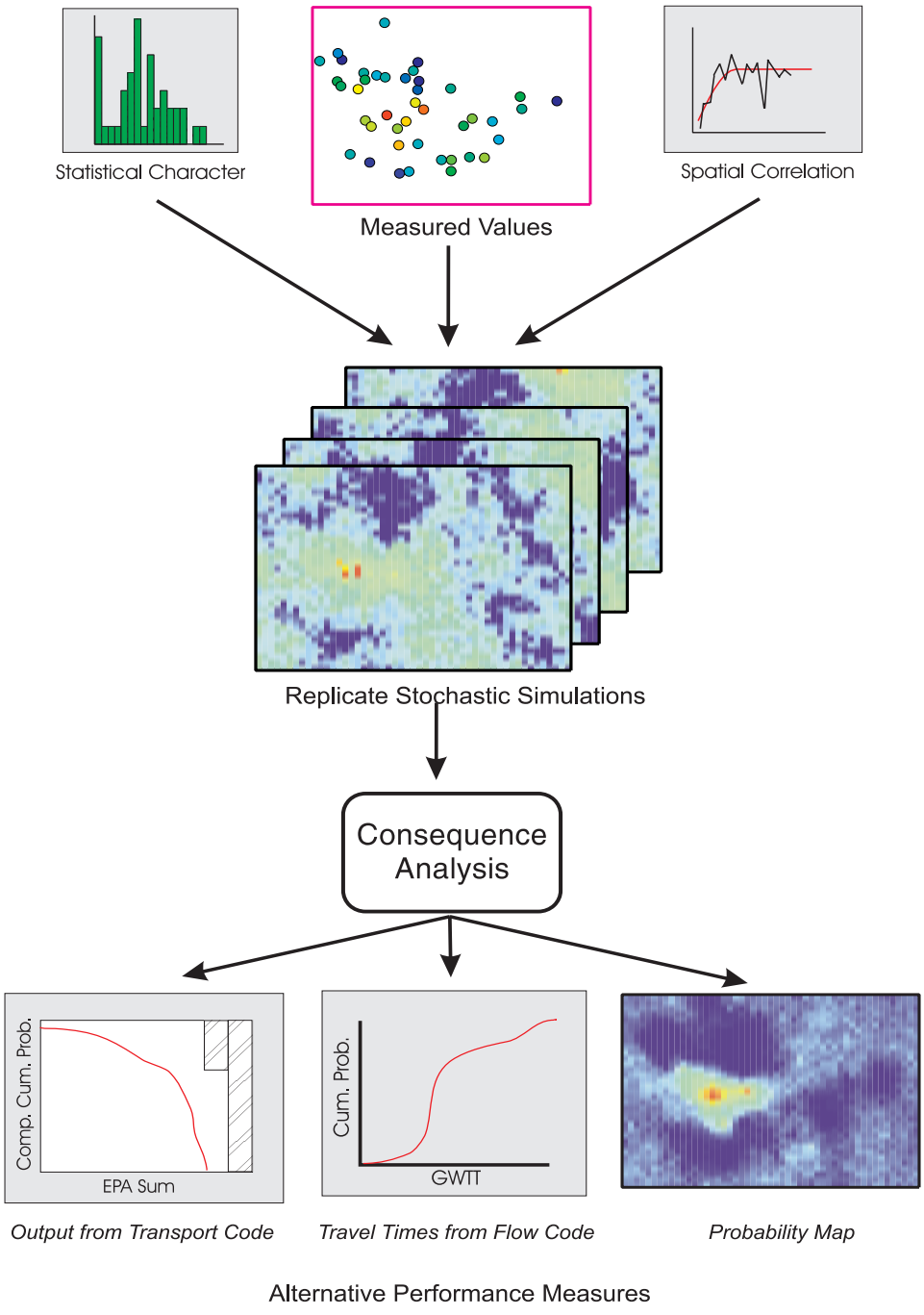

Figure 6. Conceptual representation of a Monte Carlo process incorporating geostatistical simulation techniques as the basis for assessing the impact of geologic uncertainty on a performance measure relevant to licensing of a geologic repository. A “transfer function” is any post-simulation mechanism for computing a measure of performance across the suite of replicate stochastic simulations.

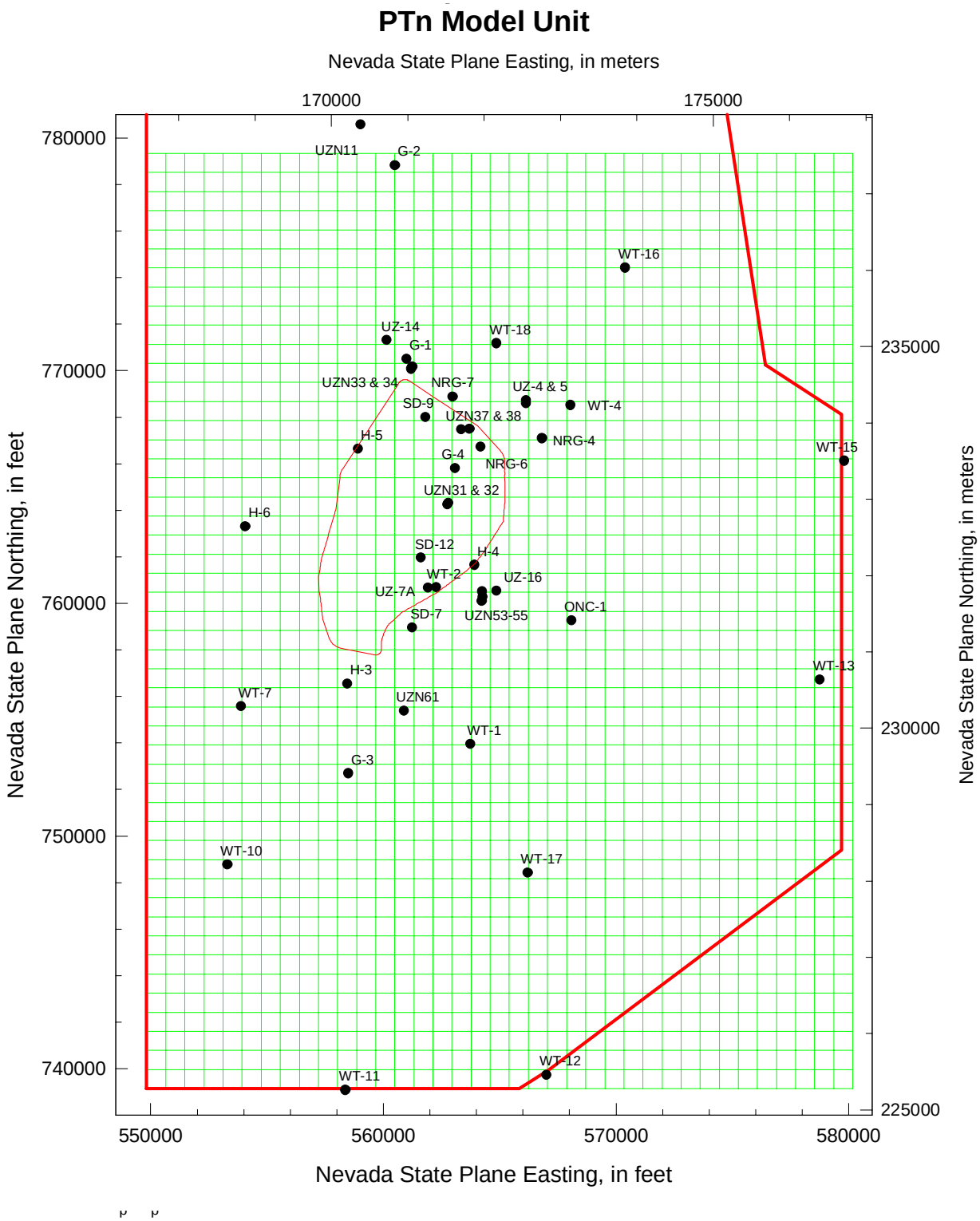

Figure 8. Drill hole locations used in modeling the PTn model unit.

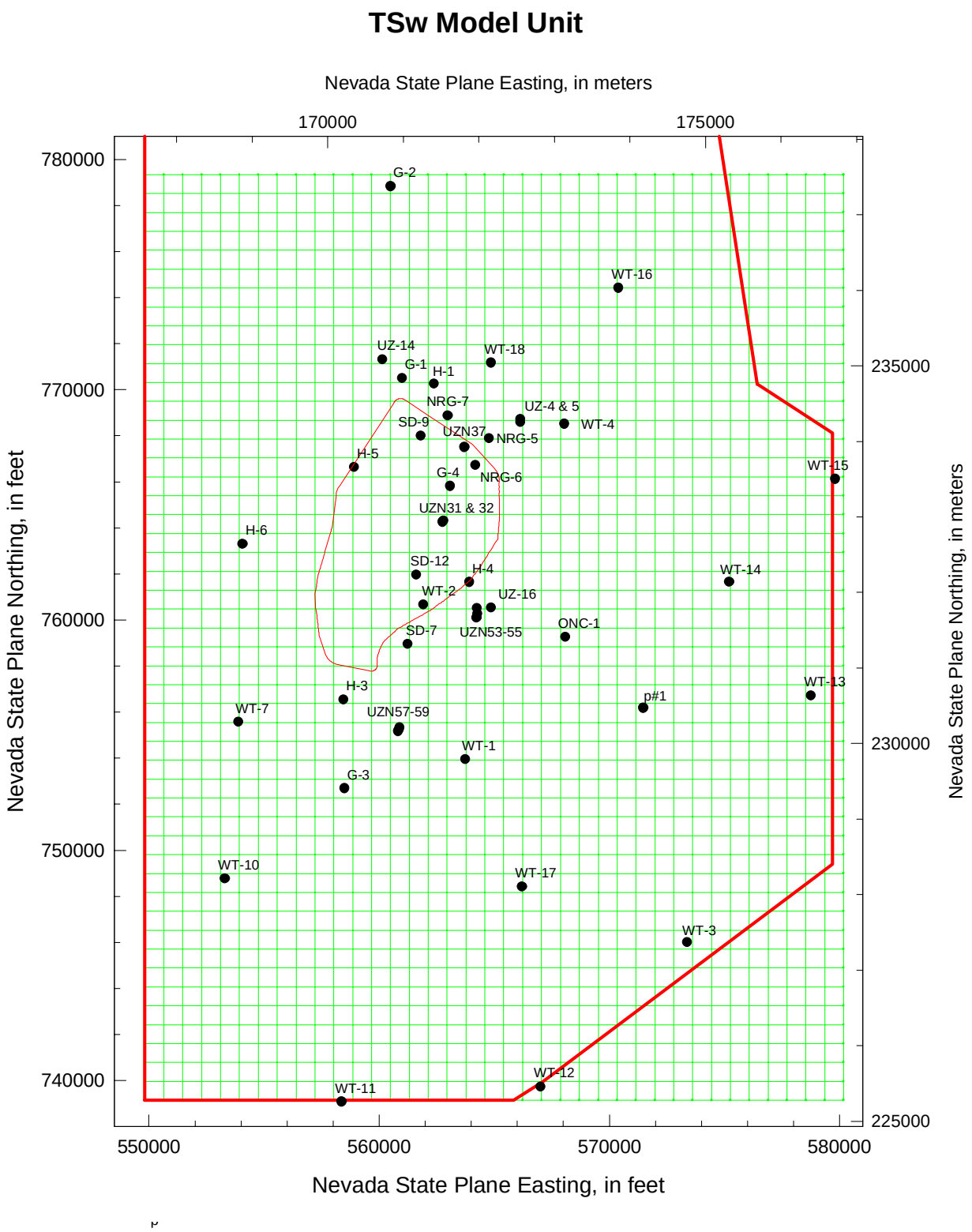

Figure 9. Drill hole locations used in modeling the TSw model unit.

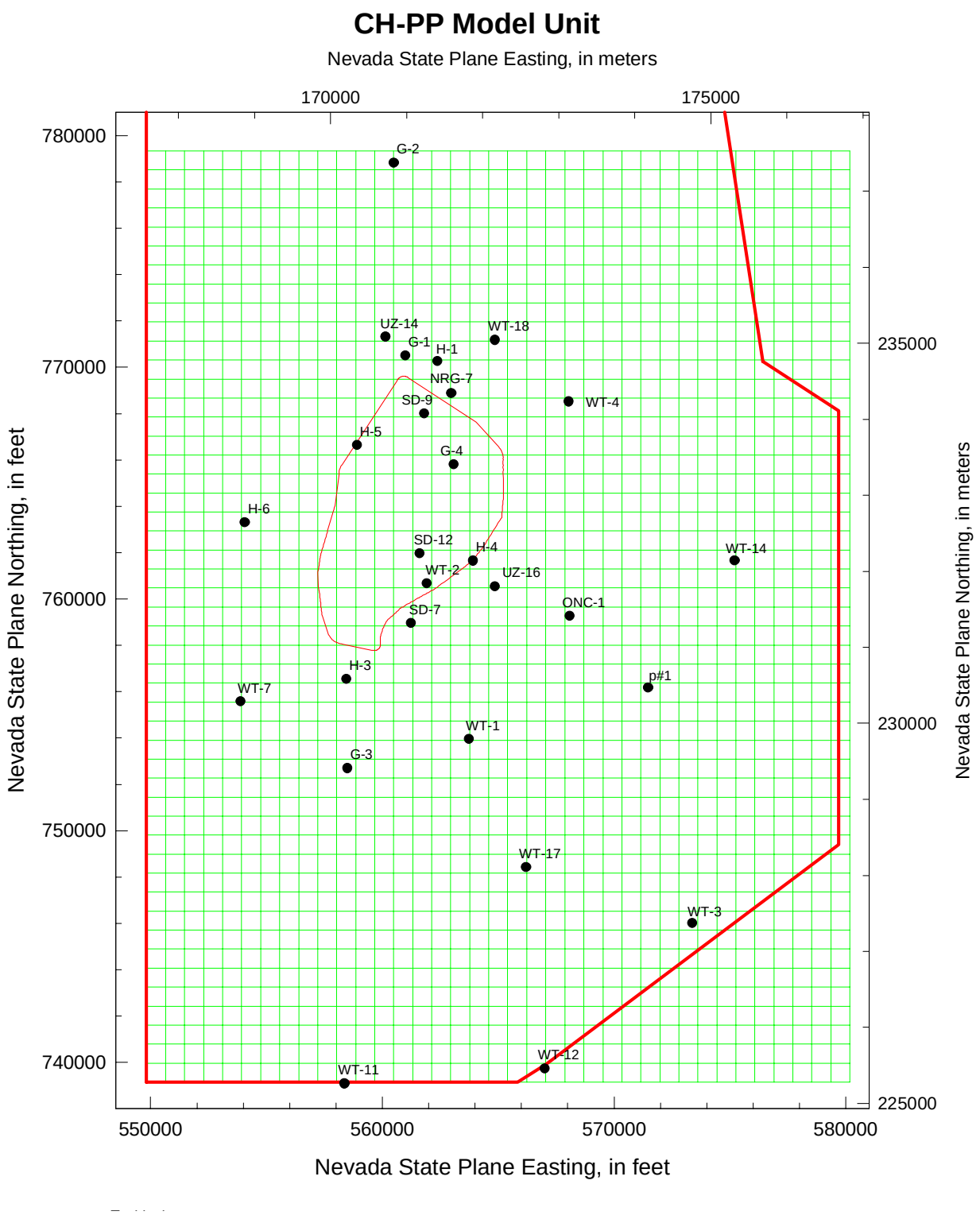

Figure 10. Drill hole locations used in modeling the CH-PP model unit.

Table 4: Drill holes used in modeling rock material properties (Continued)
[Age Designator (for petrophysical data): O– "older" hole; M–"modern" hole; N–State of Nevada drillhole. Data-availability codes: F–full penetration of unit; P–partial penetration; leaders (--)–no penetration. Location data taken from Clayton and others, 1997]

Drill Hole ID		Nevada State Plane		PTn	TSw	CH-PP
(USW- or UE-25)	Age	Easting (ft)	Northing (ft)			
H-4	O	563911.1	761643.6	F	F	P
H-5	O	558908.7	766634.3	F	F	F
H-6	O	554074.9	763298.9	P	F	F
NRG-4	M	566820.0	767080.2	P	--	--
NRG-5	M	564187.2	766726.3	--	P	--
NRG-6	M	564187.2	766726.3	F	P	--
NRG-7	M	562984.1	768880.0	F	F	P
ONC-1	N/M	568092.9	759257.3	F	F	P
p#1	O	571484.5	756171.2	--	F	F
SD-7	M	561240.3	758949.9	F	F	F
SD-9	M	561818.0	767999.0	F	F	P
SD-12	M	561606.0	761957.0	F	F	F
UZ-4	M	566139.3	768715.6	F	P	--
UZ-5	M	566135.2	768591.0	F	P	--
UZ-7A	M	562270.0	760693.0	F	--	--
UZ-14	M	560141.3	771309.4	P	F	F
UZ-16	M	564857.5	760535.2	F	F	P
WT-1	O	563739.2	753940.6	F	F	F
WT-2	O/M	561923.6	760660.5	F	F	P
WT-3	O	573384.4	745995.1	--	P	F
WT-4	O	568040.2	768511.8	F	F	P
WT-7	O	553891.3	755569.8	F	F	P
WT-10	O/M	553302.1	748770.9	F	P	--
WT-11	O	558376.8	739070.4	F	F	P
WT-12	O/M	567011.0	739725.9	F	F	P
WT-13	O	578756.7	756715.0	P	P	--
WT-14	O	575210.1	761650.6	--	P	P
WT-15	O	579805.7	766116.6	F	P	--
WT-16	O	570394.9	774419.7	F	F	--
WT-17	O	566211.9	748419.6	F	F	P
WT-18	O	564855.0	771167.1	F	F	P
UZN11	M	559020.9	780573.9	P	--	--
UZN31	M	562751.9	764245.7	F	P	--
UZN32	M	562799.6	764302.6	F	P	--

Table 4: Drill holes used in modeling rock material properties (Continued)

[Age Designator (for petrophysical data): O– "older" hole; M–"modern" hole; N–State of Nevada drillhole. Data-availability codes: F–full penetration of unit; P–partial penetration; leaders (--)–no penetration. Location data taken from Clayton and others, 1997]

Drill Hole ID		Nevada State Plane		PTn	TSw	CH-PP
(USW- or UE-25)	Age	Easting (ft)	Northing (ft)			
UZN33	M	561192.2	770069.9	P	--	--
UZN34	M	561251.5	770158.7	P	--	--
UZN37	M	563713.5	767499.1	F	P	--
UZN38	M	563343.1	767466.4	P	--	--
UZN53	M	563343.1	767466.4	F	P	--
UZN54	M	564262.2	760272.0	F	P	--
UZN55	M	564248.3	760502.9	F	P	--
UZN57	M	560829.9	755164.5	--	P	--
UZN58	M	560862.2	755240.4	--	P	--
UZN59	M	560888.4	755321.3	--	P	--
UZN61	M	560892.0	755375.9	P	--	--

Measurement Methods

Core Samples

Laboratory measurements of porosity on core samples are, perhaps, the most intuitively understandable of the several types of porosity data used in creating the material property models. These measurements are performed on core samples approximately 1–3 inches (2–8 cm) long using gravimetry and Archimedes' principle for volume determinations. This process has been described by Rautman and Engstrom (1996a, b) and by Flint.[†] Drying of samples as part of the porosity determination procedure was performed under two different temperature–relative humidity conditions, and this distinction is critical to the identification of zeolite (and other hydrous-phase) alteration elsewhere in the modeling sequence (fig. 2).

Relative-humidity-oven (RH) drying was conducted at 60°C and a controlled relative humidity of 65 percent. These environmental conditions preserve most water that is structurally bound in zeolite (and clay minerals) as well as a few-molecule-thick layer of water surrounding the individual mineral grains (Bush and Jenkins, 1970; Soeder and others, 1991). None of this water is truly "free" to participate in unsaturated-zone flow. Oven-dried (OD) samples were dried at 105°C and uncontrolled ambient (but very low) relative humidity. This stage of drying removes not only the loosely bound "residual saturation" water, but also drives off the majority of the water contained within the crystal structures of zeolite and clay minerals. Experimentation has demonstrated that these types of mineralogic changes cause irreversible changes in the measured hydraulic conductivity of the samples, which presumably are caused by differences in pore-throat geometries before and after decrepitation of the zeolite crystal structure.

A corollary of the differing porosity values (and of other bulk properties as well; figs. 3, 4) that are obtained through this progressive drying process is that the presence of "significant" zeolite and/or other hydrous-phase minerals can be identified to a first approximation without mineralogical or petrographic analyses. For purposes of these modeling exercises, "altered rocks" were defined using the following relationship:

$$I(\mathbf{x}) = \begin{cases} 1 \leftarrow \phi_{OD} > (\phi_{RH} + 0.05) \\ 0 \leftarrow \text{Otherwise} \end{cases}, \qquad (1)$$

where $I(\mathbf{x})$ is a binary *alteration indicator flag* as a function of spatial position, $\mathbf{x}$, set to 1 in the presence of alteration, and where ϕ_{OD} and ϕ_{RH} are the oven-dried and relative-humidity-oven-dried porosity values respectively. The threshold of a five-percent (0.05) higher OD porosity was selected somewhat empirically, but the value is intended to recognize that even completely unaltered rocks will retain some residual water coating the mineral grains when dried at the RH conditions. Use of a much lower threshold value leads to a designation of altered rocks in stratigraphic intervals that are known to be devoid of zeolite or meaningful clay alteration (such as densely welded, devitrified units in the Topopah Spring Tuff). Values much higher than 5 percent appeared to misidentify as unaltered, rocks within the Calico Hills Formation that are known from X-ray diffraction studies to be zeolitized.

Petrophysical Data — "Older" Drill Holes

Inferred porosity values have been computed using measurements from a suite of downhole geophysical instruments by Nelson (1996). The set of data produced using this process involves the "older" set of holes drilled at Yucca Mountain prior to release of the Site Characterization Plan (DOE, 1988; see identifiers in table 4). Inference of in-situ porosity values for the "modern" holes (table 4) drilled as part of formal characterization of the Yucca Mountain site is discussed in the next section beginning on page 25 (see also fig. 2). A schematic diagram showing the several different types of porosity values, and their relationship to the core measurements, is presented in figure 11.

The principal property from the older geophysical logging suite consists of total porosity, which is defined by Nelson (1996) as:

$$\phi_T = \phi_w + \phi_a , \qquad (2)$$

[†]Flint, L.E., in review, Matrix properties of hydrogeologic units at Yucca Mountain, Nevada: intended for publication as U.S. Geological Survey Water-Resources Investigations Report.

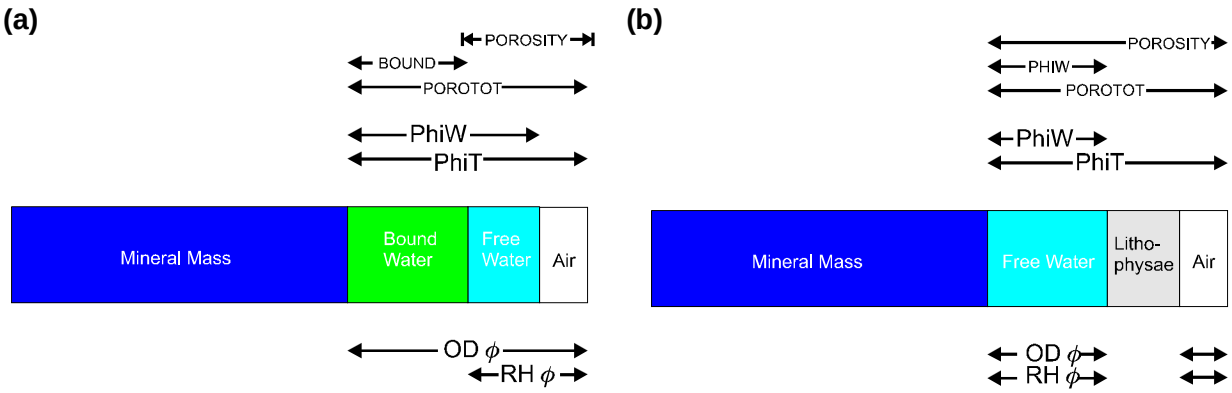

Figure 11. Diagram illustrating the conceptual relationships among the various types of "porosity" described in this report. (a) Altered rocks; (b) all other nonwelded and welded rocks. Indicated quantities refer to variable names in the original (source) data files).

where ϕ_T is total porosity, ϕ_w is the "water-filled" porosity (defined below), and ϕ_a is air-filled porosity. The principal geophysical measurement used in the computation of total porosity is the bulk density log trace, which for the older drillhole suite is derived from the gamma-gamma logging tool based on backscattering of high-energy gamma radiation from a source contained onboard the tool. The observed bulk density, ρ_b, of the in-situ rock is a weighted combination of the densities of the mineral grains themselves and of the contained water and air present in the formation. Within the saturated zone, ϕ_a = zero (all porosity is water filled), and the expression for bulk density (ρ_b) is simply:

$$\rho_b = \rho_g(1-\phi_T) + \rho_w\phi_T \quad , \qquad (3)$$

which can be rewritten in terms of porosity as:

$$\phi_T = \frac{\rho_g - \rho_b}{\rho_g - \rho_w} \quad . \qquad (4)$$

where ρ_w is the density of the pore water and ρ_g is grain density (note: ρ_g is also known as particle density). Note that equation 4 requires an estimate of grain density at each location for which a porosity measurement is desired. However, evaluation of laboratory measurements indicate that grain density is effectively constant through large stratigraphic intervals (e.g., middle columns of figs. 3, 4) at Yucca Mountain that can be independently identified using core, cuttings, and the behavior of both the raw density and other geophysical logs. Nelson (1996) used values of ρ_g as tabulated in

Table 5: Grain density values used in computing porosity from older geophysical logs
[from Nelson, 1996]

Rock Type	ρ_g (g/cm^3)
Glass	2.349
Vitrophyre	2.381
Nonwelded Tuff	2.587
Welded Tuff	2.540
Zeolitization (deep)	2.527
Zeolitization (shallow)	2.371

Use of the density log to determine total porosity in the ***un***saturated zone is complicated by the presence of two fluid phases (water + air) in the pores of the rock. Above the static water level, the relationship is thus:

$$\rho_b = \rho_g(1-\phi_T) + \rho_w\phi_w + \rho_a\phi_a \, , \qquad (5)$$

where ρ_g, ρ_w, and ρ_a are the densities of the mineral grains, water, and air (respectively). Nelson (1996) neglected the last term in equation 5, as the density of air, ρ_a, is nearly zero (0.00123g/cm^3) by comparison with the other density factors (table 5). We can rewrite the remaining terms of equation 5 as:

$$\phi_T = 1 - \frac{\rho_b}{\rho_g} + \frac{\rho_w}{\rho_g}\phi_w \, . \qquad (6)$$

Note that ϕ_w, the water-filled porosity, is simply the volumetric water content of the rock if there are no clays or zeolite minerals present in the rock matrix.

Nelson (1996) also presented a method for computing ϕ_w, which he termed the "*hydrogen index*," I_H, using the calibrated response of the epithermal neutron porosity (ENP) logging tool in air-filled boreholes above the water table. The physics underlying this measurement is that energetic ("epithermal") neutrons emitted by a downhole source onboard the logging sonde are preferentially "thermalized" or slowed by collision with hydrogen atoms in the formation. If zeolites and clays are absent, virtually all hydrogen is present in the form of pore water, and thus proper calibration of ENP devices directly indicates volumetric water content. The combination of responses from the gamma-gamma density and ENP logging instruments yields the desired total porosity via equation 7:

$$\phi_T \approx \phi_{T'} = 1 - \frac{\rho_b}{\rho_g} + \frac{\rho_w}{\rho_g} I_H \quad , \qquad (7)$$

where $\phi_{T'}$ is the *apparent* total porosity. If, however, water is present as a structurally bound component of the mineral grain framework, the neutron log will read higher than it would otherwise be for a rock of the same porosity, I_H will exceed ϕ_w, and the apparent total porosity of the rock, $\phi_{T'}$ will exceed ϕ_T by the amount of water contained in the hydrous mineral phases.

For purposes of the modeling described in this report, we have adopted a convention for identifying such altered rocks in a manner very similar to that applied to the laboratory measurements of porosity in equation 1. Thus:

$$I(\mathbf{x}) = \begin{cases} 1 \leftarrow I_H > (\phi_{T'} + 0.05) \\ 0 \leftarrow \text{Otherwise} \end{cases} \qquad (8)$$

where $I(\mathbf{x})$ is the again the binary alteration flag from equation (1) as a position of spatial location, $\mathbf{x}$. It then remains to estimate the true total porosity, ϕ_T for those intervals where the computed apparent total porosity, $\phi_{T'}$, reported in Nelson's output files is overstated.

Unfortunately, there appears to be no theoretically satisfactory estimator of true total porosity available for the older suite of drill holes. We have therefore adopted an approach that simply continues to use the computed total porosity values, $\phi_{T'}$, as the best estimator of ϕ_T. Reference to equations 6 and 7 suggests that the computed porosity value is sensitive principally to the term ρ_b/ρ_g because the bulk density of almost all rocks, ρ_b, is typically at least twice the density of water, ρ_w (~1.00 g/cm^3). In addition to a necessarily smaller value for the ratio ρ_w/ρ_g, this latter term is then multiplied by the hydrogen index, I_H, as a surrogate for the true volumetric water content ϕ_w. Even in intensely zeolitized rocks, I_H is a fractional value (generally less than 0.5), whereas the term involving bulk density contains no such fractional multiplier.

Petrophysical Data — "Modern" Drill Holes

A somewhat different approach to the determination of porosity, and particularly to the identification of structurally bound water in alteration minerals, was employed by Thompson and Rael (1996) for the "modern" set of site characterization boreholes (table 4). In addition to holes drilled since 1988 (DOE, 1988), Thompson and Rael also obtained new suites of logs in a small number of selected "older" holes. This replication of logging provides some basis for comparing the two sets of petrophysical data, although it is clear that the lapse of time between drilling and relogging appears to have induced some changes downhole.

The fundamental relationship for determining total porosity, ϕ_T, is virtually identical to that used by Nelson (1996). However, Thompson and Rael substituted computed local values of ρ_f (the density of the formation *fluid*), for ρ_w in equation (4) (saturated zone) and for the terms $[\rho_w\phi_w + \rho_a\phi_a]$ in equation (5) (unsaturated zone). Thus they write:

$$\phi_T = \frac{\rho_{g(OD)} - \rho_b}{\rho_{g(OD)} - \rho_f} \quad , \qquad (9)$$

where ρ_b is the bulk density log-trace value as before and $\rho_{g(OD)}$ is now the appropriate average grain density of the rock type as estimated from oven-dried laboratory samples (in the same or analogous drill holes). Nelson (1996) functionally used

105°C-dried grain density values in his calculations, but he did not explicitly use this term (see also the definition of effective porosity, which follows).

Thompson and Rael (1996) computed the apparent fluid density for use in equation (9) from the relationship:

$$\rho_f = \frac{\phi_w \rho_w + \phi_a \rho_a}{\phi_T} \quad , \tag{10}$$

where all terms are as defined for equation (5). Because equation (10) is, itself, dependent upon ϕ_T, Thompson and Rael computed this value in an iterative manner.

The volumetric water-content parameter (bulk water volume of Thompson and Rael), ϕ_w, was calculated using the relationship:

$$\phi_w = \phi_T S_w \tag{11}$$

where S_w is the water saturation obtained using the appropriate conductivity (resistivity) log value in the classical Archie (1942) equation:

$$S_w = \left(\frac{a}{\phi_T^{\,m}} \cdot \frac{R_w}{R_t} \right)^{\frac{1}{n}} \quad . \tag{12}$$

rather than by using calibrated ENP values, as did Nelson (1996). In equation (12), R_t is the resistivity of the formation (in ohm-meters, Ω-m) as measured by the deep induction log, R_w is the resistivity of the formation water (here approximately that of pure water, ~20Ω-m), and a, m, and n are empirically determined rock-typing constants (unit specific). Again, the interdependence of S_w and ϕ_T requires the use of an iterative solution procedure [combined with the solution of equation (10); note that rock-typing is also a quasi-separate iterative procedure as well]. Thompson and Rael did not specify a convergence criterion for the iterative solution for ϕ_T. Rather, they estimated ϕ_w initially using an uncalibrated ENP log value (in fact calibrated to so-called "limestone" units, rather than for tuff) and simply executed the iteration loop five (5) times.

To determine the quantity of water structurally bound in zeolites or other hydrous mineral phases, Thompson and Rael computed a second porosity value, ϕ_{eff}, where:

$$\phi_{eff} = \frac{\rho_{g(RH)} - \rho_b}{\rho_{g(RH)} - \rho_f} \tag{13}$$

and $\rho_{g(RH)}$ is now the unit-averaged grain density value determined through laboratory measurements for relative humidity oven-dried samples. Because the masses of samples dried under relative-humidity oven conditions include the mass of structurally bound water, the ϕ_{eff} value presumably represents open void space in the rock. The "porosity" thus represented by structurally bound water is then obtained by difference:

$$\phi_{zeol} = \phi_T - \phi_{eff} \quad , \tag{14}$$

where the "*zeol*" porosity subscript is simply shorthand for "hydrated alteration minerals." The computed porosity values from the "modern" drill hole suite were then processed to alteration indicator flags using essentially the same methodology given in equation (8):

$$I(\mathbf{x}) = \begin{cases} 1 \leftarrow \phi_T > (\phi_{eff} + 0.05) \\ 0 \leftarrow \text{Otherwise} \end{cases} \quad . \tag{15}$$

Comparison of Petrophysical Porosity Data

Comparison and evaluation of the two different approaches to the petrophysical determination of total porosity is complicated by separation of the technique into "modern" holes vs. "older" holes. Although no modern holes were logged using the older-style downhole tools, four of the old holes were relogged using the newer tools and resistivity-based S_w analysis methods. These four holes include three WT-series holes (WT-2, WT-10, and WT-12), located principally in the south and south-central portion of the site area, and drill hole G-2, which is located in the northern part of the study region (fig. 9). Scatter diagrams of total porosity from these two different petrophysical data sets are shown in figure 12(a) through (d). In each case, the older set of values are plotted on the ordinate (variable PhiT, in the original data files; fig. 11) and the "modern" porosity values (variable POROTOT; fig. 11) along the abscissa. The values shown in the crossplots are the original computed porosity val-

ues computed at 0.5 ft (approximately 15 cm) intervals downhole.

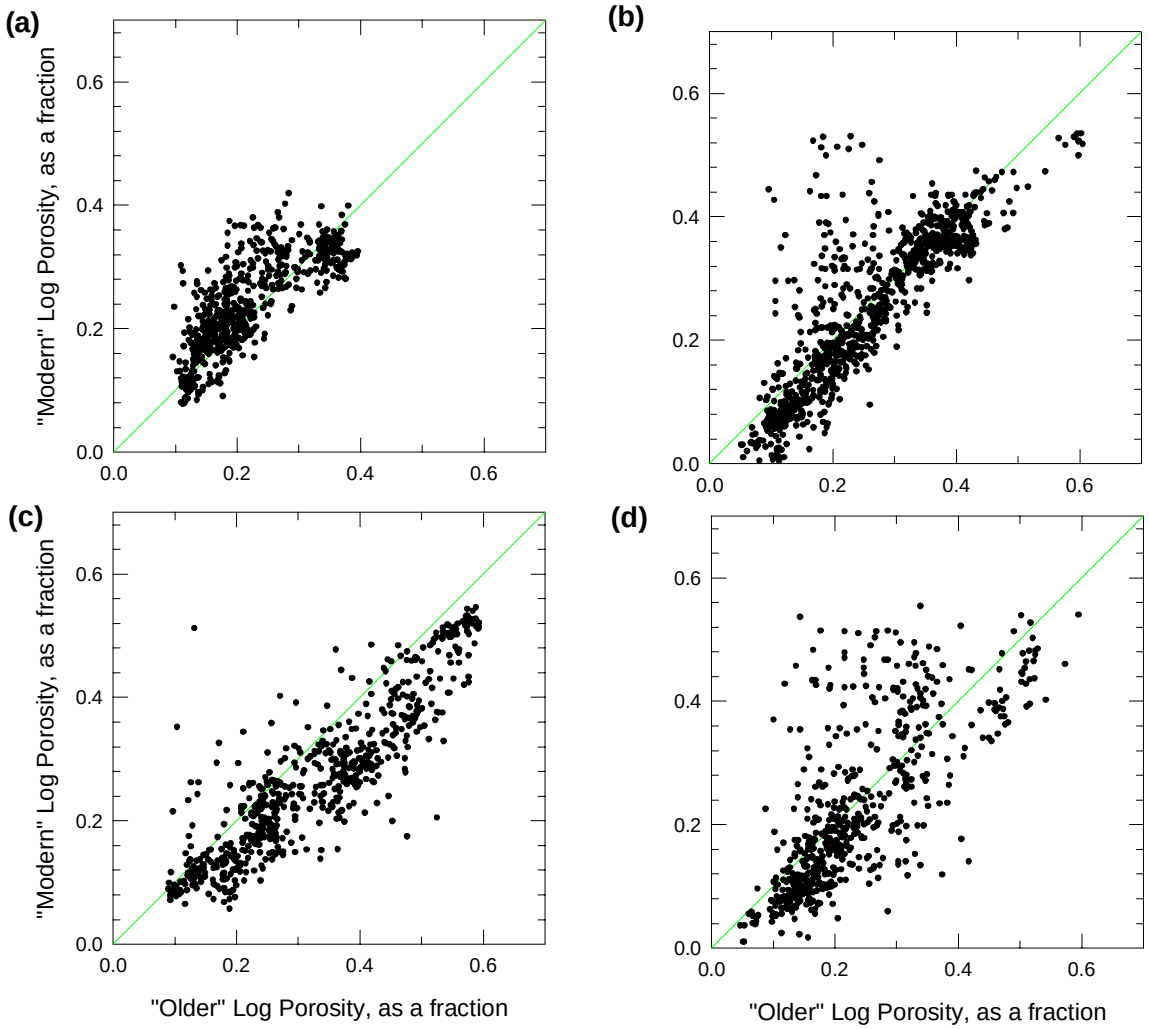

Figure 12. Comparison of petrophysical total porosity computed using two different sets of logging tools and two different data-reduction techniques from raw data acquired several years apart. Drillholes: (a) USW G-2; (b) USW WT-2; (c) USW WT-10; (d) USW WT-12. Light-grey line at 45° indicates one-to-one correspondence.

It is not entirely clear that the exact same vertical datum was identified and used for both logging runs, as for some drill holes, the measurements are separated in time by nearly two decades. Although small differences in vertical alignment may appear significant, given data on half-foot centers, the consequent variations in porosity resulting from misalignment are probably not very substantial. Most drill pads were essentially unchanged from their original condition, suggesting that such standard alignment points such as top of casing or ground level also would have been essentially unchanged. Also, the volume of rock interrogated by the geophysical logging tools is roughly 2 ft (0.6 m) in diameter (L.E. Thompson, Science Applications International Corporation, written communication, 1996), even a vertical misalignment of 2–3 sample positions would still result in substantial overlap in the volume of material being interrogated.

Examination of the four scatterplots of figure 12 indicates that the correspondence between the computed porosity values is not exact. The 45° trend of the cross plots is unmistakable, indicating clearly that both logging/data-reduction methods are capturing essentially the same lithologic effects. However, a plot such as figure 12(c) does suggest that the values from one approach may be systematically biased with respect to the other. In this specific instance, the "older" porosity values appear to be systematically higher than those reported by the "modern" readings. However, it is also clear that the passage of many years in what were effectively unmaintained boreholes may well have affected the in situ rocks such that both measurements could be "correct." To the extent that observations made "soon" after drilling are more realistic than measurements made decades later, then neither set of the petrophysical porosity data can be judged better or worse than the other, given that the direction of comparison is only one way (there are no old logs in the new holes). Note that in figure 12(a), the direction of the systematic bias appears to be in the other direction from that illustrated in figure 12(c), with the modern porosity values generally higher than the older ones. We will return to this issue of systematic bias within drill holes on page 51.

It happens that Thompson and Rael (1996) were aware of the difference in computational approach between their work and that of Nelson (1996). Figure 13 presents a comparison similar to that of figure 12, except that the "modern" porosity value plotted is no longer POROTOT (see also fig. 11), but instead a variable labeled PORNEL (fig. 11) as a mnemonic device indicating that it was determined using the ENP approach to computing ϕ_w of Nelson. Note, however, that the two sets of ENP logging tools were not necessarily calibrated in exactly the same manner; the interested reader is referred to the original references for details.

Note that the systematic downward bias of the modern computed porosity values is noticeably decreased for the older values from drillhole WT-2 [fig. 13(b)] compared with the modern values [fig. 12(b)]; the center of the cloud of data points now is more closely bisected by the 45° line of one-to-one correspondence. However, it is not evident that this improved reproduction of the older measurements in figure 13(b) is a general phenomenon associated with the Nelson (1996) computational method. For example, systematic bias is not eliminated: figure 13(c) appears just as biased as figure 12(c). Also, the spread of the points, especially those farther away from the 45° line is certainly no less in most cases, and in some [compare fig. 12(d) with fig. 13(d)], the degree of scatter is in fact greater.

In summary, the evidence does not appear to be convincing that either logging or computational method is clearly superior to the other. There is too great a likelihood that actual physical changes occurred in the formations penetrated by the four drill holes between their initial logging (Muller and Kibler, 1985; Nelson and others, 1991) and the subsequent logging conducted by Thompson and Rael (1996). Certainly, the lack of modern porosity values for the vast majority of the WT- , G-, and H-series drill holes leaves no alternative to the use of the older data at these locations.

Additional Processing of Petrophysical Porosity Data

As presented in figures 12 and 13, the petrophysically derived porosity data were recorded at uniform one-half-foot depth increments (a few holes were recorded at only one-foot intervals). The laboratory-measured core porosity values were sampled on a nominal spacing of 3 ft (1 m), although core recovery and other logistical factors combined to render this nominal spacing by no means exact. In order to maintain approximate parity between the number of core samples and petrophysical measurements per unit length of drill hole (where each type exists), the petrophysical values were resampled on a 3-ft spacing, producing a somewhat less-variable profile, similar to the example shown in figure 14.

In addition to simply selecting the petrophysical porosity values on 3-ft centers, the resampling algorithm computed a simple average of the adjoining measurements within plus and minus 1 ft of the nominal depth value. This two-foot averaging interval was based on the approximate diameter of the physical volume of rock examined by the gamma-ray logging tool. The use of such an averaged porosity based on measurements that already

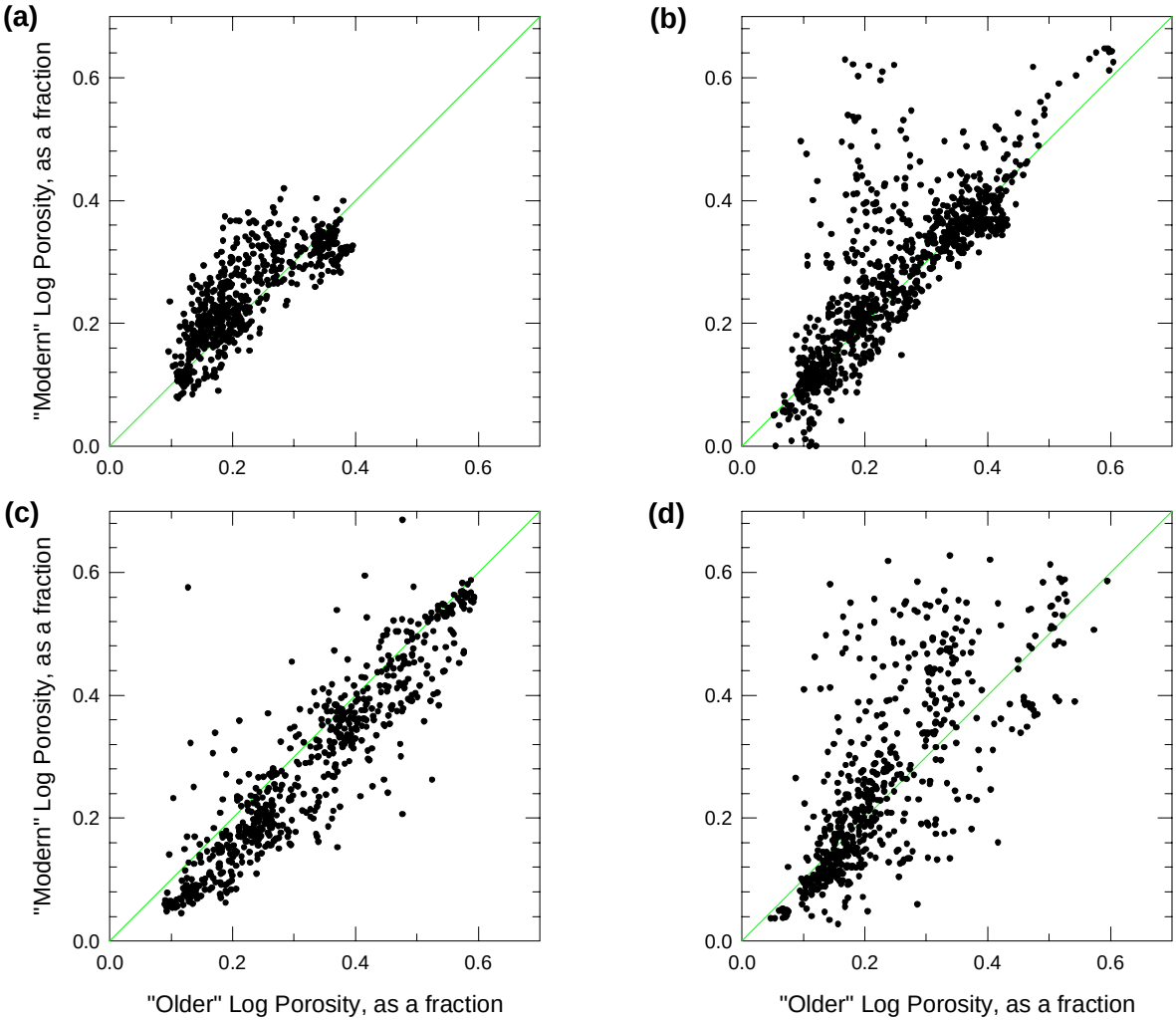

Figure 13. Comparison of petrophysical porosity values computed using two different sets of logging tools using raw data acquired several years apart, but using essentially the same computational algorithm. Drillholes (a) G-2; (b) WT-2; (c) WT-10; (d) WT-12. Light-grey line at 45° indicates one-to-one correspondence.

"average" the pore space present over a much larger sample volume than a core specimen has the effect of reducing the overall variability of the petrophysical porosity profiles. Although this reduction of variance is not particularly desirable in a statistically based study, this part of the resampling process was developed intentionally to deal with less-than-optimal downhole data. Additionally, the petrophysical data are somewhat "spiky" in their original form, even after corrections for hole conditions.

A reality of downhole geophysical logging is that hole conditions are commonly less than optimal. The gamma-gamma density tool used as the basis for the porosity calculations is a *decentralized* tool, in which the logging sonde is purposefully pressed against the side of the hole as the instrument is pulled up the borehole. If the borehole wall is particularly rough and irregular, as it is

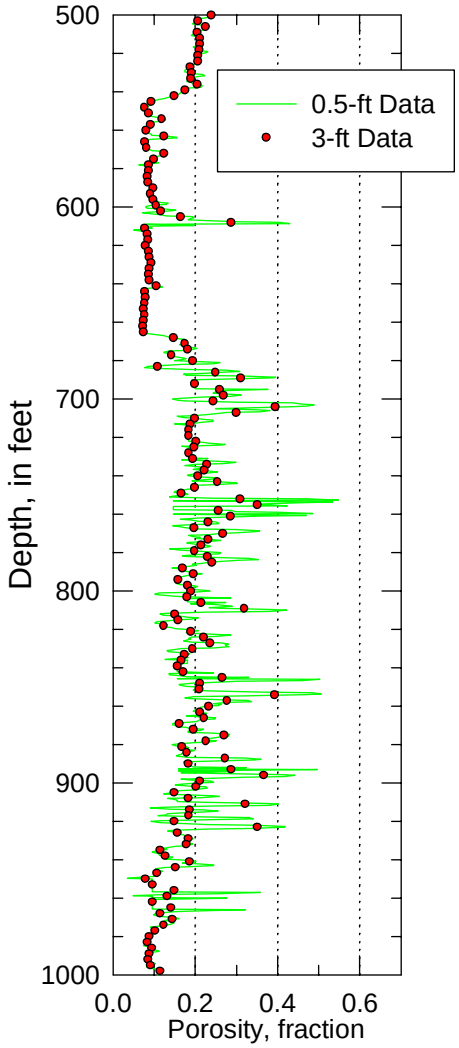

Figure 14. Comparison of original 0.5- and 3.0-ft resampled petrophysical porosity profiles for a portion of drill hole UZ-16 containing both lithophysal and nonlithophysal welded tuff.

more often than not at Yucca Mountain, particularly in the welded Topopah Spring Tuff, the gamma-ray source and/or the detector may separate from the rock mass allowing the detection of direct gamma radiation not backscattered by the formation. Alternately breaking away from and recontacting the borehole wall produces intermittent very large-amplitude readings indicating functionally zero density (infinite porosity). Although such anomalous data spikes are quite readily identified, the protocol for processing the raw petrophysical measurements into porosity values called for replacing the meaningless values with a *missing-value code* (typically a very large negative number), thus maintaining a sequence of regular depth values rather than deleting the data point entirely from the data set. As a consequence, an automated resampling algorithm could easily encounter a thick interval of spiky data and, simply by the luck of the draw, produce a long sequence of nothing but missing values, even though there were many valid porosity values within the interval.

Statistical Description

Porosity

Upper Paintbrush Nonwelded (PTn) Model Unit

Porosity data obtained from the upper Paintbrush nonwelded (PTn) model unit are portrayed in histogram and cumulative distribution function format in figure 15. A statistical summary of these data is given in table 6. Comparison of data for relative-humidity-oven and 105°C-oven dried samples, and of the total versus water-filled or effective geophysical porosity indicates that there is a large quantity of loosely bound structural water associated with some of the measured values. The implication is that hydrous-mineral alteration appears to be significant in the PTn model unit. However, the milestone schedule and defined scope of work for fiscal-year 1997 modeling activities did not allow separate investigation (and modeling) of altered and unaltered portions of the PTn model unit.

Topopah Spring Welded (TSw) Model Unit

Porosity values obtained from the Topopah Spring welded (TSw) model unit are presented graphically in figure 16; the corresponding statistical summary of these data is presented in table 6. Examination of the raw porosity data indicates that there are two different “porosity” values of interest in modeling rock material properties: “matrix” and “lithophysal.” *Lithophysal porosity*, as that term is used in this report, is taken to mean the porosity of volumes of rock many tens of centimeters in diameter, such that the porosity effect of large (centimeter scale and larger) lithophysal cavities is included. In contrast, the term *matrix porosity* is used in this report to refer to the porosity equivalent to that measured for laboratory core samples, in which the size of the matrix pores is small

enough that water is held in them under slightly unsaturated (negative pressure) conditions.

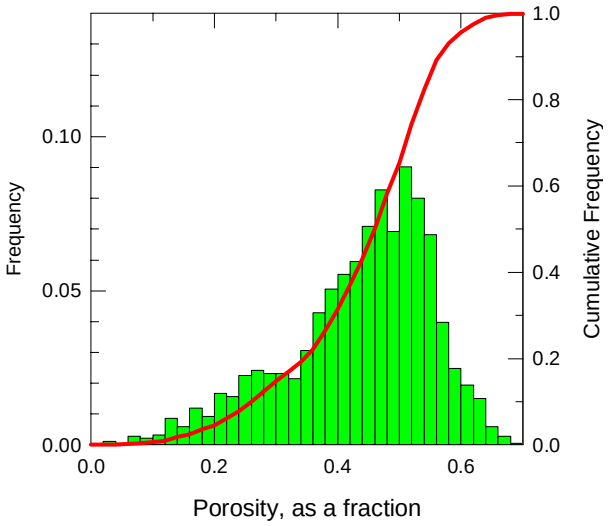

Figure 15. Histograms and cumulative distribution functions of porosity values for samples from the PTn model unit.

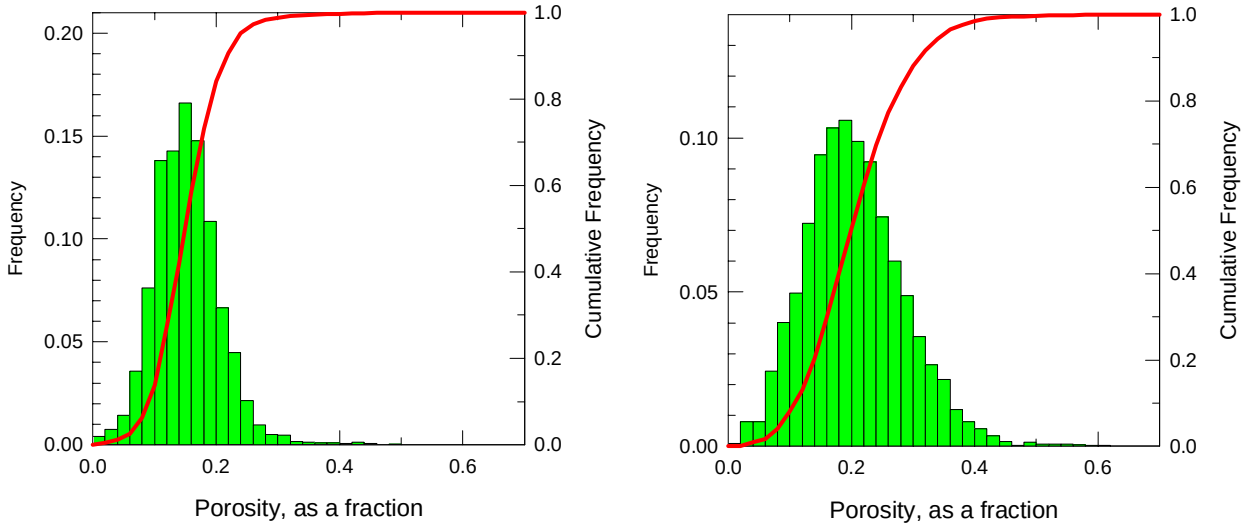

Figure 16. Histograms and cumulative distribution functions of porosity for (a) matrix and (b) lithophysal porosity values from the TSw model unit.

The difference between the two types of porosity measurements is not trivial, as illustrated in figure 17, a comparative down-hole plot of matrix and lithophysal porosity data from drill hole USW SD-7. Lithophysal porosity is indicated by the dark solid curve, whereas the matrix porosity values measured for core samples are indicated by the lighter curve with filled-circle symbols. Note the marked divergence of the porosity values indicated by these two sets of data in two vertical loca-

Table 6: Statistical summary of total porosity data used in modeling
[All values are porosity as a fraction except number of data]

	PTn	TSw		CH-PP		
		Matrix	Lithophysal	All Data	Unaltered	Altered
Mean	0.437	0.152	0.205	0.322	0.309	0.323
Std.Dev.	0.118	0.053	0.080	0.086	0.088	0.074
Minimum	0.034	0.011	0.010	0.029	0.029	0.110
Maximum	0.742	0.553	0.616	0.630	0.537	0.630
N	1863	8195	8854	4824	2878	1525

tions within the drill hole. In general, these zones of divergence correspond to the two lithophysal zones (upper and lower) defined by Buesch and others (1996). However, the correspondence is *not* at all exact, and the total (= "lithophysal") porosity curve from downhole geophysics indicates that substantial lithophysal cavity development must extend significantly above and below the limits of the formally named "lithophysal zones" (fig. 17; see also the individual drill hole plots of Appendix B). A scatterplot of these total/lithophysal porosity values versus the depth-equivalent core/matrix porosity is presented in figure 18, part (a). The region of marked divergence from the 45° one-to-one correspondence line represents high lithophysal (total) porosities matched on a nearest-sample basis to the lower matrix (core) porosity values.

Note also the third set of data plotted in figure 17; this curve is identified as "water-filled" porosity and is shown by the dashed line without symbols. This third curve is observed essentially to overlie the true matrix (= core) porosity data throughout much of the drill hole. In locations where the water-filled porosity trace does not closely match the core values, it is always observed to indicate markedly lower values than the solid total/lithophysal porosity curve. The near-equivalence of core and water-filled porosity values is demonstrated in part (b) of figure 18.

Because many drill holes lack core data from which to obtain matrix porosity for modeling purposes, we have adopted a practice (for those holes only) of identifying lithophysal intervals (as distinct from formal lithophysal zones) in those *non-cored* holes using separation of the water-filled and total porosity traces. Outside these lithophysae-bearing intervals, matrix porosity is set equal to total porosity, whereas within these intervals of curve separation, matrix porosity is set equal to the water-filled porosity values.For example, figure 19 is a scatterplot equivalent to part (a) of figure 18 for drillhole WT-2, only in this case the "matrix" porosity measurement is the water-filled porosity derived from the epithermal neutron porosity log. The behavior of the total/lithophysal porosity values in these two illustrations with respect to matrix/core porosity and its petrophysical surrogate is strikingly similar.

It is clear that this practice is merely a simple heuristic device, and that use of the water-filled values unquestionably will underestimate the actual matrix porosity within the unsaturated zone for the simple reason that all the available pore space in the unsaturated zone is not water filled. However, we believe that this approach is a reasonable approximation for several reasons. (1) Water saturation throughout much of the Topopah Spring Tuff is rather high, typically greater than about 80 percent. (2) The water-filled porosity values in zones of significant lithophysal cavity development are much closer to the true matrix porosity than are the lithophysal porosity values, which can be observed from figure 17 and 18 to be as much as double the matrix (core) porosity values for drill hole USW SD-7. And finally, (3) because one of the purposes of modeling the spatial heterogeneity of porosity is to attempt to model the variability of saturated hydraulic conductivity using porosity as a surrogate, the water-filled porosity data (at any in-situ saturation) most likely represents essentially all the pore space that is available for the transmission of water under unsaturated conditions.

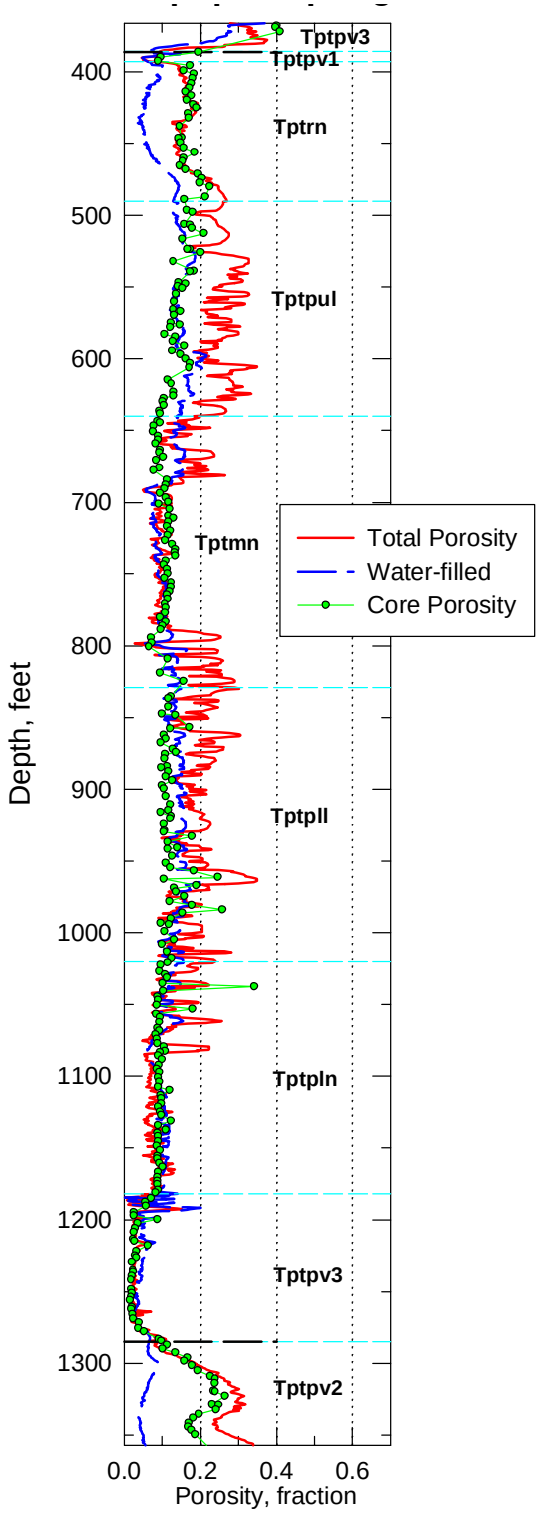

Figure 17. Comparison of different types of porosity data for drill hole USW SD-7. Horizontal dashed lines indicate lithostratigraphic units as defined by Buesch and others (1996); see also the YMP Stratigraphic Compendium (Clayton, 1996).

Note that it is possible to significantly underestimate the saturated hydraulic conductivity under true saturated conditions in this manner. However, as a practical matter, the discrepancy between the true matrix porosity and the water-filled porosity heuristic device is important essentially only in the crystal-rich nonlithophysal (Tptrn) top portion of the Topopah Spring welded model unit (fig. 17, depths of 400–500 ft). This relatively high stratigraphic interval almost invariably is present in the ***un***saturated zone throughout the entire modeled region.

Evaluation of the differences between relative humidity oven dried and 105°C dried core porosity values indicates that hydrous-phase minerals are of very modest extent within the densely welded rocks of the TSw model unit. This conclusion is compatible with other observations, which indicate that the vast majority of the Topopah Spring welded interval was devitrified and locally recrystallized by vapor-phase alteration during cooling of the originally hot pyroclastic-flow deposit. The mineral assemblages formed by these types of early alteration typically are not susceptible to zeolitization or clay formation.

Calico Hills-Prow Pass (CH-PP) Model Unit

A similar histogram and cumulative distribution function of total porosity values obtained from the combined Calico Hills–Prow Pass (CH-PP) model unit are presented in figure 20, and a statistical summary of the values is in table 6. Evaluation of individual differences between relative humidity oven dried and 105°C dried core samples and between total and "water-filled" porosity values from petrophysical logs indicates, as does independent geologic evidence, that hydrous-phase minerals are a major component of rocks from this composite geologic interval. Mineralogical data (Bish and Vaniman, 1985; Chipera and others, 1996[†]) indicates that the vast majority of hydrous-phase minerals present at these deeper stratigraphic

[†]Chipera, S.J., Vaniman, D.T., and Bish, D.L., 1996, Zeolite abundances and the vitric-to-zeolitic transition in drill holes USW SD-7, 9, and 12, Yucca Mountain, Nevada: Report LA-EES-1-TIP-96-005, Yucca Mountain Project Milestone LA4240, Los Alamos National Laboratory, Los Alamos, N. Mex., 20 p.

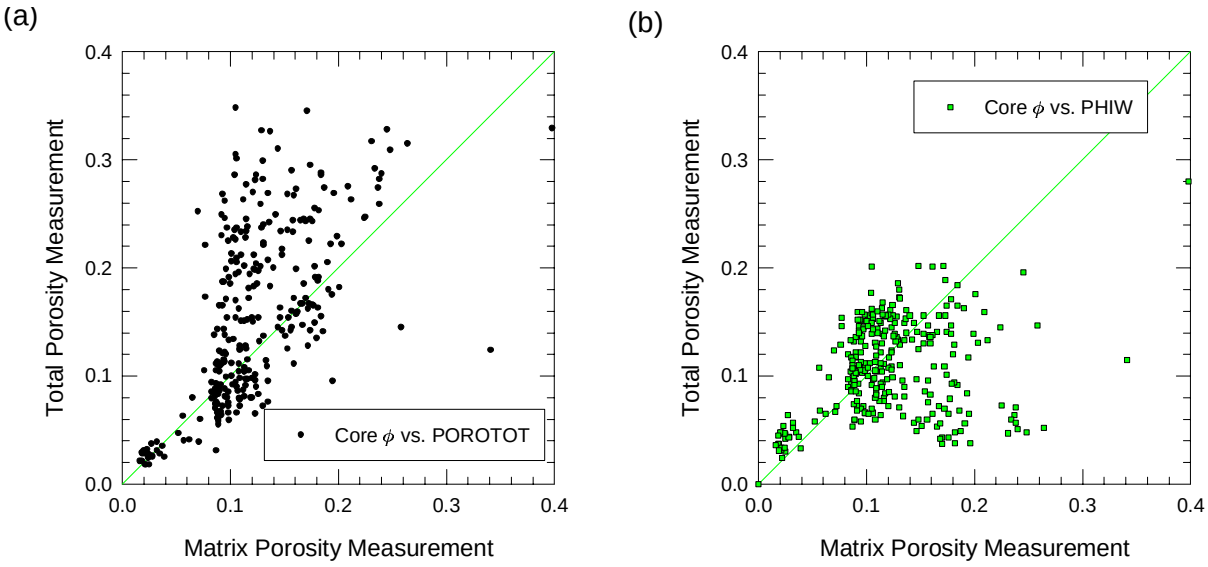

Figure 18. Crossplots of (a) total porosity vs. matrix porosity and (b) core porosity vs. water-filled petrophysical porosity for drillhole SD-7. Light grey line indicates one-to-one correspondence.

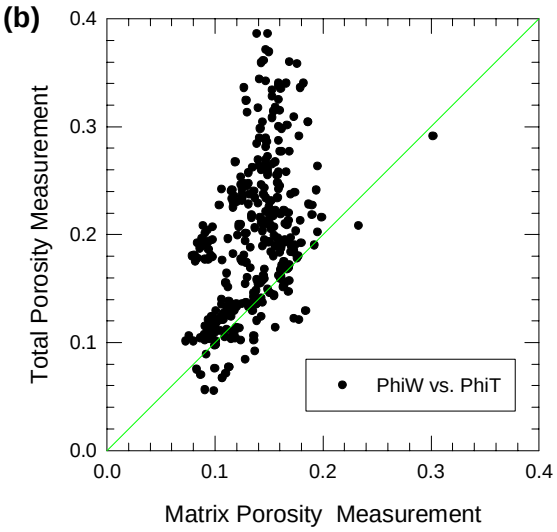

Figure 19. Crossplot of a surrogate "matrix" porosity vs. total porosity for drillhole WT-2. Light grey line indicates one-to-one correspondence.

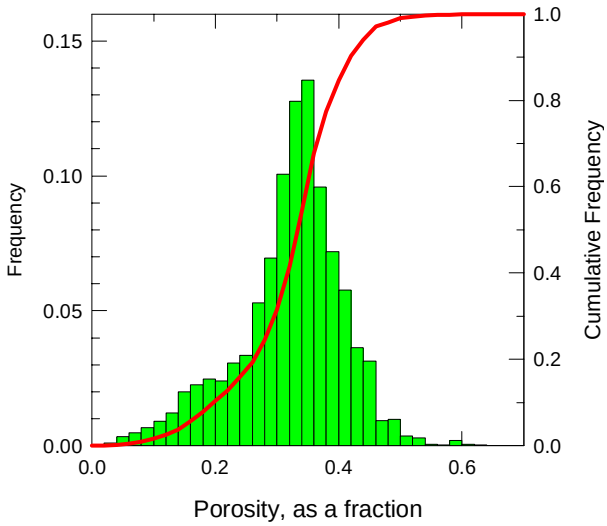

Figure 20. Histograms and cumulative distribution functions of total porosity for samples from the Calico Hills-Prow Pass model unit

levels are zeolites. No attempt has been made to distinguish different zeolite minerals, as these identifications cannot be made simply based on the presence of structurally bound water. Histograms of porosity from unaltered and hydrous-phase altered tuffaceous materials in the Calico Hills-Prow Pass model unit are shown separately in figure 21; corresponding statistical summaries are presented in table 6.

Bulk Density

The histogram and cumulative distribution function for (dry) bulk density values measured for core samples dried at 105°C are shown in figure

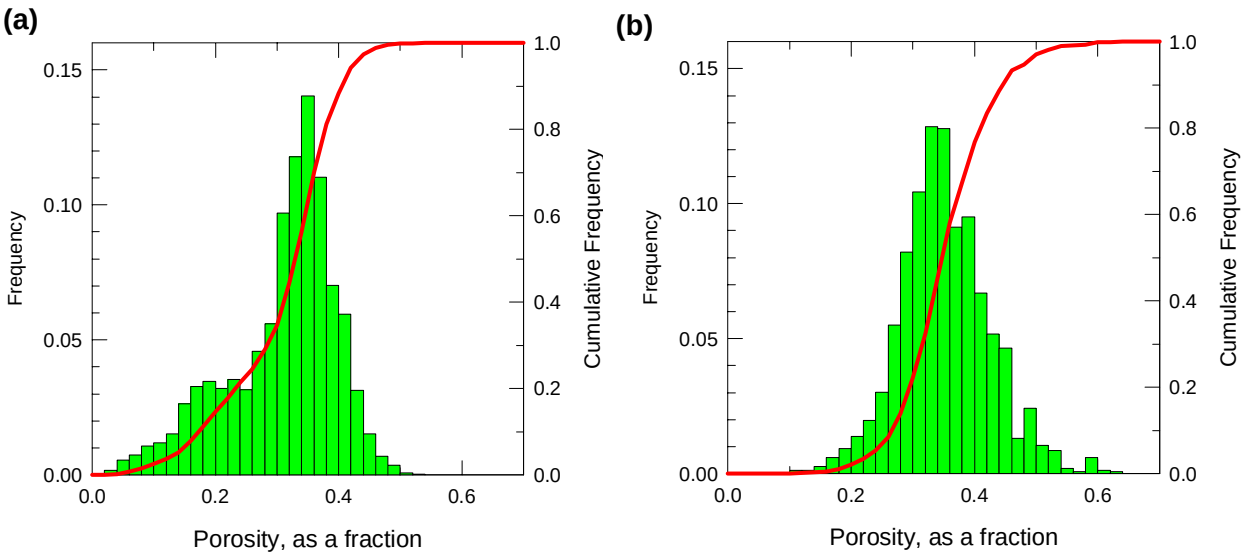

Figure 21. Histograms and cumulative distribution functions of porosity for 105°C-dried samples of (a) unaltered and (b) altered rocks from the Calico Hills-Prow Pass model unit.

22(a). A statistical summary of the bulk density values is presented in table 7. The correlation of these bulk density values with 105°C-dried porosity values measured on the same physical specimens is presented in part (b) of figure 22. Note that the points on the scatterplot are identified separately as originating from altered or unaltered materials, as determined by a separation of more than 5 porosity percent between the 105°C- and the relative humidity oven-dried porosity measurements. Although there is a suggestion of a slightly different relationship between the two different types of materials, the exceptionally high coefficient of determination ($r^2 = 0.972$) for the data considered as a whole, combined with the relative unimportance of bulk density as a flow-and-transport modeling parameter, led us to neglect alteration in modeling the spatial distribution of bulk density. Other authors, notably Istok and others (1994) and Flint (in review), have noted similar excellent correlations of bulk density with porosity as well.

Table 7: Statistical summary of bulk density data from core samples from all model units

	Bulk Density (g/cm^3)
Mean	1.972
Std.Dev.	0.367
Minimum	0.8162
Maximum	2.509
N	4888

Saturated Hydraulic Conductivity

A histogram of the available laboratory-measured saturated hydraulic conductivity data is presented in figure 23. A statistical summary of these data is in table 8, and a scatterplot of these same data against the corresponding porosity values is shown in part (b) of the figure. Note that whereas the correlation between bulk density and porosity shown in figure 22 is based on measurements obtained on the exact same physical specimen, this approach is not possible because the specimens used for hydraulic conductivity testing do not have associated total porosity values (measured after 105°C oven drying). Flint (in review) reports instead only the relative humidity oven dried porosities measured on the hydraulic conductivity plugs. Indeed, Flint's work demonstrates that the most suitable type of porosity measurement for

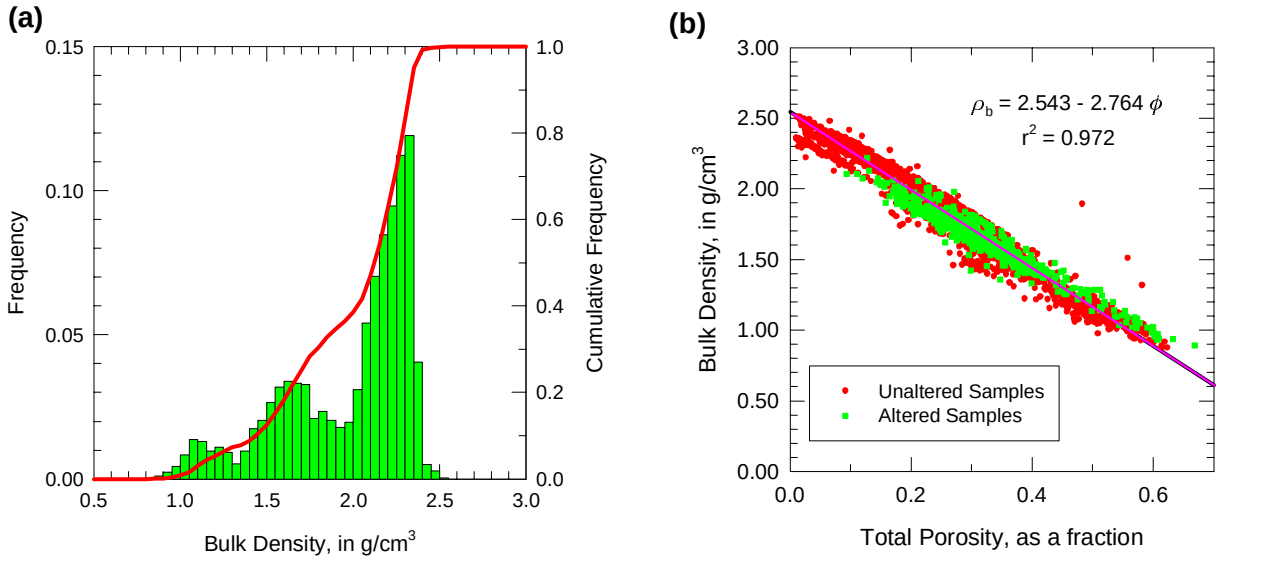

Figure 22. (a) Histogram and cumulative distribution function for bulk density measured in the laboratory on core samples dried at 105°C. (b) Cross-plot of bulk density and porosity as measured in the laboratory on core samples dried at 105°C. Distinction of "altered" and "unaltered" samples is based on the relationship: $\phi_{OD} > \phi_{RH} + 0.05$ (see text).

predicting saturated hydraulic conductivity is the RH-dried porosity. Unfortunately, although the petrophysical porosity data computed by Thompson and Rael (1996) include values of "effective porosity" [equation (13)] similar to the RH core measurements, the values computed by Nelson (1996) do not. Because the values of Nelson for the WT-series of drill holes are critical to modeling the extended site area (see figs. 8–10), we chose to rely on the correlation of hydraulic conductivity with total porosity rather than mix porosity measurements of different types.

Because Flint (in review) pursued a systematic sampling strategy whereby the specimens for hydraulic conductivity determinations were cut from samples taken immediately adjacent to specimens used for the full suite of bulk properties (ρ_b, ϕ_{RH}, $\phi_{105°C}$), the additional error introduced by using the correlation with the nearest 105°C-dried porosity value is believed to be small. Figure 24(a) is a cross plot of the relative humidity oven dried porosity values measured for the hydraulic conductivity specimens vs. the relative humidity oven dried porosity values of the immediately adjacent bulk-properties specimen. The grey solid line on the figure indicates one-to-one correspondence. Figure 24(a) indicates that there are differences between the two values that represent very small scale (order of centimeters) heterogeneity and/or measurement errors; the coefficient of determination (r^2-value) associated with the crossplot is 0.914. However, the differences in porosity value are fairly unbiased (the porosity of the adjacent sample is about equally likely to be higher than that of the hydraulic conductivity specimen as it is to be lower). Note that at the high-porosity end of the specimen, there may be a slight tendency for the porosity of the hydraulic conductivity specimen to be lower than that of the adjoining bulk-property specimen. In general, the agreement of the two porosity values is quite good, and the error induced by using the "nearby" 105°C porosity values probably is less than it would be by mixing RH and 105°C porosity values in the prediction because the 105°C values are systematically higher than the associated RH value [fig 24(b)].

Several things are notable about the hydraulic conductivity data. First, the laboratory measurements are characterized by a very significant number of "non-detect" values, indicated by the off-scale histogram bar at the left side of figure 23(a). Reference to the cumulative frequency axis

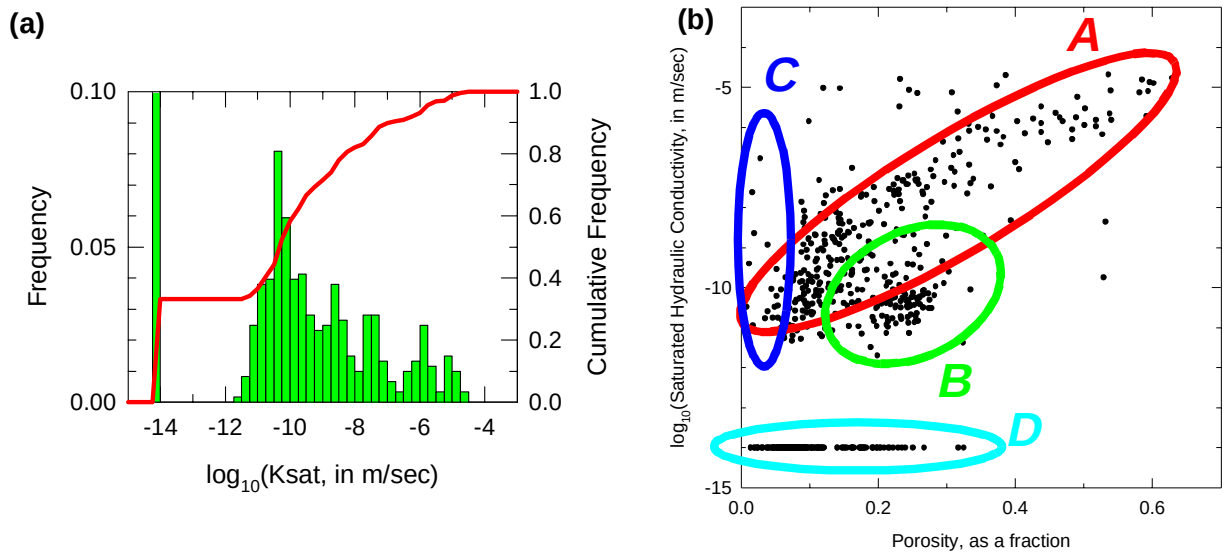

Figure 23. (a) Histogram and cumulative distribution function and (b) scatter plot for all laboratory-measured saturated hydraulic conductivity data versus matrix porosity. Note indicated clustering of data in (b). Labeled ellipses identify clusters of data discussed in text.

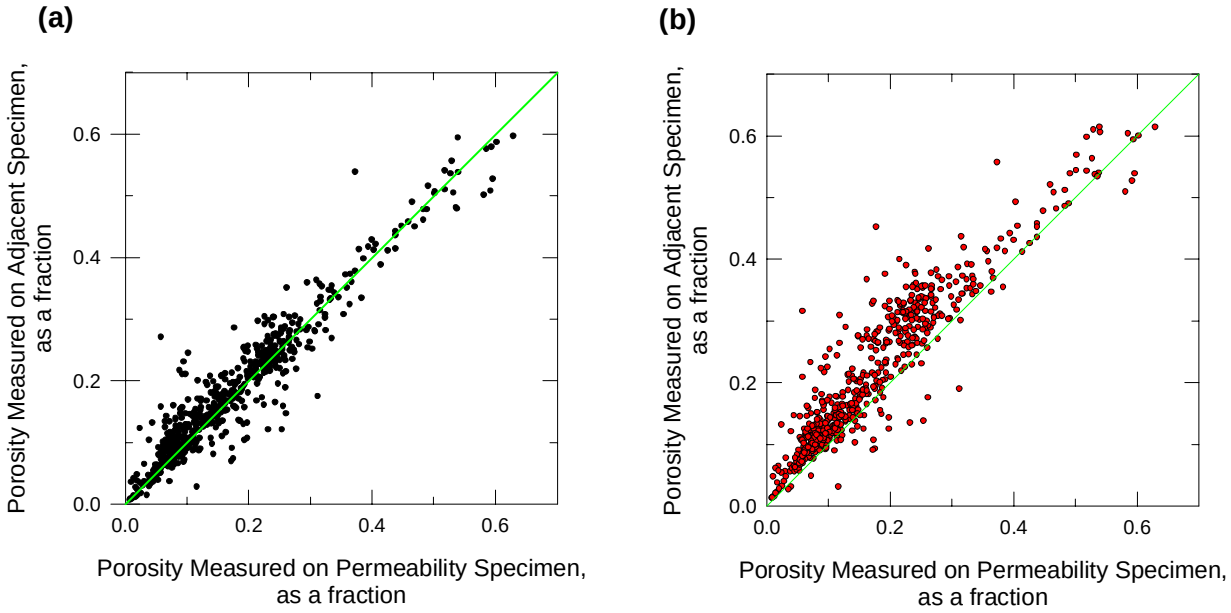

Figure 24. Scatterplot of (a) relative humidity oven dried and (b) 105°C oven dried porosity values measured on adjacent physical specimens. Light-grey line indicates one-to-one correspondence.

for the same figure indicates that approximately 35 percent of the physical specimens tested in the laboratory yielded no measurable flow. These samples have been assigned an arbitrary value of 10^{-14} m/sec for plotting purposes only. However, this treatment of the no-flow samples greatly complicates statistical description of hydraulic conductivity. As table 8 indicates, the values computed as part of a

Table 8: Statistical summary of saturated hydraulic conductivity data used in modeling
[Altered–unaltered distinction identified using difference between relative humidity and 105°C dried porosity values; see text. All units are $\log_{10}$meters per second except number of samples]

	No-flow Samples Ignored			No-flow Samples Set to -14.0		
	All Data	Unaltered	Altered	All Data	Unaltered	Altered
Mean	-8.9553	-8.6431	-9.7522	-10.6285	-10.5512	-10.8555
Std.Dev.	1.7317	1.7174	1.5034	2.7664	2.9141	2.2719
Minimum	-11.7086	-11.3360	-11.7086	-14.0000	-14.000	-14.0000
Maximum	-4.6866	-4.6955	-4.6866	-4.6866	-4.6955	-4.6866
N	405	291	114	606	452	154

statistical summary of these data are dependent on the value assigned to the no-flow samples. For example the "average" conductivity of the flowing samples is –8.9553 in $\log_{10}$ meters per second, whereas the "average" of all samples including the non-flowing ones is –10.6285 (log space), assuming the no-flow conductivity value of –14.0 used in plotting figure 23(b). However, one could generate practically any mean conductivity value desired simply by changing the conductivity assigned to the non-flowing samples, which is to a large extent related simply to the physical limits of the permeameter used for the measurements. Another interesting feature of the hydraulic conductivity data, shown in figure 23(b), is the presence of at least three somewhat distinct clusters of porosity-conductivity values, as suggested by the ellipses superimposed on the scatterplot. Note that ellipse *D* simply corresponds to the spike of no-flow samples already described.

The clusters of samples indicated as *A* and *B* in figure 23(b) correspond essentially to "unaltered" and "altered" rock types (respectively), defined as the absence or presence of zeolite (plus or minus clay) minerals. Figure 25 presents these two clusters of samples using more precise criteria for alteration. Figure 25(a) and (b) are for samples separated into unaltered and altered classes using more-or-less macroscopic criteria by Flint (in review), who developed a set of hydrogeologic units based principally (but not wholly) on the lithostratigraphic-unit classification of Buesch and others (1996). Flint ultimately assigned each laboratory specimen tested to a specific matrix-property hydrogeologic unit, and the designators for these different units have been used directly in generating these figures. Figure 25(c) and (d) present the same sample data, only here the discrimination of unaltered and altered is based on differences in sample behavior between relative humidity oven drying at 60°C and 65-percent RH and at 105°C with RH ~ 0 [see text associated with equation (1) on page 23].

Comparison of the two sets of figures indicates that subdivisions based on the two different criteria are nearly identical. Unaltered samples [parts (a) and (c) of fig. 25] exhibit a strong dependence on porosity whereas altered samples [parts (b) and (d)] show much less dependency on porosity. Histograms corresponding to these different subpopulations are presented in figure 26. Parts (a) and (c) of the figure are for unaltered samples, and parts (b) and (d) are for the altered ("zeolitized") samples. The univariate population characteristics for the two classification methods are virtually identical.

Figure 27 is a similar comparison of scatterplots and histograms for the cluster of samples identified as cluster *C* in figure 23. These samples are essentially all from the vitrophyric units that over- and underlie the main welded phase of the Topopah Spring Tuff (matrix hydrogeologic units 12 and 19, Flint, in review; units Tptrv1, Tptpv3, Buesch and others, 1996). Part (a) of the figure simply uses the Flint unit codes as the basis for selecting the samples from the overall saturated hydraulic conductivity data set, however, part (b) was constructed using a criterion of porosity < 0.05. Again, the populations identified by the hydrogeologic-unit and the material-property approaches are virtually identical. Flint (in review)

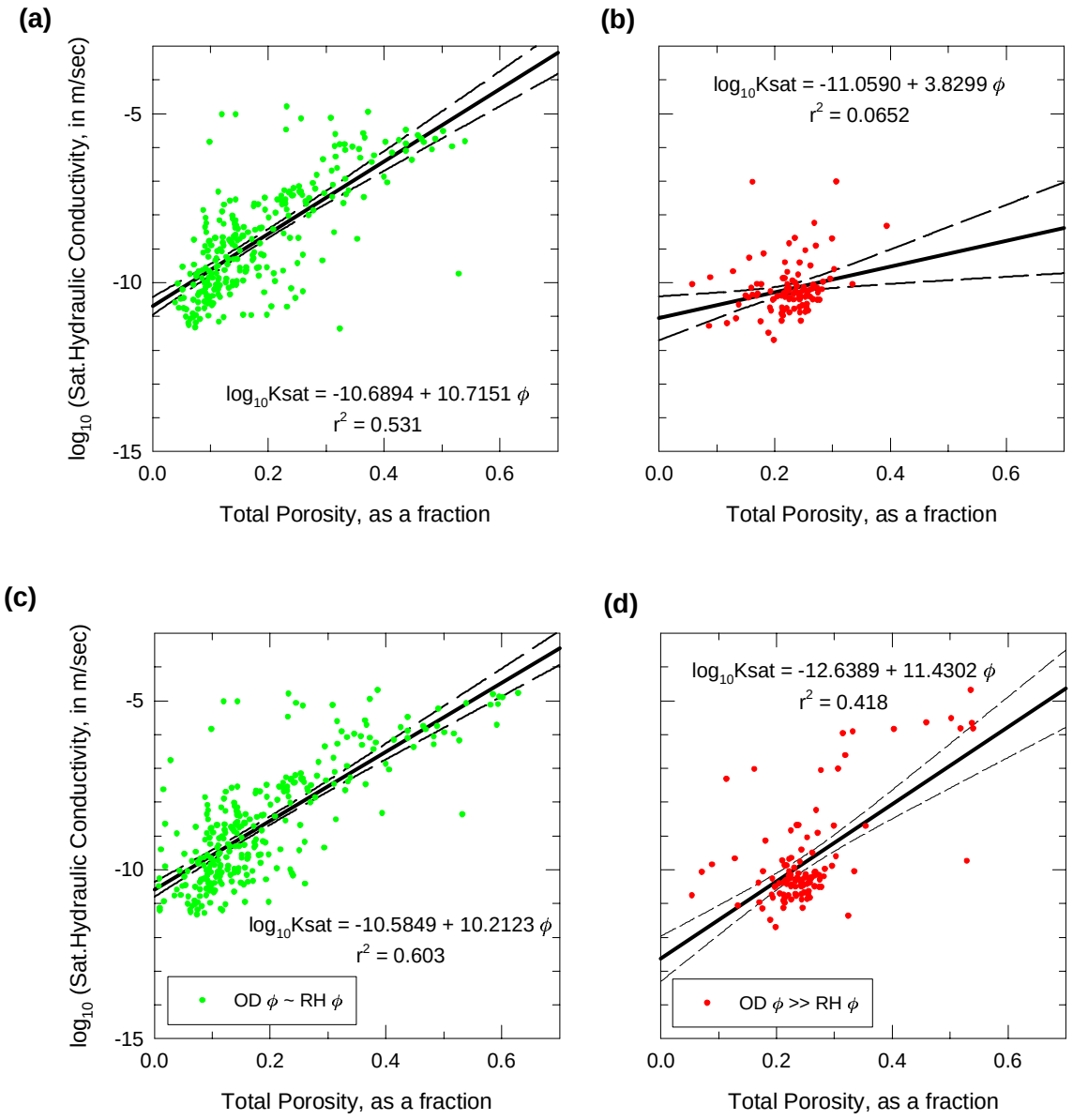

Figure 25. Scatterplots of saturated hydraulic conductivity as a function of porosity for samples separated on the basis of "alteration." (a) Unaltered and (b) altered samples discriminated using the alteration-unit codes of Flint (in review); (c) unaltered and (d) altered samples discriminated by differences in relative humidity oven vs. 105°C drying. Heavy solid line is regression fit; dashed lines are 95-percent confidence bounds.

attributed the high and quite variable hydraulic conductivity values exhibited by these low-porosity rocks to the presence of microfractures in these dominantly glassy materials, and it is quite likely that some of the higher hydraulic conductivity values exhibited for the lower-porosity samples shown in figure 25 are the result of microfracturing as well.

The ability to discriminate populations with different hydraulic conductivity characteristics using porosity extends the use of porosity-as-a-surrogate to a higher level than simply developing pre-

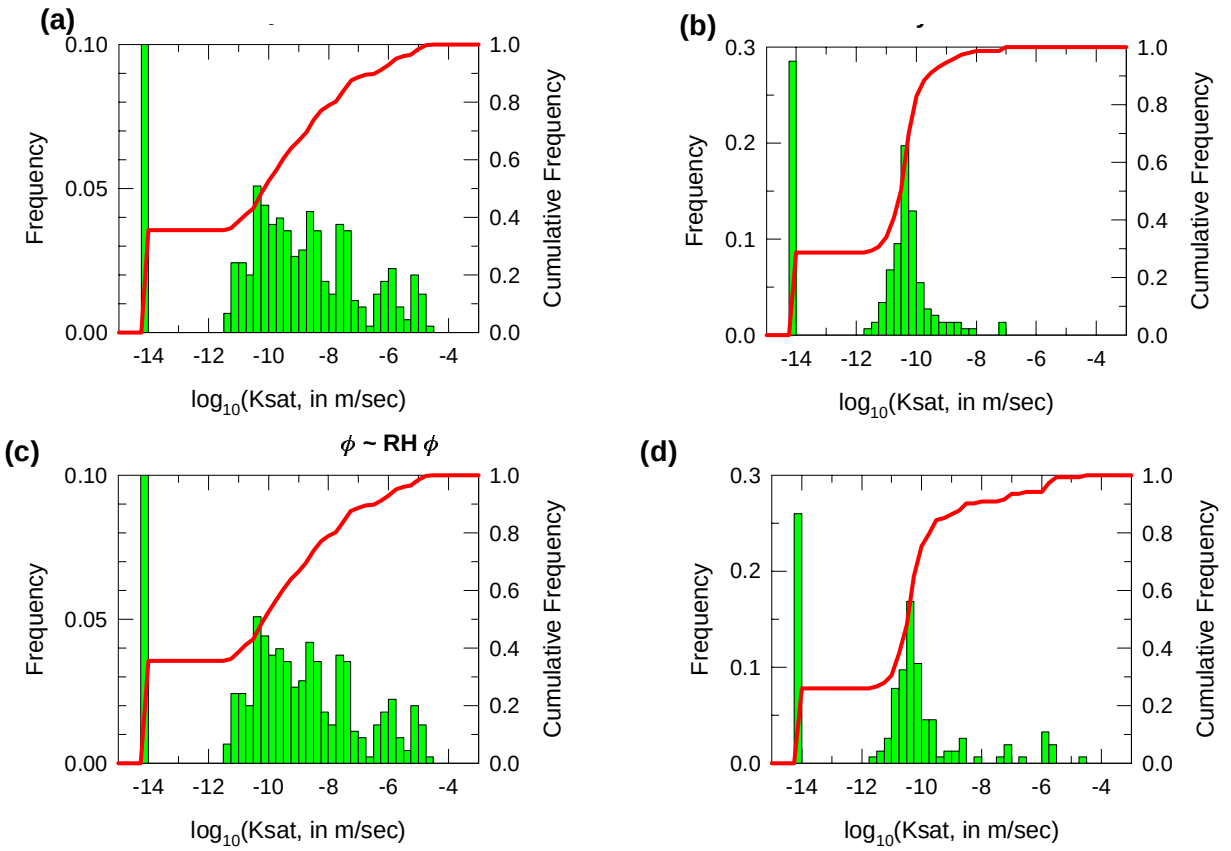

Figure 26. Histograms and cumulative distribution functions for (a) unaltered and (b) altered samples identified by matrix property hydrogeologic unit designator, and for (c) unaltered and (d) altered samples identified by differences in RH and OD behavior.

dictions of hydraulic conductivity based on a correlation with porosity. As originally suggested in figure 2, and as described in greater detail in the section on Development of the Models, the subdivision of rock-type classes based on porosity is crucial to the modeling activities described in this report.

Thermal Conductivity

Thermal conductivity and porosity data have been obtained from a modest number of samples collected from the PTn and TSw model units (Brodsky and others, 1997). Figure 28(a) presents a histogram and cumulative distribution function of the available thermal conductivity data measured at 70°C and under 105°C-dried saturation conditions. The values plotted in figure 28(b) clearly indicate a dependency on porosity, which is as expected given that the thermal conductivity of a material is closely related to its bulk density and that porosity is inversely related to bulk density in the non-zeolitized tuffs. Note, however, that *this sample suite is distinctly separate* from that used for the remainder of the bulk and hydrologic properties in this report. There are virtually no thermal conductivity data available for zeolitized tuff. A statistical summary of the available thermal conductivity data is given in table 9.

There are two major difficulties in using the existing thermal conductivity data. First, the in-situ bulk density of the Topopah Spring welded unit is most directly related to the lithophysal porosity of this unit, not to the matrix porosity. Open cavities too large to be measured as part of the matrix porosity laboratory procedure (or its petrophysical equivalent) will significantly reduce the bulk density, leading to lower *effective* thermal conductivity. Figures 17 to 19 indicate that lithophysal

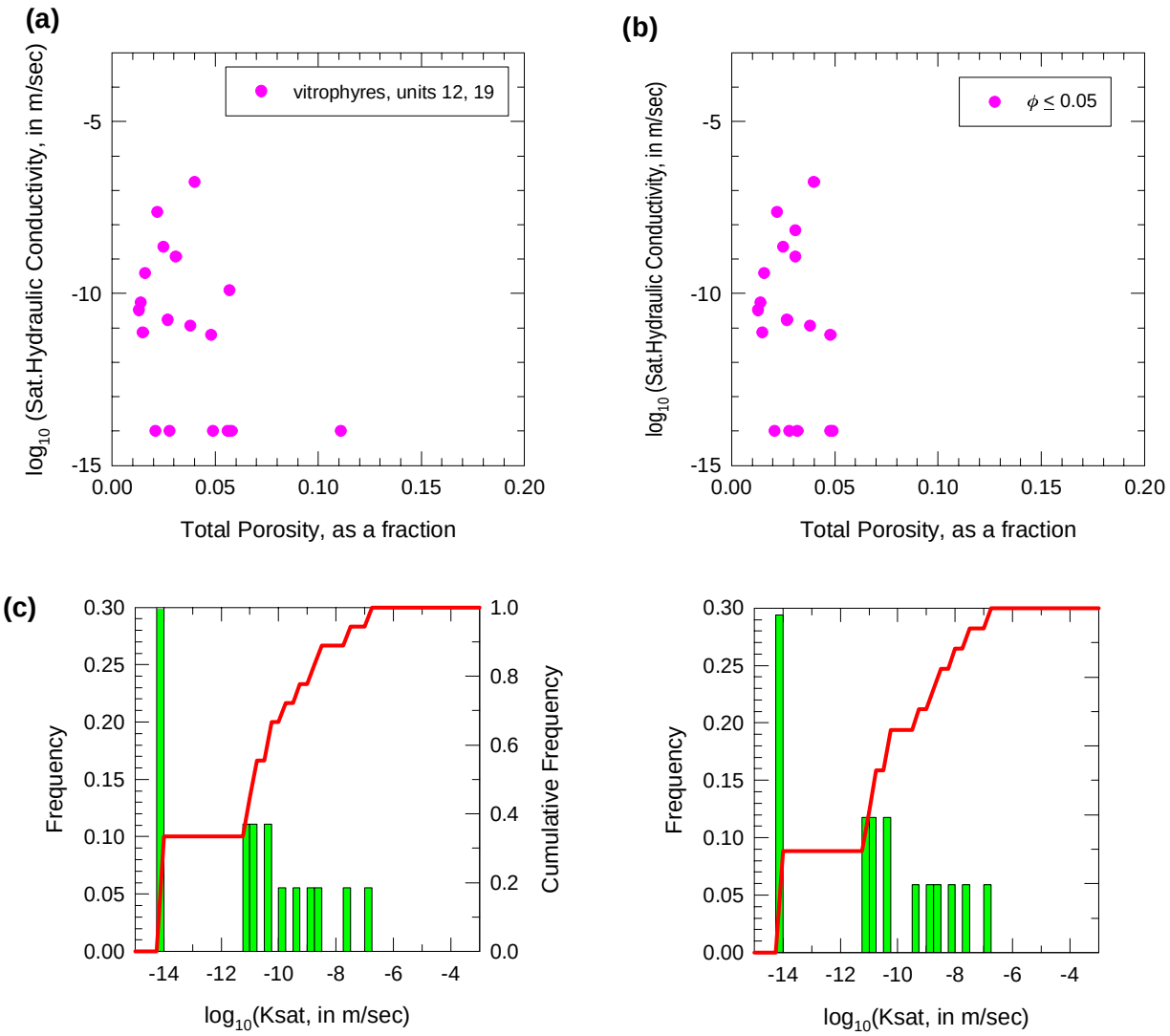

Figure 27. Scatterplots of saturated hydraulic conductivity vs. porosity for (a) vitrophyre samples corresponding to matrix hydrogeologic units of Flint (in review) and (b) samples with porosity < 0.05. Histograms and cumulative distribution functions for (c) vitrophyre samples corresponding to matrix hydrogeologic units of Flint (in review) and (d) samples with porosity < 0.05.

porosity values can be greater by a factor of two compared to the depth-equivalent matrix porosity values. Use of this factor-of-two porosity difference applied to the regression relationship shown in figure 28(b) would lead to the over-prediction errors of roughly 30–50 percent for thermal conductivity, depending on the actual porosity level considered.

A second, rather severe difficulty with the available thermal conductivity data is that the density of sampling is not great (a maximum of 52 samples; see table 9), and furthermore, those samples are highly biased both spatially and toward low-porosity materials. (1) Two of four drill holes that were sampled for thermal conductivity specimens, although located within the extended site area, are actually located some distance from the repository block itself (NRG-4, NRG-5). (2) The sampling vertically within a given drill hole is not at all systematic, and in fact, the vertical distribution of samples cannot at all be considered "representative" of the entire Topopah Spring welded model unit. (3) The only samples that represent the

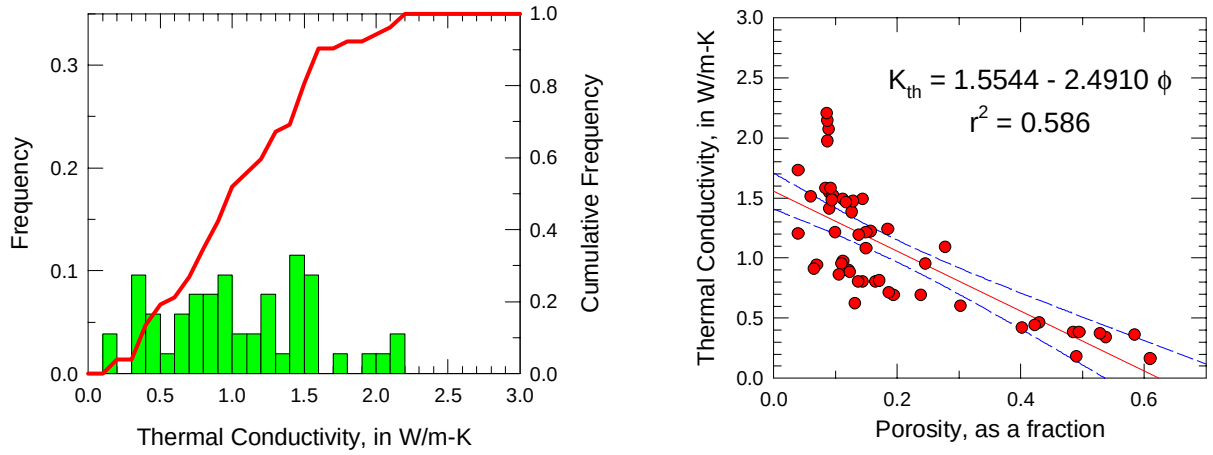

Figure 28. (a) Histogram and cumulative distribution function for thermal conductivity. (b) Scatterplot of thermal conductivity as a function of total porosity. All thermal conductivities measured at 70°C and 105°C dried conditions. Solid line in (b) is regression fit; dashed lines are 95-percent confidence interval.

Table 9: Statistical summary of all measured thermal conductivity data from non-zeolitic rock samples at Yucca Mountain

[All units are watts per meter-Kelvin, except porosity as a fraction and number of tests]

	Thermal Conductivity @ 70°C			Porosity (105°C)
	All Rock Units		TSw Only	
	Saturated	105°C Dried		
Mean	1.772	1.054	1.241	0.197
Std.Dev.	0.524	0.516	0.427	0.156
Minimum	0.730	0.160	0.620	0.040
Maximum	3.090	2.200	2.200	0.610
N	49	52	35	54

higher porosity values (needed to model the effect of lithophysal cavities on heat conduction) are taken from the PTn model unit, and thus represent nonwelded tuffs rather than the lithophysal portion of welded materials.

With respect to the several biases known to exist in the thermal conductivity data, consider figure 29, which is a histogram of the 54 porosity values measured on the thermal conductivity test specimens. Comparison of this figure with the histogram of all porosity data measured from the Topopah Spring welded unit (fig. 16) clearly indicates the extent of the sampling bias. First, figure 29 is clearly bimodal, representing, as it does, samples from both welded and nonwelded rock types. If we discount the group of samples with porosities higher than about 40 percent, the mode corresponding to the welded Topopah Spring samples is strongly skewed to lower porosity values. For example, the approximate modal value in figure 29 is 8–10 percent, whereas the modal value of the entire TSw model unit is 14–16 percent for matrix porosity and 18–20 percent for the lithophysal porosity; these latter values represents the type of

porosity measurement that would be expected to control the thermal conduction properties.

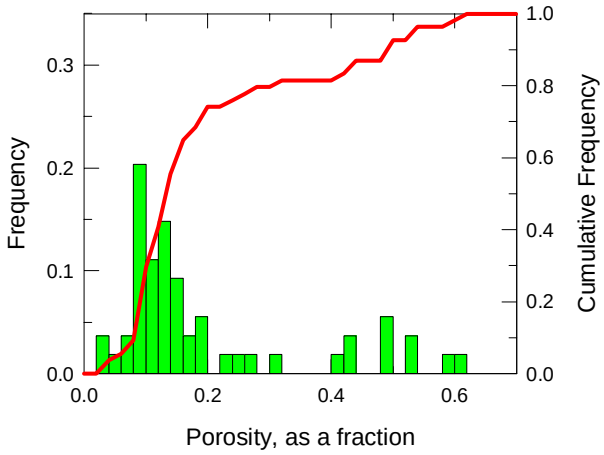

Figure 29. Histogram and cumulative distribution function of total porosity values measured for thermal conductivity test specimens.

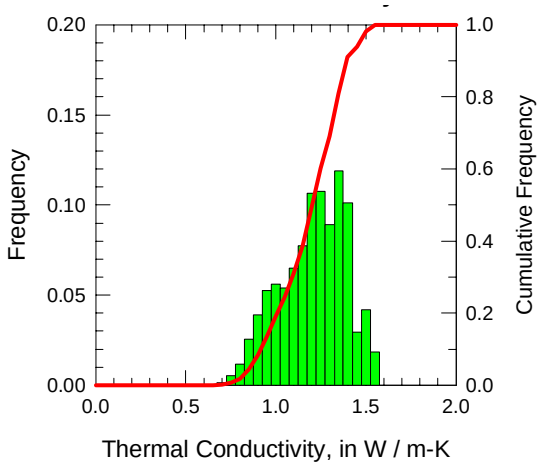

Figure 30. Histogram and cumulative distribution for thermal conductivity systematically predicted from lithophysal porosity values in drill holes USW SD-7, SD-9, and SD-12 using regression equation from figure 28(b).

We have attempted to reduce the impact of these sampling biases in the following manner. First, we assume that the regression relationship presented in the scatter plot of figure 28(b) is a valid predictor of thermal conductivity across the range of porosity values appropriate for the TSw model unit. We then predict thermal conductivity from the systematically sampled (nominal 3-ft spacing) porosity data available for three drillholes located within the footprint of the potential repository (USW SD-7, -9, and -12; fig. 31). We then aggregate these three sets of predicted values and compute the appropriate statistical quantities and histograms (fig. 30; table 10). Note that although the average thermal conductivity for both the 35 measured samples of the Topopah Spring welded model unit and the predicted thermal conductivity of the TSw unit as a whole (table 10) are remarkably similar at approximately 1.2 w/m-K, the thermal conductivity of major portions of the unit differ markedly from one another (fig. 31).

Table 10: Statistical comparison of measured and predicted thermal conductivity data for the Tsw model unit

[All units are Watts per meter-Kelvin, except number of tests]

	Measured Thermal Conductivity @ 70°C	Predicted Thermal Conductivity @ 70°C
Mean	1.241	1.183
Std.Dev.	0.427[a]	0.182[b]
Minimum	0.62	0.676
Maximum	2.200	1.550
N	35	6063

a. also includes effect of measurement errors and lithologic variability
b. includes effect of lithologic variability only

"Zeolite" Alteration in the Calico Hills–Prow Pass Unit

Alteration as a category was modeled only in the combined Calico Hills–Prow Pass model unit. Figure 32 is a histogram and cumulative distribution function for the binary alteration indicator flags from the Calico Hills–Prow Pass model unit. The relevant summary statistics for alteration category are presented in table 11. As described in the section on *Measurement Methods* beginning on page 23, the indicator alteration flag defined using the different types of porosity measurements is not truly a *mineralogic* indicator of the presence or absence of zeolites. However, the dominant hydrous-phase mineral present at these strati-

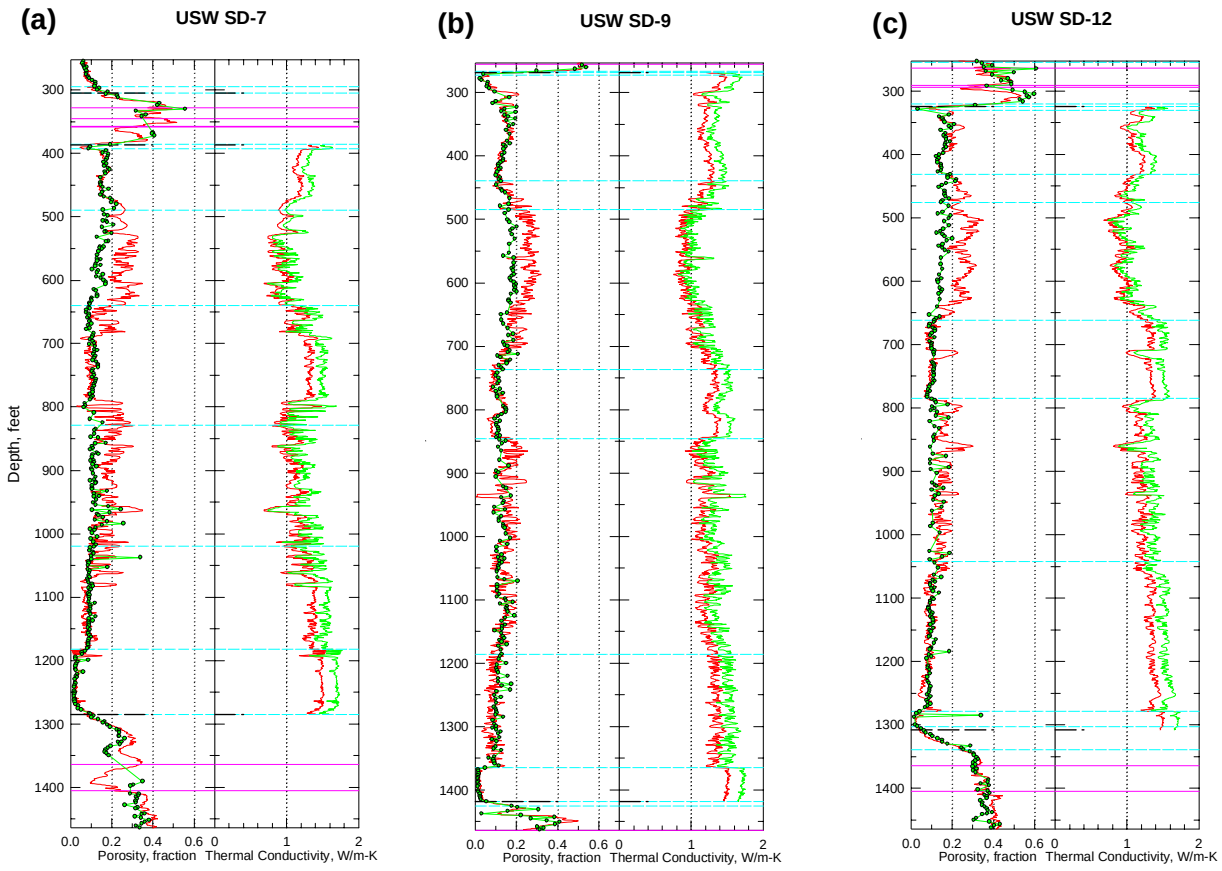

Figure 31. Downhole variation in predicted thermal conductivity values based on measured porosity data for drill holes (a) USW SD-7, (b) SD-9, and (c) SD-12. Thermal conductivity key: dark line—predicted K_{th} at 70°C and 105°C-dried conditions; light grey line—predicted K_{th} at > 100°C. Porosity key: dark line—lithophysal porosity from petrophysical logs; light grey line with symbols—matrix porosity from core samples.

graphic levels is zeolite, principally clinoptilolite with or without mordenite (Chipera and others, 1996†). Because no detailed mineralogic classification is available for samples on which saturated hydraulic conductivity was measured, we assume that all hydrous-phase alteration reduces the conductivity in the same manner. In the later stages of the modeling process (fig. 2), models of expected alteration are combined with information regarding the spatial distribution of porosity to produce a composite model of saturated hydraulic conductivity for the overall model unit.

Table 11: Statistical summary of alteration category in the Calico Hills–Prow Pass model unit

	Alteration Flag
Mean	0.525
Std.Dev.	0.499
Minimum	0
Maximum	1
N	5140

Spatial Continuity Description

Quantitative description of spatial continuity patterns (also frequently referred to as spatial correlation) employed standard variography techniques, and was conducted separately for each of the three modeling units. Three-dimensional exper-

†see unpublished citation on page 33

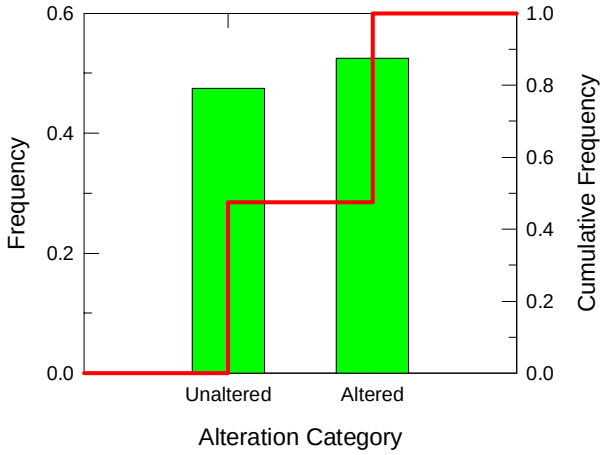

Figure 32. Histogram and cumulative distribution function of alteration category for the Calico Hills–Prow Pass model unit.

imental (semi)variograms were computed in stratigraphic coordinates using the normal-score transformed values of total porosity (see description of the normal-score transform under Development of the Models). Unless otherwise noted in the sections that follow, variograms were computed for the stratigraphically vertical direction and in the stratigraphically horizontal direction in 30-degree increments, starting from north = 0°. Additionally, variograms were also computed in the 45° and 135° directions to ensure that the 30-degree increments did not miss some particularly strong correlation structure in these intermediate directions.

The variogram estimator used in this study is the semivariogram, γ, which is traditionally defined as half the average squared difference between two attribute values approximately separated by a vector, **h**:

$$\gamma(\mathbf{h}) = \frac{1}{2N(\mathbf{h})} \sum_{i=1}^{N(\mathbf{h})} (Z_{\mathbf{x}_i} - Z_{(\mathbf{x}_i + \mathbf{h})})^2 \quad , (16)$$

where $Z_{\mathbf{x}}$ is the value of a variable at a spatial location, **x**, and $Z_{(\mathbf{x}+\mathbf{h})}$ is the value of that same variable located the vector distance, **h**, away. Note that with the exception of the factor of 2 and the fact that the comparison is between two sample values, rather than between a sample value and a mean value, equation (16) is identical to that used to estimate a variance. Thus it is no coincidence that for many earth-science applications, the variogram estimator, γ, is observed to converge on the variance of the data, σ^2, as the separation distance between the pairs of samples being compared becomes very large.

Equation (16) is computed across all available pairs of samples and all available spatial separations, **h** (note that the pair separations, **h**, are typically grouped into some modest number of distance classes). The strength of the spatial correlation, γ, *for all possible separations*, **h,** (as is typically required for modeling) is described by use a group of particular mathematical functions that have the property of yielding positive-definite covariance matrices. These models are parameterized by variables generally referred to as the *nugget*, designated *C0*, the *sill*, designated *C1*, and the *range*, designated by *a*. We can thus define:

$$\gamma = C0 + C1Sph_a(\mathbf{h}) \quad , \qquad (17)$$

where the expression $C1Sph_a(\mathbf{h})$ refers to a spherical variogram model (one of many possible functions; see Journel and Huijbregts, 1978) with range = *a* and sill =*C1*. Figure 33 presents an idealized experimental variogram, fitted by a typical variogram model, illustrating these various component quantities.

Analysis of spatial correlation is admittedly partially an art, rather than a wholly objective science. The objective is to capture the overall spatial continuity pattern(s) within a conceptual framework guided by the geologic setting and knowledge of relevant site-specific factors. Each component of a modeled variogram should have some reasonably meaningful geologic explanation. Features in the experimental variograms that conflict with geologic understanding frequently reflect artifacts of less-than-optimal sampling patterns; such features should be investigated carefully before being incorporated into a variogram model. In addition to capturing the essence of the geologic continuity of the relevant property, a fitted variogram model must comply with certain restrictions that are imposed by the use of such a model in the numerical simulation or interpolation of measured values to form a material property model. For example, if a particular structure is well developed in one direction, the same mathematical form which captures that structure must be used in all other directions, even if the

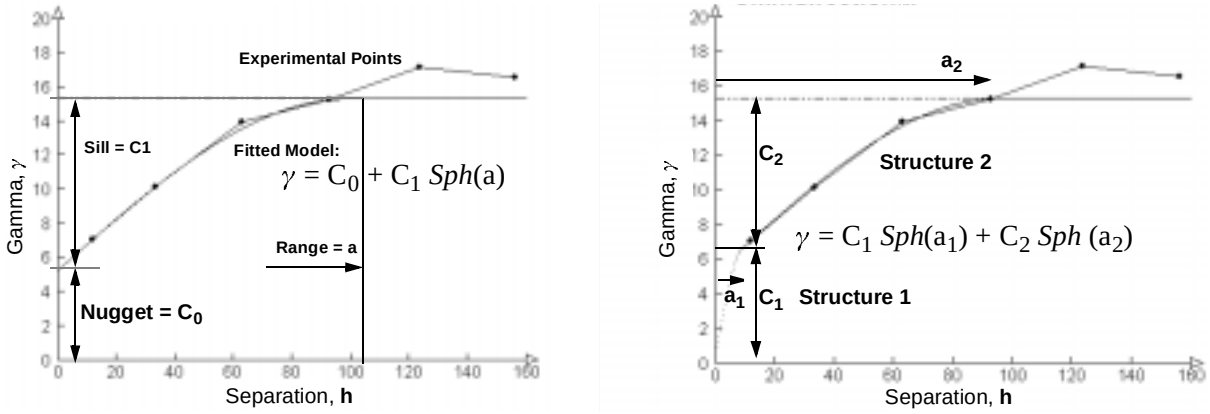

Figure 33. (a) Idealized experimental variogram with fitted model and components; (b) Example of identical experimental variogram fitted by two nested models.

structure in question is not particularly well developed in those directions. This coherence of modeled structure in three orthogonal directions can be particularly troublesome if the degree of spatial resolution is much greater in one direction (closely spaced samples down a drillhole, for example) than in others.

Anisotropy in the spatial correlation patterns of various material properties is expected in a layered sequence of rocks, such as those at Yucca Mountain. Continuity of rock properties in the stratigraphically horizontal direction generally should be greater than in the vertical direction. Properties might well be more continuous along the direction of ash-flow transport than in the horizontal direction normal to transport (or vice versa). Although standard geostatistical practice is to fit model variograms to the sample data individually in each desired direction, these separate models cannot be used directly as input to a simulation algorithm. Rather than attempt to compute the necessary spatial covariance values differently in different directions, it is typically the coordinate system describing samples and grid nodes that is modified to an isotropic system in which computation of the spatial covariance values is straightforward. This process can be conceptualized by envisioning an ellipsoid in three dimensions (or a simple ellipse in two) for which all points on the surface are at the same *structural* (geologic) distance, as opposed to the same *Euclidean* distance. Anisotropy is then described in terms of the stretching and rotation that would be necessary to transform the ellipsoid into a sphere (circle). The coordinate system is then transformed using this information, the model values are generated, and the coordinate transformations are reversed. However, a corollary that follows directly from the computation of all covariance values using an isotropic mathematical expression, is that any nested models must be of the same class of mathematical functions. One cannot, for example, fit a spherical model vertically and an exponential model for the same structure horizontally.

PTn Model Unit

Sample variograms computed in the three directions of minimum, maximum, and intermediate continuity for total porosity in the PTn model unit are presented in figure 34, together with the fitted model computed in those same three directions. The vertical variogram [fig. 34(a)] is the best defined, and it exhibits modest hole-effect phenomenon for intersample distances of about 60–120 feet. A *hole-effect variogram* is defined by a variance that increases and then decreases with increasing separation between pairs of samples; typically there is some sort of approximately periodic relationship between the peaks and troughs. The hole-effect is so named because it is most frequently observed when computing sample variograms down vertical drill holes in a (horizontally)

layered lithologic sequence. When variograms are computed for such a layered sequence, two relatively similar layers may be separated by a layer of different character. At small intersample distances, one is comparing essentially only samples from within the same unit. As the distance between sample pairs increases, one begins to compare across the different units, leading to higher computed variability. However, as the separation increases further, one begins to compare samples located in the more-similar units straddling the intervening layer and the computed variability thus decreases.

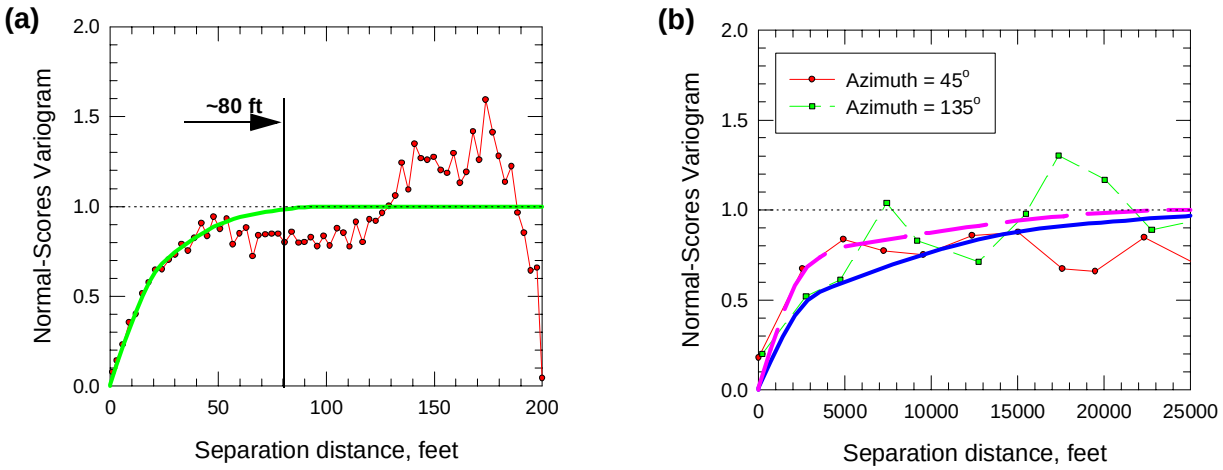

Figure 34. Variograms of total porosity normal-score values from the PTn model unit: (a) vertical; (b) horizontal. Curves with symbols represent measured data, heavy curves of corresponding line type represent fitted models; dotted line is the a priori variance of the data. Number of pairs: (a) 200–500; (b) 300–1900.

The horizontal variograms [fig. 34(b)] of total porosity in the PTn model unit are less well defined and considerably more irregular than the vertical variogram. Figure 34(b) is computed for 2500-ft lag classes, and the plot is relatively smooth, however, compared to variograms computed for shorter lag spacings (not shown). The maximum direction of spatial continuity is observed in the S 45° E (azimuth = 135°) direction, and we have inferred a modest degree of anisotropy. The orientation of the direction of maximum spatial correlation is attributed to the relative location of the source vents for the Yucca Mountain and Pah Canyon Tuffs, which are principal components of the PTn model unit, to the northwest of the repository site itself. Isopach maps of the Yucca Mountain Tuff (Clayton and others, 1997) indicate a southeast-trending lobe of thicker outflow-facies tuff in the northern part of the site area. This depositional lobe is reflected in the isopach of the total PTn interval as well. The Pah Canyon Tuff exhibits a depositional lobe of thicker tuff trending somewhat more southerly in this same region. Because the Yucca Mountain Tuff, and the Pah Canyon Tuff to a lesser extent, contain welded tuff in their thickest portions, it follows that porosity values would be more continuous along those depositional trends than at 90 degrees to them. An interesting feature of the sample variogram at an azimuth of 45° is that although some 80 percent of the total variability is reached for pairs of samples separated by approximately 5000 ft, the variability of samples separated by even greater distances does not increase, and, in fact, appears to decrease somewhat. This feature may reflect a relative lack of variability within the broad distal fringe of the Yucca Mountain and/or Pah Canyon Tuffs, the vast majority of which is nonwelded tuff and partially reworked tuffaceous sediment of relatively high porosity.

A set of three nested spherical variogram models plus a small nugget effect has been fitted to the sample data using the parameters specified in table 12. The composite spatial correlation model

appears to fit the sample variograms rather well, and the model is appropriately consistent with sample variograms computed in other directions (not shown). The horizontal variograms [fig. 34(b)] suggest a larger nugget effect than modeled here. We selected the very small nugget value of 0.01 (table 12) for a number of reasons. First, the downhole sample variogram [fig. 34(a)] indicates virtually no nugget effect and this interpretation is supported by systematic sampling on approximately 3-ft centers. The shortest average lag spacing in the horizontal directions is 7–8 ft in a few directions but is more typically 30–100 ft in others. The excellent sample control in the vertical direction is the strongest argument for a small nugget. Second, theoretical considerations require that as intersample distances approach zero, variability diminishes to zero as well. What may account for larger variability at very small sample spacings (not precisely equal to zero) is measurement error. Presumably one is not interested in reproducing measurement error in the model, so one may be justified generally in interpreting through a nugget effect to capture the underlying geologic phenomenon.

Table 12: Modeled variogram parameters for total porosity normal scores in the PTn model unit

Nest No.	Model Type	Range (ft)			Sill	Rotation Angle (degrees)			Anisotropy Ratio	
		Maximum (horizontal)	Inter-mediate	Minimum (vertical)		1	2	3	1	2
	Nugget				0.01					
1	Spherical	3500	3000	25	0.30	135	0	0	0.857	0.00714
2	Spherical	17000	5000	60	0.40	135	0	0	0.294	0.00350
3	Spherical	35000	25000	100	0.29	135	0	0	0.714	0.00286

A third reason that we have discounted the apparent nugget effect present in figure 34(b) is that the magnitude of this apparent nugget effect is (in part) a function of the vertical bandwidth used for accepting sample values into the calculation of the variogram value. Figure 35 shows the near-origin portion of a series of variograms calculated using exactly the same data and in an identical manner except that the vertical bandwidth was varied systematically from 100 ft (one-half the nominal thickness of the PTn model unit) to 5 ft. The apparent nugget effect decreases systematically as well, from a value of approximately 0.7 to less than 0.2. Of course, as the bandwidth allowed for the sample search decreases, the number of pairs of samples that can be located within this tolerance interval decreases as well, leading ultimately to a lack of statistical mass that renders interpretations suspect.

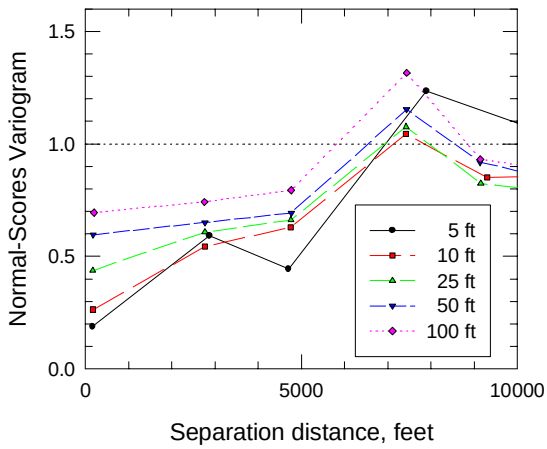

Figure 35. Variograms showing effect of vertical bandwidth on the magnitude of apparent nugget effect. Azimuth = 135°; lag spacing = 2500 ft. Dotted line is a priori variance.

We interpret the first (shortest range) structure with a = 3500 ft in the horizontal 135-degree direction to be related in some manner to the thicker depositional lobes involving the partially to moderately welded Yucca Mountain and Pah Canyon Tuffs in the northern part of the site area (much of the main masses of both the Yucca Mountain and the Pah Canyon Tuffs are located to the north

and west of the northernmost drill holes used in this study). The much more extensive second structure with a = 17,000 ft is most likely related to some average lateral extent of relatively thin individual units of air-fall tuff and pumice-fall deposits, and to partially reworked "bedded" tuffs. These thin alternating units in the more distal portions of the Yucca Mountain and Pah Canyon outflow sheets are probably also responsible for the very short ranges (25 ft and 60 ft) of these two nested structures in the vertical dimension. Interlayering of coarse grained pumice-fall deposits with much finer grained air-fall tuffs could easily account for a major part of the variability observed at these short sample-separation distances. The third nested structure with the very long range of a=35,000 ft is functionally a "dummy" structure, created to make the several sill components sum to 1.0 as required for simulation modeling, particularly in the vertical dimension. As the maximum inter-drillhole distance is generally less than about 15,000 ft for the PTn model unit [fig. 8(a)], this structure contributes very little during the modeling process.

TSw Model Unit

Matrix Porosity

Sample variograms computed using matrix porosity data from the Topopah Spring welded model unit for the minimum, maximum, and intermediate directions of spatial continuity are presented in figure 36. The fitted model variograms are also shown on the figure. Part (a) of figure 36 is the variogram computed in the minimum-continuity, stratigraphically vertical direction with a sample lag of 3 ft, whereas part (b) shows sample variograms computed horizontally at azimuths of 0 and 90 degrees (north-south and east-west), using a lag-class interval of 2000 ft. Maximum spatial correlation is observed in the north-south direction. The vertical variogram is particularly well defined because of the closely spaced sampling along drill hole traces, whereas the horizontal variograms are somewhat more irregular, largely because of the irregular pattern of surface-based drillholes.

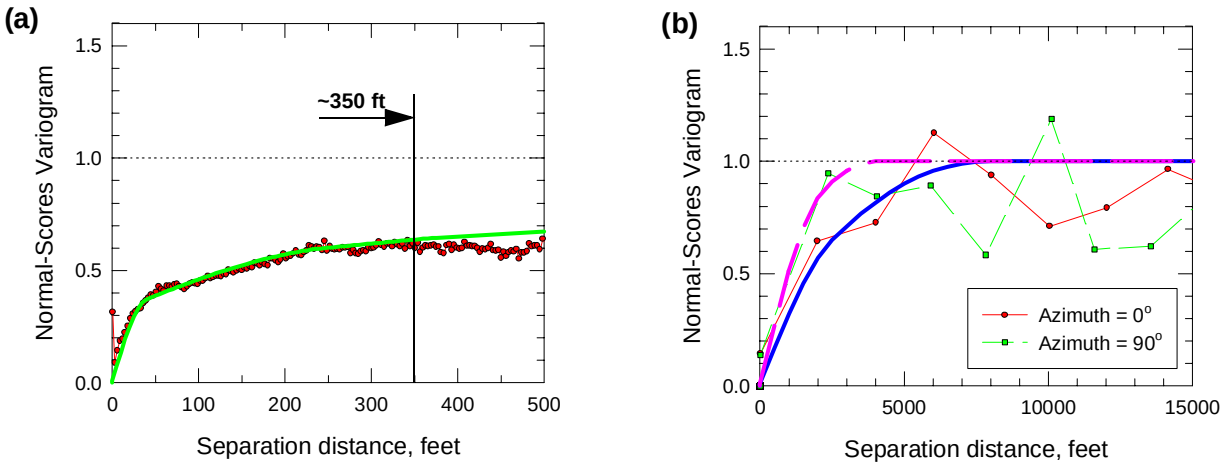

Figure 36. Variograms of matrix total porosity normal-score values from the TSw model unit: (a) vertical; (b) horizontal. Curves with symbols represent measured data, heavy curves of corresponding line type represent fitted models; dotted line is the a priori variance of the data. Number of pairs: (a) 1400–4000; (b) 1000–17000.

A particularly notable feature of the vertical variogram in figure 36(a) is that even at intersample spacings of 500 ft (which is half the nominal thickness of the TSw model unit in stratigraphic coordinates) the sample variogram value is only about 0.6 compared with the standardized a priori variance of the entire data set of 1.0. In contrast, both variograms shown in figure 36(b) clearly approximate the expected sill value of 1.0 at long separations.

The explanation of this lower-than-average variability along drillholes is not completely clear, although the behavior most likely has its origin in one of at least two causes. First, although there is no major decrease in variability, such as would be associated with a strong hole effect like that of figure 34(a), there is indeed a suggestion that the variogram values at separations slightly greater than 250 ft are somewhat lower than those associated with separations just less than 250 ft. A slight, but fairly well defined increase in the variogram values followed by a weak decrease can also be observed in the sample plot at distances between 400 and 450 ft, again potentially suggestive of a very weak hole effect. Consideration of the geology of the Topopah Spring welded unit supports the existence of some sort of hole-effect phenomenon. As is clearly illustrated by the porosity data profiles in figure 17 and in Appendix B, the TSw model unit is marked by the alternating presence vertically of lithophysal and nonlithophysal intervals. The effect of these lithologic zones on matrix porosity is much less than for the lithophysal porosity data (to be discussed below), the presence of more intense vapor-phase alteration in the lithophysae-bearing intervals may have increased the matrix porosity values by a modest amount. Interestingly, the prototypical thickness of the lithophysae-bearing intervals is approximately 200–250 ft (fig. 17).

A second, and probably more likely explanation for the variogram behavior observed in figure 36(a) may be that the lower variance computed in the vertical direction is a product of a type of zonal anisotropy involving vertically persistent areal trends in the data, as described by Kupfersberger and Deutsch (1997). Indeed, that such laterally variable vertical “zones” exist can be demonstrated by computing the vertically averaged mean matrix porosity for each vertical drill hole separately. Because each drill hole has been sampled in a consistent and essentially uniform manner (Appendix B), variability in the computed mean values is related to broad areal changes in character and not simply to artifacts of non-systematic sampling. If we further restrict our examination to the 26 drillholes that penetrate the entire thickness of the TSw model unit (table 4) in a further effort to avoid sampling artifacts, we obtain the distribution of mean values and standard deviations shown in figure 37. Although the “average” TSw matrix porosity is approximately 0.15, the individual drill hole means vary from 0.10 to 0.23. Note that this variability is zonal, rather than the effect of a systematic regional trend in porosity, as there is no evidence in the horizontal variogram (fig. 36(b) of the characteristic parabolic increase in the variogram value at large separations (Journel and Huijbregts, 1978).

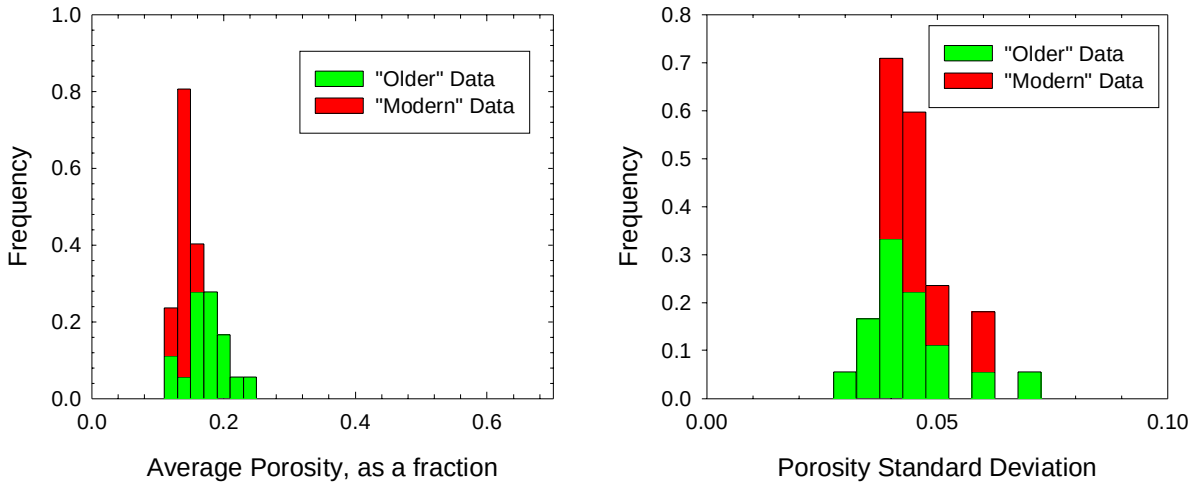

Figure 37. Histogram of (a) Drillhole-Mean Matrix Porosity Values and (b) Drillhole-Mean Standard Deviations of Porosity for the TSw Model Unit for Fully Penetrating Drillholes (n=26).

A third potential and somewhat more disturbing explanation for the variogram behavior observed in figure 36(a) might be that the low variance is an artifact related to the nature of the data used in this modeling exercise. In order to create models for the majority of the extended site area (fig. 9), it was necessary to use virtually all the available porosity data, including values from (at least) two different generations of borehole petrophysics plus laboratory-measured core values. Because of the generally quite wide inter-hole distances available in the composite data set, the search parameters used in constructing the variograms in the vertical direction have the practical effect of restricting the neighborhood of samples located to those from a single drill hole. As only one type of matrix porosity data typically exists for a given drill hole (e.g., petrophysical porosities for a WT hole; core porosities for an SD hole), any systematic differences in the magnitude or overall variability of porosity values measured by the several alternative techniques would be more or less negligible in the down-hole direction. In contrast, the horizontal variograms, which must of necessity consider data from many different drill holes, would include any systematic differences of this type, and thus the overall variability of the sample pairs might be anticipated to be higher. Note that the net effect of this type of data bias is otherwise indistinguishable from the effects of the zonal anisotropy described previously.

Support for the concept of a horizontal "hole-effect" related to alternation of data type, rather than of lithology per se, can be observed in the behavior of some of the horizontal sample variograms as well. Note that in figure 36(b), three of the four largest-separation variogram values are markedly lower than the indicated sill value of 1.0. Although this variability could easily be attributed simply to noise related to imperfections in the stratigraphic coordinate transformation or less-than-ideal drill hole locations, the observation that variogram values associated with larger separation distances are less than those associated with shorter separations is consistent across the entire suite of variograms calculated but not shown in this report. For example, figure 38 shows horizontal variograms computed at azimuths of 90, 120, and 150 degrees using a shorter lag spacing of only 1000 ft. In each of these sample variograms, the observed variability of sample pairs increases rapidly with increasing distance and then decreases to values of 0.5–0.8 for greater separations punctuated by crudely periodic, typically single-lag spikes indicating variability much greater than 1.0 at intervals of between 4000 and 5000 ft. These observations are compatible with the observation from figure 9 that drill holes separated by spacings of more than 5000 ft, and invariably by spacings greater than 10,000 ft, are members of the WT-, G-, and H-series. Porosity data from all of these holes were derived from geophysical logs run during the pre-site characterization period (Nelson, 1996), and these porosity data were processed using a consistent set of input traces and algorithms.

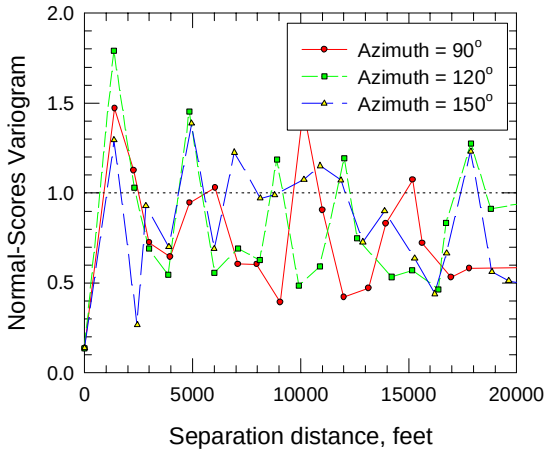

Figure 38. Sample variograms for matrix porosity data from the TSw unit computed using 1000-ft lag spacings. Note the typically lower-than-sill variability of sample pairs at lags greater than 5000 ft. Dotted line is a priori variance.

There is also one other data-related issue that may be contributing to differences in magnitude and variability between and within drill holes. Matrix porosity is essentially a core-scale property by the definitions used in this study, whereas lithophysal porosity is only defined at larger-than-core scales. The vagaries of the Yucca Mountain Project have been such that all cored drill holes have geophysical logs but not all holes with geophysical logs have core. Because the total porosity values computed using downhole geophysics are effec-

tively lithophysal porosities in lithophysae-bearing intervals and matrix porosity elsewhere, we are in the position that there are no petrophysically computed matrix porosity values for the lithophysal intervals. If there is no core in a given hole, there is no direct measurement of matrix porosity.

Because the principal set of drill holes for which this condition applies is the WT series (fig. 9), some sort of work-around was required to avoid producing models with no data whatsoever in approximately one-half the vertical thickness of the TSw model unit throughout much of the model domain. In compiling the "matrix" porosity data, we adopted the heuristic device of substituting the water-filled porosity, ϕ_w, for the total (lithophysal) porosity, ϕ_T, in the inferred lithophysal zones only [see text associated with equations (6) and (7)]. Note that as all but the very upper and lower margins of the Topopah Spring Tuff are both welded and devitrified, the issue of structurally bound water within the minerals themselves can be neglected. Of greater impact is that since $\phi_T = (\phi_w + \phi_a)$ [eq. (2)], the presence of these lithophysal intervals above the water table throughout parts of the extended site area introduces yet another source of "noise" into the modeling process. "Lithophysal intervals" for purposes of this heuristic substitution were defined by marked and abrupt separation between the total (lithophysal) and the water-filled porosity traces (see Appendix B).

In general, the approximation of matrix porosity by the water-filled porosity data is probably not far wrong. Throughout the crystal-poor lower lithophysal lithostratigraphic zone (Buesch and others, 1996) of the Topopah Spring Tuff, the rocks are relatively close to the water table so that the expected *matrix* saturations would be relatively high. It is observed empirically (for example, Rautman, 1995: UZ-16; Rautman and Engstrom, 1996a, 1996b: SD-7 and -9, respectively) that matrix saturations measured on core samples are on the order of 80–90 percent in this interval. Also, even though the specific saturation level of materials within the unsaturated zone is a complicated function of ground-water flux and relative-permeability characteristics of the porous medium, modeling studies of the UZ-16 drillhole (Flint and others, 1993) have indicated that within units of similar hydrologic character, saturations typically increase with proximity to the static water level. Because the principles of capillarity (e.g., Hillel, 1980) require that any lithophysal cavities even a few millimeters in diameter be air-filled under unsaturated (tension) conditions, it is likely that water-filled porosity values are within a 1 or 2 porosity percent of the true matrix values. The situation is somewhat more complex in the lithophysae-bearing intervals associated with the crystal-rich lithophysal and crystal-poor upper lithophysal lithostratigraphic zones of Buesch and others (1996). These lithophysal intervals are generally higher above the water table, and the available evidence indicates that the matrix saturation as measured on core samples may be on the order of 60–80 percent rather than 80–90 percent. Still for rocks of roughly 15 percent porosity at a (probable low-end) saturation of 60 percent, the total potential error should be $(1 - 0.6) \times 0.15 = 0.06$, or 6 porosity percent. At 80 percent saturation, the potential error is half of that, or 3 porosity percent.

We have modeled the sample variograms for matrix porosity in the TSw model unit (imperfections and all) using a set of three nested spherical structures and the model parameters given in table 13. The fit to the empirical values, as presented in figure 36, is really quite acceptable for the shorter lag distances. Because the total variance captured in the variogram model must be equal to one, we have dealt with the lower variability observed in the vertical variogram of figure 36(b) by increasing the range of the third nested structure in the vertical direction to a very long (compared to the vertical extent of the TSw unit) 2000 ft (= 8000 ft maximum range times an anisotropy ratio of 0.25), and then limiting the search radius used to locate sample values for modeling in the vertical direction to a maximum of 350 ft, as indicated in figure 36(a).

Vertical structure 2 with range a = 250 ft (= 6000 × 0.417) clearly is related to vapor-phase alteration of the rock matrix associated with the alternating lithophysal and nonlithophysal intervals. Because structure 3 is largely a dummy structure required in the vertical direction, as just described, structures 2 and 3 in the horizontal dimensions are effectively a single geologic structure with a range of roughly 6000–8000 ft. This

Table 13: Modeled variogram parameters for matrix porosity normal scores in the TSw model unit

Nest No.	Model Type	Range (ft)			Sill	Rotation Angle (degrees)			Anisotropy Ratio	
		Maximum (horizontal)	Inter-mediate	Minimum (vertical)		1	2	3	1	2
	Nugget				0.01					
1	Spherical	2500	2000	40	0.30	0	0	0	0.800	0.0160
2	Spherical	6000	2500	250	0.20	0	0	0	0.417	0.0417
3	Spherical	8000	4000	2000	0.49	0	0	0	0.500	0.2500

structure may represent variability associated with the maximum extent of the lithophysal intervals in stratigraphic coordinates *as captured by* the very narrow vertical-bandwidth search described on page 48 (fig. 39). Note that although structure 1 is essentially required in the vertical direction [the prominent knick-point at about 30–50 ft in fig. 36(a)], the evidence for this feature as a separate structure in the stratigraphically horizontal plane is relatively subtle, marked by a change in slope of the north–south sample variogram at about 2000–2500 ft. Given the relatively short range of this structure vertically (2500 times 0.016 = 40 ft), we interpret the origin of this structure as related to the inherent variability of small-scale cooling and devitrification conditions in a major ash-flow tuff.

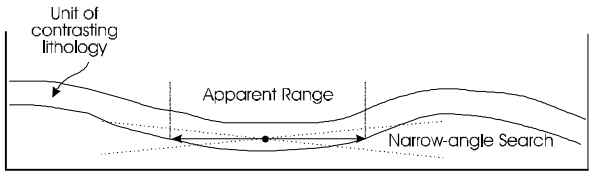

Figure 39. Sketch illustrating effect of imperfect conversion to stratigraphic coordinates on apparent range of variograms.

Some 40 percent of the hydraulic conductivity measurements conducted on samples from the Topopah Spring welded unit yielded no measurable flow [fig. 26(c–d)]. To determine the degree of spatial correlation among this group of samples, we computed an indicator variogram where non-flowing samples were assigned to one category and all flowing samples to another. Because only a small fraction of the total number of samples from the TSw model unit were measured for hydraulic conductivity, it was possible to compute this indicator variogram only in the vertical dimension (i.e., down drillholes). The resulting variogram is shown in figure 40, and it indicates that some 57 percent of the total sill variance is achieved within approximately 10 ft, and the remainder within approximately 140 ft. The prominent hole effect with a wavelength of approximately 250 ft is almost certainly related to the vertical alternation of lithophysal and nonlithophysal zones within this model unit.

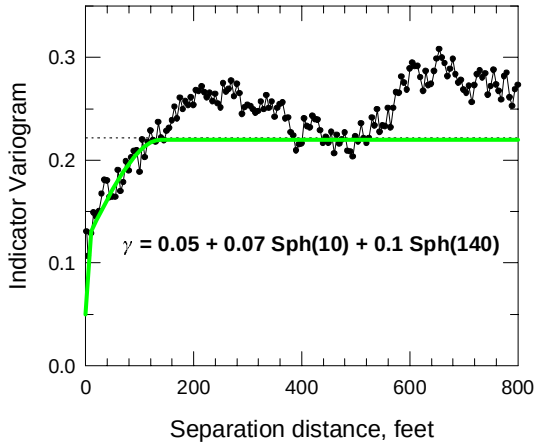

Figure 40. Vertical indicator variogram of non-flowing hydraulic conductivity samples. Curve with symbols represents measured data, heavy curve represents fitted model; dotted line is a priori variance. Number of pairs: 200–300.

Because ground-water flow in the unsaturated zone at Yucca Mountain is widely presumed to be dominantly vertical, the more important issue would appear to be the extent of spatial correlation of non-flowing welded tuff in the stratigraphically horizontal dimension. Under the assumption made for this study that hydraulic conductivity is coregionalized with matrix porosity, it is possible to use the observed vertical-to-horizontal anisotropy ratios from the matrix porosity variograms to obtain a rough idea of the likely extent of horizontal continuity for the no-flow samples. Recalling from table 13 that the vertical-to-horizontal anisotropy ratio (anisotropy ratio 2) for variogram structure number one is 0.016, the 10-ft vertical indicator range suggests that the horizontal range of the first nested indicator structure is on the order of $10 \div 0.016 = 625$ ft. Using this logic, somewhat more than half (~57 percent) of the indicator variance might be observed at approximately this 625-ft horizontal distance. If we can then assume that the remaining indicator variance vertically corresponds to matrix porosity structure 3 (which accounts for somewhat less than half of the matrix porosity variance), we can estimate the implied indicator range in the horizontal dimension as $140 \div 0.250 = 560$ ft using the appropriate value of anisotropy ratio 2.

Both of these inferred ranges are less than the horizontal grid spacing of 250 meters = 820.25 ft. The implication is that the observed non-flowing samples from the TSw model unit do not appear to be strongly correlated spatially in the horizontal dimension and thus most likely do not form a continuous barrier to flow at the site scale. This is generally in agreement with an interpretation that the non-flowing samples are simply artifacts of limited pressure capability of the permeameter used in the laboratory measurement procedure and do not represent some fundamentally different rock type.

Note, however, that approximations that are appropriate for the site scale may not necessarily be appropriate for smaller scale modeling. A worst-case estimate of the horizontal correlation exhibited by the non-flowing hydraulic conductivity specimens might be to equate the second nested structure range of 140 ft vertically with a composite of horizontal structures 2 and 3 from table 13. Anisotropy ratio 2 for structure number 2 is 0.0417, implying a horizontal indicator correlation range of more than 3300 ft. Although correlation of no-flow nodes over this distance would only involve some 3–4 grid nodes at 820.25 ft per node, horizontal barriers to flow on the order of one kilometer (four nodes at 250 m/node) might indeed be significant when modeling ground-water flow and transport at less than the site scale. It would appear prudent to investigate the actual horizontal continuity of hydraulic conductivity more directly.

Lithophysal Porosity

Sample variograms, with the appropriate fitted model values, for the minimum, maximum, and intermediate directions of spatial continuity for lithophysal porosity in the TSw model unit are presented in figure 41. Again, the experimental plot in the minimum-continuity vertical direction is very well defined because of the close down-hole sample spacings, nominally 3 ft, and the figure indicates a very small nugget value as sample spacings decrease toward zero. The horizontal variograms are more irregular because of the non-systematic spacing of the available drill holes; a mild anisotropy is observable between the sample values computed in the north-south and east-west directions

The vertical variogram exhibits a very strong hole effect with an apparent period of about 200 ft. This phenomenon is easily attributable to the marked differences in porosity values between the lithophysal and nonlithophysal lithologic intervals. Perusal of the drill hole illustrations in Appendix B confirms that the significant lithophysae-bearing intervals typically have a stratigraphic thickness of this order of magnitude. Although the maximum variance observed in the sample data again never reaches the overall sill level of 1.0, the magnitude by which the experimental values fall short is much less (approximately by 0.10 at lag separations of just less than 200 ft) than was the case for the matrix porosity data shown in figure 36(a). To some extent, this lower-than-sill variability may be attributed to the same zonal anisotropy and/or dataset effects that may be responsible in part for the very much lower-than-sill variability observed for the matrix porosity information. However, all values of lithophysal porosity within the lithophysal intervals themselves are derived from petrophysical

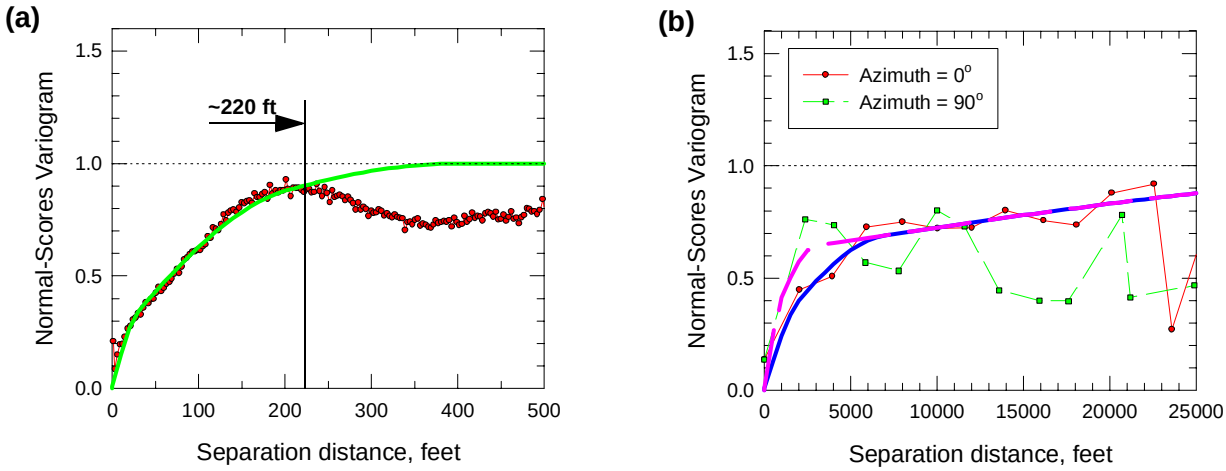

Figure 41. Variograms of lithophysal porosity normal-score values from the TSw model unit: (a) vertical; (b) horizontal. Curves with symbols represent measured data, heavy curves of corresponding line type represent fitted models; dotted line is the a priori variance of the data. Number of pairs: (a) 2000–4000; (b) 599–18,000.

calculations, as core samples a few centimeters in diameter cannot contain meaningful lithophysal cavities. The issue of two generations of petrophysical values (c.f., Nelson, 1996; Thompson and Rael, 1996) is still present. However, both sets of porosity values (and more particularly the actual gamma-gamma density log traces upon which those values are based) were obtained and computed in virtually the identical manner (compare eqs. 4 and 9). Another explanation for the smaller difference of the maximum observed variability from the a priori variance may be simply that the overall variability of the lithophysal porosity data (σ_l = 0.08) is greater than that of the matrix porosity values (σ_m = 0.05; table 6; fig. 16). With greater overall variability of the true porosity of the rocks, the small variations in measured porosity values between these two measurement techniques simply have a much smaller impact on the observed variability between drill holes.

For the lithophysal porosity variograms computed in the different horizontal directions [fig. 41(b)], we again observe that the sample variability never reaches the overall variance of the data. Quite clearly, any zonal anisotropy or data artifacts will influence the horizontal sample variograms as well. However, in this case a much more likely explanation of the lower-than-sill variability for stratigraphically horizontal searches is that the stratigraphic coordinate transformation has, in fact, worked successfully. The purpose of the stratigraphic coordinate convention is to place rocks affected by similar geologic conditions at approximately the same "elevation" within the unit. When combined with a relatively restricted vertical-search bandwidth, as discussed on page 48 (see also fig. 35), the stratigraphic coordinate convention means that the variogram search should find essentially only values within a lithophysal interval or within a nonlithophysal interval in a given computation. The apparent computed variability is thus less than the variability of the data as a whole. This search effect is probably relevant to matrix porosity as well, as the lithophysae-bearing intervals do contain rock matrix that is more affected by vapor-phase alteration than the matrix in the nonlithophysal intervals.

The sample variograms of lithophysal porosity values have been fitted with a series of three nested spherical variogram models using the parameters in table 14. Only modest anisotropy has been modeled in the horizontal dimensions, but the vertical-to-horizontal anisotropy is quite strong because of the relatively stratiform lithophysal intervals. The search in the vertical direction has been limited to 220 ft because of the hole effect. The third nested structure, with a principal range of 50,000 ft is mostly a dummy structure, as man-

Table 14: Modeled variogram parameters for lithophysal porosity normal scores in the TSw model unit

Nest No.	Model Type	Range (ft)			Sill	Rotation Angle (degrees)			Anisotropy Ratio	
		Maximum (horizontal)	Inter-mediate	Minimum (vertical)		1	2	3	1	2
	Nugget				0.01					
1	Spherical	2000	1000	30	0.20	0	0	0	0.500	0.0150
2	Spherical	7000	3000	200	0.40	0	0	0	0.429	0.0286
3	Spherical	50000	50000	400	0.39	0	0	0	1.000	0.0080

dated by the simulation requirement that the total sill be equal to 1.0. As can be observed in figure 41, the contribution of this structure is virtually nil for separation distances less than about 5000 ft (the variance contribution of the two shorter-range structures totals 0.6), and the impact of this dummy structure becomes important only for separations greater than 10,000–12,000 ft.

The approximately 200-ft vertical range (= 7000 × 0.0286 anisotropy ratio 2) for nested structure 2 is clearly related to the lithophysal–nonlithophysal layering. The origin of the approximately 30-ft vertical range [= 2000 × 0.015; prominent knick-point in figure 41(a)] is less obvious, but as a structure with a range of this magnitude was also identified for the TSw matrix porosity data (fig. 36), it probably involves the intrinsic variability of porosity in welded tuff.

Calico Hills-Prow Pass Model Unit

Porosity Variograms

Sample variograms for total porosity from the combined Calico Hills-Prow Pass model unit are presented in figure 42 for the directions of minimum, maximum, and intermediate spatial continuity. Continuity in the stratigraphically vertical minimum-continuity direction is shown in part (a) of the figure whereas part (b) shows spatial correlation in the north–south and east–west directions. Even though the CH-PP combined unit comprises unaltered (vitric) and altered (zeolitic) rock types, the presence of zeolitic alteration appears not to have affected the spatial distribution of total porosity in any meaningful manner. All data for porosity have been combined in figure 42, thus achieving greater statistical mass. The coherent spatial continuity patterns are also evidence that this aggregation of porosity data from the different rock types is appropriate.

The vertical variogram of figure 42(a) exhibits many of the same characteristics observed for vertical variograms in the other modeling units. There is a moderate hole-effect structure with an approximate periodicity of 200 ft, and the observed variability at all lags, up to somewhat more than half the total unit (stratigraphic) thickness of 800 ft, never reaches the expected sill value of 1.0. We attribute much of the hole-effect character of the vertical variogram to the inclusion of number of somewhat different lithologic units within the combined Calico Hills–Prow Pass model unit. The principal contributor to the hole effect phenomenon is most likely the so-called Prow Pass welded thermal/mechanical unit of Ortiz and others (1985; see table 1). This unit appears to constitute “ash-flow unit 3” of the Prow Pass Tuff, as described by Moyer and Geslin (1995; see also Engstrom and Rautman, 1996; Rautman and Engstrom, 1996a, b). Although Prow Pass unit 3 does appear to constitute an identifiable lithostratigraphic unit that is typically welded, the degree of welding is markedly less than that of the welded units within the overlying Paintbrush Group, and the effect of the welding process on porosity is entirely different. This distinction of welding, per se, from material properties has been noted previously by Schenker and others (1995; their appendix III). In most drill holes, the porosity values through much of the Prow Pass unit 3 interval approximate those of the nonwelded tuffs enclosing this unit (see also Appendix B). The explanations advanced on

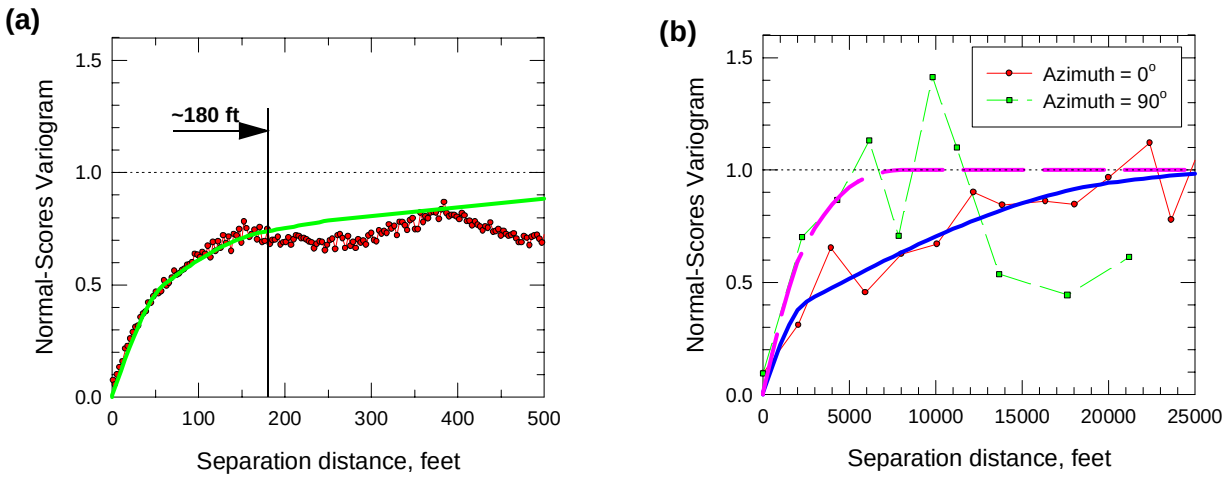

Figure 42. Variograms of matrix total porosity normal-score values from the CH-PP model unit: (a) vertical; (b) horizontal. Curves with symbols represent measured data, heavy curves of same line type represent fitted models; dotted line is the a priori variance of the data. Number of pairs: (a) 1000–3000; (b) 700–11,000.

page 51 for lower-than-sill variability (zonal anisotropy or mixing of porosity values measured by different techniques in the data set as a whole, but not in computations along individual drill holes) may also be contributing to the observed vertical spatial continuity pattern, as the horizontal variograms (next paragraph) do appear to reach the expected sill value.

The horizontal variograms of figure 42(b) are quite well defined, and in fact exhibit a less irregular pattern than the horizontal variograms from the other two model units. Spatial continuity appears greatest in the azimuth = 0° direction and the degree of anisotropy at longer lag spacings is quite pronounced. An interesting phenomenon apparent in the horizontal variograms is that whereas variability in the north–south direction appears to increase relatively steadily toward the sill value over separation distances of up to 25,000 ft, the variance in the east–west direction increases to maximum values at lags of about 5000 and 10,000 ft and then decreases markedly and remains low.

We have fitted the variograms shown in figure 42 with three nested spherical structures using the parameters given in table 15. Three structures are clearly required by the vertical variogram of figure 42(a): the knick-point at a lag of about 50 ft, the prominent intermediate sill beginning with lags of about 175–200 ft, and a third to make the total variance equal to 1.0 at very long separations. Two nested structures would appear to suffice for modeling the horizontal variograms of figure 42(b). However, use of the three-structure model in the vertical direction mandates maintenance of this model in the horizontal plane as well, and there is little practical difference between the two longer-range components. We have dealt with the hole effect in the vertical dimension by restricting the search in this direction during modeling to a maximum of about 180 ft, as noted on figure 42(a).

Zeolite Alteration Variograms

Sample indicator variograms for the two alteration categories defined in the Calico Hills–Prow Pass model unit are presented in figure 43. Part (a) of the figure is the vertical variogram (the direction of minimum continuity) and part (b) shows horizontal variograms at azimuths of 0° and 90° (maximum and intermediate directions). Notice that the sill of the indicator variogram is not equal to one, as was the case for the normal-score transformed porosity data. For indicator variograms, the expected sill can be computed as:

$$C = Var\{I\} = F - F^2 \qquad (18)$$

(Journel, 1983), where C is the indicator sill, $Var\{I\}$ is the variance of the non-zero indicator, and F is the cumulative frequency of the non-zero category (proportion of non-zero indicators). From

Table 15: Modeled variogram parameters for total porosity normal scores in the CH-PP model unit

Nest No.	Model Type	Range (ft)			Sill	Rotation Angle (degrees)			Anisotropy Ratio	
		Maximum (horizontal)	Inter-mediate	Minimum (vertical)		1	2	3	1	2
	Nugget				0.01					
1	Spherical	2500	2500	60	0.30	0	0	0	1.000	0.0240
2	Spherical	20000	5500	175	0.30	0	0	0	0.275	0.0088
3	Spherical	30000	11700	800	0.39	0	0	0	0.267	0.0267

table 11, the relative proportion of altered rocks in the CH–PP model unit is 0.5254, so $C = 0.5254 - 0.5254^2 = 0.2494$, as indicated in figure 43.

The vertical spatial continuity pattern is quite well defined, as expected with systematic sampling on nominal 3-ft centers. The variograms in the horizontal plane, however, are quite irregular, perhaps more so than any of the porosity variograms. However, with the exception of the two-point peak at lag separations between 1000 and 2000 ft, it is fairly evident that variability in the north–south direction is generally low, reaching the expected sill value of approximately 0.25 at separations greater than 5000 ft. In contrast, variability in the east–west direction reaches and generally remains at greater-than-sill values at separations of only about 2500 ft.

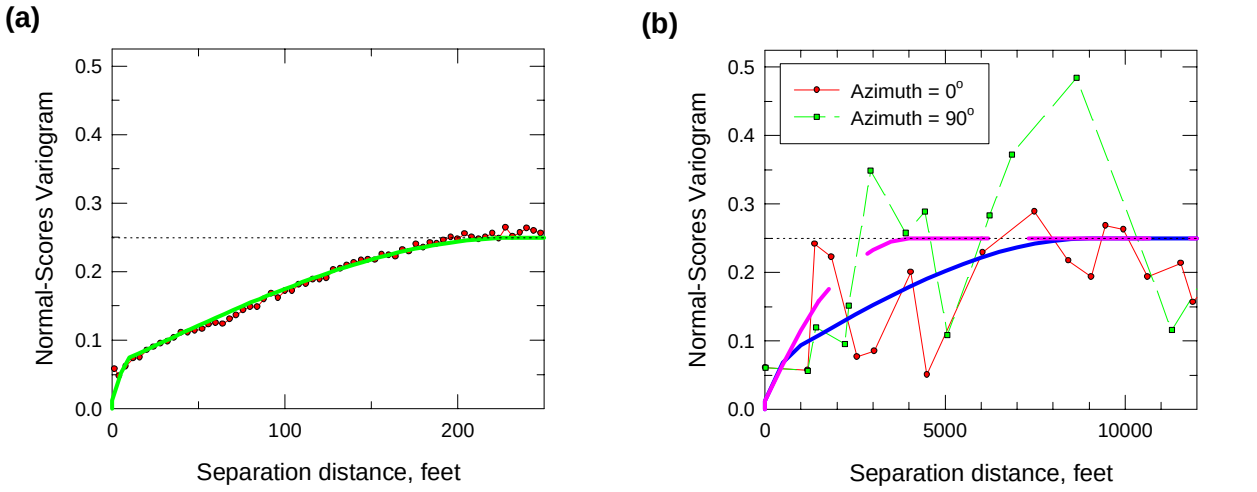

Figure 43. Indicator variograms of zeolite alteration flags in the Calico Hills-Prow Pass model unit. Curves with symbols represent measured data, heavy curves of same line type represent fitted models; dotted line is the a priori variance of the data. Number of pairs: (a) 4000–9000; (b) 400–13,000.

The variograms of figure 43 have been modeled using two nested spherical structures, the parameters for which are presented in table 16. Two structures are clearly indicated by the behavior at very short lags in figure 43(a), and this structure appears to provide a convenient surrogate for a higher nugget value in the horizontal plane. We have elected to discount the north–south variogram spike between lag separations of 1000 and 2000 ft in favor of attempting to capture the longer, low-variability information that is strongly represented by the points at lag spacings of about 3000 and at 4500 ft while at the same time attempting not to underestimate the variability at shorter lags.

Table 16: Modeled variogram parameters for alteration indicator flags in the CH-PP model unit

Nest No.	Model Type	Range (ft)			Sill	Rotation Angle (degrees)			Anisotropy Ratio	
		Maximum (horizontal)	Inter-mediate	Minimum (vertical)		1	2	3	1	2
	Nugget				0.0125					
1	Spherical	800	2000	10	0.0500	0	0	0	2.500	0.0125
2	Spherical	9000	4000	230	0.1870	0	0	0	0.444	0.0260

Indeed, as noted by a reviewer of a draft of this report, an alternative approach to modeling the horizontal variograms of figure 43(b) might be to place greater emphasis on the previously noted high variance points between 1000 and 2000 ft on the north–south experimental variogram. Were this the approach, one would conclude that the north–south direction exhibited the shorter correlation range, and that the east–west variogram and its associated 4000-ft range represented the major axis of anisotropy. Under this scenario, the lower variability associated with the north–south experimental variogram at distances between 2000 and 6000 ft could be considered as representing zonal anisotropy.

Our preference is for the former interpretation (table 16), as this is also the direction of maximum spatial correlation observed for porosity values in the Calico Hills–Prow Pass model unit (table 15; fig. 42). We are also influenced by the fact that fault blocks at Yucca Mountain tend to be elongate north–south with layering dipping to the east (see more below regarding faulting). Unquestionably, our decision with respect to modeling the alteration-indicator flags is a compromise choice, as the heavy solid curve in figure 43(b) is a rather poor fit except to the sill value.

The rather poor sample variograms exhibited by the zeolite alteration flags in the horizontal directions are most probably related to the fact that alteration within the Calico Hills–Prow Pass combined model unit reflects a wholly different physical phenomenon than the variation in porosity. Specifically, whereas porosity in effect was created at the time of deposition/emplacement of the ash-flow and air-fall units that constitute this stratigraphic interval, zeolite alteration is clearly a post-depositional process related to paleo-ground-water tables and post-cooling geochemical processes. To the extent that the zeolite alteration formed after faulting—as defined here (c.f. Clayton and others, 1997) by the observed offsets of the overlying Tiva Canyon Tuff—the stratigraphic coordinate conversion process will not remove the effects of faulting properly, and the spatial distribution of the alteration flags will appear more erratic and unpredictable than would be the case otherwise. Note that pre-Tiva Canyon Tuff faulting is known (Clayton and others, 1997), and there may well be pre-Topopah Spring Tuff faulting also.

Support for the concept of an incomplete stratigraphic coordinate transformation can be observed in the relatively strong horizontal anisotropy observed in both CH-PP porosity (table 15) and the indicator flags (table 16). For both property attributes, the direction of maximum spatial continuity is north–south. Faults in the vicinity of Yucca Mountain typically trend north–south as well, forming a series of progressively downdropped blocks from east to west. To the extent that the material properties in the transformed stratigraphic coordinates exhibit this stair-step structural pattern, one would anticipate that continuity of these properties along the structural grain would be markedly greater than across that grain. This phenomenon would also account for the noticeably zig-zag pattern exhibited by the east–west sample variogram as well. Incomplete removal of the effects of faulting would also allow the existence of the well-behaved sample variogram in the vertical direction, as variability within individual drill holes cannot be affected by faulting unless a drill hole actually penetrates a fault within the stratigraphic interval of interest.

Modeling Techniques

Geostatistical simulation comprises a large class of modeling techniques that can produce very complex, and presumably therefore highly realistic numerical representations of spatially variable properties. Simulation may be thought of as "expanding" (Journel and Alabert, 1989) the actual information available in a stochastic manner that is also compatible with additional information derived from the data ensemble and the spatial context of those data. The process builds upon the geologic intuition that unsampled locations nearby a known value "tend" to resemble that value, whereas unsampled locations at increasing distances from a known value tend progressively to resemble that datum less and less. This intuition will be observed statistically in a suite of several equiprobable simulations.

The philosophical framework of simulation is simple. Using concepts of random variables, one develops a model of the probability density function (*pdf*) for a material property of interest at all locations in space. By transforming the measured data to their respective positions on the probability density function and using simple kriging (Isaaks and Srivastava, 1989), the desired *pdf*s can be made conditional to a set of measured values. Alternative realizations are simply generated by sampling from these *pdf*s. The variance of individual, location-specific, *pdf*s will vary with the amount of geologic uncertainty. Near conditioning data [Figure 44(c)], the *pdf* associated with an unsampled location will be relatively narrow. Where less information is known, such as away from data or in the vicinity of conflicting measurements, the *pdf* will be relatively broad [figure 44(a-b)], leading to generation of a wide range of likely values across a suite of realizations. Because the underlying kriging algorithm used to derive the *pdf*s is an exact interpolator, the *pdf* degenerates to a spike with probability = 1 at a measured location [Figure 44(d)].

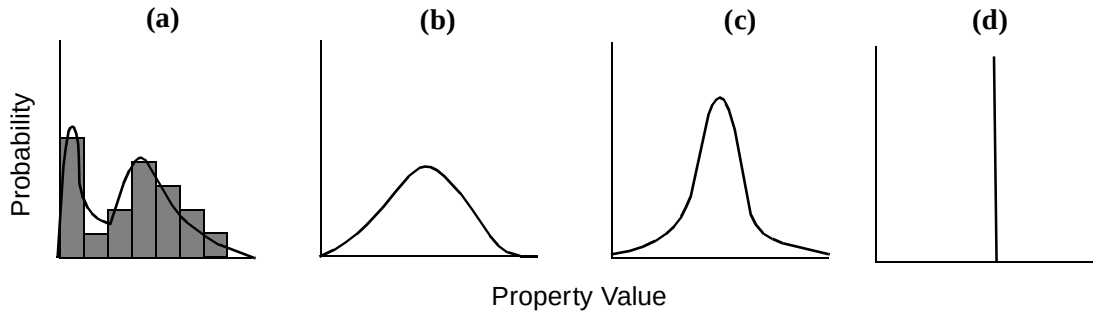

Figure 44. Conceptual probability density functions representing the uncertainty associated with various unsampled locations. (a) Beyond the range of spatial correlation: *pdf* is virtually identical to the univariate histogram; essentially all that is known about the unsampled location is what is known about the population as a whole. (b) Far away from a sample, but within the range of spatial correlation: *pdf* is broad, indicating considerable uncertainty; distribution begins to focus on expected value. (c) Nearby a sample value: *pdf* is narrower indicating lesser uncertainty. (d) Immediately adjacent to a sample value: *pdf* is nearly a spike value corresponding to the adjacent sample datum (from Cromer and Rautman, 1995).

Simulations may be conditional or unconditional. Conditional simulations are numerically anchored to a specific set of real-world data (as described in the preceding paragraph), and they possess three special properties that add to their usefulness in evaluating the effects of geologic uncertainty on physical process models. Specifically, conditional simulations:

1. reproduce the known data values at the same locations within the model as represented by the real-world samples;
2. reproduce the overall univariate descriptive statistics of the known data values; and
3. reproduce the bivariate statistics, or two-point spatial correlation structure, of the data.

Unconditional simulations are similar, except that they are not conditioned to any particular spatially anchored data, and thus item 1 does not apply. As simulations with these three characteristics cannot be distinguished statistically from the ensemble of data used in their construction, they serve as alternative, equally-likely stochastic realizations of an incompletely sampled and measured reality.

Simulations may also be developed using parametric or nonparametric techniques for mechanically inducing the desired univariate (item 2 above) and bivariate statistical properties (item 3). Parametric techniques rely upon the predictive power of well-understood multivariate probability functions, almost invariably the multivariate gaussian. A number of algorithms have been developed that implement gaussian-related simulation (for example, references in Deutsch and Journel, 1992).

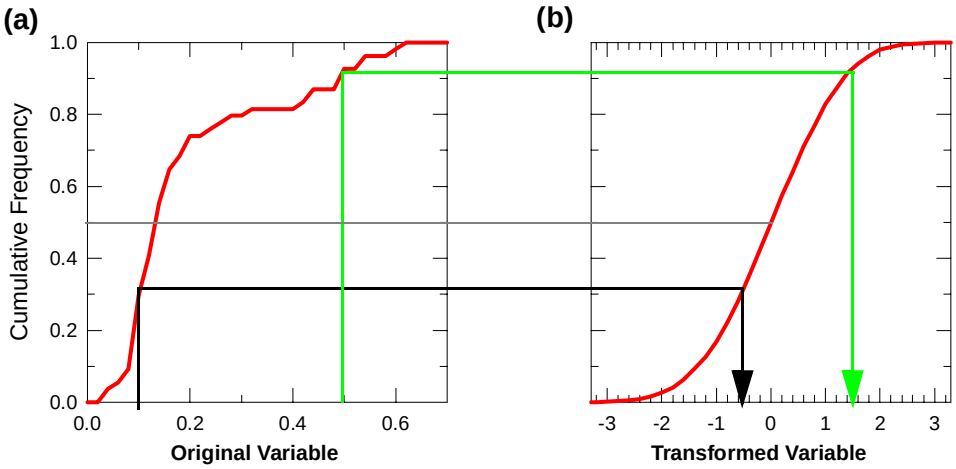

Figure 45. Graphical representation of the quantile-preserving normal-score transform process. A population with virtually any univariate distribution (a) can be transformed to any other univariate distribution (b) (here gaussian) in a manner represented by the arrows such that the quantile relationships among the data are preserved.

Sequential Gaussian Simulation of a Continuous Variable

The sequential gaussian simulation program **SGSIM** (Deutsch and Journel, 1992) was used to generate 100 replicate models of porosity for each of the three model units, conditioned to the observed porosity data from the several drill holes. The sequential modeling process is relatively straightforward and is implemented as follows:

1. All data values are converted to a univariate standard-normal (μ=0, σ^2=1) distribution using the graphical normal-score transform (fig. 45; implemented in program **NSCORE**; Deutsch and Journel, 1992). This transformation does nothing to the spatial correlation structure because the relative positions of all values with respect to each other are preserved (i.e., the transform is quantile preserving). However, the transformation does simplify the process of generating simulated values later in the algorithm.
2. The spatial correlation structure is identified using the normal-score transformed

values and modeled using standard variography.

3. The transformed measured data are mapped into the model coordinate system. Any sample data that coincide with a model grid node are assigned to that node and identified such that those nodes are not simulated.[†]
4. A random path is defined through the model grid such that each unsampled node is visited once and only once.
5. At each unsampled grid node, a search is conducted for "nearby" measured data and for any previously simulated grid nodes. The search parameters (anisotropic search radii; number of data to use) are user specified.
6. The (user specified) *N* closest nodes are identified and weighted using simple kriging (Isaaks and Srivastava, 1989) by their structural distance according to the model variogram provided as input to the algorithm. Because the normal-score transformed values are effectively relative positions on a cumulative distribution function, the resulting kriged value is also effectively as relative position on the same cumulative distribution function. This value is then taken a the *expectation* of a gaussian variable with a variance equal to the kriging variance (Isaaks and Srivastava, 1989).
7. A uniform random value between zero and one is then generated and taken as the relevant position on the cumulative distribution function defined in step 6. The corresponding *cdf* value is assigned as the simulated value for this node, the value is added to the set of data available for simulation of as-yet unsimulated grid nodes, and the simulation process moves to the next node along the random path defined in step 4.
8. After all originally unsampled grid nodes have been simulated using the logic of steps 5 through 7, the resulting spatial array of values are back-transformed to the original porosity space using the inverse of the normal-score transform of step 1 and the simulation process is complete.

Spatial correlation is induced in the simulated models through the use of previously simulated grid-node values in determining the expected value of subsequent local *cdf*s.

Sequential Indicator Simulation of a Categorical Variable

Sequential indicator simulation of a categorical variable (program **SISIMPDF**; Deutsch and Journel, 1992) was used to generate 100 replicate models of (zeolite) alteration within the combined Calico Hills–Prow Pass model unit, conditioned to the observed alteration indicator flags [page 43; eqs.(1), (8), and (18)] from the several drill holes. The sequential simulation modeling process is again relatively straightforward and utilizes much the same logic of the sequential gaussian simulation methodology described on page 61. Note that no data transformation is required in the present case. We are concerned with a categorical variable that can take on only discrete values, and because there are only two such categories—unaltered and altered—the binary zeros and ones assigned by equations (1), (8), and (15) are sufficient. The remainder of the modeling process is as follows:

1. The spatial correlation structure of the binary category distinction is identified using standard variography. Note that although "contributions" toward the numerical value of γ via equation (16) come only from the category assigned a value of one, it makes no difference to which category this value is assigned.

[†]Program **SGSIM** contains a user option as part of the search for nearby information either to relocate data values to grid nodes (in which case the search for nearby information is vastly simplified) or to leave the data values in their original spatial position (in which case the assignment and non-simulation described in this step, strictly speaking, is not true). This latter option is the one that was implemented for these simulations, because relocation of data values to grid nodes forces *all* data values to nodes, even if the physical distance from a drillhole sample to the nearest node is a full grid half-spacing. Also, data with close vertical spacing would be "collapsed" onto a single grid node, resulting in the undesirable discarding of much potential information.

2. The observed alteration indicator flags are mapped into the model coordinate system. Any flags that coincide with a model grid node are assigned to that node and identified such that those nodes are not simulated.

3. A random path is defined through the model grid such that each unsampled node is visited once and only once.

4. At each unsampled grid node, a search is conducted for "nearby" alteration flags and for any previously simulated grid notes. Again, the search parameters are user specified.

5. The *N* closest nodes are identified and weighted using simple kriging by their structural distance according to the model variogram provided as input to the algorithm. Because the indicator flags themselves are in effect representatives of a degenerate cumulative distribution function (alteration is either present with probability of 1 or it is absent with a probability of alteration equal to zero), the resulting kriged value is again a relative position on the same cumulative distribution function. This value is taken as the probability of the state: "altered rock" prevailing at that spatial location.

6. A uniform random number between zero and one is then generated and compared with the probability value. If the uniform random number is equal to or less than the probability, the node is assigned an indicator value of one (altered), whereas if the uniform random number is greater than the probability, the node is presumed to be unaltered and assigned an indicator value of zero. This simulated value is added to the set of data available for the simulation of as-yet unsimulated grid nodes, and the modeling process moves to the next node along the random path defined in step 3.

The result of this simulation process is one specific realization consisting of a spatial array of ones and zeros indicating that the rocks at each modeled location either have been or have not been altered.

Linear Coregionalization

Numerous investigations at Yucca Mountain have shown that various material properties are correlated with one another (cross-variable correlation); for example: Istok and others, 1994; McKenna and Rautman (1995); Flint and others (1996b). There are two principal methods that have been used to incorporate these correlations into rock properties models in the presence of severe undersampling of one variable. First, one may assume a coefficient of determination (r^2) equal to one and simply apply the empirically determined regression equation to predict the secondary (undersampled) variable. A second method is to model a randomly distributed error ("noise") about the regression line. Neither of these two alternatives is particularly satisfying. In many instances, $r^2 = 1.0$ implies a substantially stronger relationship than exists in fact. However, the technique has been used in past modeling of rock properties at the Yucca Mountain site (Robey, 1994). In the second case, a cross-plot of the two resulting variables reproduces the observed coefficient of determination, but any spatial correlation exhibited in nature by the secondary variable is effectively destroyed by the addition of spatially uncorrelated noise (Robey, 1993; Rautman and Robey, 1993).

The best alternative would be to use a modeling methodology that reproduces both the observed correlation between the variables and the observed spatial correlation structure. Cokriging and cosimulation (David, 1977; Journel and Huijbregts, 1978; Deutsch and Journel, 1992) are well-established mechanisms for producing such models if there are sufficient data from which to infer the necessary autocorrelation and cross correlation structures.

However, in the presence of severe undersampling of the secondary variable, such as is encountered at Yucca Mountain, an attractive practical alternative is to use a *linear model of coregionalization* (Journel and Huijbregts, 1978), in which the spatial continuity of both the secondary variable and the cross-variable spatial continuity is presumed to be approximately identical to that of the primary variable. This technique of coregionalization has been applied to the modeling of unsat-

urated flow properties at the Apache Leap Tuff site (Arizona) by Desbarats (1995; 1997), and it has also been applied recently to modeling correlated properties at Yucca Mountain (Altman and others, 1996; McKenna and others, 1996; Rautman, 1996; Ho and others, 1997†).

The mathematical basis of linear coregionalization has been described by Journel and Huijbregts (1978) and by Luster (1985), among others. The description that follows is taken broadly from Altman and others (1996) and from Desbarats (1995; 1997). Although we are concerned principally at Yucca Mountain with cases involving two variables, there is no theoretical limit to the number of variables that can be coregionalized.

Recall the following definitions from classical statistics applicable to *random variables* (see for example, Larson, 1982). Consider a set of random variables X_1, X_2, … X_n, with *expected values* $E[X_1] = \mu_1$, $E[X_2] = \mu_2$, …, and *variances* of:

$$Var[X_1] = E[(X_1 - \mu_1)^2] = \sigma_1^2 \quad \text{, and}$$

$$Var[X_2] = E[(X - \mu_2)^2] = \sigma_2^2 \text{ , ….}$$

The *covariance* of X_1 with X_2 is defined as:

$$Cov[X_1, X_2] = E[(X_1 - \mu_1)(X_2 - \mu_2)] \quad \text{, …,} \quad (19)$$

and the *correlation coefficient* between variables X_1 and X_2 is:

$$r_{12} = \frac{Cov[X_1, X_2]}{\sqrt{Var[X_1]Var[X_2]}} \text{ , ….} \quad (20)$$

Recall also that the covariance of a variable with itself (the autocovariance) is equal to the variance of that variable: i.e., $Cov[X_1, X_1] = Var[X_1]$. We can now define the following *covariance matrix* as a concise means of expressing the various relationships described above (for two variables only):

$$\mathbf{c} = \begin{bmatrix} c_{11} & c_{12} \\ c_{21} & c_{22} \end{bmatrix} \quad , \quad (21)$$

where the "**c**" denotes the (co)variance operator and the subscripts indicate the variables involved. Note that if the variables are (for convenience) in *standard normal* form with $\mu_i = 0$ and $\sigma^2_i = 1$, then the diagonal terms of $\mathbf{c}$ will be equal to 1 and the off-diagonal terms reduce to the correlation coefficient, *r*.

Now consider a *weighted linear combination* of a number of different random variables, X_i, such that the resulting random variable *Y* is defined as:

$$Y = a_1X_1 + a_2X_2 + ... + a_nX_n = \sum_{i=1}^{n} a_iX_i \quad (22)$$

where the a_i are any set of constants (weights). It is now possible to make statements about the mean and variance of *Y*. Thus (Larson, 1982):

$$\mu_Y = E[Y] = \sum_{i=1}^{n} a_iE[X_i] \quad \text{, and} \quad (23)$$

$$\sigma_Y^2 = Var[Y] = \sum_{i=1}^{n} a_i^2 Var[X_i] + 2\sum_{i<j}\sum_{j} a_i a_j Cov[X_i, X_j] \text{ .} \quad (24)$$

The case of spatially varying random variables, such as are of interest at Yucca Mountain, is essentially identical, only now the value of each variable is a function of spatial position, **x**; such spatial variables are, by convention, frequently represented as *Z*; thus $Z(\mathbf{x})$. The strength of the *spatial correlation* is typically defined through use of a covariance matrix, which, in the presence of second-order stationarity, is a function of the separation vector (**h**) between two locations, **x** and **x**+**h**. Although computations invariably are performed using the covariance matrix, $\mathbf{C}(\mathbf{h})$, most geologic descriptions of spatial variability typically make use of the (semi)variogram, $\gamma(\mathbf{h})$, related through:

$$C(\mathbf{h}) = c_{ii} - \gamma(\mathbf{h}) \text{ .} \quad (25)$$

We can thus define the following direct and cross-variable semivariograms for two variables Z_1 and Z_2 separated by **h**:

$$\gamma_1 = C0_1 + C1_1 Sph_a(\mathbf{h}) \text{ ,} \quad (26)$$

†Ho and others milestone reference

$$\gamma_2 = C0_2 + C1_2 Sph_a(\mathbf{h}) \ , \qquad (27)$$

$$\gamma_{12} = C0_{12} + C1_{12} Sph_a(\mathbf{h}) \ , \qquad (28)$$

where the expression $C1Sph_a(\mathbf{h})$ refers to a spherical variogram model with range = a and sill =$C1$.

Returning to the issue of coregionalization of two spatial variables, the objective is to obtain a *joint* model of two variables, Z_1 and Z_2, such that the spatial relationships described by equations (26) through (28) are satisfied simultaneously. To do this, we define two new variables, Y_1 and Y_2. Each of these variables has $E[Y_1] = E[Y_2] = 0$, and they are described by identical covariance functions $K_1(\mathbf{h})$ and $K_2(\mathbf{h})$. Furthermore, these variables are independent of one another, such that $K_{12}(\mathbf{h}) = 0$ for all separation vectors, $\mathbf{h} \neq 0$. We now redefine our desired variables, Z_1 and Z_2, as a weighted linear combination (equation 23) of the new variables, Y_1 and Y_2:

$$Z_1(\mathbf{x}) = a_{11} Y_1(\mathbf{x}) + a_{12} Y_2(\mathbf{x}) \qquad (29)$$

$$Z_2(\mathbf{x}) = a_{21} Y_1(\mathbf{x}) + a_{22} Y_2(\mathbf{x}) \qquad (30)$$

where the weights are defined by the terms of the matrix:

$$\mathbf{A} = \begin{bmatrix} a_{11} & a_{12} \\ a_{21} & a_{22} \end{bmatrix} . \qquad (31)$$

Note that because Y_1 and Y_2 were specified as independent (uncorrelated), $Cov[Y_1,Y_2] = 0$ and all the terms involving $Cov[X_i,X_j]$ with i ≠ j drop out of equation (24). Thus, we can express the direct and cross covariances of our desired final variables, Z_1 and Z_2, as:

$$C_1(\mathbf{h}) = a_{11}^2 K_1(\mathbf{h}) + a_{12}^2 K_2(\mathbf{h}) \ , \qquad (32)$$

$$C_2(\mathbf{h}) = a_{21}^2 K_1(\mathbf{h}) + a_{22}^2 K_2(\mathbf{h}) \ , \qquad (33)$$

$$C_{12}(\mathbf{h}) = a_{11} a_{21} K_1(\mathbf{h}) + a_{12} a_{22} K_2(\mathbf{h}) \ . \qquad (34)$$

Under the hypothesis that the variables are coregionalized (and without objective evidence to the contrary), we *assume* that these direct and cross covariances are identical. This assumptions leaves only the four weighting factors (the a_{ij}) to be determined. However, there are four unknowns with only three descriptive equations. Luster (1985) and Altman and others (1996, after Luster) dealt with this under-determined case simply by setting one of the weights to zero (choose: $a_{12} = 0$). This choice has the practical effect of setting one of the Z variables equal to one of the Y variables, thus:

$$Z_1(\mathbf{x}) = Y_1(\mathbf{x}) \text{ and} \qquad (35)$$

$$Z_2(\mathbf{x}) = a_{21} Y_1(\mathbf{x}) + a_{22} Y_2(\mathbf{x}) \ , \qquad (36)$$

with:

$$C_1(\mathbf{h}) = K_1(\mathbf{h}) , \qquad (37)$$

$$C_2(\mathbf{h}) = a_{21}^2 K_1(\mathbf{h}) + a_{22}^2 K_2(\mathbf{h}) \ , \text{ and} \qquad (38)$$

$$C_{12}(\mathbf{h}) = a_{21} K_1(\mathbf{h}) \ , \qquad (39)$$

leaving us with three equations and three unknowns. Although this arbitrary choice setting one of the weights to zero produces only one of a large number of possible values for Z_2, this number is sufficient for our purposes. This approach is also convenient in that if $a_{12} = 0$, then it can be shown that $a_{11} = 1$, a_{21} = the correlation coefficient, r, and $a_{22} = \sqrt{(1-r^2)}$, thus simplifying the computations.

If we select one of the conditional porosity simulations as $Z_1(\mathbf{x})$, and convert those values to standard normal form $Z_1'(\mathbf{x}) = Y_1(\mathbf{x})$ (with $\mu_i = 0$ and $\sigma^2_i = 1$) using the graphical normal-score transform (GSLIB program **NSCORE**; fig. 45), we are now in a position to compute (Desbarats, 1995):

$$[Z][Z]^T = [A][Y][Y]^T[A]^T = [\mathbf{c}] \ , \qquad (40)$$

which gives us the remaining coefficients of **A**. We then generate a second, independent (i.e., *un*conditional) standard-normal simulation using the same variogram parameters, and by substitution of these Y_2 values in equation (36), we obtain values of $Z_2'(\mathbf{x})$ corresponding to each input value of $Z_1(\mathbf{x})$, and which overall exhibit the desired correlation coefficient, *r*. Because $Z_2'(\mathbf{x})$ is still in standard normal form ($\mu_i = 0$ and $\sigma^2_i = 1$), we can back-transform these values to an appropriate univariate distribution for $Z_2(\mathbf{x})$ using the GSLIB routine **TRANS.**

In the modeling described in this report, the process of linear coregionalization is applied to create spatially and cross-variable correlated simulated models of thermal conductivity and $\log_{10}$ saturated hydraulic conductivity using the observed

correlation of these secondary properties with porosity. The univariate distributions used in the back-transformations are those described in the appropriate portions of the section on Statistical Description.

Post-Processing of Simulations

Porosity-as-a-Surrogate for Rock-Type Classes

Geostatistical simulation, including the generation of secondary property fields through coregionalization, produces coherent fields of spatially correlated rock properties. However, we also know from material presented in the section on the Statistical Description of hydraulic conductivity that at least three rock-type classes exist for this secondary property: viz., a vitric-through-devitrified continuum, a "zeolitic" altered continuum, and a microfractured vitrophyre continuum. Generation of the final full-field property models thus requires one or more post-processing steps to delineate these three rock types and ensure that the proper correlations of hydraulic conductivity with porosity are respected. Once the proper rock-type class has been determined the generation of the appropriate hydraulic conductivity value is mathematically trivial, once the various submodels have been generated. The steps are outlined in figure 46 for intermixed unaltered and altered ("zeolitic") rocks, and in figure 47 for microfractured vitrophyres. Current treatment of *thermal* conductivity is simplified, in that this property has been modeled for only one rock-type classification, the vitric-devitrified continuum, and for only one geologic unit, the welded portion of the Topopah Spring Tuff.

Figure 46 is the post-processing logic diagram used to generate the full-field coregionalized saturated hydraulic conductivity field for the Calico Hills–Prow Pass model unit, while accounting for the presence of hydrous-phase mineral alteration. The process begins with the simulated porosity field and a corresponding field of estimated alteration flags. Note that no changes are required to the porosity field itself, as the zeolitization process appears not to affect the total amount of pore space in the rock (see text associated with fig. 25). We begin the post-processing process by generating a coregionalized preliminary hydraulic conductivity field, for which the appropriate histogram

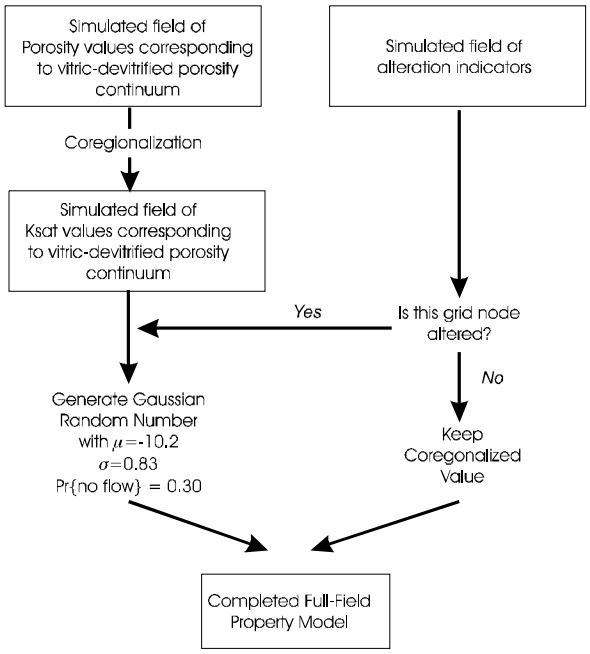

Figure 46. Logic diagram for post-processing porosity and alteration indicator simulations to recognize hydraulic conductivity dependence on alteration state. See text for discussion.

and variogram are reproduced. Each grid node within the preliminary conductivity field is then evaluated for the likely presence of (zeolitic) alteration. If specific node considered is modeled as unaltered, the preliminary hydraulic conductivity value is retained for the final, full-field conductivity model. If, however, the grid node has been modeled as "altered," the preliminary hydraulic conductivity value is discarded, and an "interim" simulated "zeolitic" hydraulic conductivity value that is not correlated with porosity is drawn randomly from a normally distributed population with the desired mean and variance for CH–PP samples (μ = –10.2; σ = 0.83 log units; see fig. 26). Because approximately 30 percent of the hydraulic conductivity samples measured in the laboratory for altered rocks from the Calico Hills–Prow Pass model unit yielded no-flow results, a second random number was generated from a uniform distribution. If the second random number was less than 0.30, the interim conductivity value was also dis-

carded and replaced by a simulated no-flow conductivity of –14.0 $\log_{10}$ m/sec. If the uniform random number was greater than or equal to the desired fraction of no-flow values, the interim conductivity value was retained for the final full-field simulation of the Calico Hills–Prow Pass model unit.

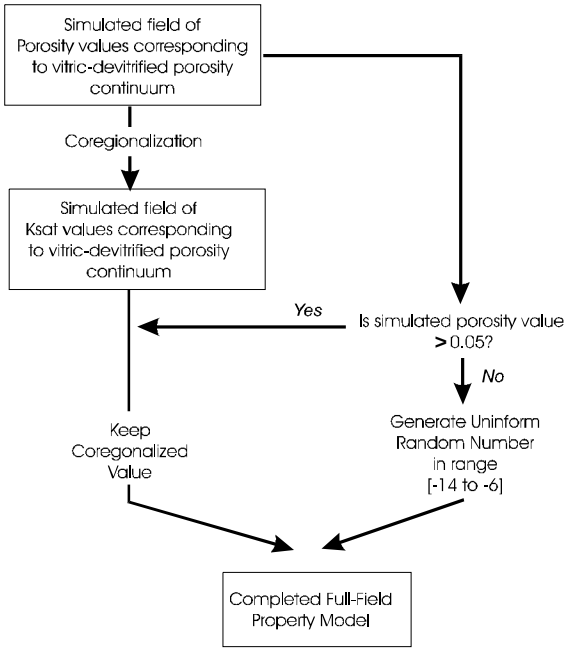

Figure 47. Logic diagram for post-processing porosity and hydraulic conductivity simulations to recognize vitrophyre rock type. See text for discussion.

A similar logic diagram is presented in figure 47 that outlines simulation of saturated hydraulic conductivity fields for the Topopah Spring welded model unit to account for the local presence of vitrophyric rocks. An input simulated model of TSw porosity is coregionalized to produce a preliminary spatially correlated conductivity field. For each grid node, the corresponding porosity value was examined to determine if the node was likely to represent a low-porosity and presumably microfractured vitrophyre. If the porosity value was greater than 0.05 (see text associated with fig. 27), the node was determined unlikely to represent a vitrophyre, and the preliminary hydraulic conductivity value was retained for the full-field simulation. If, however, the relevant porosity value was less than or equal to 0.05, the node was judged vitrophyric, and a "microfractured" hydraulic conductivity value was drawn at random from a uniform population with a range from –14.0 to –6.0 $\log_{10}$ m/sec and placed in the final, full-field model of simulated hydraulic conductivity.

Model Validation

A fundamental premise of the Monte Carlo simulation approach is that each individual realization is a plausible model of the unknown real world and that variation between the different stochastic realizations represents a variety of outcomes consistent with all that is known. Presumably, the only meaningful difference between realization 1 and realization *N* is that a different random number "seed" was used to initiate the simulation process (definition of the random path and generation of the various uniform random numbers that produce the output value at each node from the locally conditioned probability density function). Recalling that conditional simulations theoretically possess the attributes of data reproduction described on page 61 it should be possible to *test* the validity of individual models in terms of statistical similarity to the data.

Recognizing that the term *validation* has a number of frequently controversial meanings within the modeling community, we hereby restrict the meaning of this word for purposes of this report to the following empirical tests of agreement between a simulated exhaustive model of reality and the underlying partially known (i.e., sampled) vision of reality that we have obtained from site data.

1. Does the model reproduce the measured values of the particular attribute that were used to generate the model at the proper spatial position of those values?
2. Does the model as a whole reproduce the statistical character of the data ensemble used to condition the model?
3. Do the individual modeled attribute values exhibit spatial correlation consistent with the spatial continuity patterns exhibited by

the sample data and with the geologic processes that produced the real world?

Note that each of these three criteria is, by the very nature of the modeling problem, subject to certain limitations on "exactness." First and foremost among these limitations is that the underlying reality is known only imperfectly through sampling. Were the real world known exhaustively in fact, there would be no reason for producing models and estimating uncertainty. This is a very real and challenging limitation, and it is unclear how much departure from the *sample* statistics should be tolerated before declaring an exhaustive model "unrealistic." Second, constructed models are typically discretized to a grid of values of some defined resolution for computational purposes. Thus, the degree of reproduction of data values and of statistical character is influenced by the coarseness of the modeling grid. Unlike the imponderable decision of how much reliance to place on an imperfectly sampled set of data, some of these considerations can be answered, if necessary, by increasing grid resolution.

Summarized Suites of Simulations: Expected-Value Models

Monte-Carlo-style simulation modeling produces entire suites of models, all of which are proposed as statistically indistinguishable from one another (and from the known data). Dealing with suites of models is, in itself, a challenge, and furthermore, is goal dependent (see also fig. 6 on page 17). If the objective of a modeling exercise is to evaluate whether or not the ground-water travel time from point A to point B will meet or exceed some stated value with some specified degree of confidence, then it is a matter of computing the ground-water travel time (presumably using particle-tracking methods) using some flow-and-transport computer code from point A to point B in each of a group of separate material-property realizations and evaluating what proportion of those individual computations met or exceeded the stated criterion. If the objective is to evaluate the uncertainty (i.e., range of likely values) associated with a particular point in space, then it is a matter of evaluating some (large) number of equiprobable stochastic outcomes for that spatial position as suggested by the diagram of figure 48, and describing the variability using some statistical summary value (total range, interquartile range, variance, standard deviation, etc.). Recall that the ordinary kriging variance is independent of the magnitude of the kriging estimate (something that is rarely observed in earth science data), and is a quantitatively rigorous measure of local accuracy under relatively restrictive conditions of fully multigaussian spatial behavior (Deutsch and Journel, 1992; p. 15). The simulation approach, because it relies on (constrained) random number generation from the full range of physically possible values in a sequential manner in which early-simulated values influence the generation of later-simulated values, is held to be a more robust approach to the evaluation of uncertainty in the face of departures from multigaussian behavior including contradictory conditioning information.

One common method of summarizing a suite of stochastically generated models is to focus on the spatially distributed values judged as "likely" to be encountered by actual sampling according to some desired criterion. Although the mathematically *expected value*, corresponding theoretically to the arithmetic mean of a very large number of simulations is frequently selected as the object of interest (the so-called *expected-value* or *E-type model*), there is no a priori reason for selecting the material-property expectation except convention. One might as well select the *median* value (*M-type model*) of the available realizations or the *q*-quantile model where *q* is essentially arbitrary. The point is that a summary model is precisely that—a summary of something else. Accordingly, the convenient correspondence between a summary model and the observed attributes of the real world data (page 61) no longer need be present (see also *Model Validation* beginning on page 67). Note also that under strict assumptions of multivariate gaussian spatial behavior, the E-type model for an infinite number of individual realizations is identical to a kriged model (Journel and Huijbregts, 1978).

We present in this report a set of summarized models corresponding to the E-type model, computed as a grid node-by-grid node average of each set of simulated models. The computational process is effectively trivial and is illustrated schematically in figure 48.

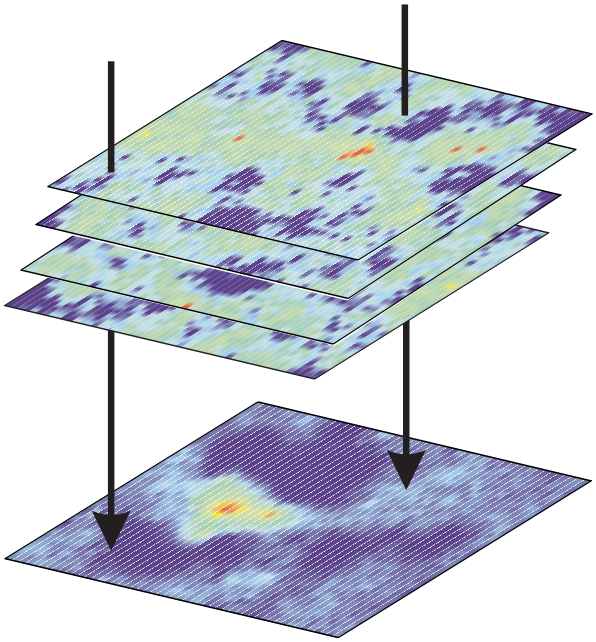

Figure 48. Conceptual representation of the process of developing a summary model from a suite of stochastic realizations for two dimensions. Note that it is possible to construct summary models showing virtually any desired statistical summary at each spatial location.

Uncertainty Measures

In addition to the somewhat conventional E-type summary models for each material property in each of the three model units presented in this report, we compute and present a set of models of uncertainty as captured by the standard deviation of the relevant realization suite. Computation of the standard deviation is relatively mechanical, and is performed in the same manner as the computation presented in figure 48. Other uncertainty measures, such as the inter-quartile range or a 95-percent confidence interval also could be computed and portrayed as models of uncertainty for a particular purpose.

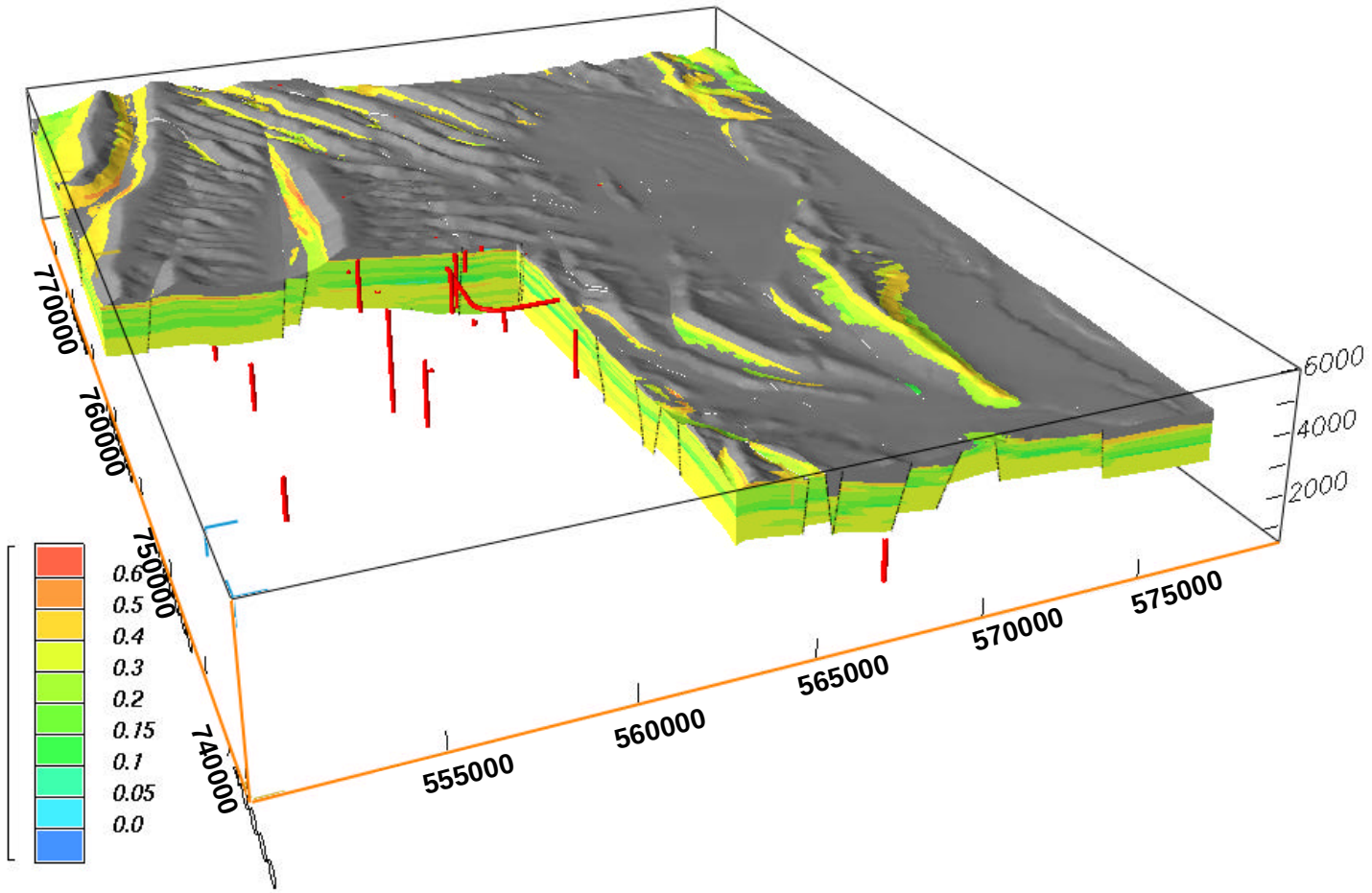

Plate 1. Perspective diagram looking northeast without vertical exaggeration of the composite total porosity model of Yucca Mountain developed as part of this study, including the upper Paintbrush nonwelded model unit, the Topopah Spring welded unit, and the Calico Hills–Prow Pass model unit. Welded rocks of the Tiva Canyon Tuff not modeled, and are shaded grey; units underlying the pre-Prow Pass tuff bedded tuff are not shown. Vertical red objects represent drillhole locations, and horizontal red object is the ESF main drift and south ramp. See also plate 2.

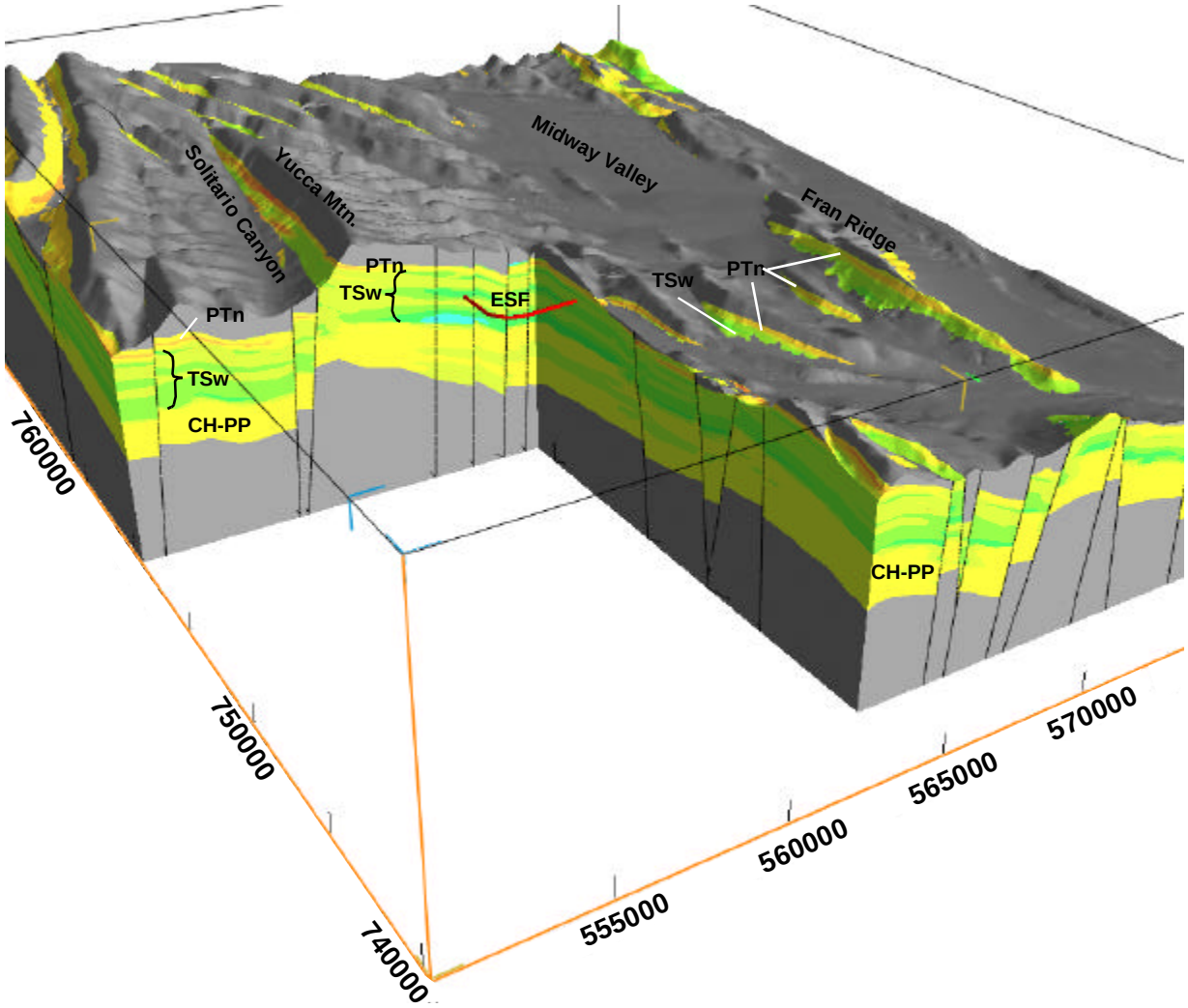

Plate 2. Closer view perspective diagram from plate 1 looking northeast with 2x vertical exaggeration of the composite total porosity model of Yucca Mountain showing additional detail of material properties heterogeneity. Porosity color scale same as plate 1. Unit abbreviations: PTn–upper Paintbrush nonwelded model unit; TSw–Topopah Spring welded model unit; CH–PP–combined Calico Hills–Prow Pass model unit. Nevada state plane coordinates in feet.

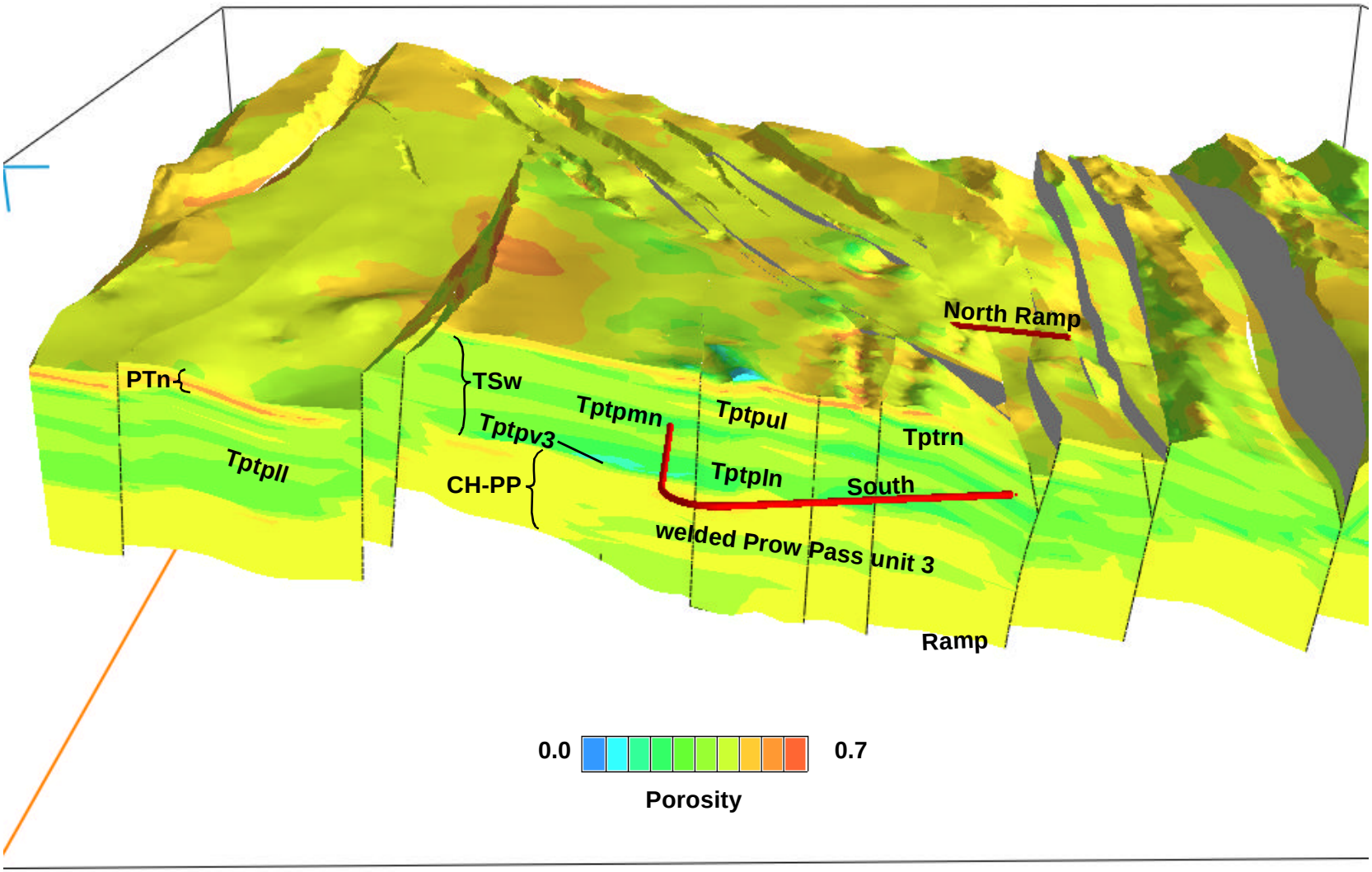

Plate 3. Perspective diagram looking north of the composite total porosity model for all three model units. Front of model is along Nevada state plane coordinate 761000 N; 2x vertical exaggeration. Red object is ESF south ramp.

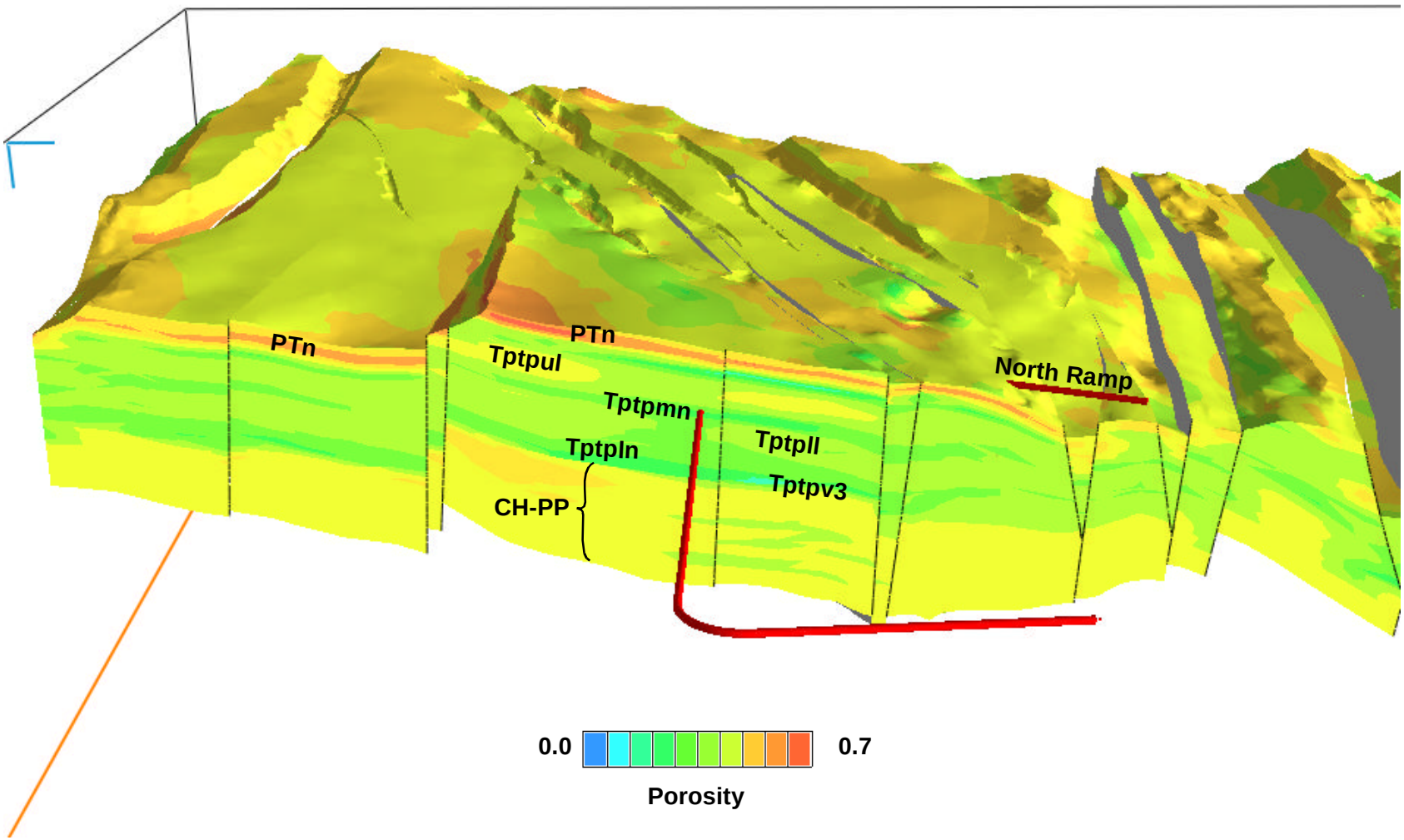

Plate 4. Perspective diagram looking north of the composite total porosity model for all three model units. Front of model is along Nevada state plane coordinate 766000 N; 2x vertical exaggeration. Red object is ESF main drift and south ramp.

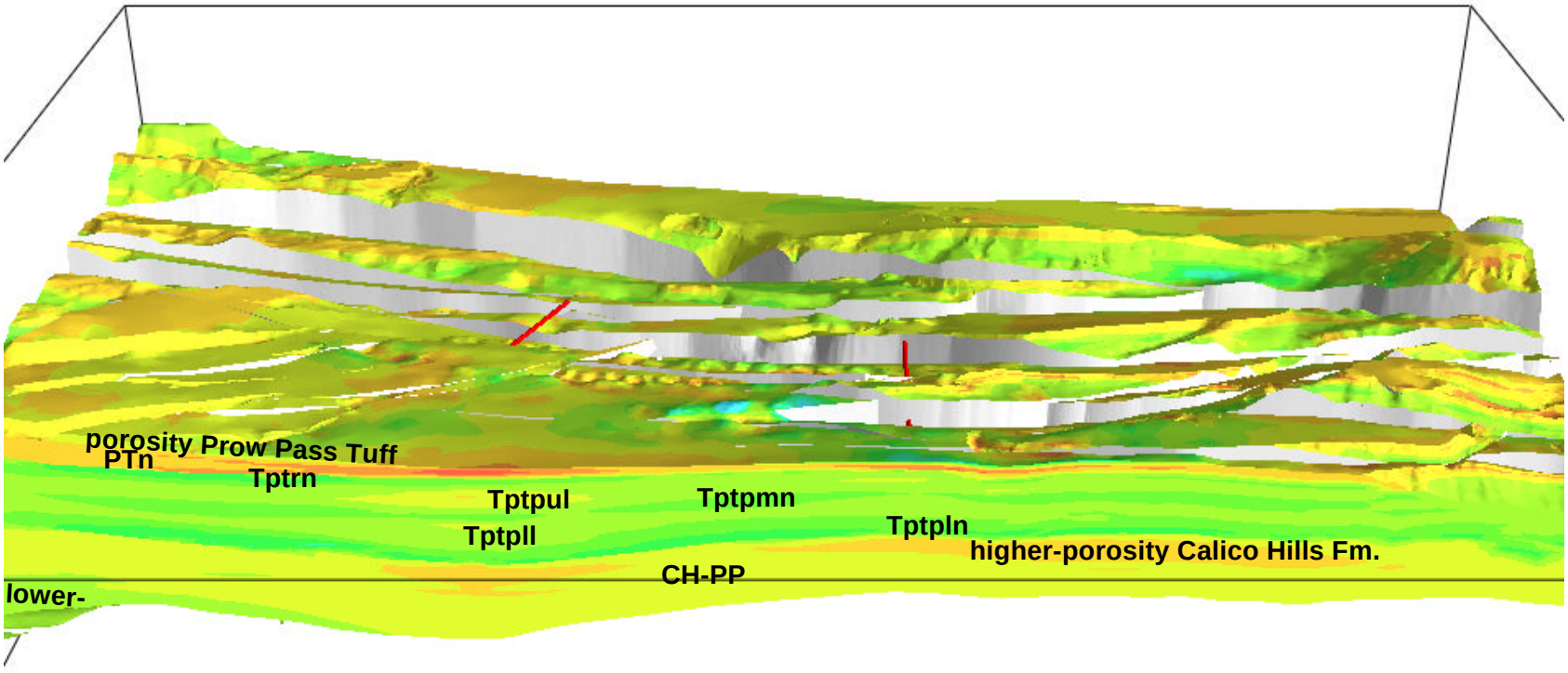

Plate 5. Perspective view looking east of the composite total porosity model for all three model units. Front of model is along Nevada state plane coordinate 560,000 E; 2x vertical exaggeration. Red objects are ESF ramps; fault surfaces are grey.

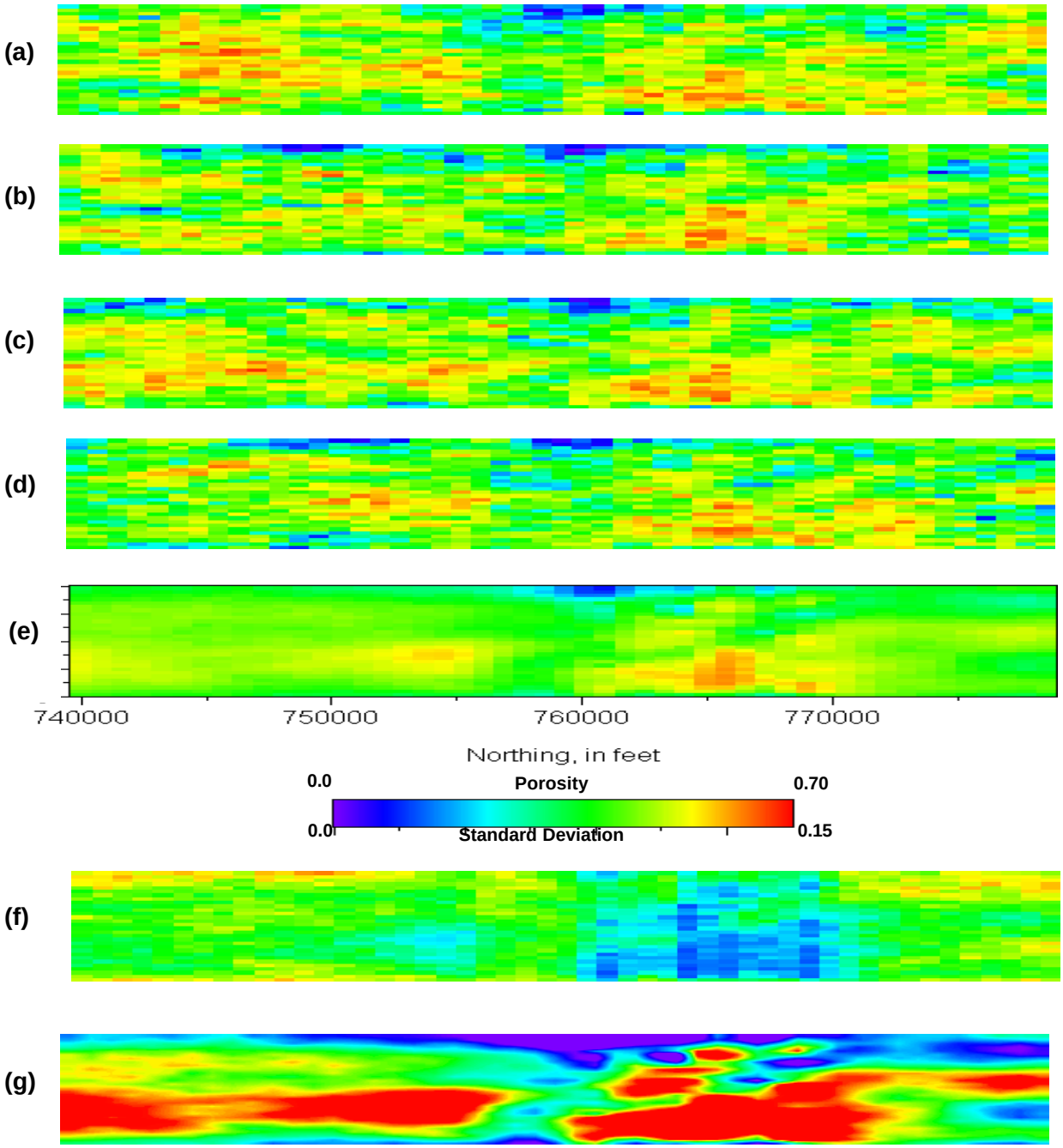

Plate 6. (a)–(d) Four simulations of porosity in the PTn model unit; (e) E-type model of porosity in the PTn model unit; (f) uncertainty of porosity in the PTn model unit; (g) E-type model with colors adjusted to show selected features. North–south cross section 15, looking west.

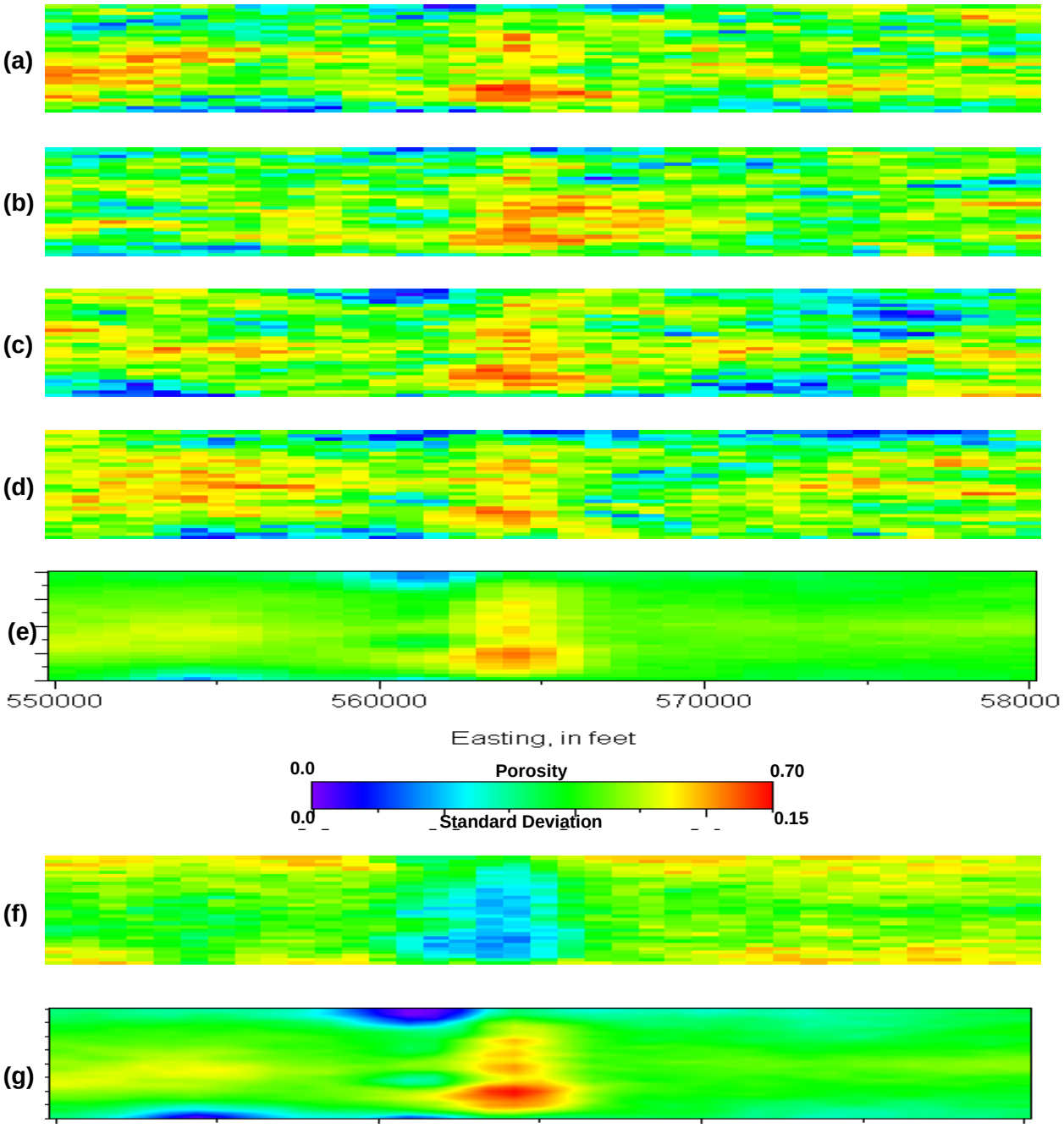

Plate 7. (a)–(d) Four simulations of porosity in the PTn model unit; (e) E-type model of porosity in the PTn model unit; (f) uncertainty of porosity in the PTn model unit; (g) E-type model with colors adjusted to show selected features. East–west cross section 28, looking north.

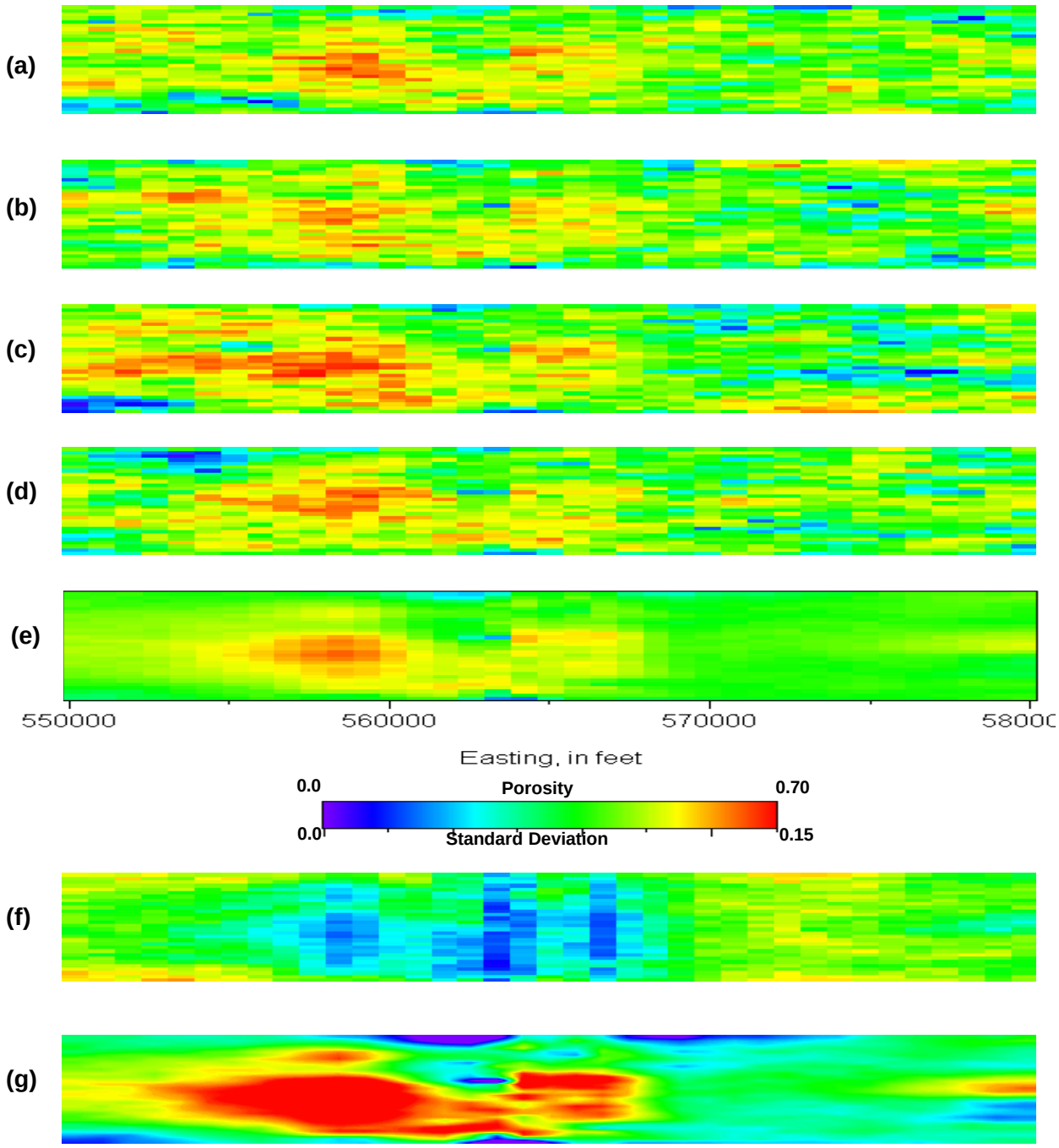

Plate 8. (a)–(d) Four simulations of porosity in the PTn model unit; (e) E-type model of porosity in the PTn model unit; (f) uncertainty of porosity in the PTn model unit; (g) E-type model with colors adjusted to show selected features. East–west cross section 34, looking north.

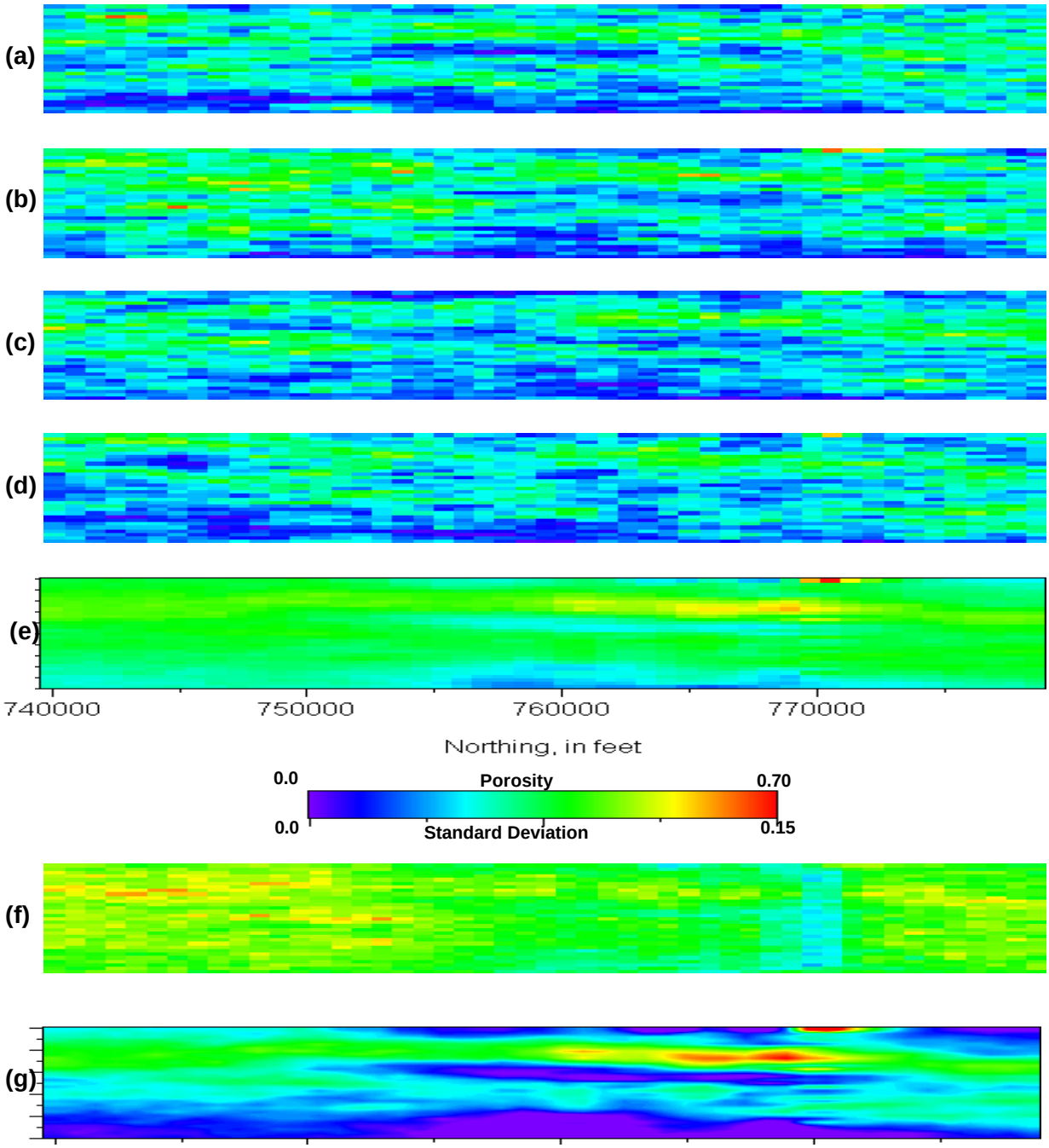

Plate 9. (a)–(d) Four simulations of lithophysal porosity in the TSw model unit; (e) E-type model of porosity in the TSw model unit; (f) uncertainty of lithophysal porosity in the TSw model unit; (g) E-type model with colors adjusted to show selected features. North–south cross section 15, looking west.

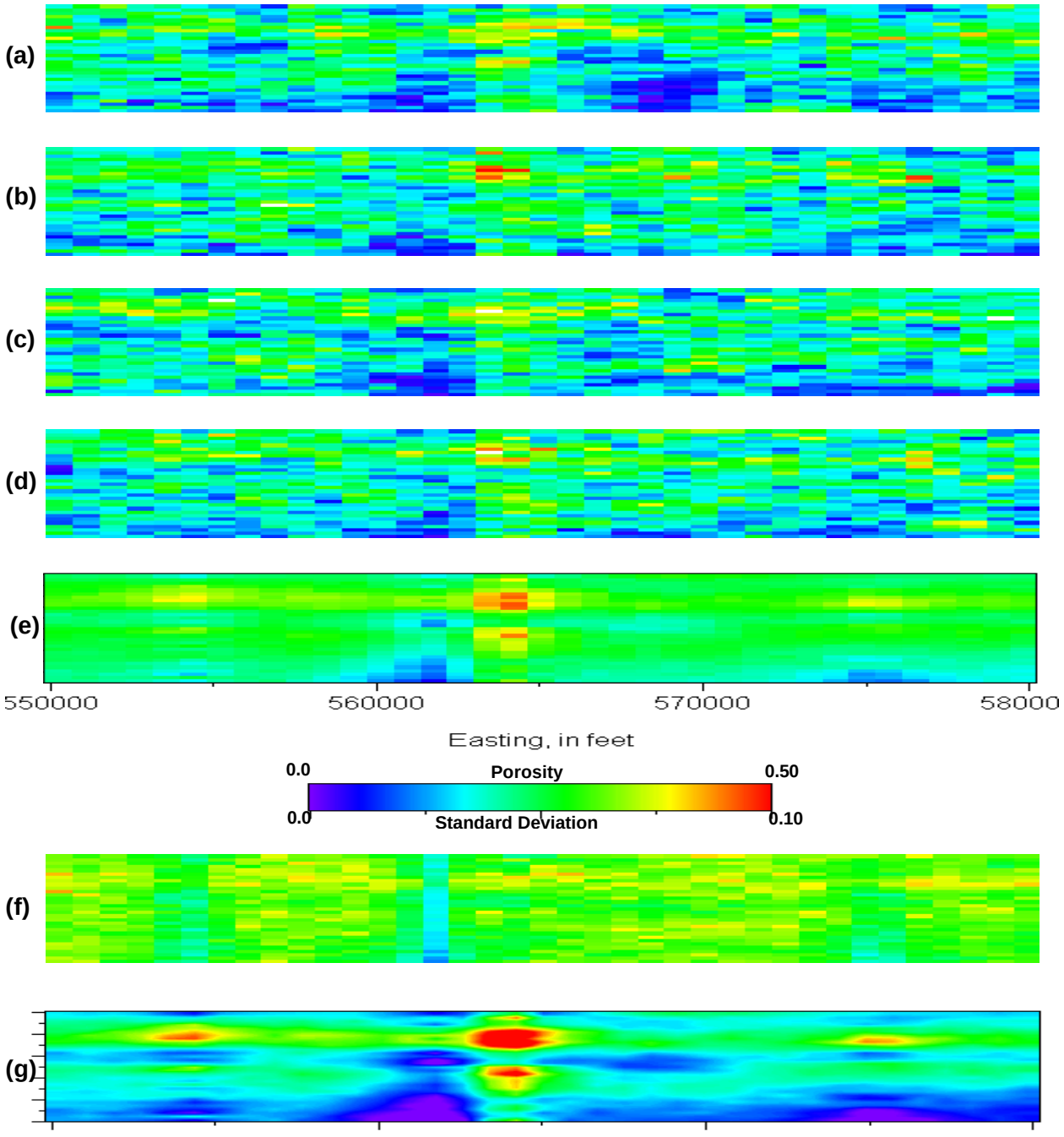

Plate 10. (a)–(d) Four simulations of lithophysal porosity in the TSw model unit; (e) E-type model of porosity in the TSw model unit; (f) uncertainty of lithophysal porosity in the TSw model unit; (g) E-type model with colors adjusted to show selected features. East–west cross section 28, looking north.

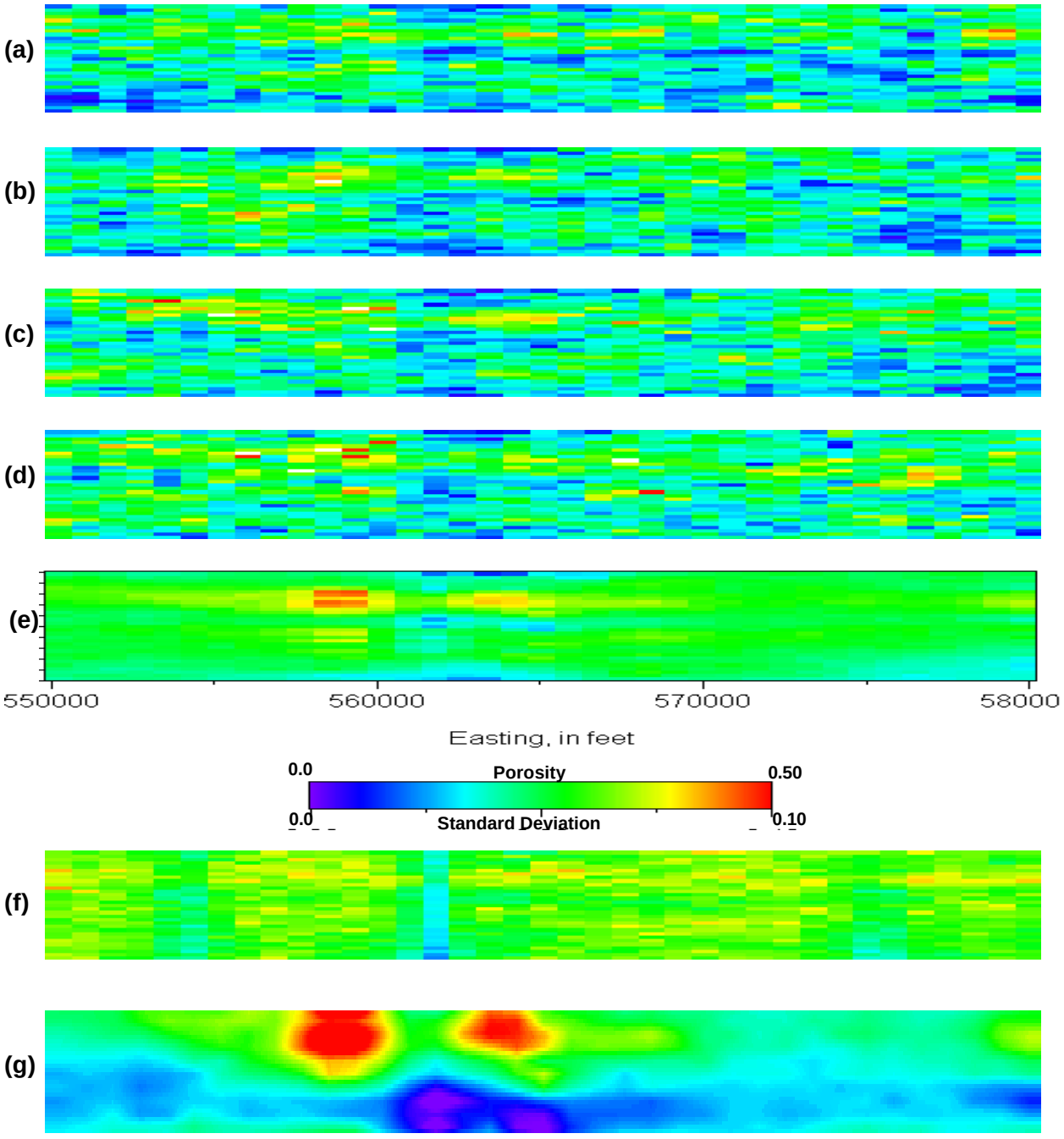

Plate 11. (a)–(d) Four simulations of lithophysal porosity in the TSw model unit; (e) E-type model of porosity in the TSw model unit; (f) uncertainty of lithophysal porosity in the TSw model unit; (g) E-type model with colors adjusted to show selected features. East–west cross section 34, looking north.

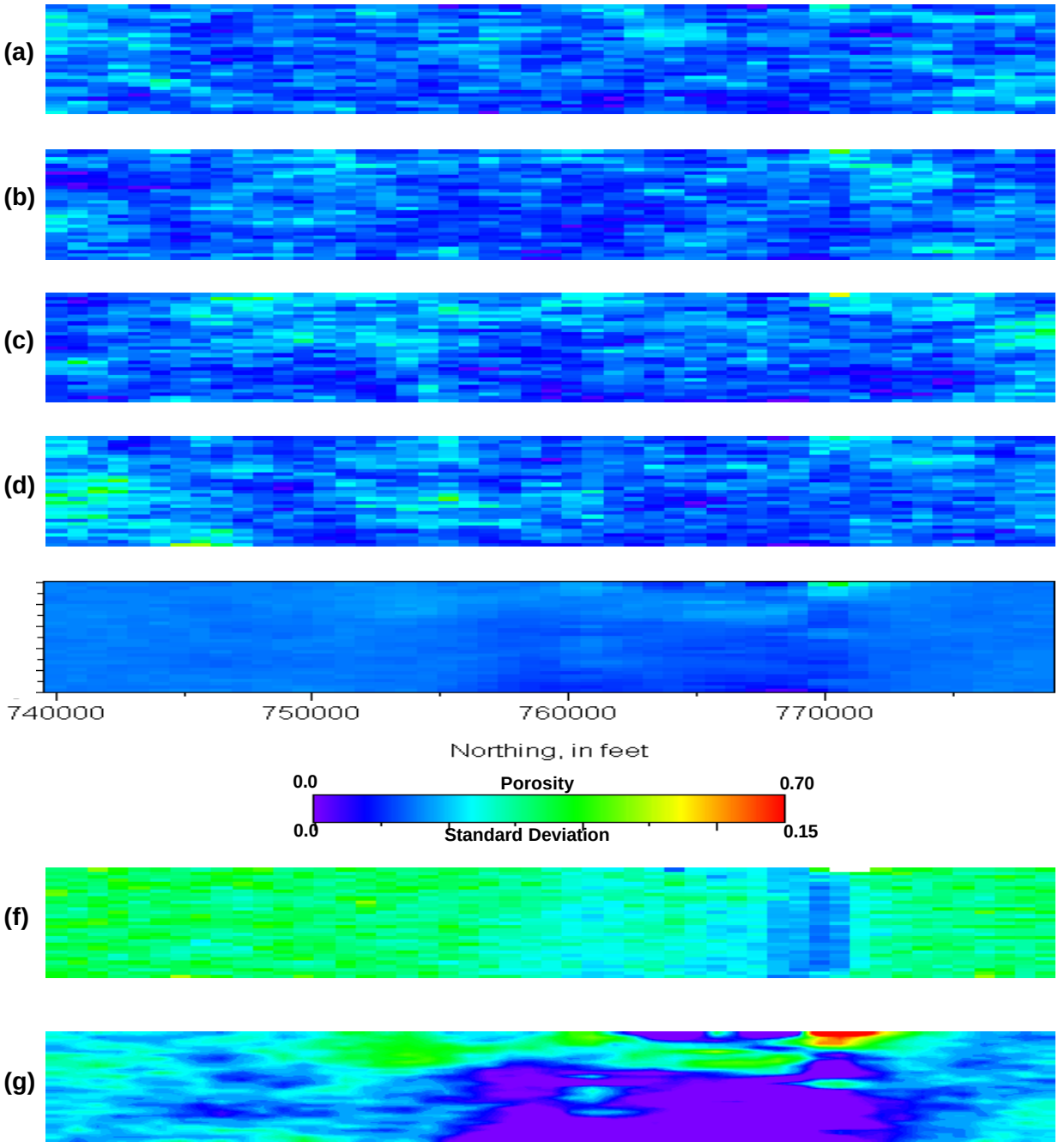

Plate 12. (a)–(d) Four simulations of matrix porosity in the TSw model unit; (e) E-type model of matrix porosity in the TSw model unit; (f) uncertainty of matrix porosity in the TSw model unit; (g) E-type model with colors adjusted to show selected features. North–south cross section 16, looking west.

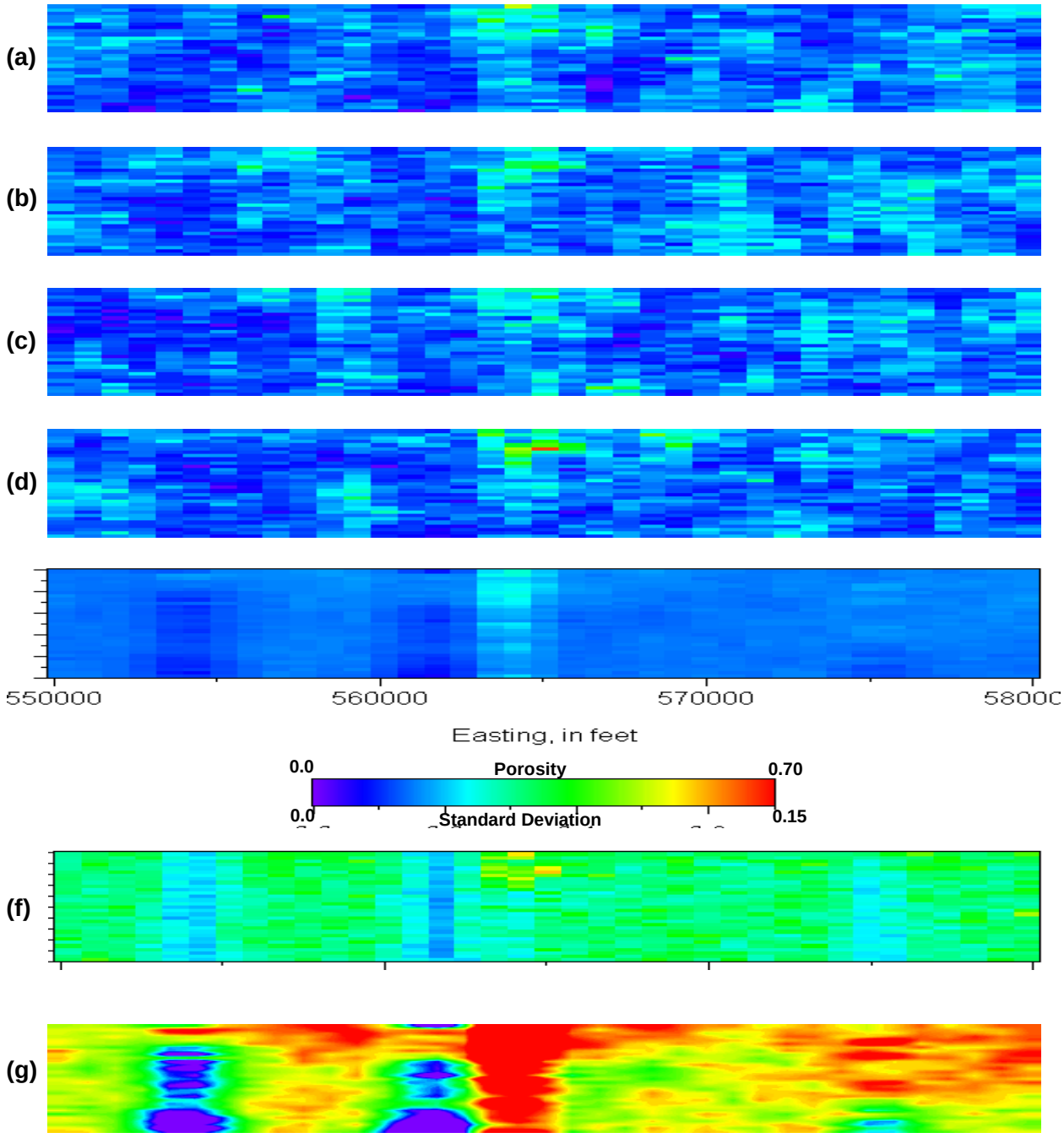

Plate 13. (a)–(d) Four simulations of matrix porosity in the TSw model unit; (e) E-type model of matrix porosity in the TSw model unit; (f) uncertainty of matrix porosity in the TSw model unit; (g) E-type model with colors adjusted to show selected features. East–west cross section looking north.

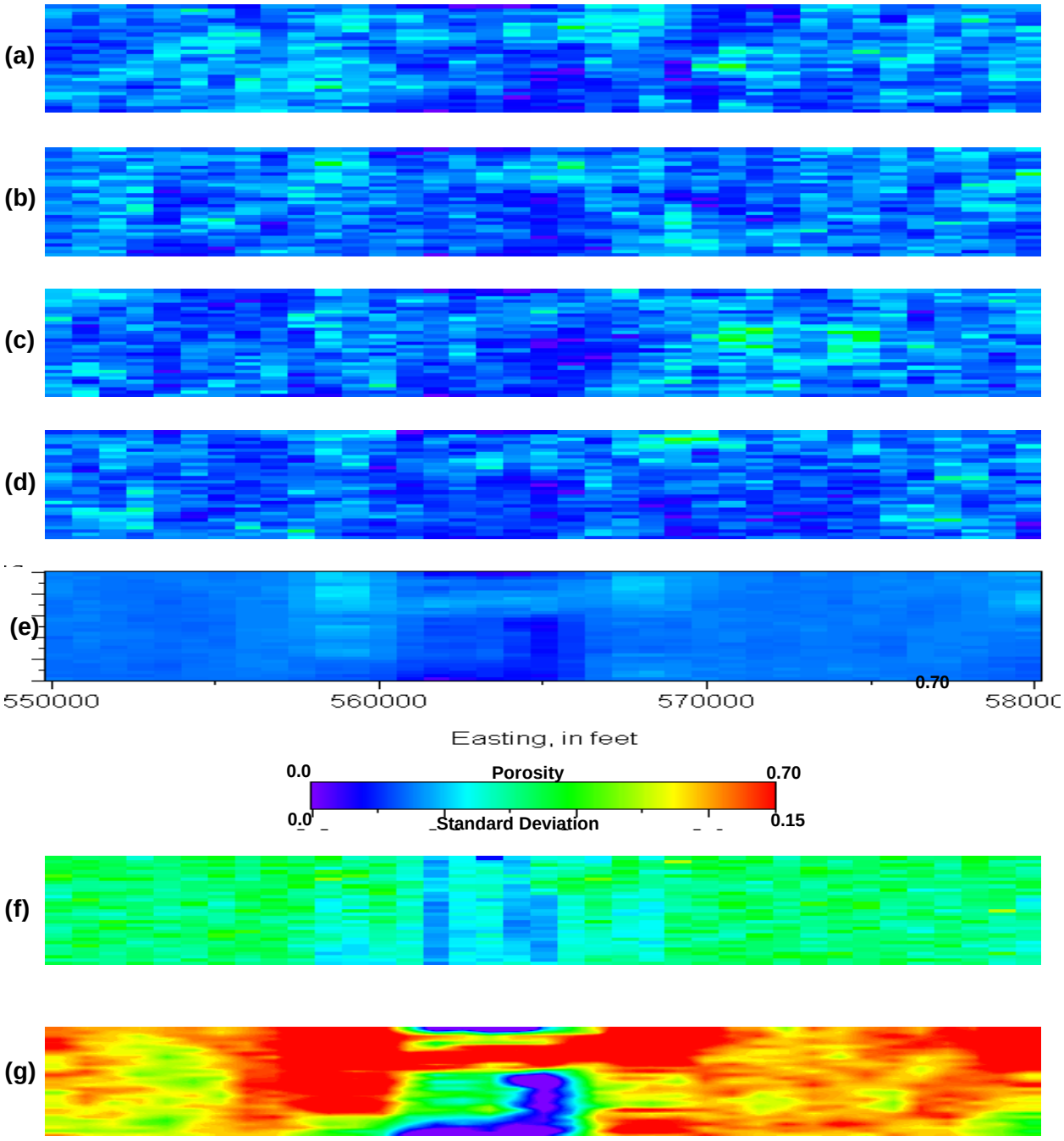

Plate 14. (a)–(d) Four simulations of matrix porosity in the TSw model unit; (e) E-type model of matrix porosity in the TSw model unit; (f) uncertainty of matrix porosity in the TSw model unit; (g) E-type model with colors adjusted to show selected features. East–west cross section 35, looking north.

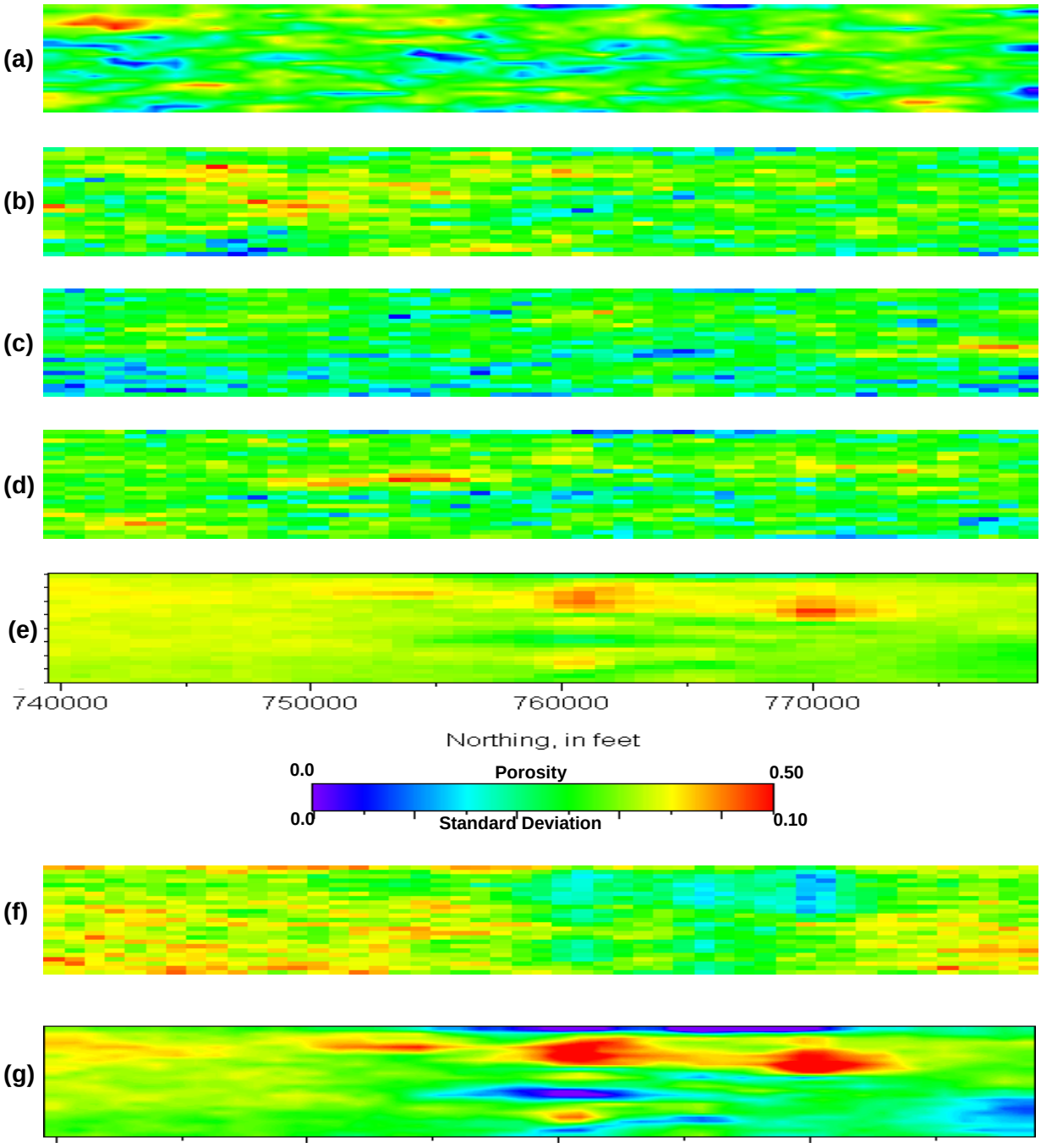

Plate 15. (a)–(d) Four simulations of porosity in the CH–PP model unit; (e) E-type model of porosity in the CH–PP model unit; (f) uncertainty of porosity in the CH–PP model unit; (g) E-type model with colors adjusted to show selected features. North–south cross section 15, looking west.

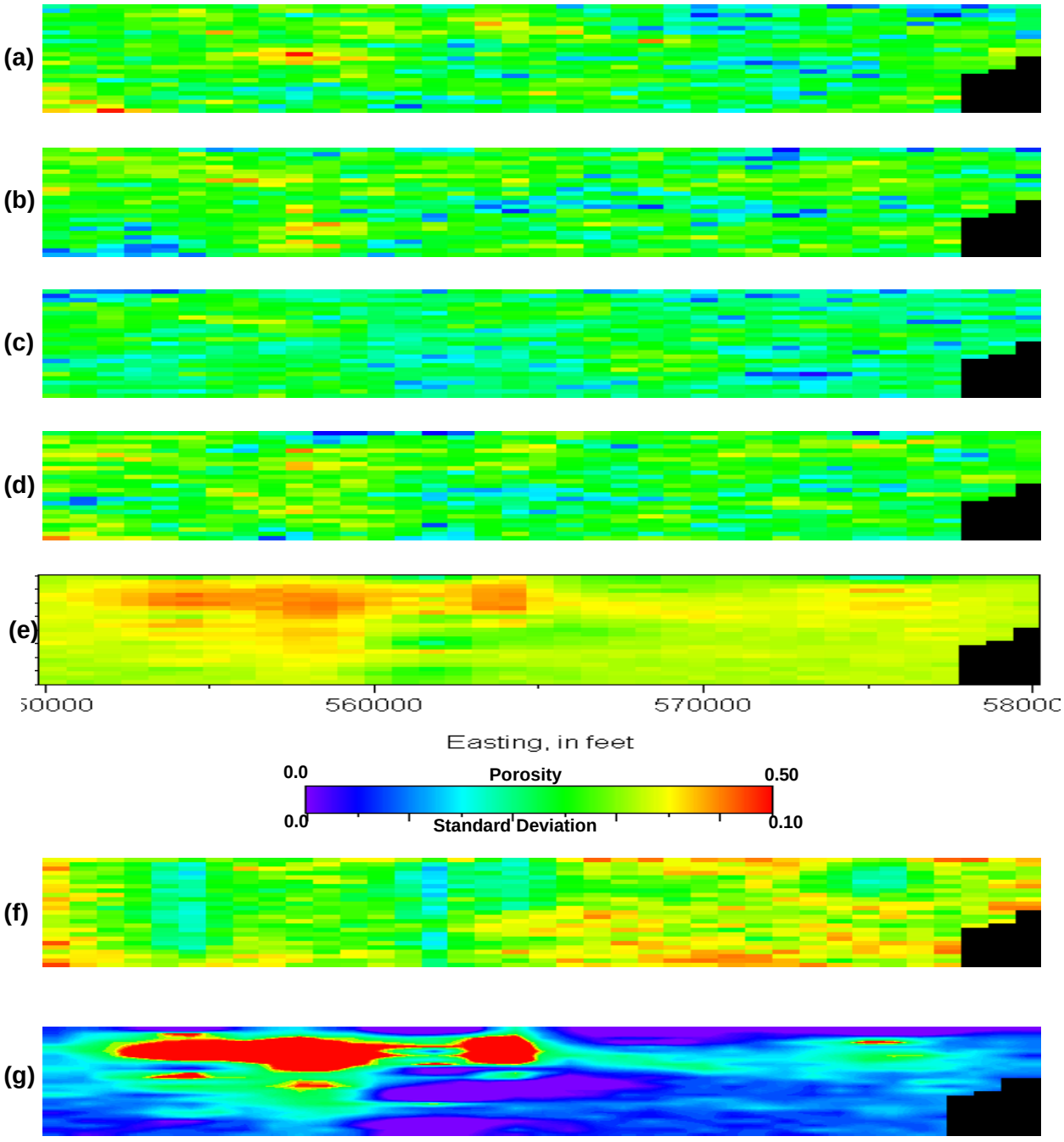

Plate 16. (a)–(d) Four simulations of porosity in the CH–PP model unit; (e) E-type model of porosity in the CH–PP model unit; (f) uncertainty of porosity in the CH–PP model unit; (g) E-type model with colors adjusted to show selected features. East–west cross section 28, looking north.

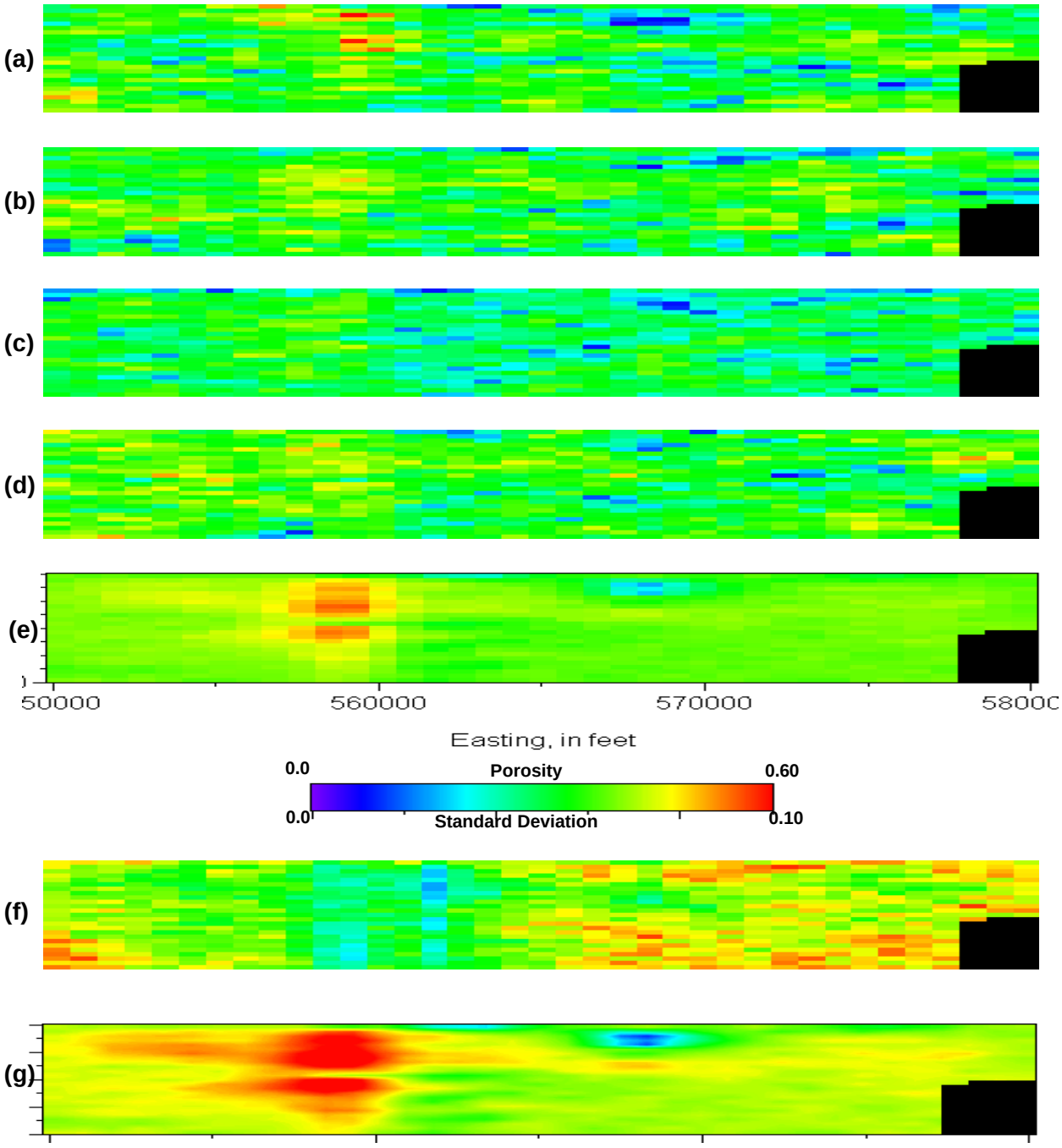

Plate 17. (a)–(d) Four simulations of porosity in the CH–PP model unit; (e) E-type model of porosity in the CH–PP model unit; (f) uncertainty of porosity in the CH–PP model unit; (g) E-type model with colors adjusted to show selected features. East–west cross section 34, looking north.

MODELING RESULTS

The material property models generated as part of this study are intended principally for use as numerical input to flow-and-transport modeling codes, and as a result the models are not particularly intended for visual presentation. Additionally, the models themselves are stochastic, and thus in essence are the products of a (sophisticated) random-number generator. We therefore place primary emphasis throughout this Modeling Results section on "validating" the simulated models statistically in terms of the three desirable features of conditional simulations, as discussed initially on page 60.

Nevertheless, in order to provide a generalized overview of the rock property models as a whole, we also present a small number of representative perspective diagrams and cross sections illustrating selected features of the models as color plates 1 through 14. Plates 1 through 5 are three-dimensional perspective views of the combined E-type summary models, and these images include all three rock-properties modeling units: PTn, TSw, and CH–PP. Plate 1 is presented with no vertical exaggeration to give some idea of the true vertical versus lateral extent of the various units at Yucca Mountain. Plates 2 through 5 are vertically exaggerated by a factor of two; however, it is still difficult to visualize the relatively thin PTn model unit even at this scale. Various of the many subunits (table 1) that have been described at Yucca Mountain are identified on the color plates. *It is important to note, however, that these smaller-scale "units" are not modeled explicitly, but exist only as porosity values that are higher or lower than their surroundings*, as conditioned by the measured porosity data throughout the model domain and the quantitative models of spatial correlation described in this report.

The locations of the several section profiles shown as plates 6 through 17 are given in figure 49. All two-dimensional sectional views of the rock properties models in this part of the report are still in stratigraphic coordinates, and the views presented include both individual simulated models, summary E-type models, and summary uncertainty models, as described on page 68.

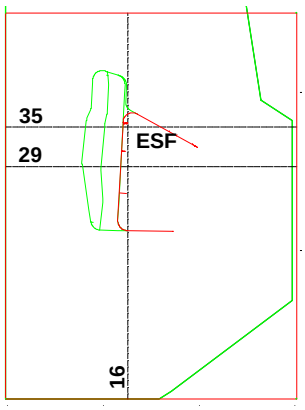

Figure 49. Location map for the sectional views of rock properties models presented in this report. Label numbers are grid node specifiers from rows and columns of modeling mesh. Area shown is same as in figures 8–10.

PTn Model Unit

Porosity

Description of Models

The PTn model unit is shown as an expected-value porosity model in perspective view in plates 1 through 5. Two cross-sections and one "long" section (i.e., parallel to structure) showing several realizations, the E-type model, and the uncertainty model are presented in plates 6, 7, and 8. Note that profiles (e) and (g) of each figure are identical, except that the uniformly varying color scale used in part (a)–(e) of each figure has been compressed and stretched in part (g) to highlight selected features of the models.

Several things are quite apparent in the sectional views of the PTn porosity models. First, the porosity values are typically high, as befits a unit dominated by nonwelded materials. Second, the high porosity values are not uniformly distributed throughout the modeled volume, but rather are generally restricted to the middle parts of the profiles (vertically). Both the top and base of the PTn model unit are defined by more or less sharp transitions from nonwelded to welded tuff. Third, it is quite clear that the top and base either have not been "picked" consistently across the drill hole data base, or else that the material property bound-

aries transgress the lithostratigraphic unit boundaries identified in the stratigraphic compendium (Clayton, 1996). Note in particular, the prominent very dark blue to purplish band of color along the top of part (g) of each figure. These cold colors represent very low porosity values associated with welded tuffs of the overlying (and not modeled) Tiva Canyon Tuff. The undulatory and discontinuous nature of this upper part of the figure suggests that the same the same degree of welding was not applied as a criterion for the distinction between lithostratigraphic units Tpcpv3 and Tpcpv2 or Tpcpv1. The same reasoning applies to the lower contact of the PTn model unit, as part (g) of each figure contains a deep blue/purple mass along the lower margin whereas the dominant porosity value is coded more of a light blue to green.

Fourth, porosity changes *within* individual lithostratigraphic units appear to be reproduced. For example, consider the extreme right-hand end of the long section shown in plate 6. Part (g) of this figure accentuates the two low-porosity zones that extend south from the general latitude of drillhole G-2 (Appendix C) that are also visible to a lesser extent in plate 6(e). These two stratigraphic intervals correspond to the welded portions of the (upper) Yucca Mountain and (lower) Pah Canyon Tuffs in this extreme northern part of the modeled area. The porosities of the Yucca Mountain Tuff appear markedly lower than those of the Pah Canyon Tuff. The change of welded materials laterally into high-porosity nonwelded tuff is quite striking for the Pah Canyon Tuff, and this change is consistent with field observations that the Pah Canyon throughout much of its extent is typified by very large yellowish-grey pumice clasts dispersed in a generally pinkish groundmass. The origin of the prominent break in high-porosity materials at approximately Nevada State Plane coordinates 758,000–760,000 feet is not immediately apparent. However, the fact that this unexplained transition is directly associated with "bulges" in the low-porosity top and base of the unit suggests that the porosity break is associated with a single drill hole.

Uncertainty, as represented by the node-by-node standard deviations of porosity across the 100 stochastic simulations used to generate the E-type model, is not the same throughout the model domain. Uncertainty is presented in part (f) of each plate, 6–8. The various shades of blue represent regions of lower uncertainty associated with the more densely drilled portions of the repository block, whereas uncertainty increases (represented by blocks colored yellow to red) in regions of more sparse drilling. The difference in the uncertainty model between the northern part of the repository block, shown for cross section 35 in plate 8(f), and the southern part of the block [cross section 29; plate 7(f)] is quite striking. Cross section 35 is influenced by drill holes UZ-14, G-1, H-1, NRG-5–7, and SD-9, whereas cross section 29 is constrained effectively by only drill holes SD12, WT-2, and H-4. Note that in plate 7, uncertainty is markedly greater west of the Ghost Dance Fault (to the west of profile 16).

Validation

Criterion number 1 for a "good" stochastically simulated rock properties model is reproduction of known data values at the same locations in the model as were sampled in the real world. The implicit assumption is that a model that does not reproduce measured values appropriately is immediately distinguishable from reality, and hence, a distortion. The complicating factor in making the required comparison is that whereas drillhole data have unique and specific sets of three-dimensional coordinates related to the sampling process itself, the simulated models as constructed are discretized on a relatively coarse three-dimensional grid.

In this study, the grid spacing for the PTn model unit is 250x250x2 meters (x:y:z; table 3). Because of the coarse spacing in the horizontal plane, a drillhole with its contained data may be located as much as 176 m (some 580 ft) distant from the nearest grid node. Given that the ranges of spatial correlation described in the section on *Spatial Continuity Description* are, in some cases, on the order of 2000–5000 ft (for the first nested structure), it is evident that there may be non-trivial differences for some drill holes that are poorly situated with respect to the simulation grid. Another consideration is that even with a 2-m (about 6 ft) vertical discretization interval, it is clearly impossible to individually represent each and every downhole sample where the nominal

sample spacing is only about 1 meter (3 ft). Note that vertical discretization effects will be markedly more pronounced in the other two model units, for which a 10-m vertical grid spacing was used. Subject to these mechanical limitations, the several drillhole profiles should be reflected generally in a porosity profile extracted from the model in the immediate vicinity of that hole.

In general, reproduction of the input porosity

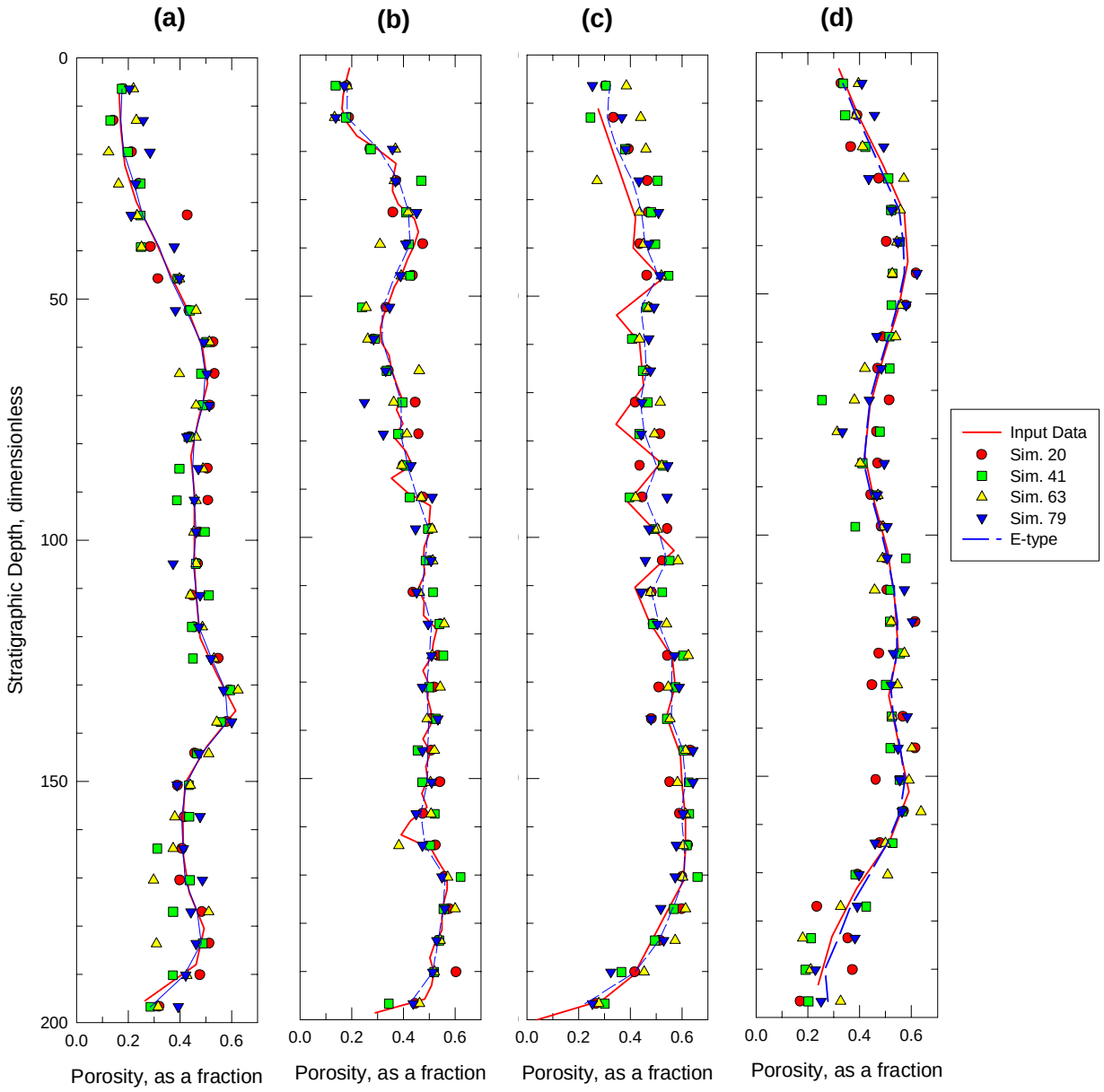

Figure 50. Comparison of porosity profiles extracted from simulated models of total porosity with input porosity data and with the E-type model results for the PTn model unit at grid nodes nearest drillholes (a) G-3, (b) SD-9, (c) UZ-16, and (d) WT-17.

data in the four simulations selected randomly from the suite of realizations for the PTn model unit is quite good, as illustrated in figure 50. The overall character of the vertical changes in porosity

(shown in the solid heavy line) is definitely captured in each simulation. Most of the more evident discrepancies are related to short-wavelength features in the input data (corresponding to the thin reworked depositional units?); these differences are most pronounced where the feature in the original data is located midway between two adjacent grid nodes. In a few instances, three of the four simulations closely approximate the measured data curve, whereas the fourth indicates a rather different simulated porosity value [e.g., specific examples in fig. 50(a) at approximately 42, 65, 105, 125, 183 ft., etc.]. These disparate data points are attributed to interaction between imprecise coincidence of drill hole and grid node with the randomness of the sequential path through the model domain along which the unit is simulated. At every point not precisely coincident with a measured value, there is a finite probability of generating an "odd" property value. If an adjoining grid node (located yet farther away from the conditioning drill hole) simulated early in the sequential filling process by chance receives a low-probability value that is much higher (lower) than those at the drill hole, this value will influence later simulation of the node closest to the drill hole in proportion to its spatial position and magnitude. Across a large number of simulations, however, the impact of these statistical fluctuations should be minimal, and indeed, the profile of the expected-value model (shown in fig. 50 as the dashed line without symbols) is observed to pass through the cluster of values more similar to the nearest measured porosity.

Criterion number 2 for reasonable simulations involved the univariate statistical character of the ensemble of data used to condition the simulation process. In essence, this criterion involves reproduction of the histogram, including both the mean and the variance. Because simulations do, in general, reproduce the input data histogram quite closely, it is important to ensure that the data used to condition a modeling exercise are as unbiased as possible. Preferential sampling of either high or low values because of some external criteria (including logistical limitations) will, if left uncorrected (for example Deutsch, 1989) lead to the production of simulated models for which the values tend to be either too high or too low.

Figure 51, parts (a) through (d), presents histograms of the four simulated porosity models of the PTn model unit that were summarized for specific drill hole locations in figure 50. For comparison, figure 51(e) is a representation of the original porosity values used to condition the simulations of parts (a) through (d); see also fig 15. In addition to the histograms themselves, figure 51 includes several summary statistical measures for each relevant population. Clearly, the simulated models of PTn porosity not only reproduce the mean of the measured values, but they also reproduce the full range of observed variability (i.e., standard deviation) and, by implication, the high-order moments (skewness; kurtosis) as well. Reproduction of the high-order moments is demonstrated by the near-identical shapes of the histogram plots and by the highly asymmetric quartile intervals and minimum–maximum relationships.

Figures 52 and 53 present three-dimensional variograms of the simulated porosity models of the PTn model unit.[†] Part (a) shows the vertical variograms, whereas part (b) and (c) show the horizontal variograms in the directions of maximum (azimuth 135°) and minimum (45°) continuity. Figure 52 represents a summary of all 100 simulated models as the average variogram and 95-percent confidence intervals, and figure 53 compares the variograms from the four simulated models from figure 51 and from the expected-value summary model. Also shown for comparison in the heavier line weights are the modeled variograms from figure 34.

Reproduction of the desired vertical variograms by the simulated models is excellent. All four simulations in figure 53 plot essentially on top of the input model. However, the variogram from the E-type summary porosity model does not. This latter variogram indicates that for each given distance less than the range of spatial correlation, the E-type model exhibits a lower degree of variability than do the individual stochastic realizations and the modeled summary of the actual measured data.

In the stratigraphically horizontal dimension, the variograms of the individual simulated porosity

[†]See also discussion of variograms in Appendix D.

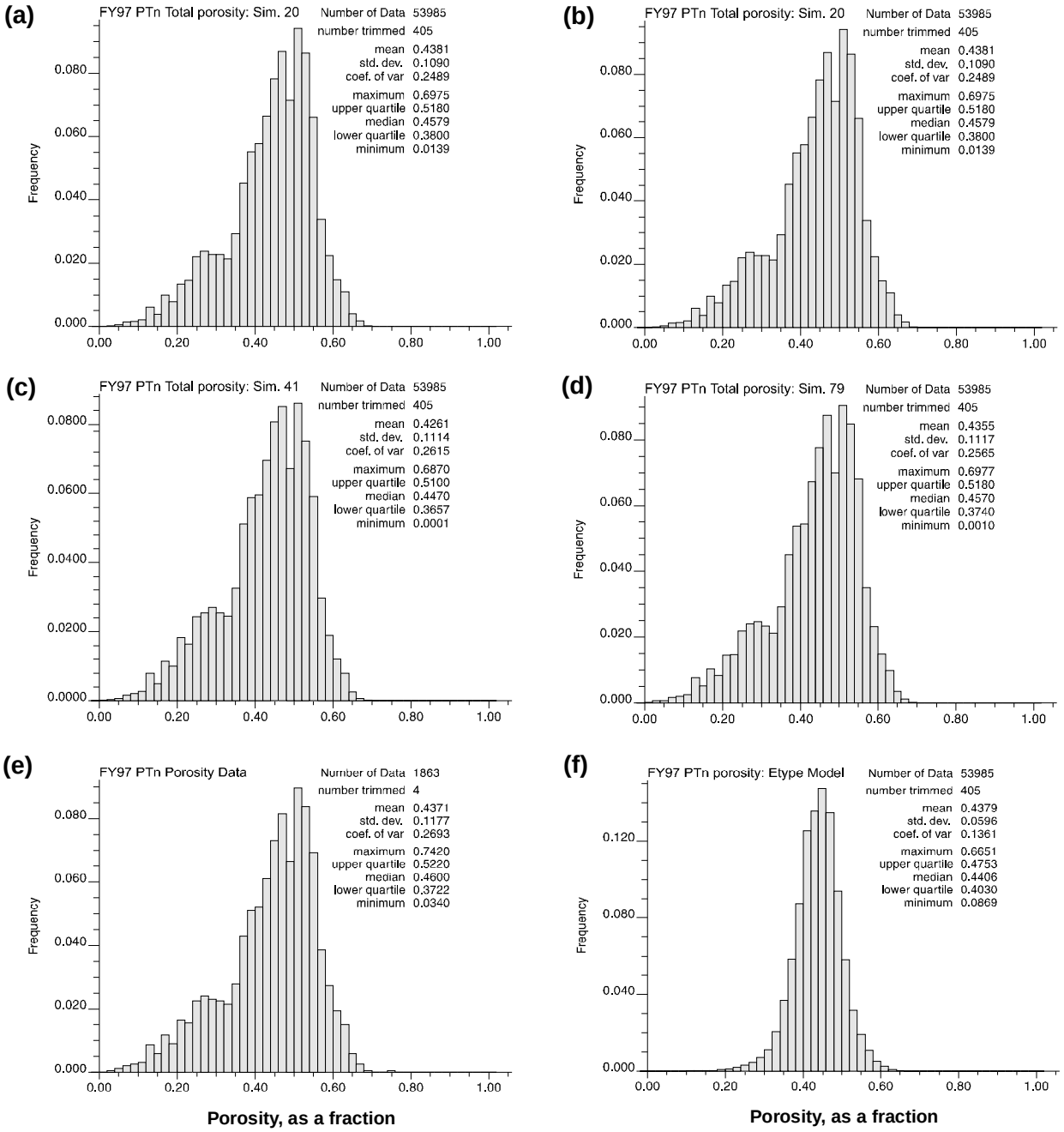

Figure 51. Histograms of four individual simulations of total porosity in the PTn model unit [(a)–(d)] compared to the original porosity data [(e)] and E-type summarized model [(f)]. Associated statistical summary shown for each histogram.

models indicate a modest degree of anisotropy, but the apparent maximum range of correlation is somewhat less than was specified by the input variogram (heavy curves). The variogram curves in figure 53(b) also include the sample variogram plots in the appropriate directions (the irregular lines with circular symbols; see also fig. 34). Note that for each of the stochastic realizations shown in figure 53(b), the variograms of the simulations appear to resemble the *sample* variograms more closely

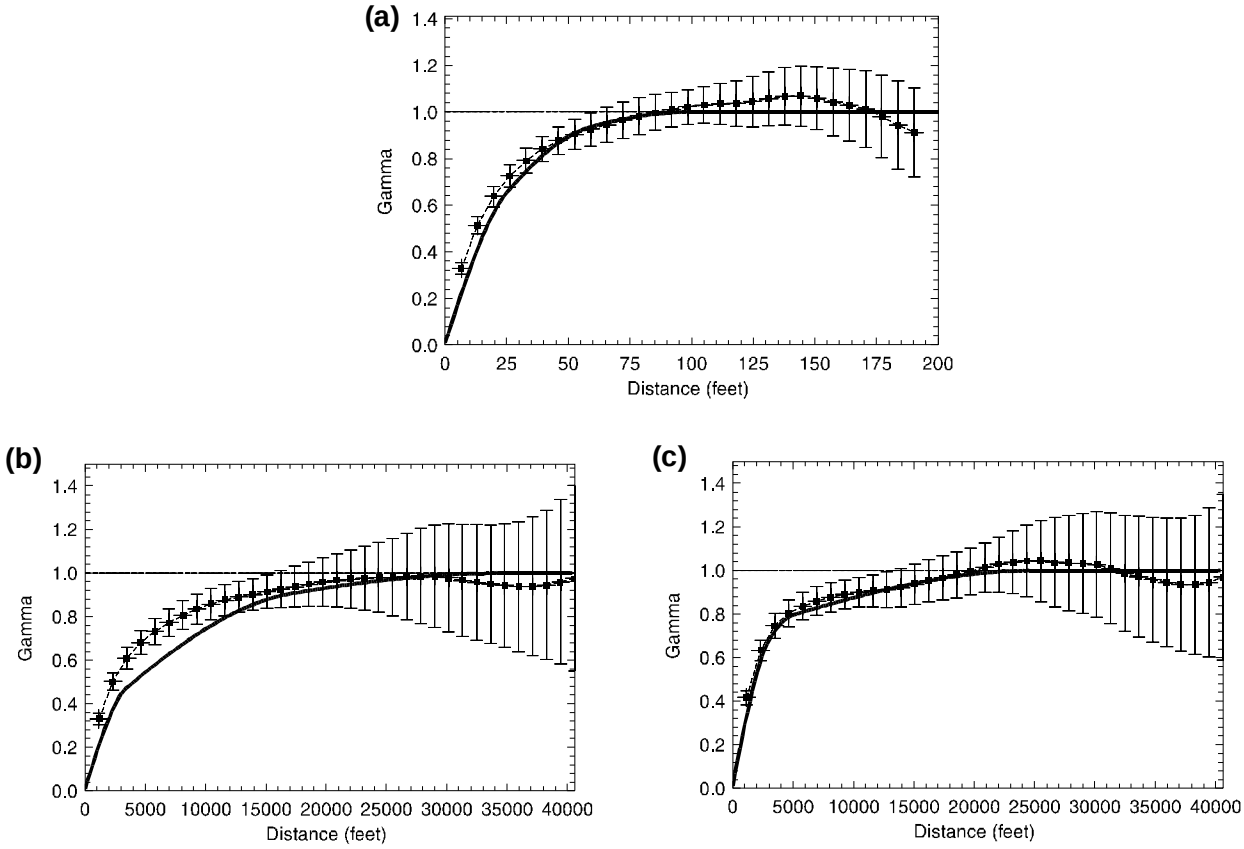

Figure 52. Reproduction of input variograms for simulated porosity models of the PTn model unit: (a) stratigraphic vertical, (b) stratigraphic horizontal, azimuth = 135°; (c) stratigraphic horizontal, azimuth = 45°. Dashed line with error bars is average variogram with plus/minus 95-percent confidence interval; heavy solid line is input variogram model.

than the input *modeled* variogram. This effect is particularly noticeable for the variogram at azimuth = 135°. We had inferred the model variograms in figure 34 giving somewhat more weight to the low-variance value at separation distances of about 13,000 ft because the guiding conceptual model of ash-flow deposition suggests that one might expect long-range spatial correlation. However, the conditioning data in this case appear to work to influence the simulated models in the opposite direction: giving more weight to the sample variogram points at 7000 and 9000 ft. This type of *robust behavior with respect to the influence of data* is a hallmark generally of geostatistical methods.

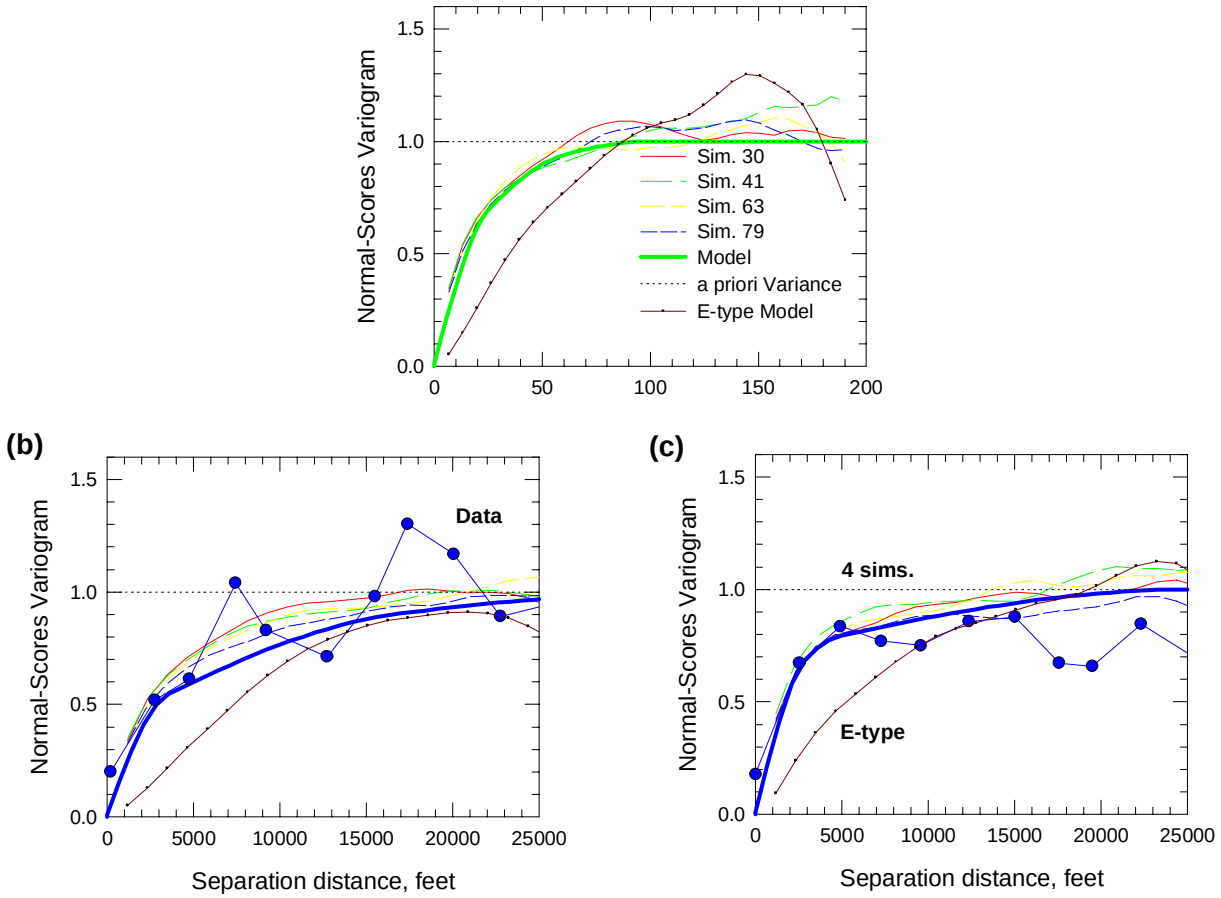

Figure 53. Variograms from four simulated porosity models of the PTn model unit. (a) Stratigraphic vertical; (b) stratigraphic horizontal, azimuth = 135°; (c) stratigraphic horizontal, azimuth = 45°.

Bulk Density

The model of bulk density for the PTn model unit was created using direct regression on total porosity. Bulk density is predicted by the relationship:

$$\rho_b = 2.543 - 2.764\phi \quad , \qquad (41)$$

as presented previously in figure 22(b). The coefficient of determination (r^2 value) for this regression is 0.972. Note that in contrast to the models of other secondary material properties described in this report, the bulk density model is simply an expected-value-type model, and it was generated simply by applying equation (41) to the summary E-type model of porosity.

Saturated Hydraulic Conductivity

Models of saturated hydraulic conductivity for the PTn model unit were created by linear coregionalization with each of the individual porosity models for this unit. There are thus 100 separate stochastic realizations of hydraulic conductivity, which have also been summarized through the creation of a single E-type hydraulic conductivity model.

Histograms of four of the individual coregionalized saturated hydraulic conductivity models for the PTn model unit are shown in figure 54, parts (a)–(d). A histogram of the 64 measured PTn hydraulic conductivity values is shown for comparison in part (e) of the figure. Note that this latter histogram represents a subset of the entire measured Ksat data set (PTn–TSw–CHPP) shown in

figure 26(a). The histogram of the summary E-type model of hydraulic conductivity for the PTn model unit is presented in part (f) of figure 54.

Saturated hydraulic conductivity was demonstrated to be correlated quite strongly with porosity for unaltered rocks in the section on *Saturated Hydraulic Conductivity* beginning on page 35. The coefficient of determination is approximately 0.6. This partial correlation has been reproduced through the coregionalization process, as indicated in figure 55, for the four individual realizations that have been used previously as illustrations [compare to fig. 25(c)]. The irregularly clustered appearance of the plots is largely an artifact related to the limited number of actual Ksat measurements from the PTn model unit (64) that has been used to describe the univariate characteristics of the simulated models. Also, the scatterplots of figure 55 were generated using only a 5-percent subsample of each full simulated model in order to generate logistically feasible diagrams (the full simulations each contain more than 54,000 values, too many to plot in a reasonably sized computer file). Although the 5-percent sample was selected at random, the subsampling process may have accentuated the clustering caused by the somewhat blocky data histogram of figure 54(e).

As indicated in figure 55, the strength of the correlation between simulated hydraulic conductivity and simulated porosity is somewhat stronger than that observed from the measured data (original r^2 = 0.603). However, the original correlation between porosity and hydraulic conductivity, shown in figure fig. 25(c) and used in the coregionalization algorithm, was based on all available Ksat values measured for all unaltered core samples [N = 291; table 8; fig. 26(c)]. These data included specimens from the PTn model unit, the TSw model unit, and the combined Calico Hills–Prow Pass interval to achieve the benefits of greater statistical mass (there are only 64 available samples from the PTn unit itself). As the PTn model unit consists almost entirely of nonwelded rock types, the correlation exhibited by these simulations might be expected to be stronger than for an aggregation of different rock types including nonwelded, densely welded, and even microfractured vitrophyric samples.

Figure 56 is an equivalent scatter diagram showing the correlation between the E-type models of saturated hydraulic conductivity and porosity for the PTn model unit. In distinct contrast to the crossplots of figure 55, which indicated distinct-yet-not-perfect cross-variable correlation of these two properties, figure 56 indicates a nearly one-to-one relationship for which the coefficient of determination is virtually 1.0. This behavior is consistent with the behavior of an expectation operator. Values from both tails of the two distributions "regress toward the mean." The result is an increasingly strong apparent correlation, despite the only modest correlation [r^2 = 0.603; see fig. 25(c)] between the actual laboratory measurements. Carried to its logical-though-extreme end, the expectation operator results in a single "representative" value for both porosity and hydraulic conductivity in an effort to summarize what is a modestly complex state of being.

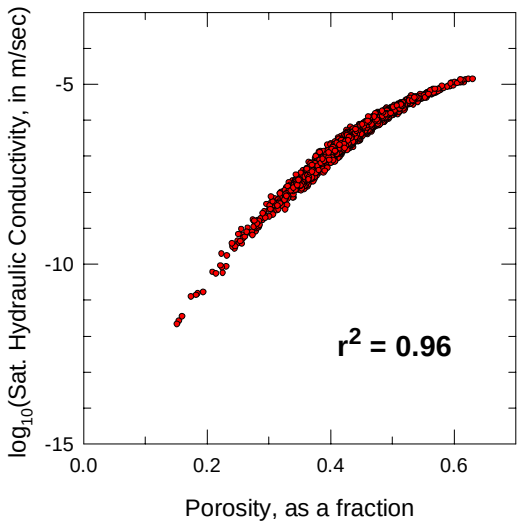

Figure 56. Scatterplot of saturated hydraulic conductivity and porosity for the summary E-type models of the PTn model unit (5-percent subsample).

A very interesting and somewhat unexpected observation can be made from the scatter diagram presented in figure 56. Despite the name of the simulation process for deriving Ksat from porosity, *linear* coregionalization, the relationship between the two correlated E-type models is anything but

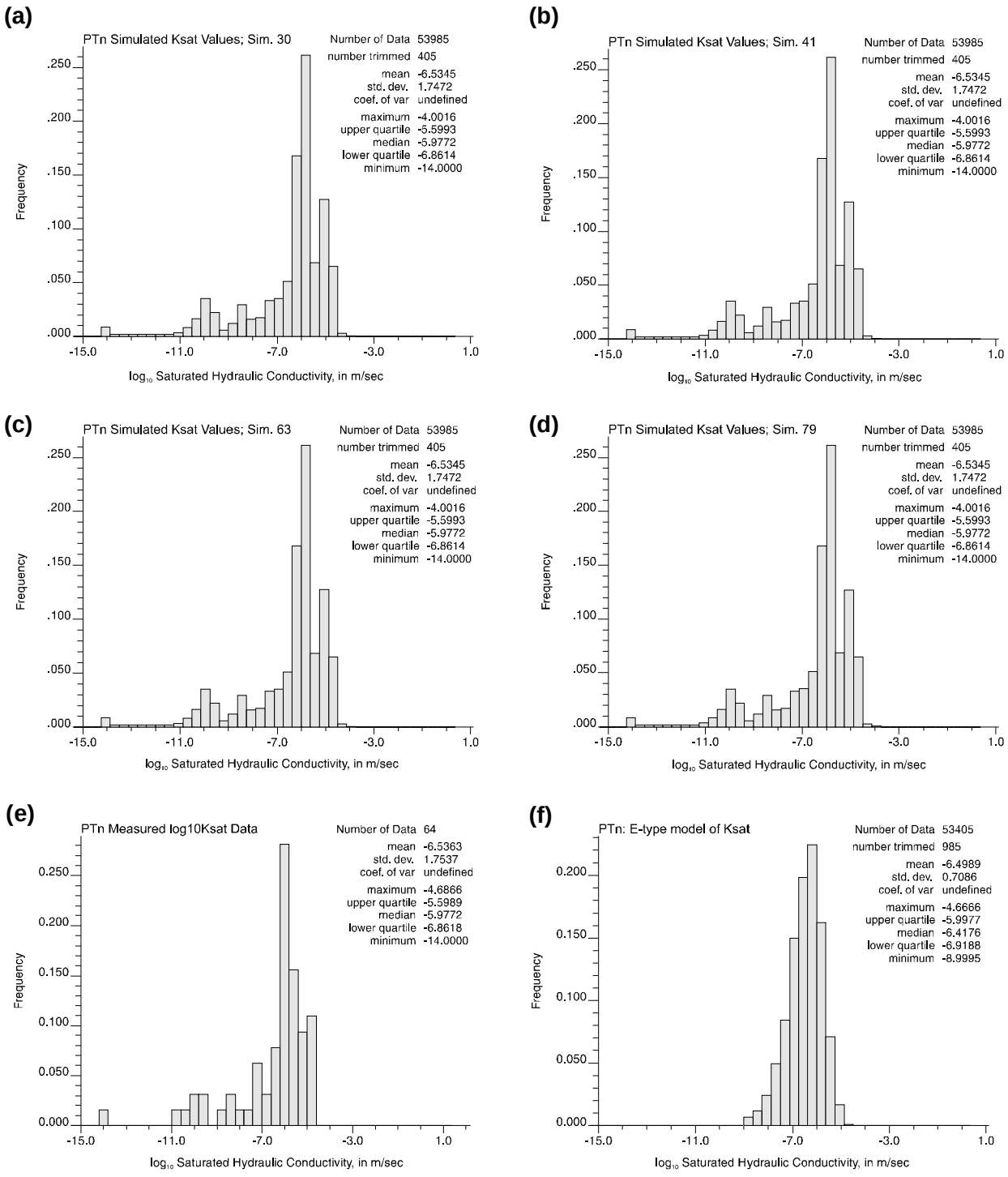

Figure 54. Histograms of four coregionalized models of saturated hydraulic conductivity corresponding to the four porosity models presented in figure 51(a) through (d) compared to histograms of original measured data [(e)] and E-type model [(f)].

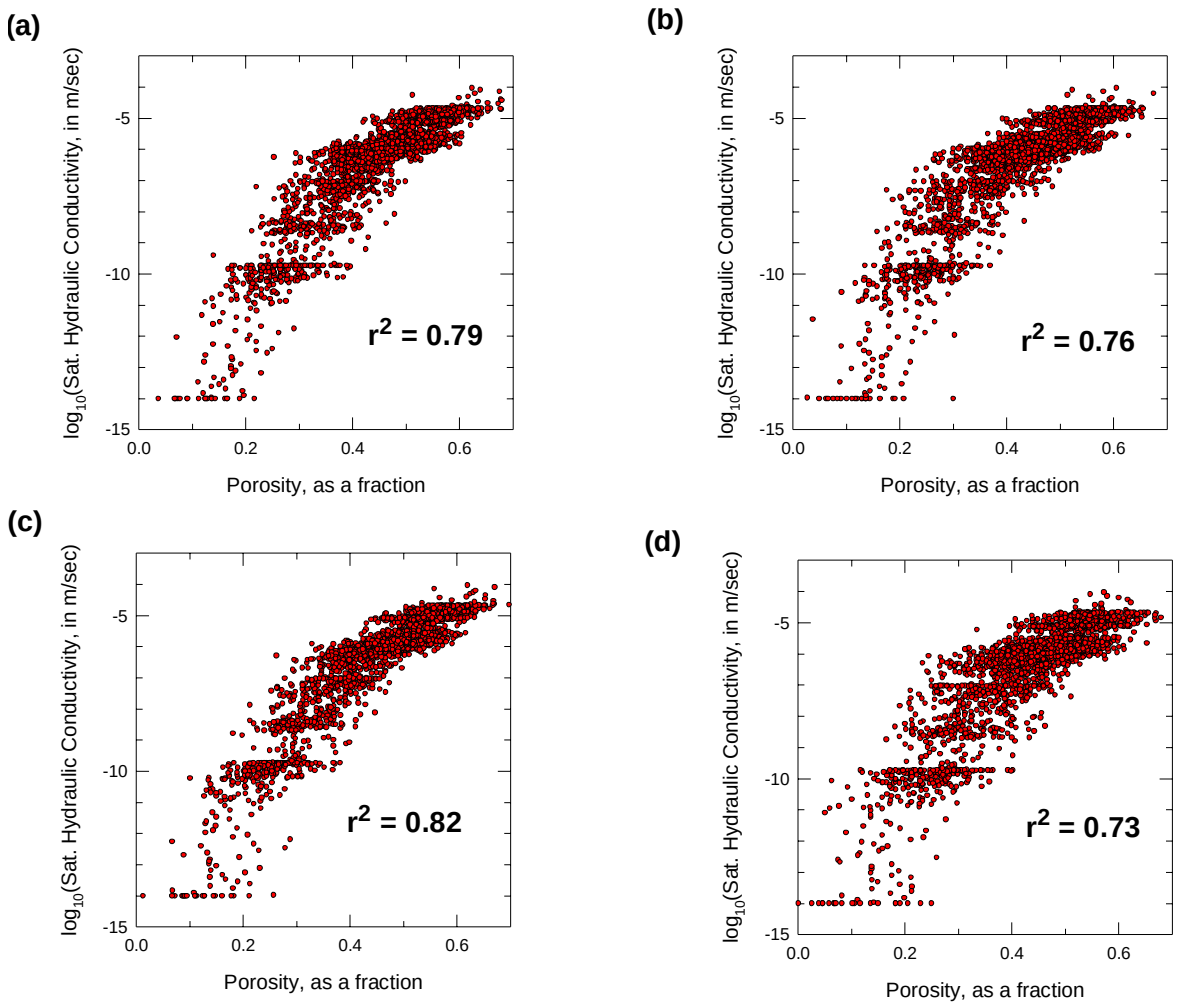

Figure 55. Scatterplots of modeled saturated hydraulic conductivity as a function of modeled porosity for the PTn model unit. (a) Simulation no. 30; (b) no. 41; (c) no. 63; (d) no. 79 (5-percent subsample).

linear. The same curvilinear relationship can also be observed in the scatterplots of the individual simulated models (fig. 55); however, the nature of the relationship is more clearly defined with the markedly diminished variability of figure 56. In fact, that there would be an upper bound on hydraulic conductivity with increasing porosity is somewhat intuitive. Because the porosity of closely packed uniform spheres is only about 30 percent, it is clear that much of the porosity for some samples from Yucca Mountain must be intra-granular: specifically related to "froth" bubbles in coarse pumice clasts. Clearly some of this intraparticle porosity is connected and will conduct fluid, increasing the hydraulic conductivity of the samples. However, the flow of fluid (water in the laboratory) cannot increase indefinitely, as the rock specimens must be sufficiently consolidated to withstand handling and testing. Note that is possible to obtain a higher coefficient of determination for the original scatterplot of the laboratory data shown in figure 25 (r^2 = 0.611 vs 0.603) simply by fitting a polynomial regression of order two to the data instead of a simple linear fit. L. E. Flint (in review) has developed predictive equations for

hydraulic conductivity from porosity that use such complex regression relationships.

Uncertainty Model

Geostatistical simulation provides a powerful tool for addressing geologic uncertainty, that which results from less-than-exhaustive observation of a particular site. Although for the Yucca Mountain repository program, the real interest in uncertainty focuses on uncertainty in the *predicted performance* of the potential repository. However, this predicted performance uncertainty is to no small extent dependent on the uncertainty associated with input parameters to the performance models (c.f. fig. 6), and thus we present here a short description of the uncertainty associated with the simulated models of material properties. Figure 57 presents histograms representing the standard deviations of the 100 stochastic realizations (each) of total porosity [part (a)] and saturated hydraulic conductivity [part (b)] for the PTn model unit. The uncertainty models are computed in association with the generation of the expected-value-type models, and they are nothing more than the node-by-node standard deviations of the 100 input simulations (see See "Uncertainty Measures" on page 68.). Although the uncertainty varies spatially as shown in plates 6 to 8, these histograms provide a somewhat global view of the uncertainty associated with the suite of simulated models.

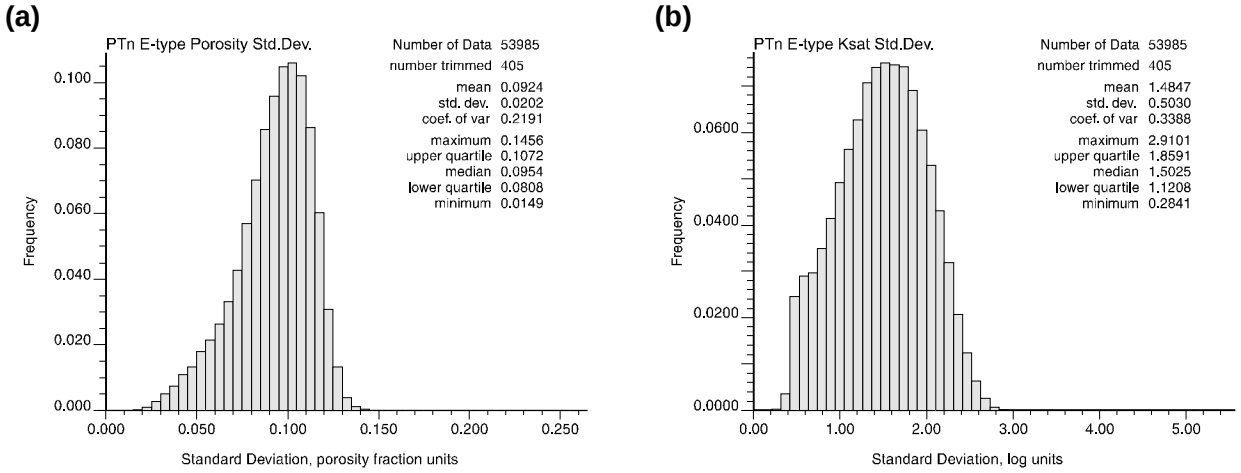

Figure 57. Uncertainty associated with (a) simulated porosity models and (b) simulated hydraulic conductivity models, as expressed by the standard deviations of individual grid nodes. Uncertainty estimates derived from E-type models.

Figure 57(a) indicates that across the entire PTn model domain, the average standard deviation is plus-or-minus just over 9 porosity percent (0.092). This is with respect to a global average porosity of 44 percent (0.438; fig. 51). The distribution of uncertainty is asymmetric, with a maximum uncertainty of 14.5 percent (0.146). The skewed tail of low uncertainties is directly and immediately related to the spatial positions of model grid nodes with respect to conditioning data. Simulated values close to conditioning information vary only slightly, whereas simulated values far from data are much more highly variable. Note that there appears to be a lower limit to uncertainty of about plus-or-minus 2 porosity percent. The existence of a limiting value is most likely related to discretization of the model domain on an arbitrary grid, as the numerical implementation of the sequential simulation algorithm will reproduce exactly sample data collocated with a grid node. The magnitude of this limit is also a function of model discretization; however, it is also directly related to the small-scale variability exhibited by the 3-ft spaced closest samples.

Figure 57(b) is an identical presentation of uncertainty associated with hydraulic conductivity; recall that Ksat in this report is expressed in units

of $\log_{10}$ m/sec. Uncertainty in the simulated values of saturated hydraulic conductivity appears relatively high. The global average standard deviation is approximately 1.5 log units, and at worst, the variability may be estimated at plus-or-minus three orders of magnitude (standard deviation = 2.9). The best-constrained grid nodes are simulated with a standard deviation of 0.4 log units, with a lower bound of plus-or-minus 0.28. Again, these uncertainty measures are spatially distributed, and figure 57(b) provides only a global overview.

TSw Model Unit

Lithophysal Porosity

Description

Lithophysal porosity values for the TSw model unit is presented in perspective-diagram format in plates 1 through 5. Two-dimensional profile views are presented for the same cross- and long-sections as for the PTn model unit (location map in fig. 49) in plates 9, 10, and 11. As before, parts (a) through (d) of the 2-D figures are individual simulations and part (e) is the E-type summary model. Part (f) of each plate is the uncertain model associated with the suite of simulations. Finally, part (g) is the same as (e) except that the color scale has been adjusted to bring out selected features of each profile.

"On average," i.e for the E-type model, the two prominent lithophysae-bearing intervals of the Topopah Spring Tuff are reproduced quite faithfully, although identifying these distinctive units in the individual simulated models requires more effort. The upper and lower lithophysal "zones" are most readily identified on the north–south long-section in stratigraphic coordinates (plate 9). Note that the upper lithophysal interval is modeled by cells of higher porosity than the lower interval. This is consistent with field observations (and core observations) that indicate abundant and very large lithophysal cavities (decimeter size) in the upper lithophysal zone and typically smaller and locally flattened lithophysae in the lower interval. There also appears to be a large amount of lateral variability to the upper lithophysal interval in particular. A first impression from this apparent lateral heterogeneity is that it might be related to differences in borehole "vintage;" see plate 10, particularly the very high porosity values associated with drillhole H-4 and the nearby much lower porosity values corresponding to drillhole SD-12. However, plate 11 contains a parallel example of high lithophysal porosities associated with drillhole NRG-6 and nearby much lower porosity values corresponding to drillhole SD-9, both of which were logged using post-1988 geophysical instruments. Farther to the west on cross section 35 (plate 11), drillhole H-5 (pre-site characterization logs) is again associated with very high lithophysal porosity values. We interpret the evidence as weighing most heavily toward real lateral heterogeneity in the extent of development of mesoscale lithophysal cavities.

There is at least one example of some significant problems with identification of the boundaries of the TSw model unit. Plate 9(e) shows a very anomalous high-porosity interval at the very top of the unit at Nevada state plane coordinate 770,000 ft north. The red-colored block in plate 9(e) clearly is anomalous, as it represents a porosity of some 40–50 percent associated with what "should" be the caprock vitrophyre (zone Tptrv1) of the densely welded Topopah Spring Tuff. The same high-porosity material is indicated in the enhanced image of plate 9(g), which also indicates an undulating interval of dark blue to purple partially broken by lighter blue shades all across the top of this north–south profile. Note also that the very low porosity lower (sometimes called "basal") vitrophyre of the TSw model unit (lithostratigraphic unit Tptpv3) is not particularly continuous throughout the model domain—at least not as a low-porosity unit.

The uncertainty model for the Topopah Spring welded model unit [part (f) of plates 9–11] indicates strong vertical zonation controlled by proximity of the several sections to individual drill holes. Uncertainty is observed to increase toward the northern and (particularly) the southern ends of the long-section shown in plate 9. Uncertainty in this southern area appears to be accompanied by a more blurred distinction of the upper and lower lithophysae-bearing intervals.

Validation

Figure 58 presents four randomly selected porosity profiles of lithophysal porosity from the TSw model unit and compares them to the lithophysal porosity data derived from downhole petrophysical logging and other information. As was the case for the PTn model unit, reproduction of measured values at the locations of those values, subject to the limitations of grid discretization, appears to be acceptable in the simulated models shown in the figure. The overall trend of alternating higher- and lower-porosity lithophysal and nonlithophysal intervals has clearly been captured, given the fairly coarse 10-m (roughly 33-ft) spacing of the grid in stratigraphic coordinates. In addition to the zonation of lithophysae-bearing intervals, the two vitrophyre units of the Topopah Spring welded section (units Tptrv1 and Tptpv3; Buesch and others, 1996) are appropriately captured as well; the simulated values fall essentially on the heavy solid line indicating the measured porosities of these low-porosity glassy zones at the very top and base of the TSw model unit. Given that the true thickness of the upper ("caprock") vitrophyre is typically only 1–2 ft (less than a meter) thick (Appendix B), the simulated models would appear to be quite realistic in detail. What the simulated models cannot do, is reproduce on a 10-m discretization the high-frequency information content of the measured porosity data for which the sample spacing is nominally less than 1 meter (3 ft). For example, profile (d) of figure 58 completely misses the prominent very high porosity interval in the lower lithophysal zone at a stratigraphic depth of about 640 ft.

An interesting phenomenon may be observed in figure 58(b), the profile nearest the location of drill hole SD-9. The simulated porosity values closely track the data, as indicated by the heavy solid line, to a stratigraphic depth of approximately 730 nominal feet; the replicate values are also quite closely grouped about the true values. However, below this stratigraphic depth, the spread of the simulated values plotted in the figure become much larger, although the lighter-weight dashed line representing the E-type model values appears to agree rather well with the general porosity trends observable in the lower portions of the remaining parts of figure 58, including a suggestion of the lower vitrophyre unit equivalent in porosity to that indicated in hole WT-18 [part (a) of the same figure] and only slightly higher than that in parts (c) and (d). The cause of this behavior is that conditioning data values for drill hole SD-9 are absent below this 730-ft depth. Measured porosity values from below the lower lithophysal interval of the TSw model unit were inadvertently omitted from the input data file.

In fact, this inadvertent omission offers the opportunity for a small exercise in blind validation of the simulation modeling process. The actual core porosity data from the SD-9 drill hole are available, and these values have been plotted in figure 59, together with the E-type model values and the individual sets of values from the four different simulated models.

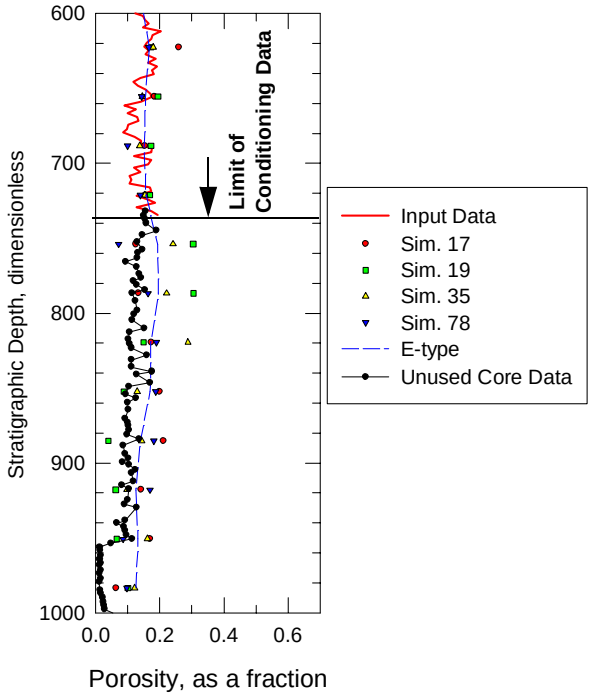

Figure 59. Lower portion of porosity profile from figure 58(b) showing measured core data inadvertently omitted from drill hole SD-9 in the simulation data set. Compare core values to E-type model plot (dashed line).

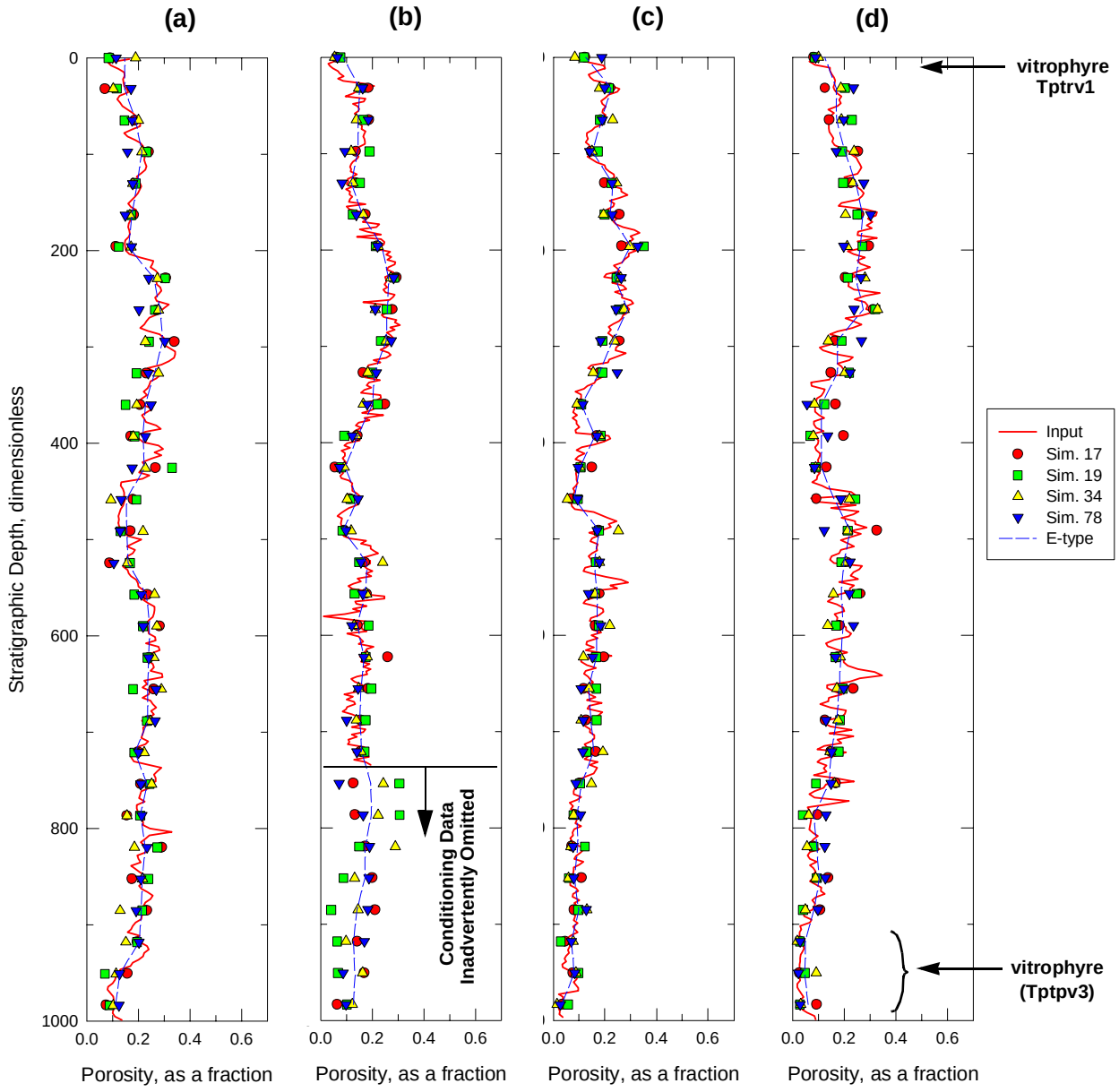

Figure 58. Comparative porosity profiles extracted from simulated models of lithophysal porosity in the TSw model unit for grid nodes nearest drillholes (a) WT-18, (b) SD-9, (c) SD-12 and (d) SD-7.

The univariate statistical character of the simulated models of lithophysal porosity for the TSw model unit is shown in figure 60, parts (a)–(d), for the four randomly selected realizations shown as porosity profiles in figure 58. Also shown in figure 58(e) are the histogram of the original measured lithophysal porosity values used to condition the models [see also plate 16(b)] and the his-

togram of the summarized E-type model [figure 58(f)]. A number of descriptive statistical measures are shown adjacent to each histogram.

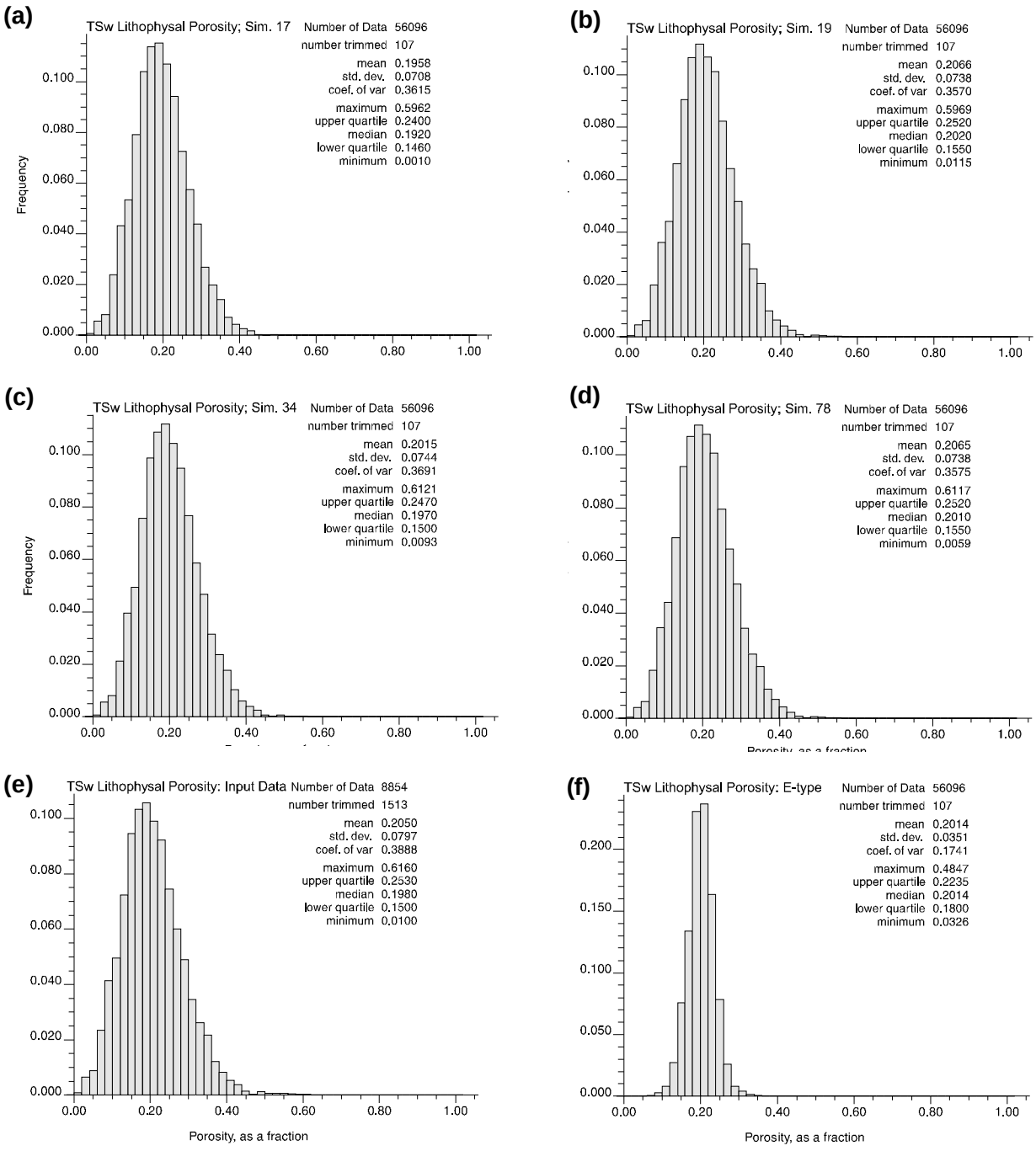

Figure 60. Histograms of four individual simulations of lithophysal porosity in the TSw model unit [(a)–(d)] compared to the original porosity data [(e)] and E-type summarized model [(f)]. Associated statistical summary shown for each histogram.

The several histograms indicate that the overall univariate statistical character of the simulated models is virtually indistinguishable from that of the original data. Because there is no objective means of deciding among the various realizations (the full suite consists of 100 equiprobable realizations), we hold that each realization represents a plausible model of the real world distribution of lithophysal porosity values. In contrast, as was the case for total porosity in the PTn model unit (fig. 51), the statistical character of the E-type summary model is quite different from that of the underlying data. Even though the measured data themselves are reproduced, the expectation operator has greatly reduced the tails of the distribution of modeled values and produced an essentially gaussian-appearing population. To the extent that (in this case) the very high porosity lithophysae-bearing intervals affect the performance of the potential repository, the systematically lower expected porosity values represented in the E-type model may distort subsequent engineering analyses.

Figure 61 presents a summary of the computed variograms for the 100 simulated lithophysal porosity models.[†] A comparison of variograms from the four individual porosity models compared to both the input variogram model and the original sample variogram of the data is presented in figure 62. Part (a) of the figure contains the variograms computed in the stratigraphically vertical direction, whereas parts (b) and (c) are computed in the stratigraphically horizontal plane, one in the direction of maximum spatial continuity at azimuth = 0° (b) , and the other at 90° to it (c).

In all three parts of both figures, the simulated porosity models indicate somewhat shorter correlation lengths than had been inferred from the sample data. The simulated models exhibit more variability at each separation distance than do the inferred variogram models. However, note that for both horizontal cases, [figure 62, parts (b) and (c)], the variograms of the simulated models are not incompatible with the *sample* variograms computed in the same directions. In figure 62(b), the simulation variograms plot directly on top of the second point of the sample variogram at a separation distance of about 2000 ft. The third sample variogram point appears too low by comparison, but the fourth sample point representing separations of about 6000 ft is again closely approximated in the simulated models. In figure 62(c), the simulation variograms clearly are more closely akin to the sample variogram values, with the exception of the hole-effect-like decreases in observed variability at 5000–8000 ft and again at 13,000–18,000 ft distances. The simulated models appear to be robust, reproducing characteristics of the actual sample data that appear to have been over-interpreted in light of a prior conceptual model of geology.

In contrast with the variograms computed for the four simulations shown in figure 62, the variograms of the E-type porosity model clearly emphasizes the intuitive geologic expectation of continuity. At each separation distance examined, the variability of the E-type model is less than half the magnitude of the other three types of variograms (data, model, simulations) presented in the figure. This type of distortion of real-world quantitative correlation structure is typical of E-type models, and it poses a serious conundrum for users of rock property models in numerical physical process modeling. Clearly, there is something very basic about fairly large-scale spatial continuity of rock units at Yucca Mountain. If there were not, it would not be possible to create geologic maps with map units that extend across broad areas (e.g., Day and others, in prep.[‡]). At the same time, however, it is also apparent that quantitative measurements of material properties do exhibit quite significant variability over quite short separation distances both vertically and horizontally. Unless we are to assume that this type of variability is simply measurement error subject to disproof by replicate measurements or measurement by multiple techniques, we are driven to the conclusion that the material properties of the rock mass are, in fact,

[†]See also discussion of variograms in Appendix D.

[‡]Day, W.C., Dickerson, W.P., Potter, C.J., Sweetkind, D.S., San Juan, C.A., Drake, R., and Fridrich, C.J., in prep., Geologic map of the Yucca Mountain Area, Nye County, Nevada: intended for publication as USGS open-file report., scale 1:24,000.

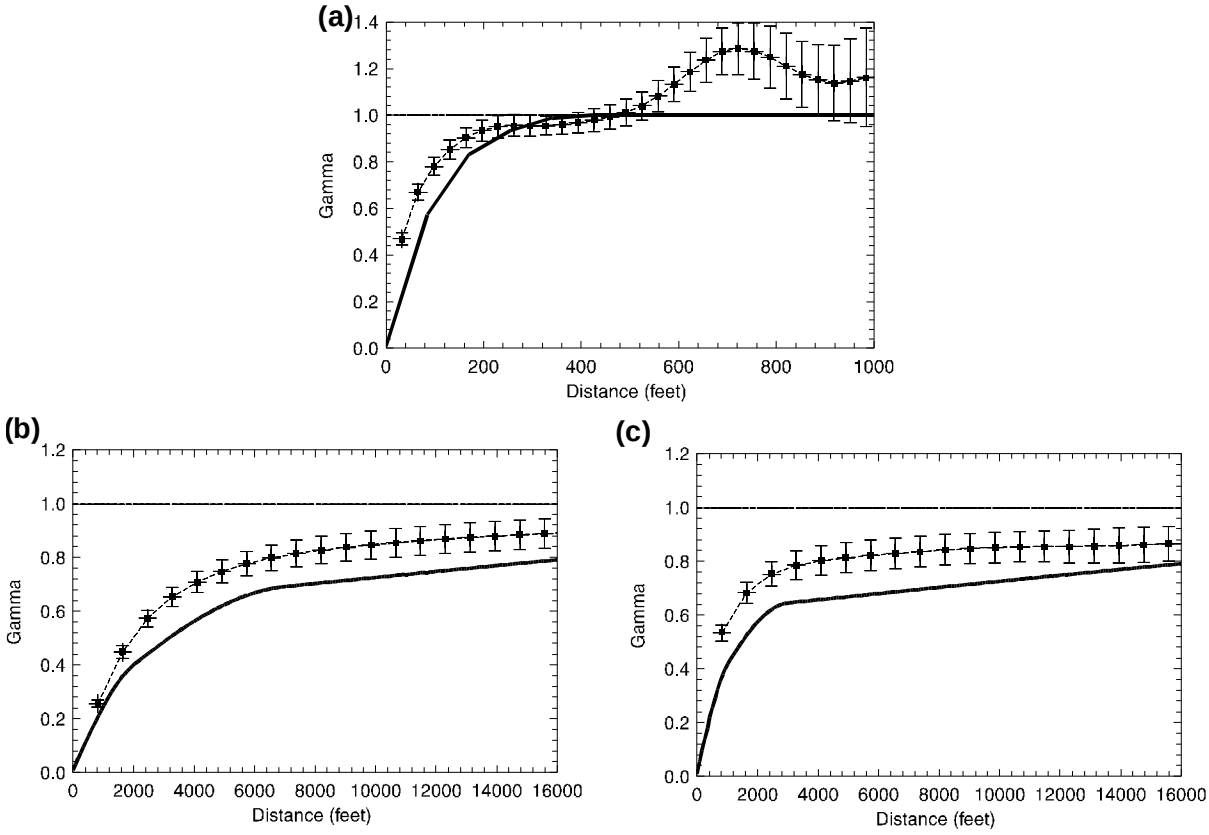

Figure 61. Reproduction of input variograms for simulated lithophysal porosity models of the TSw model unit: (a) stratigraphic vertical, (b) stratigraphic horizontal, azimuth = 135°; (c) stratigraphic horizontal, azimuth = 45°. Dashed line with error bars is average variogram with plus/minus 95-percent confidence interval; heavy solid line is input variogram model.

more heterogeneous than our geologic intuition tells us.

Matrix Porosity

Description

Several representative two-dimensional profiles extracted from the simulated models of matrix porosity for the TSw model unit are shown in plates 12 through 14. Note that the porosity values shown on the perspective views of the E-type models (plates 1–5) are *lithophysal*, not matrix, porosities, and thus the variability in porosity attributable to the megascopic lithophysae-bearing intervals of the unit is much subdued (compare with plates 9–11). Figure 63 presents drillhole profiles of matrix

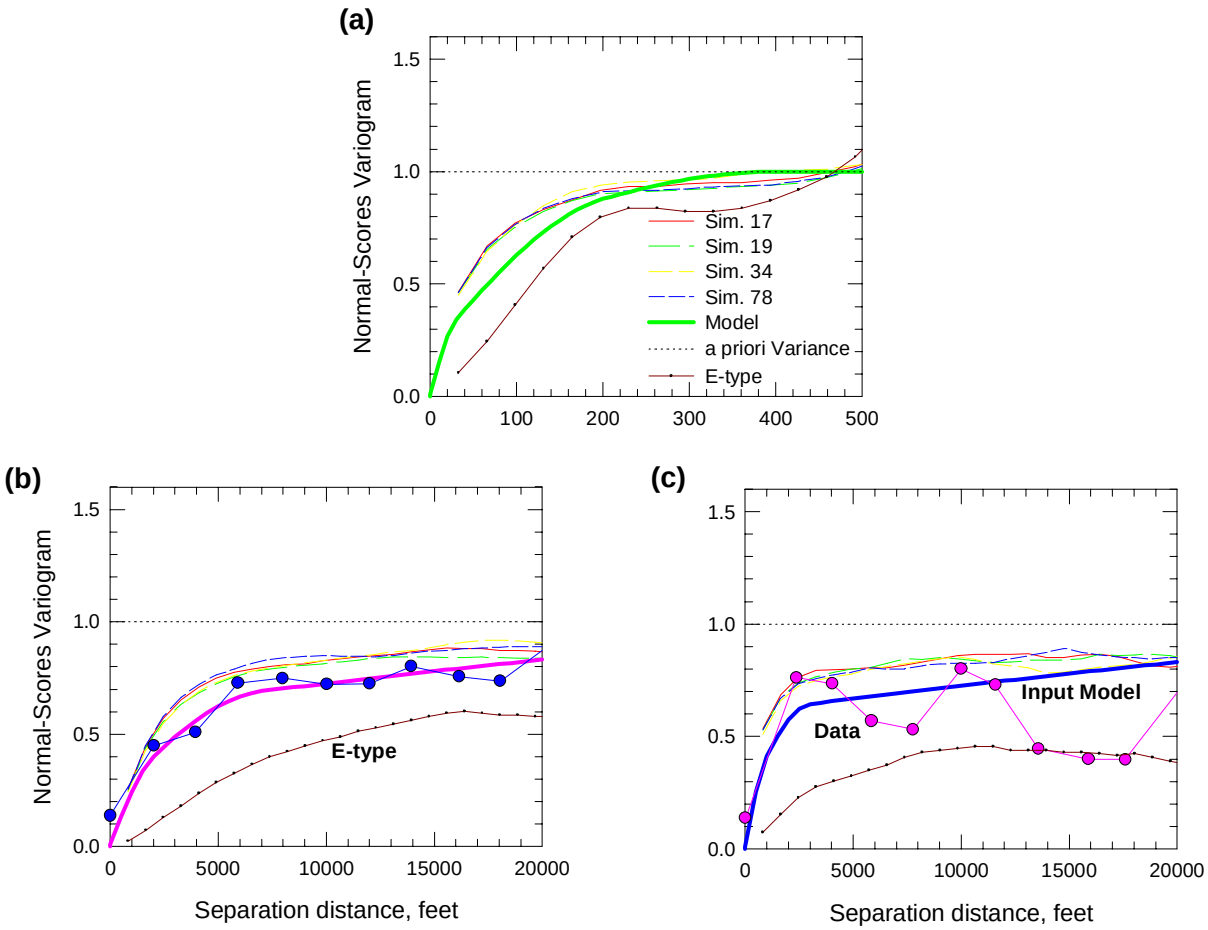

Figure 62. Variograms from four simulated lithophysal porosity models of the TSw model unit compared to input model and original data. (a) Stratigraphic vertical; (b) stratigraphic horizontal, azimuth = 0°; (c) stratigraphic horizontal, azimuth = 90°.

porosity for four randomly selected simulated models. Also shown on each figure are the original conditioning data (core or petrophysical) and the expected-value summary profile. These porosity profiles are relatively uniform and featureless by comparison with those for lithophysal porosity. However, the important features of the input data are reproduced in the simulated models to an acceptable degree. These features include slight increases in matrix porosity associated with the lithophysae-bearing intervals (compare with fig. 58, lithophysal porosity), generally higher porosity associated with the uppermost part of the Topopah Spring Tuff, and the very low porosity values associated with both the caprock vitrophyre and the lower vitrophyre units.

Validation

Validation of the simulated matrix porosity models is upheld in part by reproduction of the character of the input drillholes at the nearest grid nodes (fig. 63). Additionally, the univariate statistical character of these four simulated models of matrix porosity are shown in the histograms of figure 64, parts (a) through (d). A histogram of the original measured matrix porosity data is shown for comparison in figure 64(e). Comparison of the histogram plots and the several statistical measures associated with each data set in the figure indicates that the simulated models are, in fact, virtually indistinguishable from the actual observations of Yucca Mountain. In contrast, examination of the univariate character of the E-type summary model, shown in histogram format in figure 64(f), indi-

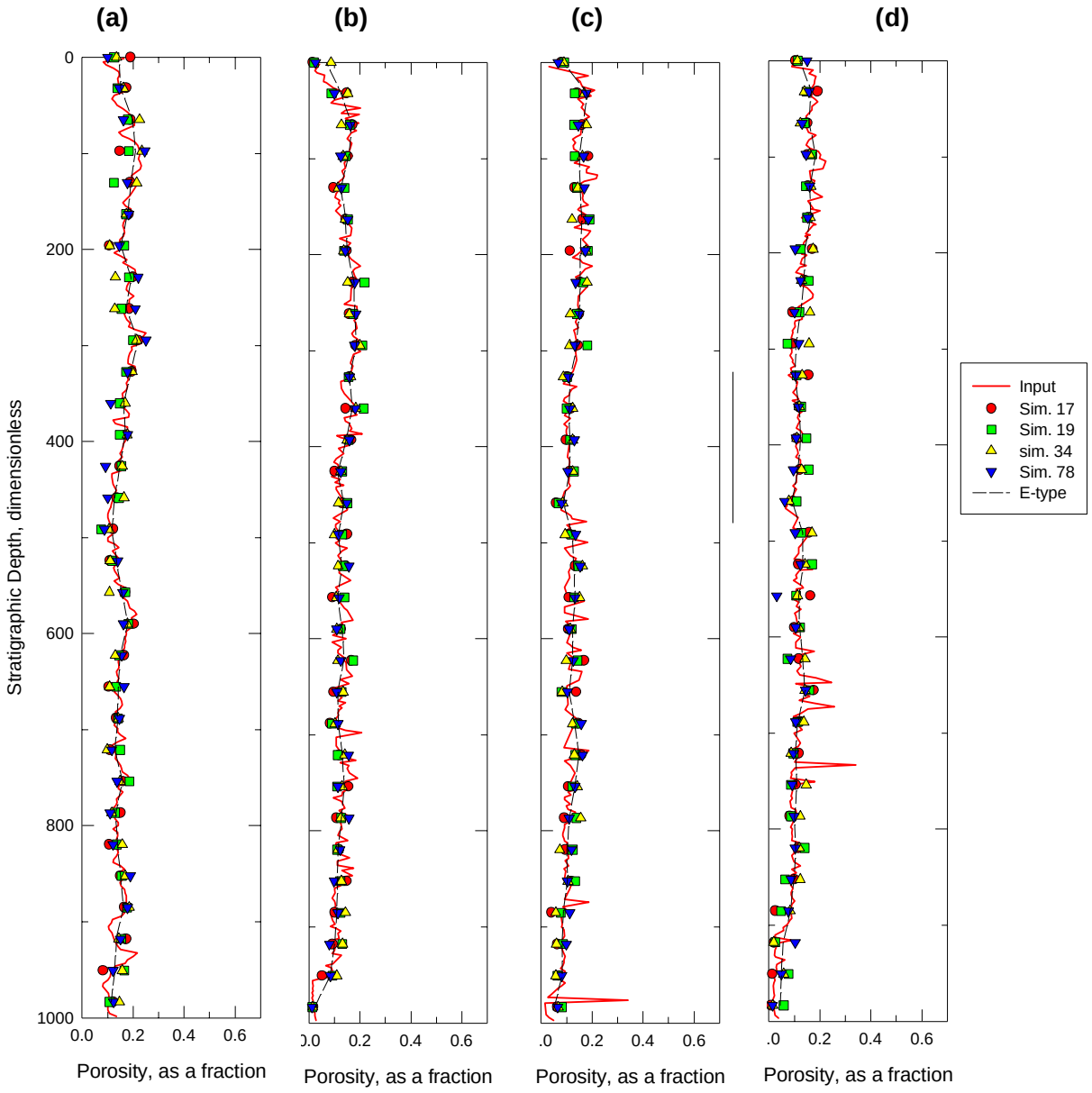

Figure 63. Comparative porosity profiles extracted from simulated models of matrix porosity in the TSw model unit for grid nodes nearest drillholes (a) WT-18, (b) SD-9, (c) SD-12, and (d) SD-7.

cates clear differences between this numerical model and both the simulated models and the samples from the site. Variability has been significantly compressed and the tails of the sample distribution have been mostly truncated. Note particularly the interquartile range of the modeled porosity values, which has been reduced to just over one porosity percent (0.0108) from nearly 7 porosity percent (0.066).

Figures 65 and 66 continue the comparison of the simulated matrix porosity models to our knowledge of matrix porosity at Yucca Mountain. Figure 65 presents the overall reproduction of the desired input model of spatial correlation across

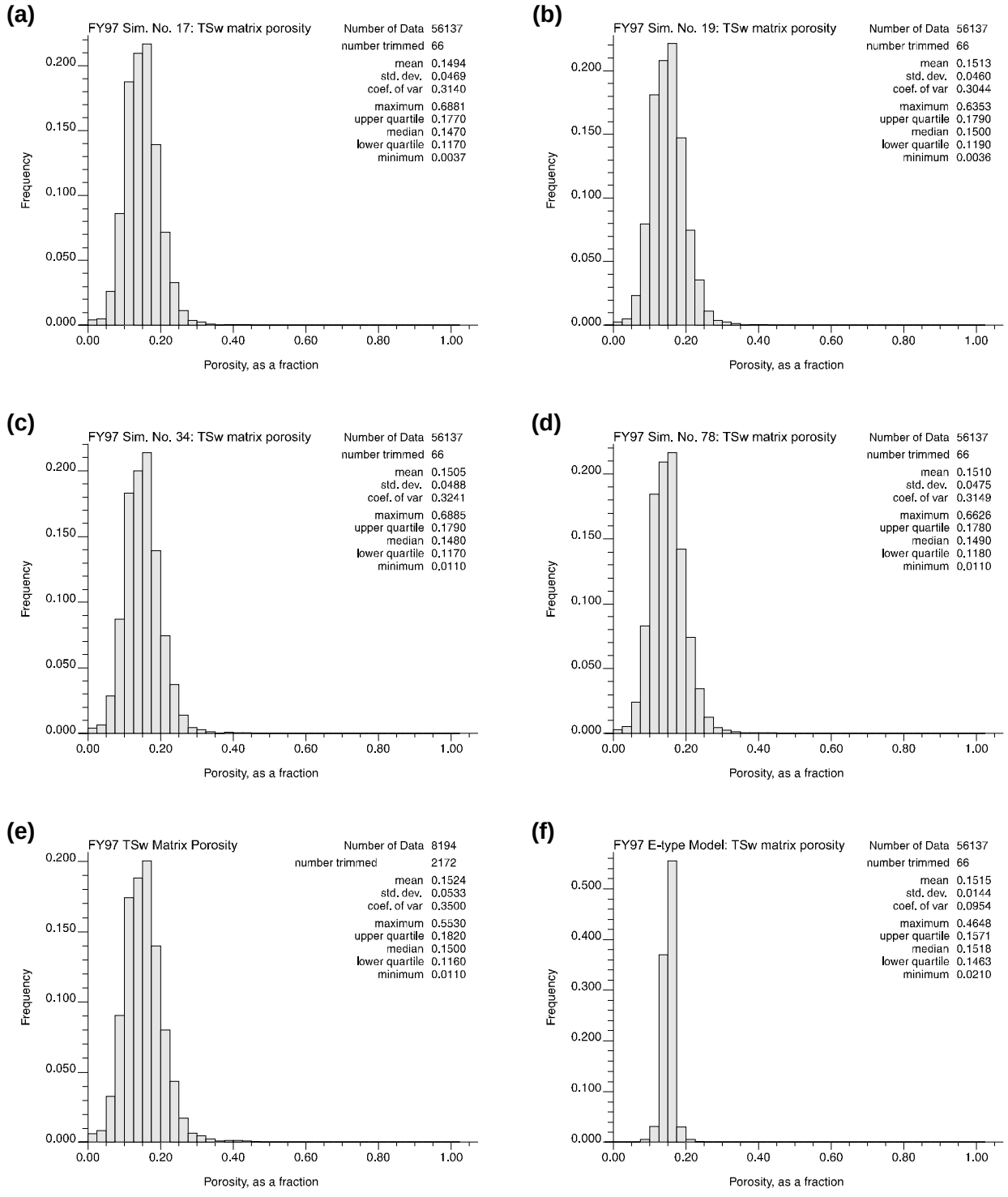

Figure 64. Histograms of four individual simulations of matrix porosity in the TSw model unit [(a)–(d)] compared to the original porosity data [(e)], and the E-type summarized model [(f)]. Associated statistical summary shown for each histogram.

the ensemble of simulations, and figure 66 shows variograms of four of the simulated models and the E-type model.† Parts (a) through (c) of both figures show spatial continuity patterns in the directions of minimum (vertical), maximum (horizontal, azimuth 0°), and intermediate correlation. The four simulated models (fig. 66) exhibit spatial continuity patterns that are quite similar to both the input variogram and the sample variogram from which that theoretical input model was developed. The one exception is in the stratigraphically vertical direction [fig. 66(a)], for which the input spatial model did not reach the sill value until the separation distances became very large (see discussion on page 51). Recall that the third and longest-range structure fitted to the sample variograms of matrix porosity in the TSw model unit (table 13) was a dummy structure to bring the total variability captured by the variogram model to the sill of 1.0, as required by Gaussian simulation theory. The underlying cause of the observed phenomenon of the too-low apparent sill for the sample data is inferred to be the computation of the sample variogram using data from only one drillhole and one type of porosity measurement at a time. Such dummy structures are neither necessary nor possible in a simulated material properties model, which is generated as a unified whole.

†See also discussion of variograms in Appendix D.

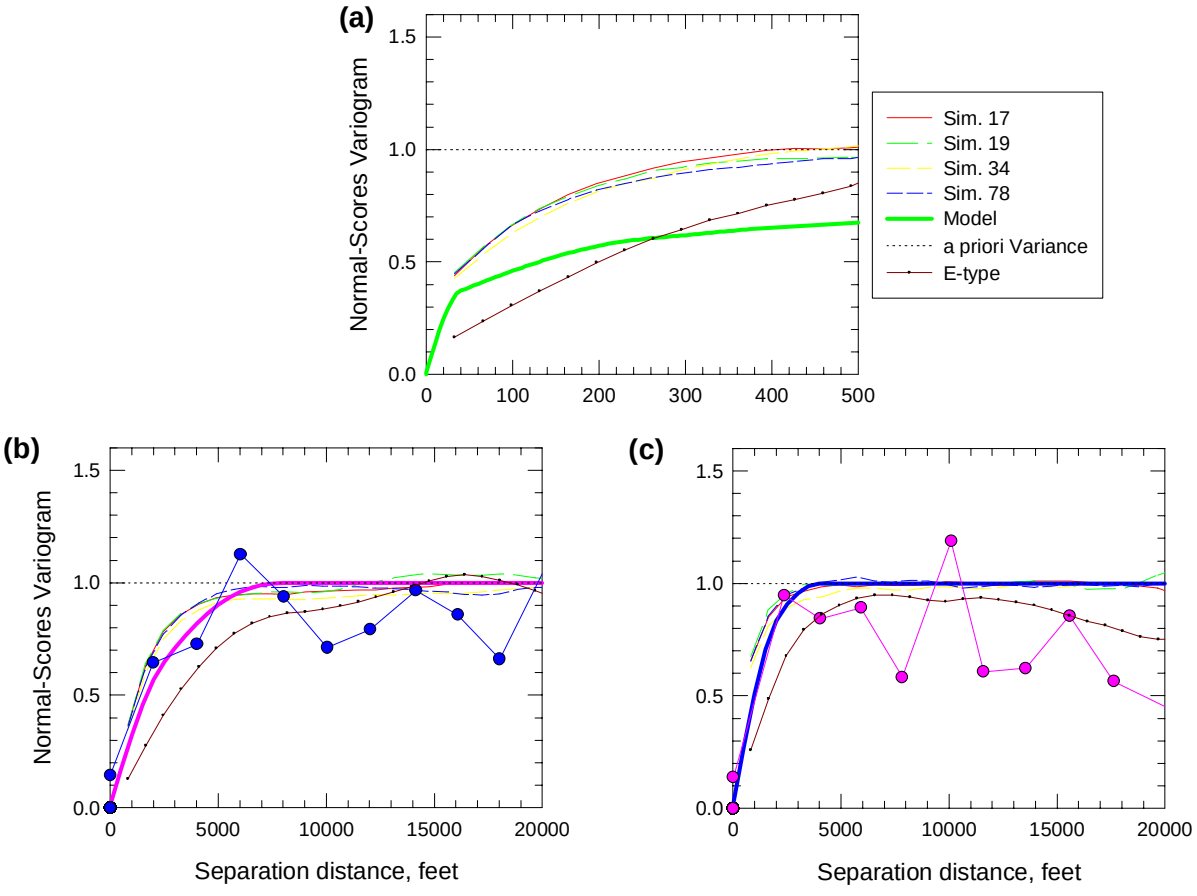

Figure 66. Variograms from four simulated matrix porosity models of the TSw model unit compared to input model and original data. (a) Stratigraphic vertical; (b) stratigraphic horizontal, azimuth = 0°; (c) stratigraphic horizontal, azimuth = 90°.

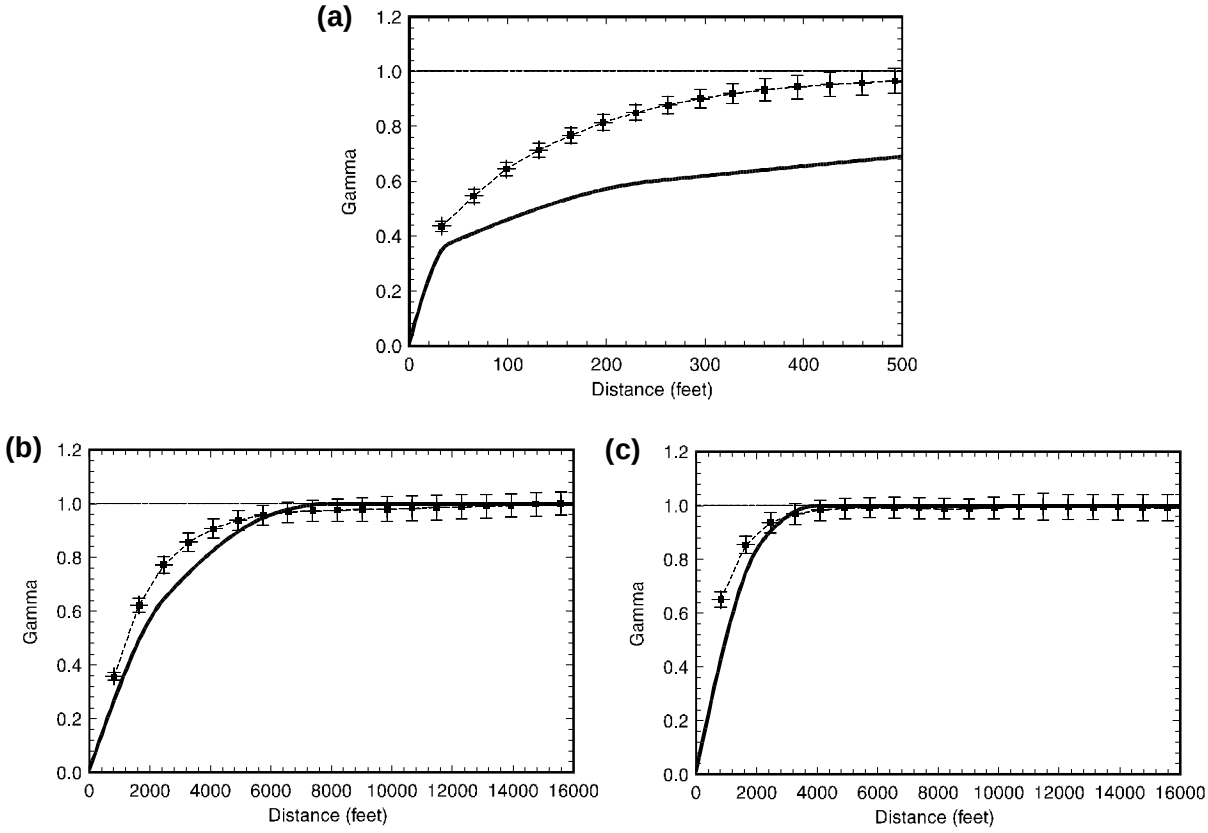

Figure 65. Reproduction of input variograms for simulated matrix porosity models of the TSw model unit: (a) stratigraphic vertical, (b) stratigraphic horizontal, azimuth = 135°; (c) stratigraphic horizontal, azimuth = 45°. Dashed line with error bars is average variogram with plus/minus 95-percent confidence interval; heavy solid line is input variogram model.

Also shown in each part of figure 66 is the variogram of the summary E-type matrix porosity model, computed in the appropriate direction in each part of the illustration. In each case, the E-type model variogram indicates less variability than is observed in the underlying simulated models; this is simply another manifestation of the compression of variability exhibited by the histograms of figure 64. Such limited variability, although it may be helpful in conceptualizing the generalized distribution of material properties at the Yucca Mountain site, is not compatible with the degree of spatial heterogeneity actually observed and measured quantitatively in the field.

Bulk Density

The bulk density model of the TSw model unit was created directly from the E-type lithophysal porosity summary model, in a manner identical to that used in creating the bulk density model for the PTn unit. The prediction relationship is given by equation (41) on page 93.

Saturated Hydraulic Conductivity

Simulated models of saturated hydraulic conductivity were created for the Topopah Spring welded unit using the linear coregionalization algorithm applied to the simulated models of matrix porosity. The rationale for using matrix, rather than lithophysal, porosity for the coregionalization is that under unsaturated conditions, such as prevail within the Topopah Spring Tuff throughout much of the immediate repository area, water will exist only in the matrix-sized pores of the welded tuff; recall previous discussion of lithophysal porosity beginning on page 30.

Because the models of hydraulic conductivity have been generated using coregionalization with the *matrix* porosity models, *the use of these models for ground-water flow and transport calculations under* ***saturated*** *conditions is not valid*. Under widespread conditions of saturation, such as exist below the water table and as distinct from local quasi-saturated conditions within the unsaturated zone, water may flow not only in the rock matrix (as herein defined), but also through the centimeter- to decimeter-scale pores comprised of lithophysal cavities. No objective evidence is known that would allow coregionalization of true fully saturated hydraulic conductivity values with lithophysal porosity. It is also likely that flow through fractures would dominate ground-water movement throughout the entire welded interval of the Topopah Spring Tuff, including both lithophysal and nonlithophysal portions.

Figure 67, parts (a) through (d), presents histograms and associated summary statistics for four coregionalized hydraulic conductivity simulations. Figure 67(e) is the histogram of the available laboratory measurements of saturated hydraulic conductivity for the entire TSw model unit, and part (f) of the same figure is the histogram of the summary E-type hydraulic conductivity model.

Comparison of the univariate character of the simulated models with that of the measured data suggests that the individual coregionalized material property models are faithful statistical replicas of the "real" Yucca Mountain. Even the forty-odd percent of the laboratory specimens that yielded no measurable flow have been reproduced. These no-flow values have been arbitrarily assigned a hydraulic "conductivity" of 10^{-14} m/sec (–14.0 log units). Although spatial correlation among the no-flow laboratory specimens was not explicitly modeled as part of the coregionalization process (see discussion of the no-flow indicator variogram beginning on page 53), the quantile-preserving univariate transformation applied as part of the coregionalization algorithm has the effect of assigning the lowest simulated normal-score conductivity values as no-flow grid nodes.

In contrast to the simulated (coregionalized) models of hydraulic conductivity, the histogram of the expected-value summary model [fig. 67(f)] clearly indicates a different statistical character from that of the measured laboratory data. No-flow grid nodes are absent, and the modal hydraulic conductivity of the model as a whole has been reduced from a broad "peak" centered at a log Ksat value of between –8 and –10 log units to a sharp spike of values with a conductivity of less than –11.0 log units. Note, however, that the modal conductivity value for the E-type model is strongly influenced by the value assigned to the simulated non-flowing grid nodes. Because the no-flow values are generated essentially at random, the existence of a no-flow grid node in one simulation says nothing about the occurrence of no-flow values at the same location in the next simulated model. In any event, the symmetrization of the histogram and the reduction in overall variability noted in other E-type models appears to operate here as well.

Figure 68 presents scatterplots of simulated saturated hydraulic conductivity with simulated porosity for the appropriate pairs of coregionalized models. The general relationship of increasing hydraulic conductivity values with increasing porosity expected from the physics of ground-

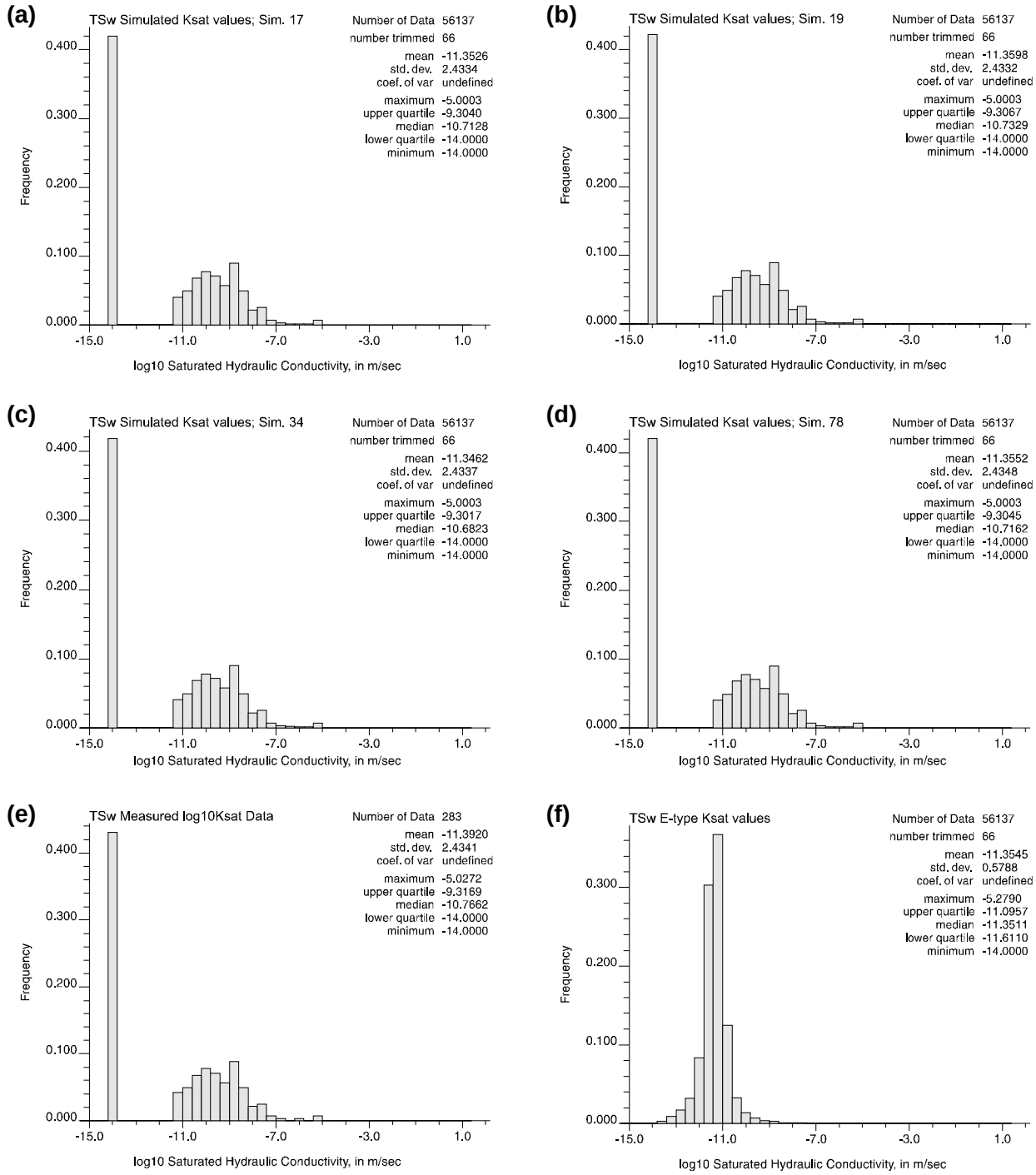

Figure 67. Histograms of four coregionalized models of saturated hydraulic conductivity corresponding to the four porosity models presented in figure 58(a) through (d) compared to histograms of original measured Ksat data (e), and E-type summary model (f).

water flow in a welded tuff is respected. Coefficients of determination (r^2 values) appear to be on the order of 0.5 to 0.6, approximately the same order of magnitude as was observed for the laboratory data; see figure 25. Note that non-flowing lab-

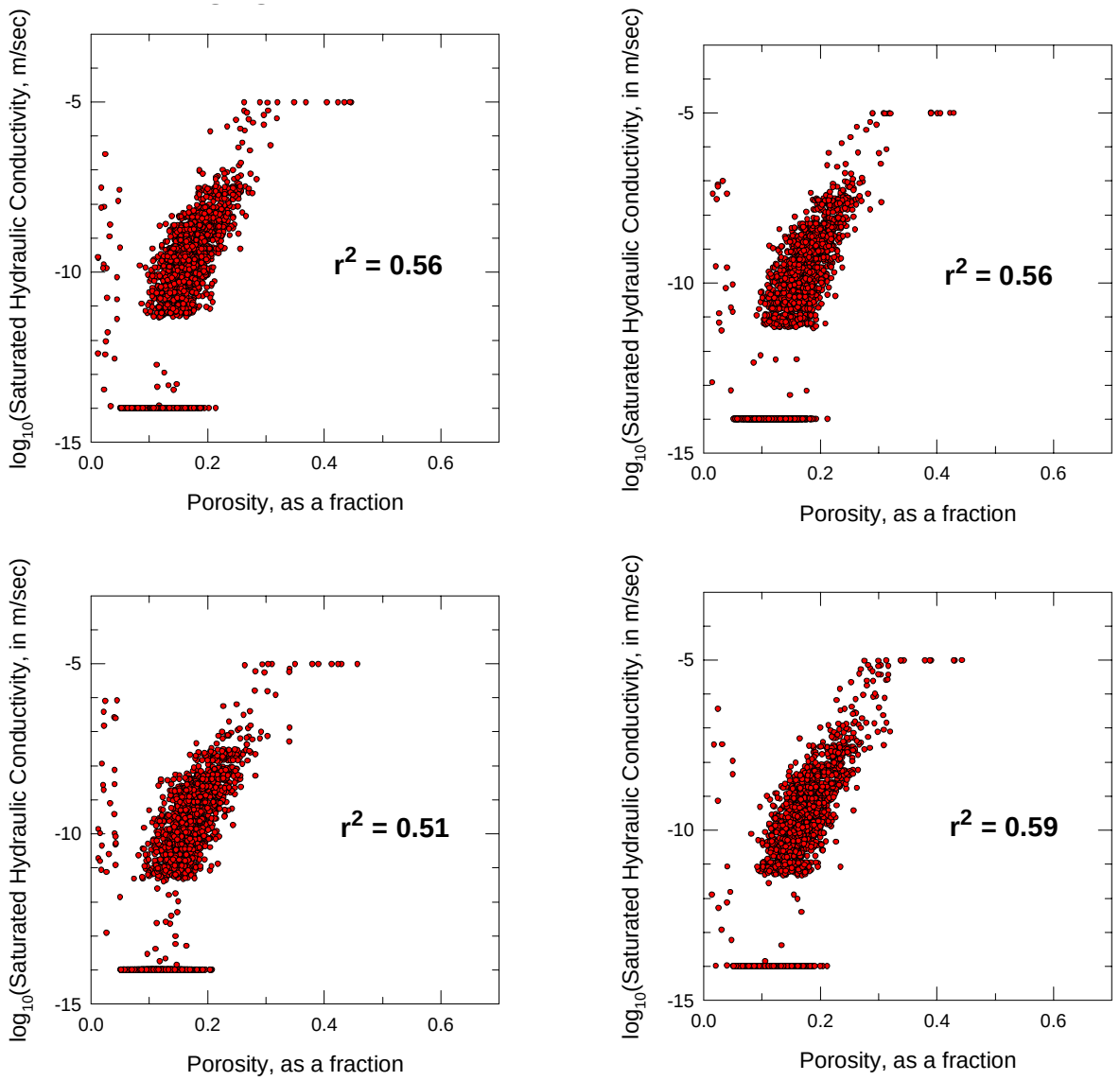

Figure 68. Scatterplots of modeled saturated hydraulic conductivity as a function of modeled matrix porosity for the TSw model unit. (a) Simulation no. 17; (b) no. 19; (c) no. 34; (d) no. 78 (5-percent subsample). Compare with parts (a) and (c) of figure 25.

oratory samples were excluded from the analysis of laboratory data, whereas the simulated no-flow grid nodes have been included in the plots of figure 68. However, comparison of the scatter "clouds" for both diagrams suggests that the correlation is approximately correct, regardless of the treatment of these non-numeric property values. Included in the correlation analysis for both data and simulated models are the presumed-microfractured conductivity values associated with the vitrophyric test specimens (group "C" of fig. 23; see also fig. 27 at an expanded porosity scale).

Figure 69 is a similar scatterplot of hydraulic conductivity vs porosity for the E-type summary of the suite of coregionalized simulations of TSw model unit. What was observed to be a fairly diffuse (r^2 = 0.6) correlation of properties has been modified by the expectation operator to a relationship just short of one-to one; the computed r^2 value for figure 69 is 0.90. As a matter of "expectation," porosity and hydraulic conductivity are generally fairly strongly correlated. On a sample-specific (location-specific, in the case of the simulated models) basis, however, the relationship is not as strong.

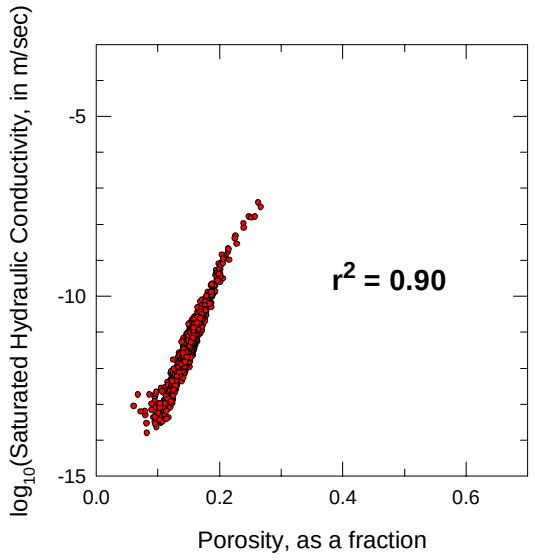

Figure 69. Scatterplot of saturated hydraulic conductivity and matrix porosity for the summary E-type model of the TSw model unit (5-percent subsample).

The effect of the expectation operator on the modal value of the flowing grid nodes is emphasized graphically in comparing figures 68 and 69. In addition to the variance reduction in figure 69, the entire correlation "cloud" has been shifted vertically downward a full 3 log-conductivity units, whereas the porosities remain unchanged, varying between about 10 and 30 percent (0.10–0.30). Again, the magnitude of this modal shift is determined largely by the hydraulic conductivity value assumed to represent the non-flowing grid nodes.

Thermal Conductivity

Simulated models of thermal conductivity were created for the Topopah Spring welded unit using linear coregionalization applied to the *lithophysal porosity* models. The rationale for this approach is that although the correlation relationship of thermal conductivity with porosity shown in figure 28(b) is based upon measured *matrix* porosities, heat will be conducted within the actual Yucca Mountain by rocks with markedly higher porosities than were measured in the laboratory. As such, the conductivity of the lithophysae-bearing intervals will be reduced by the presence of large void spaces that may be at least equal to the amount of micro-scale matrix porosity. The presumption in this study is that a densely welded tuff containing a total of 40-percent void space comprised of both small-scale matrix pores and large-scale lithophysal cavities will exhibit approximately the same thermal conduction behavior as a nonwelded tuff containing the same 40-percent total void space made up of inter-particle pores and intra-particle voids (e.g., "frothy" pumice clasts). Although there is unquestionably some error introduced by this currently unverified assumption, we believe that the physics of heat conduction imply that thermal conductivity modeled for the TSw model unit in this manner more closely resembles the true thermal conductivity than were we to ignore the presence of the lithophysal cavities and use only matrix porosity in the prediction.

Figure 70, parts (a) through (d), present histograms and associated summary statistics of four coregionalized thermal conductivity models. Figure 70(e) is an unbiased histogram of the true distribution of thermal conductivity, as inferred by applying the regression relationship of figure 28(b) to the systematic vertical distribution of porosity identified from drill holes SD-7, SD-9, and SD-12 (see discussion on page 43 regarding sampling and testing biases; also figs. 31 and 30). The histogram shown in figure 70(f) is that of the summarized E-type thermal conductivity model.

The histograms of figure 70(a)–(d) indicate that the coregionalized models of thermal conductivity are faithfully reproducing the statistical nature of the systematically "sampled" thermal

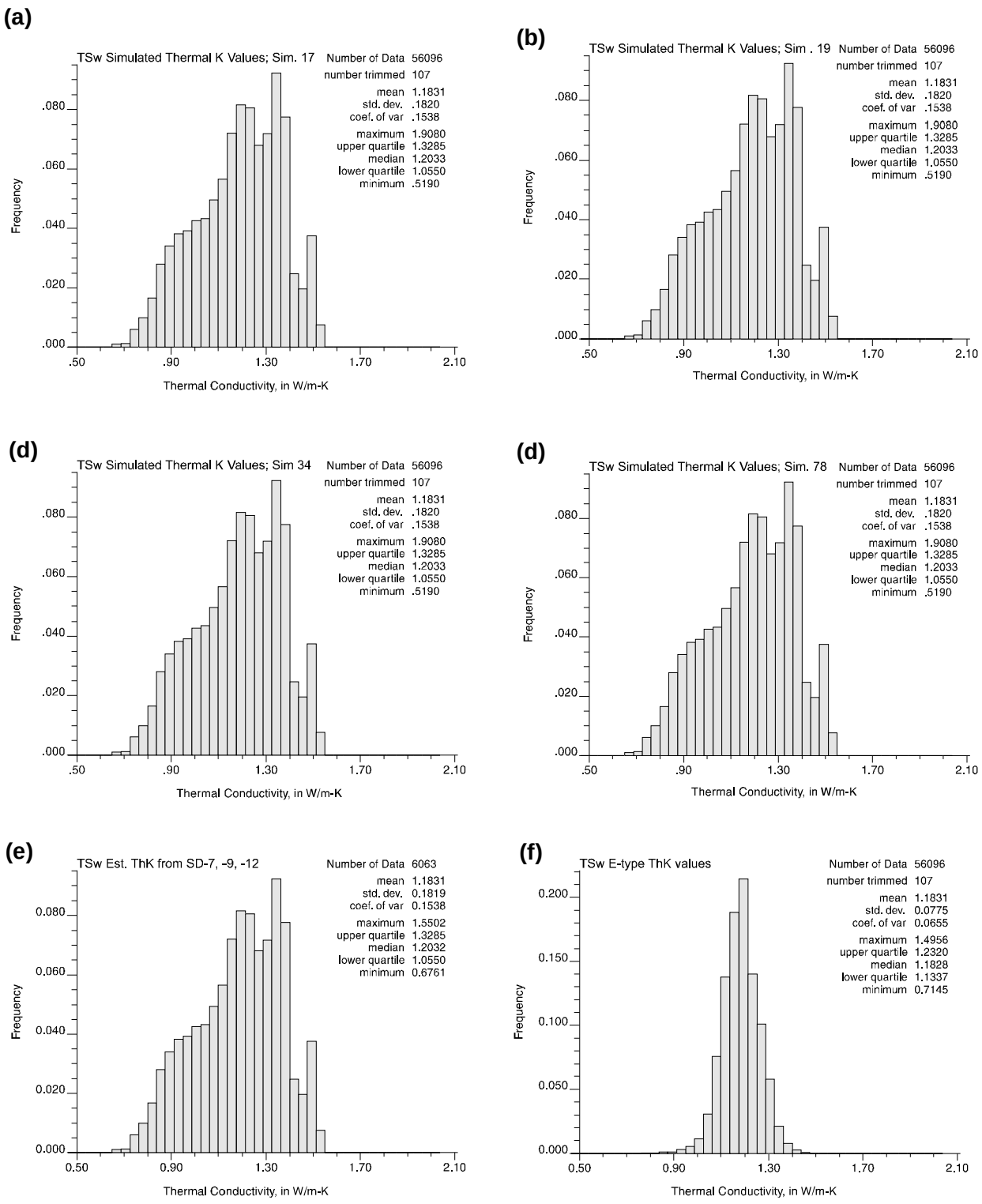

Figure 70. Histograms and summary statistics for four coregionalized models of thermal conductivity for the TSw model unit.

conductivity data. Clearly, it would be better if there were measured thermal conductivity values that directly address the issue of lithophysal cavities on the heat-carrying capabilities of the rocks at Yucca Mountain [fig. 70(e)]. However, given the mechanical limitations of laboratory experiments that require small, intact test specimens, reproduction of the estimated thermal conductivity of the entire Topopah Spring welded unit as described on page 43 is probably the most reasonable approach to material properties modeling, pending completion of larger-scale in-situ thermal testing. It is unclear, however, that these in-situ testing activities will affect a sufficiently large volume of material over the time-scales available for testing to extend above and below the repository horizon to include a meaningful volume of material containing the large lithophysal cavities. Note that if our hypothesis regarding the impact of lithophysal cavities is correct, the simple distribution of measured thermal conductivity values presented in figure 28 significantly distorts the actual thermal conductivity of the Paintbrush Group tuffs at Yucca Mountain.

As has been the case in previous sections presenting the results of material properties modeling, the histogram of the E-type summary model, shown in figure 70(f), indicates strong truncation of tail conductivity values from the univariate distribution. The figure also shows the strong symmetrization of the distribution of values typical of the expectation operator; both high and low values have been eliminated. The impact of the loss of both high and low conductivity materials from the numerical property models may have detrimental effects on the results of numerical modeling of the redistribution of heat from an actual repository.

Figure 71 presents the cross-variable correlations of thermal conductivity with the underlying simulated lithophysal porosity values used in the coregionalization process for the same four realizations shown in figure 70. The strength of the correlation for each realization is indicated on the different parts of the figure, and they range from an r^2 value of 0.71 to an r^2 of 0.78. These values are markedly higher than the original r^2 obtained from the measured thermal conductivity data of 0.586 [see fig. 28(b)]. Reference to figure 28 strongly suggests, however, that the low coefficient of determination obtained from the laboratory data may have been strongly influenced by the four data points corresponding to measured thermal conductivities of 2.0 W/m-K and higher (recalculation of the coefficient of determination omitting the 4 samples shown in figure 28 that yielded measured thermal conductivities of approximately 2.0 and higher gives a revised r^2 of approximately 0.663). These samples may not be representative of the bulk of the Topopah Spring welded unit, as the larger majority of the laboratory data fall much closer to the fitted regression line shown in figure 28(b). Indeed, application of the prediction equation even to porosity values less than 5 percent (0.05), results in no estimated thermal conductivity values greater than about 1.6 W/m-K (figs. 30, 70). Even among the existing data, these samples appear to represent outliers. Additionally, there is a lack of high porosity-low thermal conductivity samples in general, which might have served to strengthen the experimentally observed correlation, simply from a computational standpoint.

Figure 72 presents the cross variable correlation of porosity with thermal conductivity for the E-type model. The form of the relationship is correct, with higher porosity grid nodes corresponding to lower thermal conductivity values. However, the expectation operator has worked to obscure the fact that the observed correlation of thermal conductivity with porosity is not one to one. The coefficient of determination for the scatterplot shown in figure 72 is 0.98, far higher than the observed r^2 value of 0.586.

Uncertainty Model

Figure 73 presents a global summary of uncertainty associated with the 100 stochastic simulations of lithophysal porosity, as measured by the node-by-node standard deviations developed during computation of the E-type lithophysal porosity model. The average standard deviation is approximately 6.3 porosity percent, compared with a global average porosity of just over 20 percent (0.205; table 6; fig. 58). The distribution of standard deviations is asymmetrical, with a maximum simulated uncertainty of approximately 10 porosity percent. The less-uncertain portion of the uncertainty distribution exhibits a relatively progressive decrease in

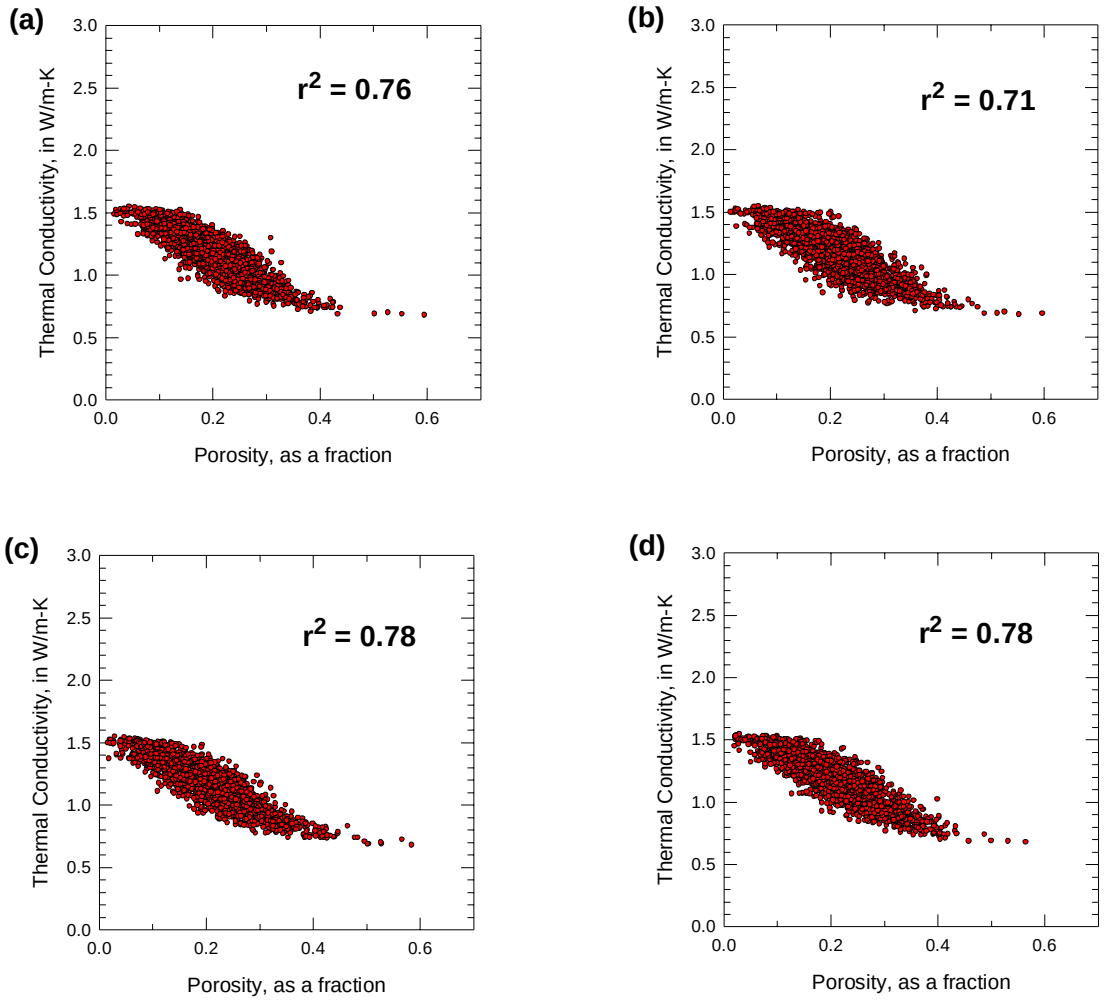

Figure 71. Scatterplots of modeled thermal conductivity in the TSw model unit as a function of simulated lithophysal porosity (5-percent subsample). (a) Simulation 17; (b) simulation 19; (c) simulation 34; (d) simulation 78.

standard deviation to a minimum uncertainty of between 1 and 2 porosity percent. Grid nodes exhibiting this low degree of variation among the different realizations of the lithophysal porosity model are located close to conditioning sample data.

A visual summary of the global uncertainty associated with the simulated models of matrix porosity (excluding the effect of large lithophysal cavities) is presented in figure 74. This histogram shows the node-by-node standard deviations computed across the suite of 100 stochastic models of matrix porosity. The "average" uncertainty associated with the models of matrix porosity in the TSw model unit is plus-or-minus approximately 4.5 porosity percent (0.045). This average standard deviation value is smaller than the equivalent uncertainty measure for lithophysal porosity (fig. 73), which is appropriate given the smaller range of matrix porosity values compared to that for the lithophysal porosity measure. The minimum uncertainty associated with the matrix porosity models is just over 1 percent, and the maximum uncertainty is just under 14 porosity percent. The corresponding values for the lithophysal porosity models are 0.01 and 0.10, respectively. The larger maximum uncertainty value (0.137, fig. 74) is somewhat sur-

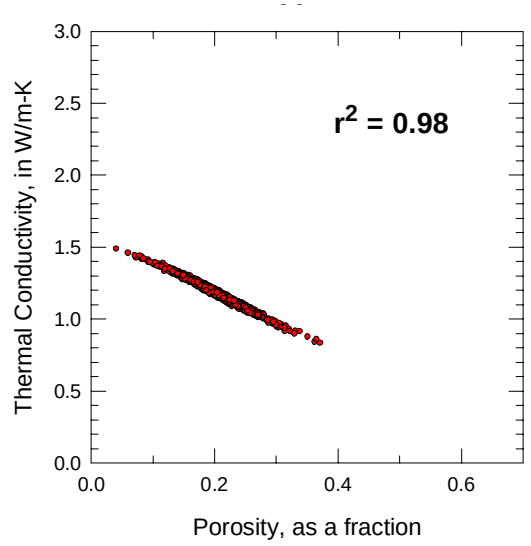

Figure 72. Scatterplot of thermal conductivity as a function of lithophysal porosity for the summary E-type model of the TSw model unit (5-percent subsample).

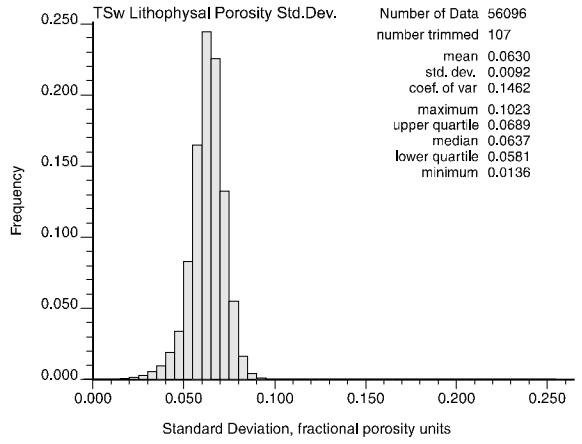

Figure 73. Uncertainty associated with simulated models of lithophysal porosity for the TSw model unit.

prising, given the smaller overall range of variability for matrix porosity. However, comparison of the statistical summaries associated with figures 73 and 74 indicates that the interquartile range for the standard deviations of matrix porosity is appropriately smaller than that range for lithophysal porosity, the explanation of the larger maximum uncertainty value clearly lies in the spatial positions of various drill hole data with respect to the modeled grid nodes.

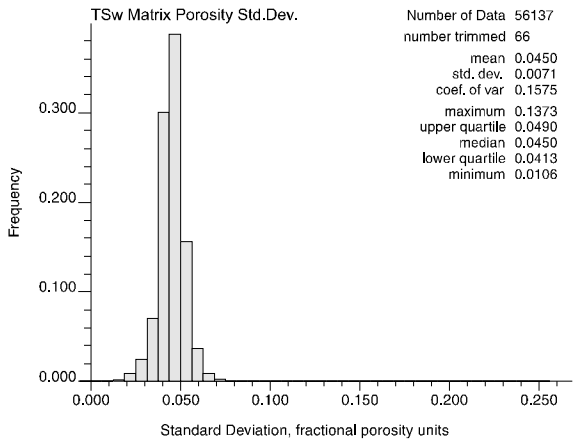

Figure 74. Uncertainty associated with simulated models of matrix porosity for the TSw model unit.

Global uncertainty associated with the coregionalized models of saturated hydraulic conductivity is presented in figure 75; the uncertainty estimates are again based on the node-by-node standard deviations computed during generation of the E-type hydraulic conductivity model. The globally typical or average uncertainty associated with the simulated models of hydraulic conductivity is plus-or-minus 2.4 log units ($\log_{10}$ m/sec), compared with a global average conductivity of –11.35 log units. The maximum observed uncertainty is somewhat less than plus-or-minus 3 log units (2.8768). The actual uncertainty associated with any particular location within the modeled domain is spatially variable, and is a function of the distance from the location considered to the nearest set of constraining porosity values.

A similar presentation of the global uncertainty associated with the simulated models of thermal conductivity is presented in histogram format in figure 76, again expressed as the standard deviations of the 100 stochastic coregionalized models. The average standard deviation across all grid nodes in the discretized model is 0.164 W/m-K, with a maximum simulated uncertainty on the order of 0.22 W/m-K. These values may be compared with the estimated average thermal conduc-

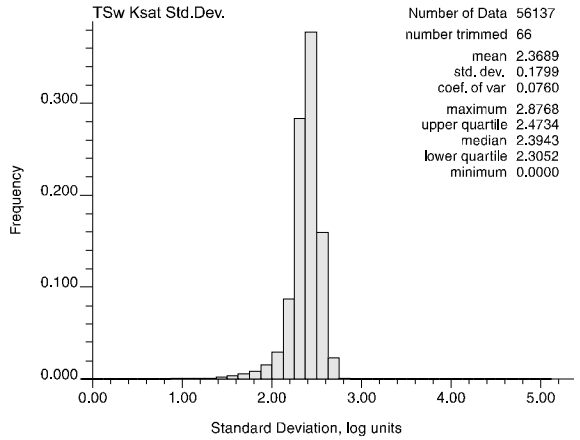

Figure 75. Uncertainty associated with simulated models of saturated hydraulic conductivity for the TSw model unit.

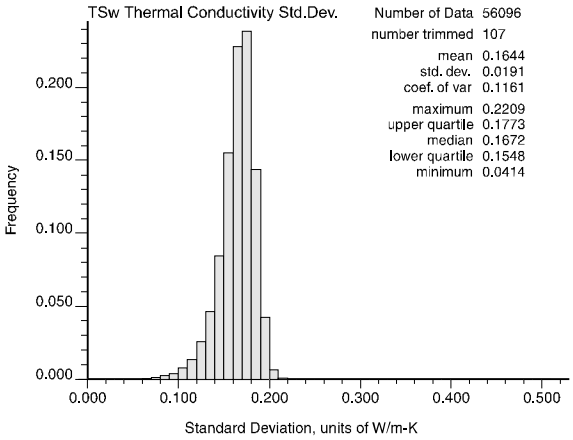

Figure 76. Uncertainty associated with simulated models of thermal conductivity for the TSw model unit.

tivity of the Topopah Spring welded interval of about 1.2 W/m-K [fig. 59(e)]. However, the data from which this unit-specific average thermal conductivity was derived were the *estimated* conductivity values predicted using the observed regression of thermal conductivity on porosity shown in figure 28; the mean of the non-systematically sampled, spatially biased *measured* thermal conductivities was 1.77 W/m-K (table 9). Uncertainty decreases smoothly and progressively to a lower bound of approximately plus-or-minus 0.05 W/m-K for grid nodes located at shorter distances from the locations of the best-conditioned lithophysal porosity values.

Calico Hills–Prow Pass Model Unit

Porosity

Description

An overall perspective view of the expected porosity within the combined Calico Hills–Prow Pass stratigraphic interval is presented in plates 1 through 5. More specific sectional profiles of the CH–PP model unit by itself are shown in plates 15, 16, and 17. Note that the solid black blocks in the right-hand side of plates 16 and 17 represent grid nodes that were left unsimulated because the distance from these nodes to the nearest drillhole information exceeded 12,000 ft.

Because the Calico–Prow model unit is a composite one, it is important to examine how this modeling approach reproduces the separate identities of the Calico Hills Formation and the Prow Pass Tuff. The most prominent materials properties feature of the Prow Pass Tuff, as distinct from the Calico Hills Formation, is where ash-flow unit 3 of the Prow Pass Tuff is partially welded (Moyer and Geslin, 1995). Markedly lower porosity values are present locally in the lower half of the combined CH–PP model unit as shown in plates 15 and 16, and to a lesser extent in plate 17 [shown as green colors in part (e) and green to blue colors in part (g) of each figure]. Note, however, that the degree of welding and concomitant porosity reduction is never as pronounced in the Prow Pass Tuff as it is in the Topopah Spring and Tiva Canyon Tuffs. According to the porosity model, the most-welded part of the Prow Pass Tuff is restricted to the area north of about Nevada state plane coordinate 750,000 ft north (plate 15).

In contrast to the Prow Pass Tuff, the rocks of the Calico Hills Formation in the upper part of the CH–PP model unit are generally of quite high porosity, as befits nonwelded ash-flow deposits. An exception to this involves the blue-shaded interval in the upper part of the cross section shown in plate 17. The spatial position of this region corresponds

to drillhole WT-4. In fact, drillhole WT-4 contains rhyolitic lava and breccia in the upper part of the Calico Hills Formation (R. W. Spengler, U.S. Geological Survey, written communication, 1994; cited in Clayton, 1996), in addition to the more prototypical ash-flow tuff lithology. Note that drillhole WT-16, located some 6500 ft north-northeast of WT-4, contains only rhyolitic lavas and was excluded from this modeling effort as properly belonging to an entirely different geologic terrane. Despite the atypical lithology, however, the simulated porosity model captured the low apparent porosity of these flow rocks, as indicated in the drill hole logs of Appendix B.

The uncertainty model [part (f) of each plate] clearly indicates that uncertainty is relatively high except in the vicinity of the several drill holes that penetrate to this stratigraphic level. Uncertainty, as expressed by a larger standard deviation of the 100 replicate stochastic simulations, is particularly high in the southern half of the area, as shown in plate 15. Uncertainty is also high along the western margin of the modeled domain (plate 16, 17); uncertainty is even higher in the deeper portions of this western area. Uncertainty also increases east of the immediate repository region in the eastern half of the region. Again uncertainty is greater in the deeper part of the stratigraphic section. An interesting feature of the uncertainty model shown in plate 16(f) is the green-colored region of low uncertainty associated with drillhole WT-14. Hole WT-14 penetrates only the upper part of the Calico Hills Formation, and extent of this hard, conditioning data is clearly reflected in the abrupt transition from green-shaded grid blocks to yellow and red colors in the lower two-thirds of the composite profile.

Validation

Another set of four randomly selected simulated porosity profiles has been extracted from the suite of porosity models for the Calico Hills–Prow Pass combined stratigraphic unit and these are presented in figure 77(a) through (d). Also shown for comparison are traces representing the original measured porosity data used to generate the simulations (heavy solid line) and the summarized E-type model (lighter dashed line). As was the case for the other model units discussed previously, the simulated values closely approximate the associated measured porosity values, as does the line representing the expectation of porosity over the full suite of 100 realizations. As was also the case for the Topopah Spring welded model unit, the simulated profiles, which are discretized on 10-m (33-ft) vertical spacings, simply cannot capture all of the finer-scale variability represented in the 3-ft (1-m) nominal sampling density in each drill hole. Finer discretization of the model domain almost unquestionably would allow additional detail to be modeled, particularly in the Calico Hills part of the combined CH–PP unit where there are thin reworked intervals between the several ash-flow tuff main units (see Moyer and Geslin, 1995).

Note also that the porosity profiles in figure 77 illustrate a logistical fact of life that becomes progressively worse in attempting to model the deeper volcanic units at Yucca Mountain: specifically the profiles of figure 77(c) and (d) indicate that the density of conditioning information becomes rather sparse below the level of the Calico Hills Formation. The paucity of measured data from the deeper units is one of the major reasons why we elected to treat the generally nonwelded Calico Hills Formation and Prow Pass Tuff as a single entity, lest modeling of the Prow Pass interval be conditioned solely to a very limited number of drill holes. In this manner, we are able to reproduce the overall statistical character of the generalized interval even though site-specific conditioning information is lacking throughout much of the modeled volume (see list of partial drillhole penetrations for the CH–PP model unit in table 4).

The most important feature to understand from figure 77(c) and (d) is that although the E-type model values (light dashed profile) are essentially constant at approximately the mean/median porosity of somewhat more than 30 percent for the model unit as a whole [fig. 20(a)], the individual simulated porosity profiles retain much of the heterogeneous character of the Prow Pass Tuff as represented in parts (a) and (b) of figure 77. Note that although there is a fairly broad range of simulated values at each vertical position, the simulated values are not entirely random, figuratively bouncing across the range of possible porosities from zero to 100 percent. There is considerable spatial correla-

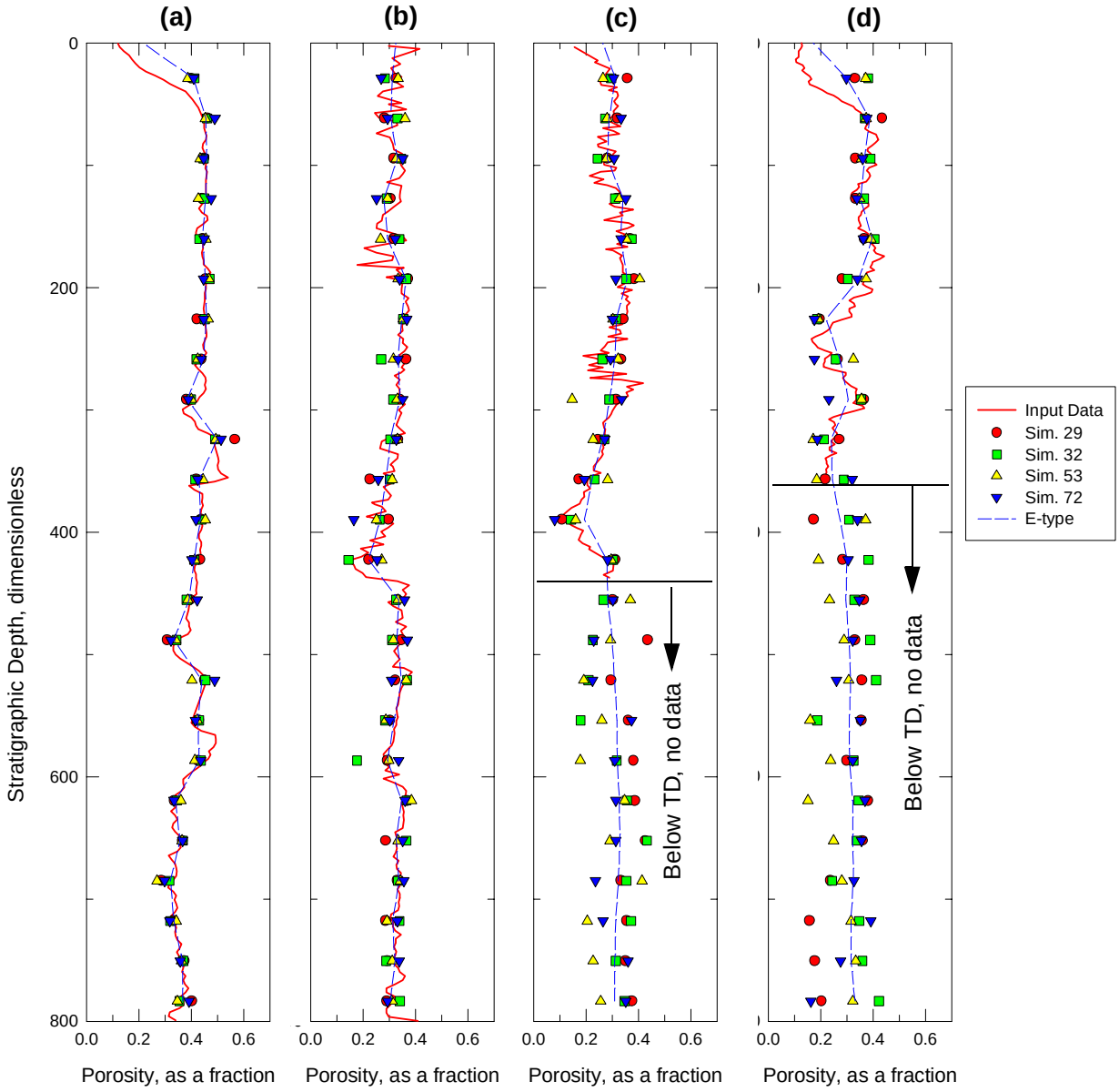

Figure 77. Comparative porosity profiles extracted from simulated models of porosity in the CH-PP model unit for grid nodes nearest drillholes (a) G-3, (b) UZ-14, (c) UZ-16, and (d) WT-17.

tion in the stratigraphically vertical direction as required by the variogram of figure 42(a). Additionally, there is continuity in the stratigraphically horizontal dimensions as well [figure 42(b)] that reflects property correlations "brought in" from geologically nearby drill holes.

Histograms representing the univariate statistical character of the modeled CH–PP combined unit are presented in figure 78, parts (a) through (d). Comparison of the histograms and summary statistics for the four randomly selected simulated models in the upper two rows of figure 78 with the corresponding histogram and summary statistics for the original measured porosity values [part (e)] indicates that the simulated porosity models of this model unit are, indeed, functionally identical to the real world in terms of univariate statistical charac-

ter. Notice that the relatively large number of "trimmed" data represents the fact that grid nodes constituting the model were not simulated unless conditioning data could be located within 12,000 ft horizontally or 180 ft vertically (in stratigraphic coordinates); see discussion of porosity variography for the CH–PP model unit beginning on page 56. Such unsimulated grid nodes were assigned a missing-value code consisting of a large negative integer, which is then ignored in computing the histogram summary.

The histogram and summary statistics of the E-type model presented in part (f) of figure 78 stand in marked contrast to the rest of the illustration. The distribution has been made effectively symmetrical, and more than 70 percent of the modeled porosity values fall between 30 and 35 percent (roughly mean plus-and-minus one standard deviation). Porosity values greater than 40 percent, most likely representing the extremely high porosity pumice fall deposits known to exist in the Calico–Prow interval (includes both inter-particle void space and intra-particle frothy pore space), are almost wholly absent in the E-type model. Porosities of less than 25 percent, including a non-trivial number of measured values of less than 10-percent porosity most likely representing thin very fine grained ashy or reworked layers, are missing from the summarized model as well. The reader is referred to the geologic descriptions of Moyer and Geslin (1995) for detail regarding the various lithologic materials present in this stratigraphic interval.

Figures 79 and 80 present variograms computed for the simulated models.[†] Figure 79 is for the overall ensemble of simulations, whereas figure 80 is a comparison of variograms computed for the four simulated porosity models used previously as examples. Parts (a) of the figures show variograms in the vertical direction, whereas parts (b) and (c) are for the stratigraphic horizontal. The direction of maximum spatial continuity is azimuth = 0° [north–south; fig. 80(b)].

The vertical variograms of the simulated porosity models shown in figure 80(a) do not match the input modeled variogram description very well at all. Variability in the vertical direction in the simulated models is much greater at any given separation distance than called for by the theoretical variogram. Note, however, it appears as though one could simply shift the input model by approximately 0.3 normal-score units and match the simulation variograms almost exactly. We tentatively attribute this systematic vertical offset of output spatial continuity patterns with respect to the input modeled variogram (the differences in variance) to the phenomenon described in the descriptive section that presented the sample variograms for the CH-PP model unit on page 56, specifically the "horizontal hole-effect" presumed to be caused by use of (at least) two different sets of porosity data. Recall that the sample vertical variogram of figure 42(a) never reached its sill value, and that a very long range third structure was added to the theoretical variogram model to force the total sill to equal 1.0, as required for the sequential gaussian simulation algorithm.

The variograms of the simulated porosity models for the stratigraphically horizontal dimension of maximum spatial continuity, shown in figure 80(b), indicate a markedly shorter range than was implied by the input variogram provided to the simulation algorithm. These variograms of the simulations computed at azimuth = 0° still exhibit a longer range, however, than do the equivalent variograms for azimuth = 90° [fig. 80(c)], indicating that anisotropy in the horizontal plane is not as extreme as had been modeled originally. Recall that table 15 indicated a stronger anisotropy ratio 1 (~0.27 for both nested structures 2 and 3 than had been inferred for any of the other units (typically on the order of 0.4–0.5). Given that the third data point on the sample variogram of figure 80(b) is matched quite closely by the four simulated models, it appears that the lower-variability points 4–6 on the sample (data) variogram are anomalous, and may in fact be related to the horizontal hole effect evident in the vertical variograms discussed in the preceding paragraph. The east–west variograms reproduce the input model in this direction quite closely.

[†]See also discussion of variograms in Appendix D.

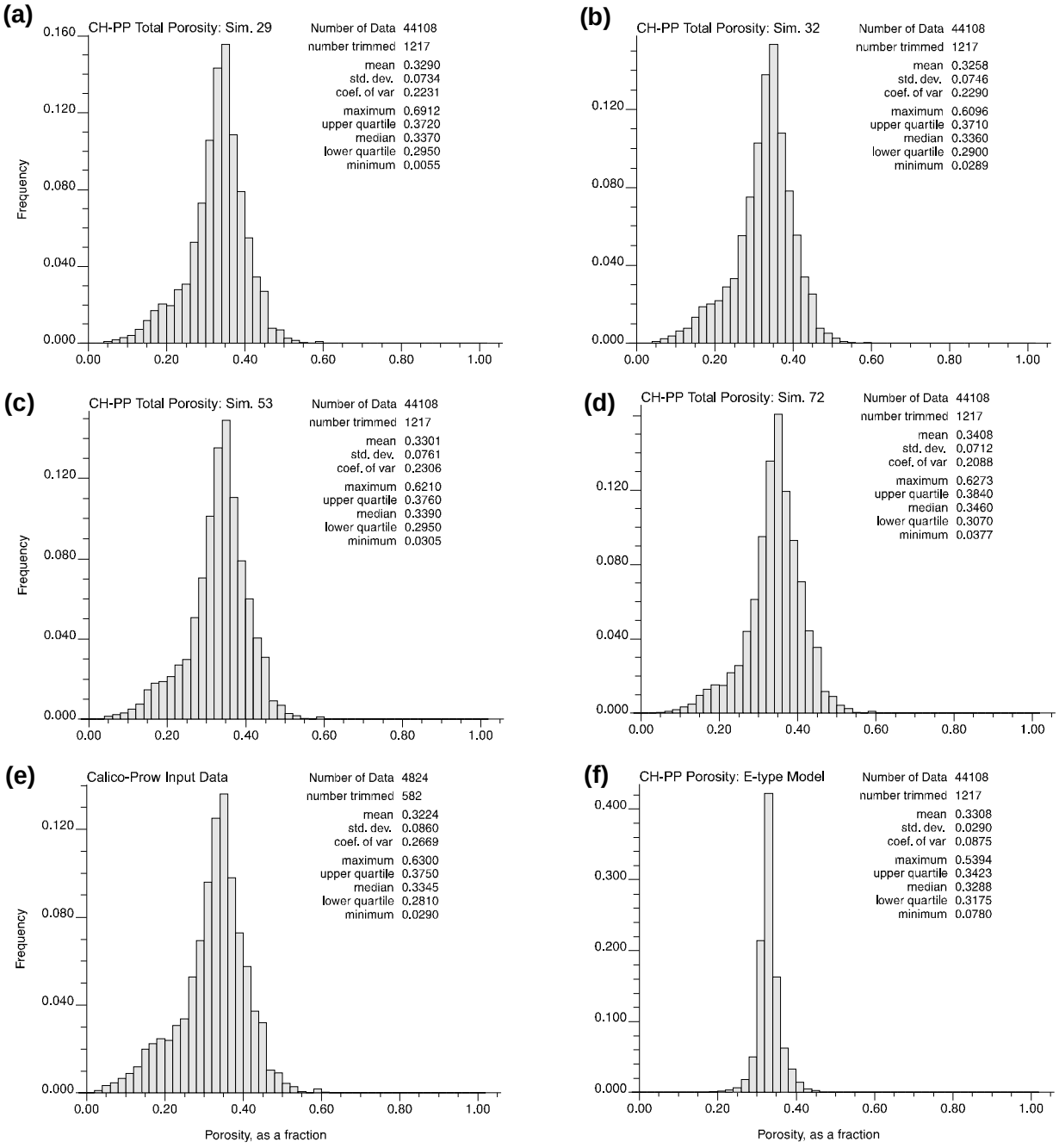

Figure 78. Histograms of four individual simulations of porosity in the combined CH–PP model unit [(a)–d)] compared to original porosity data [(e)] and E-type summarized model [(f)]. Associated statistical summary shown for each histogram.

Bulk Density

Bulk density for the combined CH–PP model unit was modeled directly from the summary model of expected porosity. The prediction relationship is given by equation (41) on page 93.

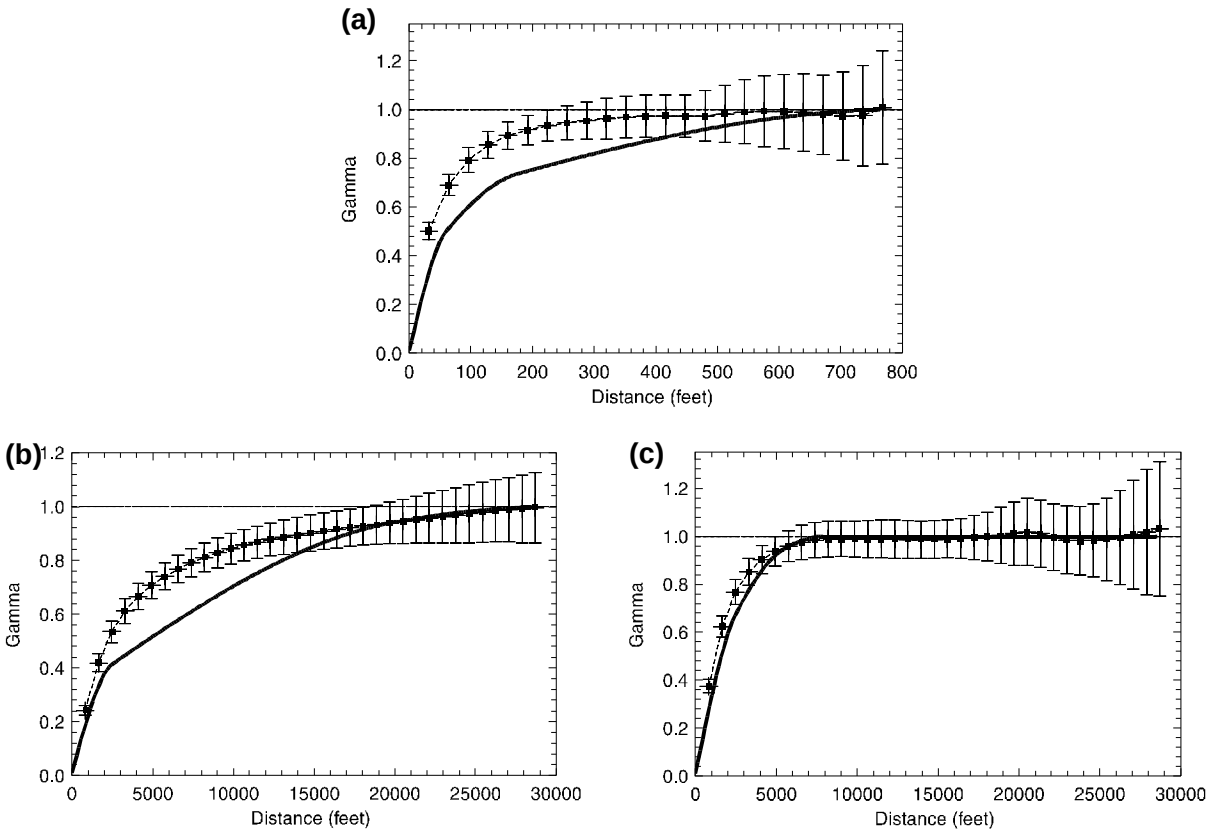

Figure 79. Reproduction of input variograms for simulated porosity models of the combined CH–PP model unit: (a) stratigraphic vertical, (b) stratigraphic horizontal, azimuth = 0°; (c) stratigraphic horizontal, azimuth = 90°. Dashed line with error bars is average variogram with plus/minus 95-percent confidence interval; heavy solid line is input variogram model.

Alteration Indicators

Zeolitic alteration is a prominent, but spatially variable, feature of the deeper part of the volcanic section at Yucca Mountain. In addition to the simulated porosity models for the combined Calico Hills–Prow Pass model unit, we have also created 100 simulated models of (presumed zeolite) alteration in this stratigraphic interval. Although the alteration models were created using sequential indicator simulation of a categorical variable (see page 62), the resulting simulated models should resemble their real-world equivalent when evaluated according to the same three validation criteria previously applied to the simulated models of a continuous variable (page 67).

Figure 81 is a presentation of alteration profiles corresponding approximately to four different drill hole locations for four randomly selected simulated alteration models compared with the conditioning indicator flags that were provided as input to the simulation algorithm. The manner of presentation is somewhat different than the profiles of porosity presented previously. The widest set of horizontal bars correspond to the input indicator flags; a dark bar indicates the presence of alteration in the relevant drill hole data, shorter bar extending only one-quarter of the distance across the column indicates the presence of no alteration. Blank intervals indicate no information. For the drill holes of interest, the alteration flags are available on a fairly uniform 3-ft (1-m) nominal spacing. The exception to this state is drill hole WT-18, for which the total depth of the hole is indicated on the figure. The

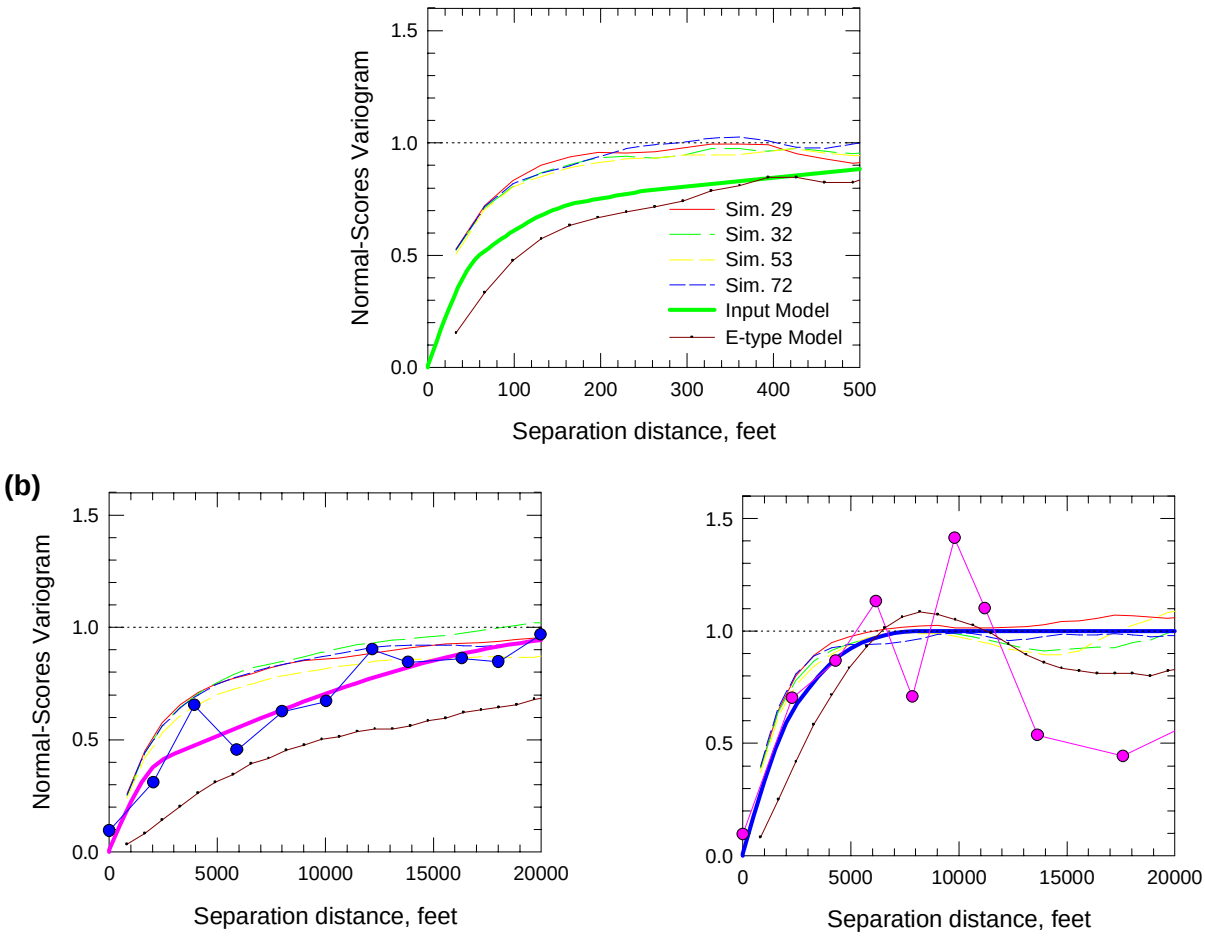

Figure 80. Variograms for simulated porosity models of the CH-PP model unit compared to input model and original data. (a) Stratigraphic vertical; (b) stratigraphic horizontal, azimuth = 0°; (c) stratigraphic horizontal, azimuth = 90°.

narrower sets of bars indicate the simulated presence (dark) or absence (white) of alteration at the grid node nearest to the relevant drill hole.

In keeping with the analogy of actual rocks, simulated rocks are either altered ($I(\mathbf{x}) = 1$) or not altered ($I(\mathbf{x}) = 0$). In contrast to this binary logic, the functioning of the expectation operator, which produces the E-type model of alteration, yields a value between zero and one that is interpreted as the *probability of alteration* at the specific location. Very large (or very small values) within this [0,1] interval represent rocks almost certain to be altered (unaltered), whereas values of approximately 0.5 are about equally likely to be altered as to be unaltered. Because of this probabilistic interpretation of the E-type model in this case, we present these values as symbols connected by a dashed line at the appropriate [0,1] location at the vertical position of the actual grid nodes involved. Note that for purposes of assigning secondary property values within the CH–PP model unit based on coregionalization with porosity, we have elected to work with the most likely (expected) rock type at each node. Accordingly if the probability value is less than or equal to 0.5, the simulated material was presumed to be unaltered; if the probability of alteration was greater than 0.5, alteration was assumed to be present and the secondary property generated accordingly.

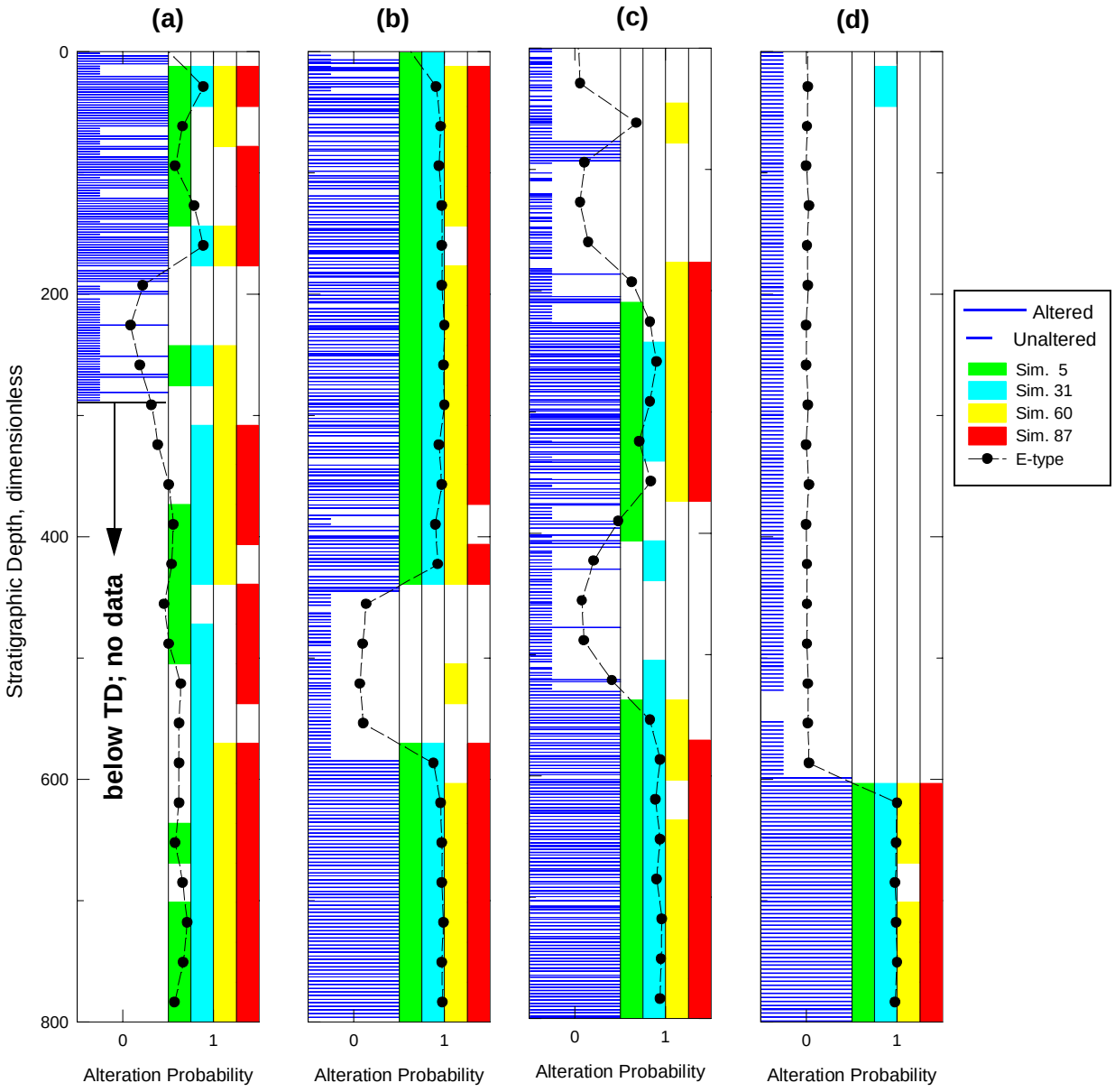

Figure 81. Comparative profiles of alteration indicators extracted from simulated models of alteration in the CH–PP model unit for grid nodes nearest drillholes (a) WT-18, (b) SD-9, (c) SD-7, and (d) G-3. Left- hand side of each diagram represents input data: wide bar indicates altered (flag=1), short bar indicates unaltered (flag = 0); note intervals of no data. Right-hand side of each diagram represents four simulated models; shaded bar indicates altered, unshaded indicates unaltered. E-type model curve represents *probability* of alteration at the indicated depths across all 100 simulated alteration models and is scaled from zero to one as indicated.

The profiles of figure 81 are consistent with what is generally known about zeolitic alteration at the Yucca Mountain site. In the northern portion of the site area, the entire vertical extent of the Calico Hills Formation and Prow Pass Tuff typically is altered *except* where the Prow Pass Tuff has been partially welded and devitrified; drillholes WT-18 [fig. 81(a)] and SD-9 [fig. 81(b)] are examples. The high-temperature-crystallization mineral assemblage is effectively stable at low temperatures, whereas uncrystallized glass is inherently unstable and will alter readily to zeolite minerals in the presence of ground waters of the proper-composition. The unit principally affected by such partial welding and early crystallization is informally named ash flow unit 3 of Moyer and Geslin (1995), and the presence of this interval is clearly shown as the approximately 100-ft (nominal) interval at stratigraphic depths of about 500 ft in profiles (b) and (c) [as well as (d)]. In the southern (and southwestern) portions of the site area, the rocks typically have been preserved above the ground-water table essentially since their formation. Thus, unaltered vitric materials are preserved at the higher stratigraphic levels in addition to any welded–devitrified rocks. Compare the preserved unaltered top of drill hole SD-7 [profile (c)] with the even more extensive presence of unaltered tuff in the upper three-quarters of drill hole G-3 [profile (d)], which is located farther south than UZ-16. Even for drillhole WT-18, for which there is no direct evidence of alteration state below TD (total depth) at approximately a stratigraphic depth of 290 ft, there is a suggestion of a lower likelihood of alteration at a depth of about 450 ft, in contrast to the higher (but still fairly uncertain) probability of alteration at stratigraphic depths of, say 700–800 ft.

Note that an independent three-dimensional model of alteration mineralogy for Yucca Mountain has recently been developed by Chipera and others (1997).[†] This model was constructed using an entirely different deterministic approach based upon the presumption that thin lithostratigraphic layers subject to preferential alteration can be identified and projected across the model domain using only sparse drillhole data. Abundances of alteration (and other) minerals similar to those construed as "altered" rocks in the current study have been interpolated (and extrapolated) throughout those layered volumes using an inverse-distance-squared algorithm. Uncertainty in the predicted mineral content is not estimated, and all layers represent vertically averaged mineral contents. Despite the very significant differences in approach and modeling methodology, the results are quite similar in that "altered" and "unaltered" rock types occur in grossly interstratified vertical sequences. A more detailed comparison of the two modeling efforts is not yet available.

Figure 82 presents the simulated proportions of unaltered and altered rock types at Yucca Mountain for four randomly selected stochastic realizations of alteration indicator flags. Recall that the proportions of actual rock types, as identified using the differential separation between the RH and OD core porosity data or the water-filled vs total porosity or bound-water fraction for the petrophysical logs is 47.5-percent unaltered, 52.5-percent altered (table 11) with a standard deviation of effectively 50 percent (0.499). More reasonably, given the fairly wide spacing of the underlying drill holes, unaltered and altered rocks appear to be present in roughly subequal proportions. Given this interpretation, it appears that the results for the four simulated models shown in figure 82 are quite reasonable. Out of four randomly selected simulated models, two are dominated by altered rocks and two by unaltered. The differential between the two rock types is approximately correct at roughly a difference of 5 percent. A reasonable conclusion is that we cannot distinguish the simulated alteration models from our observations of the real world, based only on relative proportions.

Figure 83 presents a comparison of variograms from the four alteration simulations compared to both the input variogram model and the original experimental variogram plot.[‡] Figure 83(a)

[†]Chipera, S.J., Carter-Krough, K., Vaniman, D.T., Bish, D.L., and Carey, J.W., 1997, Preliminary three-dimensional mineralogic model of Yucca Mountain, Nevada: Yucca Mountain Site Characterization Project Deliverable Product No. SP321AM4, Los Alamos National Laboratory, Los Alamos, N. Mex., 26 p.

[‡]See also discussion of variograms in Appendix D.

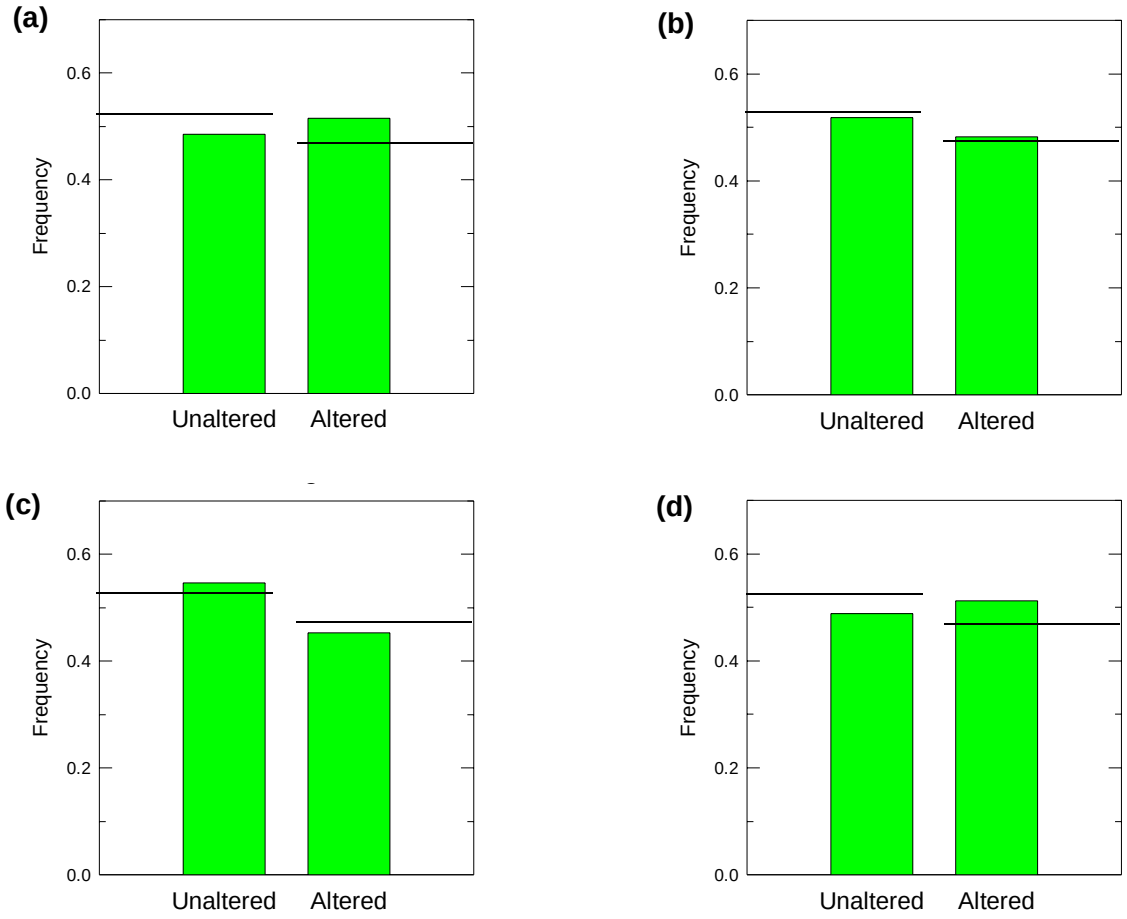

Figure 82. Histograms showing the relative proportions of four randomly selected alteration-flag simulations. (a) Simulation no. 5, (b) no. 31, (c) no. 60, (d), no.87. Target proportions shown by horizontal lines: 0.475 unaltered, 0.525 altered (table 11).

shows the spatial continuity pattern of the simulated models in the vertical direction whereas figure 83(b) and (c) are the equivalent variograms in the stratigraphic horizontal directions in the direction of maximum and intermediate continuity. Figure 84 continues the validation comparison for the full suite of 100 simulations.

The first impression from figure 83 is that the simulated models exhibit a shorter range of correlation than did the input model, although the match in the stratigraphic horizontal east–west direction is actually quite good. Again, as in several previous instances, the simulated variograms appear to resemble the original experimental (data) variogram more closely than the inferred model; note especially figure 83(b), the third and fourth experimental points. It would appear that points five, six, and eight represent anomalously low variability. The interpretation is that there is more vertical to horizontal anisotropy and less anisotropy in the stratigraphic plane than we had originally inferred. The somewhat shorter range of the simulated models in the vertical direction of figure 83(a) is somewhat unexpected, as the original experimental variogram [figure 43(a)] was quite well constrained by the close downhole sampling pattern. However, the pattern is consistent with observations involving variograms for porosity in the CH–PP unit [fig. 80(a)].

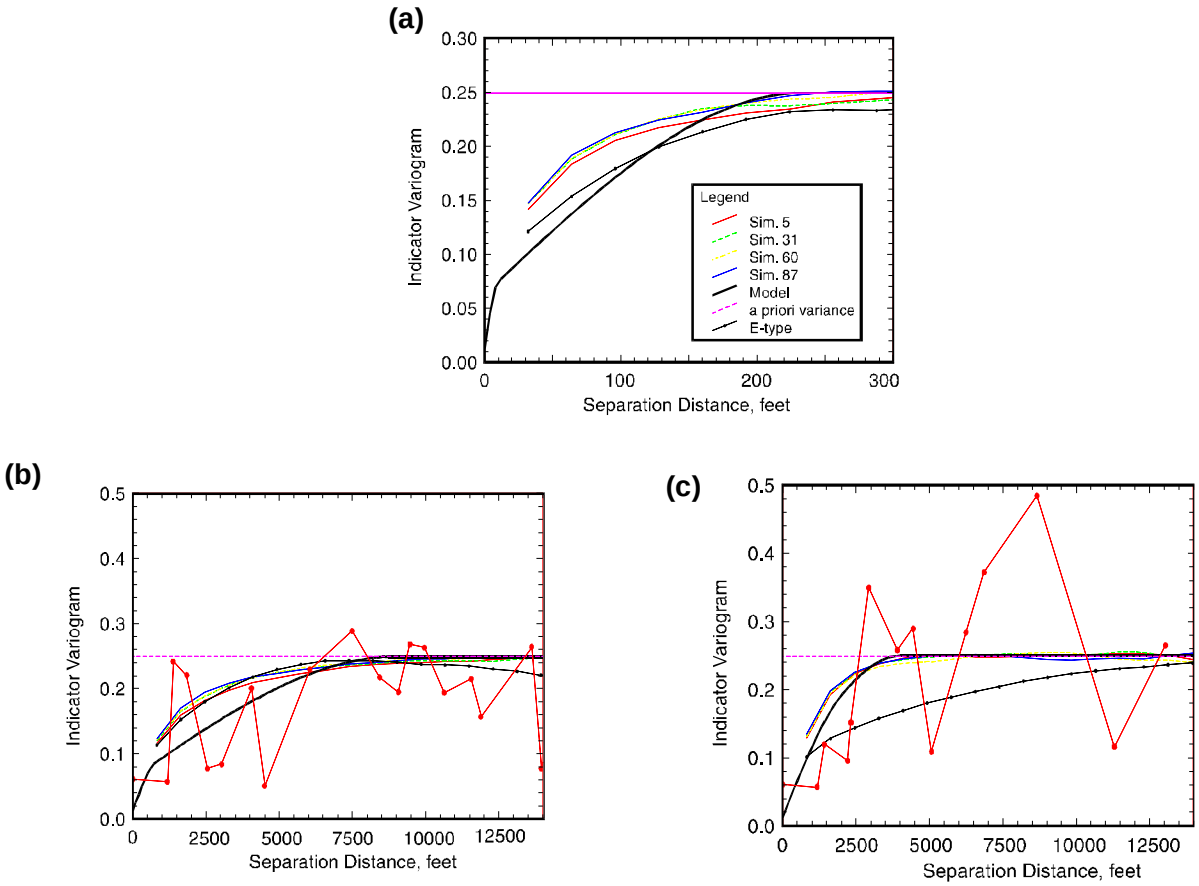

Figure 83. Indicator variograms from four simulated models of alteration in the CH-PP model unit compared to input model and original data. (a) Stratigraphic vertical; (b) stratigraphic horizontal, azimuth = 0°; (c) stratigraphic horizontal, azimuth = 90°.

Saturated Hydraulic Conductivity

Modeling of secondary properties, such as saturated hydraulic conductivity, for the combined Calico Hills–Prow Pass model unit is complicated by the existence of alteration phenomena that change the gross character of those secondary properties. In this study, we have generated full-model coregionalized fields of hydraulic conductivity from the individual simulated porosity models. These hydraulic conductivity fields thus exhibit the desired statistical properties, such as reproduction of the histogram and spatial continuity patterns. The assumption here is that these

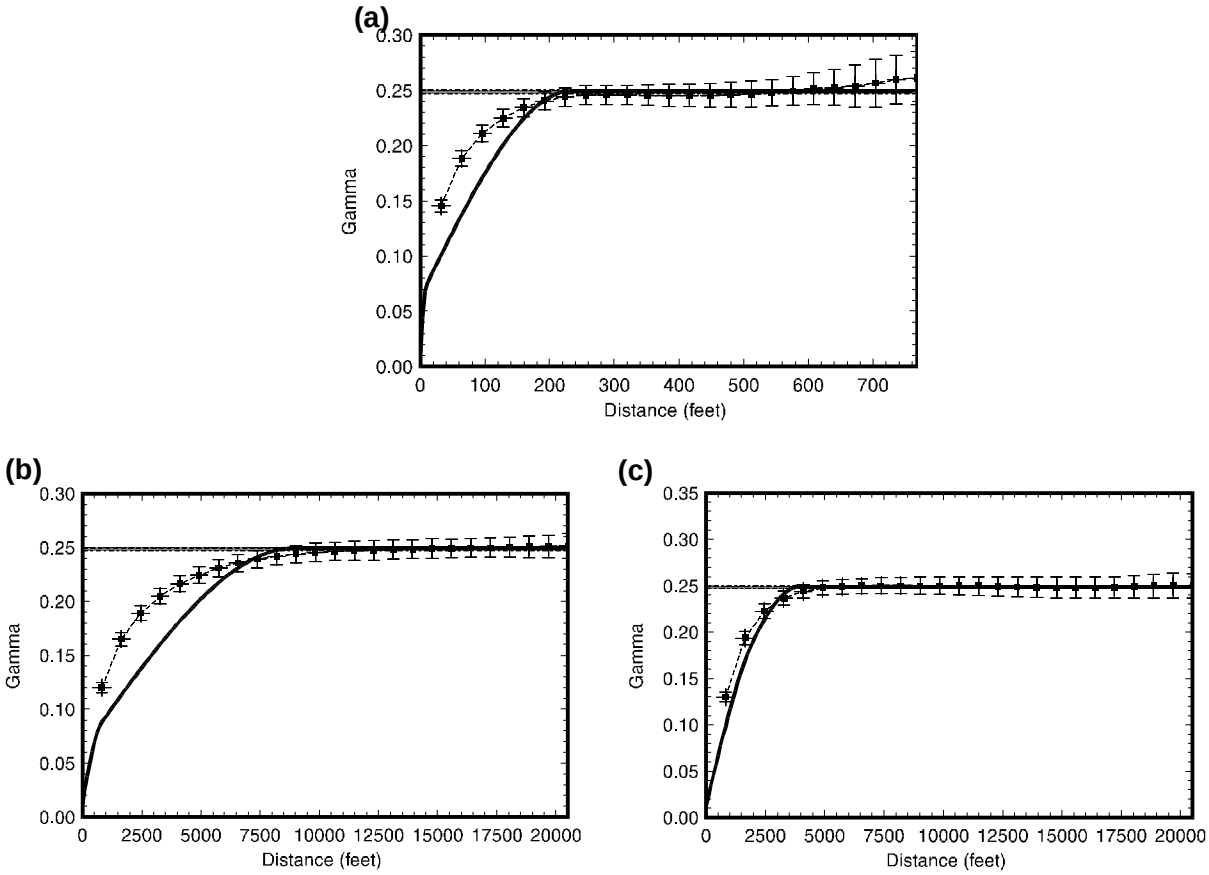

Figure 84. Reproduction of input variograms for simulated alteration indicator models of the combined CH–PP model unit: (a) stratigraphic vertical, (b) stratigraphic horizontal, azimuth = 135°; (c) stratigraphic horizontal, azimuth = 45°. Dashed line with error bars is average variogram with plus/minus 95-percent confidence interval; heavy solid line is input variogram model.

characteristics were produced in the rocks close to the time of original deposition. The rocks were then altered (zeolitized, for the most part), and the alteration process is presumed to have imparted its own characteristics to those rocks so affected. In practice, this late-stage alteration has been modeled using the alteration-indicator approach described on page 62 and the spatial correlation parameters described on page 57. The E-type alteration indicator model was then superimposed as a template or "cookie cutter" onto the full-model hydraulic conductivity model. If the rock at a particular grid node is expected to be unaltered, the coregionalized hydraulic conductivity value was retained. If the rock at that grid node is expected to be altered, the coregionalized conductivity value was discarded and replaced by a simulated "zeolitic" hydraulic conductivity value drawn at random from a gaussian distribution with the mean and variance specified in table 8 (without no-flow samples; fig. 26).

Statistical validation of the final altered-plus-unaltered models of saturated hydraulic conductivity for the CH–PP model unit is complicated by the composite nature of these models. We therefore present first validation statistics for the full-model unaltered hydraulic conductivity fields to demonstrate that these "pre-zeolitization" models exhibit the desired geostatistical attributes. We then allow the models to be "altered", and repeat the validation exercise.

Figure 85, parts (a) through (d), presents histograms of four randomly selected full-model,

unaltered hydraulic conductivity fields. The histogram of the 76 available measured hydraulic conductivity data is shown in part (e) of the figure. Visually, the simulated full-field models appear to be reproducing the measured data quite closely. The summary statistics associated with each individual histogram also indicate close agreement of models with measurements. The slight differences between models and data in the configuration of the lower-conductivity mode at approximately log Ksat = –10.5 are attributed to the fact that the sample size for the laboratory-measured values is quite small, samples come in integer increments and thus a single sample may exert a major influence on the shape of specific parts of the histogram.

Parts (a) through (d) of figure 86 show histograms of the same four simulated models after the "rocks" have been "altered". Part (e) of the figure is the composite histogram of all measured saturated hydraulic conductivity values from the laboratory data set, and part (f) of figure 86 is the histogram of the summarized, E-type hydraulic conductivity model.

Note that there are several interesting effects of the "alteration" process. First, compared to the unaltered models of figure 85, the "zeolitized" models of figure 86 exhibit a much larger number of no-flow values, here arbitrarily set equal to -14.0. Second, the modal peak of low-conductivity values at about log Ksat = –10.5 is more prominent as a result of the combined influence of the unaltered model mode at this value and the very high mode of this approximate value from the altered sample data. The low-value mode in the unaltered simulations is attributed to the presence of partially welded rocks in the Prow Pass portion of the composite CH-PP stratigraphic interval, whereas the higher modal peak at log Ksat $\approx$ –7.3 is attributed to the highly porous and permeable nonwelded pumiceous materials also present in this interval.

The major discrepancy between the magnitude of the low-conductivity histogram mode for the combined measured data and the equivalent part of the composite models is a direct consequence of the fact that the two rock types were not sampled for laboratory measurement in proportion to their relative abundances in the field; the sampling was biased with respect to rock type. Figure 32 indicates that the proportions of altered and unaltered rocks, as identified from the entire systematically-sampled CH–PP porosity data set, are about equal: 52.5 vs 47.5 percent. In contrast, the laboratory data set contains 134 values from altered rocks, some 63.8 percent, whereas unaltered samples number only 76, or 36.2 percent. Simply combining the two sets of laboratory values without proper weighting over-accentuates the fraction of low-conductivity altered materials. The simulated models, on the other hand, reproduce the identified proportions of altered and unaltered indicator flags, and thus presumably constitute a more accurate representation of the real world rocks.

The E-type model histogram presented in figure 86(f) is interesting as well. Rather than representing a trimodal population as might be expected (nonwelded, welded/altered, and no-flow), the mode of no-flow values prominent in both figures 85(a)–(e) and 86(a)–(e) is completely absent. Instead, the modes of high-conductivity nonwelded values and of low-conductivity welded or altered values have merged into a single mode at log Ksat $\approx$ –9.0. Because altered rocks were represented in all simulated models by the same "expected-alteration" model, the centralization of this latter mode must represent the collapse of the two major modes shown in the several other parts of figure 85. The low-conductivity modal value in figure 86(f) must therefore represent the combination of the randomly occurring no-flow node values with the prominent unimodal histogram peak of the altered-rock conductivity values.

Because the saturated hydraulic conductivity values for the final, composite conductivity simulations are associated with the E-type alteration flags, we are able to examine the correlation behavior of porosity and hydraulic conductivity separately for the two rock types, as indicated in figures 87 and 88. Parts (a) and (c) of each figure show the relationship for unaltered materials, whereas parts (b) and (d) of each figure are for the altered (presumably zeolitized) grid nodes. These scatterplots should be compared with figures 23(b) and 25 on page 37 and page 39, respectively.

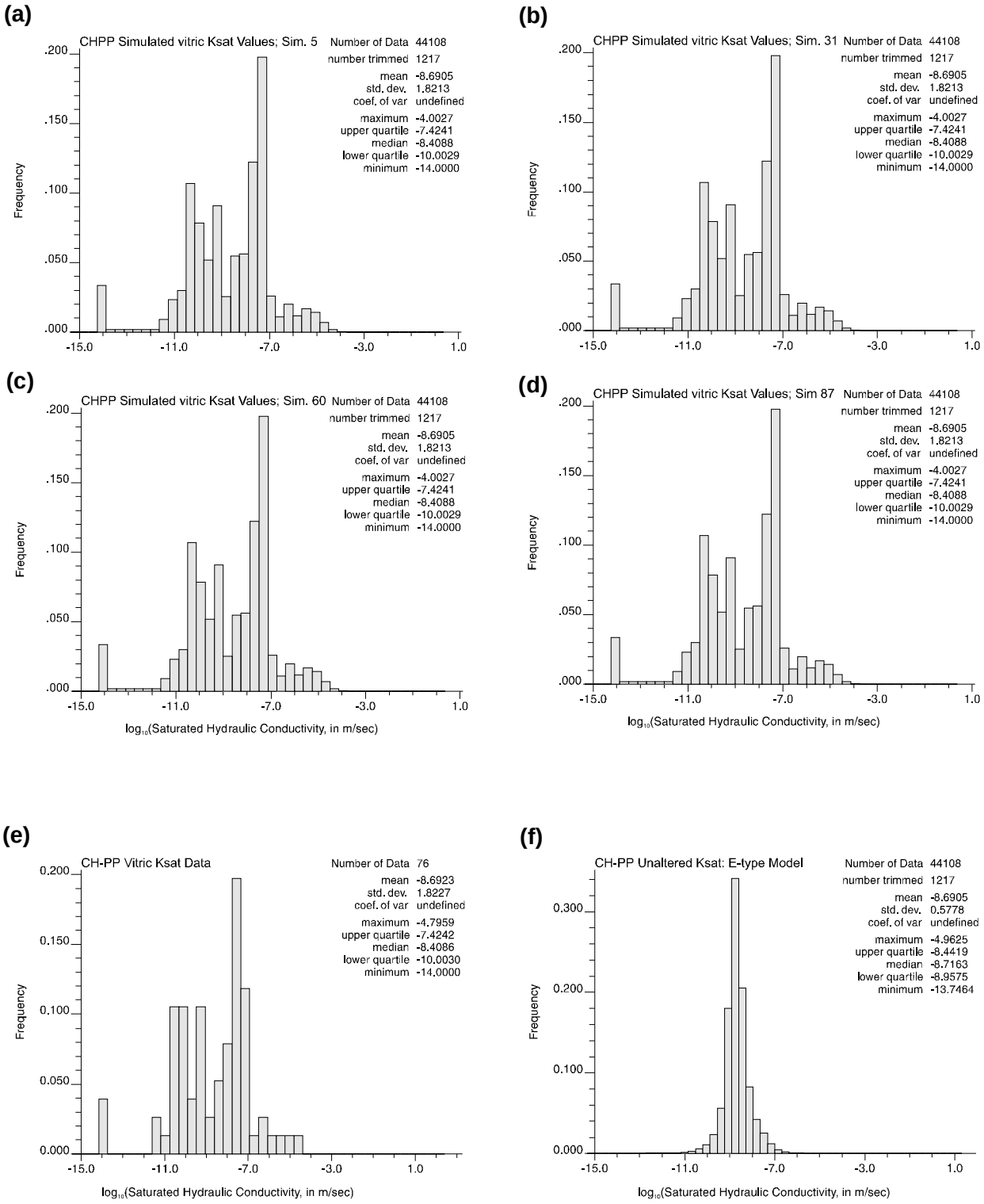

Figure 85. Histograms of four coregionalized models of saturated hydraulic conductivity corresponding to the four porosity models presented in figure 77(a) through (d) compared to histograms of original measured data [(e)] and E-type model [(f)].

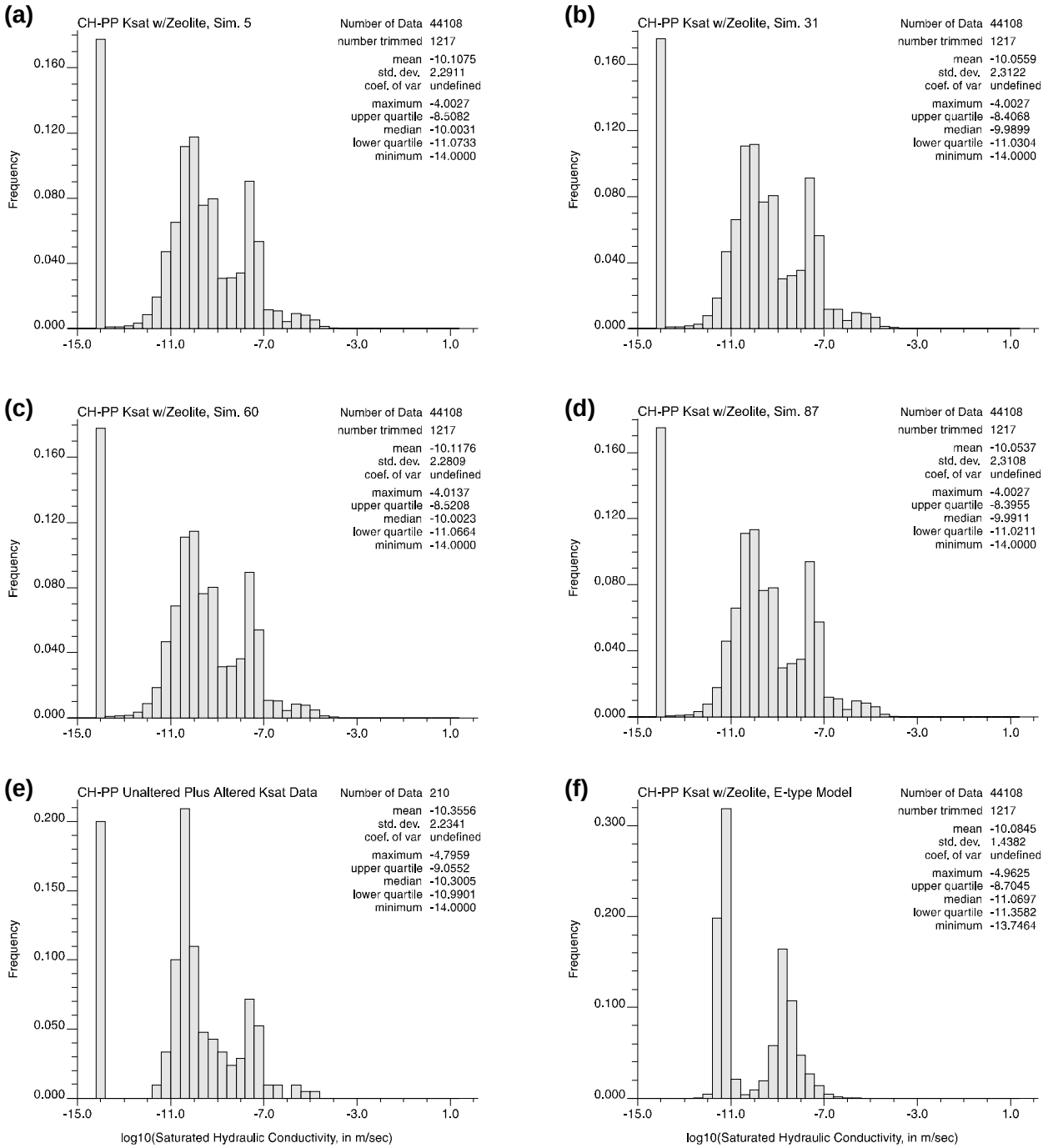

Figure 86. (a)–(d): Histograms of four coregionalized models of saturated hydraulic conductivity after conductivity values representative of altered rock types have been inserted at the locations of probable alteration; (e): histogram of combined unaltered and altered laboratory measurements from the CH-PP unit; and (f): histogram of E-type model.

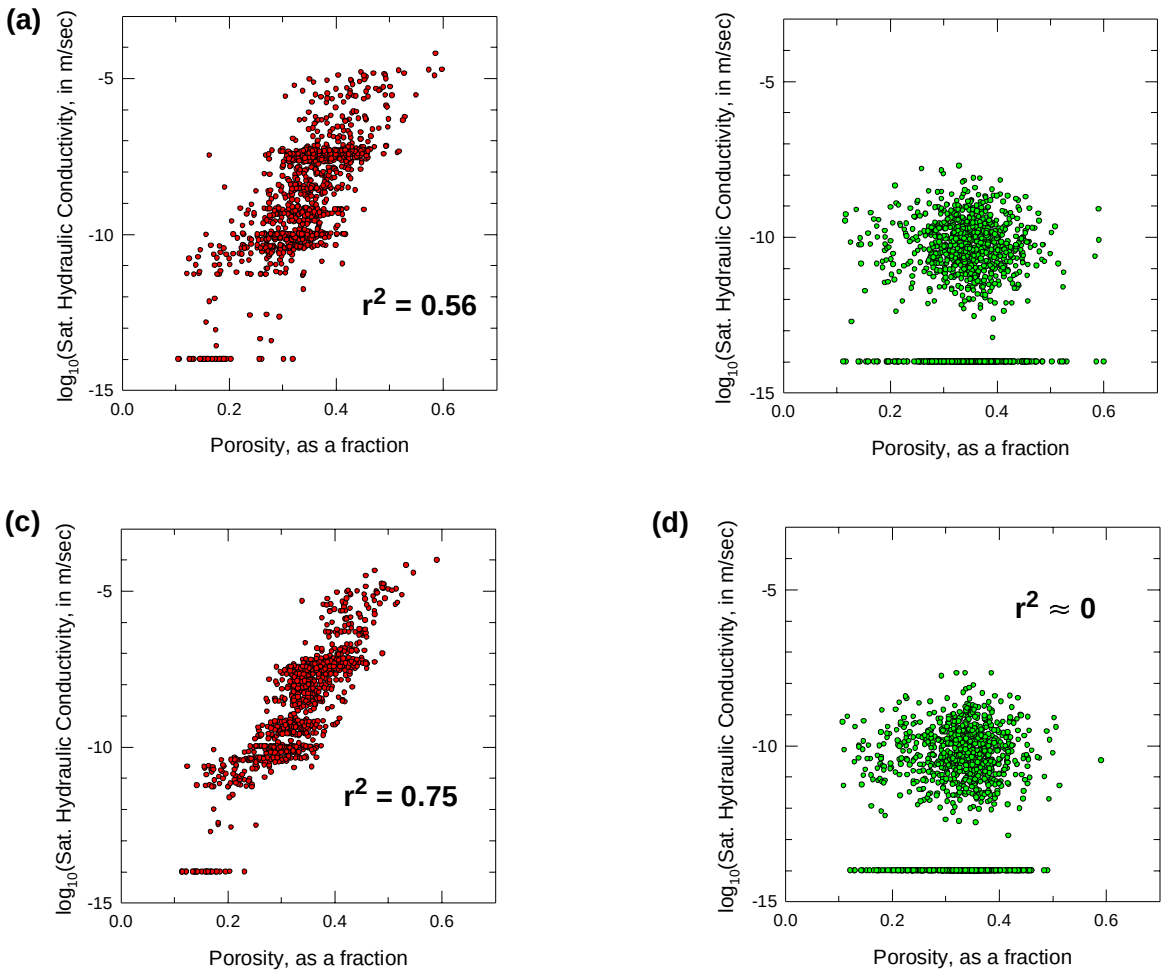

Figure 87. Scatterplots of modeled saturated hydraulic conductivity as a function of simulated porosity for the CH-PP model unit. (a) Simulation no. 5, unaltered rocks; (b) no. 5, altered rocks. (c) Simulation no. 41, unaltered rocks; (d) no. 41, altered rocks.

The unaltered modeled values do, indeed, exhibit a definite positive correlation with porosity, as did the unaltered laboratory sample values. In general, the strength of the relationship is somewhat higher than that of the original (target r^2 = 0.60); however, this can be attributed largely to the *ex*clusion of no-flow values from the diagram of figure 25(a) and (c), and the *in*clusion of those no-flow simulated values in the scatterplots of figures 87 and 88. Clearly dealing with samples that exhibited no measurable flow in the laboratory complicates modeling, and it is possible to "drive" statistical summaries of either data or models in almost any direction desired through different treatment of these non-numeric quantities.

Correlation between porosity and altered hydraulic conductivity values in the simulated models is essentially non-existent. All r^2 values were less than 0.01, which is appropriate given that they were produced using a gaussian random-number generator. The correlation of altered conductivity with porosity in figure 25(d) was 0.42, but examination of this figure and of figure 25(b) suggests that the higher r^2 value can be attributed to inclusion of a few high-conductivity samples that were misclassified on the basis of the RH vs OD drying values. An alteration mechanism that produces recrystallized mineral phases in pore throats without meaningfully changing the total pore vol-

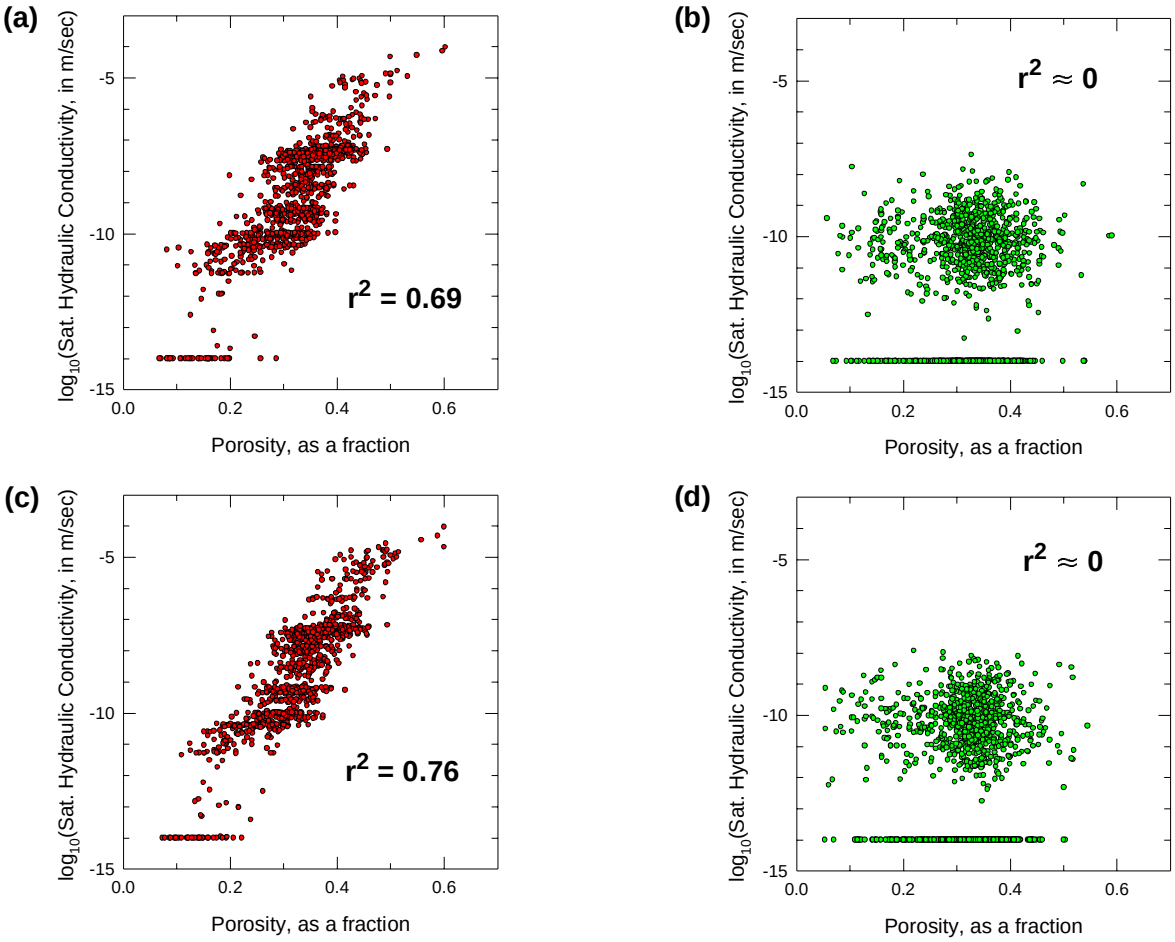

Figure 88. Scatterplots of modeled saturated hydraulic conductivity as a function of simulated porosity for the CH-PP model unit. (a) Simulation no. 60, unaltered rocks; (b) no. 60, altered rocks. (c) Simulation no. 87, unaltered rocks; (d) no. 87, altered rocks.

ume is expected to destroy the correlation of porosity and conductivity.

Figure 89 shows the correlation of porosity and saturated hydraulic conductivity models for the expected-value type models. The two different populations corresponding to the unaltered and altered rock types are quite apparent in the figure. Also, as has been the case for the other coregionalized E-type summary models, the strength of the correlation relationship is far greater than justified by the observed data [fig. 23(b), fig. 25]. Notably missing from figure 89 are the no-flow samples from the laboratory data. As described previously, these simulated values are randomly distributed throughout the individual models, and as such have been averaged out of existence in the summary model.

Uncertainty Model

A global summary of uncertainty associated with the simulated models of porosity within the CH–PP composite model unit is presented in figure 90 as a histogram of node-by-node standard deviations computed during generation of the E-type summary porosity model. The expected uncertainty associated with porosity prediction, disregarding location of the modeled values with respect to conditioning data, is approximately 7 porosity percent. The maximum observed uncertainty is about 10

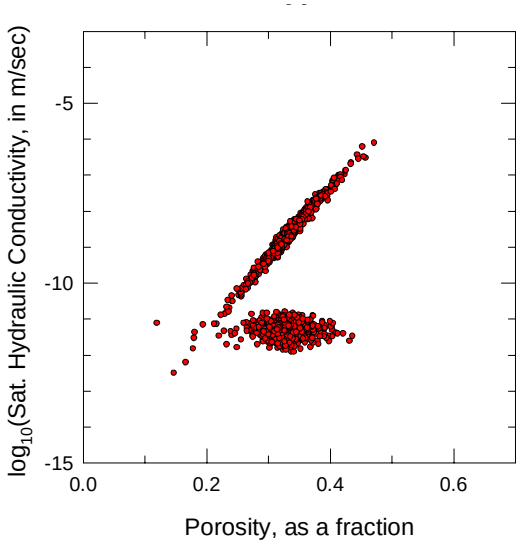

Figure 89. Scatterplot of saturated hydraulic conductivity and porosity for the summary E-type models of the CH–PP model unit (5-percent subsample).

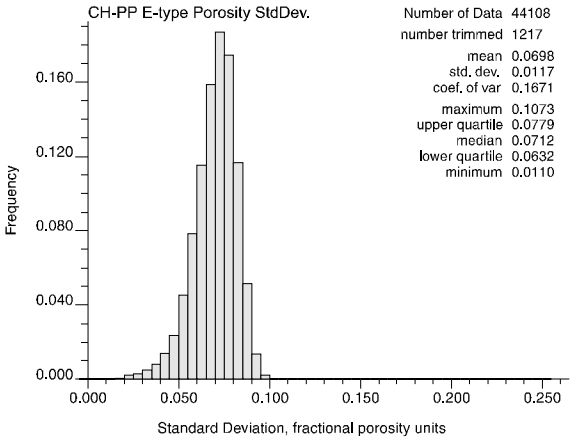

Figure 90. Uncertainty associated with simulated models of porosity for the CH–PP model unit.

porosity percent, and the observed minimum standard deviation is just over 1 porosity percent. The univariate distribution of these uncertainty values is strongly skewed, with a long low-uncertainty tail representing the values that are strongly influenced by local conditioning drillhole data.

Figure 91 presents corresponding histograms of standard deviations of log values of saturated hydraulic conductivity. Part (a) of figure 91 is the most relevant measure of uncertainty, as this histogram was computed during generation of the composite unaltered/altered E-type model. Part (b) of the figure shows the distribution of uncertainty measures for the underlying full-field spatially correlated values of unaltered hydraulic conductivity, prior to application of the alteration template. This global summary of uncertainty associated with the simulated models of hydraulic conductivity indicates that variability of between one and two orders of magnitude is observed among the suite of stochastic simulations at the “average” grid location. Furthermore, with the exception of a very few grid nodes, the best-constrained Ksat values are uncertain by about an order of magnitude (one log unit). Although an order of magnitude is quite a bit of geologic uncertainty adjacent to measured data from a drill hole, this uncertainty overall is less than that associated with the “typical” predicted Ksat value within the PTn model unit; compare to figure 57. Note however, that the best-constrained predictions of Ksat in the PTn model unit were uncertain by only about 0.3 log units, even though the global uncertainty associated with the somewhat more heterogeneous PTn interval is higher. We attribute this somewhat contradictory observation to the much finer-scale discretization of the PTn model grid (2 m vertically, vs 10 m).

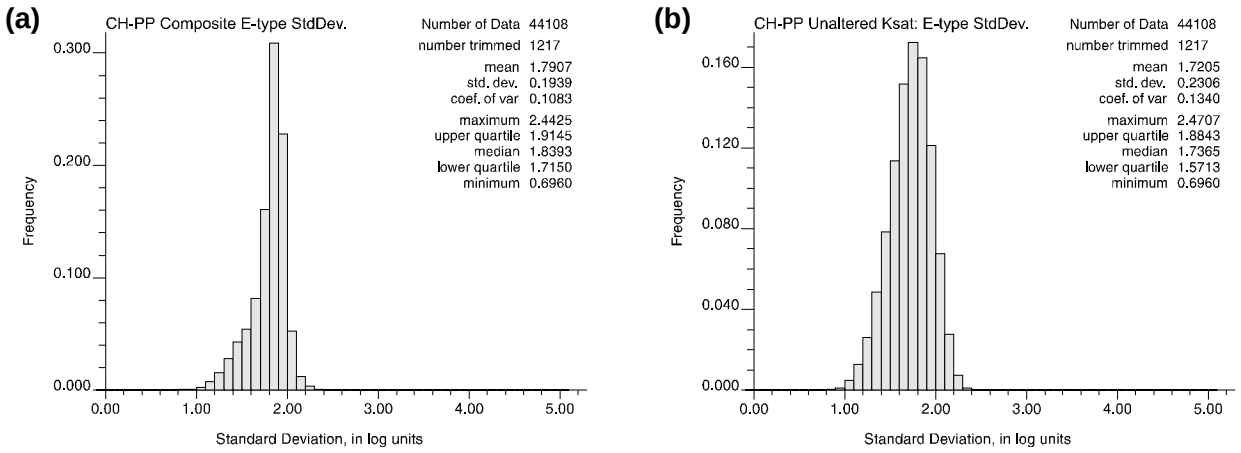

Figure 91. Uncertainty associated with simulated models of saturated hydraulic conductivity for the CH–PP model unit. (a) Final composite models; (b) full-domain unaltered model prior to merging with "zeolitic" alteration model.

SUMMARY AND DISCUSSION

The simulated numerical rock properties models presented in the preceding section of this report appear to be reasonable discretized representations containing much of what is known about the actual distribution of material properties at Yucca Mountain. The primary, conditionally simulated porosity models for the three major modeling units have been demonstrated to (1) reproduce the measured conditioning porosity measurements at the grid nodes closest to the physical location of the several drillholes in an appropriate manner, (2) to reproduce quite closely the statistical character of the ensemble of conditioning porosity values, and (3) to reproduce approximately the same spatial correlation structure that is observed (and has been modeled) using the raw drillhole porosity data. To this extent, the replicate simulated models are statistically indistinguishable from what is known about the actual rocks at Yucca Mountain. Because the only objective difference among the members of a given suite of simulations is the random number seed used to define the sequential simulation path through the discretized domain and initiate the stochastic generation of porosity values, we conclude that the individual simulations are equally probable, given our current state of knowledge of the Yucca Mountain site. The secondary coregionalized material property models of thermal and hydraulic conductivity appear to reproduce closely the statistical character of the actual measurements of these undersampled physical properties, although these individual models do not reproduce exactly the measured values of these properties at the locations of those data. This limitation is inherent in our decision to represent these secondary property fields using coregionalization rather than a more data-intensive cokriging/cosimulation approach.

The several suites of simulated material properties models have been summarized through the preparation of expected-value-type models, computed as the arithmetic average of the simulated values at corresponding grid nodes across the entire set of replicate models. This process, which results in the "most likely" property value given the surrounding conditioning data, does continue to reproduce measured data at data locations, but the resulting univariate and bivariate statistical character of the E-type models no longer directly resembles the statistics of the data ensemble. Variability within the summary-type models is much decreased, compared with the variability of the data themselves, and values within the tails of the data distribution are truncated. To the extent that such "extreme" values are important in further numerical modeling of physical processes anticipated to occur at the Yucca Mountain site, the inferred consequences of those physical processes modeled using the E-type models may be significantly in error. Specifically, rocks characterized by material properties from the tails of the overall population may constitute a relatively small fraction of the total volume of a flow-and-transport model. However, if the tail values are spatially connected, those rocks may form very significant conduits or barriers to ground-water flow. Even if rocks with extreme property values are not strongly interconnnected, flow (and transport) will be focused through local regions of higher than average hydraulic conductivity with results that are not necessarily predictable simply from volumetric proportions. This latter topic takes on issues involved in the upscaling of rock properties measured on a small scale to "represent" much larger volumes within a flow-and-transport model. The scaling issue is complex (McKenna and Rautman, 1996) and resolution of the problem is quite beyond the scope of this report. Note however, that connectivity of extreme values probably is less significant for a diffusive process, such as heat convection, than it is for the advective processes involving ground water.

The individual simulated property models and the summary E-type representations provide a rigorous and quantitative description of geologic heterogeneity, the inherent variability of rock properties within a complex volcanic accumulation caused by both large-scale and small-scale heterogeneity in the physical conditions that effected the formation, emplacement, and subsequent alteration of these earth materials. The material properties at Yucca Mountain are heterogeneous and do vary spatially. Because each individual simulated property model is consistent with what is known about the Yucca Mountain site, these models collectively provide a quantitative description of our knowl-

edge-based uncertainty regarding the likelihood of encountering specific rock property values at specific locations within the modeled domain. In similar manner to the material properties themselves, our uncertainty also is spatially variable. Thus, knowledge is demonstrated to be heterogeneous as well.

Issues and Concerns Identified Through Modeling

Construction of the simulated and summarized rock properties models described in this report involved the compilation, evaluation, and use of a fairly broad assemblage of laboratory and field data acquired over many years and through a number of different measurement techniques. Inevitably, not all pieces of information used in this large-scale synthetic effort are directly comparable, and some data may be partially incompatible with others. We enumerate in this section a number of the more significant of these data issues and the resulting concerns regarding the usefulness of these models in Yucca Mountain project activities.

Data Concerns

Use of Different Porosity Measurements

The integrated use of porosity data of different types and vintages as the underlying basis for the primary porosity models allows construction of a coherent, unified model for the entire Yucca Mountain site area, and at the same time, poses a number of difficulties. First, the volume of physical substance interrogated by core sampling and laboratory measurement is quite different than the volume examined through the use of downhole geophysical methods. Although the physical volume of rock involved in a laboratory porosity determination is only a few tens of cubic centimeters compared to many tens of thousands of cubic centimeters for the downhole petrophysical measurement, the porosity profiles produced using geophysics are observed to be much more variable than those created using only the core measurements. One might reasonably have expected the variance of two sets of measurements to be inversely proportional to the relative sample volumes.

The effect of these differences between porosity as measured by core sampling and through geophysics are identified in the variograms of figures 36 and 42. The (stratigraphically) vertical variograms in these figures considered only porosity data of a single type when comparing pairs of samples. For the TSw matrix porosity computation, a drillhole such as SD-9 contains only core-derived matrix porosity data, whereas a drillhole from the outlying parts of the site, such as WT-18, contains only petrophysically derived water-filled porosity data as a surrogate for the true matrix porosity. The average squared differences between pairs of like values is clearly demonstrated to be smaller that the average squared differences between pairs of unlike measurements, as indicated by the markedly different apparent sill values shown in figure 36. The horizontal variograms include comparisons of core–petrophysical pairs as well as comparisons of core-to-core and petrophysics-to-petrophysics; increased variance is the result, approximating the univariate variance of the entire data set.

Additionally, we are confronted with the differences between one generation of petrophysically derived porosity and another, as well as the differences between two different computational methods involving differences in the type of input geophysical response from different logging tools used in the calculations. That the different generations (“older,” “modern”) of petrophysical porosity data are not exactly equivalent is clearly indicated by figures 12 and 13. Although changes of in-situ rock conditions over the time separating the different borehole logging runs are certainly a logical explanation for some of the scatter exhibited in these crossplots of what should be overlapping data sets, the point is well taken that integration of diverse data is more difficult if the data are not precisely comparable to one another.

One of the results of the use of “mixed” porosity data in the modeling process is that some changes in the resulting material property models may be artifacts, rather than true changes in geology. Such artifacts may be identified in the simulated porosity models by the presence of vertical “striping,” particularly if the stripe occurs at a number of grid nodes in the vicinity of a particular drill hole. “Single-point” anomalies of any type are

always suspect in geology. Striping may be most noticeable in the summary E-type models, for which the associated change in material property expectation of necessity has been generated in a substantial number of the underlying stochastic realizations. Note that uncertainty in predicted material properties associated with such systematic biases cannot be addressed through geostatistical simulation, as presented in this report. Variability among individual simulated models will be low in the vicinity of the involved drill hole, decreasing theoretically to zero at the hole location itself.

Sampling and Testing Biases

Evaluation of the compiled database of material properties clearly indicates that the objective of "systematic" sampling, as described in Study 8.3.1.4.3.1 of the Site Characterization Plan (DOE, 1988), has not been achieved across different work areas on the Yucca Mountain Project. A lack of systematic ("representative") sampling (and testing) for material properties is particularly significant for geostatistical modeling using simulation, in that characteristics of the data ensemble (read: histogram) are used to extend our knowledge of property heterogeneity into regions where direct measurements are absent. If the statistical character of the data ensemble is distorted by preferential sampling related to external criteria, those distortions can be propagated into the individual stochastic models and any subsequent numerical process modeling using those models as input.

Modeling of thermal properties clearly is the most significantly affected by systematic biases in the underlying laboratory data. As shown in two pairs of figures, 28 & 30 and 16(b) & 29, the laboratory thermal conductivity measurements are not particularly representative of the overall thermal conductivity of the welded Topopah Spring Tuff. We have endeavored to compensate at least partially for the systematic selection of the lower-porosity–higher-thermal-conductivity materials for laboratory testing by generating simulated (coregionalized) models that reflect a thickness-weighted univariate frequency distribution (fig. 30) derived using the observed regression relationship [fig. 28(b)] between lithophysal porosity and thermal conductivity. The situation involving thermal properties is made worse by the fact that heat conduction through earth materials is a function of large-scale, bulk porosity combined with the occurrence of a locally quite large proportion of that "bulk" porosity as centimeter- to decimeter-sized lithophysal cavities that simply cannot be sampled and tested in the laboratory.

Systematic biases also exist in the hydraulic conductivity data set, although in this case, there is much more "statistical mass" available as partial compensation. Some of the modern drill holes were sampled quite systematically for laboratory hydraulic conductivity testing (UZ-16, for example), whereas the effort for other such holes is much more biased toward the higher-conductivity units. Compare, for example, the hydraulic conductivity profiles published by Engstrom and Rautman (1996; their figure 10) for drillhole SD-9 with the equivalent profile for drillhole SD-7 (Rautman and Engstrom, 1996a; their figure 9). Although a thickness-weighted correction to the univariate frequency distribution of hydraulic conductivity could have been performed in parallel with the correction for thermal conductivity, we did not undertake such a correction for this study in light of the order-of-magnitude larger number of hydraulic measurements (400–600 vs. 50).

Although modeling of saturated hydraulic conductivity was not complicated by an issue directly comparable to the physical impossibility of performing laboratory tests on thermal conductivity specimens containing decimeter-scale lithophysal porosity, a significant additional complicating factor involves the issue of the "non-detect" flow measurements. Figure 23 clearly indicates that a very large fraction (more than 35 percent) of the laboratory hydraulic testing yielded no measurable flow. Although simulation of hydraulic conductivity models that exhibit the proper, unit-specific, fraction of non-flowing grid nodes is relatively straightforward, the summary of a suite of such stochastic models into some reasonable model of "representative" or "expected" hydraulic conductivity is not so direct. Mathematically, the alphabetic string, *no-flow*, cannot be averaged with simulated values given in meters per second. However, omitting a full third of one's knowledge of the Yucca Mountain site cannot lead to a "representa-

tive" hydraulic conductivity value by almost any definition. Attempting to substitute a very low numeric value for the non-flowing grid nodes is, arguably, the most "honest" method of dealing with this issue. However, unlike the results of this substitution on a numerical process model computed for an individual simulation, computation of a physical process model for an E-type property model averaging arbitrarily small hydraulic conductivities with conductivities typical of the flowing laboratory test specimens can be driven in virtually any desired direction through (in)judicious selection of that arbitrary value. Spatial continuity analysis of the vertical distribution of no-flow hydraulic conductivity values indicated that although such no-flow values are distributed effectively at random for a model with grid spacings such as this site-scale modeling effort, there is sufficient spatial correlation that a model involving random non-flowing grid nodes may not be appropriate for more detailed numerical modeling of the site. (see discussion beginning on page 112).

Issues Involving Geologic Interpretations as Input

Construction of the simulated material properties for this study has identified a modest number of "interpretive" type issues that are highlighted by the results of the modeling process. A number of these are discussed in a subsequent section of this *Summary and Discussion*. However, there are also several issues that have been identified during data compilation and model generation that are more directly related to data used as input in this modeling process.

Lithophysal Zones and Rock-Property Units

The presence of laterally extensive intervals of lithophysal cavity development is a prominent visual feature of the welded tuffs at Yucca Mountain, even to the untrained eye. As these intervals, which contain individual lithophysae varying in size from a centimeter or less to cavities the better part of a meter across, clearly persist both laterally and vertically for large distances, it is evident that this type of alteration phenomenon will affect the distribution of rock material properties. However, attempts to map formally named lithophysal zones to bodies of rock exhibiting consistently higher porosity have been less than successful. A summary of this evidence is presented in Appendix C, in the form of a porosity cross section (fig. C-2, in stratigraphic coordinates) from north to south across the entire site-scale model domain, in which abrupt, major changes in porosity are demonstrated to occur at vertical positions that have nothing to do with the "breaks" between named stratigraphic zones. Moreover, it is unclear in some locations that "units" of consistent character can be traced across the modeled area, nor should this sort of "layer-cake" stratigraphy be expected within a complex volcanic accumulation that has been affected by numerous post-depositional alteration processes.

Additional information bearing on the presence or absence of true stratigraphic control of lithophysal porosity is presented in the individual drillhole porosity plots of Appendix B. The results discussed in Appendix C are perhaps the principal reason this study adopted the approach of treating porosity as an attribute to be modeled within larger-scale geologic "units," rather than as a stratigraphically controlled entity in and of itself.

"Contacts" between Major Rock Units

One of the fundamental assumptions underlying the rock properties modeling conducted as part of this study was described on page 6 as involving the "separation of the geologic column into several discrete geologic units, each of which is more internally 'homogeneous' in some manner than subdivisions based on other criteria." Indeed, the convention of using stratigraphic coordinates also described on page 6 and in more detail in the section beginning on page 11 is dependent upon our ability to define unit-bounding contacts and to project those contacts reliably into regions where a drill hole did not penetrate the boundary of a particular unit. However, examination of two-dimensional cross sections extracted from the three-dimensional models while still in stratigraphic coordinates indicates some local material-property anomalies that suggest that the contacts of these major stratigraphic units may not always have been picked in a consistent manner—at least with respect to changes in material properties. An alternative explanation of these same anomalies is that

the boundaries of bodies of similar material properties do not correspond to even the more major lithostratigraphic subdivisions. This is a disturbing possibility that calls into question the utility of these subdivisions in modeling the performance of the Yucca Mountain site.

This issue of lithostratigraphic and material-property contacts is most easily addressed by considering what is perhaps the most pronounced material-property distinction at Yucca Mountain: that between welded and nonwelded materials. As described previously (see figs. 3, 4), we elected to aggregate densely welded rock types into a "TSw model unit" of uniformly low porosity, and to aggregate both nonwelded and more variably porous rocks into an overlying "PTn unit" and an underlying "CH–PP model unit." These latter two subdivisions are effectively "homogeneous in their inhomogeneity," as they both include material of generally high, but locally quite variable, porosity.

In keeping with the concept of "homogeneous inhomogeneity," the top of the PTn model unit has been taken as the boundary between the Tpcpv2 (crystal-poor moderately welded) or Tpcpv1 (partially to nonwelded) lithostratigraphic unit and the overlying densely welded (vitric or devitrified) neighbor. In a similar manner, the top of the CH–PP model unit has been presumed to be the boundary between the Tptpv2 or Tpcpv1 lithostratigraphic unit and its overlying densely welded (here, vitric) neighbor, Tptpv3. Thus, the more nonwelded and/or more variably welded materials would be assigned to the PTn or CH–PP model units, leaving essentially only densely welded materials within a "homogeneous homogeneous" TSw model unit. A part of our reasoning was also that such a fundamental change in rock type should be easy to identify with or without continuous core, leading to a more consistent subdivision of the rock column across cored and non-cored drillholes.

However, examination of figures 6 through 8, which are profiles of the PTn model unit shorn of distractions such as fault offsets, clearly indicates local occurrences of very low porosity–presumably densely welded tuff within this unit, principally near the top contact. The presence of these out-of-character materials is most evident in part (g) of each figure, for which the color scale has been adjusted to highlight what may otherwise be fairly subtle changes in porosity. The entire center section of the top of figure 6(g) is shaded deep purple, corresponding to the lowest possible porosity values, whereas the outer extremities of this same profile are characterized by relatively light-blue-coded porosity values. That this change in material properties is an artifact, rather than part of the (heterogeneous) geology of Yucca Mountain is suggested more strongly by figures 7 and 8, which are at right angles to that of figure 6. The former two cross sections contain a total of three very localized dark-purple property "anomalies" that indicate densely welded-type porosity values within this generally nonwelded modeling unit. A similar "excursion" of very low porosity values into the base of the PTn model unit is also indicated in the center of figure 8(g), as the small dark-purple mass rising between two downward-convex bulges of red- and yellow-coded higher porosity. Reference to the individual drillhole porosity profiles of Appendix B also suggests either that the moderately/nonwelded-to-densely-welded boundary between PTn and TSw has not been picked consistently across drill holes (Clayton, 1996), or that the moderately/nonwelded to densely welded distinction has little or nothing to do with porosity. Figure 15(g) illustrates this same phenomenon at the top of the Calico Hills–Prow Pass "nonwelded" unit. Here, the upper contact of the CH–PP unit is marked by yellow- to green-coded porosities on the left-hand (west) side of the figure and by dark-purple-coded porosity values on the center-right.

Although the modeling conducted as part of this study could have been performed using modified upper (and/or lower) contacts picked directly using the indicated changes in porosity as the criterion, we have elected to continue with the formal lithostratigraphic boundaries as defined by Clayton (1996). Although re-picking contacts on the basis of porosity would have ensured properly "homogeneous" modeling units, we would be unable to back-transform the completed rock-property models from stratigraphic to real-world coordinates because there would be no framework geologic model available (Clayton and others, 1997) from which to extract the required structure-contour and thickness information. The point of this modeling

exercise is not simply to produce "nice" appearing stratigraphic models, but rather it is to distribute material properties realistically within a numerical representation of the real Yucca Mountain that includes faults, stratigraphic thinning and pinch-outs, and other less-than-ideal features of the actual site.

We note that to some extent, the actual impact of these imperfections in picking contacts and including minor low-porosity rocks in a high-porosity unit (and vice-versa) is negligible, to the extent that what is missed on one side of a contact is included on the other side thereof. The physical dimensions of these misclassification errors (if indeed they are truly misclassifications) are on the order of about 10 meters or less (10-30 ft). For situations involving the Topopah Spring welded interval, which is nominally some 300 m (1000 ft) thick, the physical mis-positioning of the numerical model is a few percent of the thickness at most. Although consistency is a virtue to be valued, the most serious consequences of such mis-picked contacts would occur at the top of the PTn model unit where there is no equivalently modeled overlying unit to take up the discrepancy. The Tiva Canyon welded thermal/mechanical unit (table 1) was not included in this material properties modeling exercise for reasons discussed on page 9. However, if subsequent process-modeling activities are unaware of the inconsistencies just described, it would be possible to assume "welded" = low porosity for the entire TCw thermal/mechanical unit, whereas the unit locally would include materials of 20–40-percent porosity in its lower part (for example, drillholes G-4, WT-17; Appendix B).

Interpretive Observations

Topopah Spring Vitrophyres

The two vitrophyre units (zones Tptrv1 and Tptpv3) of the Topopah Spring Tuff form distinctive low-porosity, glassy marker units in many outcrops of this formation of the Paintbrush Group. The "outer" limits of these units were also selected as the boundaries of the TSw model unit because they bound relatively uniformly low-porosity densely welded tuff and were anticipated to be readily distinguishable from the less-welded rocks both above and below. Although there are some questions as to the consistency of "picking" for these outer limits to the TSw model unit (see discussion above), there are other observations that may be made for these well-known marker intervals that appear to be real features of the rocks at Yucca Mountain and not mere artifacts to be argued over by stratigraphers.

For example, consider the lower ("basal") vitrophyre of the Topopah Spring Tuff, a unit that has been identified previously (Ortiz and others, 1985; see table 1) as sufficiently distinctive to warrant its own separate thermal/mechanical identity. Abundant evidence exists from much of the Yucca Mountain site that characterizes the lower Topopah Spring vitrophyre as an extremely low-porosity, black, glassy rock some 10 m or more in thickness. Ground-water flow through this unit would be anticipated to be almost entirely through microfractures and larger fractures because "matrix" conductivity is nearly non-existent in rocks of 2–5 percent porosity (see fig. 27 and associated discussion on page 38). Because this unit is typically at or near the water table within the local repository region, saturations are generally quite high, and there has been concern that the thermal pulse from the repository might alter the metastable glassy material to low-permeability but mechanically incompetent clays or zeolites that might form a permeability barrier beneath the repository (Knauss, 1987; Whitbeck and Glassley, 1995,[†] 1996).

Although this material-property modeling effort does not include a stratigraphic subdivision separately identifiable as thermal/mechanical unit TSw3 (table 1), we have succeeded in producing a unit of lower-than-typical Topopah Spring welded porosity at the base of the TSw model unit (as defined in this study). This low-porosity "vitrophyre" is shown to advantage in figure 9(g) as the dark-purple-coded pixels near the base of these

[†]Whitbeck, M., and Glassley, W.E., 1995, Preliminary bounds on the water composition and secondary mineral development that may influence the near-field environment: Yucca Mountain Site Characterization Project milestone MOL205, Lawrence Livermore National Laboratory, Livermore, Calif.

two-dimensional stratigraphic-coordinate cross sections. However, as suggested by part (e) of figures 9 through 11, in which the porosity coding follows a linear gradation from low to high, the absolute magnitude of the porosity throughout much of the presumed lower Topopah vitrophyre is significantly higher than the less-than-five-percent anticipated vitrophyre-like values. In fact, examination of the individual drillhole porosity plots contained in Appendix B confirms that the porosity values used to condition the simulations in lowermost part of the TSw model unit *do not indicate the presence of a uniformly low-porosity "vitrophyre" rock-property unit*.

Figure C-2 of Appendix C provides a convenient summary of lower vitrophyre character from the northern part of the model area to the south. Some drill holes (e.g., NRG-7, SD-9, SD-12, SD-7) appear to meet the prototypical low-porosity external expectation at this stratigraphic level. However, for holes such as WT-1 and WT-17 (and others in Appendix B), the porosity of the lower vitrophyre interval is clearly different and not compatible with a straightforward interpretation of low-porosity glass. Note that figures 9 through 11(e) suggest that the vitrophyre, as a continuous, low-porosity glassy unit, does not extend throughout the site area. If vitrophyre, as in glassy material, is in fact present in the indicated higher-porosity regions, the character, and alteration propensity under hydrothermal conditions, may be quite different from that heretofore understood.

Existence of Other-Than-Expected Thermal Conductivity in the TSw Model Unit

That the existing thermal conductivity measurements from the Yucca Mountain site are spatially and lithologically biased appears quite clear (see *Thermal Conductivity* beginning on page 40). What is not so clear is the actual impact of these biased measurements on the real heat-transfer behavior of the site. Comparison of the histograms of measured and predicted thermal conductivity presented as figures 28(a) and 30 in this report suggests, however, that it will be other than as expected for two reasons. First, the existence of high-lithophysal-porosity intervals in the upper portion of the Topopah Spring Tuff suggests that the insulating qualities of the upper Topopah Spring, above the level of the potential repository, may be greater than indicated by straightforward application of measured thermal conductivity values obtained for core samples taken from this same interval. Second, and in some ways counteracting the first effect, is the observation that the thickness-porosity-weighted histogram of predicted thermal conductivity values (fig. 30) indicates that the Topopah Spring welded interval as a whole may be *more* conductive thermally than indicated (again) by straightforward application of measured thermal conductivity values obtained from core samples.

What does appear to be clear, is that it may be very important to identify and properly consider *local geologic heterogeneity* in the thermal properties of the site during modeling of waste-isolation performance. Examination of figures 9 through 11(e) and (g) suggests that lithophysal porosity (and, by extension, bulk-rock thermal conductivity) is quite variable over relatively short distances in the immediate vicinity of the potential repository. The insulating effect of the lower lithophysae-bearing interval below the proposed repository horizon is also problematic, given that the physical effect of even small, centimeter-scale lithophysal cavities is unknown from actual laboratory testing. A final imponderable at this time regarding thermal conductivity involves the influence in the vicinity of the potential repository of the various proportions of the thickness-porosity-weighted predicted high thermal conductivity values shown in the histogram of figure 30. Many of the highest thermal conductivity values in the "representative" distribution of values are unquestionably associated with the lower-porosity lower portion of the TSw model unit. What does appear likely is that bulk-rock thermal conductivities on the order of 2.0 W/m-K are quite unlikely given the modeled distribution of lithophysal (total) porosities in the mountain.

Alteration in the PTn Model Unit and its Effect on Secondary Properties

The individual porosity profiles presented on a drillhole-by-drillhole basis in Appendix B, and in particular, the relative behavior of the two main porosity traces, suggests that there is a non-negligible fraction of the upper Paintbrush nonwelded

interval that exhibits significant hydrous-phase alteration. Although the alteration indicators developed in this study are not specific as to mineral phase, montmorillonitic clays have been described from the welded-to-nonwelded transition near the base of the Tiva Canyon Tuff (Buesch and others, 1996). A number of iron-stained and oxidized horizons are present within the nonwelded to "bedded" (reworked) tuffs within the PTn stratigraphic interval as well, both in core and on outcrop.

Regardless of the specific identity(ies) of the alteration minerals present within the PTn model unit, the simple existence of alteration raises the question of whether straightforward coregionalization of hydraulic conductivity to simulated porosity is an appropriate modeling technique for this part of the geologic section. We conclude that it would be preferable to develop a two-part coregionalization strategy for modeling hydraulic conductivity in the PTn model unit, similar to that developed for and applied in the modeling of the combined Calico Hills–Prow Pass model unit. The methodology for modeling altered and unaltered materials separately is quite straightforward, and the number of drill holes containing data from the PTn combined with the relatively thin nature of this model unit suggest that the modeling exercise should be quite feasible.

A second, more speculative, interpretation to be drawn from our conclusion of hydrous-phase alteration in the PTn model unit is that—subject to more explicit modeling, such as proposed in the preceding paragraph—there may exist a significant reservoir(s) of loosely bound structural water within this stratigraphic interval in the immediate vicinity of the potential repository. To the extent that the majority of tuffaceous material lying between the devitrified lowermost Tiva Canyon welded tuff and the uppermost devitrified Topopah Spring welded interval is vitric, mobilization of this loosely held structural water in association with elevated temperatures by the thermal pulse of a constructed repository might allow the alteration of metastable glass to more widespread clays or zeolites in a similar manner to that proposed elsewhere (Whitbeck and Glassley, 1996) for the lower vitrophyre of the Topopah Spring Tuff. Although quite speculative at this time, the formation of a clay "cap" overlying an actual repository might significantly change post-waste-emplacement hydrology by sealing fractures and diverting infiltrating ground water away from the cooling waste. Note that the additional thermal "insulation" provided by the very-high-porosity upper lithophysae-bearing interval within the TSw model unit—and which has not been well characterized by laboratory measurements of thermal conductivity—may interact with in unpredictable ways with the loosely held structural water identified within the PTn stratigraphic interval.

SUMMARY AND CONCLUSIONS

This work has successfully used data from a diverse set of site-characterization measurements to provide the first known areally extensive, site-scale, fully three-dimensional model of material properties at the Yucca Mountain site. We have successfully generated discretized numerical models of several important hydrologic and thermal properties for three distinctly different major rock units at Yucca Mountain. The models have been constructed using geostatistical simulation methods conditioned to drillhole measurements of porosity, with the result that the individual stochastic models are spatially correlated and essentially indistinguishable statistically from the set of measured values. These simulated models of porosity have been provided as input to a linear coregionalization algorithm, which has been used to generate simulated models of secondary material properties, such as hydraulic and thermal conductivity. These secondary property models are also spatially correlated and are close statistical replicates of the set of measured secondary material properties. Cross-variable correlations exist, and the strength of these correlations is approximately that described by the sample correlation coefficients.

Sets of 100 individual simulations for each material property in each different geologic unit have been summarized in an single "expected-value" type model for each property, together with a quantitative description of geologic uncertainty associated with each material property. Although these summary models may represent the most-likely values expected within the geologically heterogeneous model domain, the statistical character

of these interrelated summary models is markedly different from the statistical character of the input measured values. Overall variance is much reduced in the summary material property models compared with the input stochastic simulations, and the range of the expected values models is significantly smaller than that observed in the measured data. Concomitantly, the cross-property correlations are much stronger, and may approximate a one-to-one (perfect correlation) relationship.

This work has also identified a number of differences among the data from different sources that complicate modeling and the interpretation of the output models. Rock properties measured by one technique may be moderately but systematically biased with respect to measurements of the same property by another technique. Additionally, external factors have led to the existence of spatially and lithologically biased data sets that may not fairly represent the overall material property distributions on a thickness-weighted basis. Evidence presented using downhole geophysical measurements suggests that laboratory testing of thermal conductivity of core samples may not accurately represent the thermal conductivity of the in-situ bulk rocks because larger-than-core-scale lithologic features cannot be sampled and tested.

The final sets of simulated and summarized models indicate that the distribution of major hydrologic and thermal properties at the Yucca Mountain site are heterogeneous, both vertically and laterally, and that geologically based heterogeneity exists on several scales. These models provide useful insights regarding the spatial variability of rock properties on the site scale. Furthermore, they provide the basis for quantitative estimates of the spatially variable geologic uncertainty, that which results from less-than-exhaustive site characterization, associated with these models.

REFERENCES

Altman, S.J., Arnold, B.W., Barnard, R.W., Barr, G.E., Ho, C.K., McKenna, S.A., and Eaton, R.R., 1996, Flow calculations for Yucca Mountain groundwater travel time (GWTT-95): Sandia National Laboratories Report SAND96-0819, 170 p.

Archie, G.E., 1942, The electrical resistivity log as an aid in determining some reservoir characteristics: American Institute of Mining, Metallurgical, and Petroleum Engineers Transactions, v. 146, p. 54–62.

Atkins, J.E., Lee, J.H., Lingineni, S., Mishra, S., McNeish, J.A., Sassani, D.C., and Sevougian, S.D., 1995, Total system performance assessment-1995—An evaluation of the potential Yucca Mountain Repository: Las Vegas, Nev., TRW Environmental Safety Systems, Civilian Radioactive Waste Management System Management and Operating Contractor Report B00000000-01717-2200-00136, Rev. 01, 677 p.

Barnard, R.W., and Dockery, H.A., eds., 1991, Technical summary of the performance assessment calculational exercises for 1990 (Pace-90), Volume 1, "Nominal configuration" hydrogeologic parameters and calculational results: Sandia National Laboratories Report SAND90-2726, 180 p.

Barnard, R.W., Wilson, M.L., Dockery, H.A., Gauthier, J.H., Kaplan, P.G., Eaton, R.R., Bingham, F.W., and Robey, T.H., 1992, TSPA 1991—An initial total-system performance assessment for Yucca Mountain: Sandia National Laboratories Report SAND91-2795, 376 p.

Bish, D.L., and Vaniman, D.T., 1985, Mineralogic summary of Yucca Mountain, Nevada, Los Alamos National Laboratory Report LA-10543-MS, 55 p.

Brodsky, N.S., Riggins, M., Connolly, J., and Ricci, P., 1997, Thermal expansion, thermal conductivity, and heat capacity measurements for boreholes UE25 NRG-4, UE25 NRG-5, USW NRG-6, and USW NRG-7/7A: Sandia National Laboratories Report SAND95-1955, 398 p.

Buesch, D.C., Spengler, R.W., Moyer, T.C., and Geslin, J.K., 1996, Proposed stratigraphic nomenclature and macroscopic identification of lithostratigraphic units of the Paintbrush Group exposed at Yucca Mountain, Nevada: U.S. Geological Survey Open-File Report 94-469, 47 p.

Bush, D.C., and Jenkins, R.E., 1970, Proper hydration of clays for rock property determinations: Journal of Petroleum Technology, v. 22, p. 800-804.

Cas, R.A.F., and Wright, J.V., 1987, Volcanic successions, modern and ancient: New York, Chapman and Hall, 528 p.

Clayton, R.W., 1996, Yucca Mountain Project Stratigraphic Compendium: Las Vegas, Nev., TRW Environmental Safety Systems, Inc., Civilian Radioactive Waste Management System Management and Operating Contractor Document BA0000000-01717-5700-00004 Rev. 01.

Clayton, R.W., Zelinski, W.P., and Rautman, C.A., 1997, ISM2.0—A 3D geologic framework and integrated site model of Yucca Mountain, Rev. 00: Las Vegas, Nev., TRW Environmental Safety Systems, Inc., Civilian Radioactive Waste Management System Management and Operating Contractor Report B00000000-01717-5700-00004 Rev. 00.

Cressie, N.A.C., 1991, Statistics for spatial data: New York, John Wiley & Sons, 900 p.

Cromer, M.V., and Rautman, C.A., 1995, Use of stratigraphic models as soft information to constrain stochastic modeling of rock properties—Development of the GSLIB-Lynx integration module: Sandia National Laboratories Report SAND95-2080, 34 p.

David, M., 1977, Geostatistical ore reserve estimation: New York, Elsevier Scientific Publishing Co., 364 p.

Desbarats, A.J., 1995, Upscaling capillary pressure-saturation curves in heterogeneous porous media: Water Resources Research, v. 31, p. 281–288.

Desbarats, A.J., 1997, Geostatistical modeling of unsaturated flow parameters at the Apache Leap Tuff site, *in* Baafi, E.Y. and Schofield, N.A., eds., Geostatistics Wollongong, '96, volume 1: Boston, Kluwer Academic Publishers, p. 621–633.

Deutsch, C.V., 1989, DECLUS—A Fortran 77 program for determining optimum spatial declustering weights: Computers & Geosciences, v. 15, p. 325–332.

Deutsch, C.V., and Journel, A.G., 1992, GSLIB geostatistical software library and user's guide: New York, Oxford University Press, 340 p.

DOE (U.S. Department of Energy), 1988, Site Characterization Plan, Yucca Mountain Site, Nevada

Research and Development Area, Nevada: U.S. Department of Energy, Office of Civilian Radioactive Waste Management Report DOE/RW-0199, 9 volumes.

Dudley, A.L., Peters, R.R., Gauthier, J H., Wilson, M.L, Tierney, M.S., and Klavetter, E.A., 1988, Total System Performance Assessment Code (TOSPAC); Volume 1—Physical and Mathematical Bases: Sandia National Laboratories Report SAND85-0002, 216 p.

Engstrom, D.A., and Rautman, C.A., 1996, Geology of the USW SD-9 drill hole, Yucca Mountain, Nevada: Sandia National Laboratories Report SAND96-2030, 128 p.

Fisher, R.V., and Schmincke, H.-U., 1984, Pyroclastic rocks: New York, Springer-Verlag, 472 p.

Flint, A.L., and Flint, L.E., 1994, Spatial distribution of potential near surface moisture flux at Yucca Mountain, *in* High-Level Radioactive Waste Management, Proceedings of the Fifth Annual International Conference, May 22–26, 1994, Las Vegas, Nev.: La Grange Park, Ill., American Nuclear Society, p. 2352–2358.

Flint, A.L., Flint, L.E., and Hevesi, J.A., 1993, The influence of long term climate change on net infiltration at Yucca Mountain, Nevada, *in* High-Level Radioactive Waste Management, Proceedings of the Fourth Annual International Conference, April 26–30, 1994, Las Vegas, Nev.: La Grange Park, Ill., American Nuclear Society, p. 152–159.

Flint, L.E., Flint, A.L., and Rautman, C.A., 1996a, Porosity as a surrogate for modeling hydrologic properties at Yucca Mountain, Nevada [abs.]: Geological Society of America Abstracts with Programs, v. 28, no. 7, p. A-521.

Flint, L.E., Flint, A.L., Rautman, C.A., and Istok, J.D., 1996b, Physical and hydrologic properties of rock outcrop samples at Yucca Mountain, Nevada: U.S. Geological Survey Open-File Report 95-280, 52 p.

Gomez-Hernandez, J.J., and Srivastava, R.M., 1990, ISIM3D—An ANSI-C three-dimensional multiple indicator conditional simulation program: Computers and Geosciences, v. 16, p. 395–440.

Hillel, D., 1980, Fundamentals of soil physics: New York, Academic Press, 413 p.

Isaaks, E.H., and Srivastava, R.M., 1989, Applied geostatistics: New York, Oxford University Press, 578 p.

Istok, J.D., Rautman, C.A., Flint, L.E., and Flint, A.L., 1994, Spatial variability in hydrologic properties of a volcanic tuff: Ground Water, v. 32, p. 751–760.

Journel, A.G., 1983, Nonparametric estimation of spatial distributions: Mathematical Geology, v. 15, p. 445–468.

Journel, A.G., and Alabert, F., 1989, Non-gaussian data expansion in the earth sciences: Terra Nova, v. 1, p. 123–134.

Journel, A.G., and Huijbregts, Ch.J., 1978, Mining geostatistics: New York, Academic Press, 600 p.

Knauss, K.G., 1987, Zeolitization of glassy Topopah Spring Tuff under hydrothermal conditions, *in* Bates, J.K., and Seefeldt, W.B., eds., Scientific Basis for Nuclear Waste Management X, Materials Research Society Symposia Proceedings, December 1–4, 1986, Boston, Mass.: Boston, Materials Research Society, v. 84, p. 737–745.

Kupfersberger, H., and Deutsch, C.V., 1997, Determination of 3-D variogram models from analogue information, *in* SCRF Report 10, May 1997: Stanford, Calif., Stanford Center for Reservoir Forecasting, Department of Petroleum Engineering, Stanford University, 41 p.

Larson, H.J., 1982, Introduction to probability theory and statistical inference (3rd ed.): New York, John Wiley & Sons, 637 p.

Lipman, P.W., Christiansen, R.L., and O'Connor, J.T., 1966, A compositionally zoned ash-flow sheet in southern Nevada: U.S. Geological Survey Professional Paper 524-F, 47 p.

Longenbaugh, R., Rautman, C.A., and Ryder, E.E., 1995, Yucca Mountain thermal response—An evaluation of the effects of modeled geologic structure and thermal property descriptions: Sandia National Laboratories Report SAND94-2247, 131 p.

Luster, G.R., 1985, Raw materials for Portland cement: Applications of conditional simulation of coregionalization: Stanford, Calif., Stanford University, Ph.D. dissertation, 531 p.

McKenna, S.A., and Rautman, C.A., 1995, Summary evaluation of Yucca Mountain surface transects with implications for downhole sampling: Sandia

National Laboratories Report SAND94-2038, 46 p.

McKenna, S.A., and Rautman, C.A., 1996, Scaling of material properties for Yucca Mountain—Literature review and numerical experiments on saturated hydraulic conductivity: Sandia National Laboratories Report SAND95-2338, 117 p.

McKenna, S.A., Cromer, M.V., Rautman, C.A., and Zelinski, W.P., 1996, Addressing uncertainty in rock properties through geostatistical simulation, *in* Uncertainty in the Geologic Environment—From Theory to Practice, Proceedings of Uncertainty 96, July 31–August 3, 1996, Madison, Wis.: New York, American Society of Civil Engineers, p. 297–311.

Moyer, T.C., and Geslin, J.K., 1995, Lithostratigraphy of the Calico Hills Formation and Prow Pass Tuff (Crater Flat Group) at Yucca Mountain, Nevada: U.S. Geological Survey Open-File Report 94-460, 59 p.

Muller, D.C., and Kibler, J.E., 1985, Preliminary analysis of geophysical logs from the WT series of drill holes, Yucca Mountain, Nye County, Nevada: U.S. Geological Survey Open-File Report 86-46, 30 p.

Nelson, P.H., Muller, D.C., Schimschal, U., and Kibler, J.E., 1991, Geophysical logs and core measurements from forty boreholes at Yucca Mountain, Nevada: U.S. Geological Survey Geophysical Investigations Map GP-1001, 10 sheets, 64 p.

Nelson, P.H., 1996, Computation of porosity and water content from geophysical logs, Yucca Mountain, Nevada: U.S. Geological Survey Open-File Report 96-078, 64 p.

Ortiz, T.S., Williams, R.L., Nimick, F.B., Whittet, B.C., and South, D.L., 1985, A three-dimensional model of reference thermal, mechanical, and hydrologic stratigraphy at Yucca Mountain, southern Nevada: Sandia National Laboratories Report SAND84-1076, 76 p.

Rautman, C.A., 1995, Preliminary geostatistical modeling of thermal conductivity for a cross section of Yucca Mountain, Nevada: Sandia National Laboratories Report SAND94-2283, 50 p.

Rautman, C.A., 1996, Integrated rock properties models at Yucca Mountain, Nevada [abs.]: Geological Society of America Abstracts with Programs, v. 28, no. 7, p. A-521.

Rautman, C.A., and Engstrom, D.A., 1996a, Geology of the USW SD-12 drill hole, Yucca Mountain, Nevada: Sandia National Laboratories Report SAND96-1368, 132 p.

Rautman, C.A., and Engstrom, D.A., 1996b, Geology of the USW SD-7 drill hole, Yucca Mountain, Nevada: Sandia National Laboratories Report SAND96-1474, 164 p.

Rautman, C.A., and Flint, A.L., 1992, Deterministic geologic processes and stochastic modeling, *in* High-Level Radioactive Waste Management, Proceedings of the Third International Conference, April 12–16, 1992, Las Vegas, Nev.: La Grange Park, Ill., American Nuclear Society, p. 1617–1624.

Rautman, C.A., and Robey, T.H., 1993, Recent developments in stochastic modeling and upscaling of hydrologic properties in tuff, *in* High-Level Radioactive Waste Management, Proceedings of the Fourth Annual International Conference, April 26–30, 1993, Las Vegas, Nev.: La Grange Park, Ill., American Nuclear Society, p. 1437–1445.

Rautman, C.A., and Robey, T.H., 1994, Development of stochastic indicator models of lithology, Yucca Mountain, Nevada, *in* High-Level Radioactive Waste Management, Proceedings of the Fifth Annual International Conference, May 22–26, Las Vegas, Nev.: La Grange Park, Ill., American Nuclear Society, p. 2510–2519.

Robey, T.H., 1993, Numerical methods for fluid flow in unsaturated heterogeneous tuff, *in* High-Level Radioactive Waste Management, Proceedings of the Fourth Annual International Conference, April 26–30, 1993, Las Vegas, Nev.: La Grange Park, Ill., American Nuclear Society, p. 138–145.

Robey, T.H., 1994, Development of models for fast fluid pathways through unsaturated heterogeneous porous media: Sandia National Laboratories Contractor Report SAND93-7109, 104 p.

Ross, C.S., and Smith, R.L., 1961, Ash-flow tuffs—Their origin, geologic relations, and identification: U.S. Geological Survey Professional Paper 366, 81 p.

Sawyer, D.A., Fleck, R.J., Lanphere, M.A., Warren, R.G., Broxton, D.E., and Hudson, M.R., 1994, Episodic caldera volcanism in the Miocene southwestern Nevada volcanic field—Revised stratigraphic framework, $^{40}Ar/^{39}Ar$ geochronology, and implications for magmatism and exten-

sion: Geological Society of America Bulletin, v. 106, p. 1304–1318.

Schenker, A.R., Guerin, D.C., Robey, T.H., Rautman, C.A., and Barnard, R.W., 1995, Stochastic hydrogeologic units and hydrogeologic properties development for total-system performance assessments: Sandia National Laboratories Report SAND94-0244, 89 p.

Scott, R.B., and Bonk, J., 1984, Preliminary geologic map of Yucca Mountain, Nye County, Nevada, with geologic sections: U.S. Geological Survey Open-File Report 84-494, scale 1:12,000.

Soeder, D.J., Flint, L.E., and Flint, A.L., 1991, Effects of sample handling and measurement methodology on the determination of porosity in volcanic rock samples [abs.]: Agronomy Abstracts, 1991 Annual Meeting, p. 232.

Thompson, L.E., and Rael, H.P., 1996, Determining porosity, balanced water content and other rock properties from geophysical logs for the modern borehole data set at Yucca Mountain, Nevada, June 1996: Las Vegas, Nev., TRW Environmental Safety Systems, Inc., Civilian Radioactive Waste Management System Management and Operating Contractor Document BAAA00000-01717-0200-00013 REV 00.

Whitbeck, M., and Glassley, W.E., 1996, Thermal effects in the altered zone—Preliminary bounds on the water composition and secondary mineral development in the altered zone that may influence the near-field environment, Section 10.4.3 *in* Wilder, D.G., Near-Field and Altered Zone Environment Report, v. 2.: Lawrence Livermore National Laboratory Report UCRL-LR-124998, p. 10.4-17–10.4-23.

Wilson, M.L., Gauthier, J.H., Barnard, R.W., Barr, G.E., Dockery, H.A., Dunn, E., Eaton, R.R., Guerin, D.C., Lu, N., Martinez, M.J., Nilson, R., Rautman, C.A., Robey, T.H., Ross, B., Ryder, E.E., Schenker, A.R., Shannon, S.A., Skinner, L.H., Halsey, W.G., Gansemer, J., Lewis, L.C., Lamont, A.D., Triay, I.R., Meijer, A., and Morris, D.E., 1994, Total-System Performance Assessment for Yucca Mountain—SNL Second Iteration (TSPA-1993): Sandia National Laboratories Report SAND93-2675, 882 p.

Wittwer, C., Chen, G., Bodvarsson, G.S., Chornack, M., Flint, A., Flint, L., Kwicklis, E., and Spengler, R., 1995, Preliminary development of the LBL/USGS three-dimensional site-scale model of Yucca Mountain, Nevada: Lawrence Berkeley National Laboratory Report LBL-37356, 69 p.

(This page intentionally left blank.)

Appendix A: DATA TRACKING NUMBERS

Table A-17: Data tracking numbers for data used to model rock material properties

Tracking Number	Q/ NQ	Title of Technical Data Information Form
GS960708312132.001	Q	Qualified geophysical logs (as listed on the qualification checklists) collected at 26 boreholes; and water content, poroisty and saturation computations derived from logs of USW H-6, USW WT-1, USW WT-2, UE-25 WT#4, UE-25 WT#6, USW WT-7, USW WT-10, USW WT-11, UE-25 WT#12, UE-25 WT#13, UE-25 WT#14, UE-25 WT#15, UE-25 WT#17, and UE-25 WT#18
GS960708312132.002	NQ	Non-qualified geophysical logs (as identified on the qualification checklists), and stratigraphy, lithology, mineralogy, fracture characteristics, and water levels collected from 26 boreholes; and water content, poroisty and saturation computations derived from geophysical logs of USW H-1, USW H-3, USW H-4, USW H-5, USW G-1 USW G-2, USW G-3/GU-3, USW G-4, and UE-25 P#1
GS950608312231.007	Q	Physical properties and water content of core from borehole USW NRG-6
GS951108312231.010	Q	Physical properties and water content from borehole USW NRG-7/7A
GS951108312231.009	Q	Physical properties, water content, and water potential for borehole USW SD-7
GS960808312231.004	Q	Physical properties, water content, and water potential for samples from lower depths in boreholes USW SD-12 and USW SD-7
GS950408312231.004	Q	Physical properties and water potentials of core from borehole USW SD-9
GS950608312231.006	Q	Water permeability of core from SD-9
GS960808312231.002	Q	Relative humidity calculated porosity measurements on samples from borehole USW SD-9 used for saturated hydraulic conductivity
GS950308312231.002	Q	Laboratory measurements of bulk density, porosity, and water content for USW SD-12
GS951108312231.011	Q	Physical properties, water content, and water potential for borehole USW UZ-7a
GS950308312231.005	Q	Physical properties and water potentials of core from borehole USW UZ-14
GS940508312231.006	Q	Core analysis of bulk density, porosity, particle density, and in situ saturation for borehole UE-25 UZ#16
GS960808312231.005	Q	Water permeability and relative humidity calculated porosity for on samples from boreholes USW SD-7, USW SD-9, USW SD-12 and USW UZ-14
GS930108312231.006	Q	USW UZ-N53 core analysis: bulk density, porosity, particle density, and in situ saturation for core dried in 105°C oven
GS960808312231.001	Q	Water permeability and relative humidity calculated porosity from boreholes USW UZ-N27 and UE-25 UZ#16
GS940108312231.002	Q	Core analysis of bulk density, porosity, particle density, and in situ saturation for seventeen neutron boreholes: Data for core dried in RH oven and 105°C oven for USW UZ-N31, UZ-N32, UZ-N33, UZ-N34, UZ-N35, UZ-N38, UZ-N58, UZ-N59, UE25 UZN#63 and USW UZ-N64; data for core dried in 105°C only for USW UZ-N11, UZ-N15, UZ-N16, UZ-N17, UZ-N27, UZ-N36, and UZ-N37
GS940408312231.004	Q	Core analysis of bulk density, porosity, particle density, and in situ saturation for three neutron holes USW UZ-N57, UZ-N61, and UZ-N62

Table A-17: Data tracking numbers for data used to model rock material properties (Continued)

Tracking Number	Q/ NQ	Title of Technical Data Information Form
GS920508312231.012	Q	USW UZ-N54 and USW UZ-N55 core analysis: bulk density, porosity, particle density, and in situ saturation for core dried in 105°C oven
TMUSWNRG600097.001	Q	Output data from synthesis of borehole and surface geophysical studies at Yucca Mountain, Nevada and vicinity
TMUSWNRG7A0097.001	Q	Output data from synthesis of borehole and surface geophysical studies at Yucca Mountain, Nevada and vicinity
TMUSWSD7000097.001	Q	Output data from synthesis of borehole and surface geophysical studies at Yucca Mountain, Nevada and vicinity
TMUSWSD9000097.001	Q	Output data from synthesis of borehole and surface geophysical studies at Yucca Mountain, Nevada and vicinity
TMUSWSD1200097.001	Q	Output data from synthesis of borehole and surface geophysical studies at Yucca Mountain, Nevada and vicinity
TMUSWWT2000097.001	Q	Output data from synthesis of borehole and surface geophysical studies at Yucca Mountain, Nevada and vicinity
TMUSWWT10-0097.001	Q	Output data from synthesis of borehole and surface geophysical studies at Yucca Mountain, Nevada and vicinity
TMUE25WT120097.001	Q	Output data from synthesis of borehole and surface geophysical studies at Yucca Mountain, Nevada and vicinity
TMUSWG20000097.001	Q	Output data from synthesis of borehole and surface geophysical studies at Yucca Mountain, Nevada and vicinity
TMUE25UZ400097.001	Q	Output data from synthesis of borehole and surface geophysical studies at Yucca Mountain, Nevada and vicinity
TMUE25UZ500097.001	Q	Output data from synthesis of borehole and surface geophysical studies at Yucca Mountain, Nevada and vicinity
TMUSWUZ7A00097.001	Q	Output data from synthesis of borehole and surface geophysical studies at Yucca Mountain, Nevada and vicinity
TMUSWUZ1400097.001	Q	Output data from synthesis of borehole and surface geophysical studies at Yucca Mountain, Nevada and vicinity
TMUE25UZ160097.001	Q	Output data from synthesis of borehole and surface geophysical studies at Yucca Mountain, Nevada and vicinity
TMUE25ONC10097.001	Q	Output data from synthesis of borehole and surface geophysical studies at Yucca Mountain, Nevada and vicinity
SNL03042594001.002	Q	Average grain density for thermal properties test samples from boreholes UE25 NRG4, UE25 NRG-5, and USW NRG-6
SNL03042594001.003	Q	Average grain density for thermal properties test samples from borehole USW NRG-7/7A
SNL02030193001.014	Q	Mechanical properties data (grain density, porosity, unconfined strength, elastic properties & indirect tensile strength) for drillhole UE25 NRG-4 samples from depth 378.1 to 695.8 ft
SNL02030193001.017	Q	Mechanical properties data (tensile strength, average grain density & porosity) for drillhole USW NRG-7/7A samples from depth 18.0 to 495.0 ft

Table A-17: Data tracking numbers for data used to model rock material properties (Continued)

Tracking Number	Q/ NQ	Title of Technical Data Information Form
SNL02030193001.018	Q	Mechanical properties data (ultrasonic velocities, static elastic properties, triaxial strength, dry bulk density & porosity) for drillhole USW NRG-7/7A samples from depth 344.4 ft
SNL02030193001.019	Q	Mechanical properties data (grain density, porosity, unconfined strength, confined strength, elastic properties and indirect tensile strength) for drillhole USW NRG7/7A samples from depth 507.4 to 881.0 ft
SNL02030193001.020	Q	Mechanical properties data (ultrasonic velocities, static elastic properties, unconfined strength, triaxial strength, dry bulk density & porosity) for drillhole USW NRG-7/7A samples from depth 554.7 to 1450.1 ft
SNL02030193001.021	Q	Mechanical properties data (ultrasonic velocities, static elastic properties, triaxial strength, dry bulk density & porosity) for drillhole USW NRG-7/7A samples from depth 345.0 to 1408.6 ft
SNL02030193001.022	Q	Mechanical properties data (ultrasonic velocities, static elastic properties, triaxial strength, dry bulk density & porosity) for drillhole USW NRG-6 samples from depth 5.7 to 1092.3 ft
SNL01A05059301.005	Q	Laboratory thermal conductivity data for boreholes UE25 NRG-4, NRG-5, USW NRG-6 and NRG-7/7A, dated 01/19/96
SNL02030193001.009	Q	Mechanical properties data (tensile strength, average grain density & porosity for drillhole UE25 NRG-5 samples from depth 781.0 to 991.9 ft

Appendix B: DRILLHOLE POROSITY DATA

Introduction

This appendix contains downhole plots of all porosity data used in generation of the hydrologic and thermal property models described in this report. The data are presented by drillhole, first in true coordinates for the drillhole as a whole and then for each of the three model units in both true and stratigraphic coordinates. Note that all drillholes are referred to using a number composed of a simple "series" designator, a hyphen, and a number. Prefixes such as USW and UE-25 are omitted, and the drillhole plots are organized quasi-alphabetically, with the shallow neutron series last.

Stratigraphic Coordinates

As described on page 12, sample depths, Z, associated with measured properties data reported by the original principal investigator were converted to stratigraphic depths, Z', using the formula:

$$Z' = \frac{UnitTop - Depth}{UnitThickness} \cdot C, \qquad (42)$$

where *UnitTop* is the depth in the borehole corresponding to the top of the specific model unit, and where:

$$UnitThickness = UnitBottom - UnitTop. \qquad (43)$$

Note that *UnitTop* and *UnitBottom* were projected if necessary above or below the physical extent of the hole using information obtained from the three-dimensional geologic framework model of Clayton and others (1997). If required, *UnitTop* and *UnitBottom* were also adjusted to account for post-depostional erosion or for omission of part of a unit by normal faulting using regional thickness trends extracted from the 3-D framework model.

Note also that the stratigraphic depths defined by equation (42) are rescaled and normalized to an arbitrary value corresponding to a nominal or prototypical thickness of the model unit across the entire model domain. The values of C for equation (42) are given in table B-1.

Stratigraphic depths were then converted to stratigraphic elevations, Z'', prior to input to the geostatistical algorithms, as:

$$Z'' = C - Z'. \qquad (44)$$

Note that although it is convenient to maintain a thought pattern that expresses stratigraphic depths and elevations as possessing measurement units ("… a stratigraphic depth of 250 'feet'…") these stratigraphic dimensions truly are dimensionless.

Table B-1: Scaling constants, *C*, for nominal thicknesses of model units

Model Unit	Scaling Constant *C*
PTn	200
TSw	1000
CH-PP	800

The completed property models, which consist of an implicit structured array of simulated values tied to the input grid specifications of table 3, were back-transformed from stratigraphic elevations to real-world Nevada state-plane coordinates, using the equations provided for such conversions by Deutsch and Journel (1992, p. 21). Because this conversion produces values of stratigraphic elevation, Z'', an additional step was required to account for the relevant structure contour and isopach information for the appropriate model unit, as extracted from the 3-D geologic framework model (Clayton and others, 1997), effectively:

$$TrueElevation = \frac{Z''}{C} \cdot Isopach + StructureTop. \qquad (45)$$

The result is elevation above sea level. Nevada state-plane Eastings and Northings were added at the same time based on the grid-specification information given in table 3. Downhole deviation of the borehole from vertical was not considered in this study.

Unit Contacts

Three sets of rock-unit contacts are shown in the figures of this appendix, as indicated in the explanation (fig. B-1). Formation-level contacts (e.g., Topopah Spring Tuff) and the contacts of the informal lithostratigraphic subdivisions of Buesch and others (1996) (e.g., crystal-poor middle nonli-

thophysal zone) were taken from a November 1996 digital revision of the tables of Yucca Mountain Stratigraphic Compendium (Clayton, 1996). Note that certain of these latter contacts were revised from the original issue of Clayton (1996), dated September, and the information presented in these appendix figures suggests that there remain certain inconsistencies and probable defects in the vertical positions of these informal units. Although aesthetically displeasing, the vast majority of these uncertainties and/or inconsistencies are irrelevant to the modeling activities described in this report because of the "major rock unit" approach used in this study.

The boundaries of the three modeling units, PTn, TSw, and CH–PP, have been taken by definition to coincide with the boundaries of selected lithostratigraphic "contacts" that on paper define the breaks between welded and nonwelded lithosomes, as defined in table A-2. Note that because the full nominal sequence of lithostratigraphic units defined by Buesch and othes (1996) is not present in all locations, the specific units described on either side of the major rock unit boundaries varies by drillhole.

Table B-2: Listing of lithostratigraphic units typically defining modeling-unit contacts
[Unit abbreviations after Buesch and others (1996) and/or Moyer and Geslin (1995)]

	top of PTn	top of TSw	top of CH–PP	base of CH–PP
Above	Tpcpln Tpcpv3	bt2 Tptrv3 Tptrv2	Tptpln Tptpv3	Tcp Tcpbt
Below	Tpcpv2 Tpcpv1 bt4 Tpy bt3	Tptrv1 Tptrn	Tptpv2 Tptpv1 bt1 Tac	Tcb

In some cases, the figures presented in this appendix indicate that the most prominent change in porosity from low (welded) to high (nonwelded) is not as expected from the nominal descriptions of Buesch and others. At the time these data were "frozen" for modeling purposes, it was unclear whether these apparent porosity-lithostratigraphic unit mismatches were caused by the application of inconsistent criteria in describing the lithostratigraphic units or because of location-specific alteration that have increased or decreased the porosity of specific intervals. In all cases, the borehole depths of these few critical boundaries were selected to be consistent with the same boundary in the three-dimensional geologic framework model of Clayton and others (1997) because of the need to use structure-contour and isopach information from this model in the conversion to and from stratigraphic coordinates.

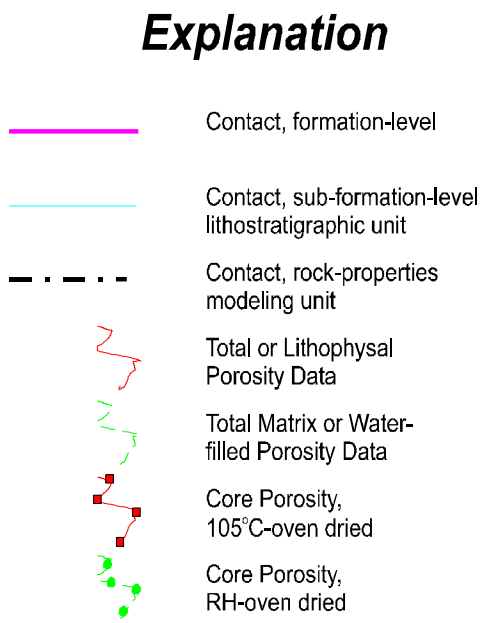

Figure B-1. Explanation for drillhole porosity data plots in Appendix B

Drillhole G-1

Drillhole G-1 is one of the earliest core holes drilled at Yucca Mountain and the hole provides partial penetration of the PTn model unit and full penetration of the TSw and CH–PP units. Porosity data from the G-1 drillhole consist principally of petrophysical porosity values from the older set of geophysical data, although a few older (NQ) core data are available for the TSw model unit.

We have selected only petrophysical porosity values for use in modeling.

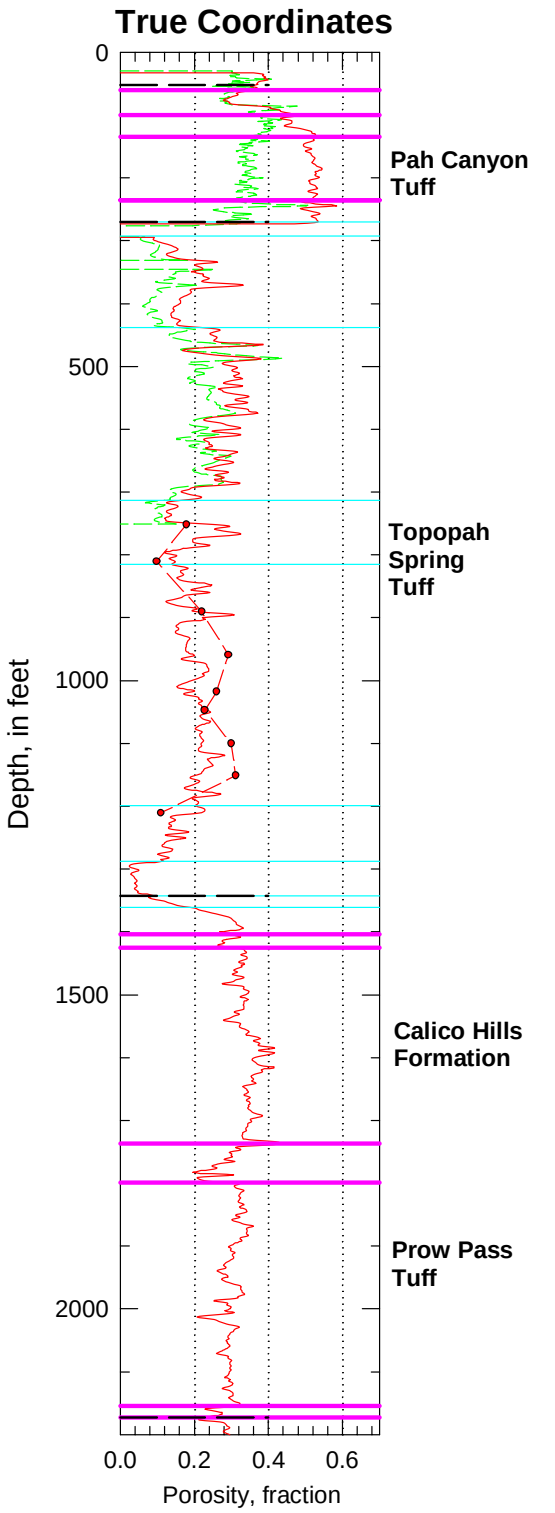

Figure B-2. Porosity data in true coordinates from drillhole G-1 for the entire drill hole through the top of the Bullfrog Tuff.

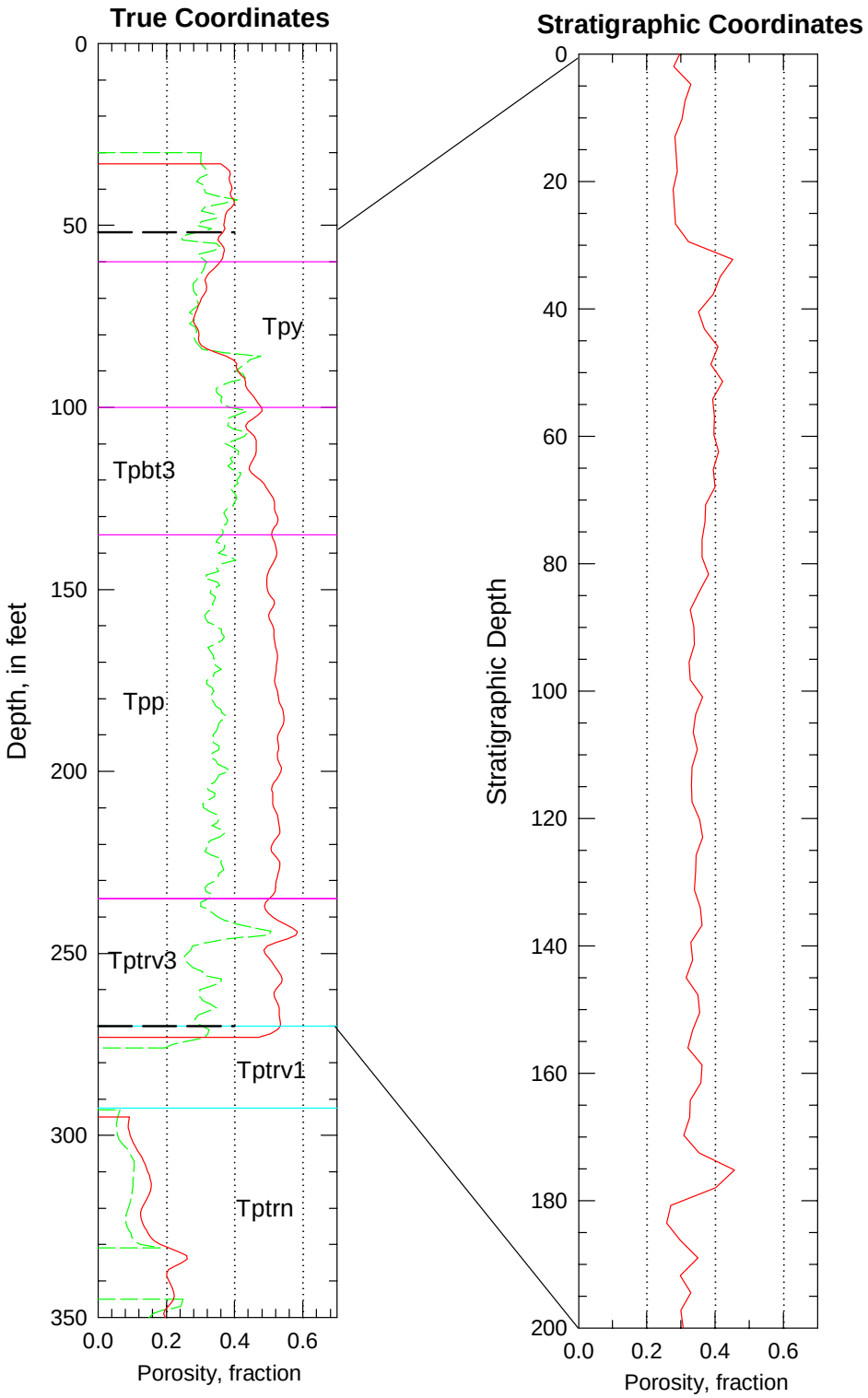

Figure B-3. Porosity data in real-world and in stratigraphic coordinates for the PTn model unit in drillhole G-1.

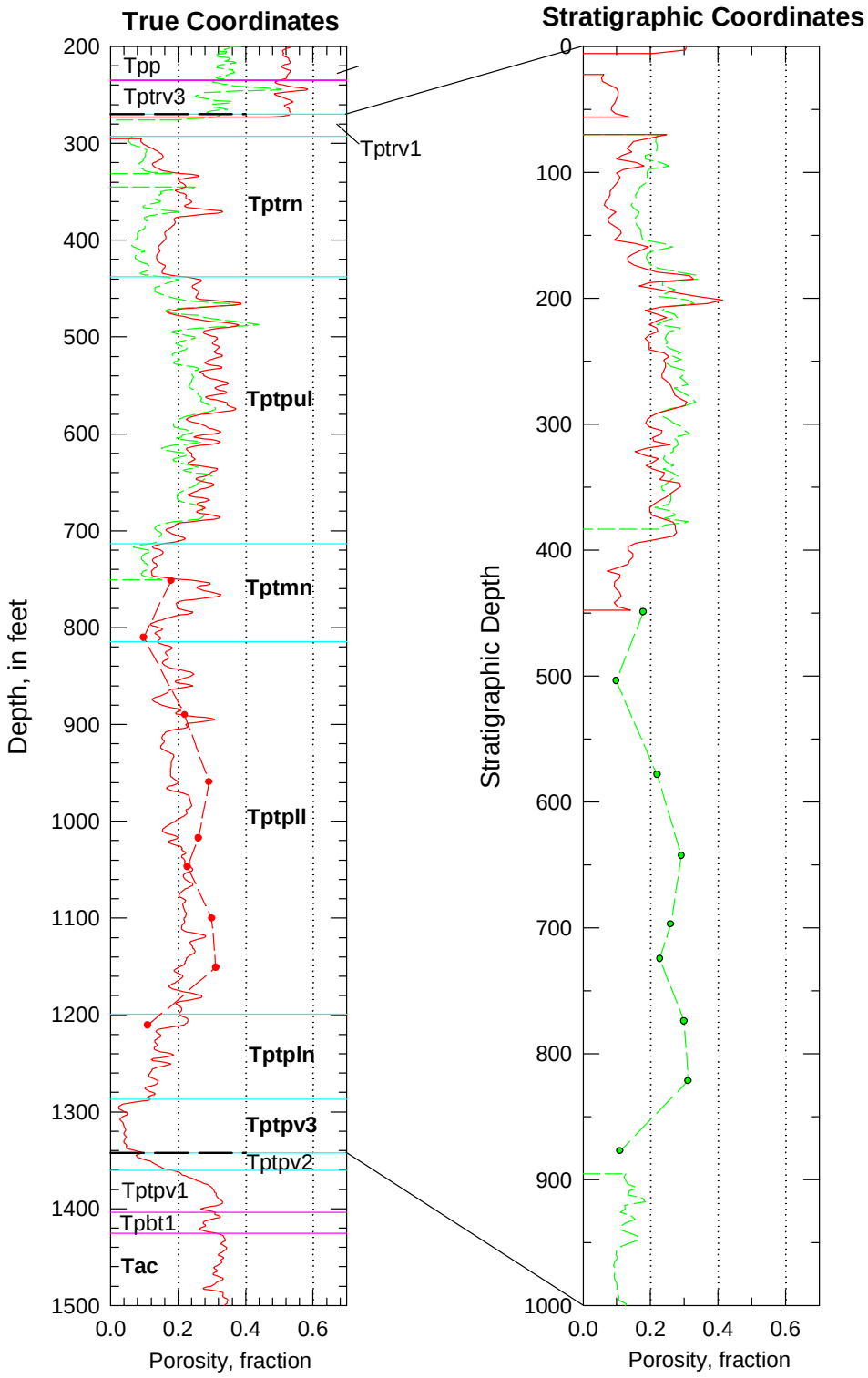

Figure B-4. Porosity data in real-world and in stratigraphic coordinates for the TSw model unit in drillhole G-1.

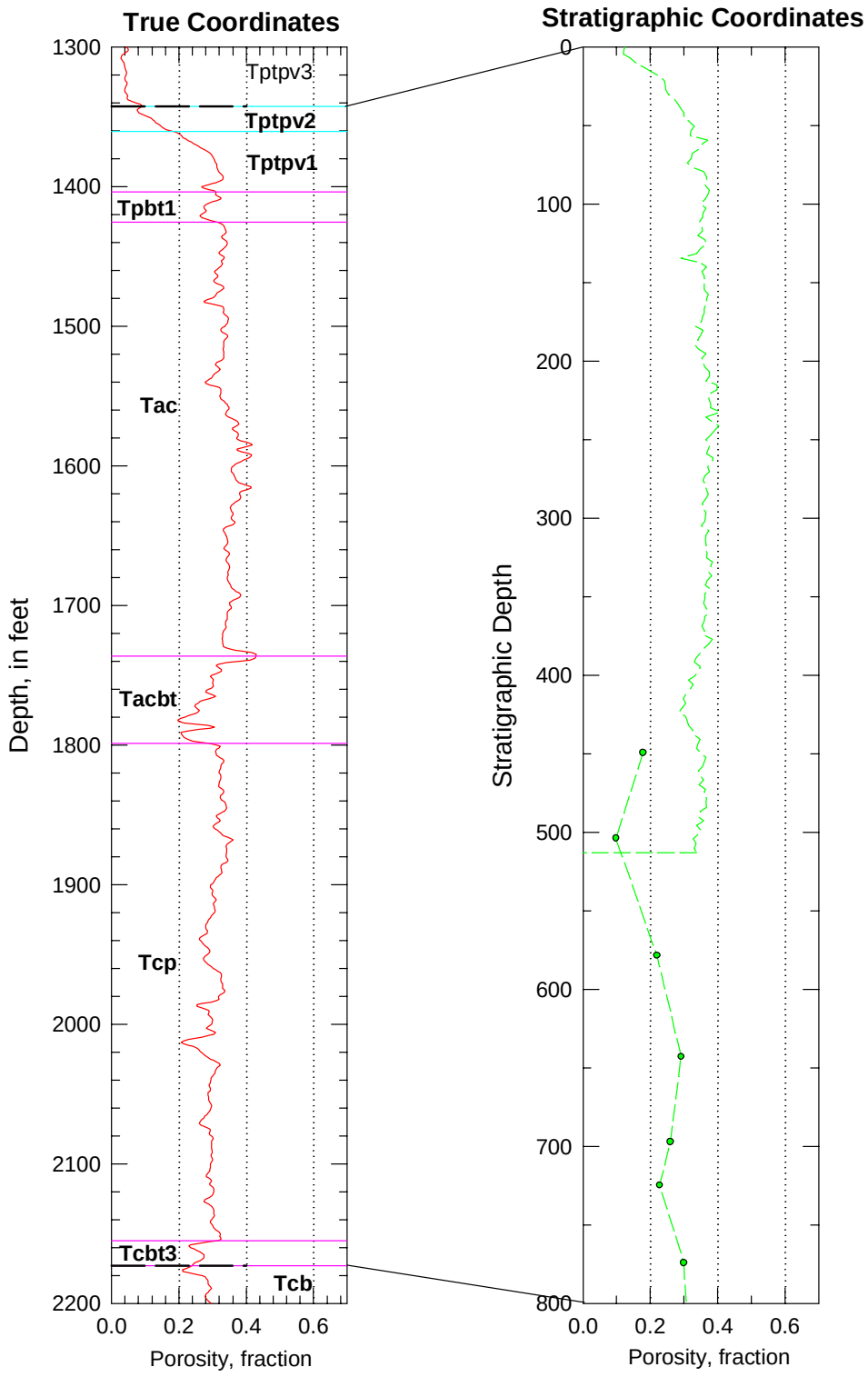

Figure B-5. Porosity data in real-world and in stratigraphic coordinates for the combined CH–PP model unit in drillhole G-1.

Drillhole G-2 (older data)

Drillhole G-2 is also one of the earliest holes drilled at Yucca Mountain; it is also the northernmost of the deep drillholes. The drillhole provides nearly full penetration of all three material properties model units. Some older core data is available, but this information has not been included in the modeling described in this report.

Petrophysically derived porosity data include values from both older and modern data sets. We have used selected intervals from both vintages of petrophysical data as follows: PTn model unit—no modern logs, use older values; TSw model unit—poor spatial distribution of valid older data, use modern values except insert older data 768–789 ft true depth (no modern values); CH–PP model unit—use older data as there is only partial modern coverage.

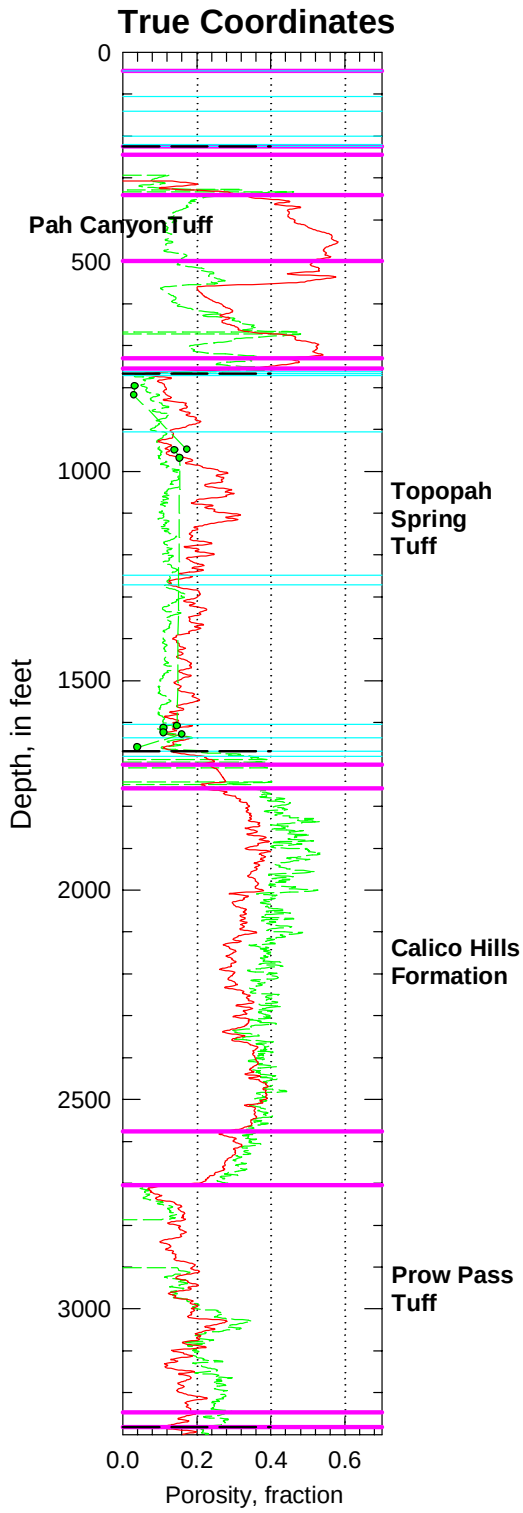

Figure B-6. Porosity data from the older set of petrophysical logs for the entire G-2 drillhole. Compare with figure B-10.

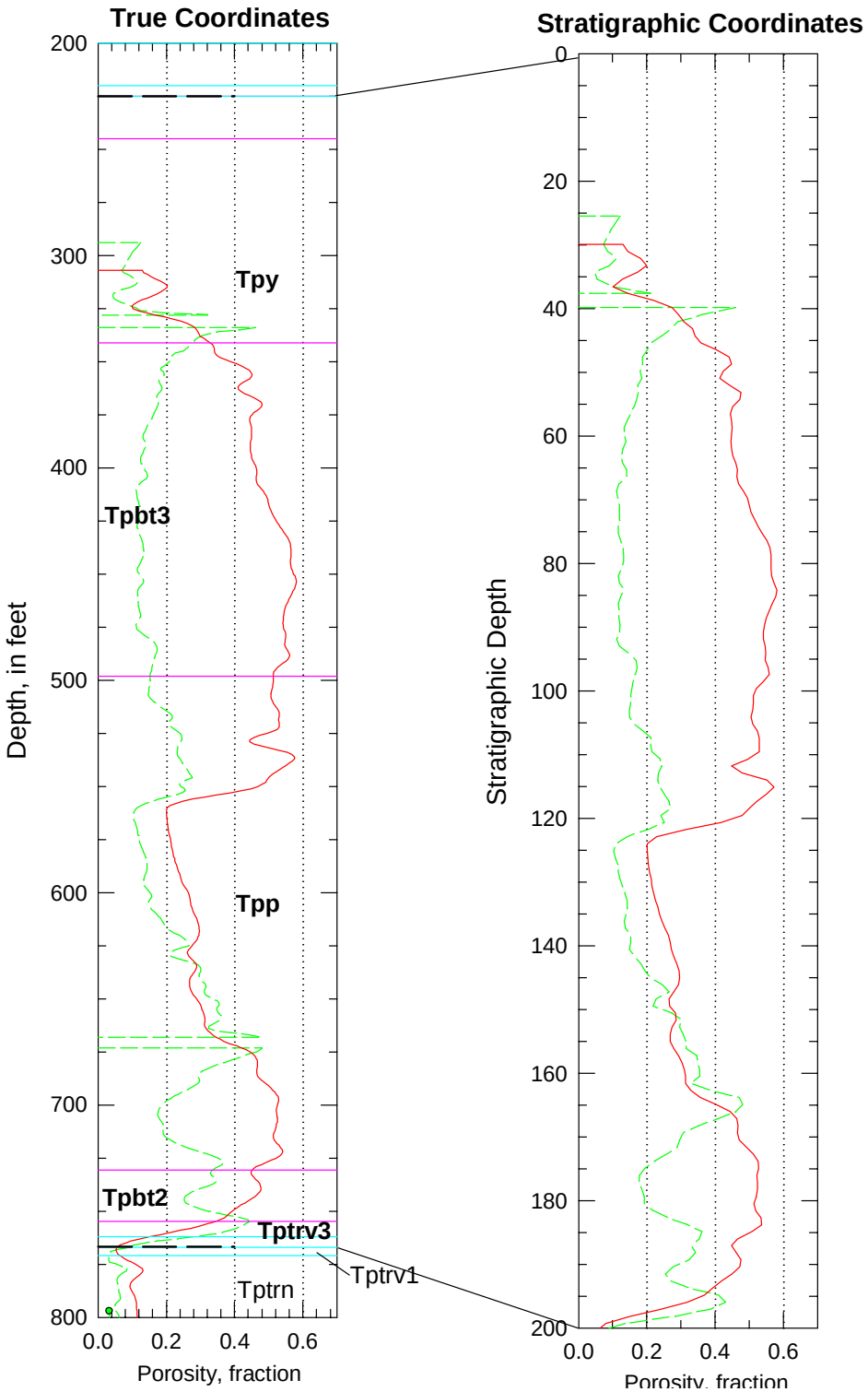

Figure B-7. Porosity data from the older set of petrophysical logs in real-world and in stratigraphic coordinates for the PTn model unit in drillhole G-2.

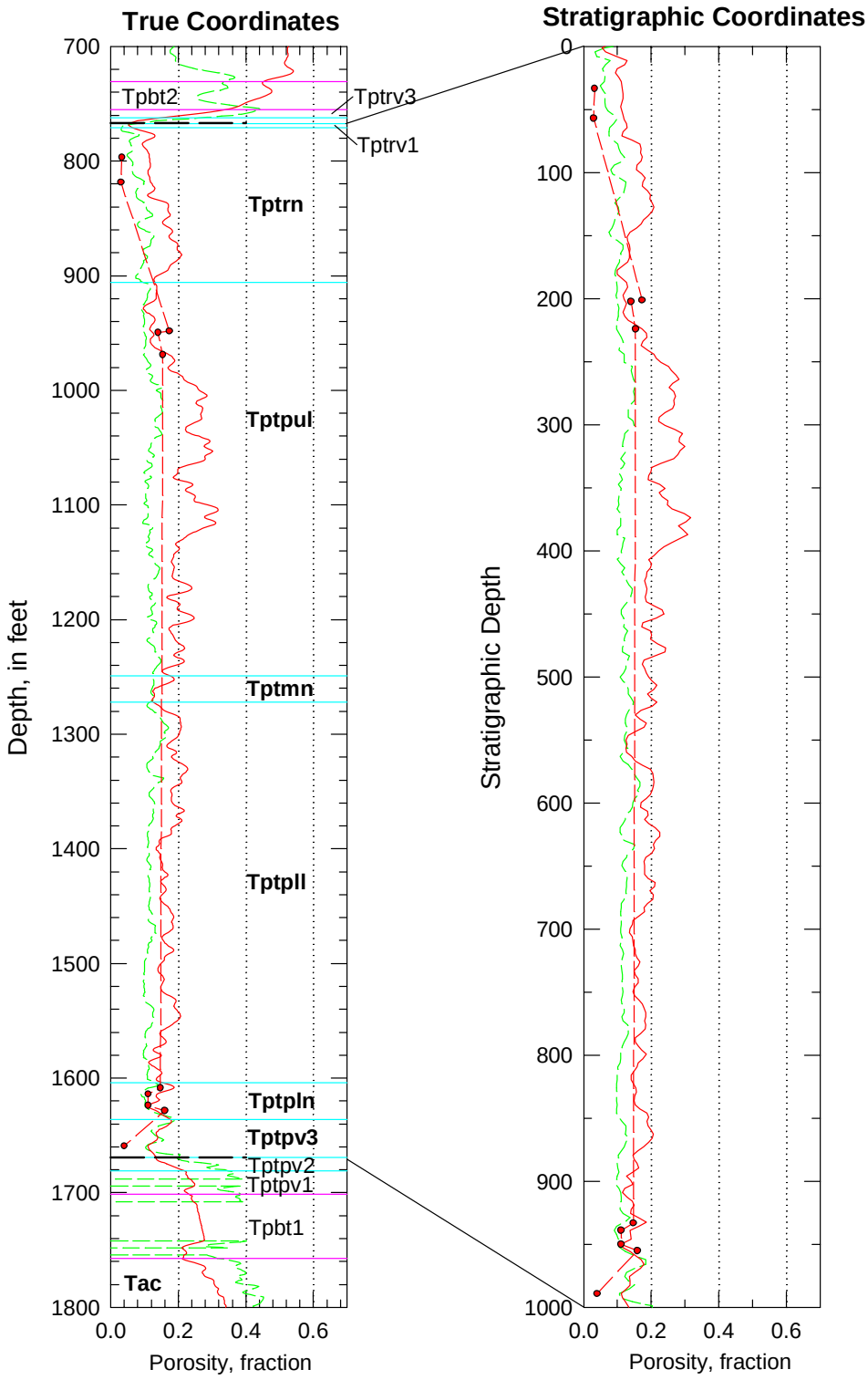

Figure B-8. Porosity data from the older set of petrophysical logs in real-world and in stratigraphic coordinates for the TSw model unit in drillhole G-2.

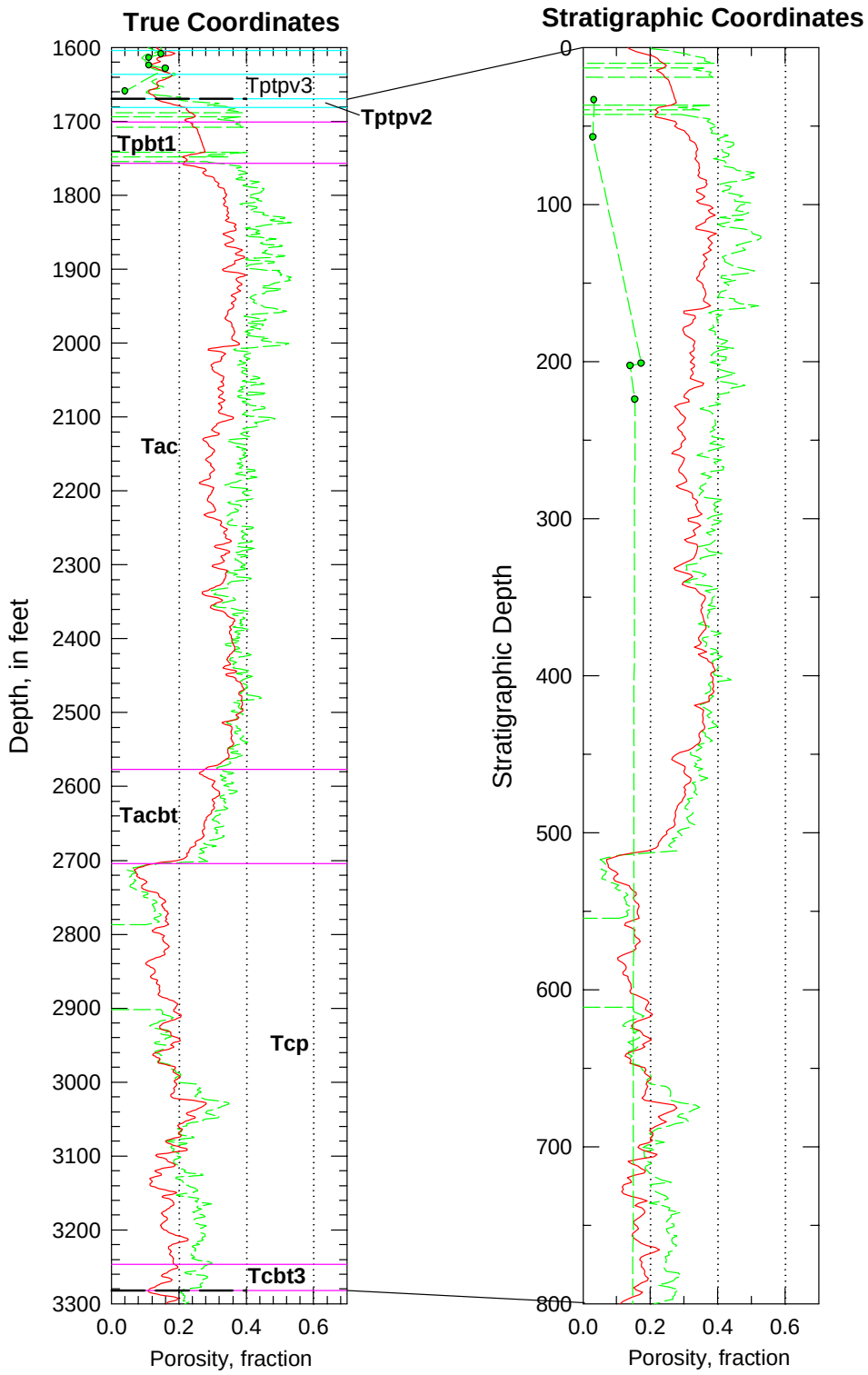

Figure B-9. Porosity data from the older set of petrophysical logs for the combined CH–PP model unit in the G-2 drillhole.

Drillhole G-2 (modern data)

Refer to the description of data from drillhole G-2 on page 162.

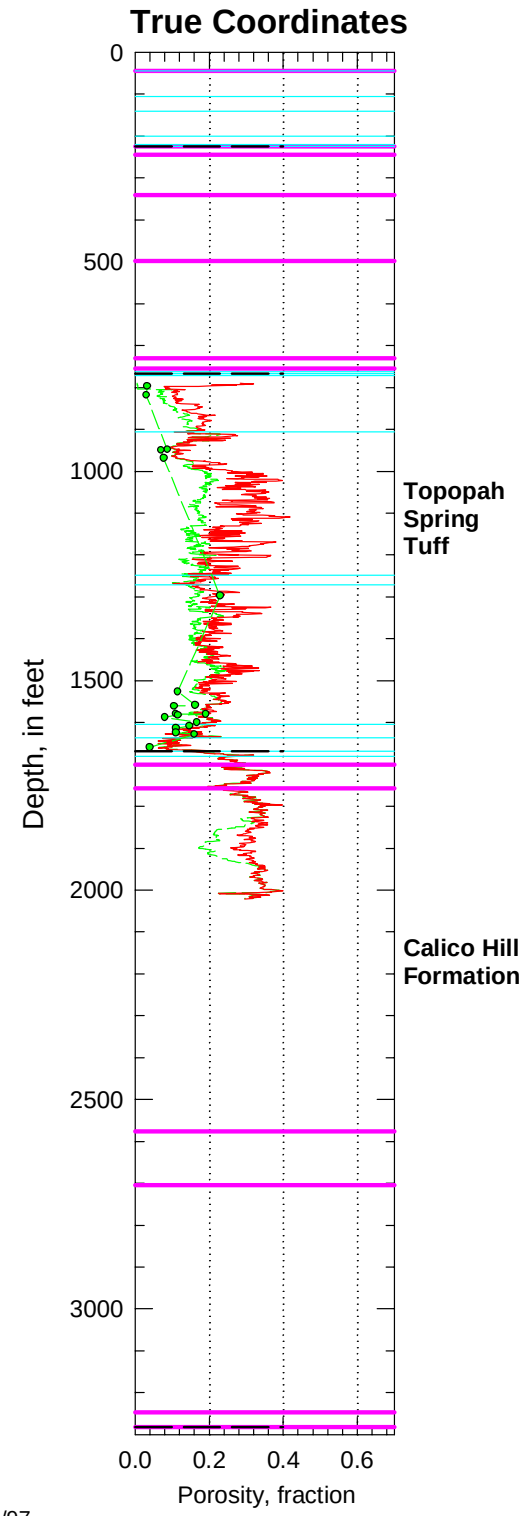

Figure B-10. Porosity data from the modern set of petrophysical logs for the entire G-2 drillhole. Compare with figure B-6.

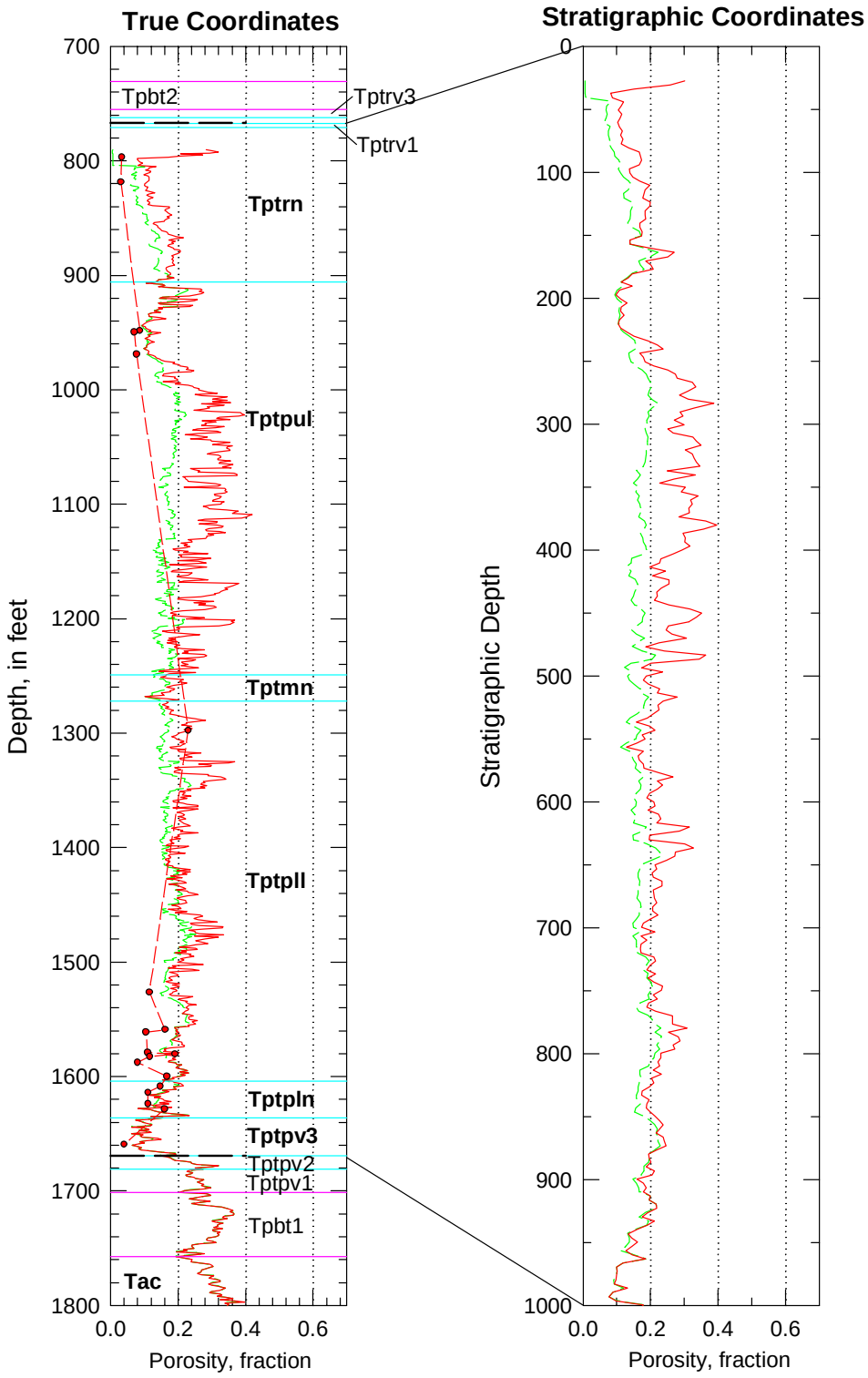

Figure B-11. Porosity data from the modern set of petrophysical logs in real-world and in stratigraphic coordinates for the TSw model unit in drillhole G-2.

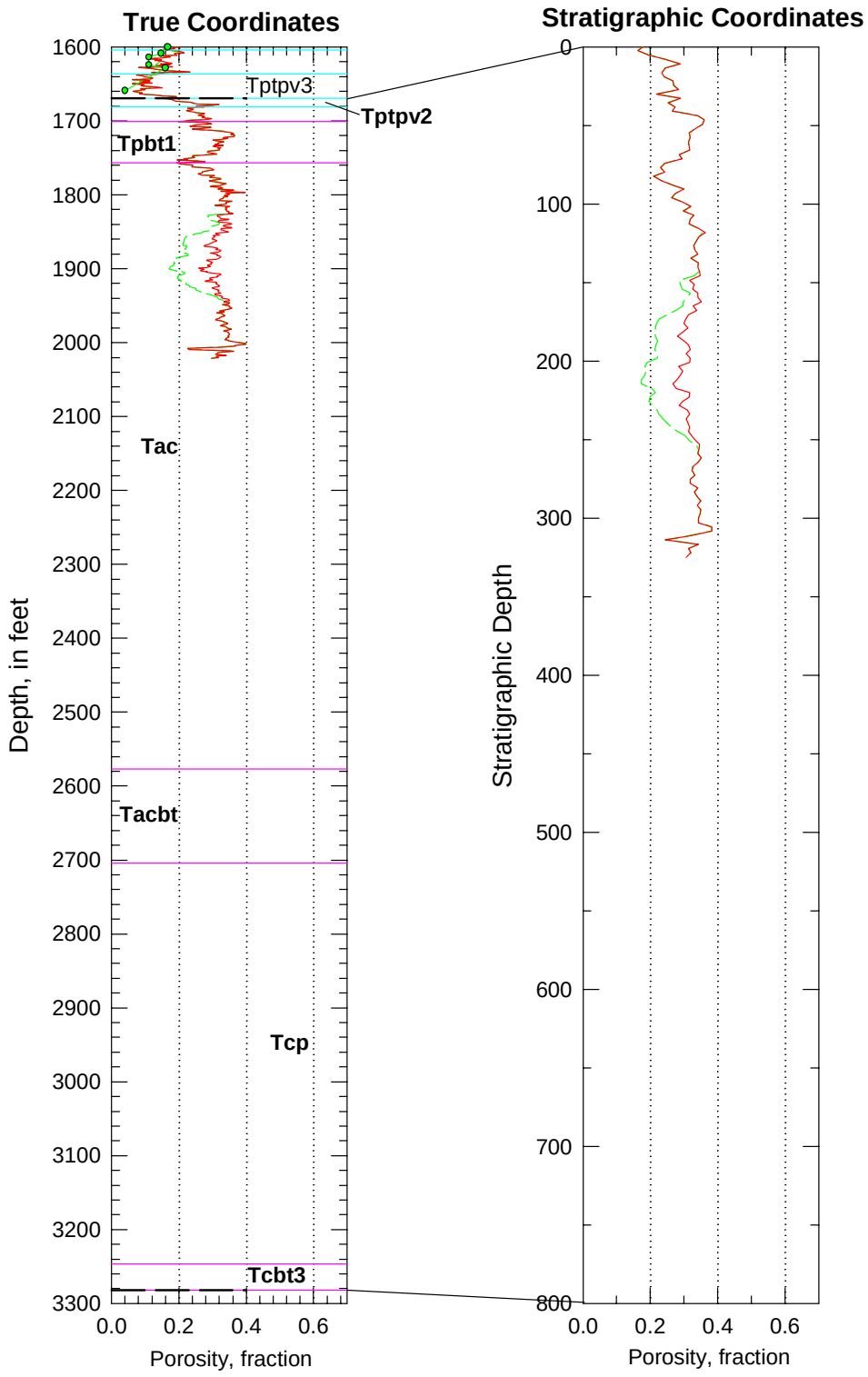

Figure B-12. Porosity data from the modern set of petrophysical logs for the combined CH–PP model unit in the G-2 drillhole.

Drillhole "G-3"

Drillhole "G-3" actually consists of two separate drillholes, both located on the same drillpad, one for the unsaturated zone and one for the interval below the static water level. The interval modeled as part of this report consists solely of the unsaturated portion of the hole, and thus the data are actually from drillhole GU-3

Petrophysical porosity data are available only from the older set of downhole geophysical logs, and these include principally total (or lithophysal) porosity values. Accordingly we have inserted a relatively systematically collected set of older (NQ) core porosity values to represent matrix porosity in the intervals from approximatley 500–675 and 775–1100 ft true depth that appear to be lithophysae-bearing, as indicated by the total porosity petrophysical trace. We have also substituted core values for matrix porosity in the lower vitrophyre unit of the TSw model unit from approximately 119–1270 ft true depth.

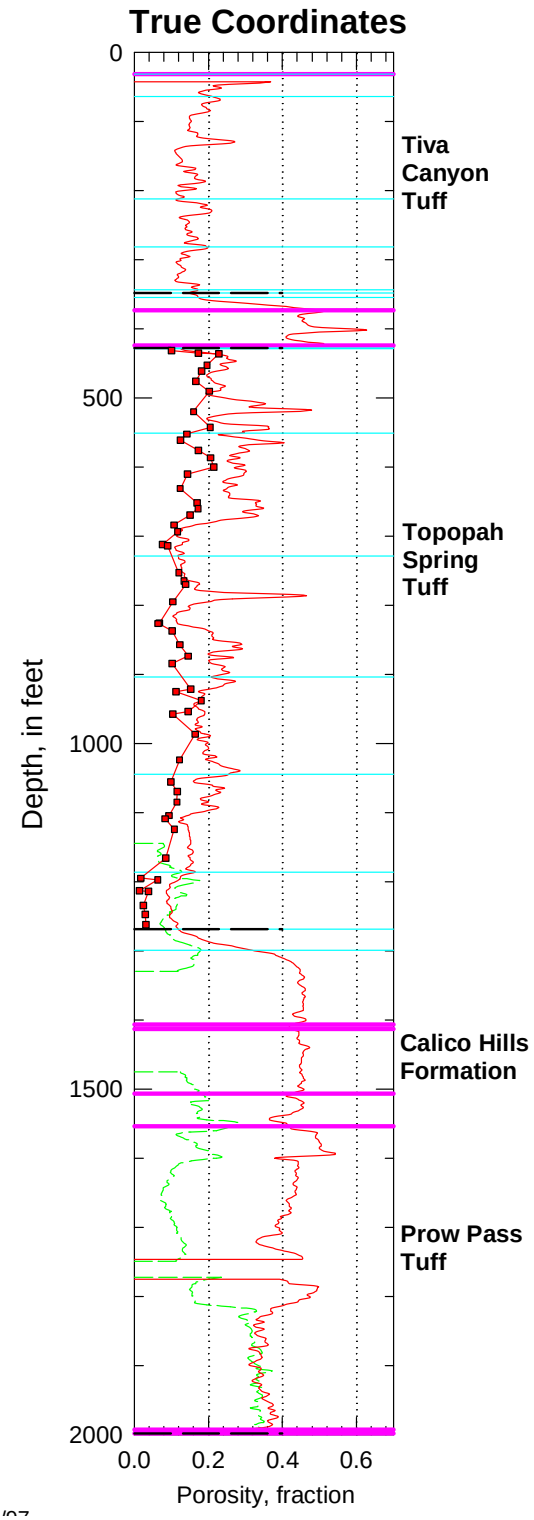

Figure B-13. Porosity data in true coordinates from drillhole G-3 for the entire drill hole through the top of the Bullfrog Tuff.

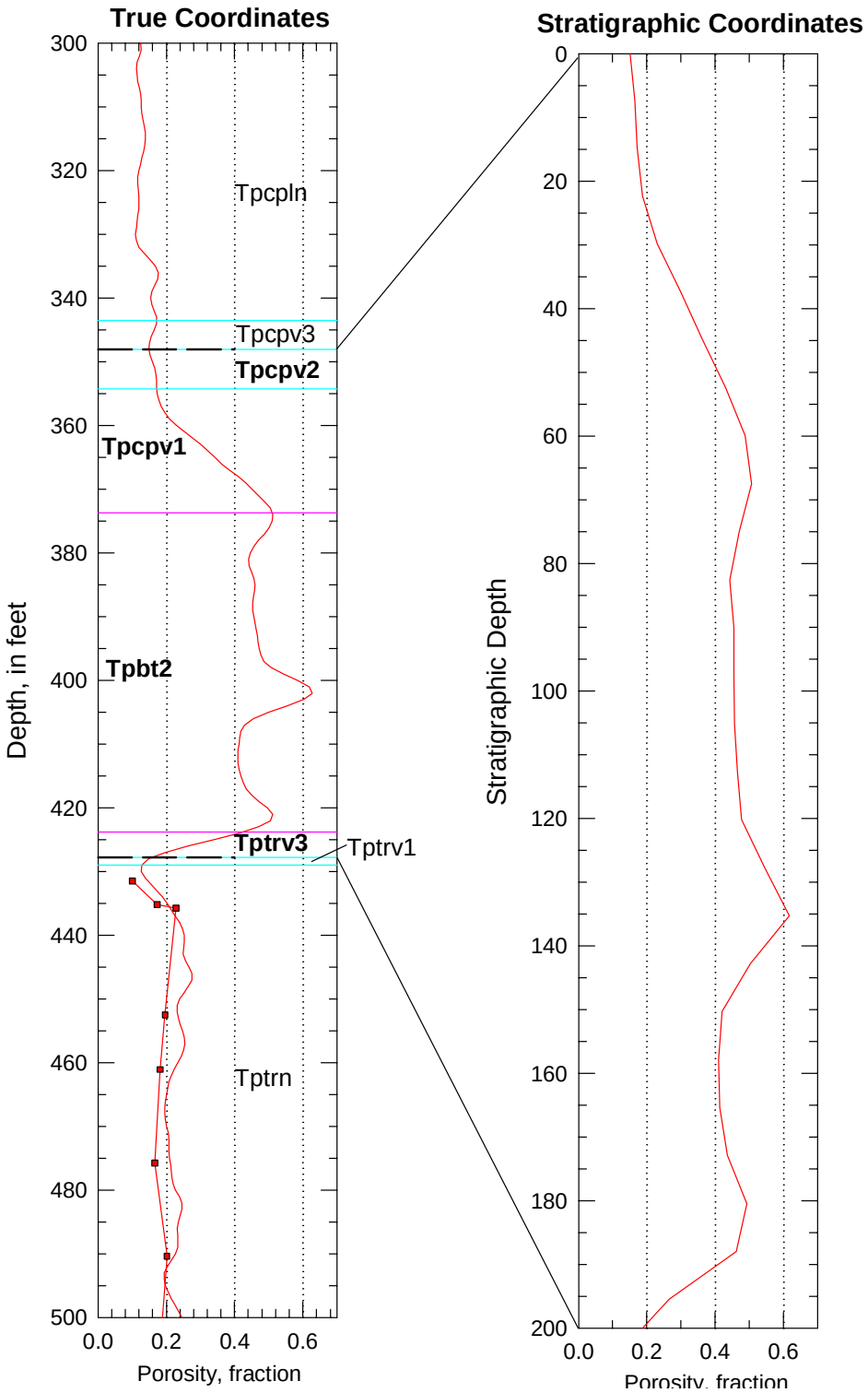

Figure B-14. Porosity data in real-world and stratigraphic coordinates for the PTn model unit for drillhole G-3.

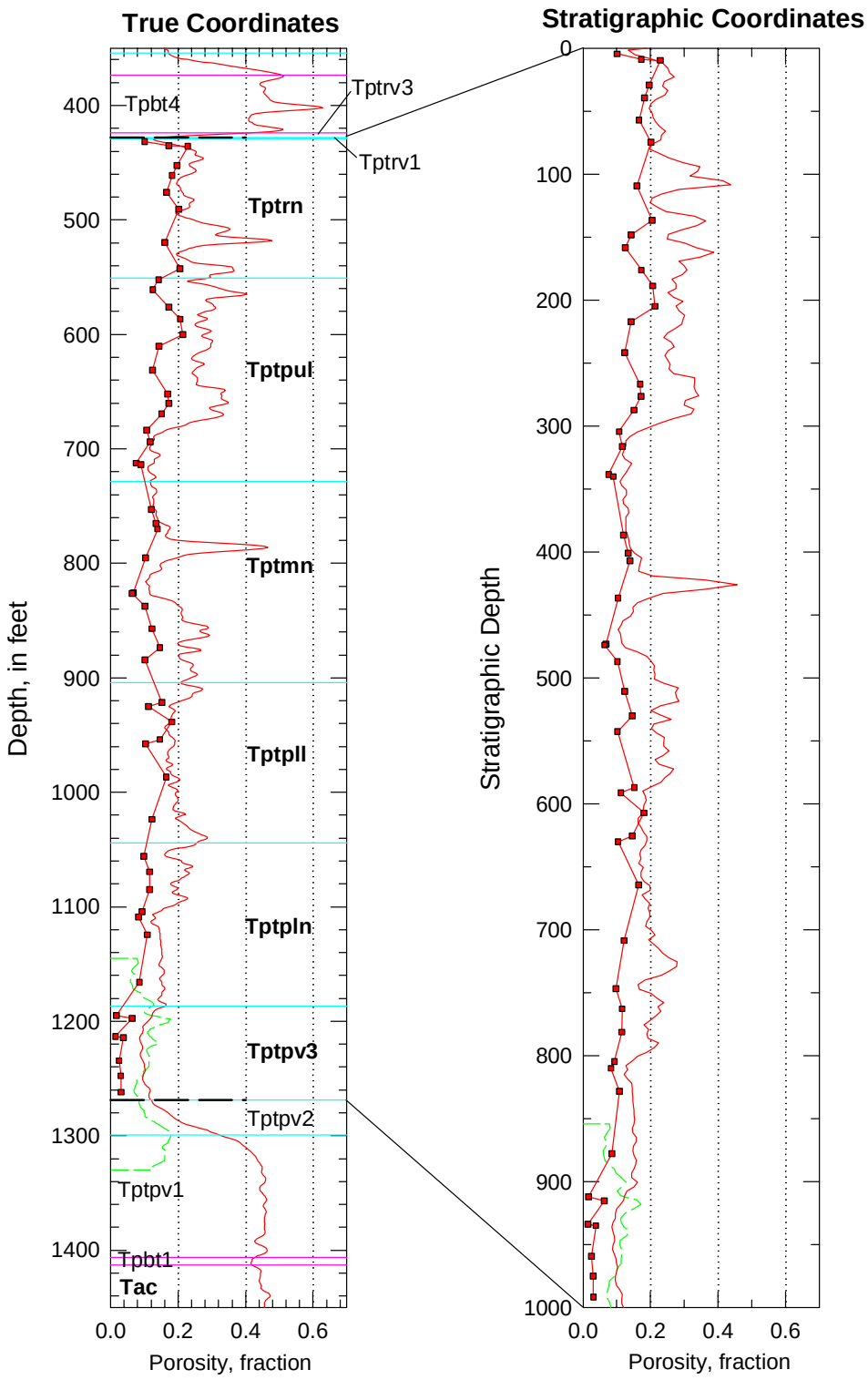

Figure B-15. Porosity data in real-world and stratigraphic coordinates for the TSw model unit in drillhole G-3.

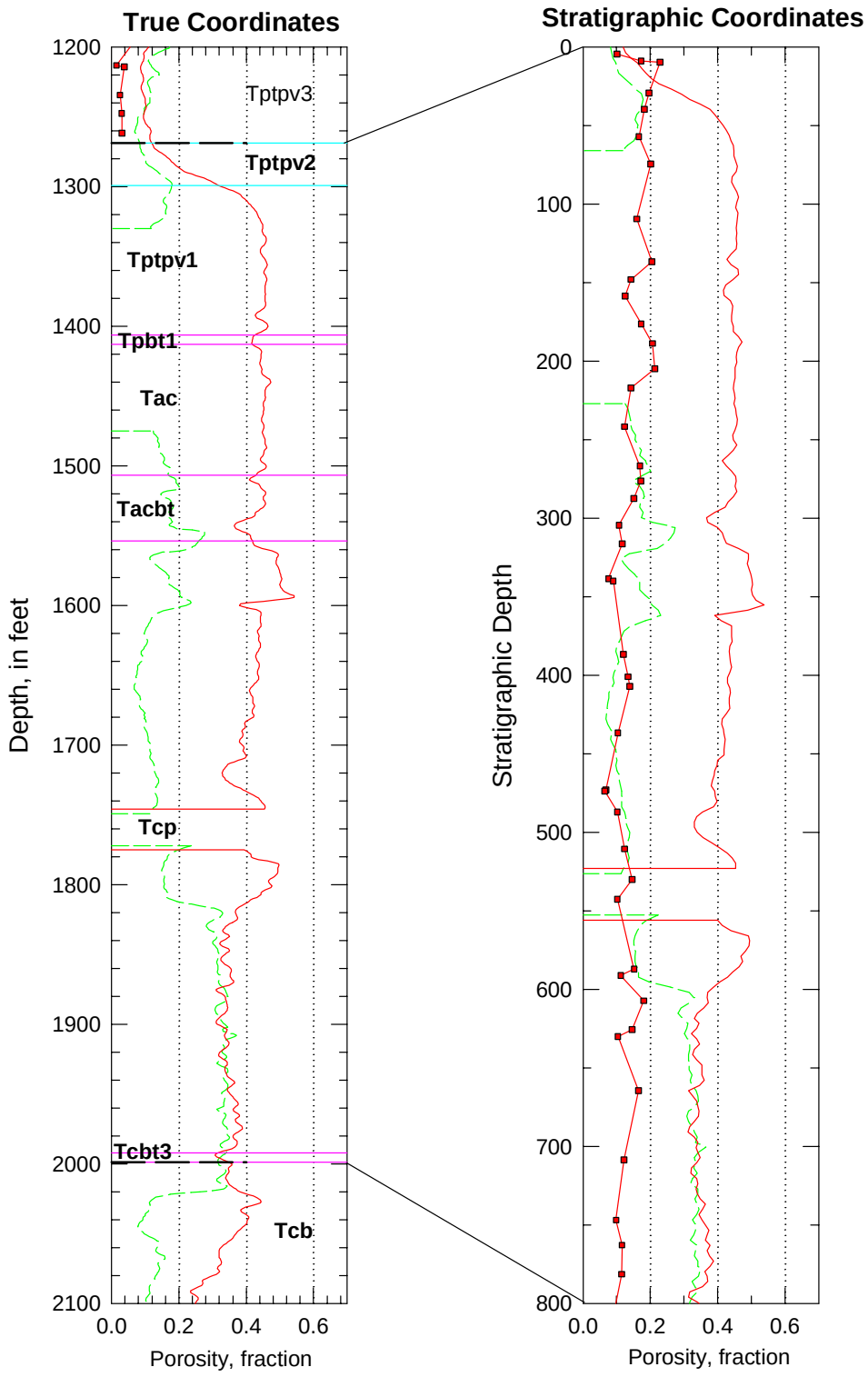

Figure B-16. Porosity data in real-world and in stratigraphic coordinates for the CH–PP model unit from drillhole G-3.

Drillhole G-4

Drillhole G-4 is the newest of the pre-site-characterization cored drillholes and is unquestionably the most systematically sampled of that set. Petrophysically derived porosity data are from the older set of downhole geophysical logs.

We have used the petrophysical porosity values throughout the hole, except that core porosity measurements have been substituted for matrix porosity in the inferred lithophysae-bearing intervals from 400–680 and from 770–1310 ft true depth.

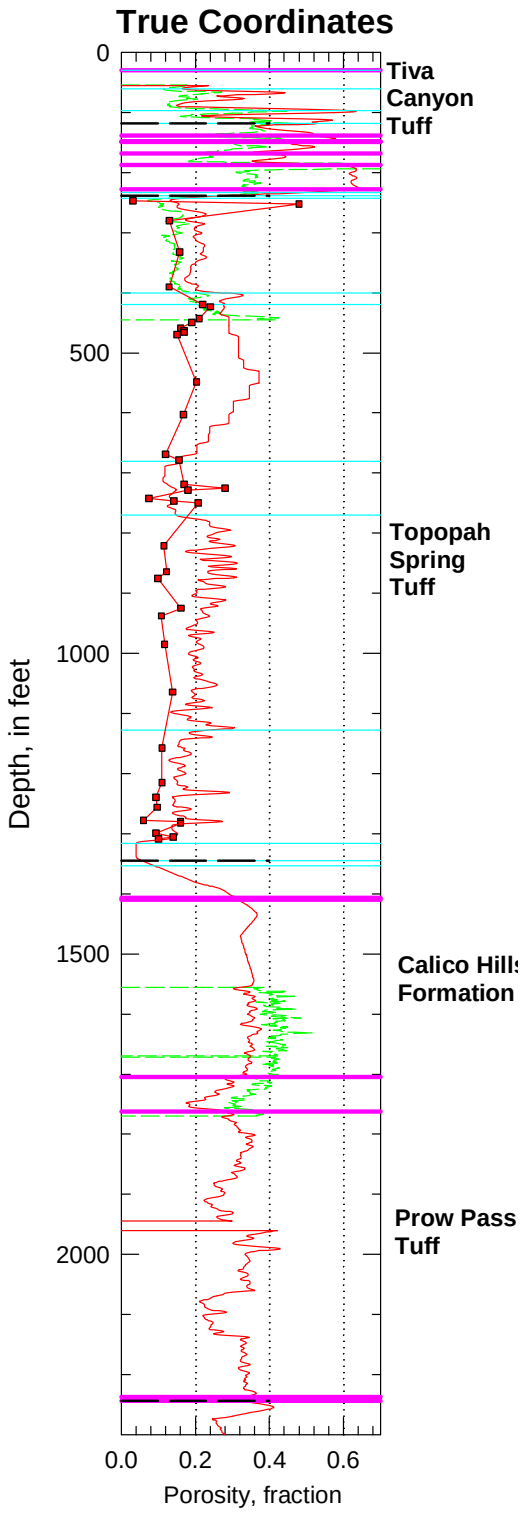

Figure B-17. Porosity data in true coordinates from drillhole G-4 for the entire drill hole through the top of the Bullfrog Tuff.

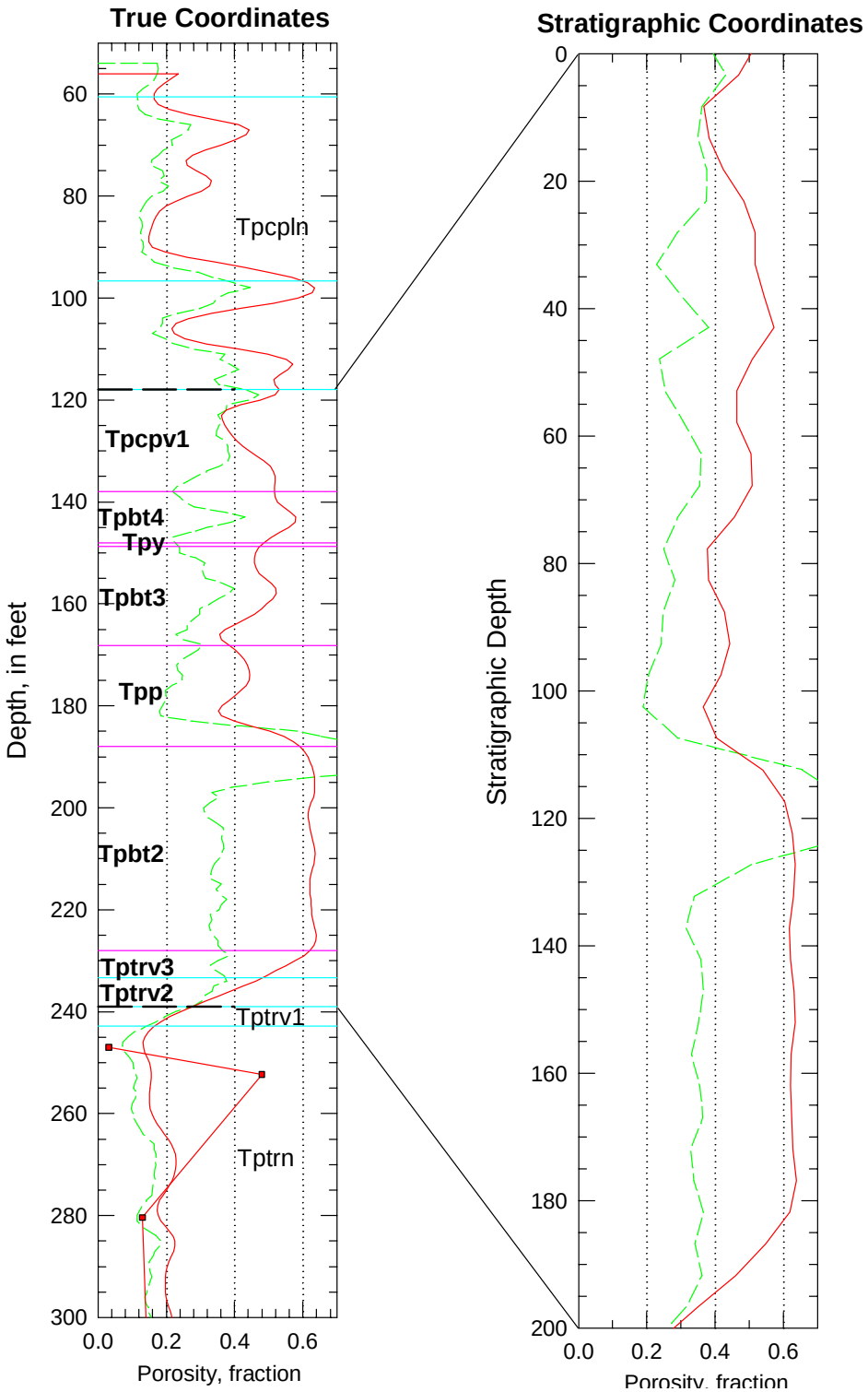

Figure B-18. Porosity data in real-world and in stratigraphic coordinates for the PTn model unit in drillhole G-4.

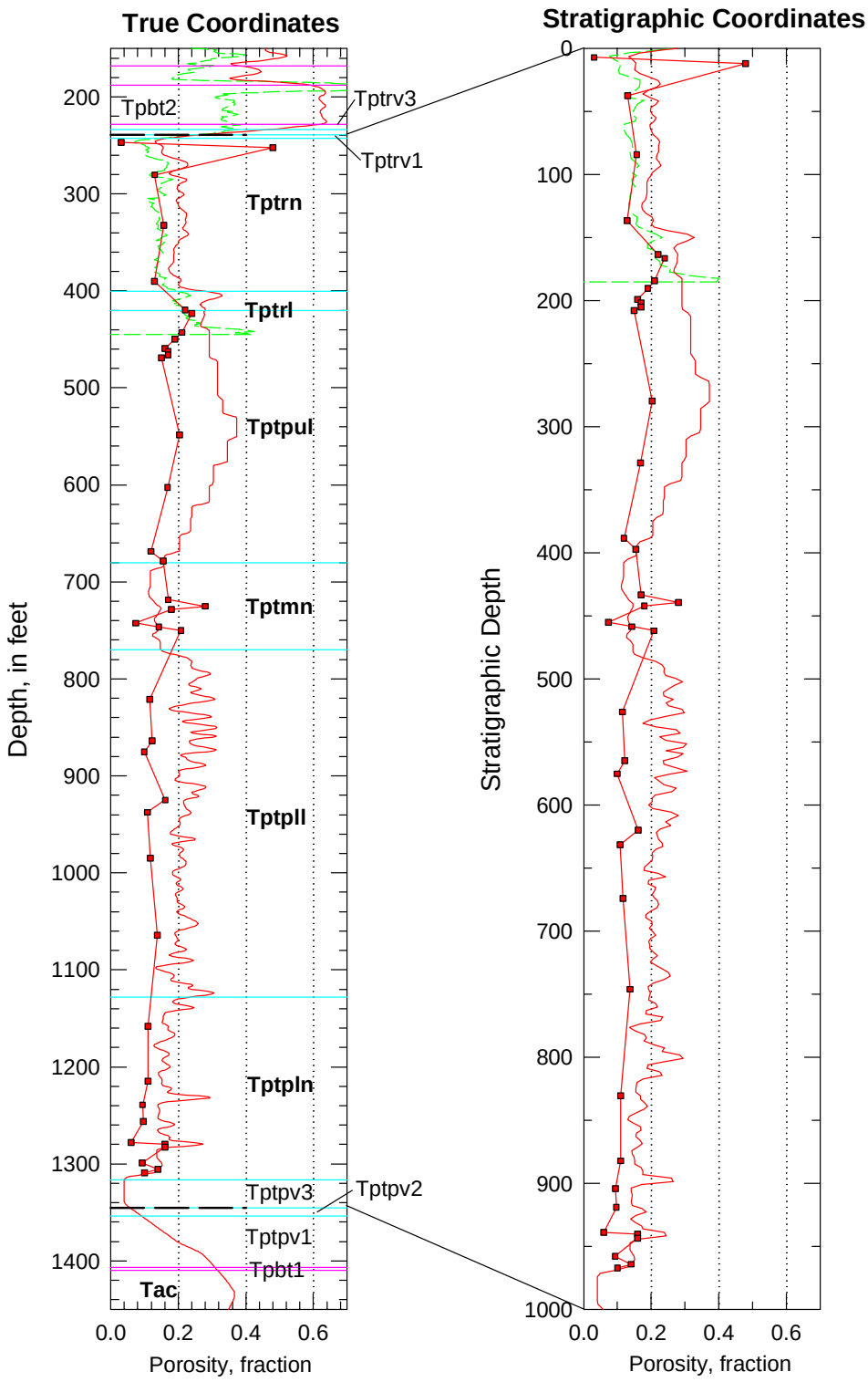

Figure B-19. Porosity data in real-world and in stratigraphic coordinates for the TSw model unit in drillhole G-4.

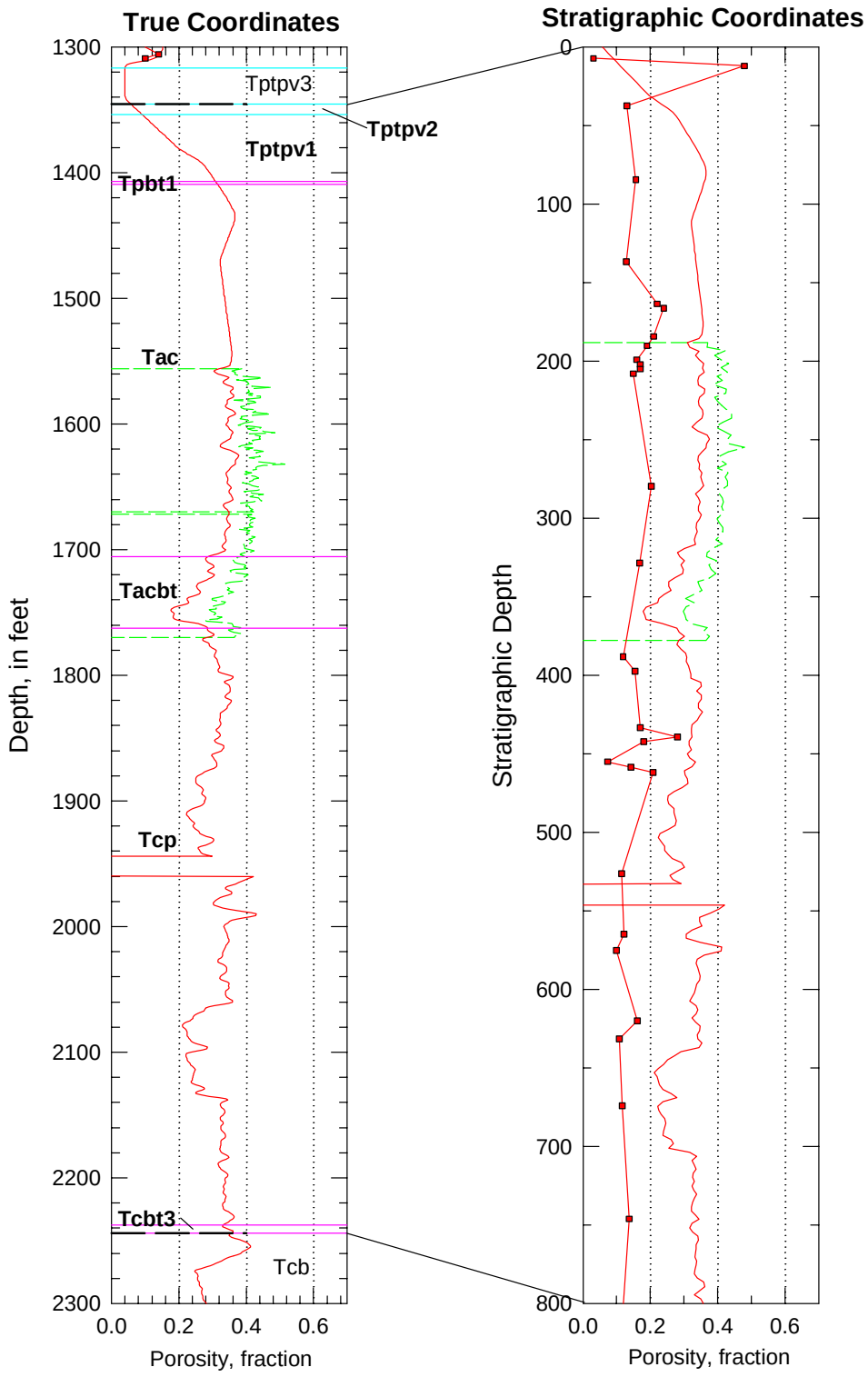

Figure B-20. Porosity data in real-world and in stratigraphic coordinates for the combined CH–PP model unit in drillhole G-4.

Drillhole H-1

Drillhole H-1 is a non-cored hydrologic hole for which the available petrophysically derived porosity value belong to the older set of geophysical data. Note that there are some abrupt shifts in the indicated porosity data within the PTn model unit (particularly noticeable in figure B-22). These values were not used in modeling the PTn unit.

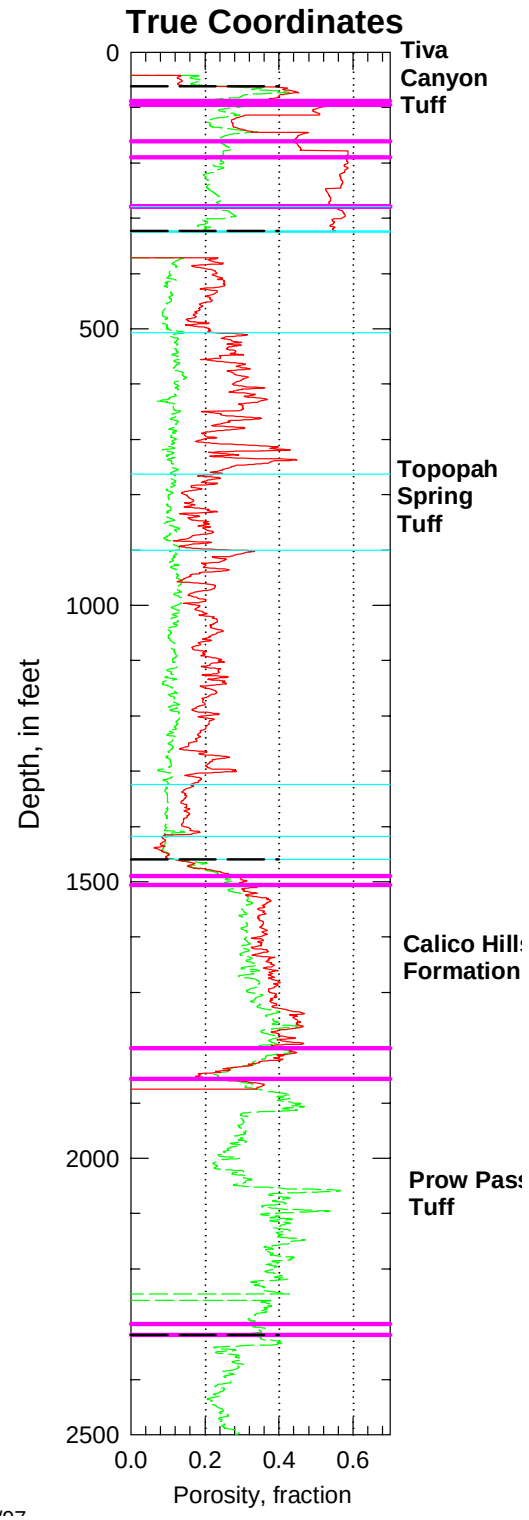

Figure B-21. Porosity data in true coordinates from drillhole H-1 for the entire drill hole through the top of the Bullfrog Tuff.

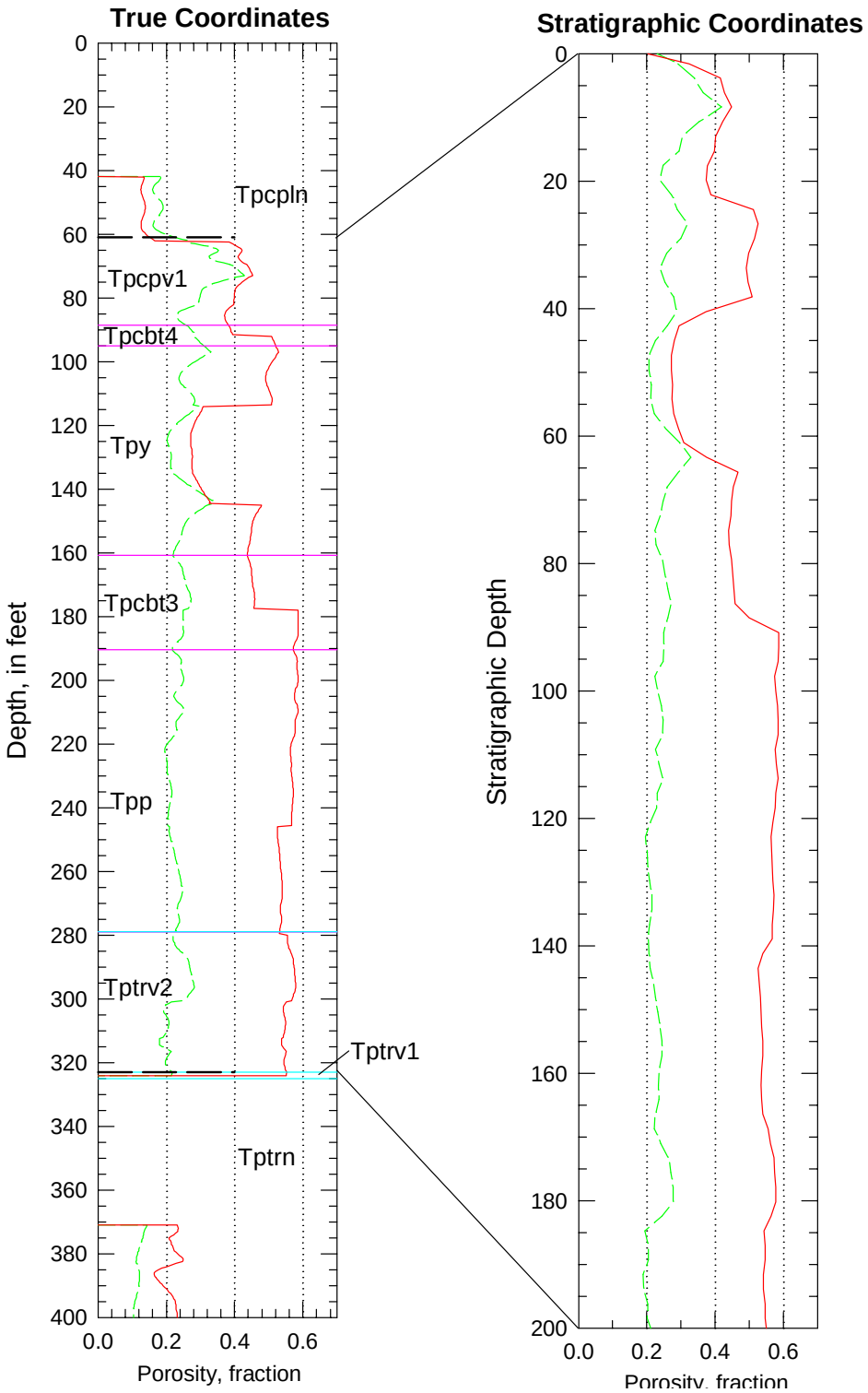

Figure B-22. Porosity data in real-world and in stratigraphic coordinates for the PTn model unit in drillhole H-1.

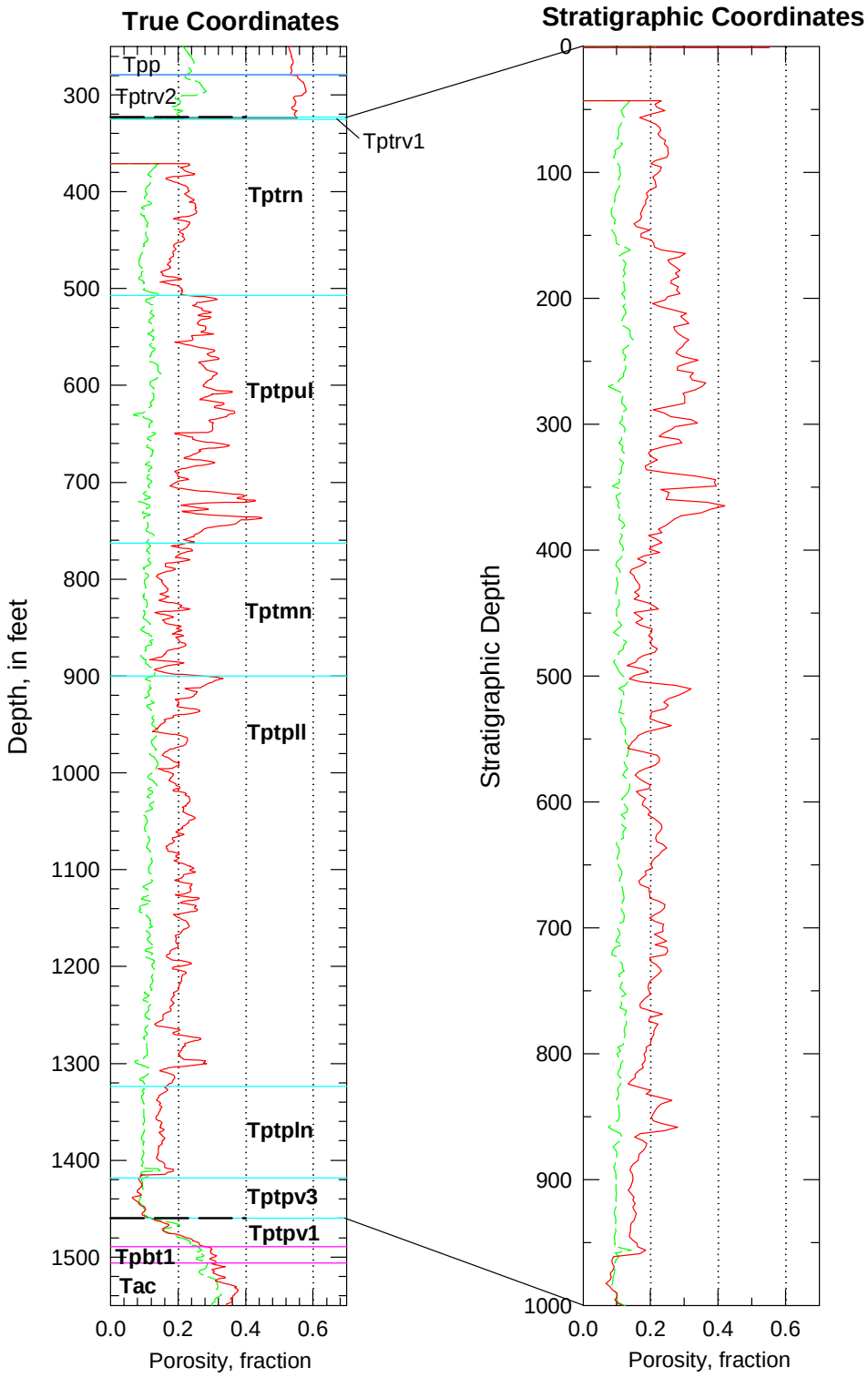

Figure B-23. Porosity data in real-world and in stratigraphic coordinates for the TSw model unit in drillhole H-1.

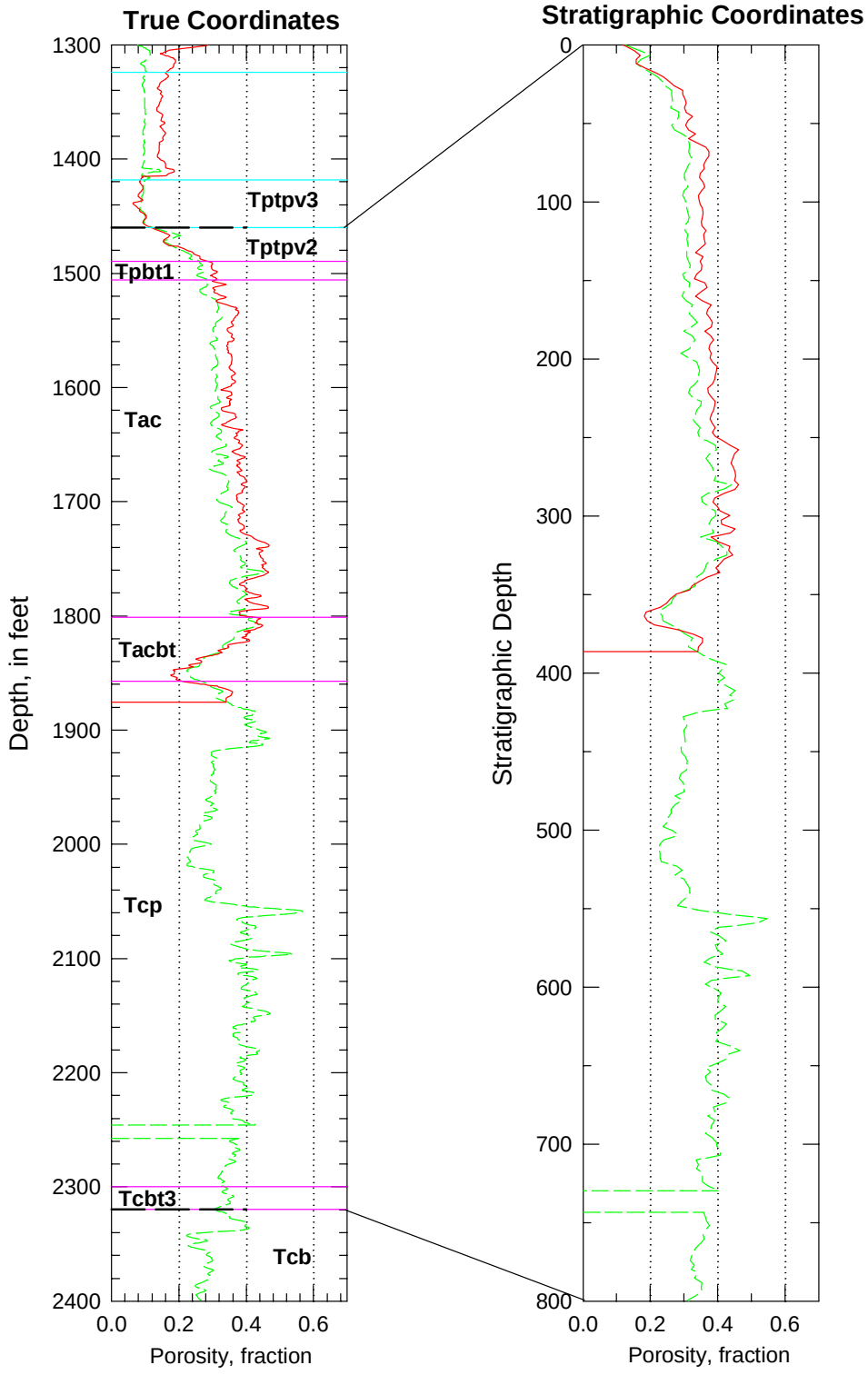

Figure B-24. Porosity data in real-world and in stratigraphic coordinates for the combined CH–PP model in drillhole H-1.

Drillhole H-3

Drillhole H-3 is an uncored hydrologic test hole located near the southern end of Yucca Mountain. Porosity data are based on downhole geophysical logs of the older suite.

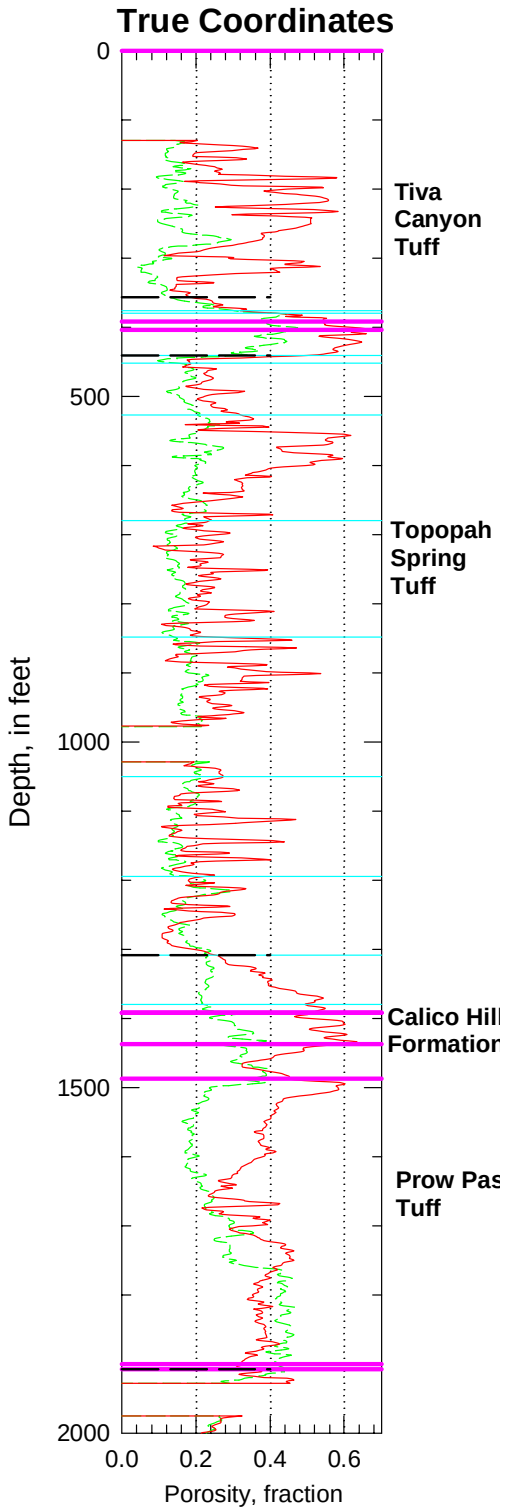

Figure B-25. Porosity data in true coordinates from drillhole H-3 for the entire drill hole through the top of the Bullfrog Tuff.

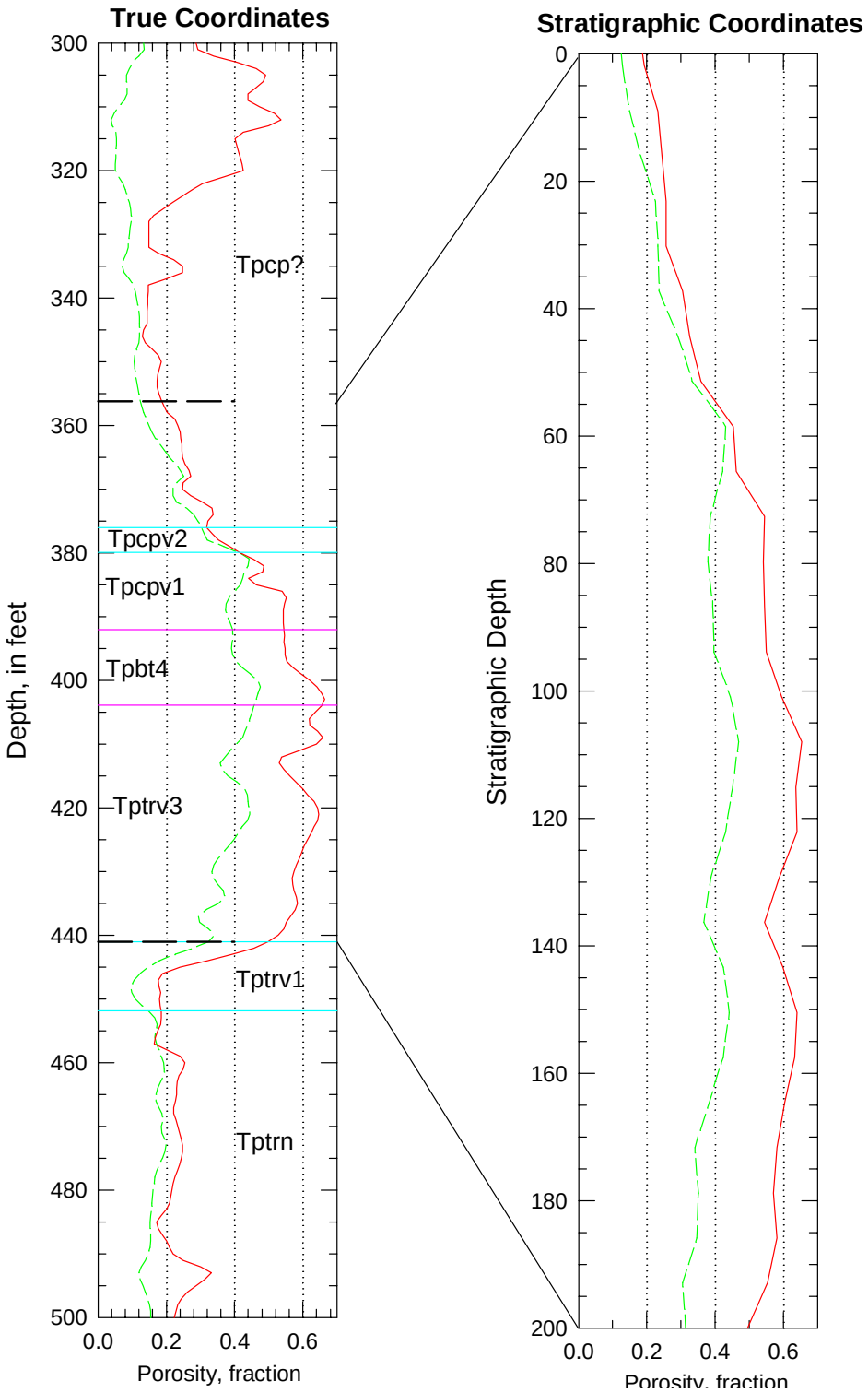

Figure B-26. Porosity data in real-world and in stratigraphic coordinates for the PTn model unit in drillhole H-3.

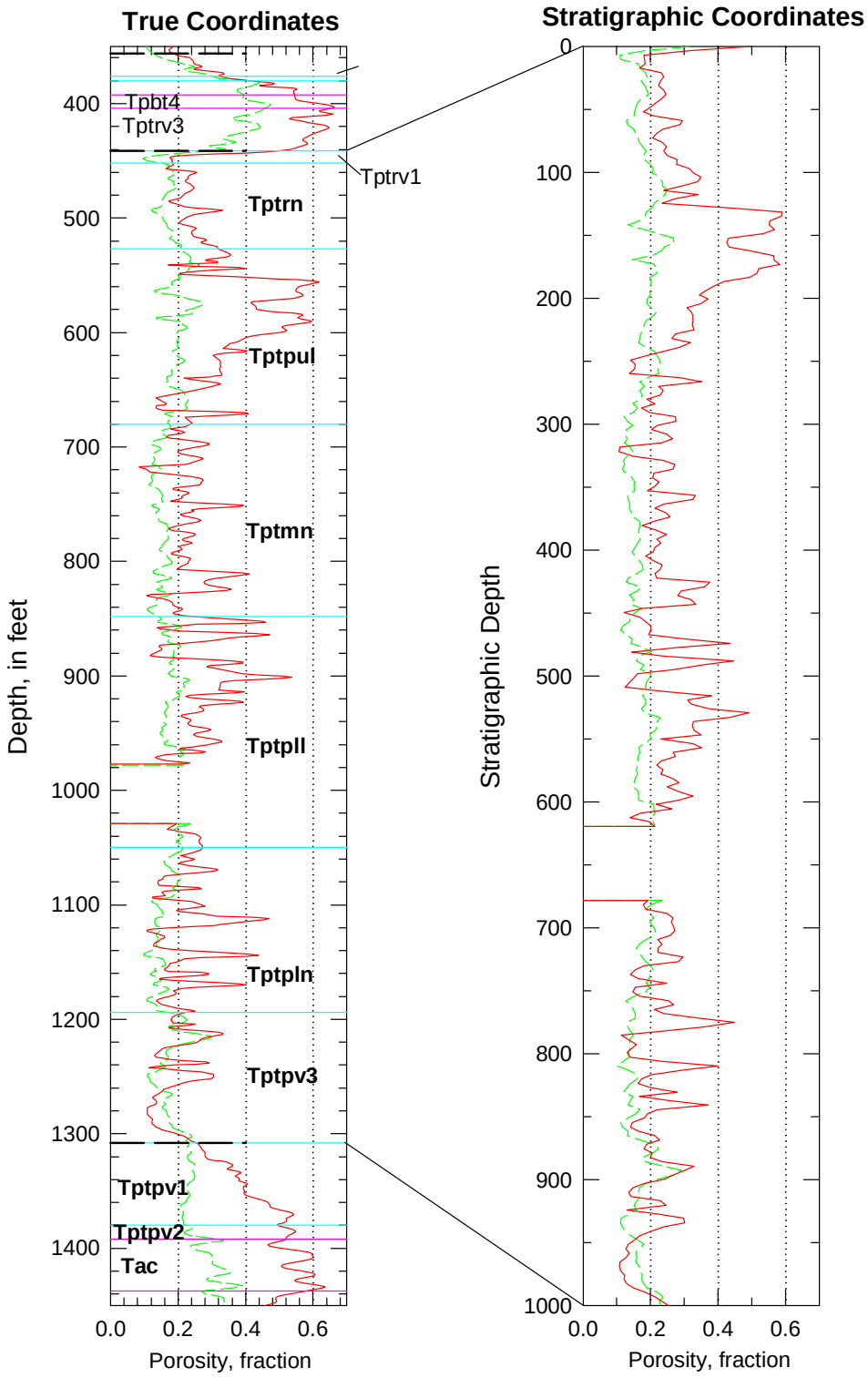

Figure B-27. Porosity data in real-world and in stratigraphic coordinates for the TSw model unit in drillhole H-3.

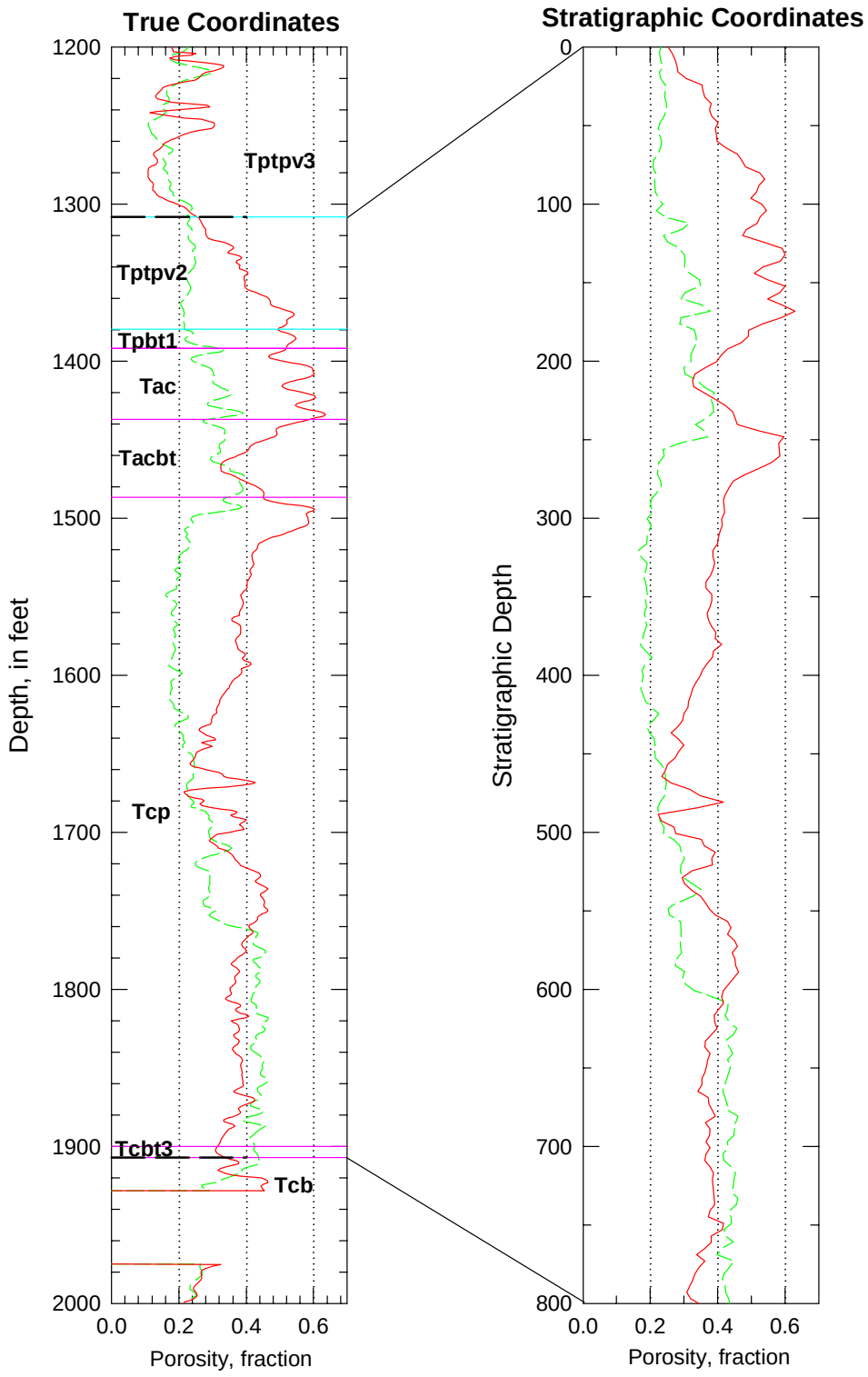

Figure B-28. Porosity data in real-world and in stratigraphic coordinates for the combined CH–PP model unit in drillhole H-3.

Drillhole H-4

Drillhole H-4 is an uncored hydrologic test hole. The available porosity values are petrophysically based and are derived from the older set of downhole geophysical logs.

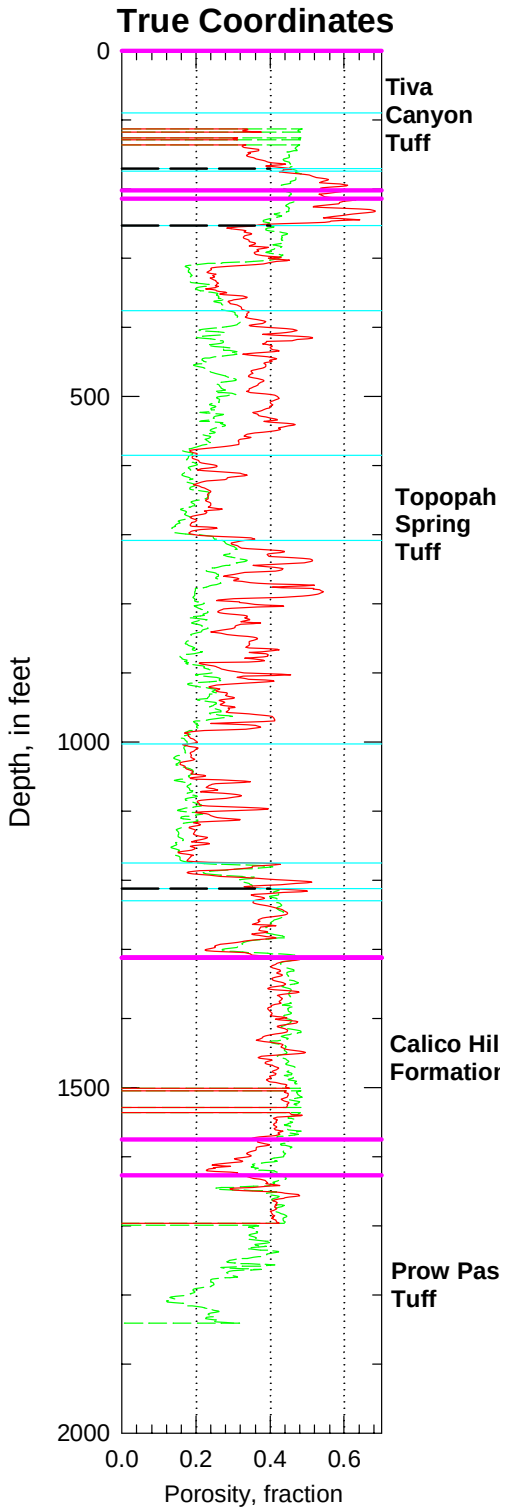

Figure B-29. Porosity data in true coordinates from drillhole H-4 for the entire drill hole through the top of the Bullfrog Tuff.

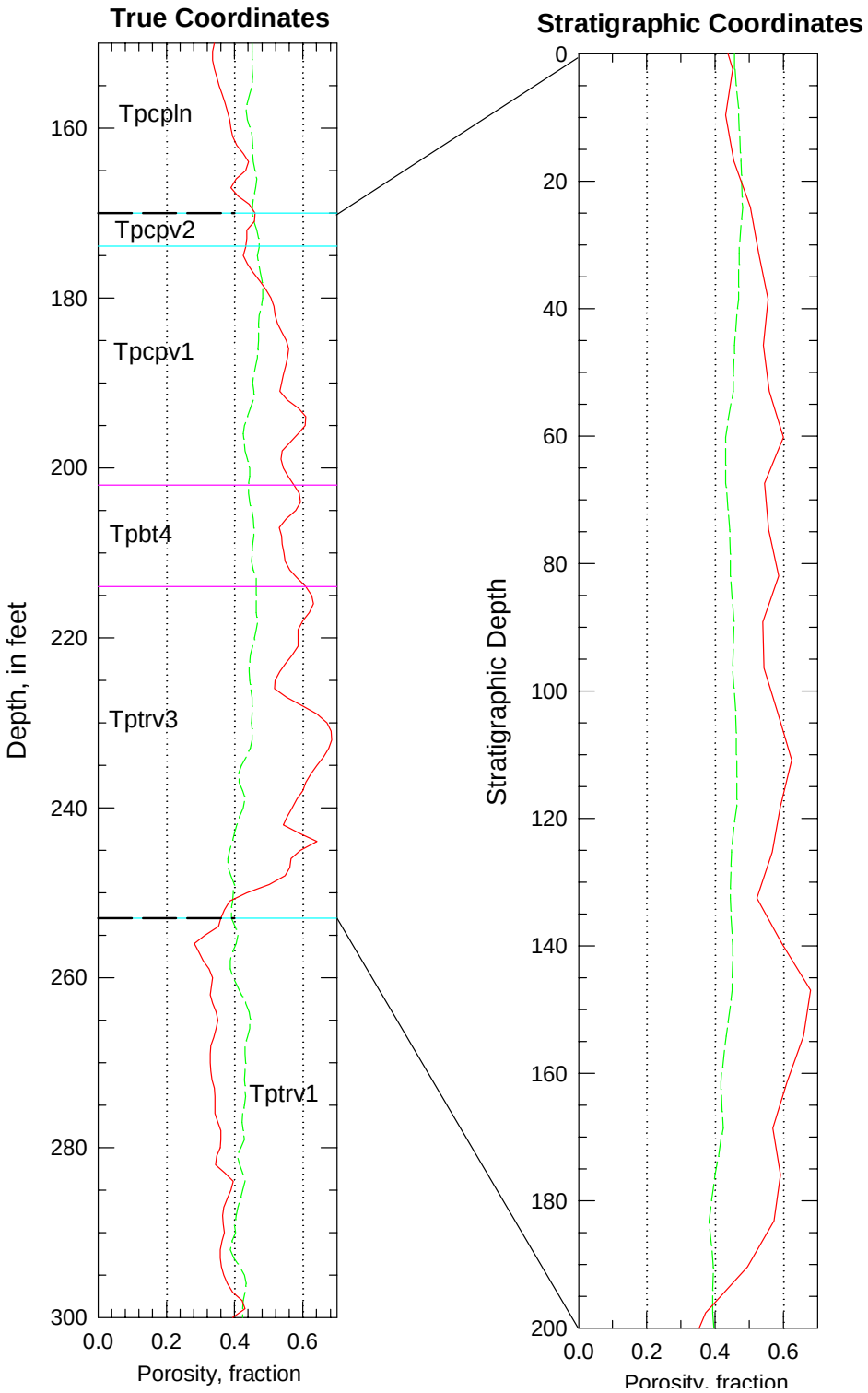

Figure B-30. Porosity data in real-world and in stratigraphic coordinates for the PTn model unit in drillhole H-4.

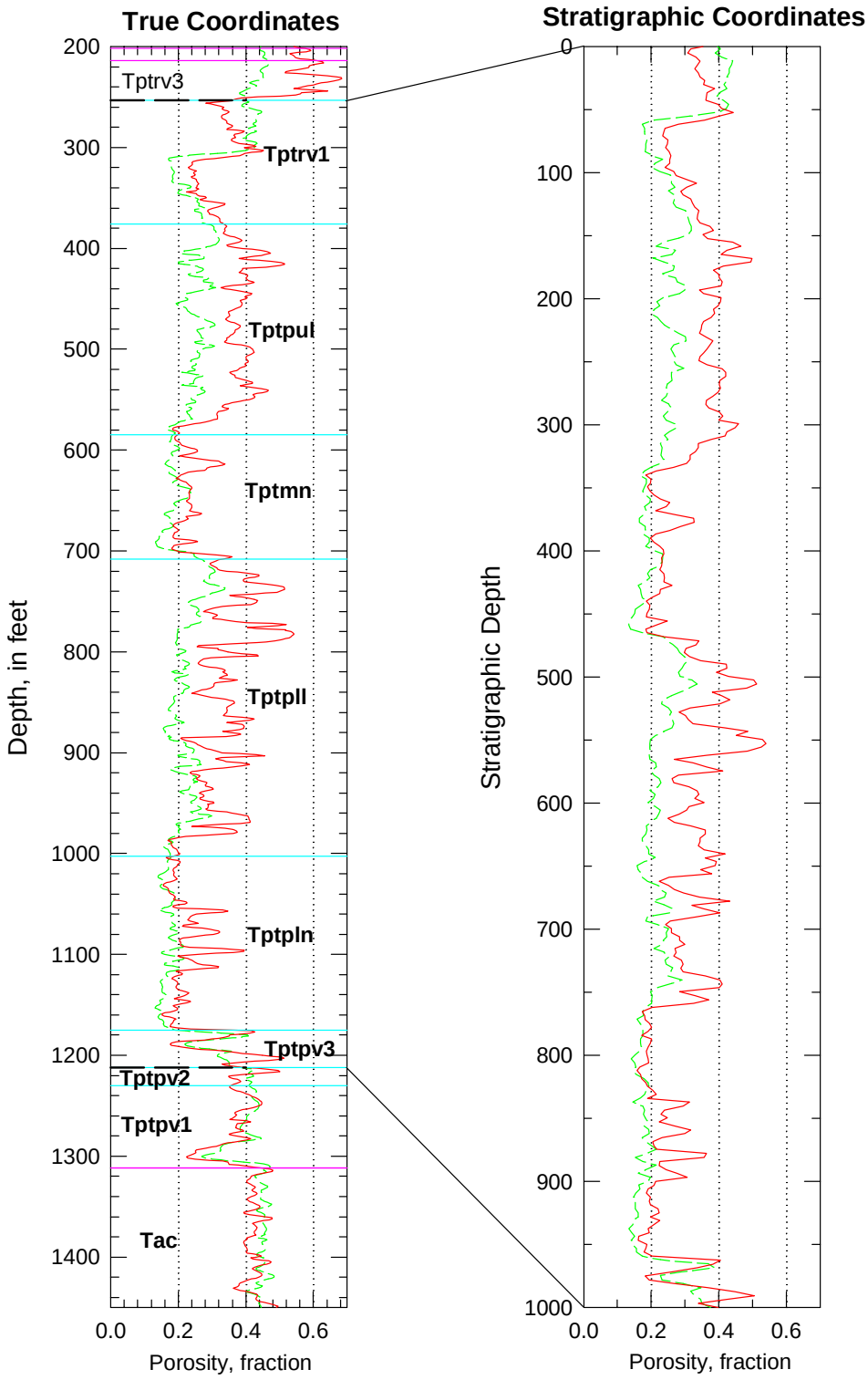

Figure B-31. Porosity data in real-world and in stratigraphic coordinates for the TSw model unit in drill hole H-4.

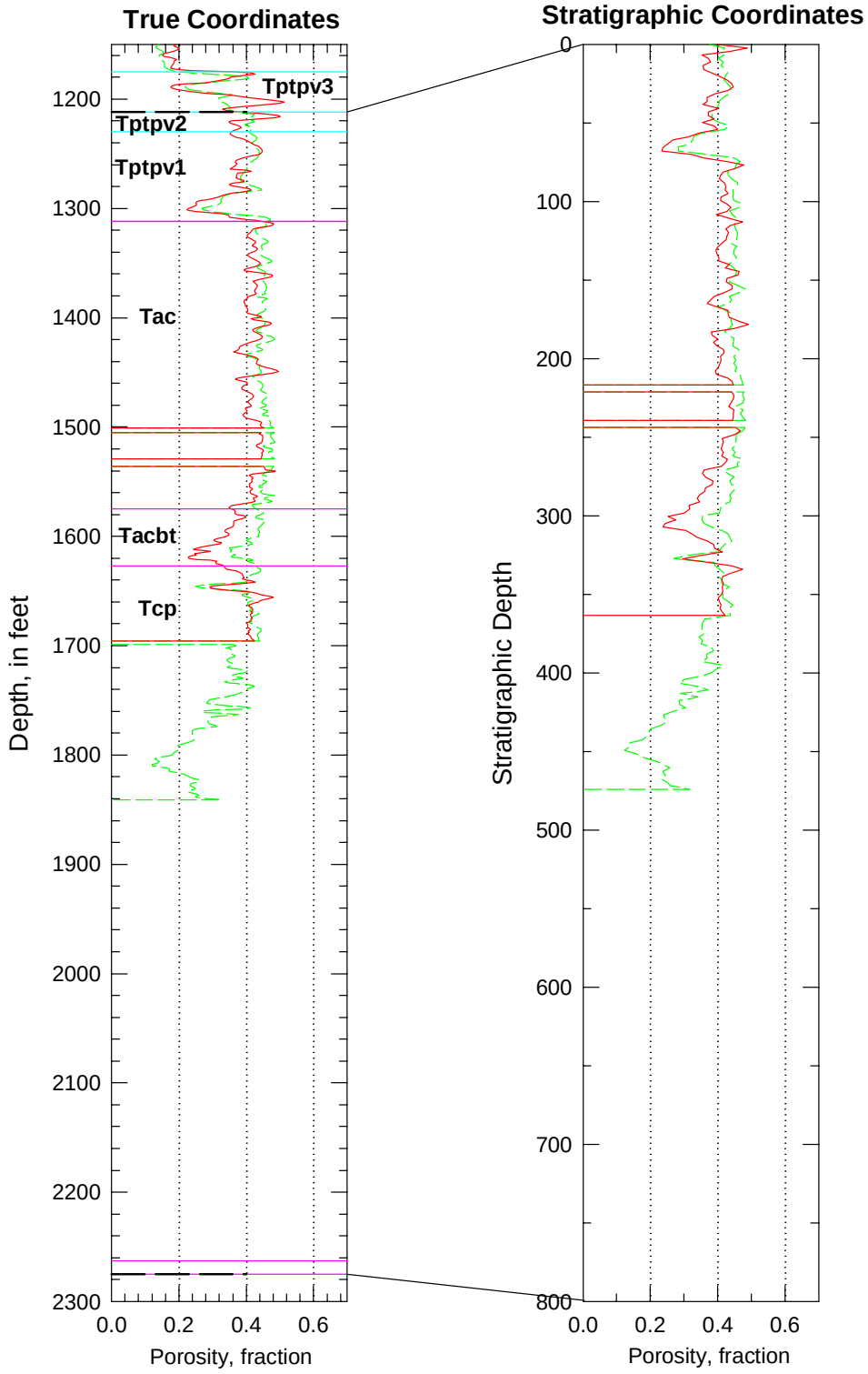

Figure B-32. Porosity data in real world and in stratigraphic coordinates for the combined CH–PP model unit in in drillhole H-4.

Drillhole H-5

Drillhole H-5 is an uncored hydrologic test hole located in the northern portion of the immediated repository block. The available porosity data are based on petrophysical calculations using data from the older set of downhole geophysical logs.

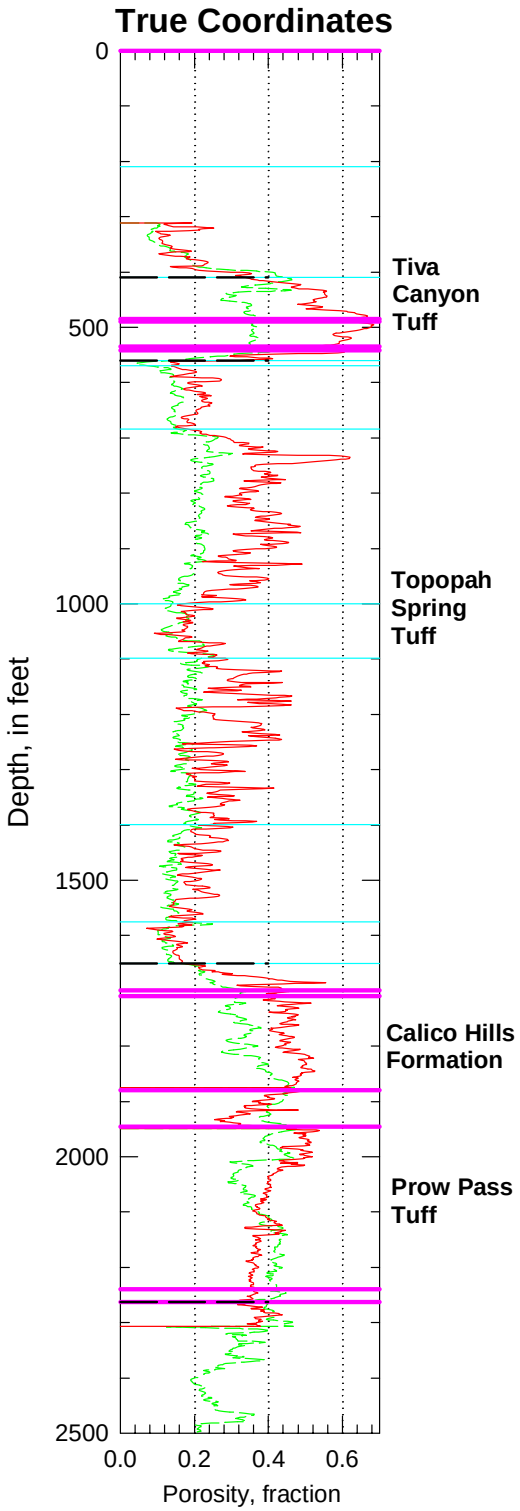

Figure B-33. Porosity data in true coordinates from drillhole H-5 for the entire drill hole through the top of the Bullfrog Tuff.

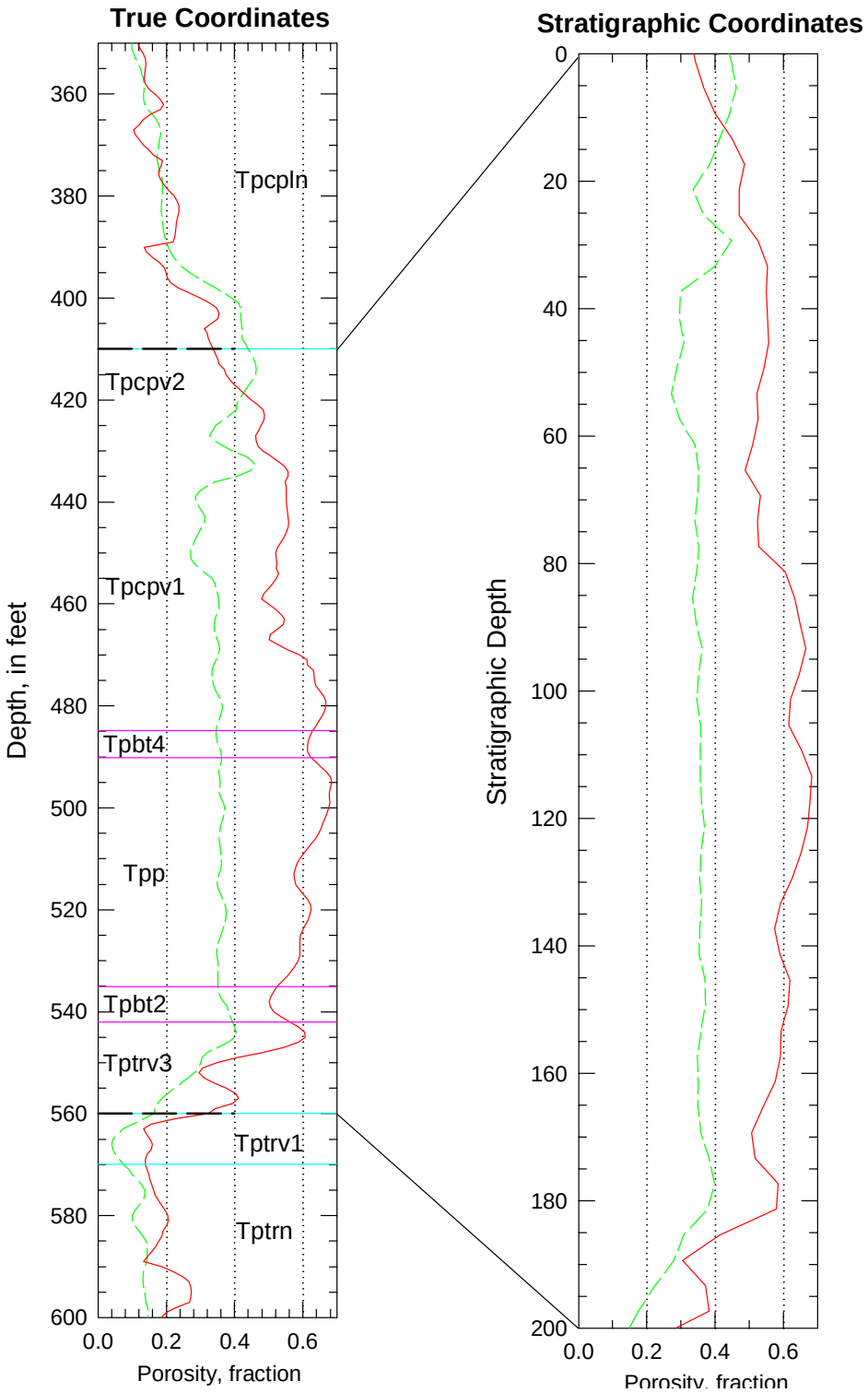

Figure B-34. Porosity data in real-world and in stratigraphic coordinates for the PTn model unit in drillhole H-5.

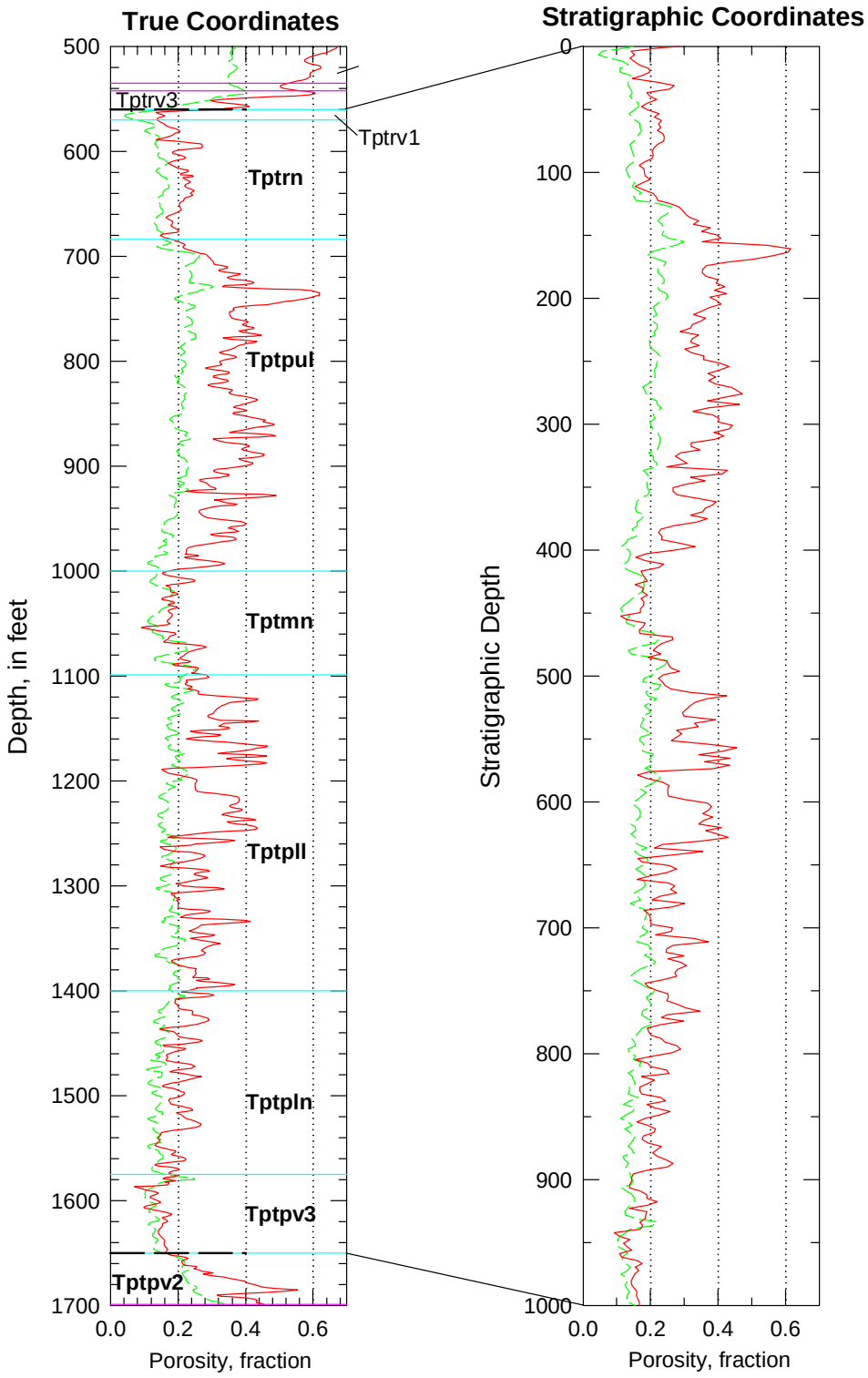

Figure B-35. Porosity data in real-world and in stratigraphic coordinates for the TSw model unit in drillhole H-5.

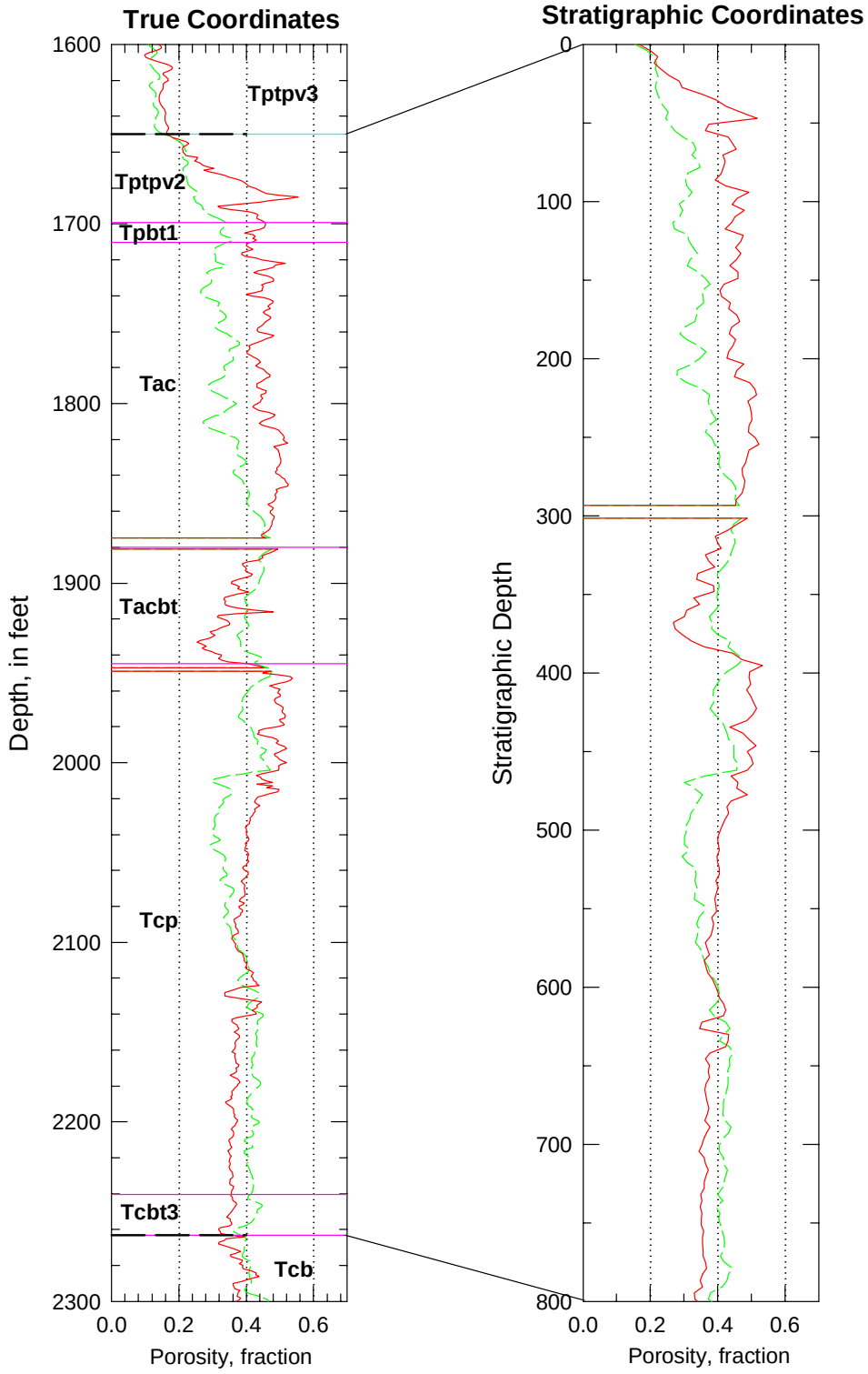

Figure B-36. Porosity data in real-world and in stratigraphic coordinates for the combined CH–PP model unit in drillhole H-5.

Drillhole H-6

Drillhole H-6 is an uncored hydrologic test hole located to the west of the immediate repository block on the downthrown side of the Solitario Canyon fault.

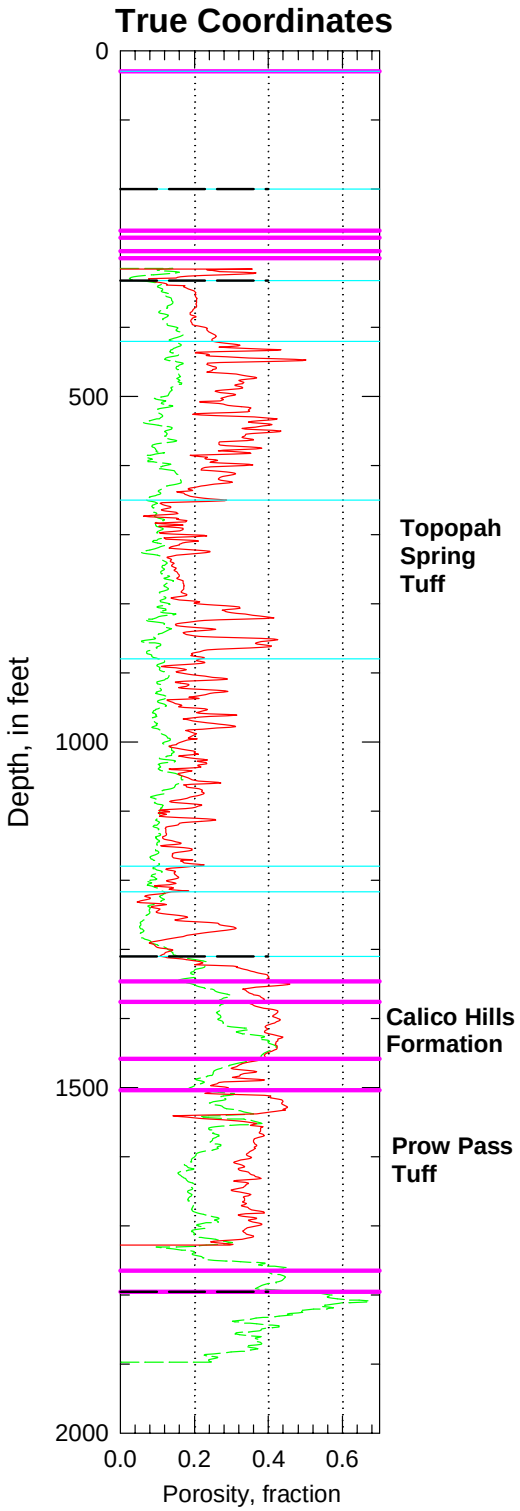

Figure B-37. Porosity data in true coordinates from drillhole H-6 for the entire drill hole through the top of the Bullfrog Tuff.

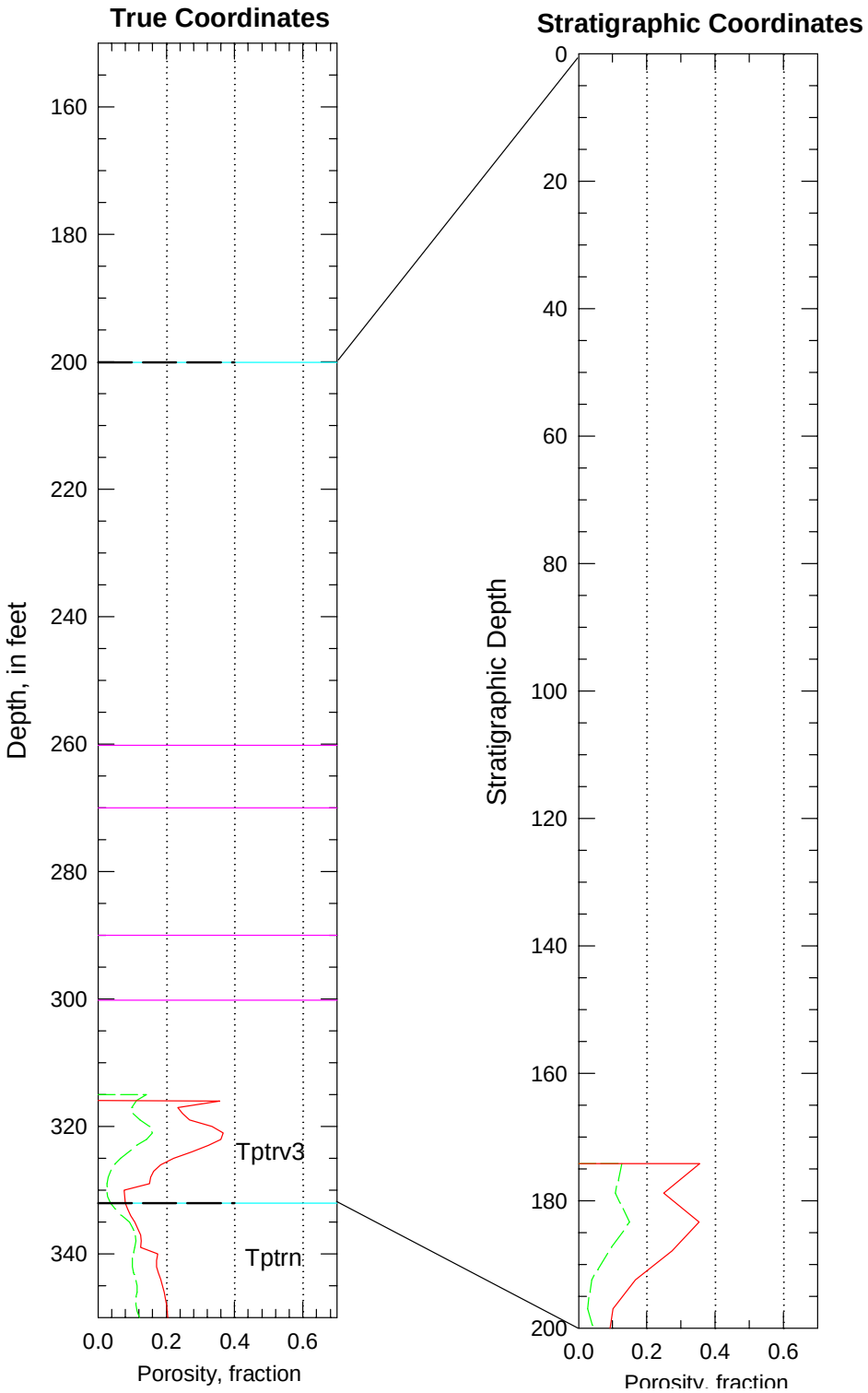

Figure B-38. Porosity data in real-world and in stratigraphic coordinates for the PTn model unit in drillhole H-6.

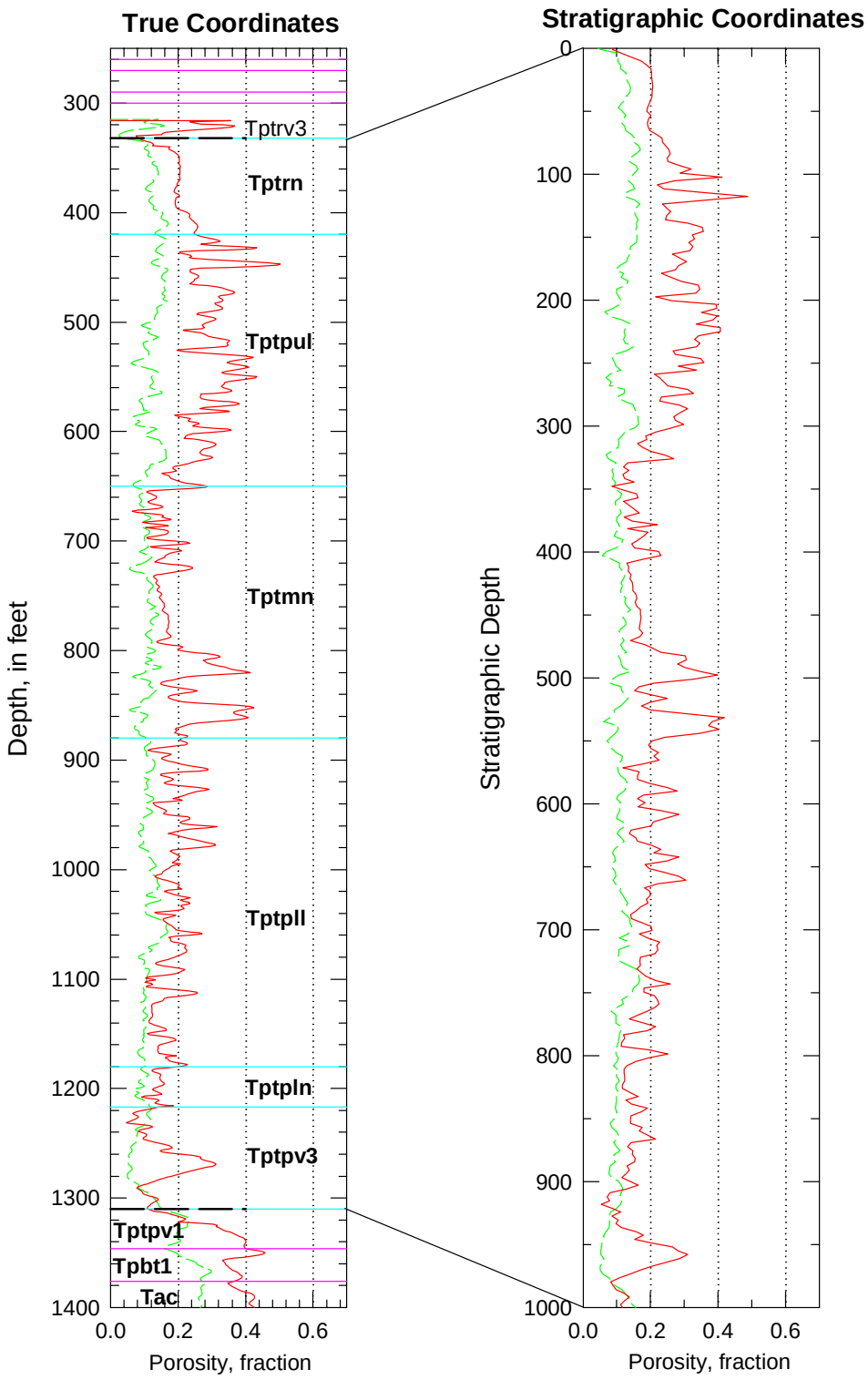

Figure B-39. Porosity data in real-world and in stratigraphic coordinates for the TSw model unit in drillhole H-6.

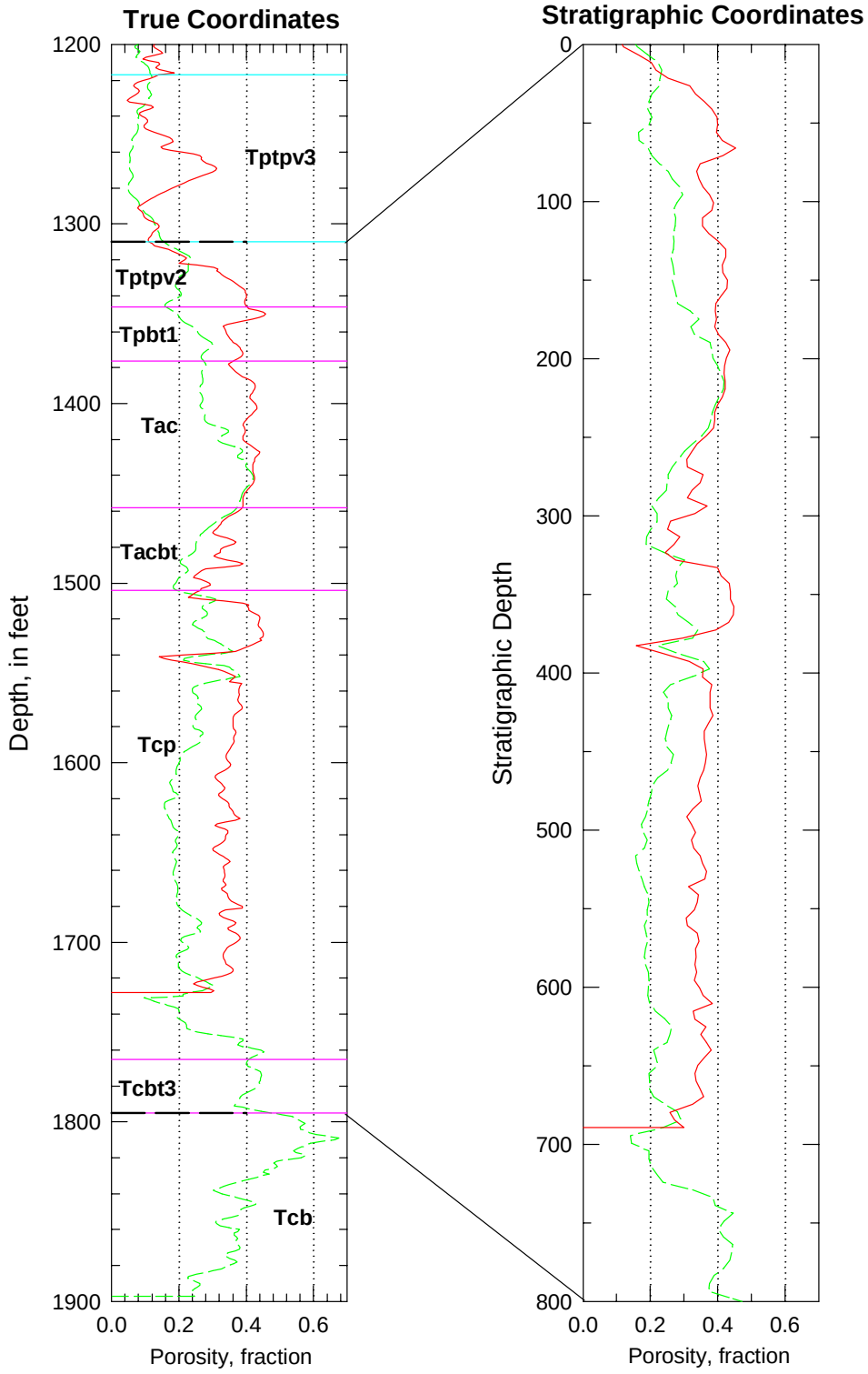

Figure B-40. Porosity data in real-world and in stratigraphic coordinates for the combined CH–PP model unit in drillhole H-6.

Drillhole NRG-4

Only petrophysical porosity values are available from the NRG-4 drillhole, and the geophysical logs were run only for a portion of the drillhole through the stratigraphic interval through which the Exploratory Studies Facility North Ramp decline was anticipated the pass. The data are usable essentially only for the PTn model unit. The approximately 200 ft of data from the TSw model unit were not used because of structural complications involved in projecting the lower contact of the Topopah Spring welded interval required to make the stratigraphic-coordinate transformation.

The lower contact of the PTn model unit appears reasonable geophysically. However, the upper contact with the overlying welded portion of the Tiva Canyon Tuff appears to have been picked too low in the Stratigraphic Compendium (Clayton, 1996), as the selected contact assigns rocks with an indicated porosities in excess of 20 percent to the overlying welded interval of the Tiva Canyon Tuff.

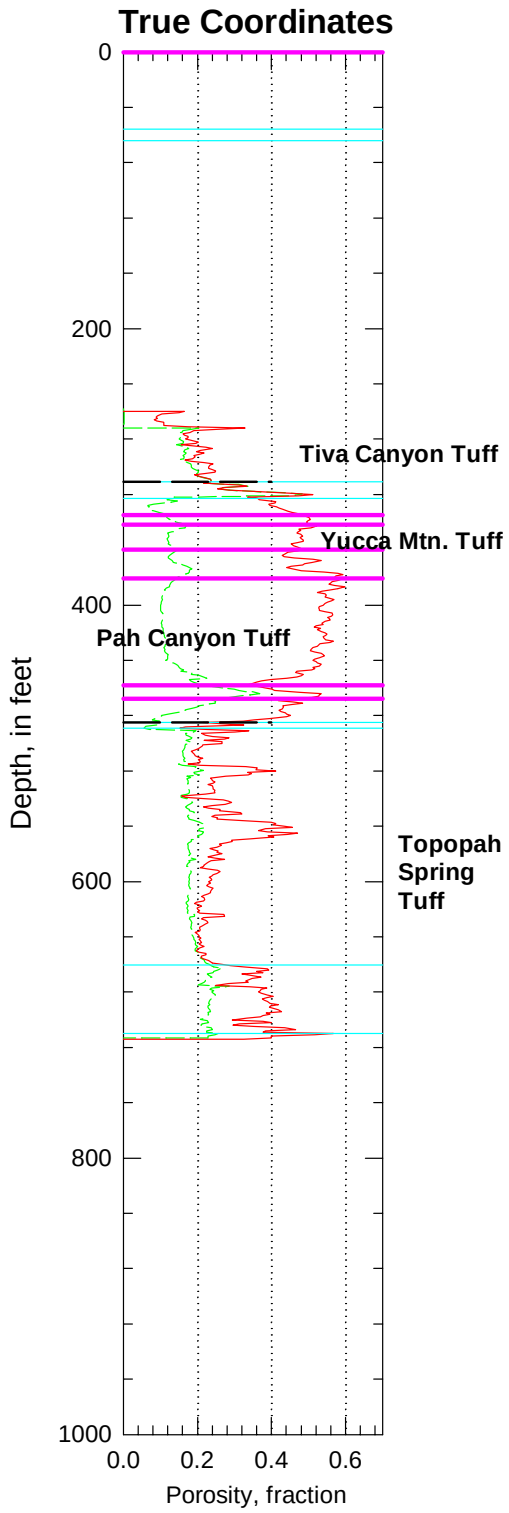

Figure B-41. Porosity data in true coordinates from drillhole NRG-4 for the entire drill hole.

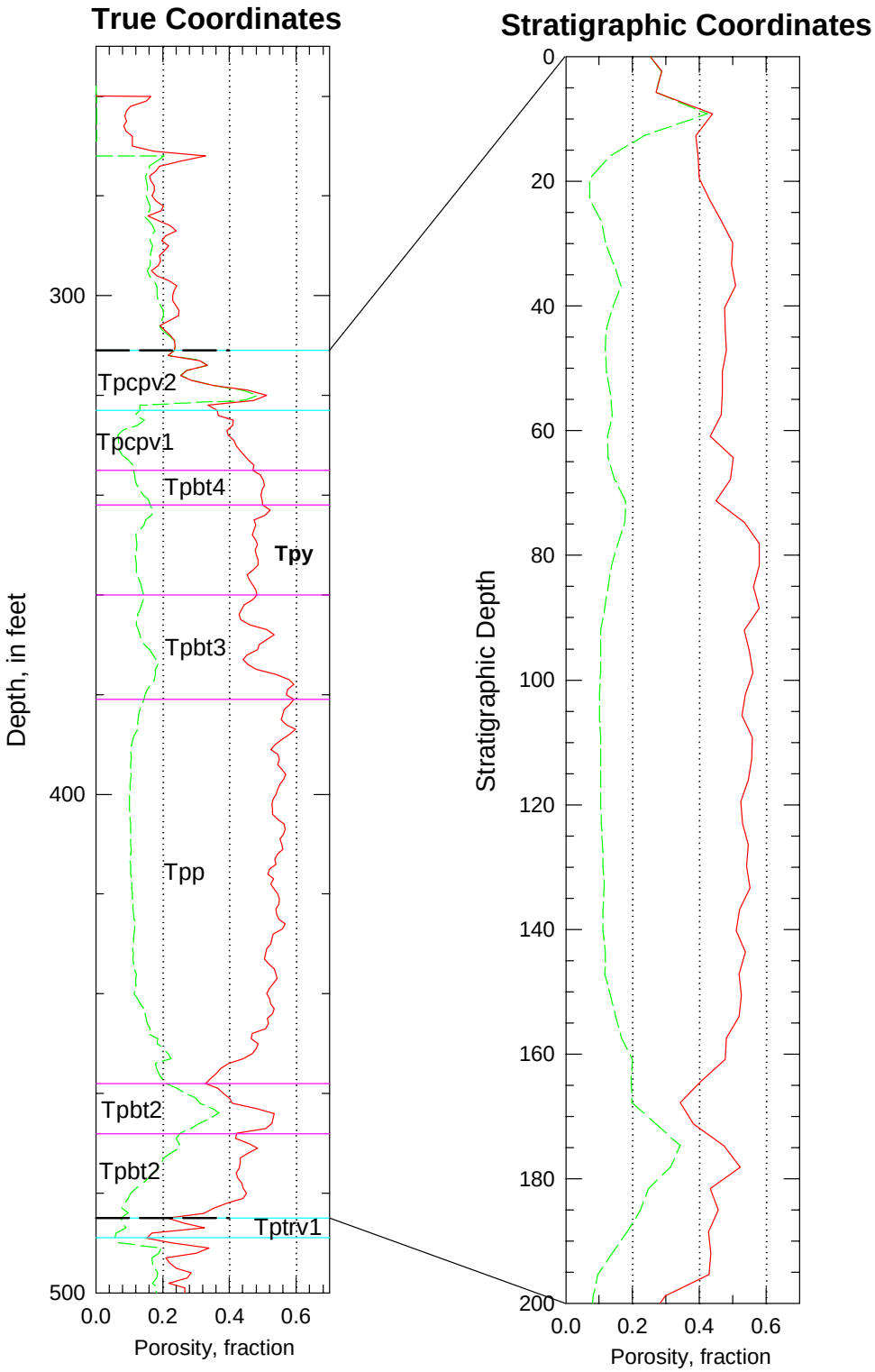

Figure B-42. Porosity data in real-world and in stratigraphic coordinates for the PTn model unit in drillhole NRG-4.

Drillhole NRG-5

Only petrophysical porosity values are available for the NRG-5 drillhole, and the geophysical logs were run only through the portion of the Topopah Spring Tuff through which the ESF North Ramp decline was anticipated to pass at the time the hole was drilled. In fact, the North Ramp passed the vicinity of hole NRG-5 at a redesigned depth of approximately 500 ft.

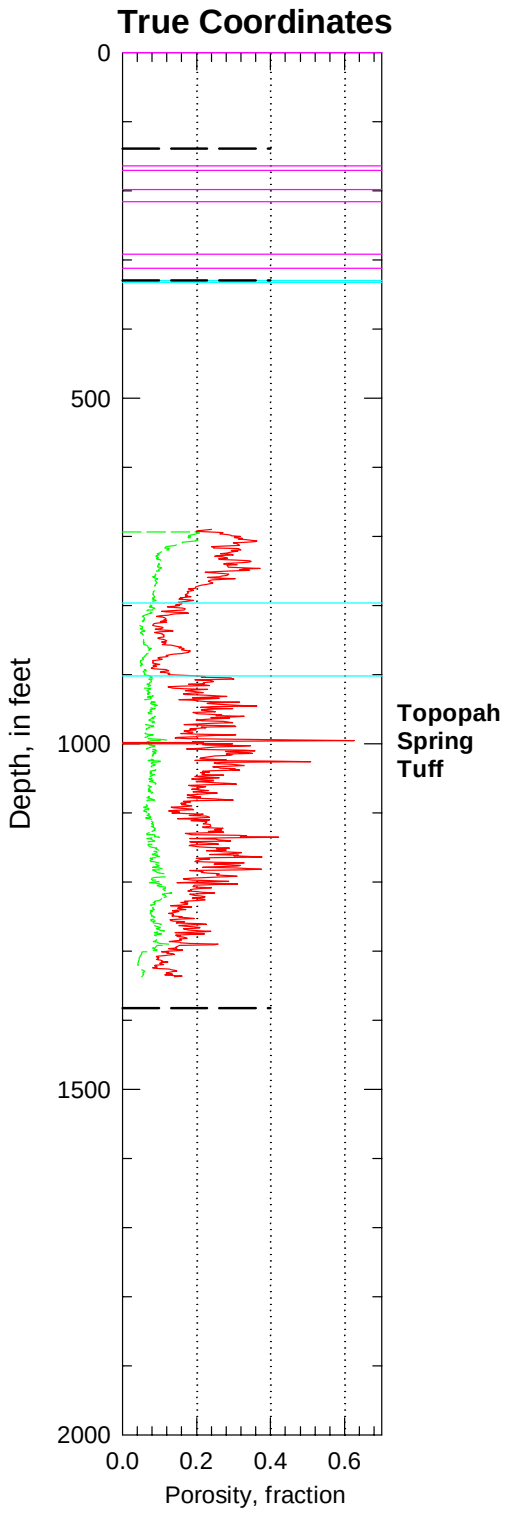

Figure B-43. Porosity data in true coordinates from drillhole NRG-5 for the entire drill hole.

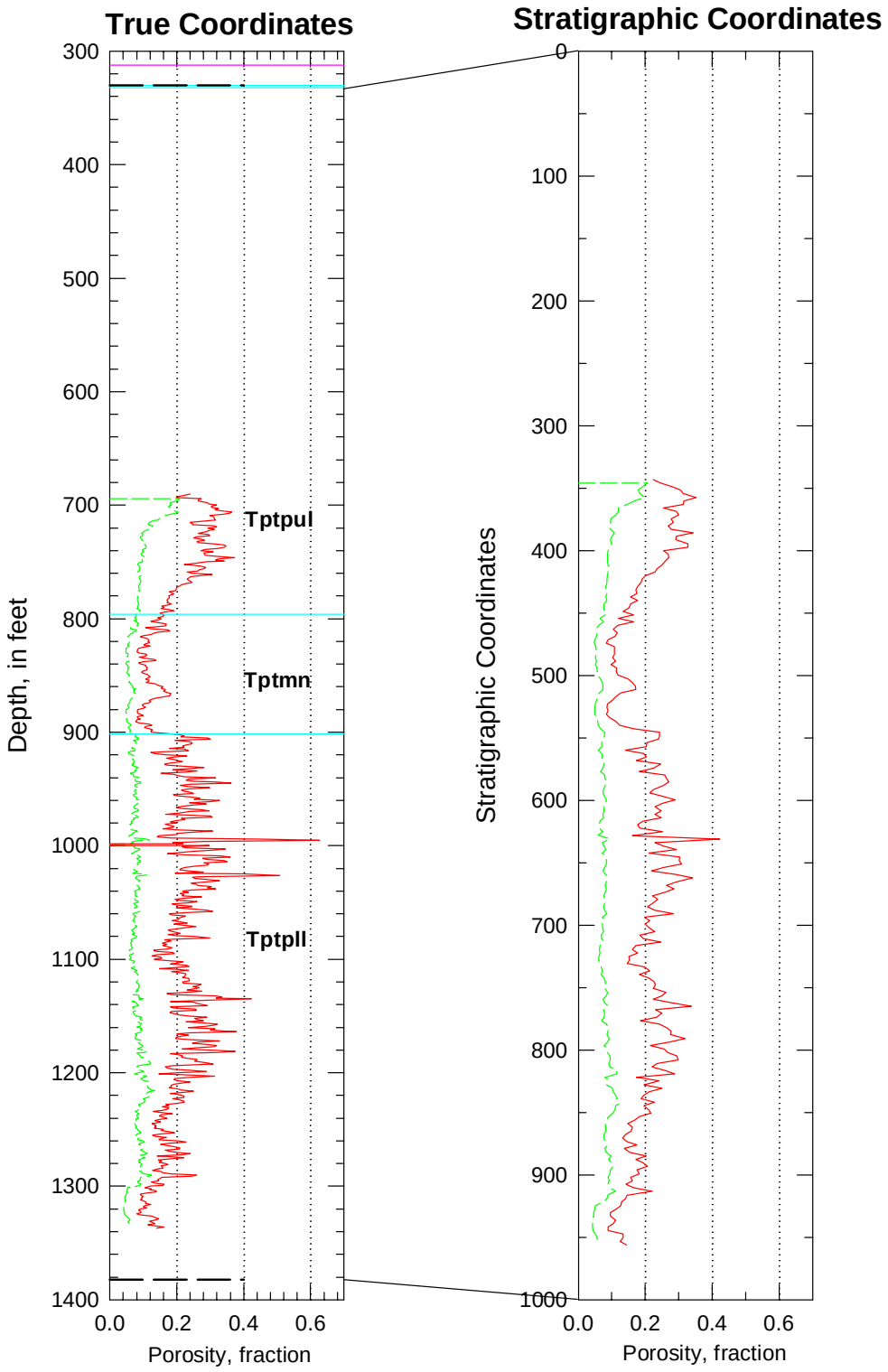

Figure B-44. Porosity data in real-world and in stratigraphic coordinates for the TSw model unit in drillhole NRG-5.

Drillhole NRG-6

Both petrophysical porosity values and core measurements are available for the NRG-6 drill hole. The hole begins in the unmodeled welded interval of the Tiva Canyon Tuff and provides a complete penetration of the PTn model unit and a nearly complete section of the TSw unit. Agreement of the geophysical- and laboratory-determined porosity data is quite good, with the anticipated exception of the lithophysae-bearing intervals.

Two of the three contacts required for the stratigraphic-coordinate transformation are present in the drill hole. The lower contact of the TSw model unit was projected using the three-dimensional geologic framework model (Clayton and others, 1997). The upper contact of the PTn model unit appears low, assigning rocks of nearly 20 percent porosity to the overlying Tiva Canyon welded interval.

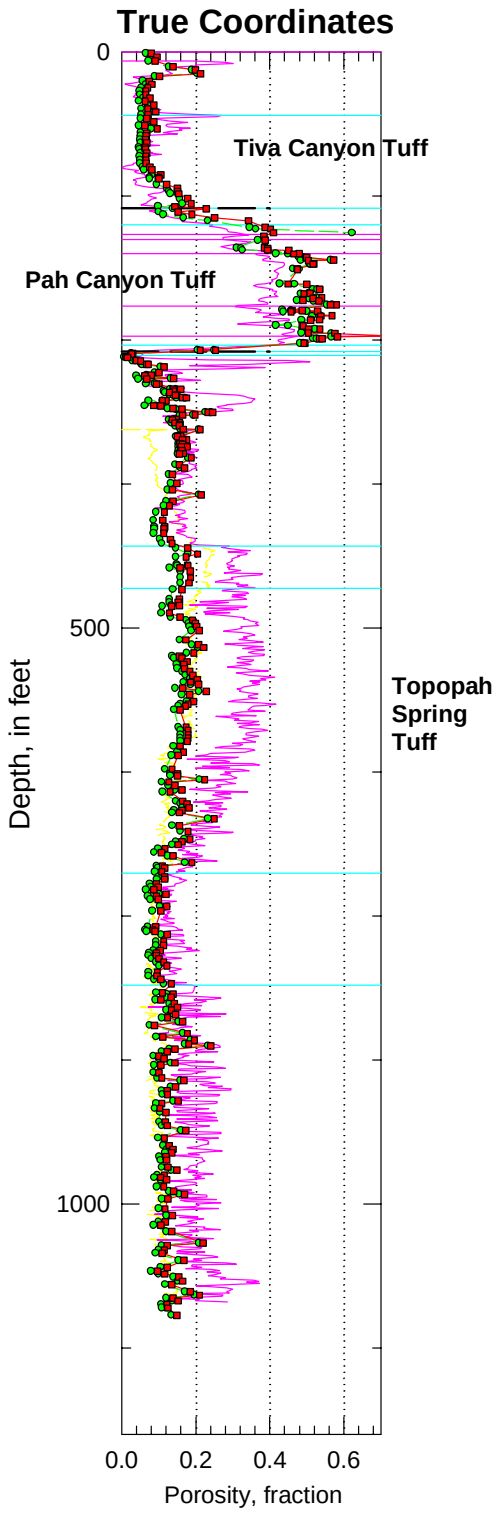

Figure B-45. Porosity data in true coordinates from drillhole NRG-6 for the entire drill hole.

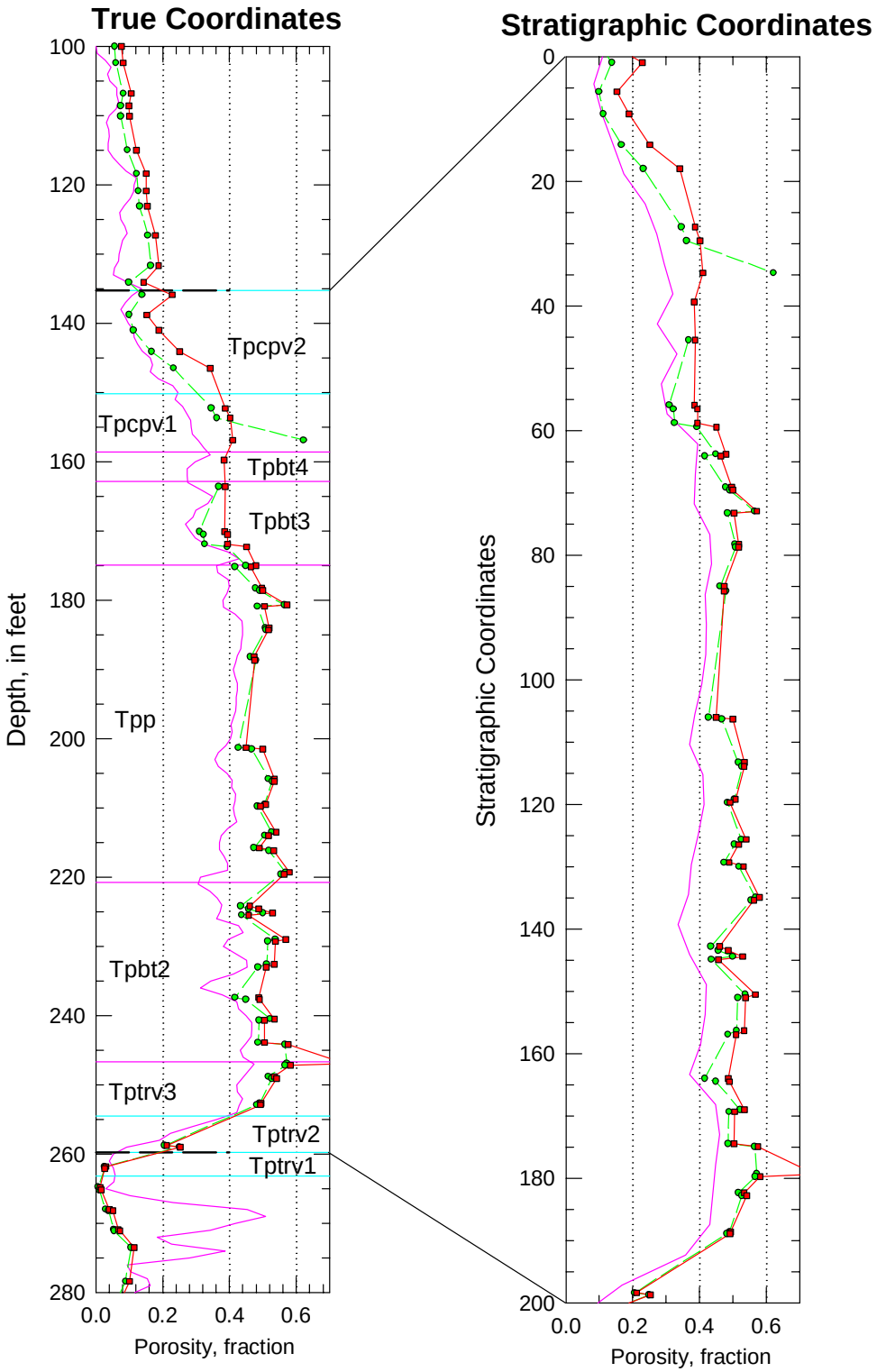

Figure B-46. Porosity data in real-world and in stratigraphic coordinates for the PTn model unit in drillhole NRG-6.

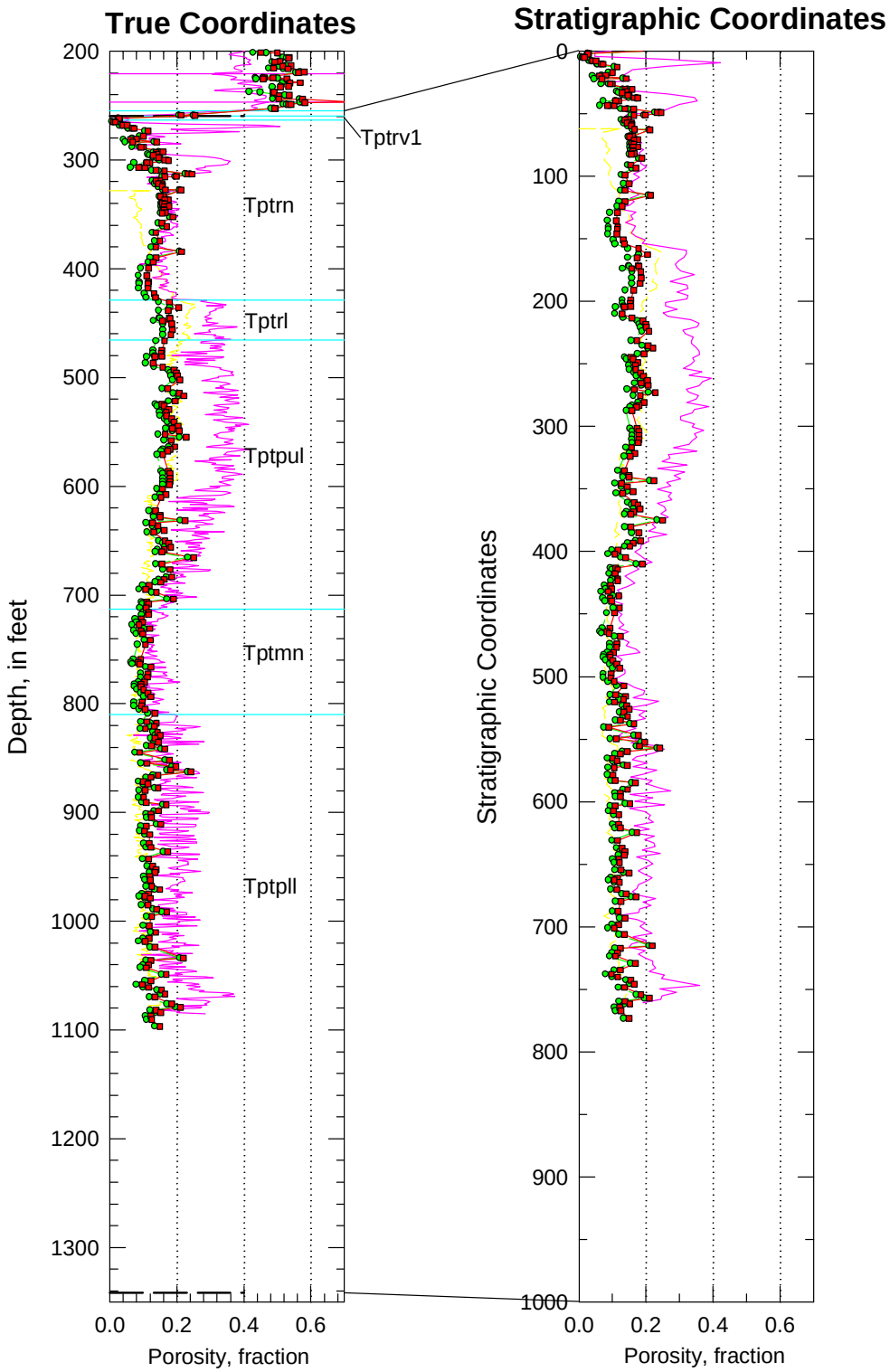

Figure B-47. Porosity data in real-world and in stratigraphic coordinates for the TSw model unit in drillhole NRG-6.

Drillhole NRG-7

Both petrophysical and laboratory-determined porosity data are available for the NRG-7 drillhole, providing full sections of both the PTn and TSw modeling units. Agreement of the core and geophysically computed porosity values is quite good for the upper part of the hole, again with the exception of the lithophysal intervals for which agreement is not expected. However, the petrophysical porosity data and the core measurements diverge markedly below a actual depth of approximately 1200 ft. The core values have been used for matrix porosity throughout the hole

All the required contacts are present in the core from the hole. The upper contact of the PTn model unit appears low, with rocks of 20-percent porosity assigned to the overlying "welded" interval.

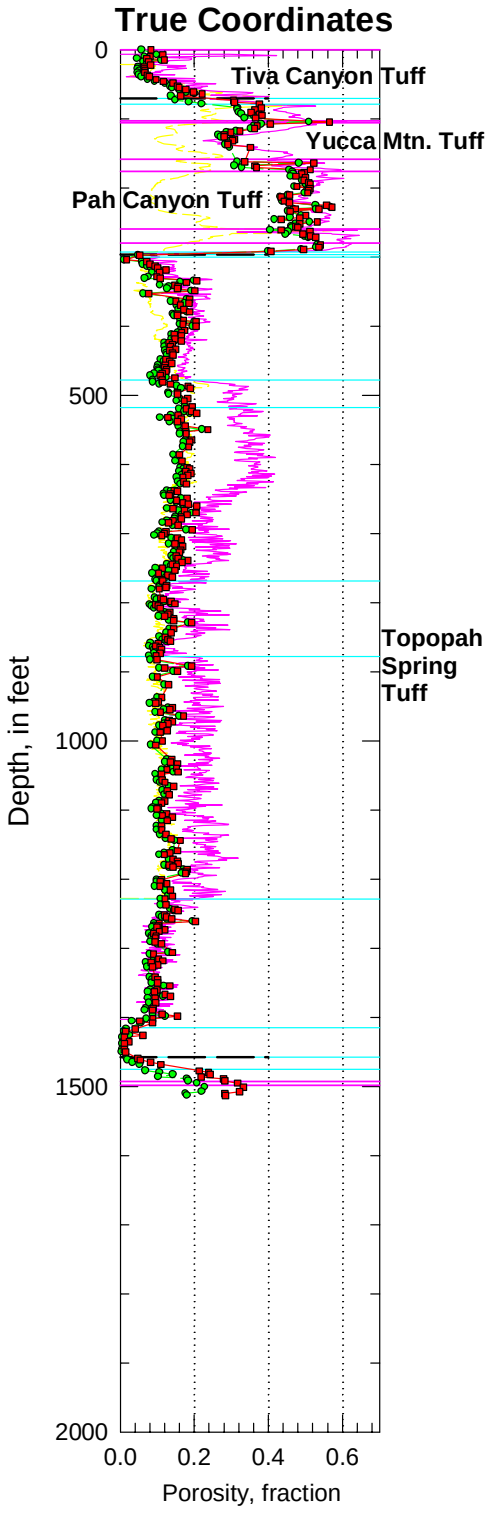

Figure B-48. Porosity data in true coordinates from drillhole NRG-7 for the entire drill hole.

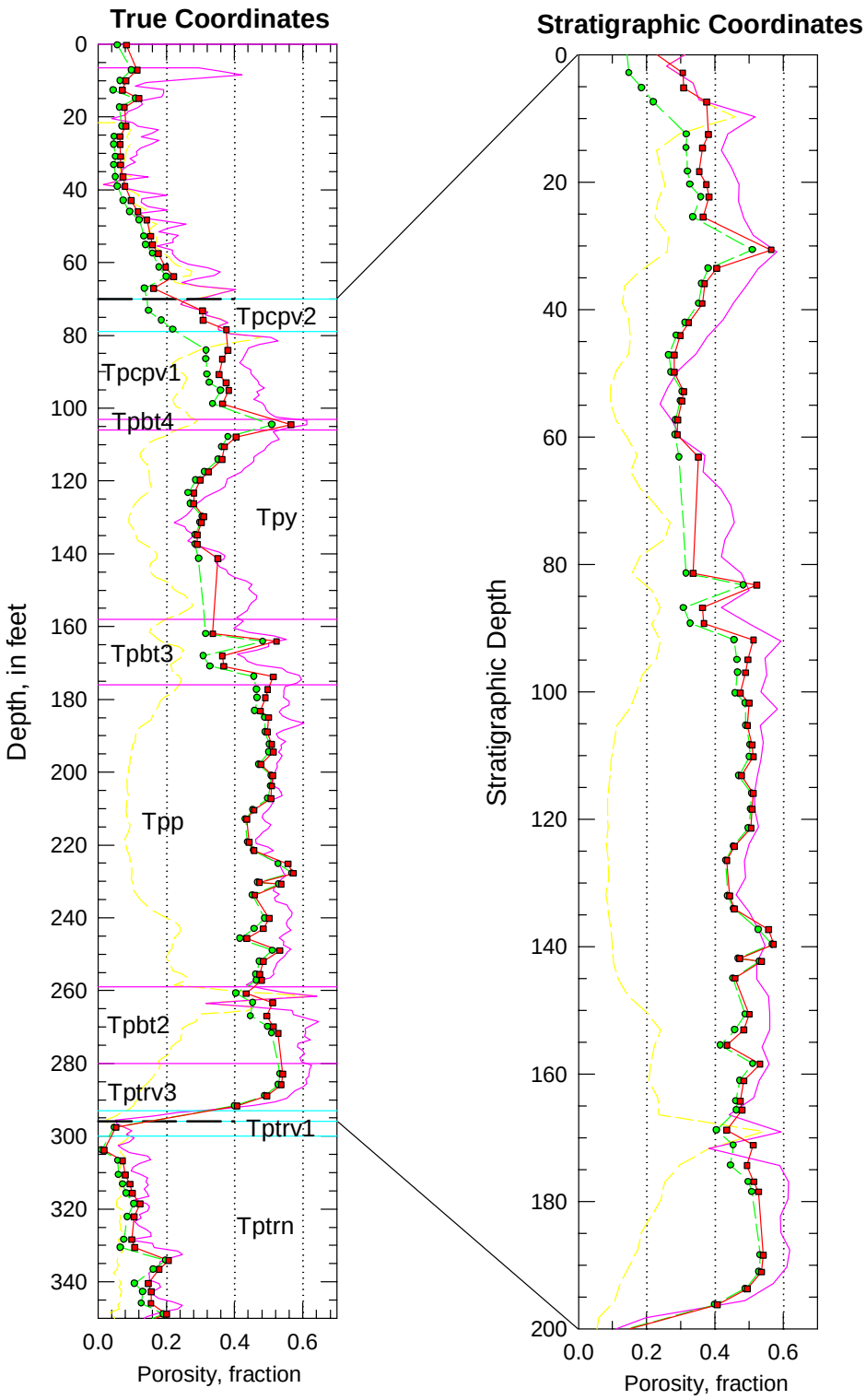

Figure B-49. Porosity data in real-world and in stratigraphic coordinates for the PTn model unit in drillhole NRG-7

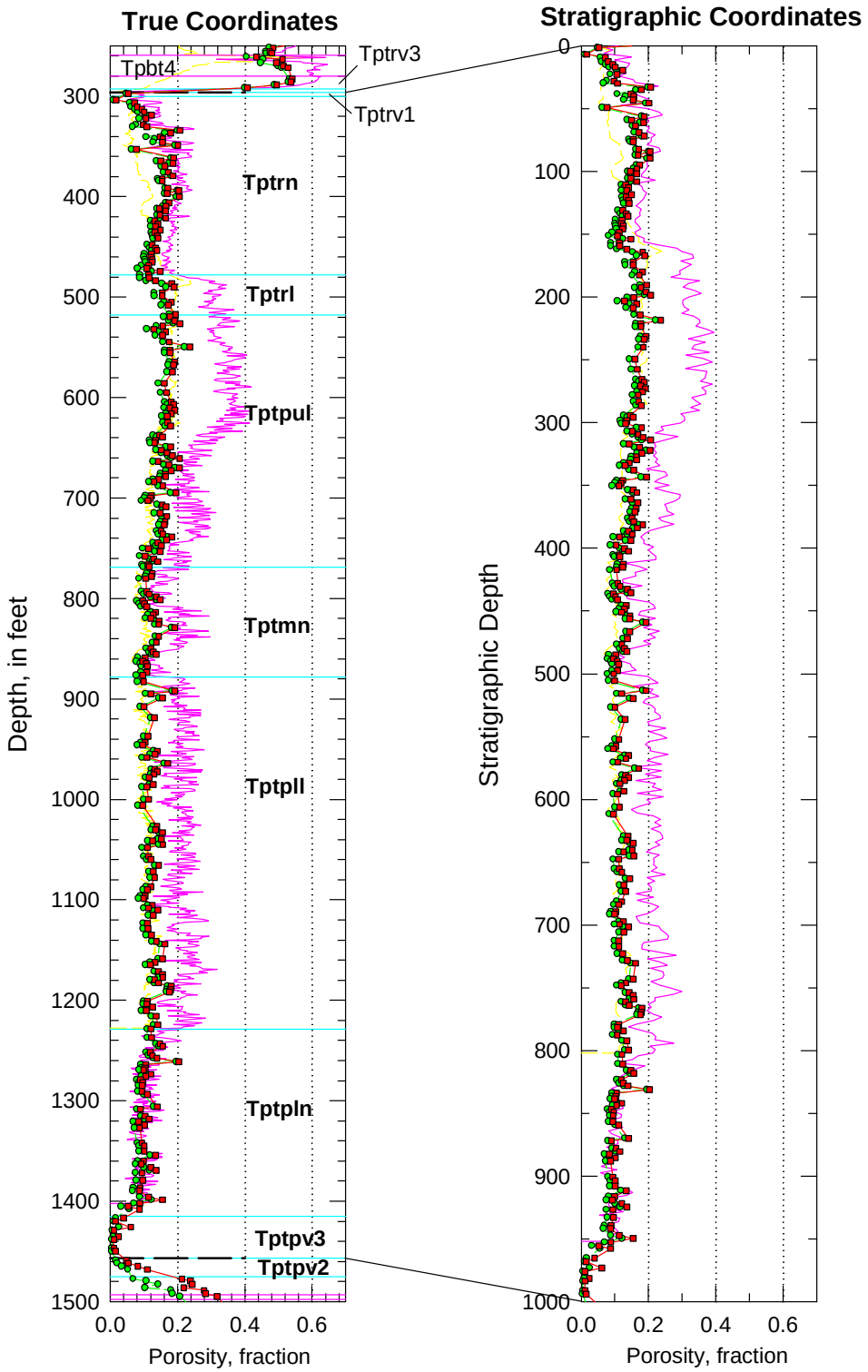

Figure B-50. Porosity data in real-world and in stratigraphic coordinates for the TSw model unit in drillhole NRG-7.

Drillhole SD-7

Drillhole SD-7 is one of six recent site-characterization drillhole that is located within the main repository block at Yucca Mountain, slightly to the west of the Ghost Dance fault. The drillhole contains a full suite of modern geophysical logs for which total and water-filled porosities have been calculated, and the hole was cored from top to bottom producing a full suite of both RH and 105°C-dried porosity measurements.

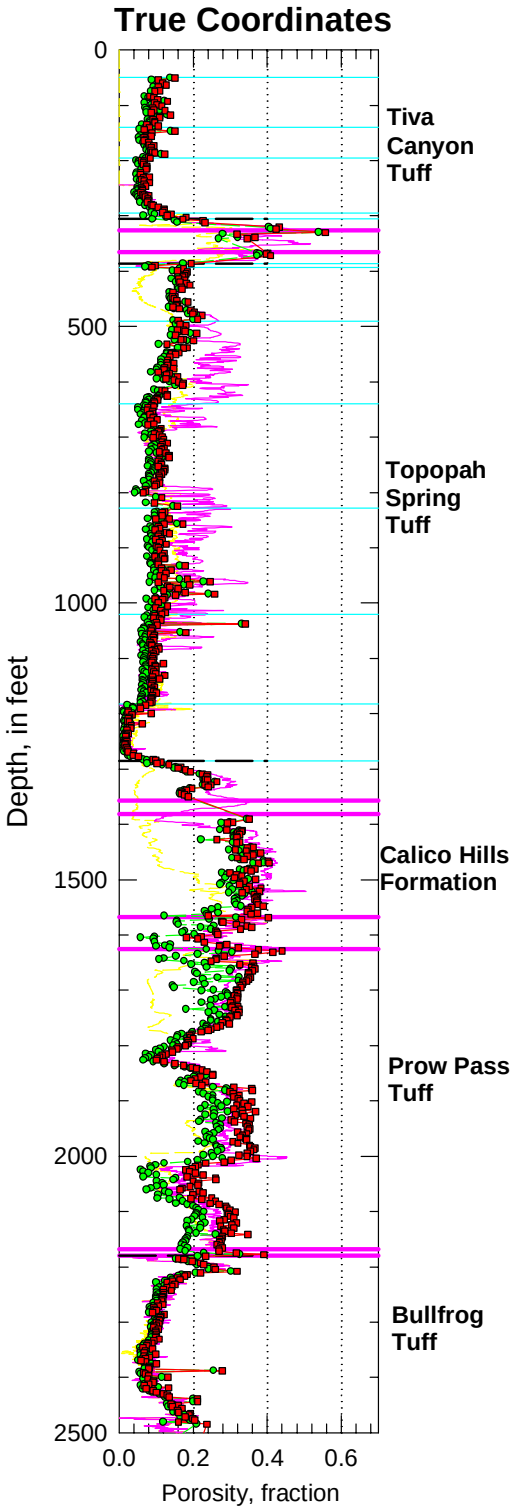

Figure B-51. Porosity data in true coordinates from drillhole SD-7 for the entire drill hole through the top of the Bullfrog Tuff.

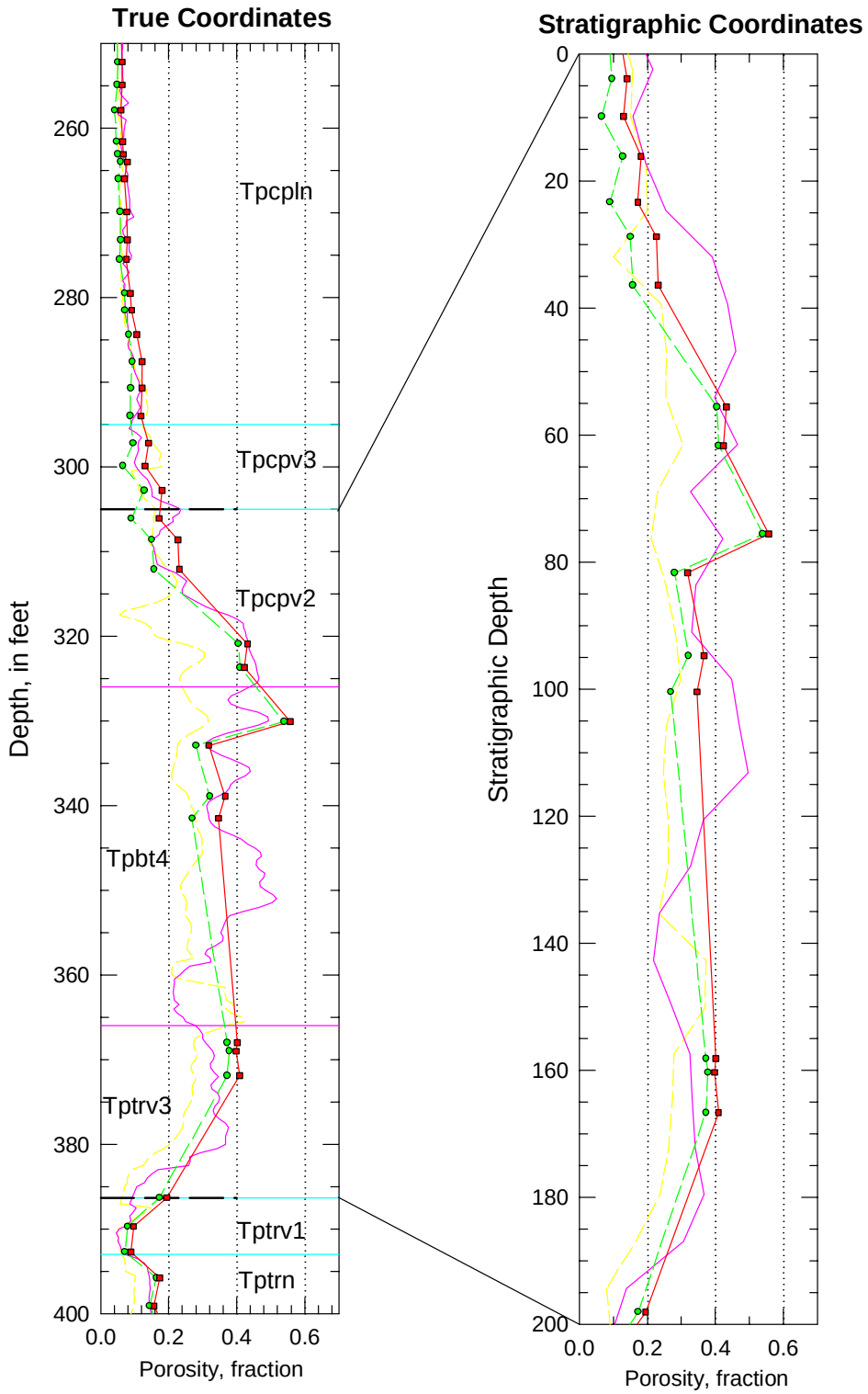

Figure B-52. Porosity data in real-world and in stratigraphic coordinates for the PTn model unit in drillhole SD-7.

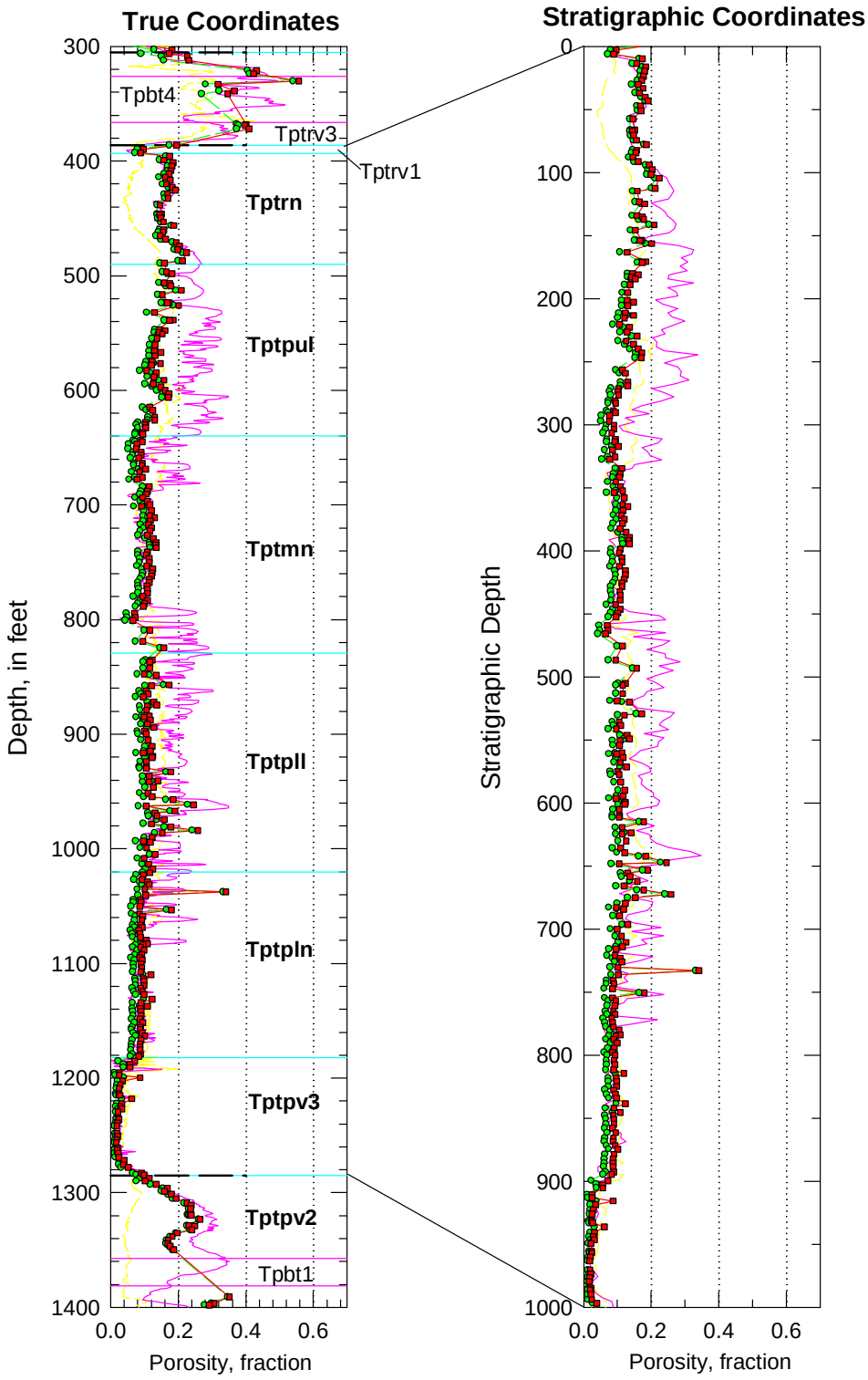

Figure B-53. Porosity data in real-world and in stratigraphic coordinates for the TSw model unit in drillhole SD-7.

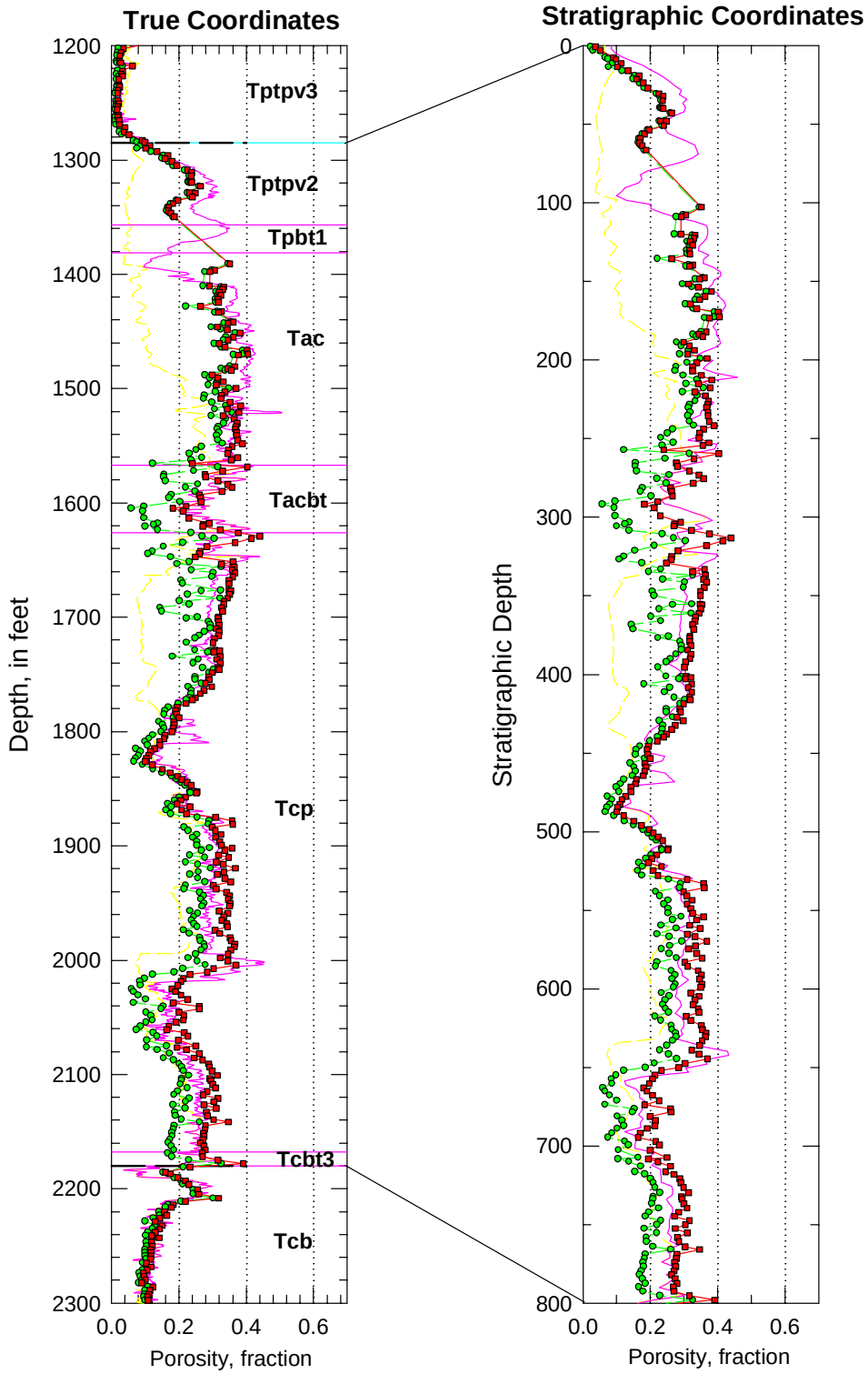

Figure B-54. Porosity data in real-world and in stratigraphic coordinates for the combined CH–PP model unit in drillhole SD-7.

Drillhole SD-9

Drillhole SD-9 is one of six site characterization drillholes and is located within the main repository block at Yucca Mountain, slightly to the west of the Ghost Dance fault. The drillhole contains a full suite of modern geophysical logs for which total and water-filled porosity values have been calculated. The hole was cored from top to bottom, and there is a full suite of both RH- and 105°C-dried laboratory porosity measurements.

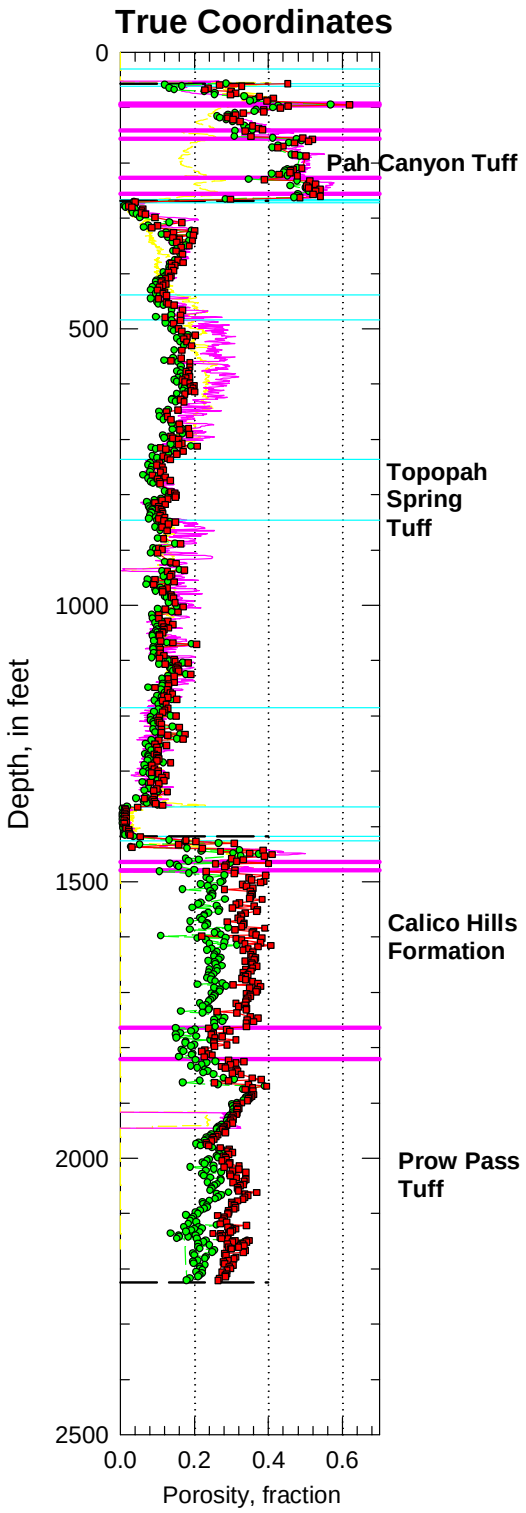

Figure B-55. Porosity data in true coordinates from drillhole SD-9 for the entire drillhole.

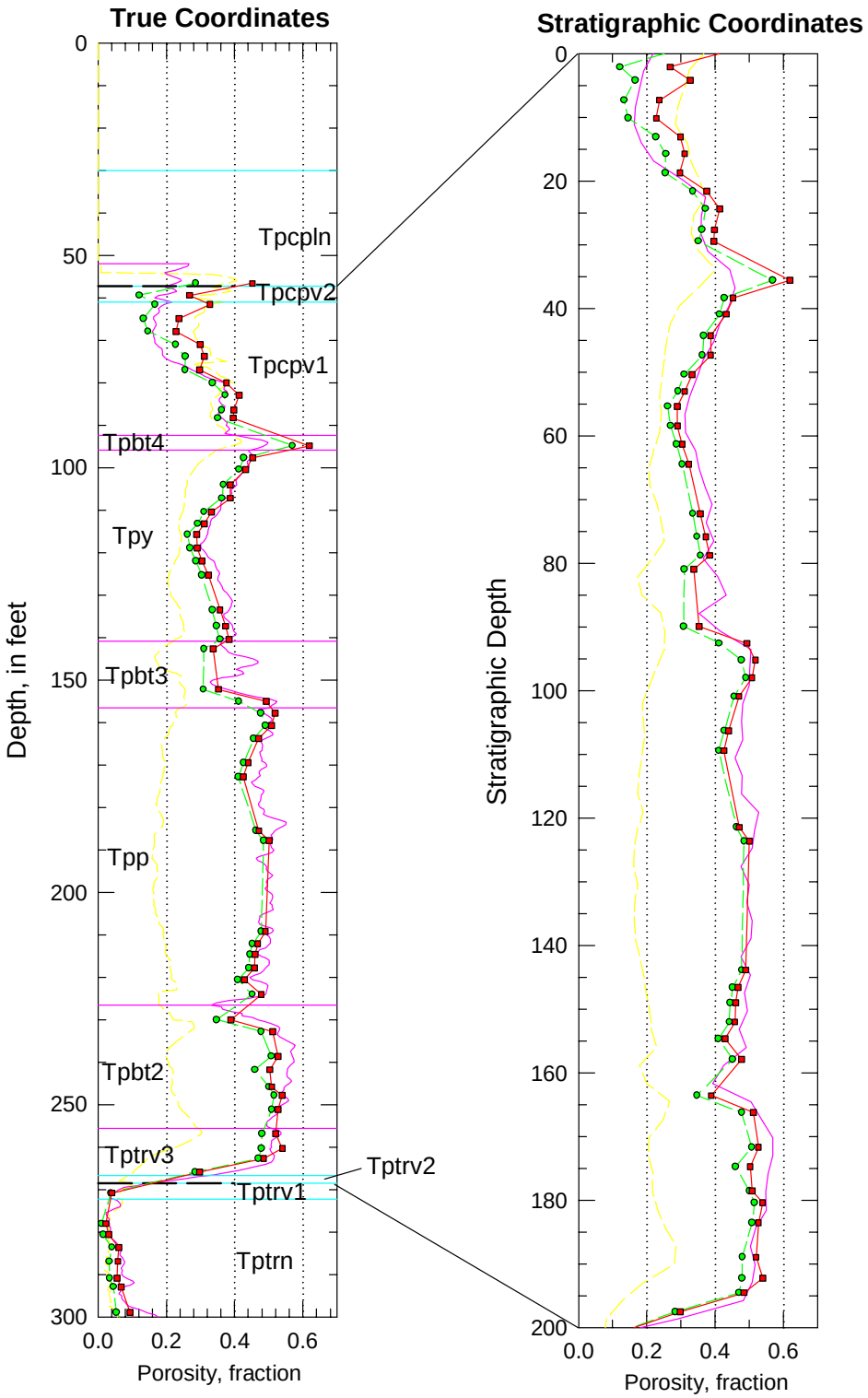

Figure B-56. Porosity data in real-world and in stratigraphic coordinates for the PTn model unit in drillhole SD-9.

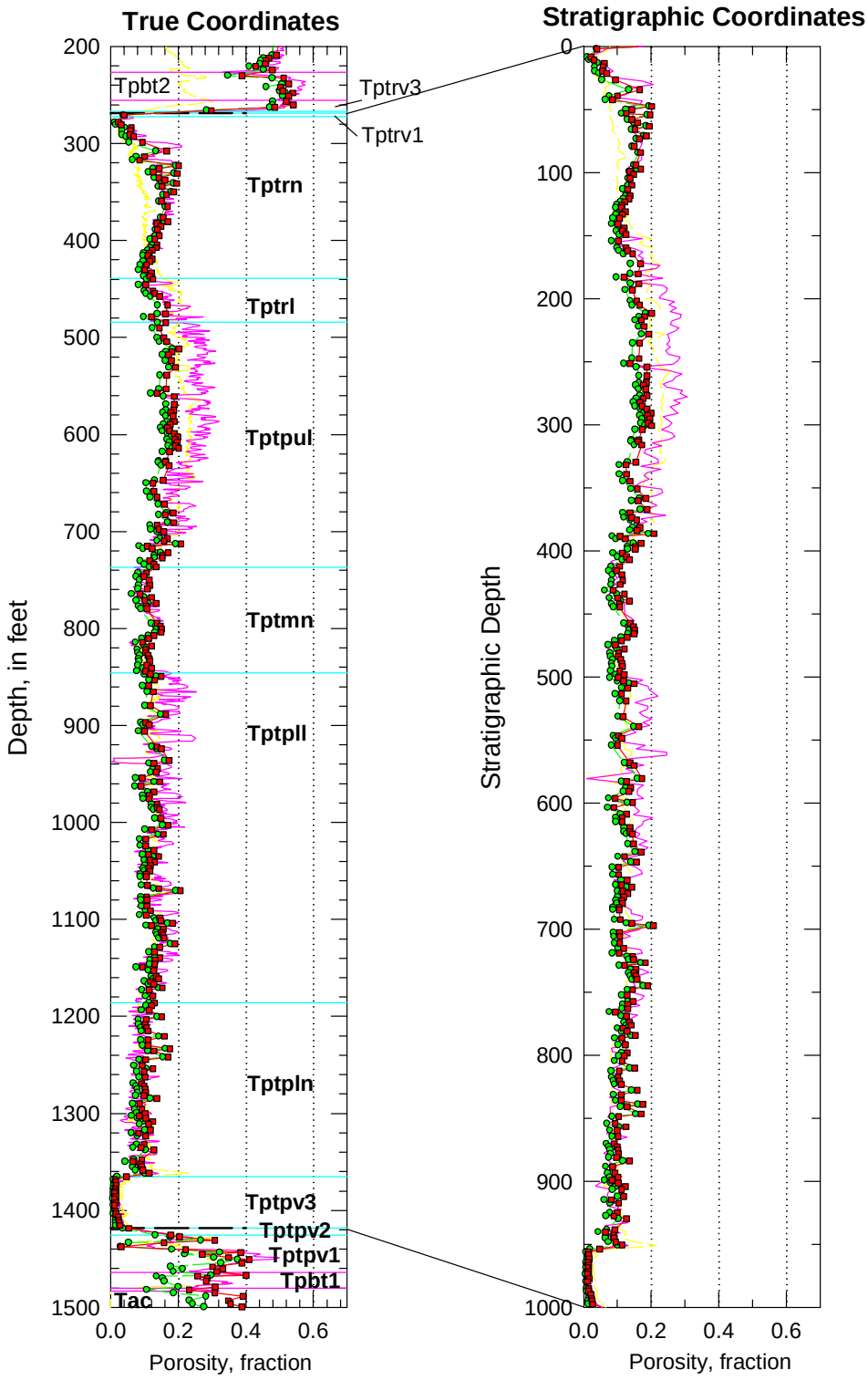

Figure B-57. Porosity data in real-world and in stratigraphic coordinates for th TSw model unit in drillhole SD-9.

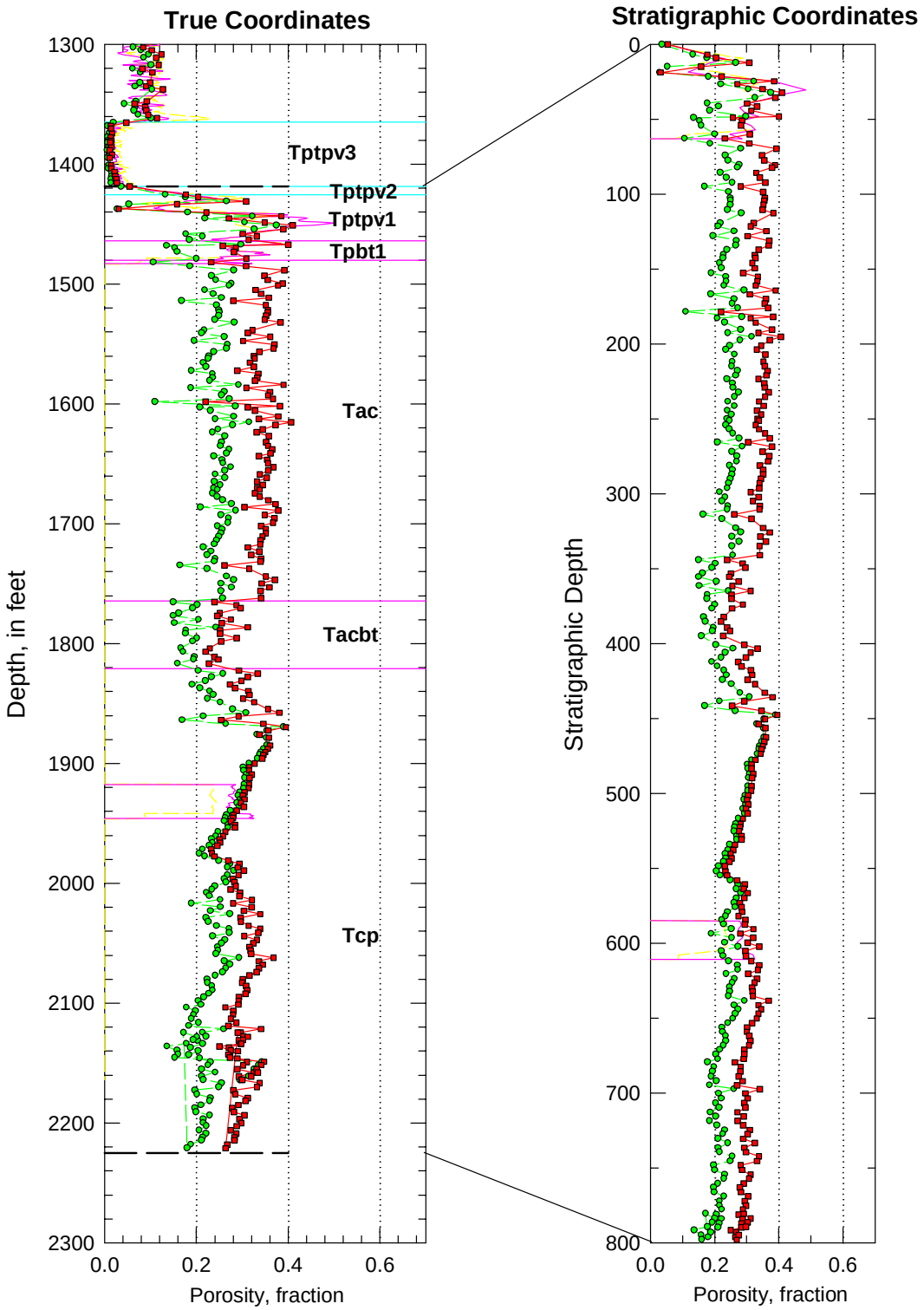

Figure B-58. Porosity data in real-world and in stratigraphic coordinates for the combined CH–PP model unit in drillhole SD-9

Drillhole SD-12

Drillhole SD-12 is one of six deep site-characterization drillholes and is located wihtin the main repository block at Yucca Mountain, slightly to the west of the Ghost Dance fault. The drillhole provides a complete suite of modern petrophysical logs, from which total and water-filled porosity values have been calculated. The hole was cored from top to bottom, and there are a full suite of both RH- and 105°C-dried porosity measurements.

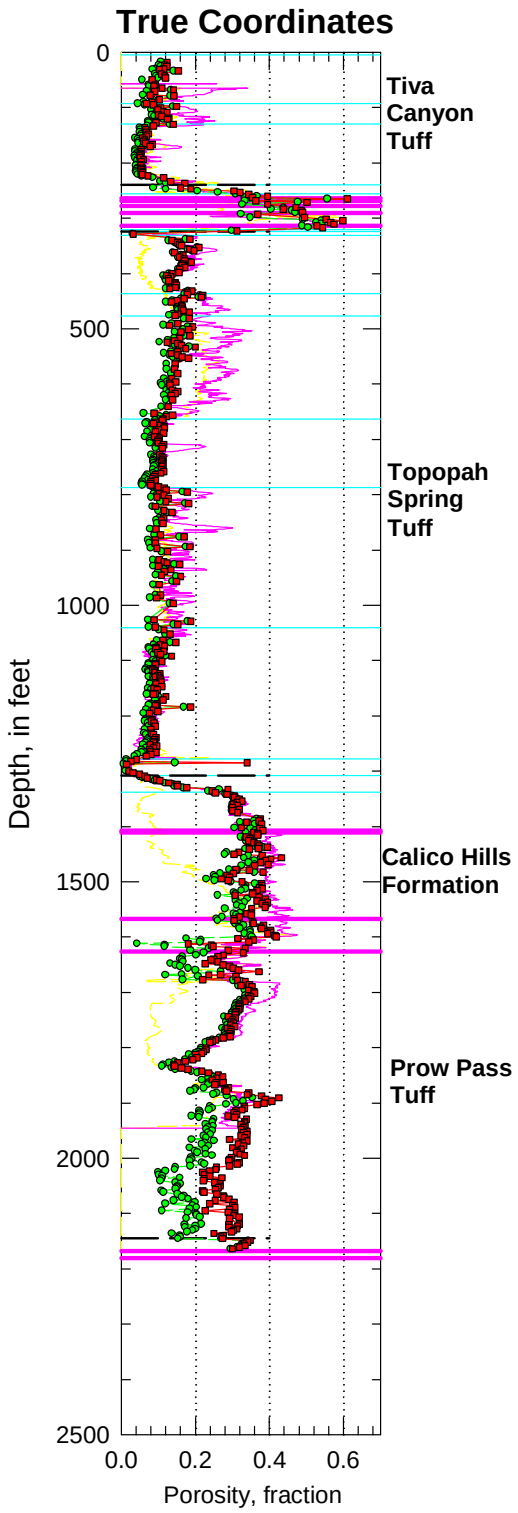

Figure B-59. Porosity data in true coordinates from drillhole SD-12 for the entire drillhole through the top of the Bullfrog Tuff

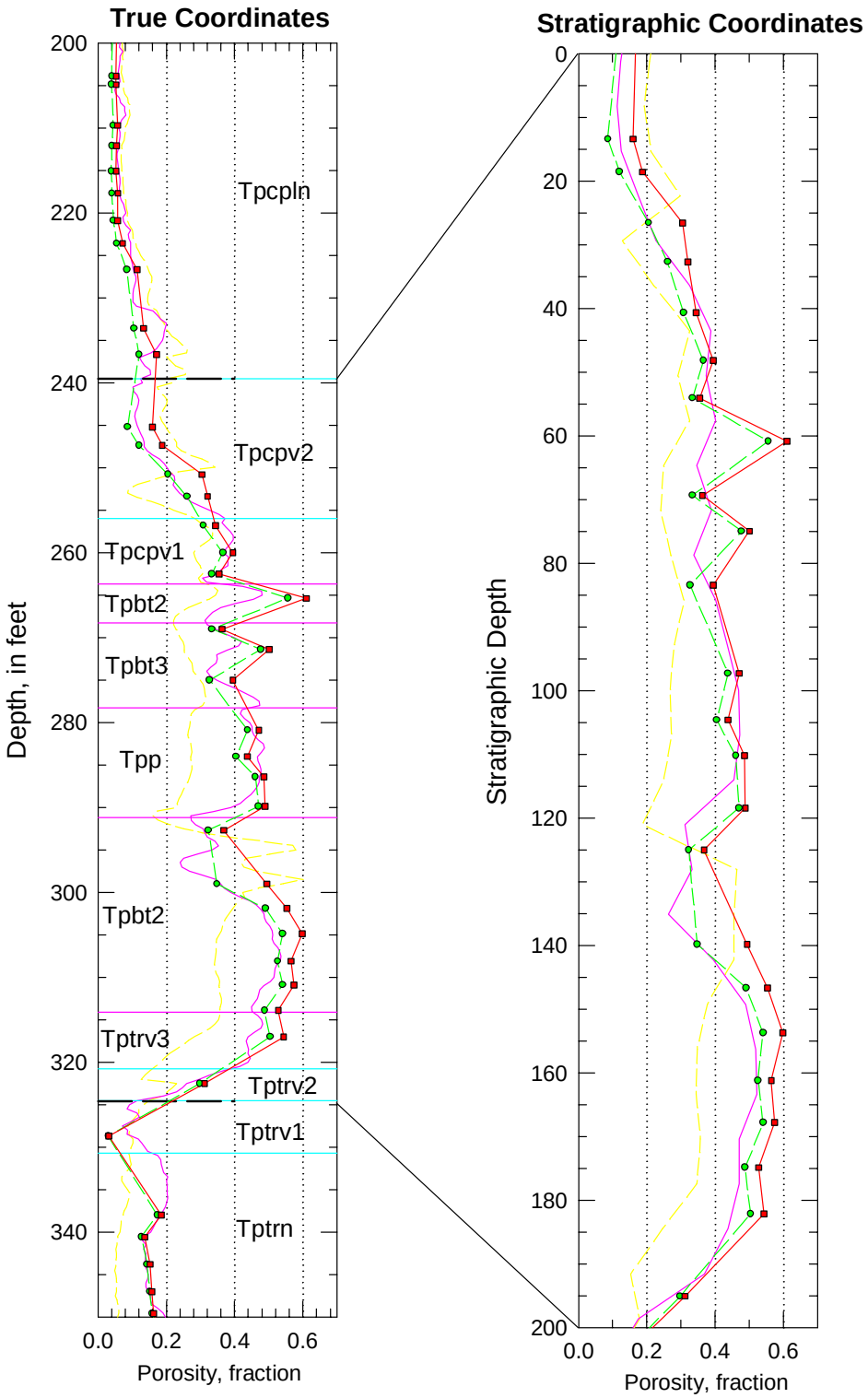

Figure B-60. Porosity data in real-world and in stratigraphic coordinates for the PTn model unit in drillhole SD-12.

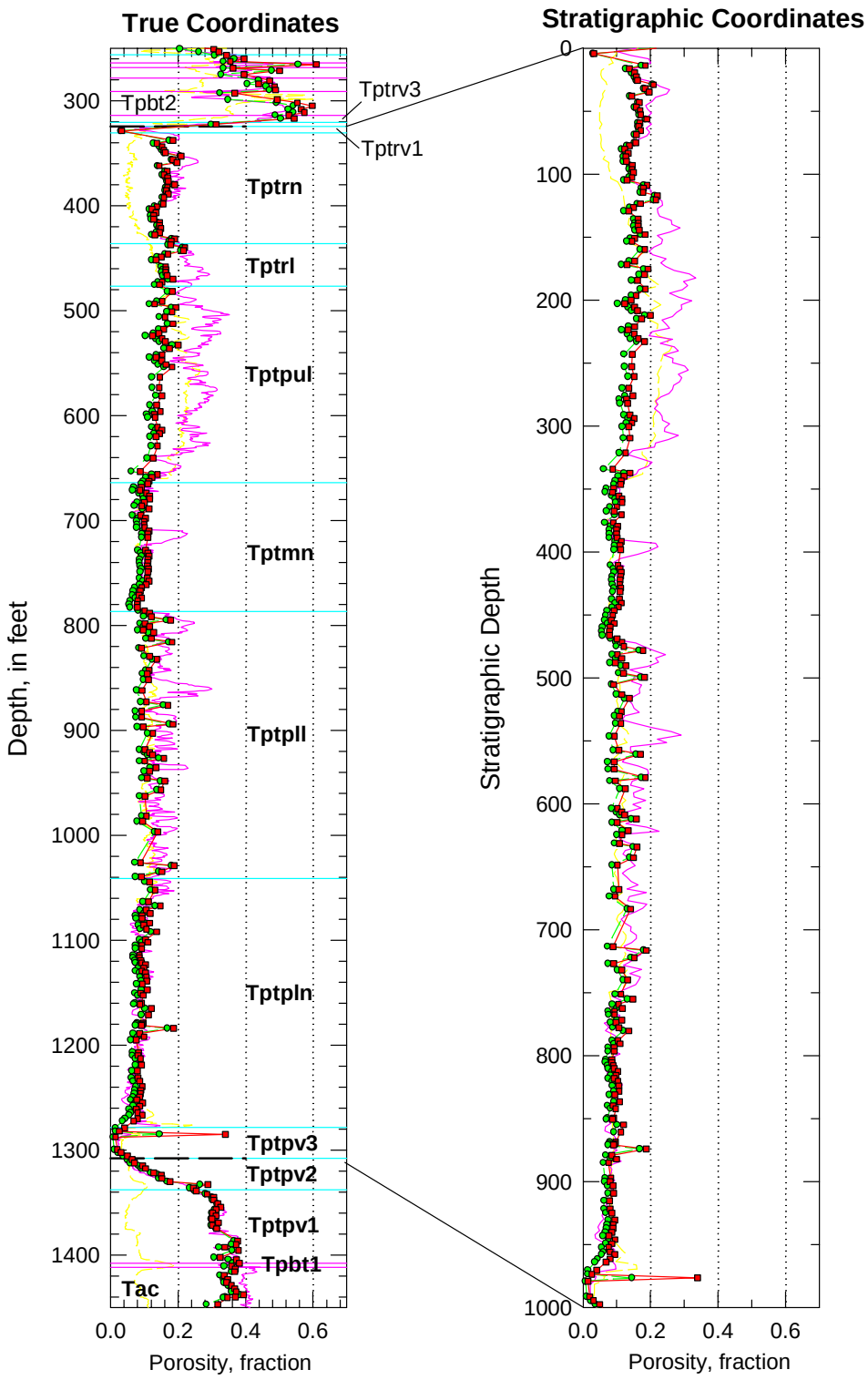

Figure B-61. Porosity data in real-world and in stratigraphic coordinates for the TSw model unit in drillhole SD-12.

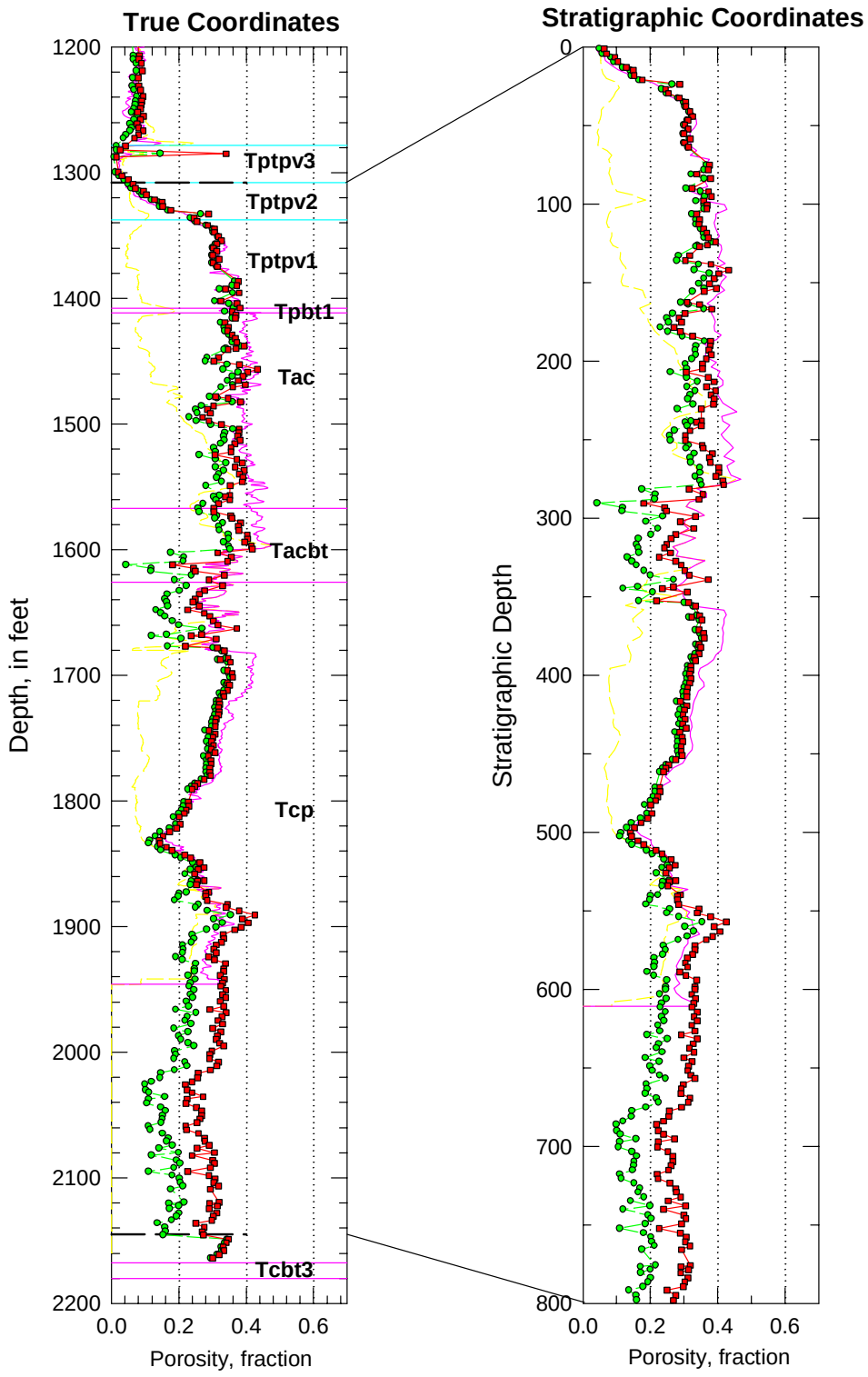

Figure B-62. Porosity data in real-world and in stratigraphic coordinates for the combined CH–PP model unit in drillhole SD-12.

Drillhole UZ-7A

Drillhole UZ-7A is a special-purpose site characterization drill hole that was started in the hanging wall of the Ghost Dance fault and drilled to intersect the fault at depth. The hole contains a full suite of modern petrophysical logs from which total and water-filled porosity values have been calculated. Although core recovery was locally quite poor, the hole was cored from top to bottom, and there are a full suite of both RH- and 105°C-dried laboratory porosity measurements.

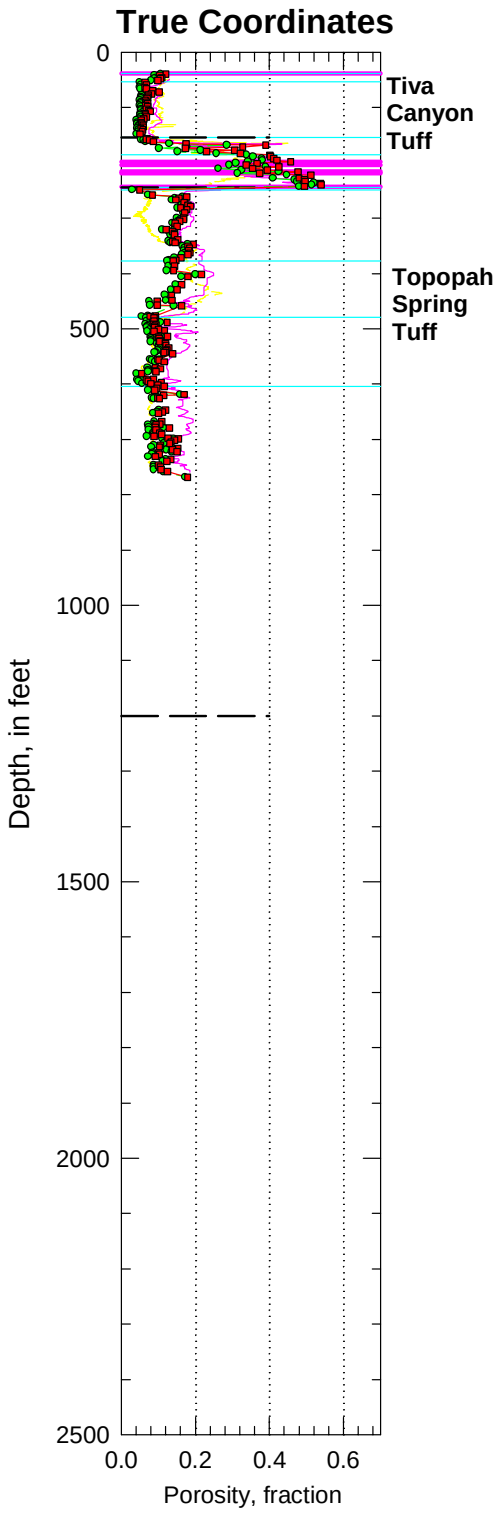

Figure B-63. Porosity data in true coordinates from drillhole UZ-7A for the entire drillhole.

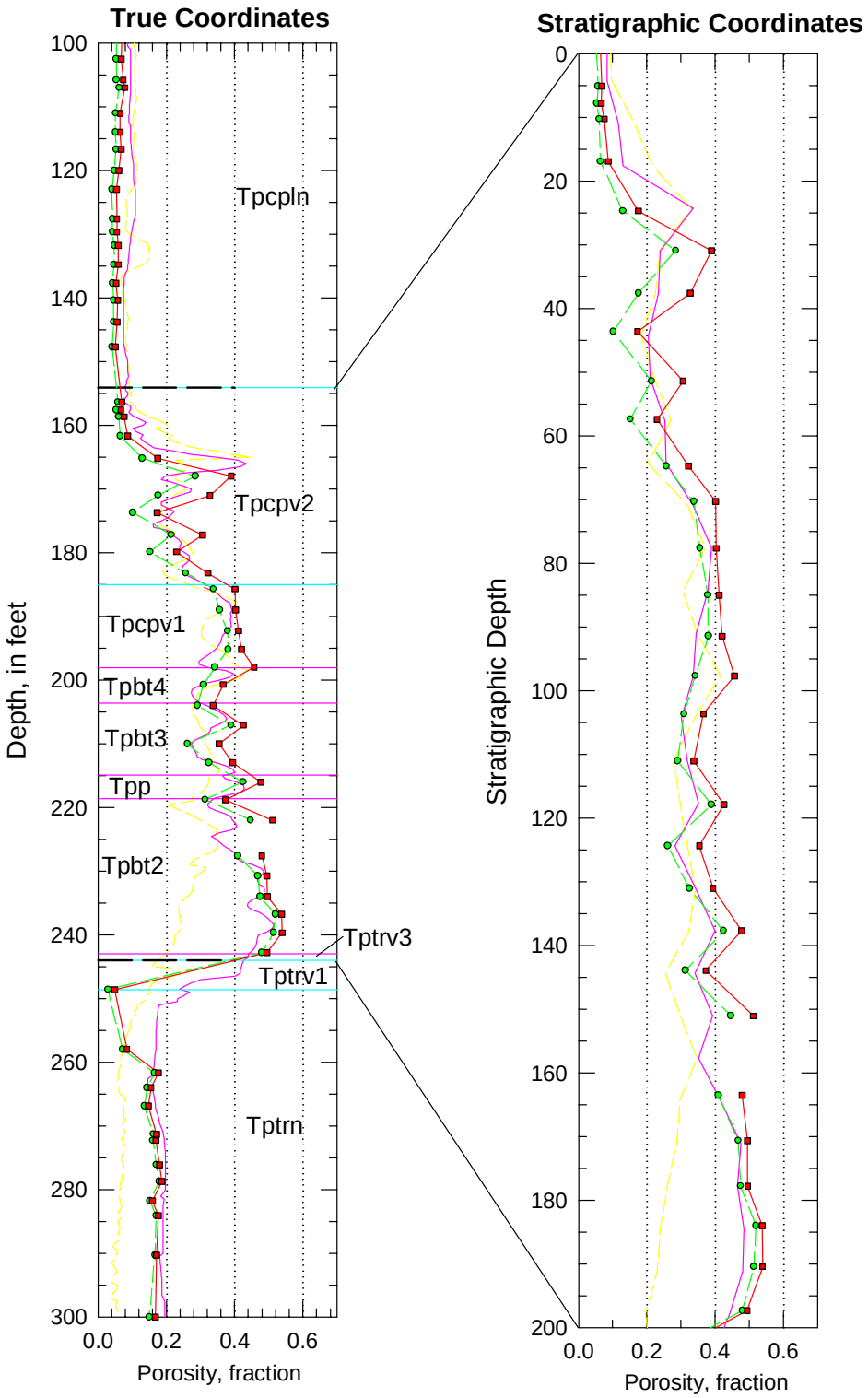

Figure B-64. Porosity data in real-world and in stratigraphic coordinates for the PTn model unit in drillhole UZ-7A.

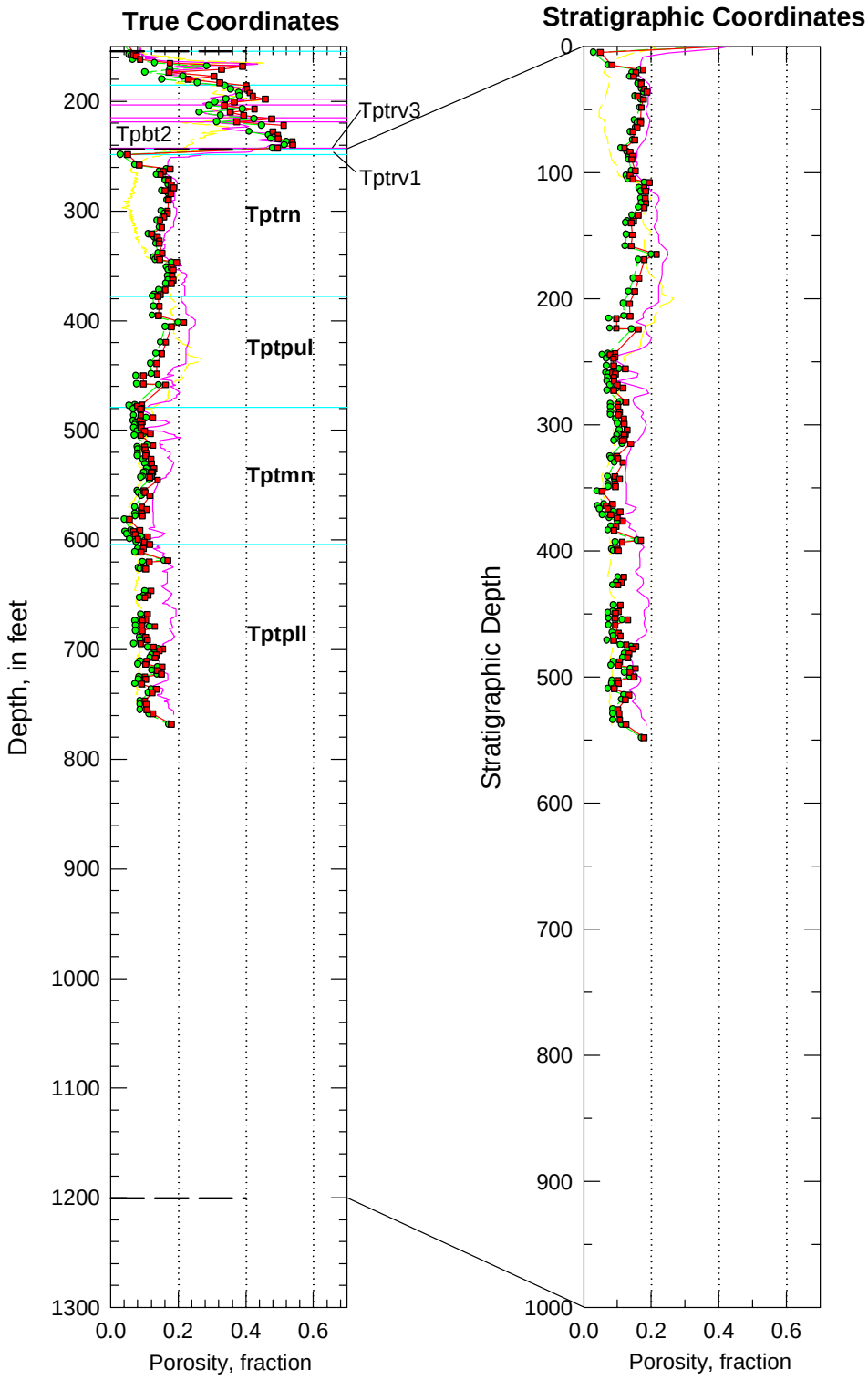

Figure B-65. Porosity data in real-world and in stratigraphic coordinates for the TSw model unit in drillhole UZ-7A.

Drillhole UZ-14

Drillhole UZ-14 is one of six deep site characterization drillholes at Yucca Mountain. The hole is located immediately to the northwest of the main repository block. The hole provides a complete suite of modern petrophysical logs, from which total and water-filled porosity values have been calculated. The hole was cored from top to bottom, and there are a full suite of both RH- and 105°C-dried laboratory porosity measurements, with the exception of the very lowermost portion of the hole for which only petrophysical porosity data are available.

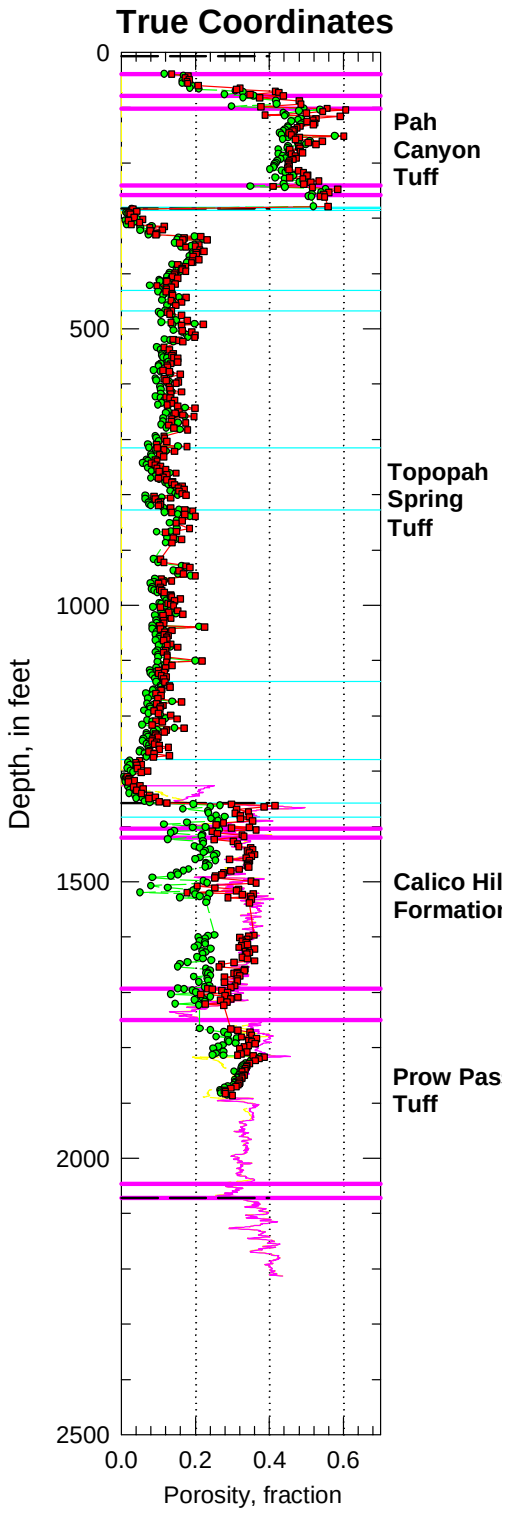

Figure B-66. Porosity dat in true coordinates from drillhole UZ-14 for the entire drillhole.

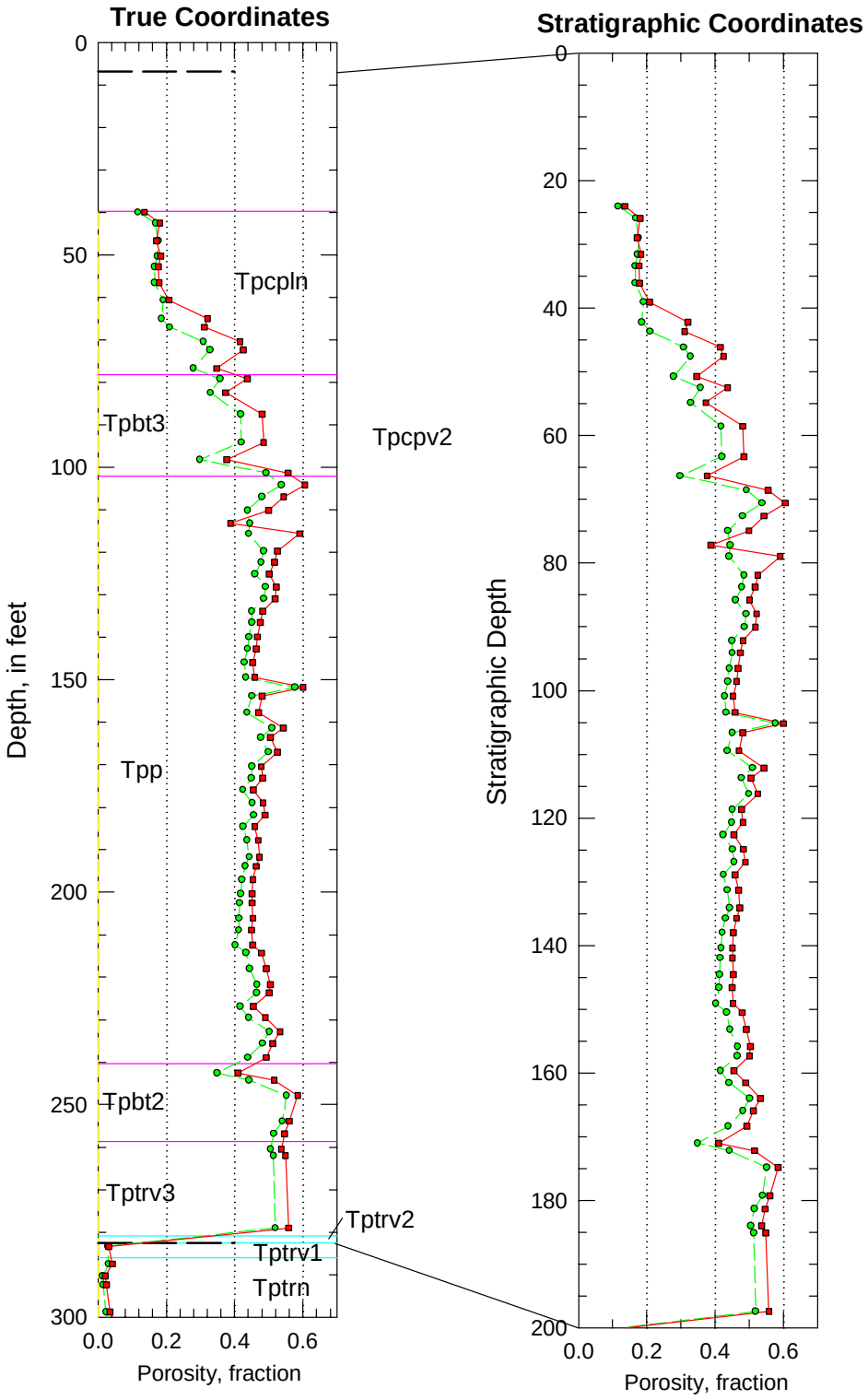

Figure B-67. Porosity data in real-world and in stratigraphic coordinates for the PTn model unit in drillhole UZ-14.

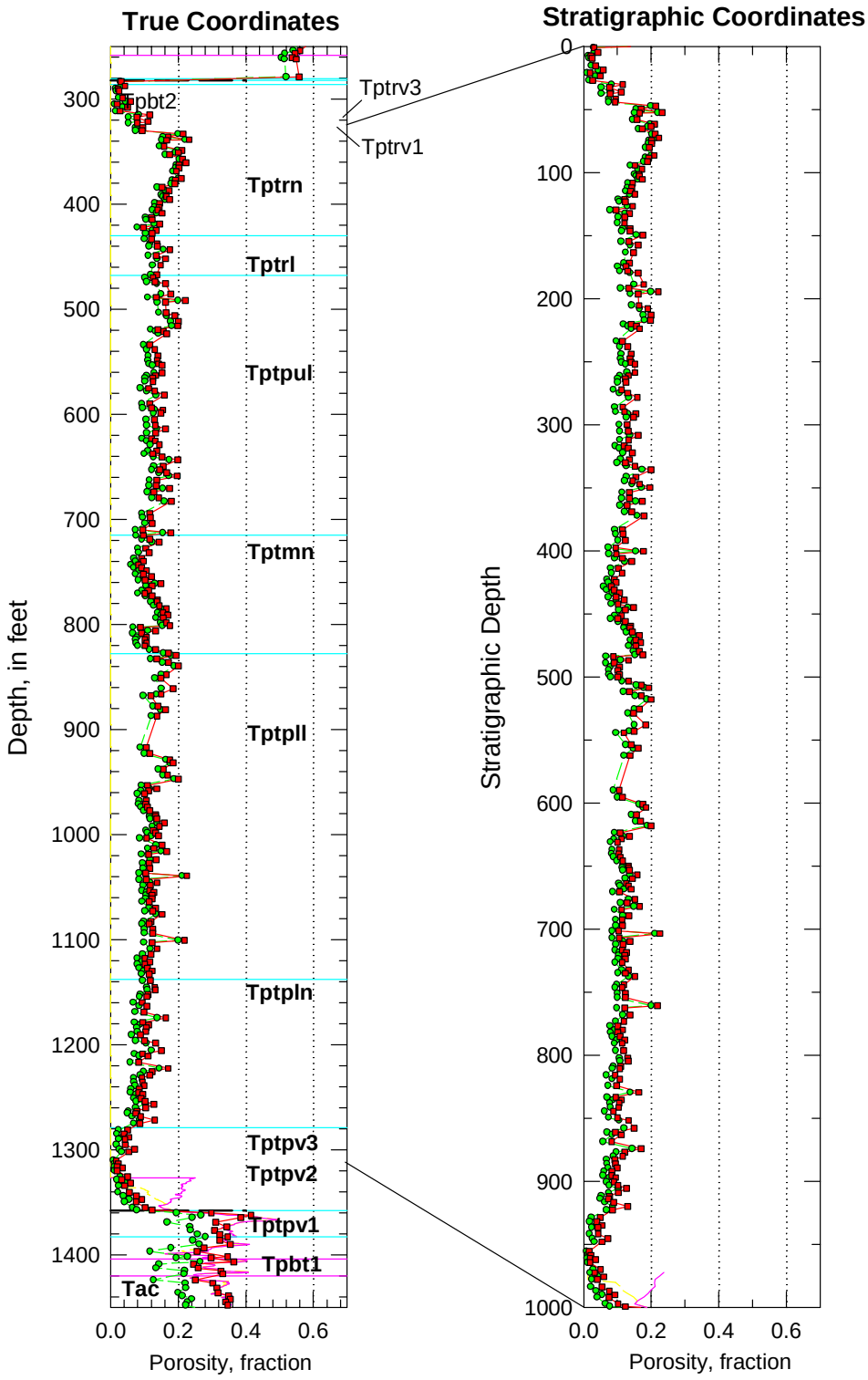

Figure B-68. Porosity data in real-world and in stratigraphic coordinates for the TSw model unit in drillhole UZ-14.

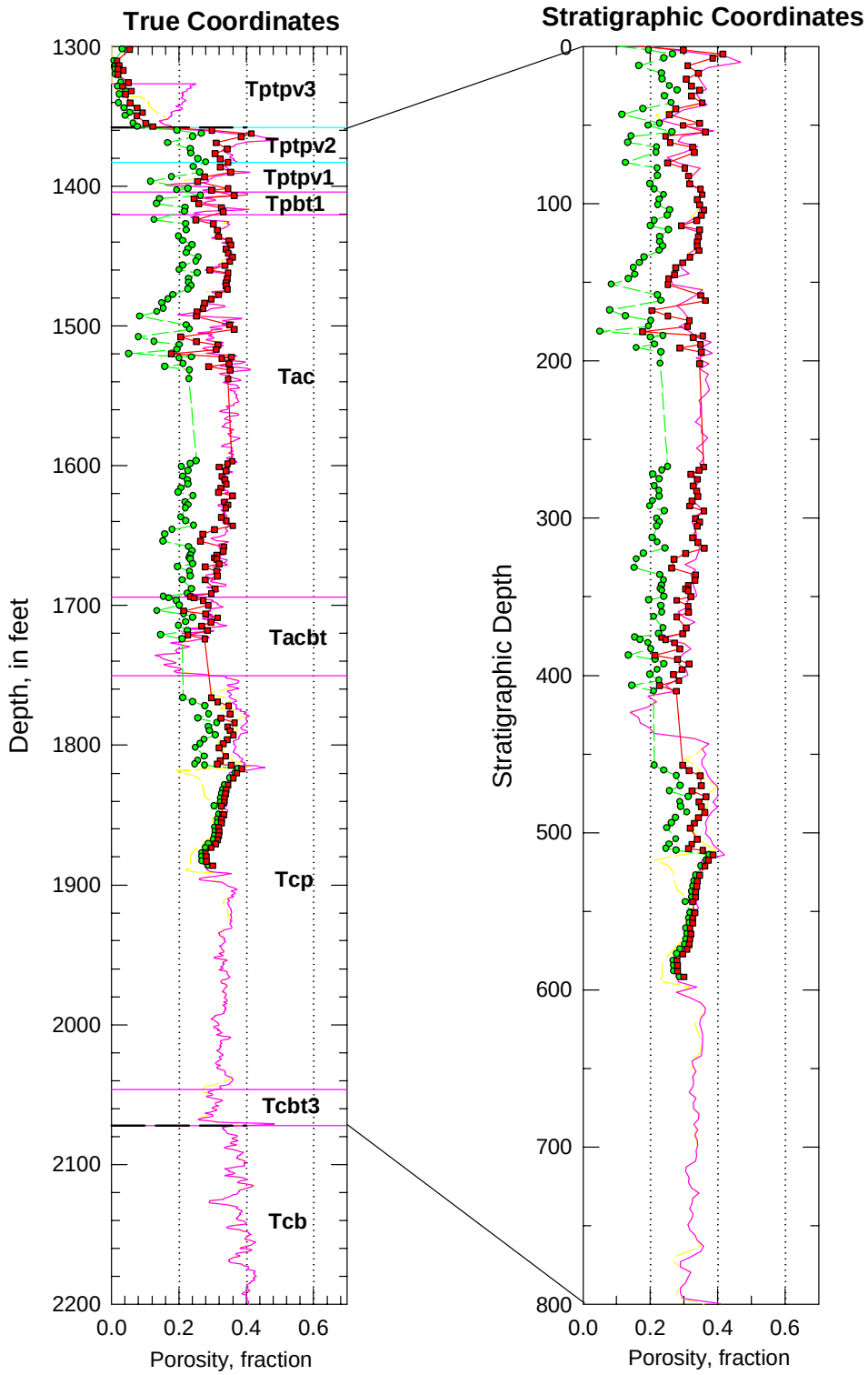

Figure B-69. Porosity data in real-world and in stratigraphic coordinates for the combined CH–PP model unit in drillhole UZ-14.

Drillhole UZ-16

Drillhole UZ-16 is one of six deep site characterization drillholes at Yucca Mountain. The hole is located to the southeast of the main repository block, and it provides a full suite of modern geophysical logs from which total and water-filled petrophysical porosity values have been calculated. The hole was cored from top to bottom, and there are a full suite of both RH- and 105°C-dried laboratory porosity measurements.

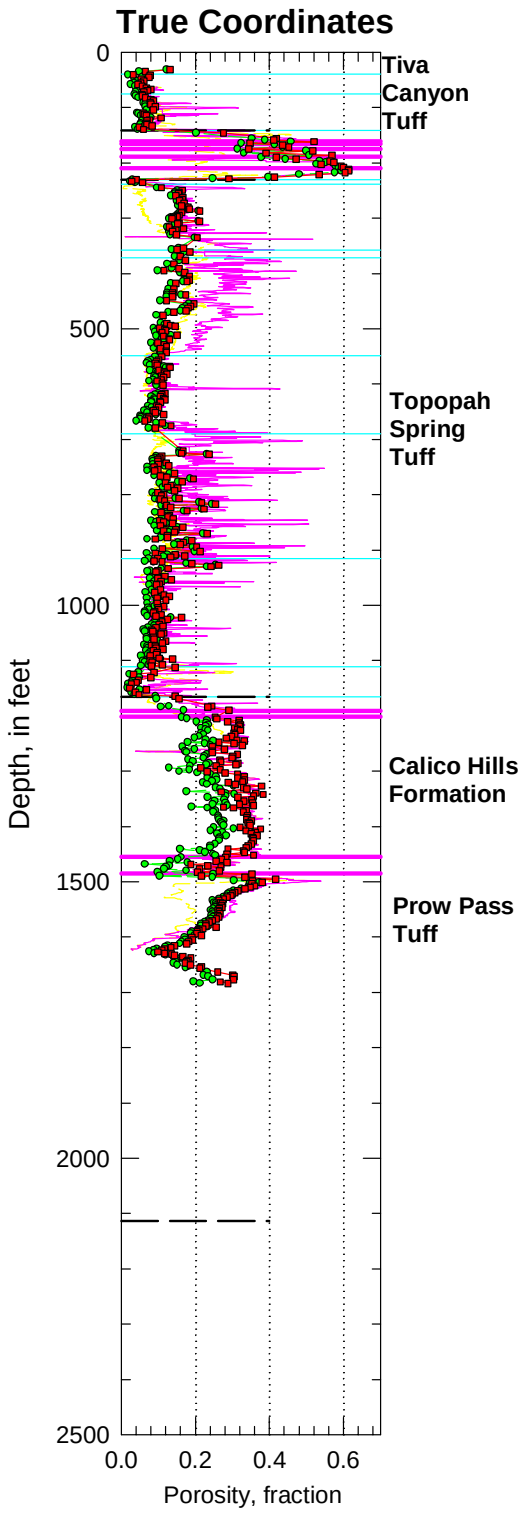

Figure B-70. Porosity data in true coordinates for drillhole UZ-16 for the entire drillhole.

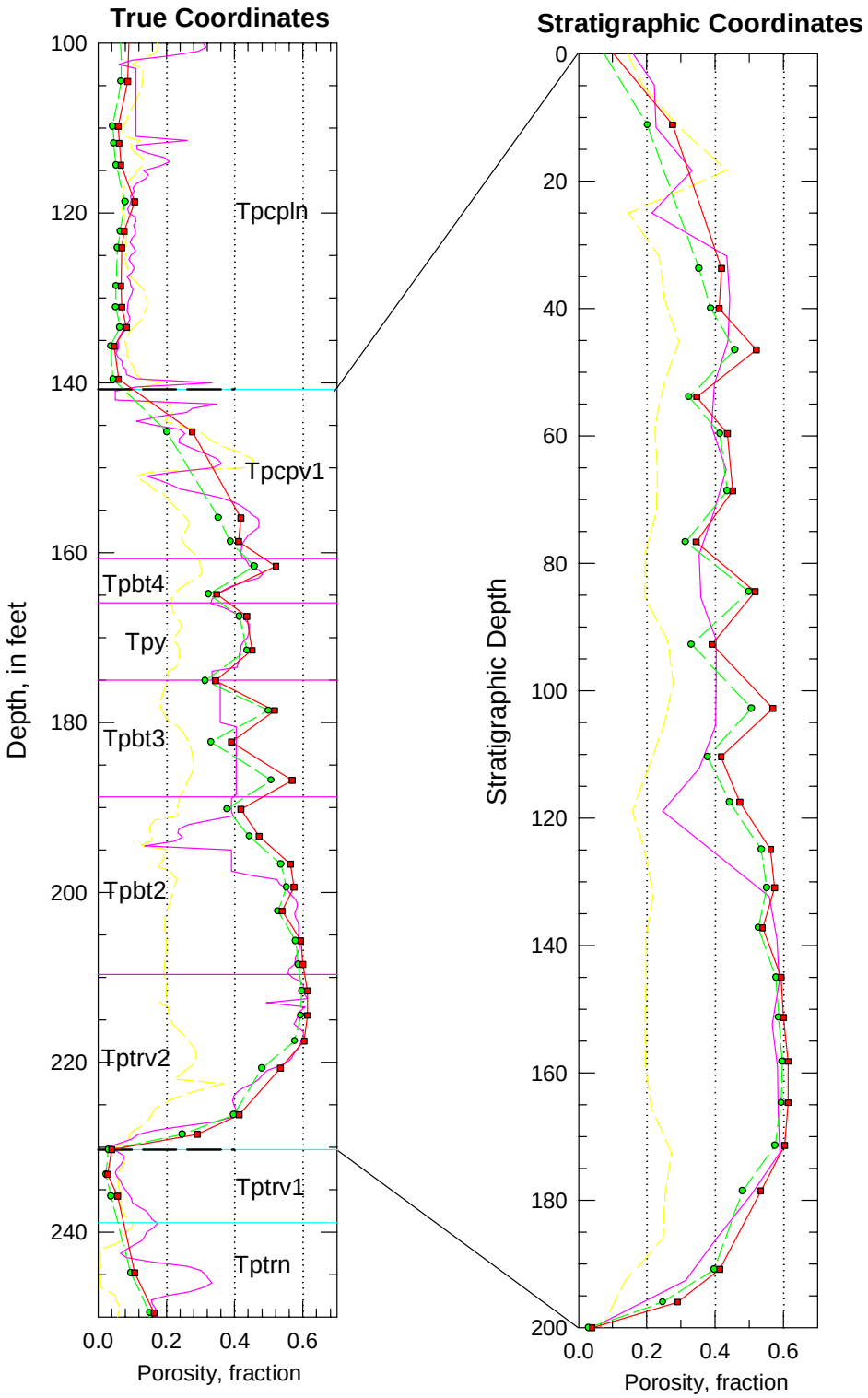

Figure B-71. Porosity data in real-world and in stratigraphic coordinates for the PTn model unit in drillhole UZ-16.

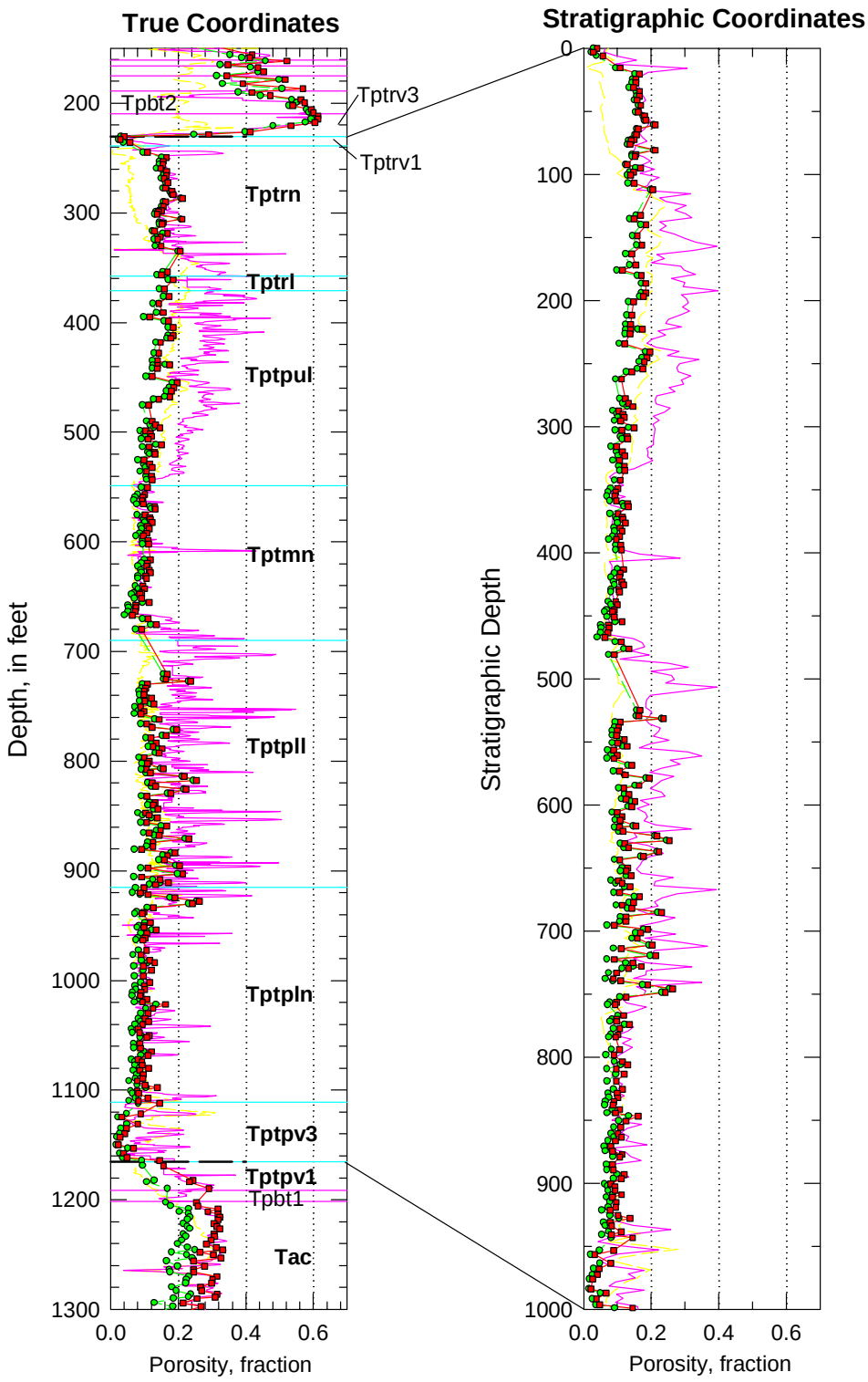

Figure B-72. Poroisty data in real-world and in stratigraphic coordinates for the TSw model unit in drillhole UZ-16.

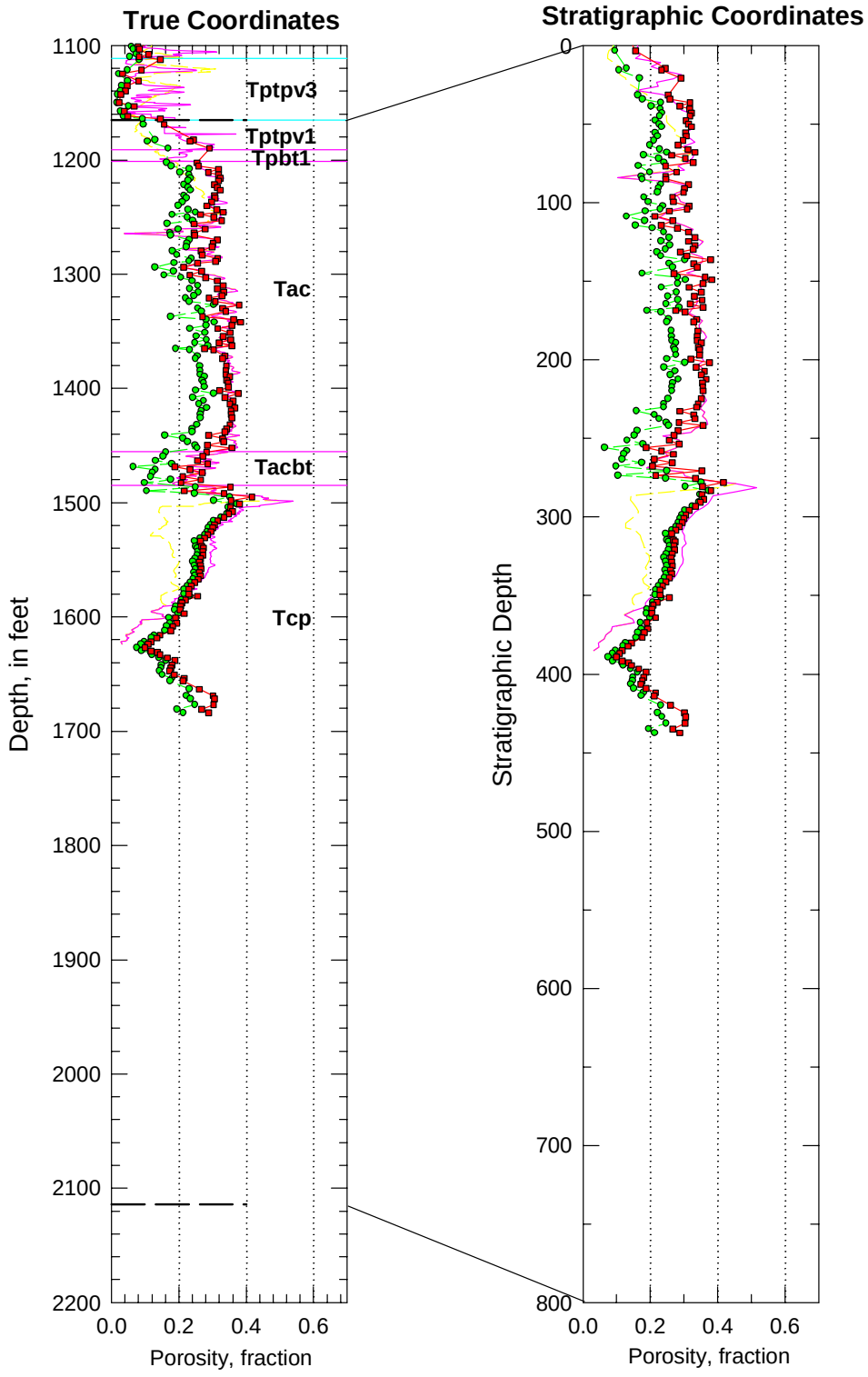

Figure B-73. Porosity data in real-world and in stratigraphic coordinates for the combined CH–PP model unit in drillhole UZ-16.

Drillhole WT-1

Drillhole WT-1 is one of an older series of holes drilled to obtain hydrologic information principally from the saturated zone at Yucca Mountain. The hole was not cored, and the geophysical logs belong the older suite of petrophysical data. These data have been converted to values of total and water-filled porosity. The lower part of the Calico Hills Formation and the entire Prow Pass Tuff are missing at this location because of a fault. Stratigraphic coordinates for the CH–PP model unit are based upon the inferred true thickness of this interval reconstructed from regional thickness trends.

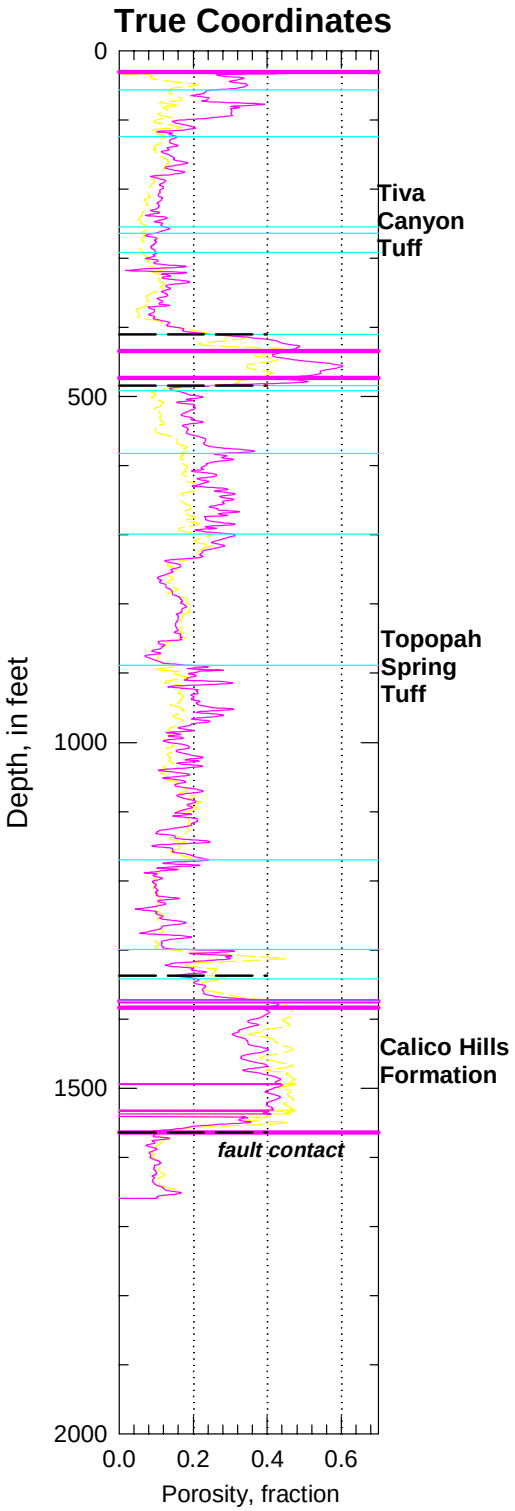

Figure B-74. Porosity data in true coordinates from drillhole WT-1.

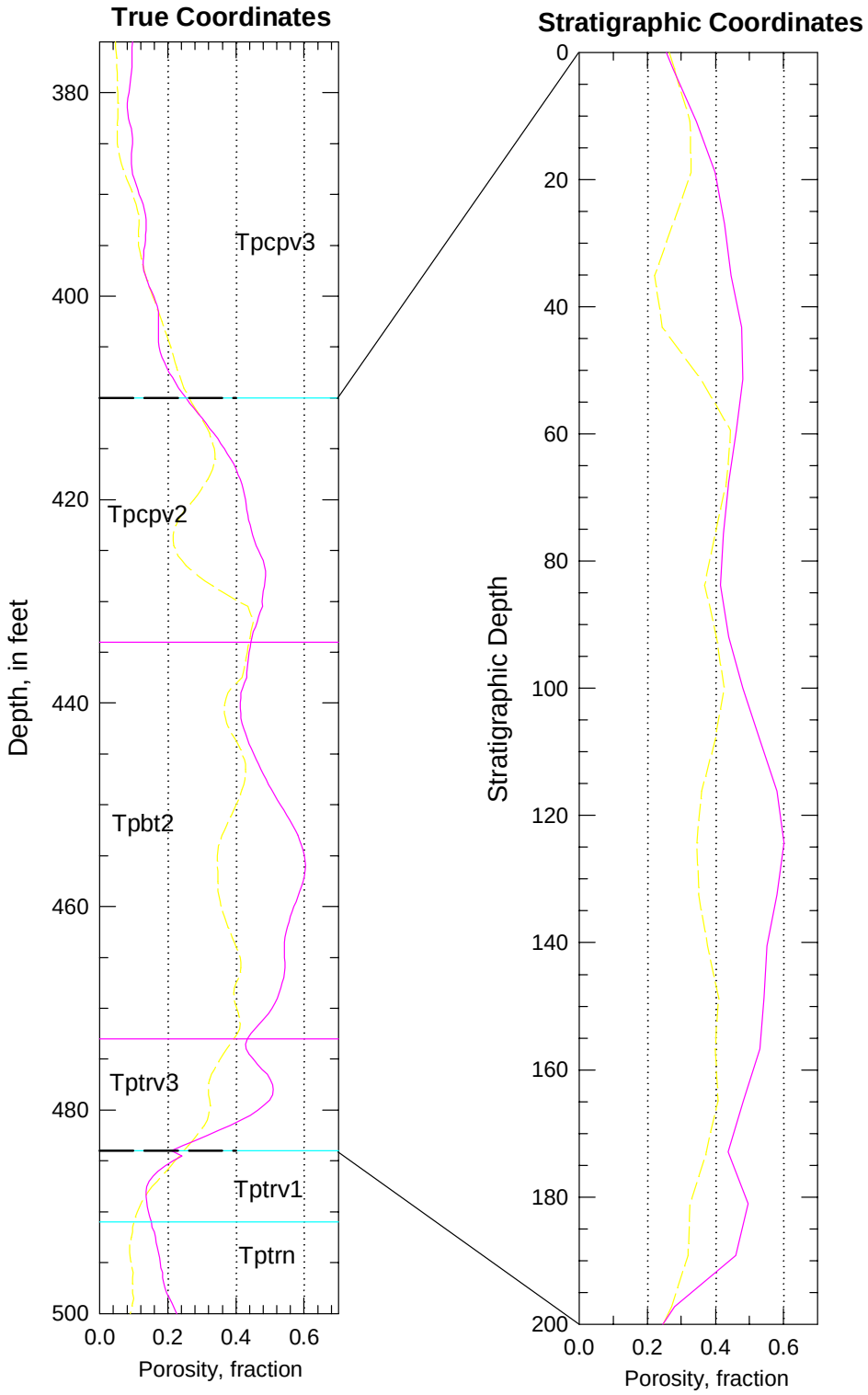

Figure B-75. Porosity data in real-world and in stratigraphic coordinates for the PTn model unit in drillhole WT-1.

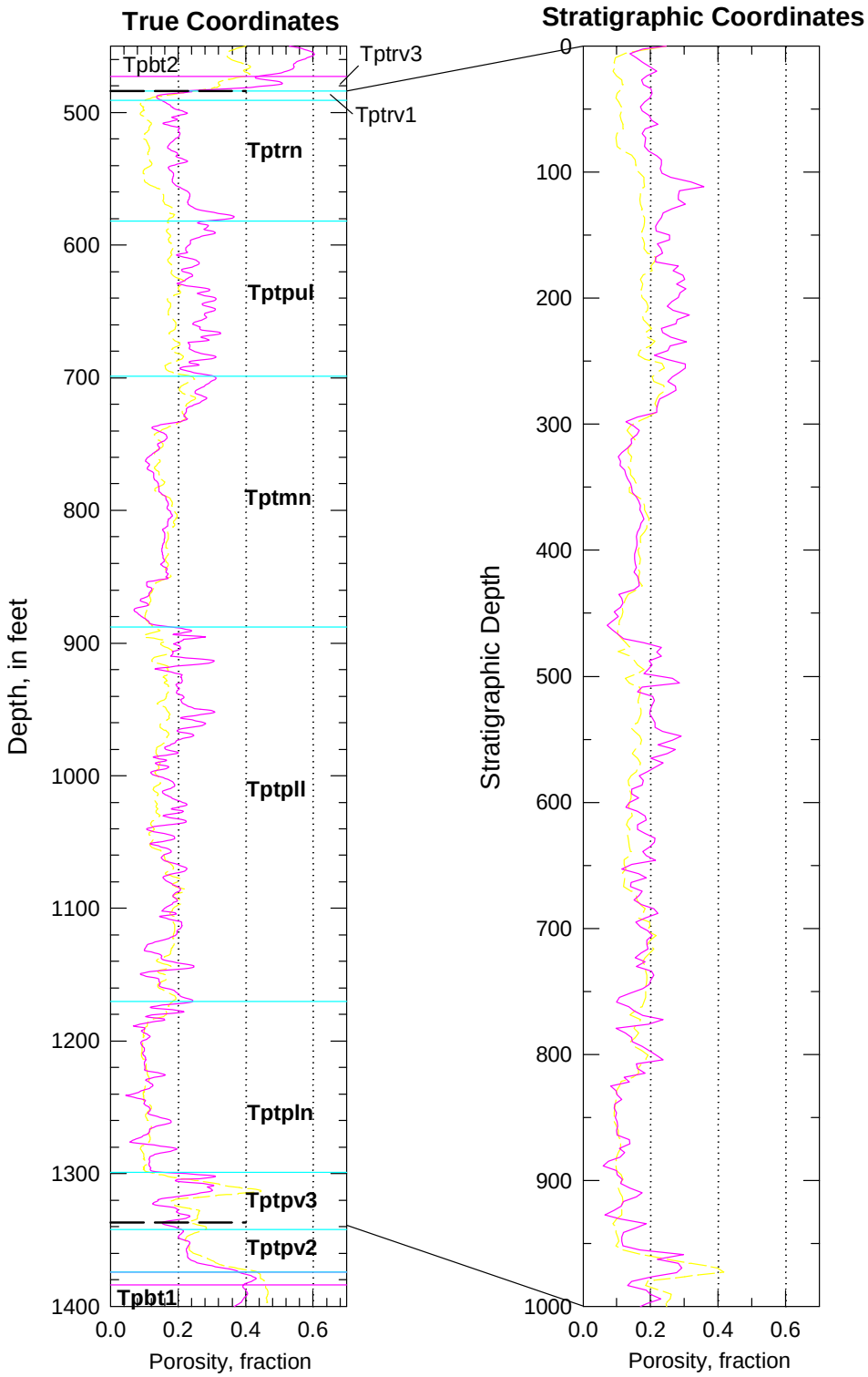

Figure B-76. Porosity data in real-world and in stratigraphic coordinates for the TSw model unit in drillhole WT-1.

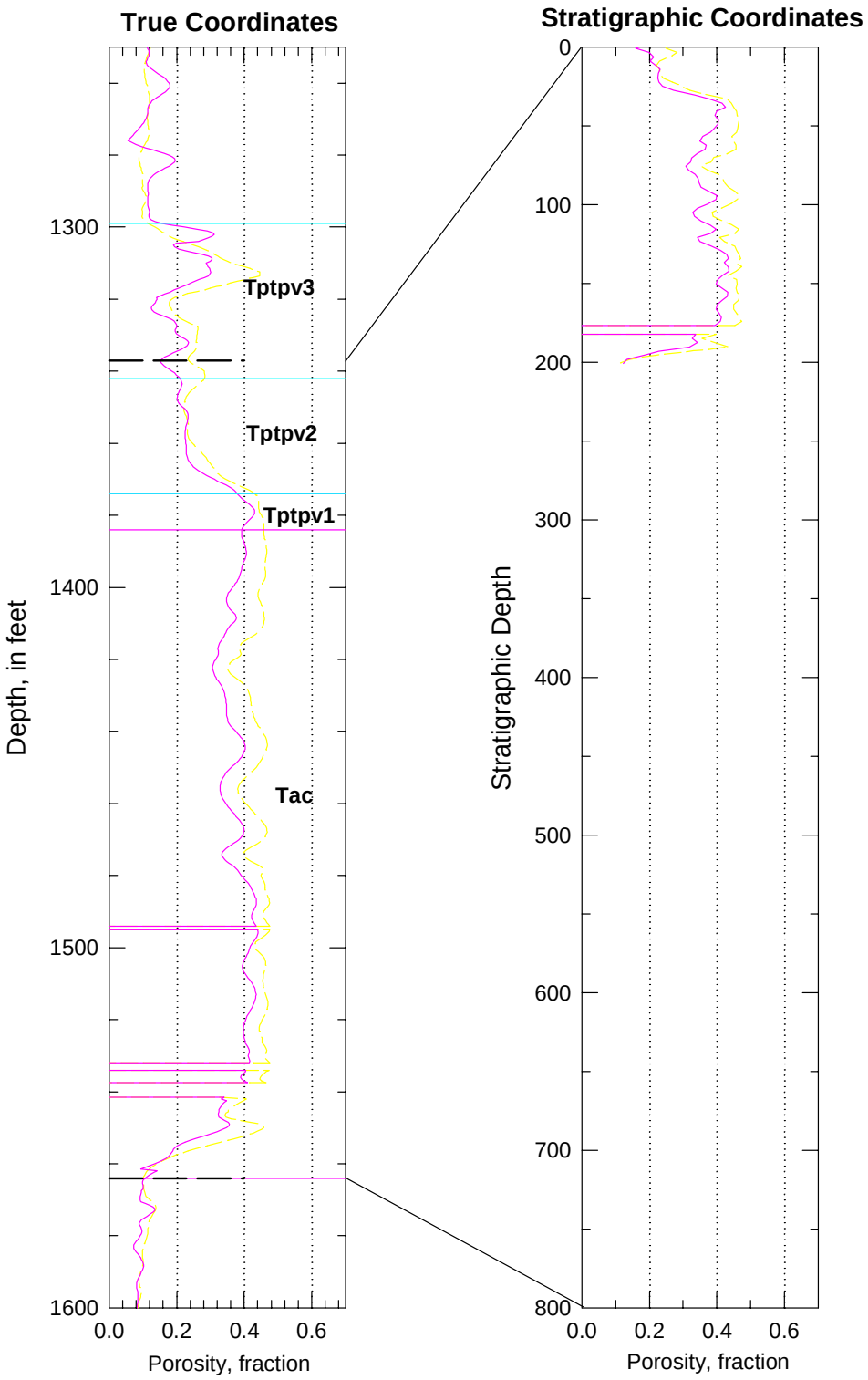

Figure B-77. Porosity data in real-world and in stratigraphic coordinates for the combined CH–PP model unit in drillhole WT-1. The lower part of the Calico Hills Formation and the entire Prow Pass Tuff are missing at this location because of a fault.

Drillhole WT-2 (Older Data)

Drillhole WT-2 is one of an older series of holes drilled to obtain hydrologic information principally from the saturated zone at Yucca Mountain. The hole was not cored, and the earliest geophysical logs belong the older suite of petrophysical data. The hole has been relogged as part of site characterization at Yucca Mountain, and there is also a full suite of modern geophysical information. These data have been converted to values of total and water-filled porosity.

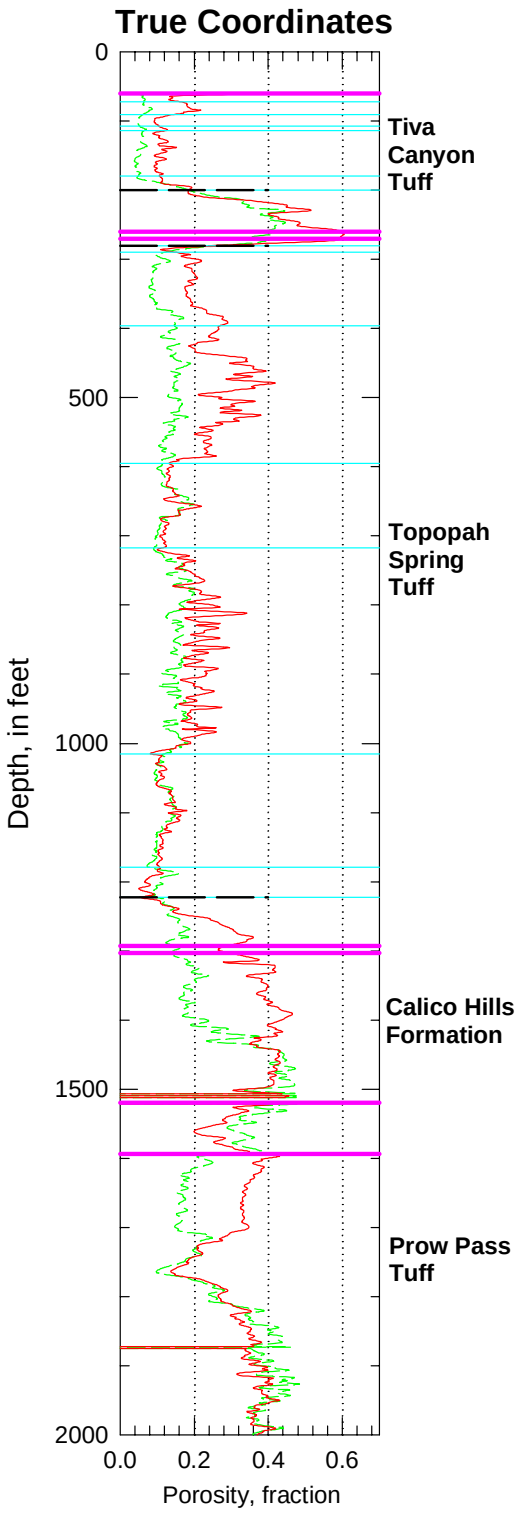

Figure B-78. Porosity data in true coordinates from drillhole WT-2 for the entire drillhole down to the top of the Bullfrog Tuff using the older petrophysical data.

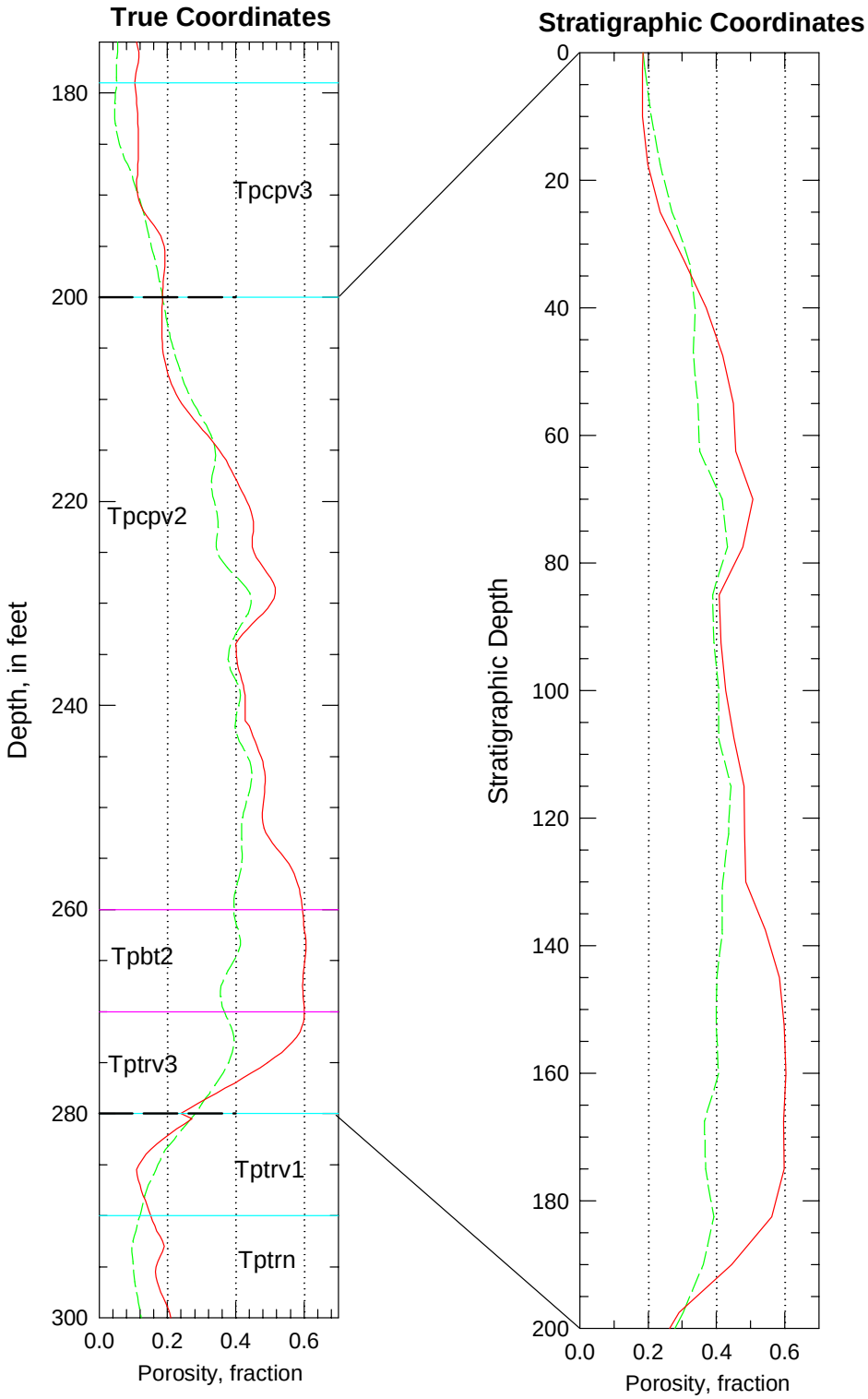

Figure B-79. Porosity data in real-world and in stratigraphic coordinates for the PTn model unit in drillhole WT-2, computed from the older series of petrophysical logs.

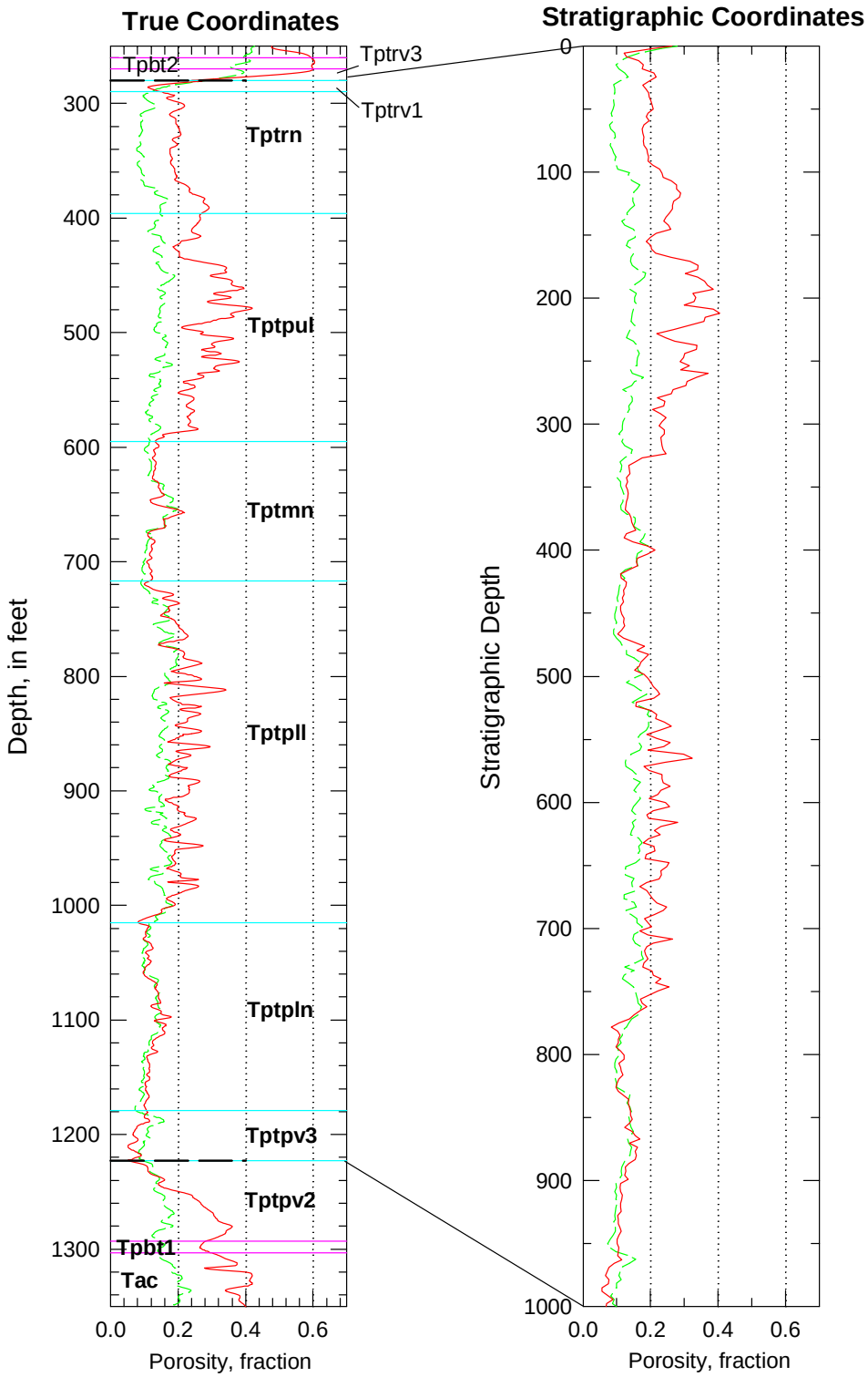

Figure B-80. Porosity data in real-world and in stratigraphic coordinates for the TSw model unit in drillhole WT-2, computed from the older series of petrophysical logs.

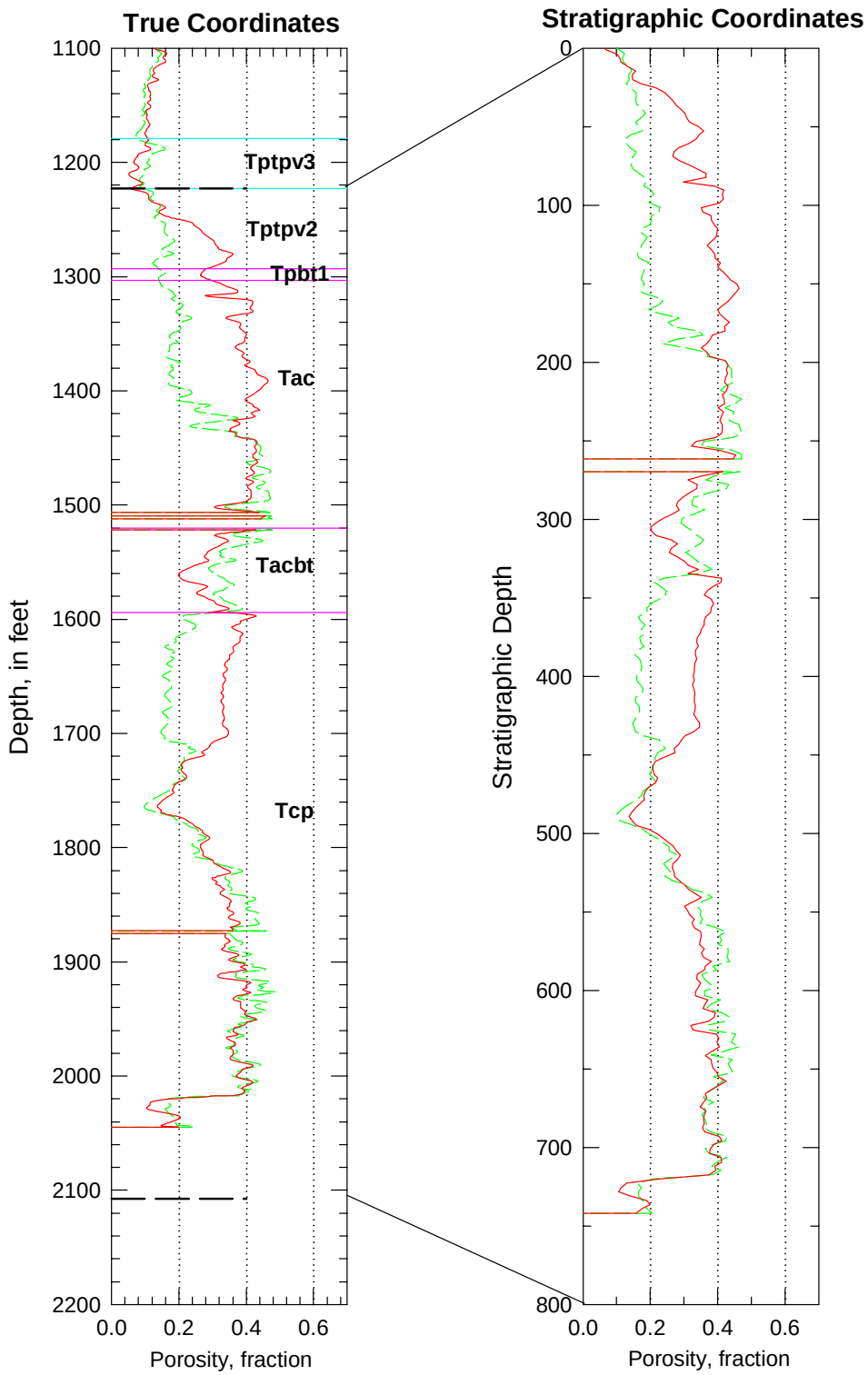

Figure B-81. Porosity data in real-world and in stratigraphic coordinates for the combined CH–PP model unit in drillhole WT-2, computed from the older series of petrophysical logs.

Drillhole WT-2 (Modern Data)

Drillhole WT-2 is one of an older series of holes drilled to obtain hydrologic information principally from the saturated zone at Yucca Mountain. The hole was not cored, and the hole has been relogged as part of site characterization at Yucca Mountain, and there is a full suite of modern geophysical information in addition to the older suite of logs that were obtained shortly after drilling. These data have been converted to values of total and water-filled porosity.

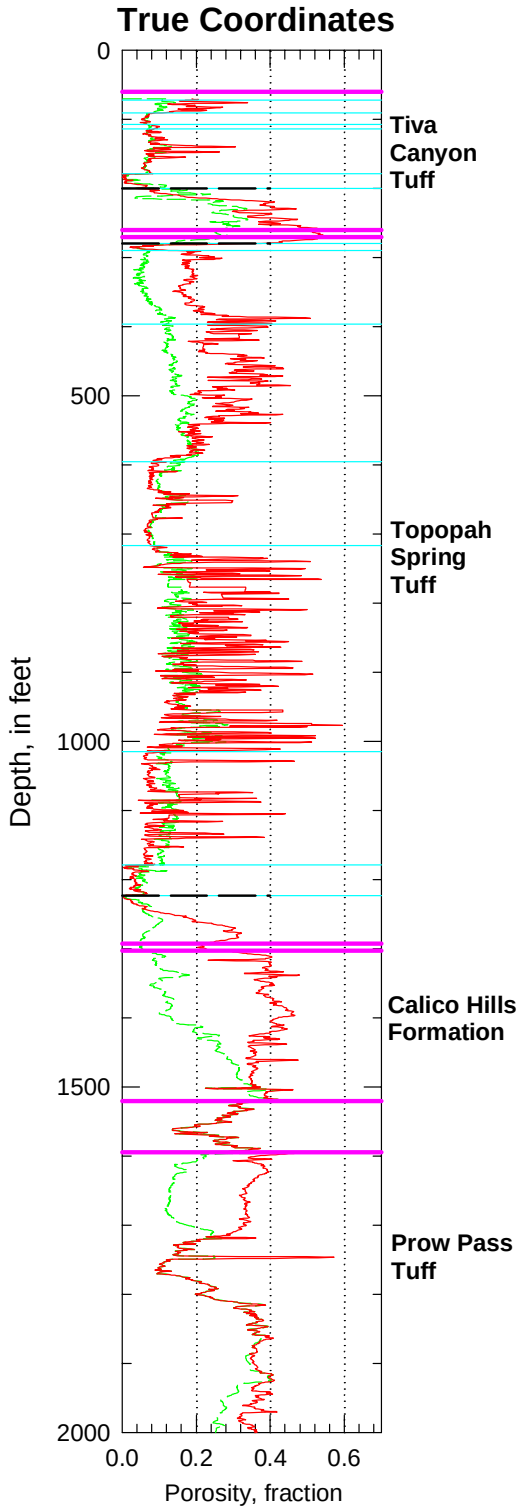

Figure B-82. Porosity data in true coordinates from drillhole WT-2 for the entire drillhole down to the top of the Bullfrog Tuff using the modern petrophysical data.

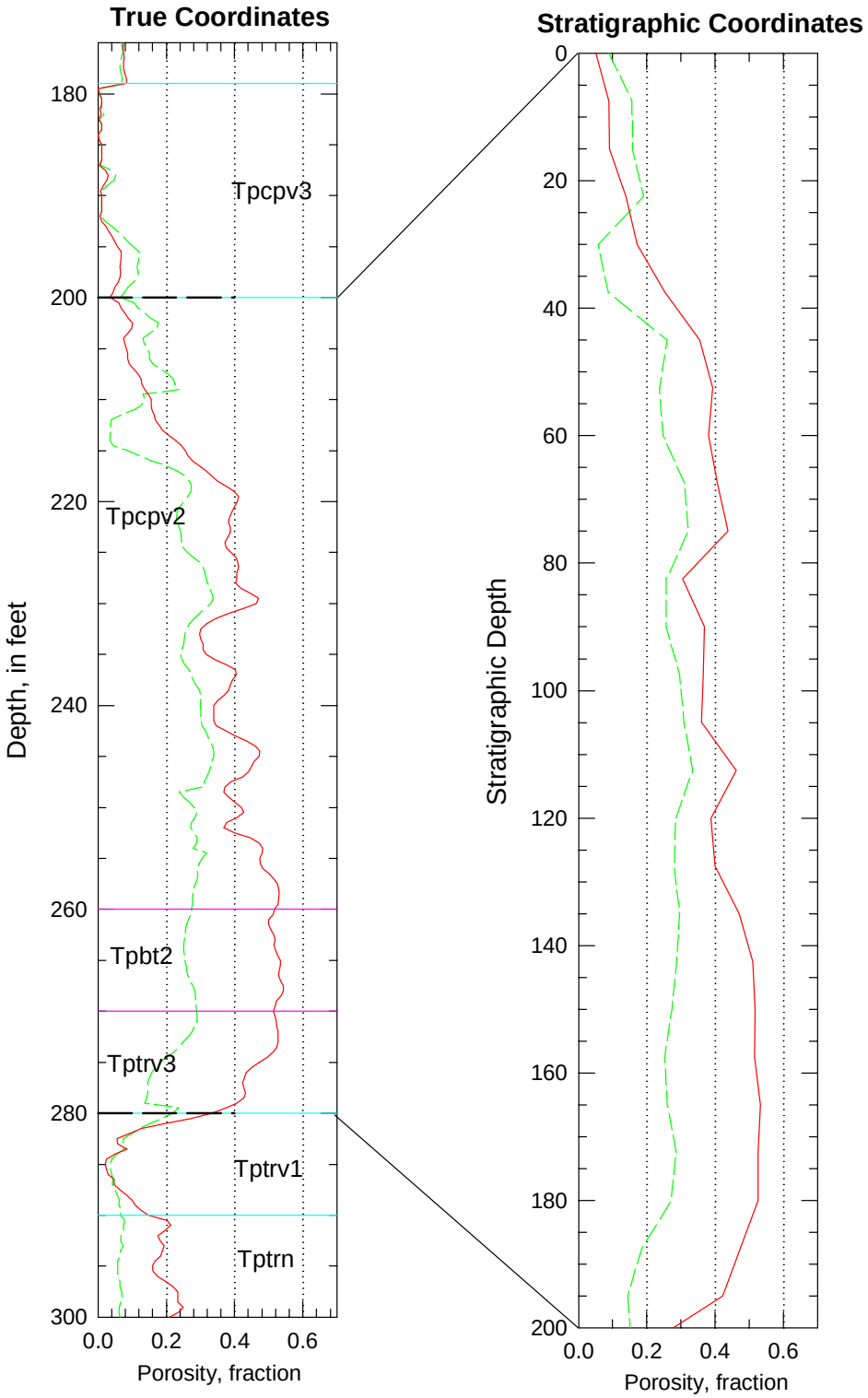

Figure B-83. Porosity data in real-world and in stratigraphic coordinates for the PTn model unit in drillhole WT-2, computed from the modern series of petrophysical logs.

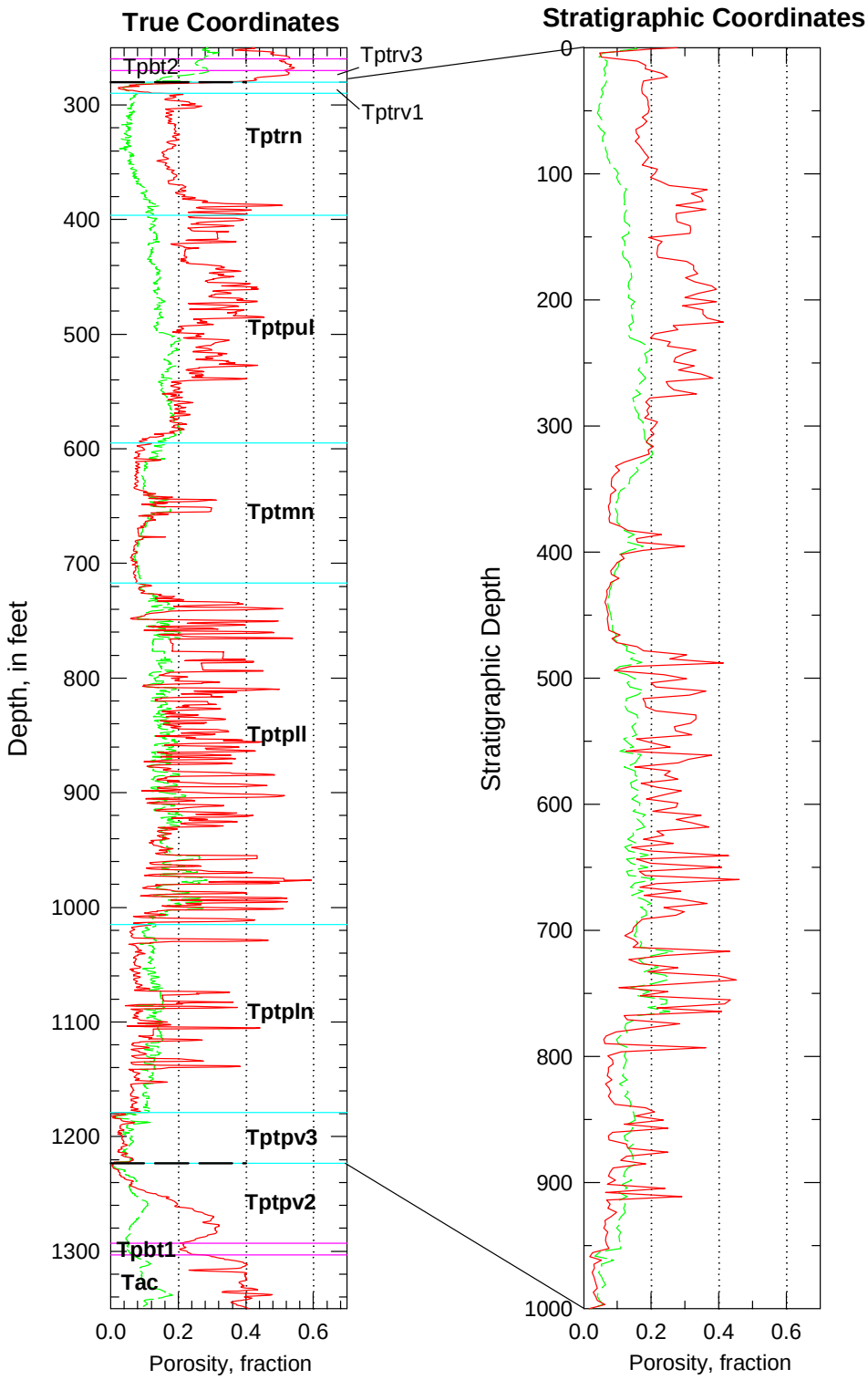

Figure B-84. Porosity data in real-world and in stratigraphic coordinates for the TSw model unit in drillhole WT-2, computed using the modern series of petrophysical logs.

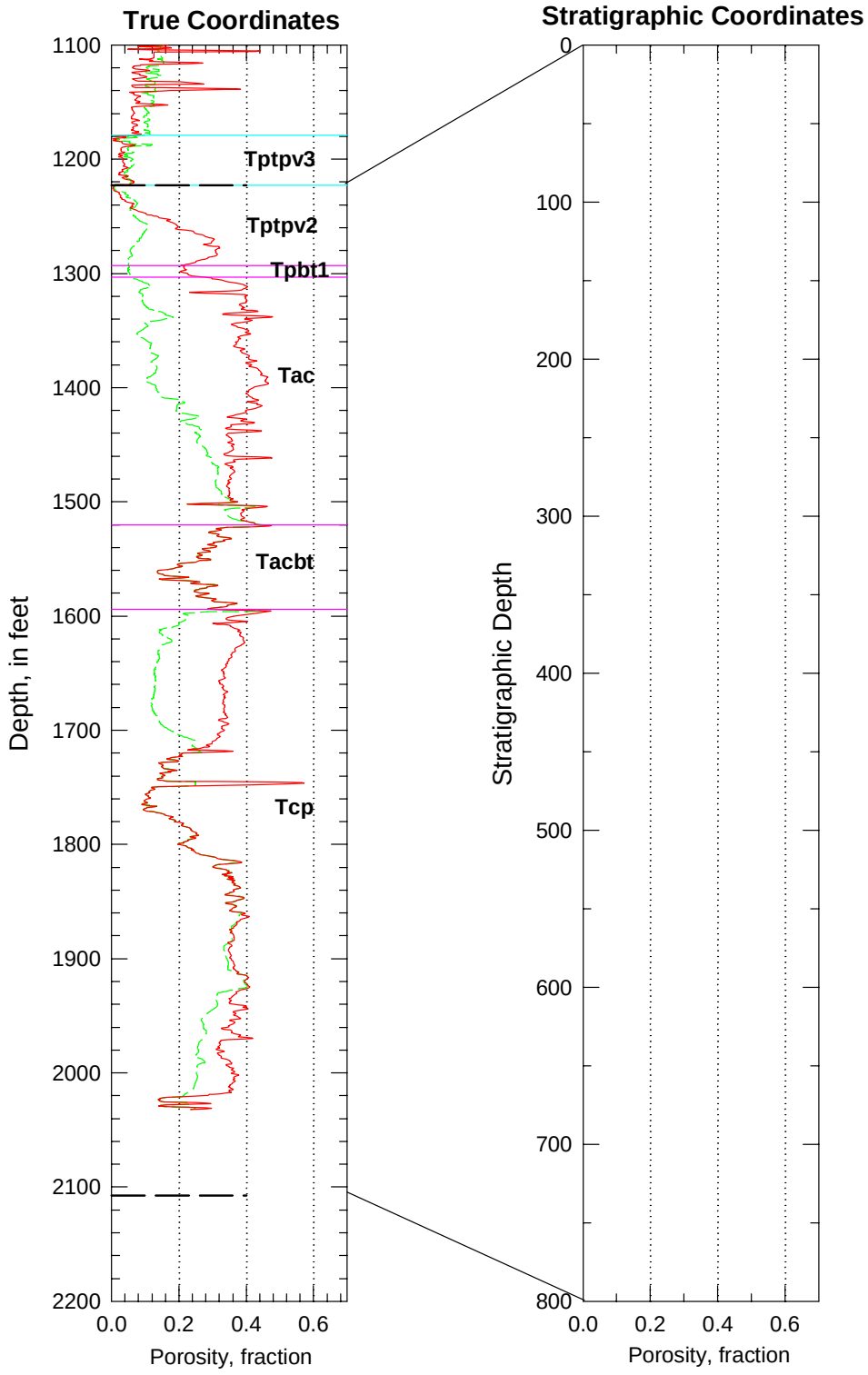

Figure B-85. Porosity data in real-world and is stratigraphic coordinates for the combined CH–PP model unit in drillhole WT-2, computed from the modern series of petrophysical logs.

Drillhole WT-3

Drillhole WT-3 is one of an older series of holes drilled to obtain hydrologic information principally from the saturated zone at Yucca Mountain. The hole was not cored, and the geophysical logs belong the older suite of petrophysical data. These data have been converted to values of total and water-filled porosity.

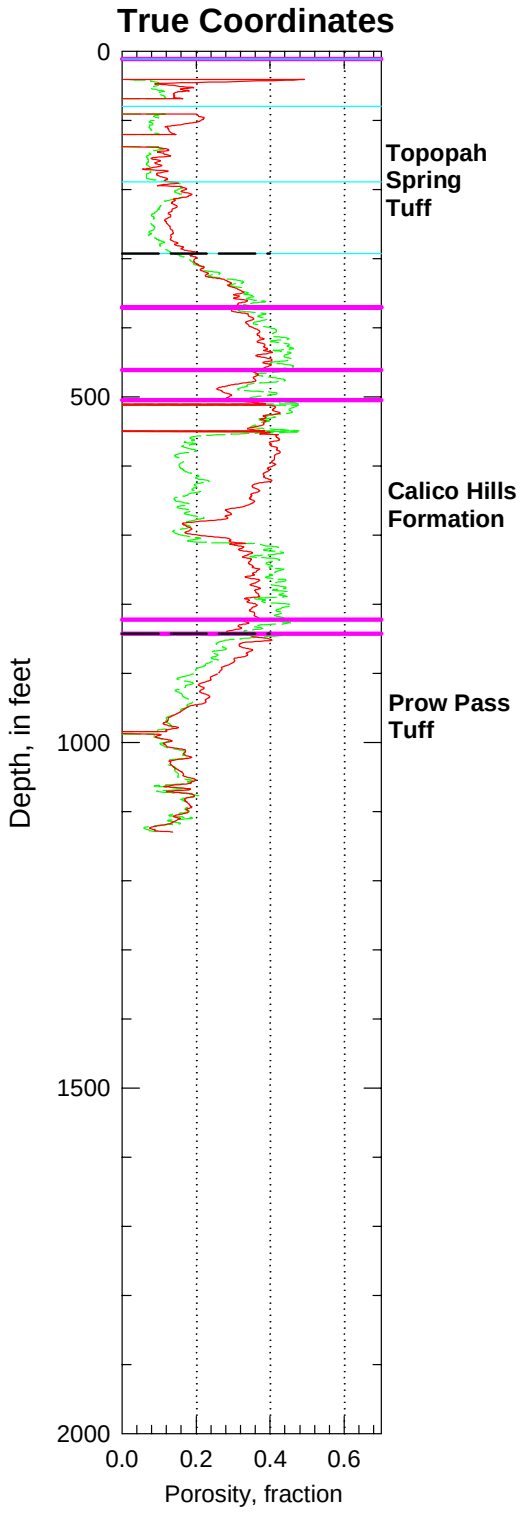

Figure B-86. Porosity data in true coordinates from drillhole WT-3 for the entire drillhole.

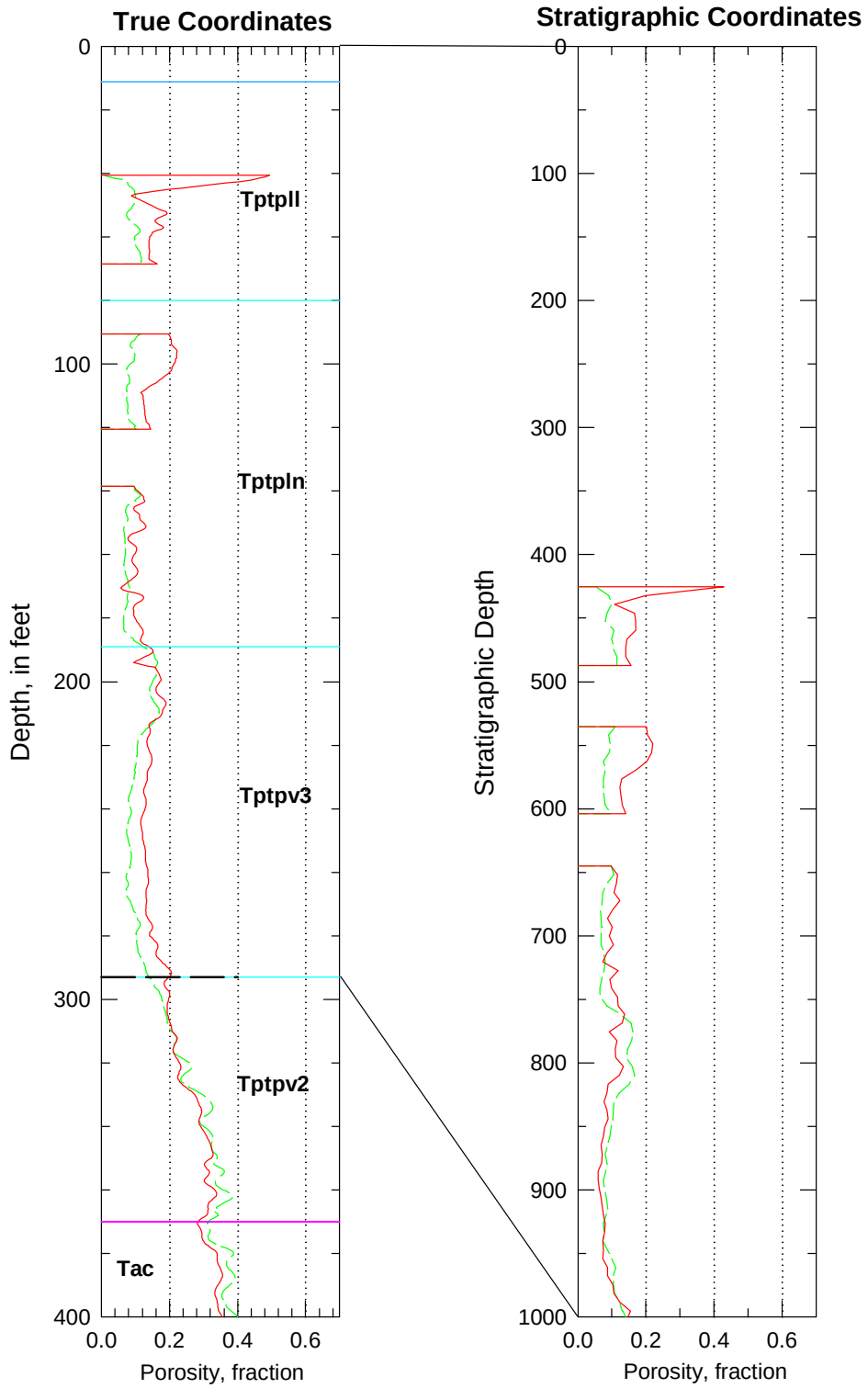

Figure B-87. Porosity data in real-world and in stratigraphc coordinates for the PTn model unit in drillhole WT-3.

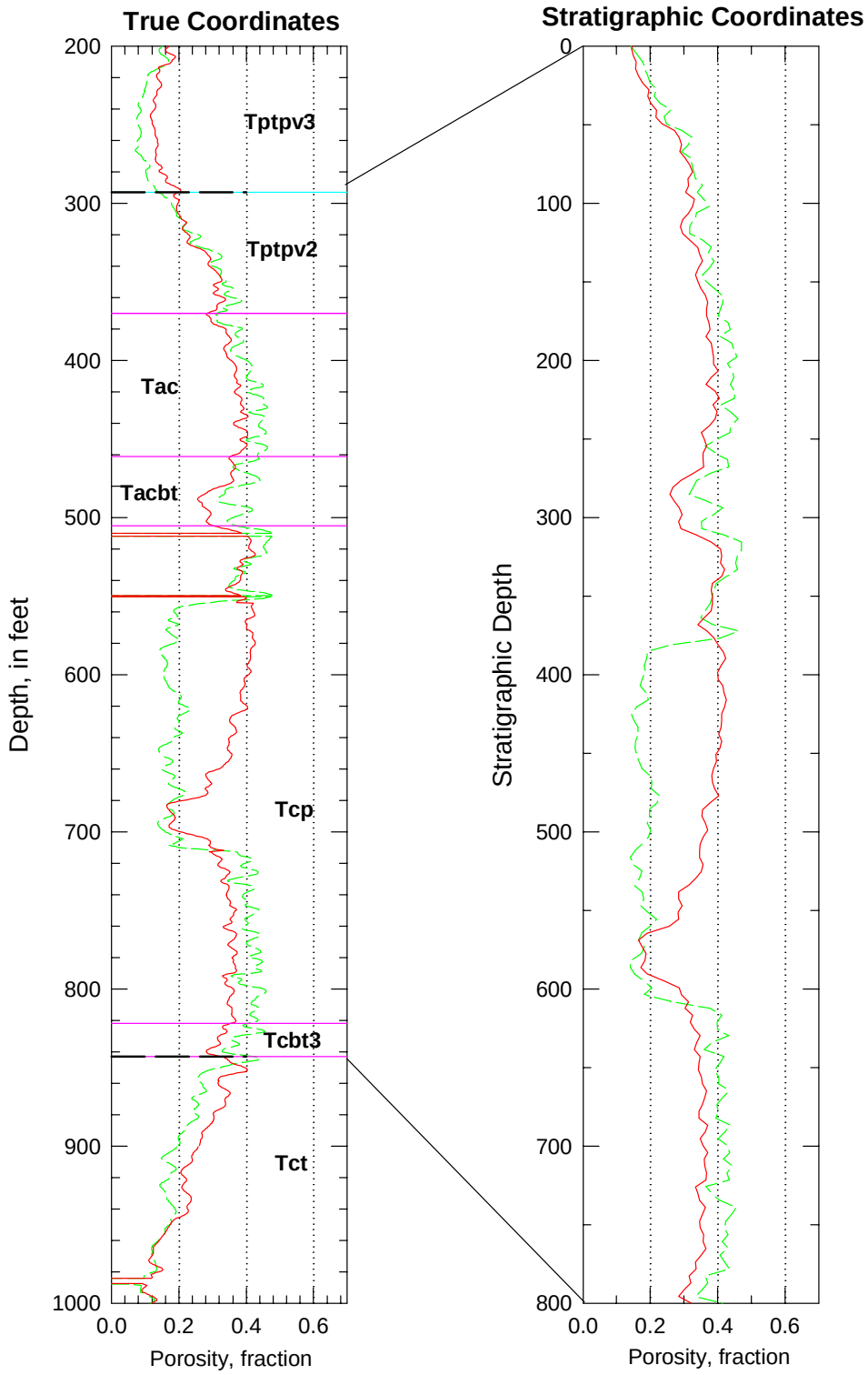

Figure B-88. Porosity data in real-world and in stratigraphic coordinates for the TSw model unit in drillhole WT-3.

Drillhole WT-4

Drillhole WT-4 is one of an older series of holes drilled to obtain hydrologic information principally from the saturated zone at Yucca Mountain. The hole was not cored, and the geophysical logs belong the older suite of petrophysical data. These data have been converted to values of total and water-filled porosity.

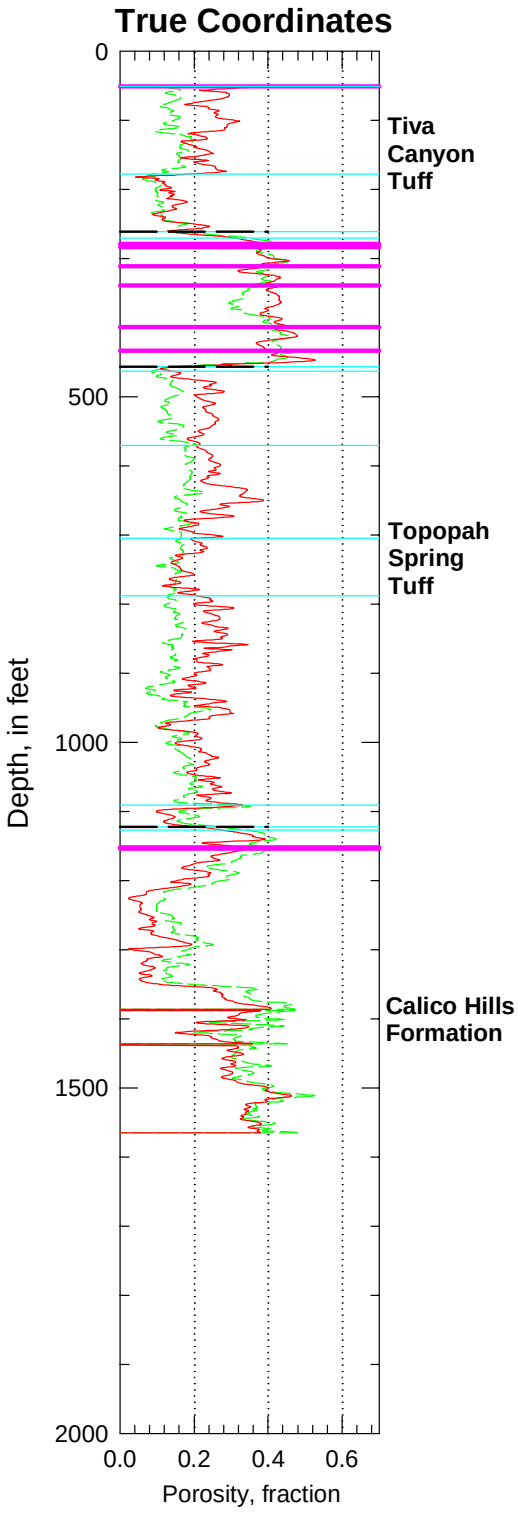

Figure B-89. Porosity data in true coordinates from drillhole ST-4 for the entire drill hole.

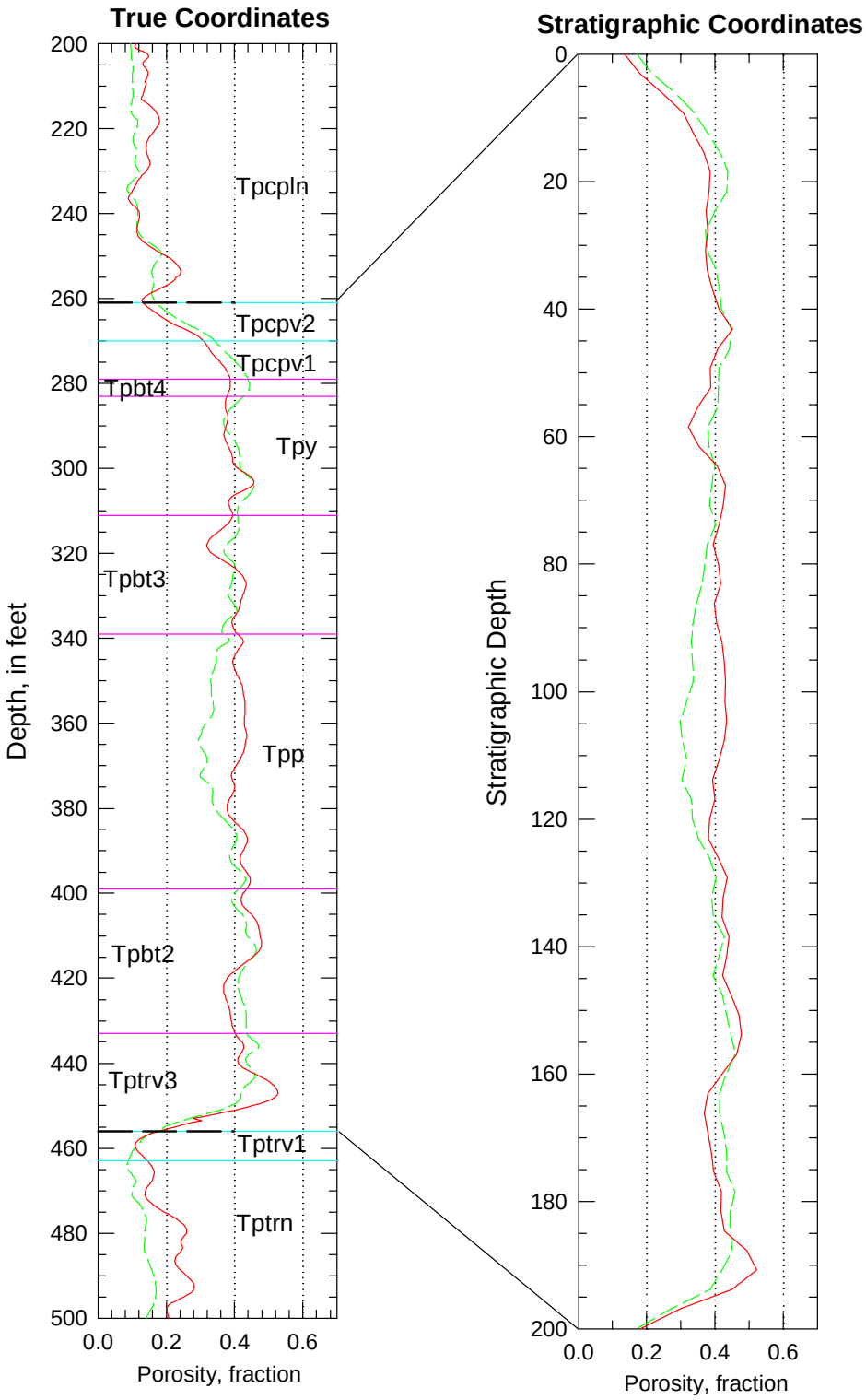

Figure B-90. Porosity data in real-world and in stratigraphic coordinates for the TSw model unit in drillhole WT-4.

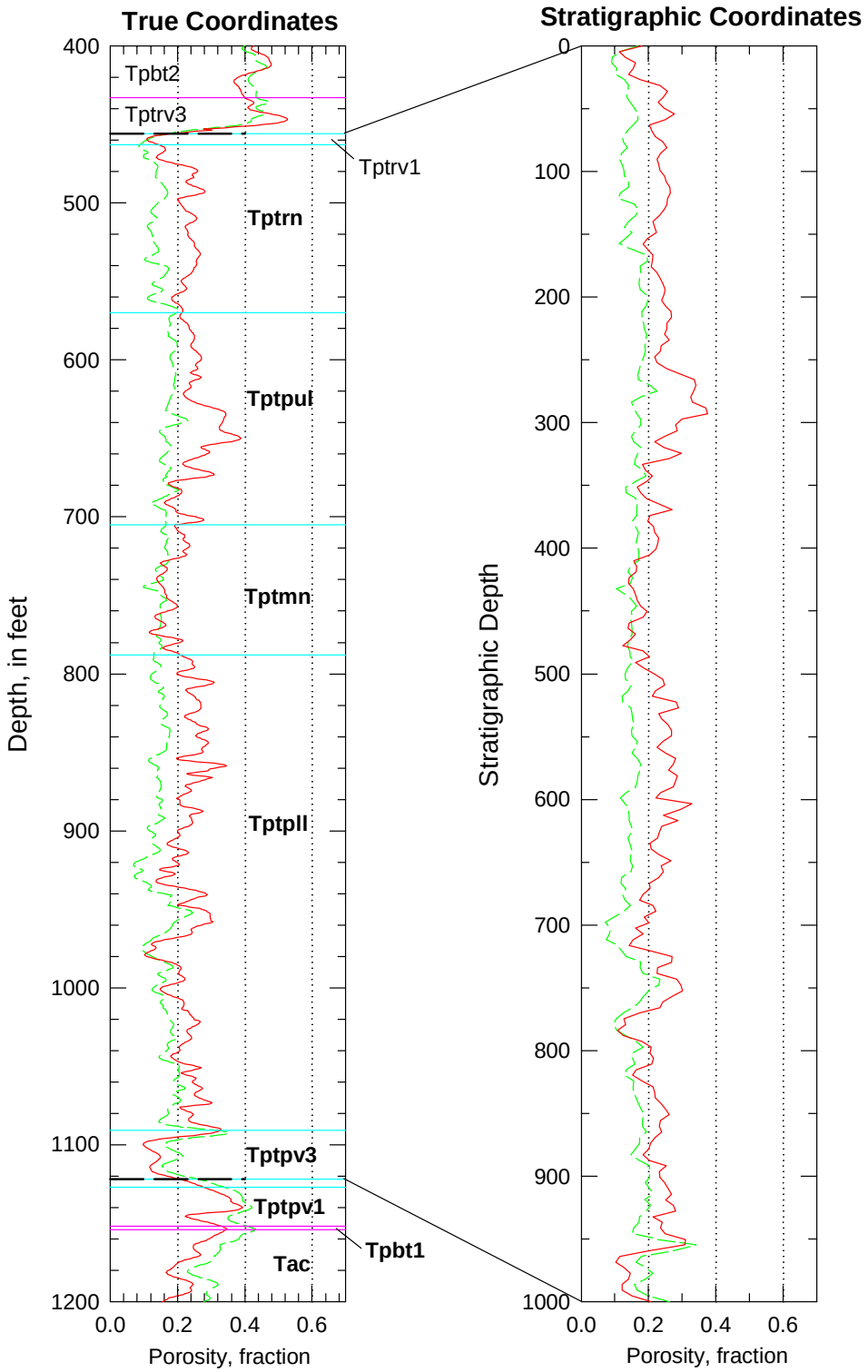

Figure B-91. Porosity data in real-world and in stratigraphic coordinates for the TSw model unit in drillhole WT-4.

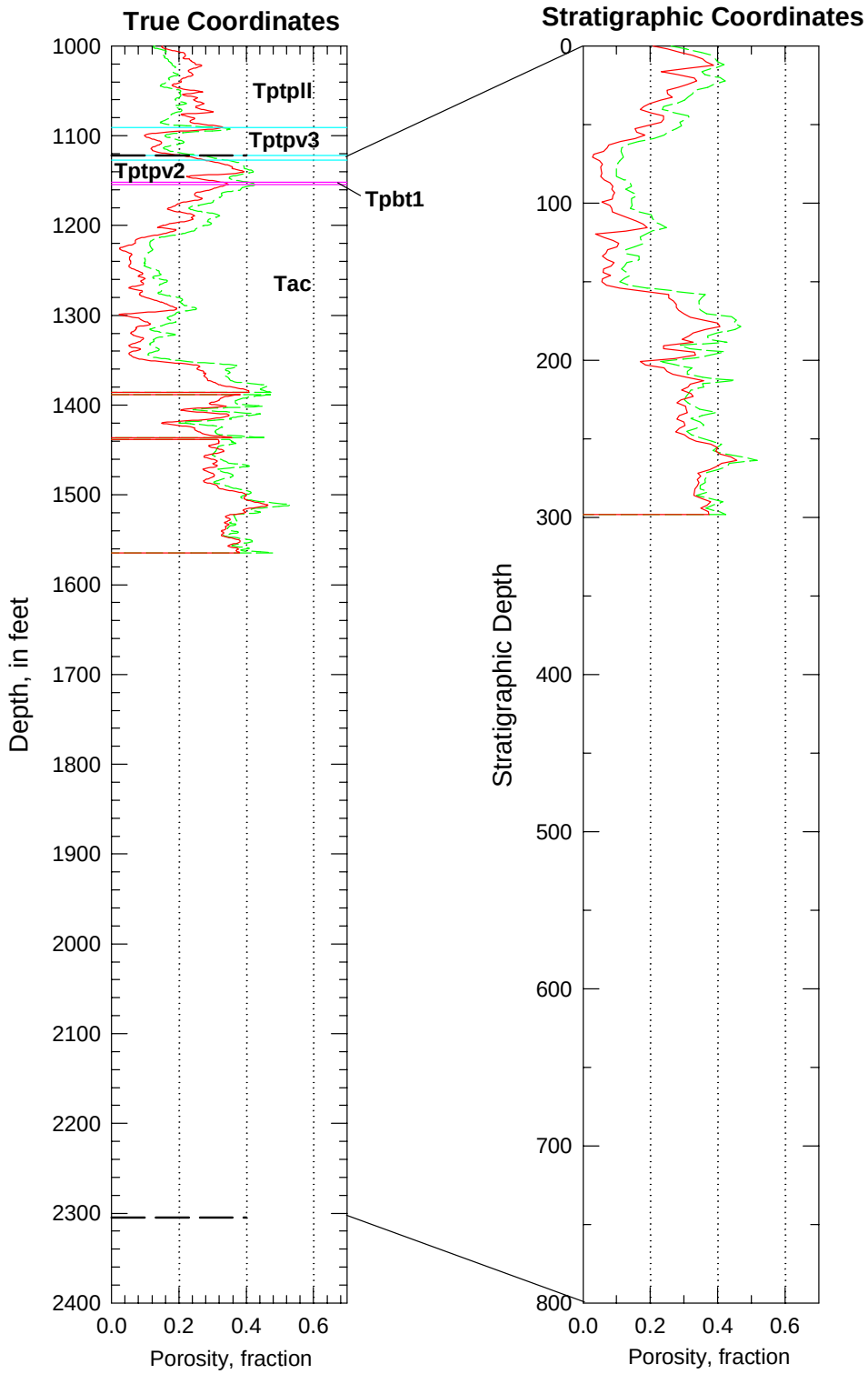

Figure B-92. Porosity data in real-world and in stratigraphci coordinates for the combined CH–PP model unit in drillhole WT-4.

Drillhole WT-6

Drillhole WT-6 is one of an older series of holes drilled to obtain hydrologic information principally from the saturated zone at Yucca Mountain. The hole was not cored, and the geophysical logs belong the older suite of petrophysical data. These data have been converted to values of total and water-filled porosity.

The Topopah Spring tuff is anomalously thin in the vicinty of the WT-6 drill hole, and virtually the entire thickness of the Calico Hills Formation that was penetrated in this drillhole consists of rhyolitic lavas rather than of pyroclastic rocks. Because the rocks in WT-6 are distinctly atypical of the majority of the volcanic units in the Yucca Mountain area, these data were not used in modeling rock material properties in this study. Indeed, the nature of the rocks changes profoundly between drillholes G-2 and WT-6, and this discontinuity has been used to define the northern limit of the modeled area. Rocks to the north of this latitude belong to a different geologic terrane, and their properties should be modeled separately from those to the south. Accordingly, data from this hole are not presented in stratigraphic coordinates.

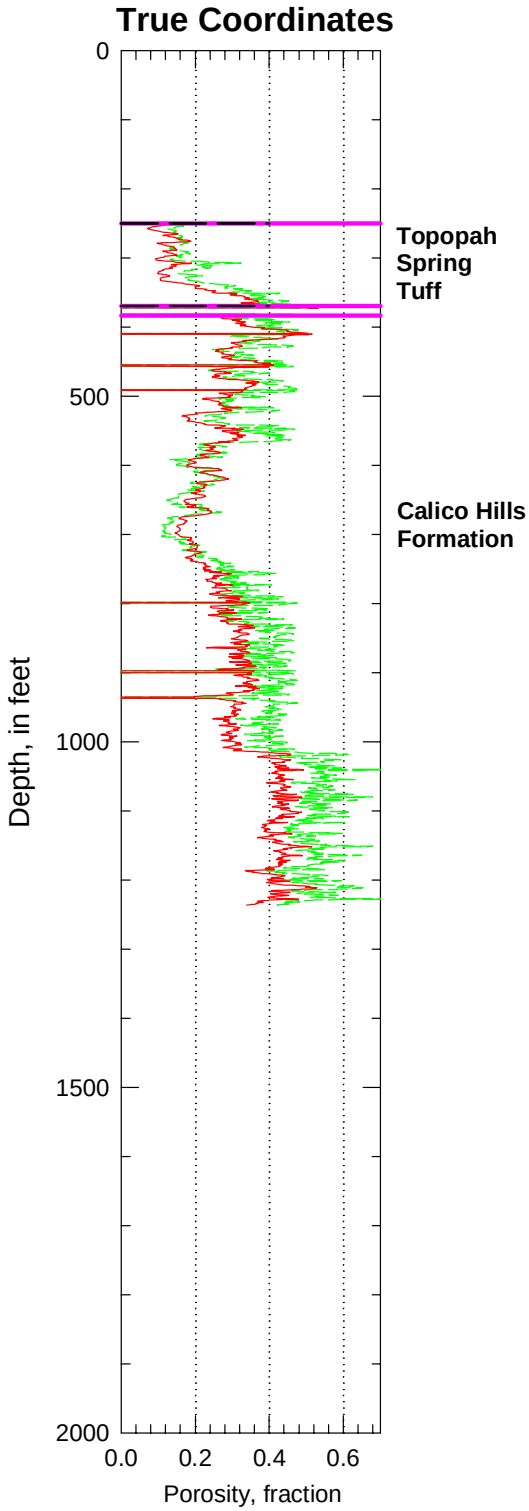

Figure B-93. Porosity data in true coordinates from drillhole WT-6 for the entire drillhole.

Drillhole WT-7

Drillhole WT-7 is one of an older series of holes drilled to obtain hydrologic information principally from the saturated zone at Yucca Mountain. The hole was not cored, and the geophysical logs belong the older suite of petrophysical data. These data have been converted to values of total and water-filled porosity.

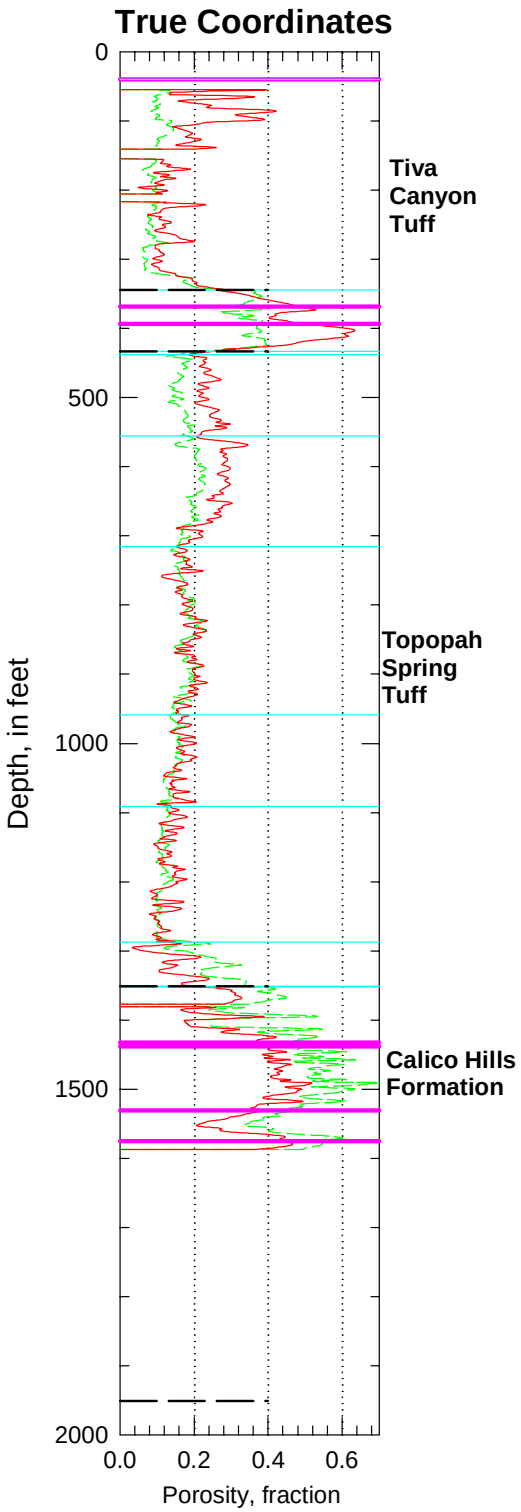

Figure B-94. Porosity data in true coordinates from drillhole WT-7 for the entire drillhole.

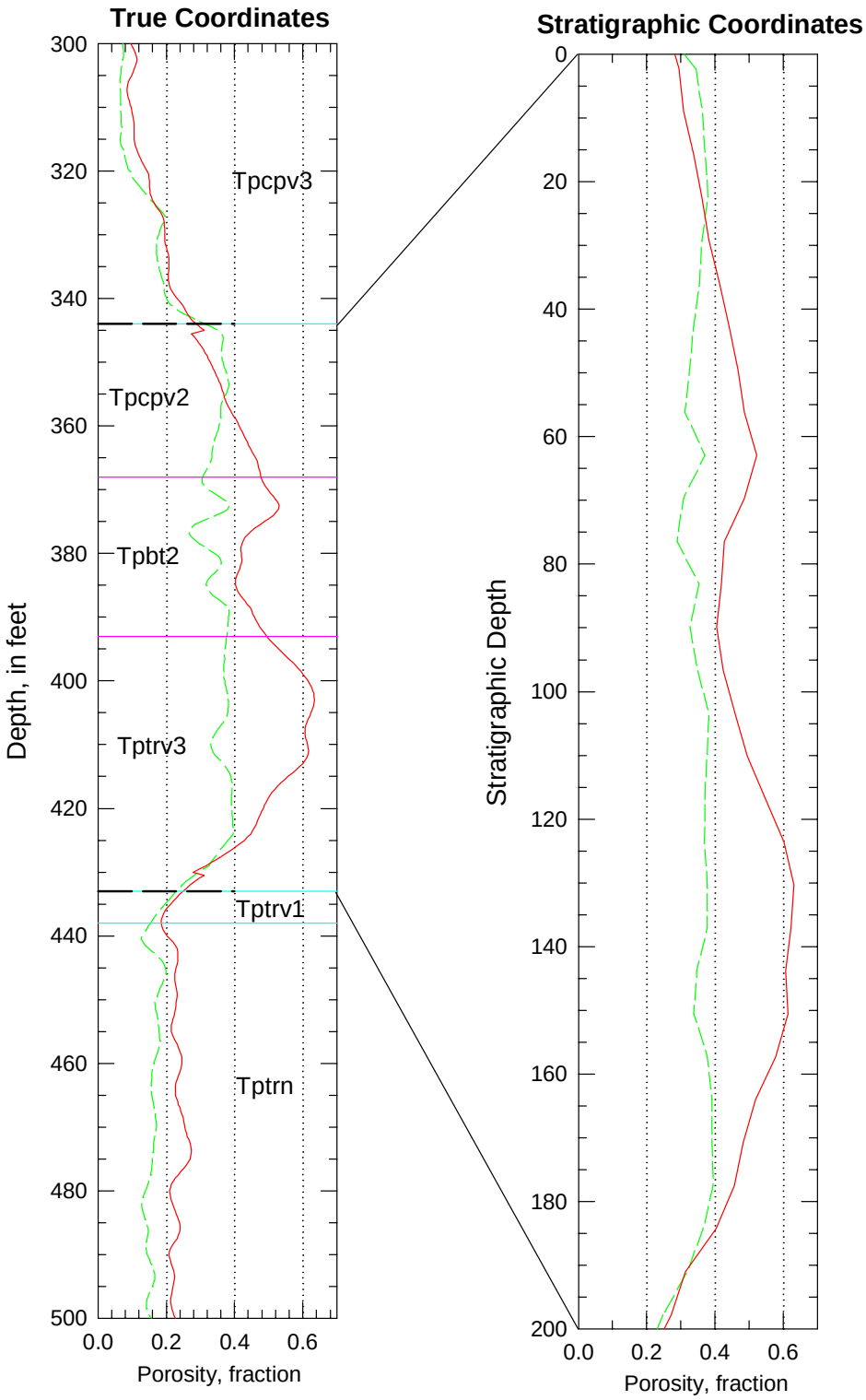

Figure B-95. Porosity data in real-world and in stratigraphic coordinates for the PTn model unit in drillhole WT-7.

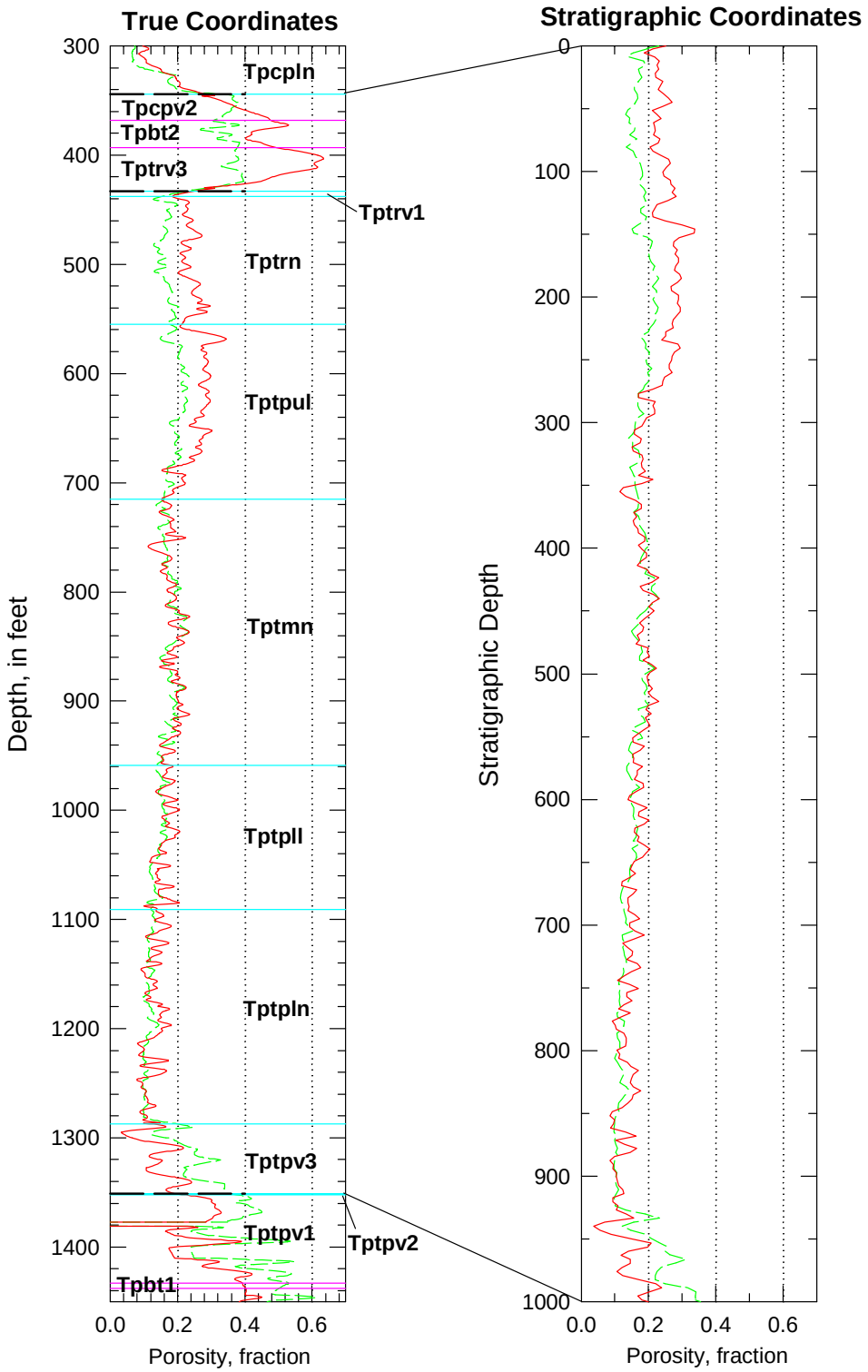

Figure B-96. Porosity data in real-world and in stratigraphic coordinates for the TSw model unit in drillhole WT-7.

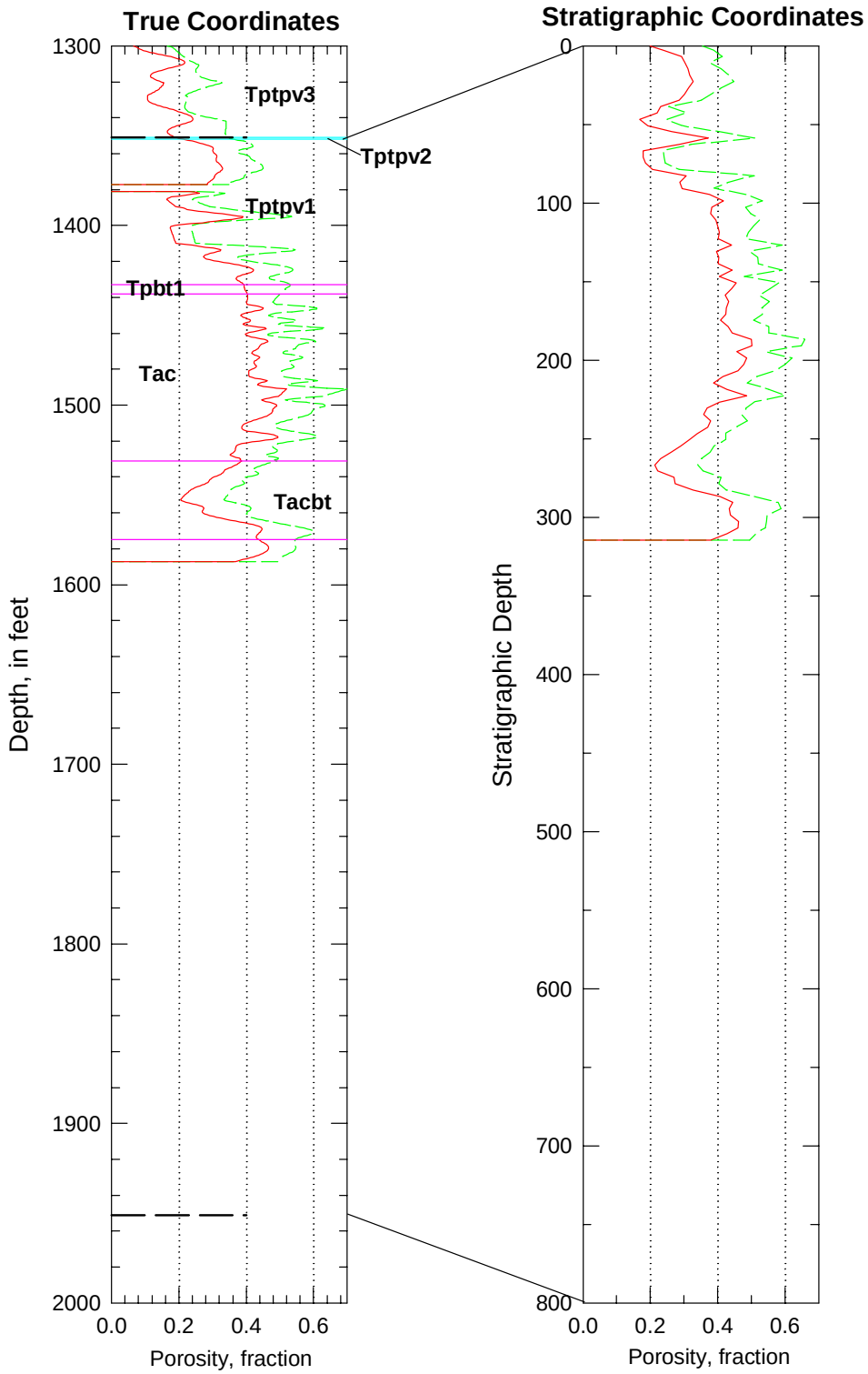

Figure B-97. Porosity data in real-world and in stratigraphic coordinates for the combined CH–PP model unit in drillhole WT-7

Drillhole WT-10 (Older Data)

Drillhole WT-10 is one of an older series of holes drilled to obtain hydrologic information principally from the saturated zone at Yucca Mountain. The hole was not cored, and the earliest geophysical logs belong the older suite of petrophysical data. The hole was relogged as part of site characterization efforts, and there is also a full suite of modern geophysical data. These data have been converted to values of total and water-filled porosity.

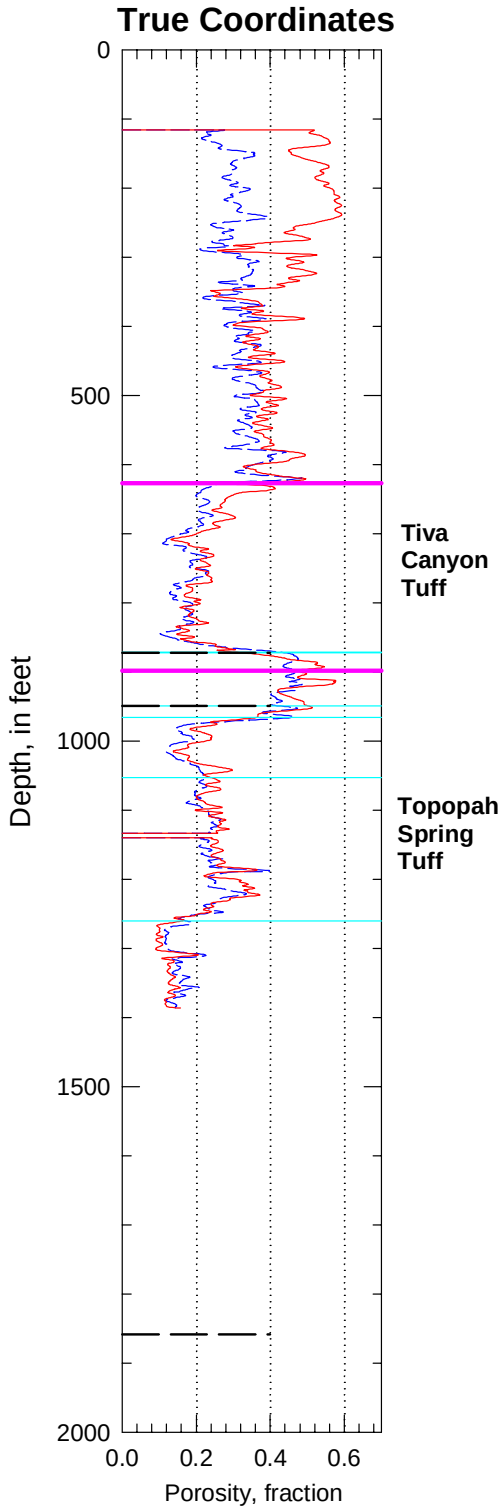

Figure B-98. Porosity data in true coordinates from drillhole WT-10 for the entire drillhole.

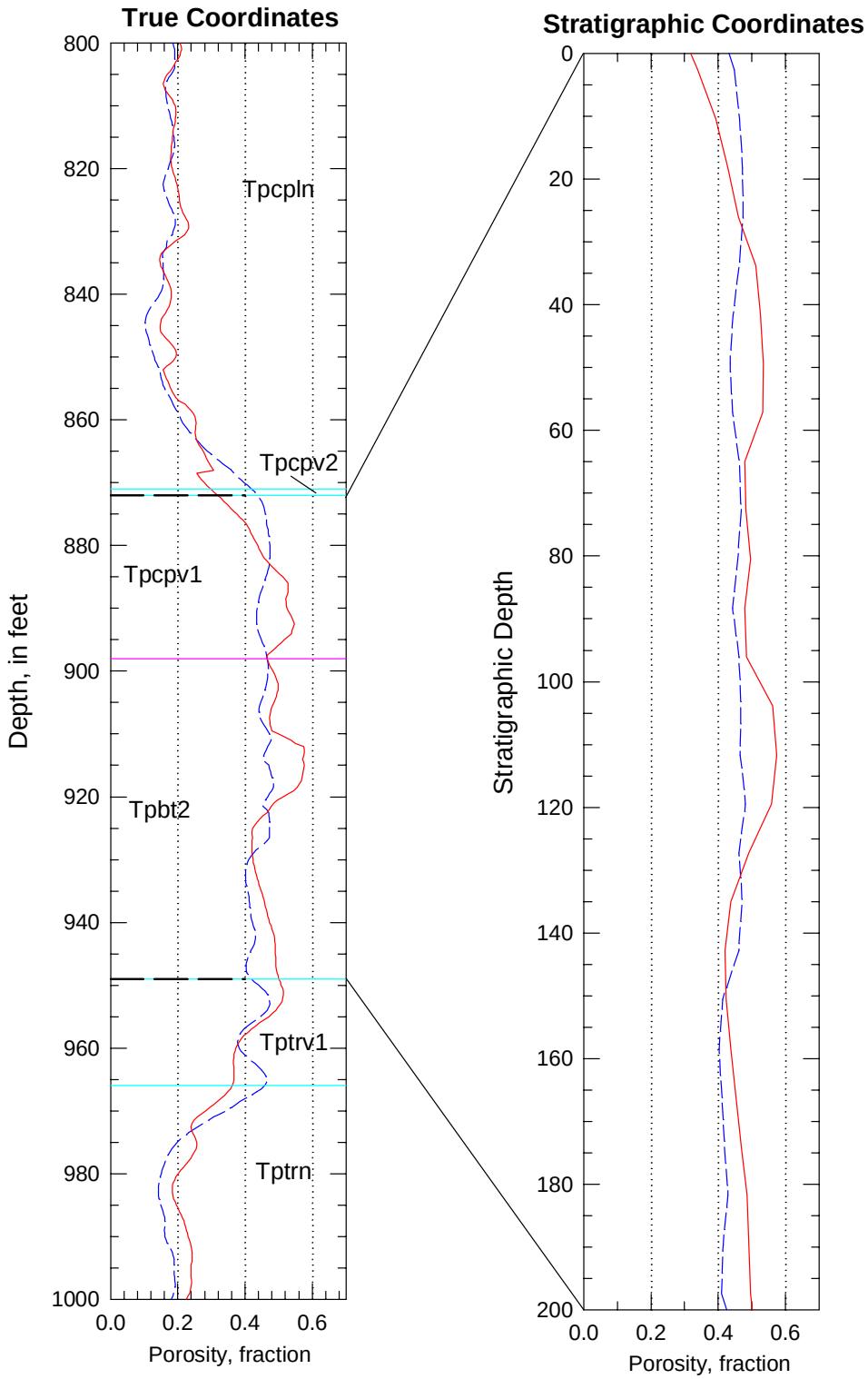

Figure B-99. Porosity data in real-world and in stratigraphic coordinates for the PTn model unit in drillhole WT-10.

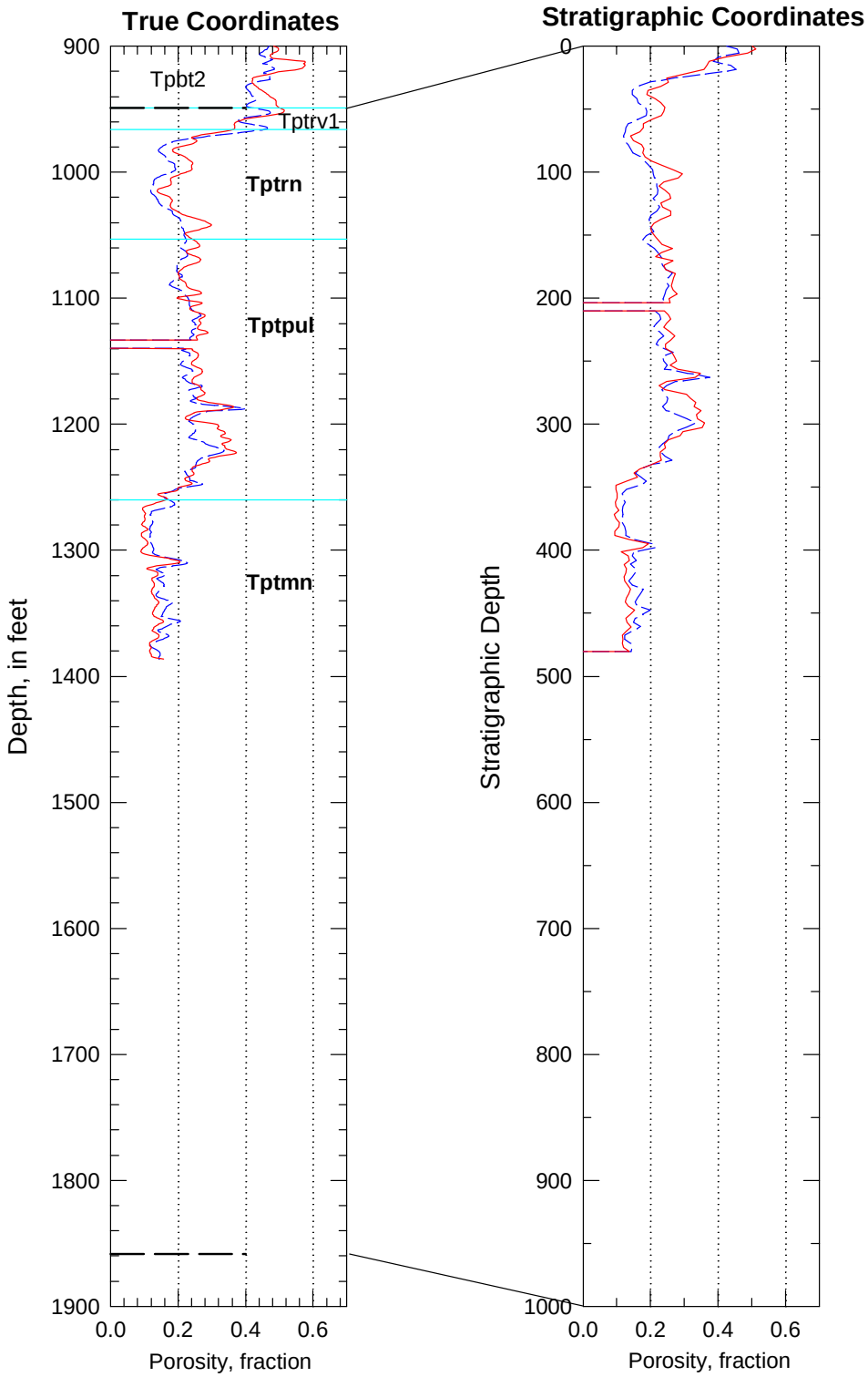

Figure B-100. Porosity data in real-world and in stratigraphic coordinates for the TSw model unit in drillhole WT-10.

Drillhole WT-10 (Modern Data)

Drillhole WT-10 is one of an older series of holes drilled to obtain hydrologic information principally from the saturated zone at Yucca Mountain. The hole was not cored, and the earliest geophysical logs belong the older suite of petrophysical data. The hole was relogged as part of site characterization efforts, and there is also a full suite of modern geophysical data. These data have been converted to values of total and water-filled porosity.

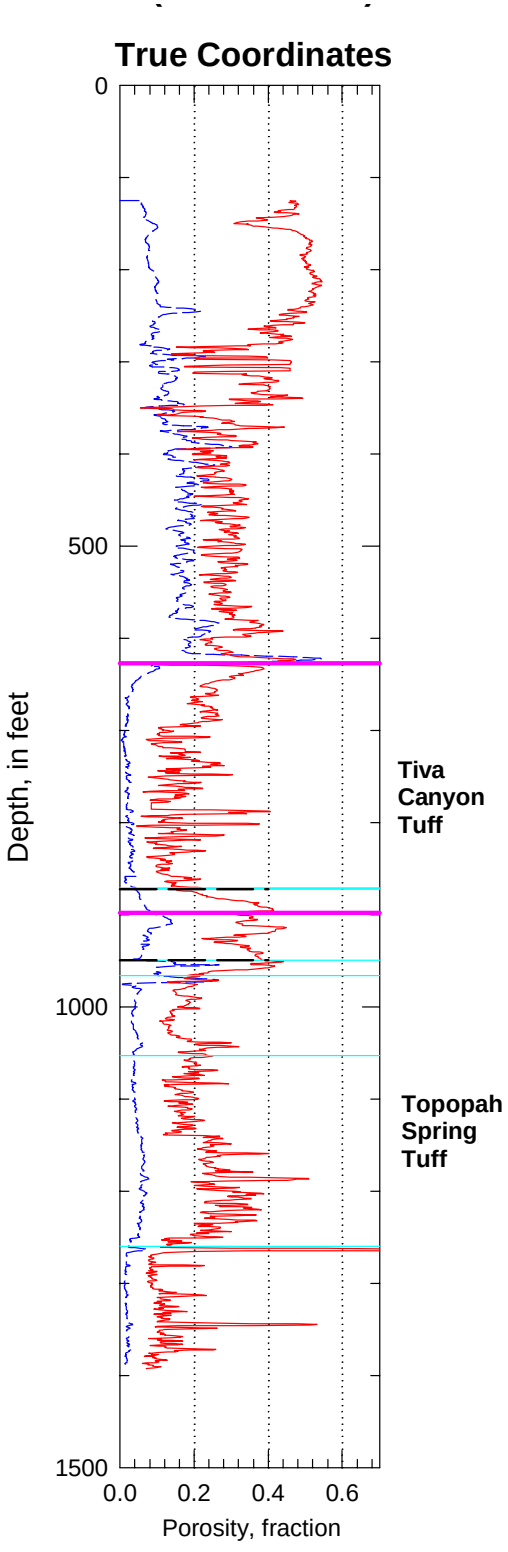

Figure B-101. Porosity data in true coordinates from drillhole WT-10 for the entire drillhole using petrophysical data from the modern data set.

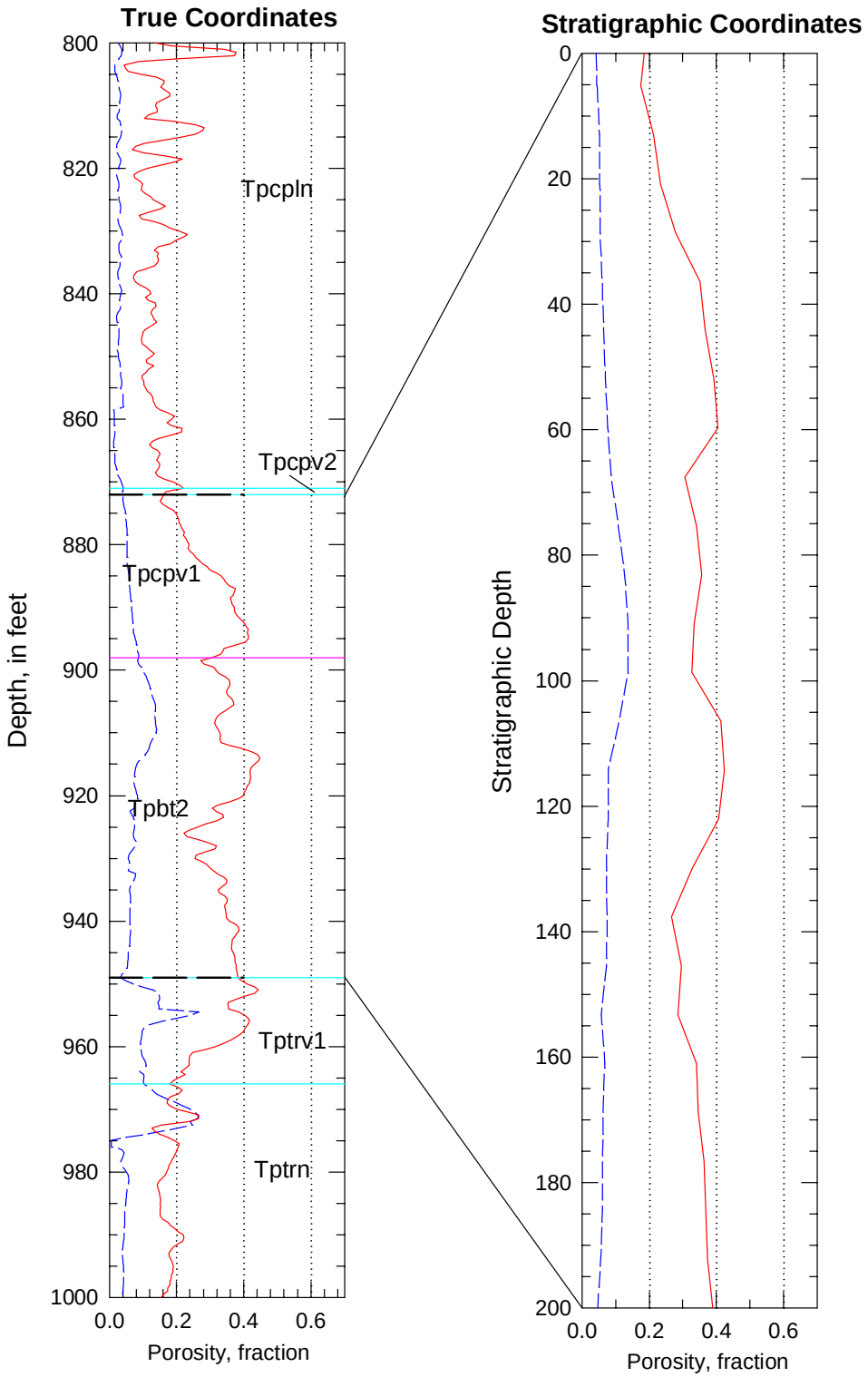

Figure B-102. Porosity data in real-world and in stratigraphic coordinates for the PTn model unit in drillhole WT-10 using petrophysical data from the modern data set.

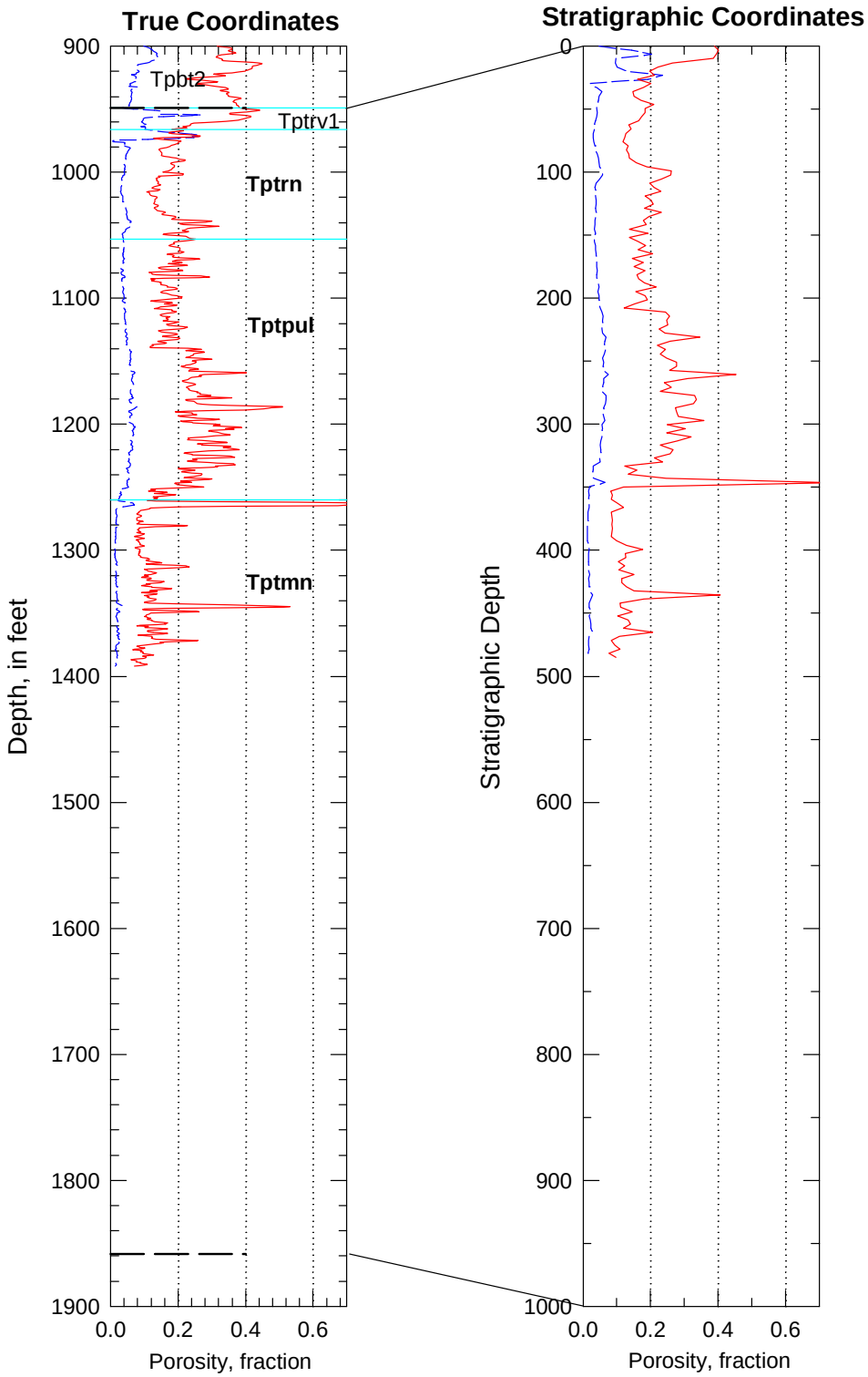

Figure B-103. Porosity data in real-world and in stratigraphic coordinates for the TSw model unit in drillhole WT-10 using petrophysical data from the modern data set.

Drillhole WT-11

Drillhole WT-11 is one of an older series of holes drilled to obtain hydrologic information principally from the saturated zone at Yucca Mountain. The hole was not cored, and the earliest geophysical logs belong the older suite of petrophysical data. These data have been converted to values of total and water-filled porosity.

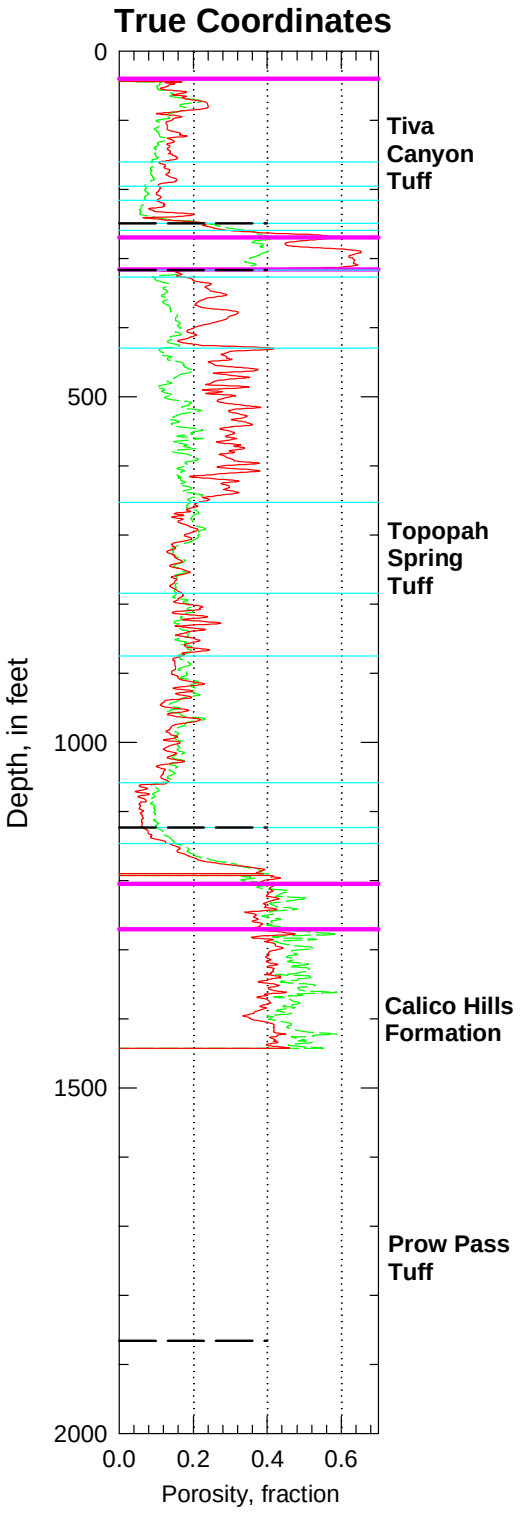

Figure B-104. Porosity data in true coordinates from drillhole WT-11 for the entire drillhole.

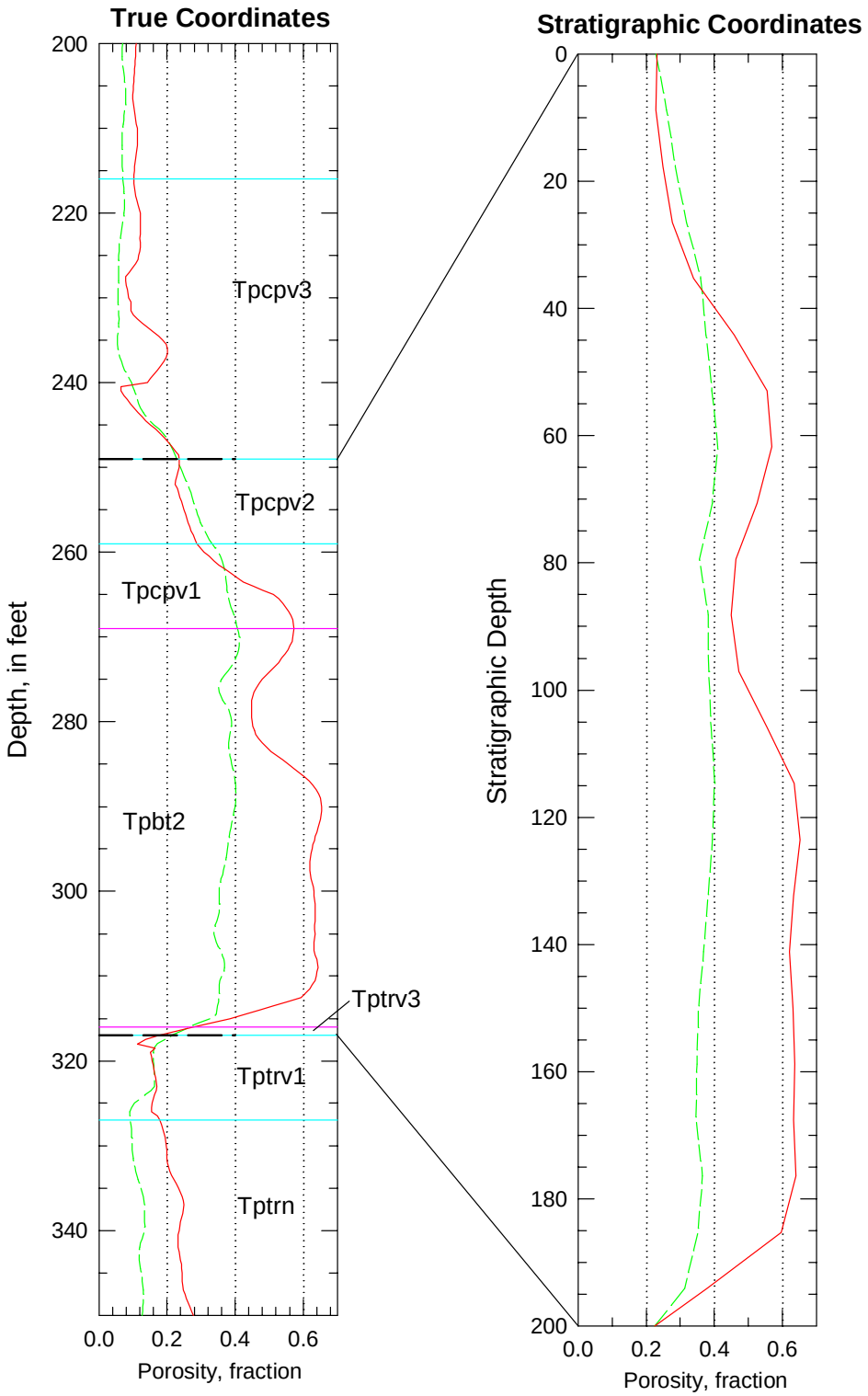

Figure B-105. Porosity data in real-world and in stratigraphic coordinates for the PTn model unit in drillhole WT-11.

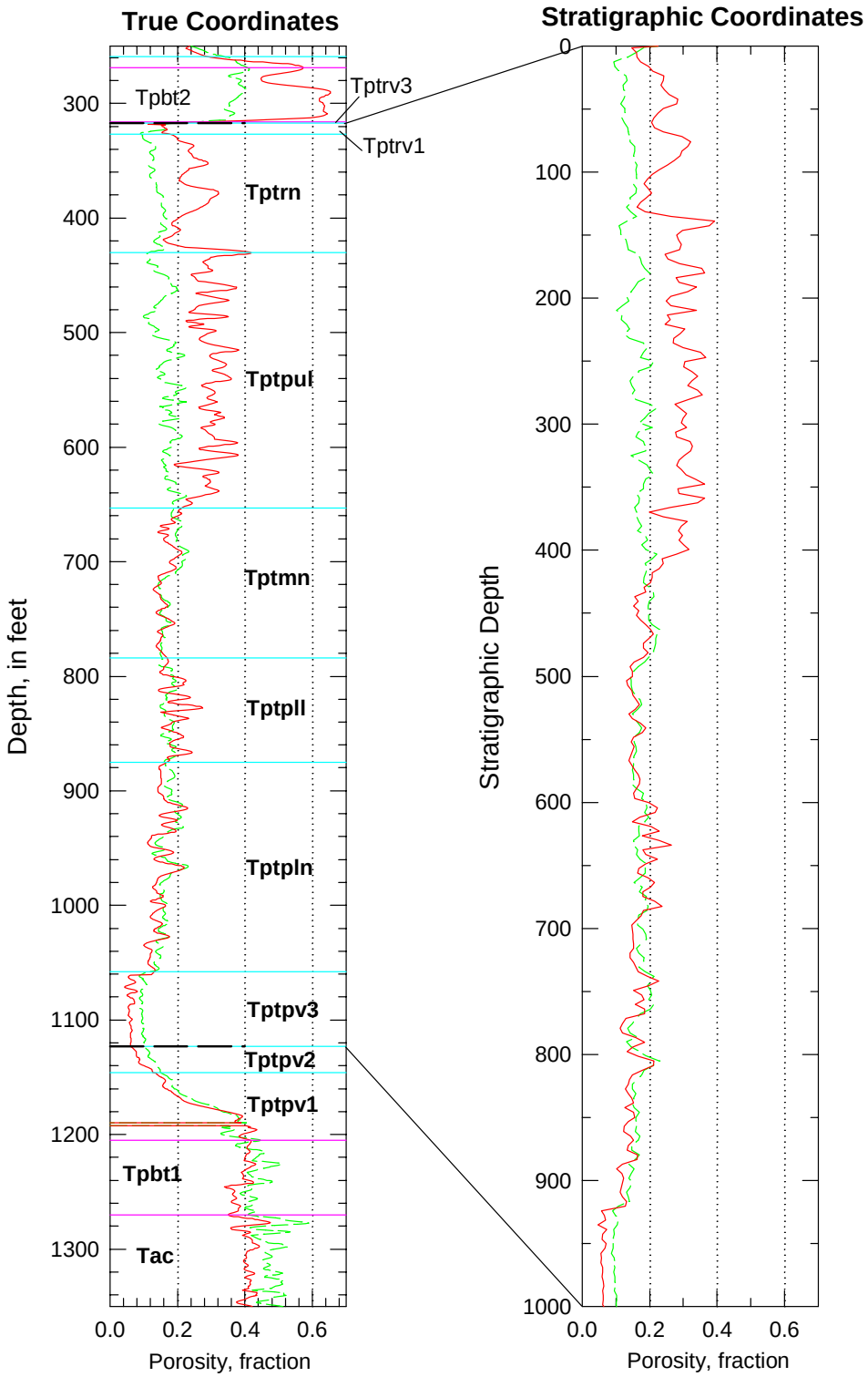

Figure B-106. Porosity data in real-world and in stratigraphic coordinates for the TSw model unit in drillhole WT-11.

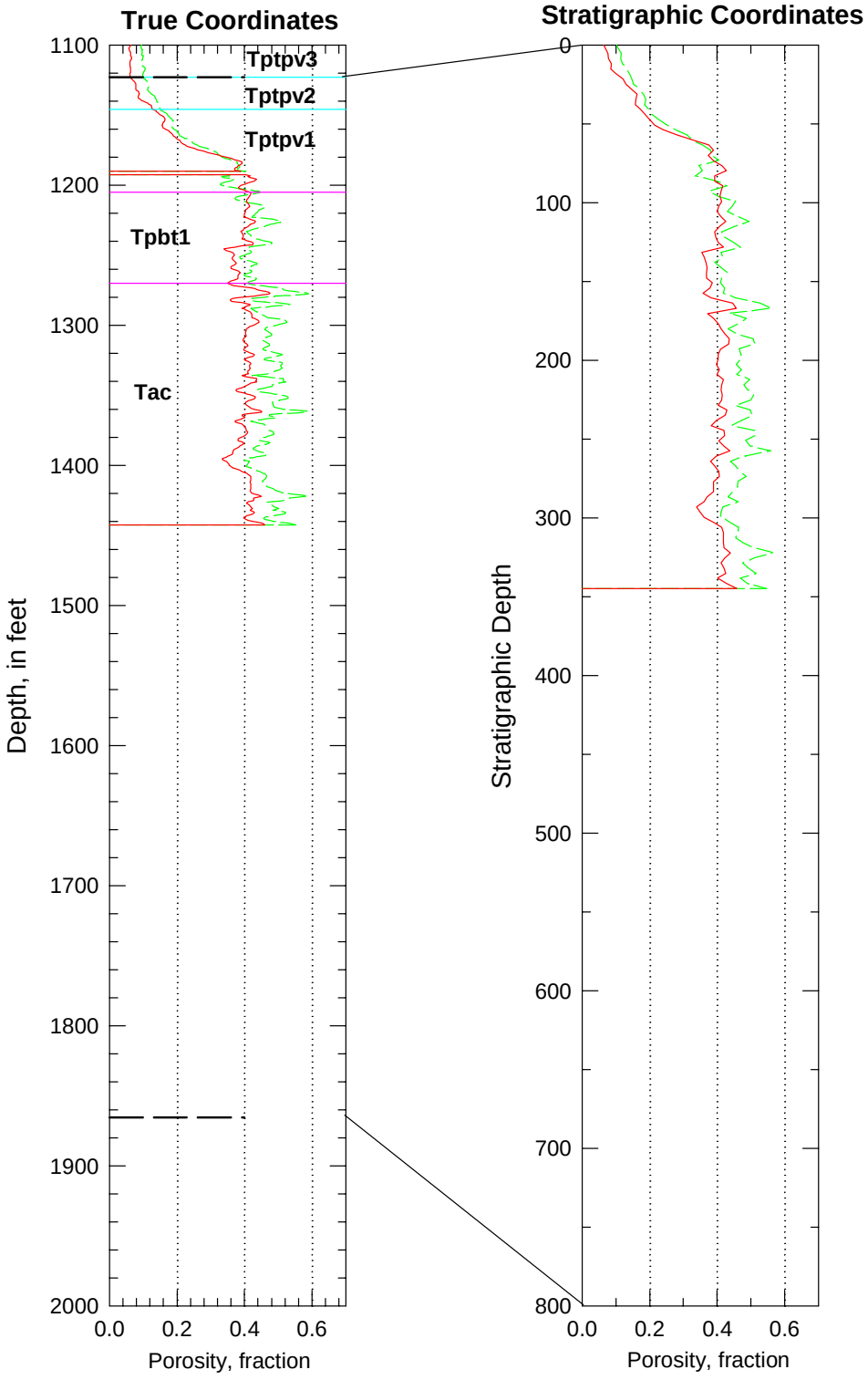

Figure B-107. Porosity data in real-world and in stratigraphic coordinates for the combined CH–PP model unit in drillhole WT-11.

Drillhole WT-12 (Older Data)

Drillhole WT-12 is one of an older series of holes drilled to obtain hydrologic information principally from the saturated zone at Yucca Mountain. The hole was not cored, and the earliest geophysical logs belong the older suite of petrophysical data. The hole was relogged as part of site characterization efforts, and there is also a full suite of modern geophysical data. The older data have been used in the rock properties modeling effort in order to provide greater consistency with other WT-holes for which only older data are available.

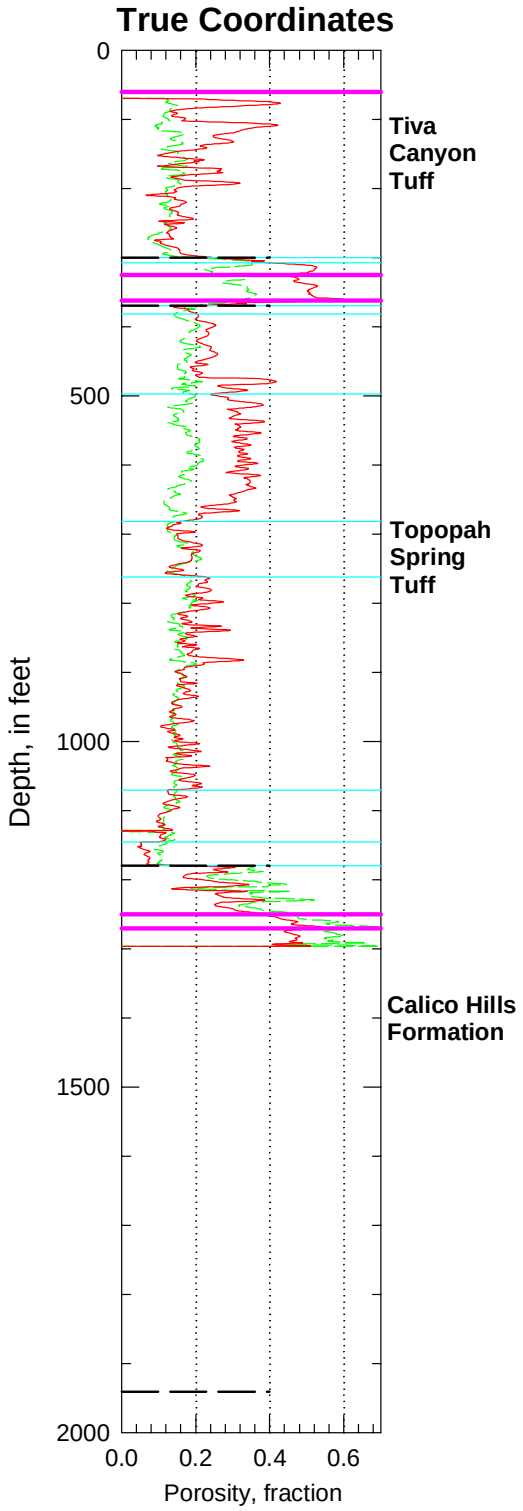

Figure B-108. Porosity data in true coordinates from drillhole WT-12 for the entire drillhole.

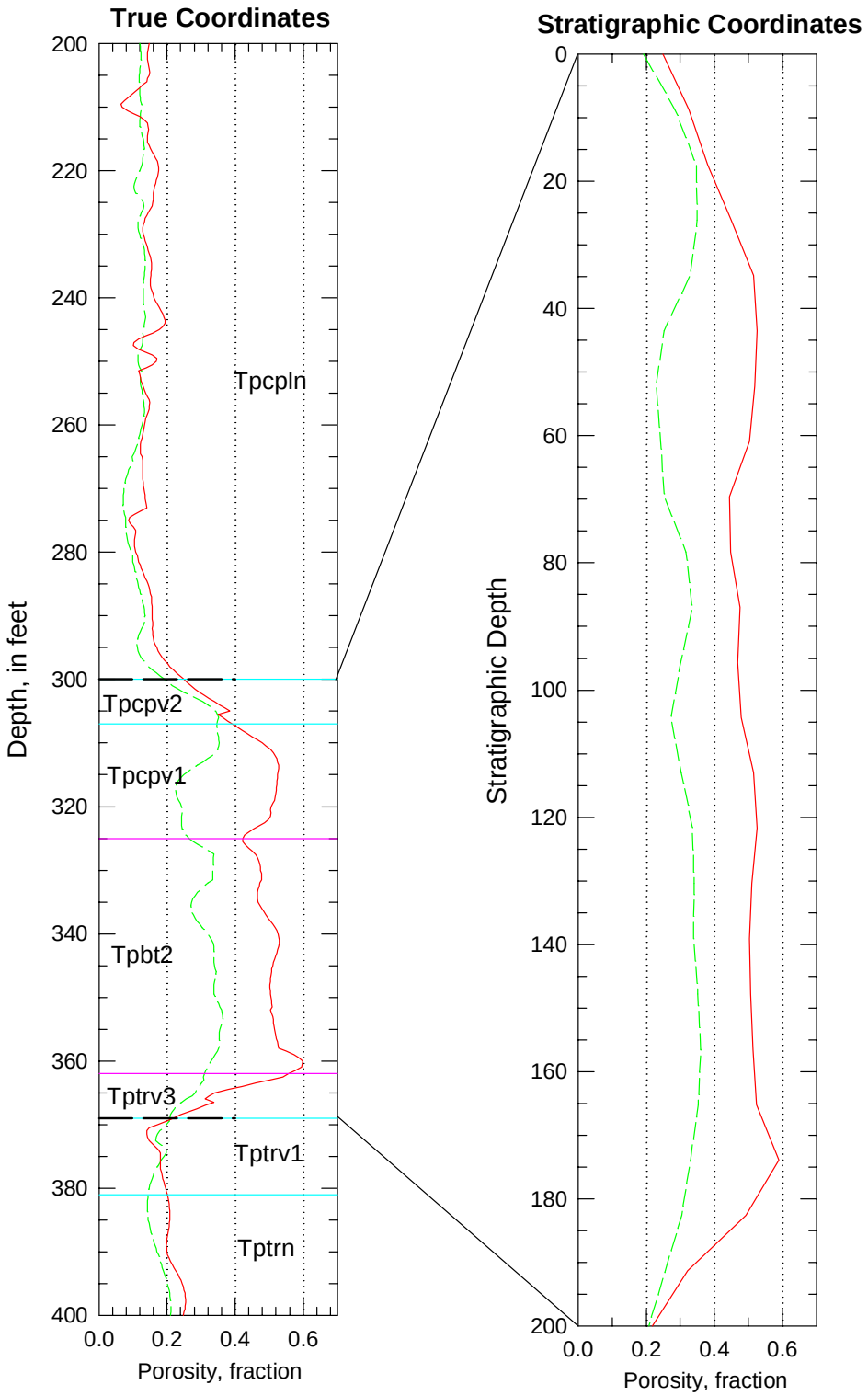

Figure B-109. Porosity data in real-world and in stratigraphic coordinates for the PTn model unit in drillhole WT-12.

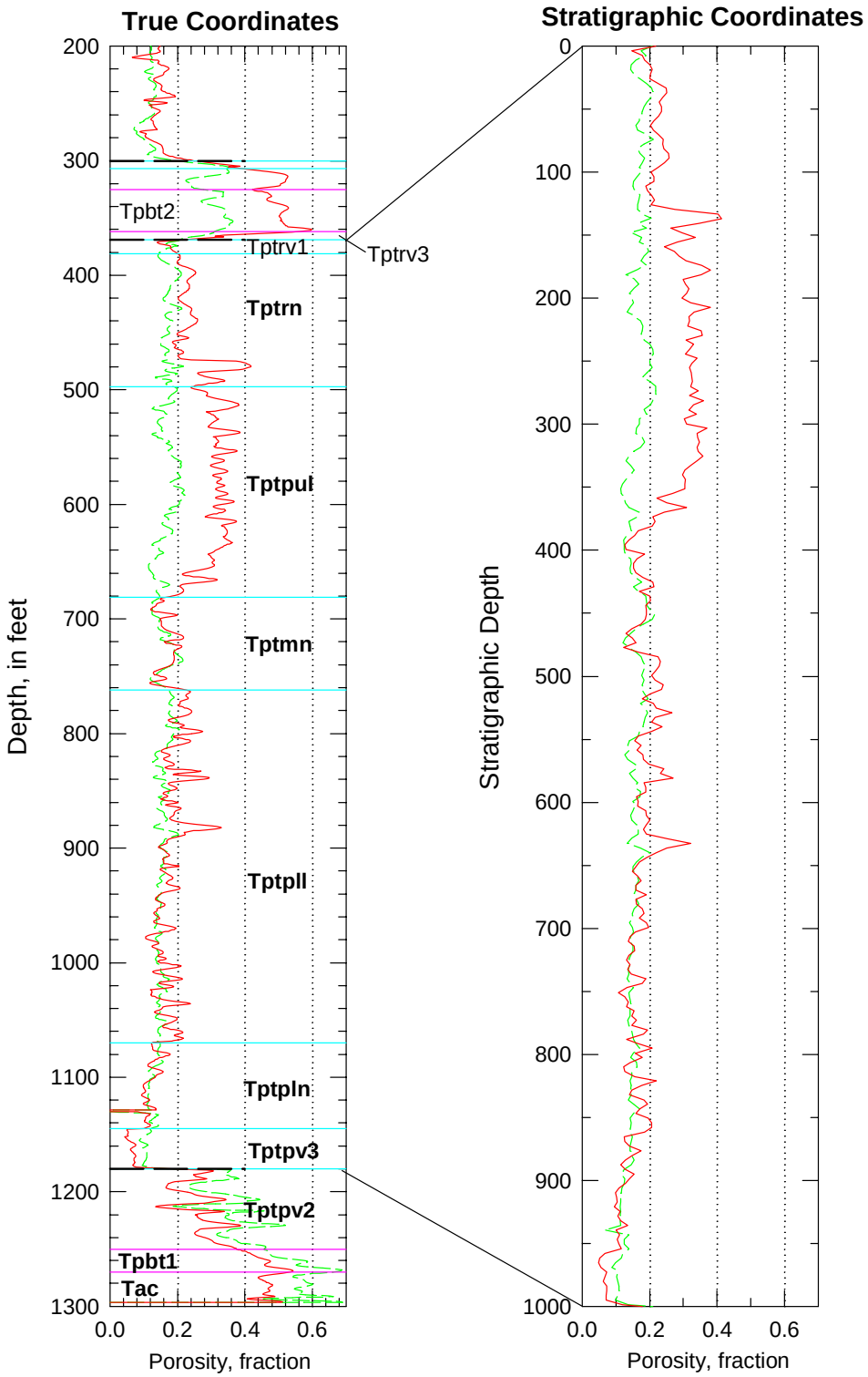

Figure B-110. Porosity data in real-world and in stratigraphic coordinates for the TSw model unit in drillhole WT-12.

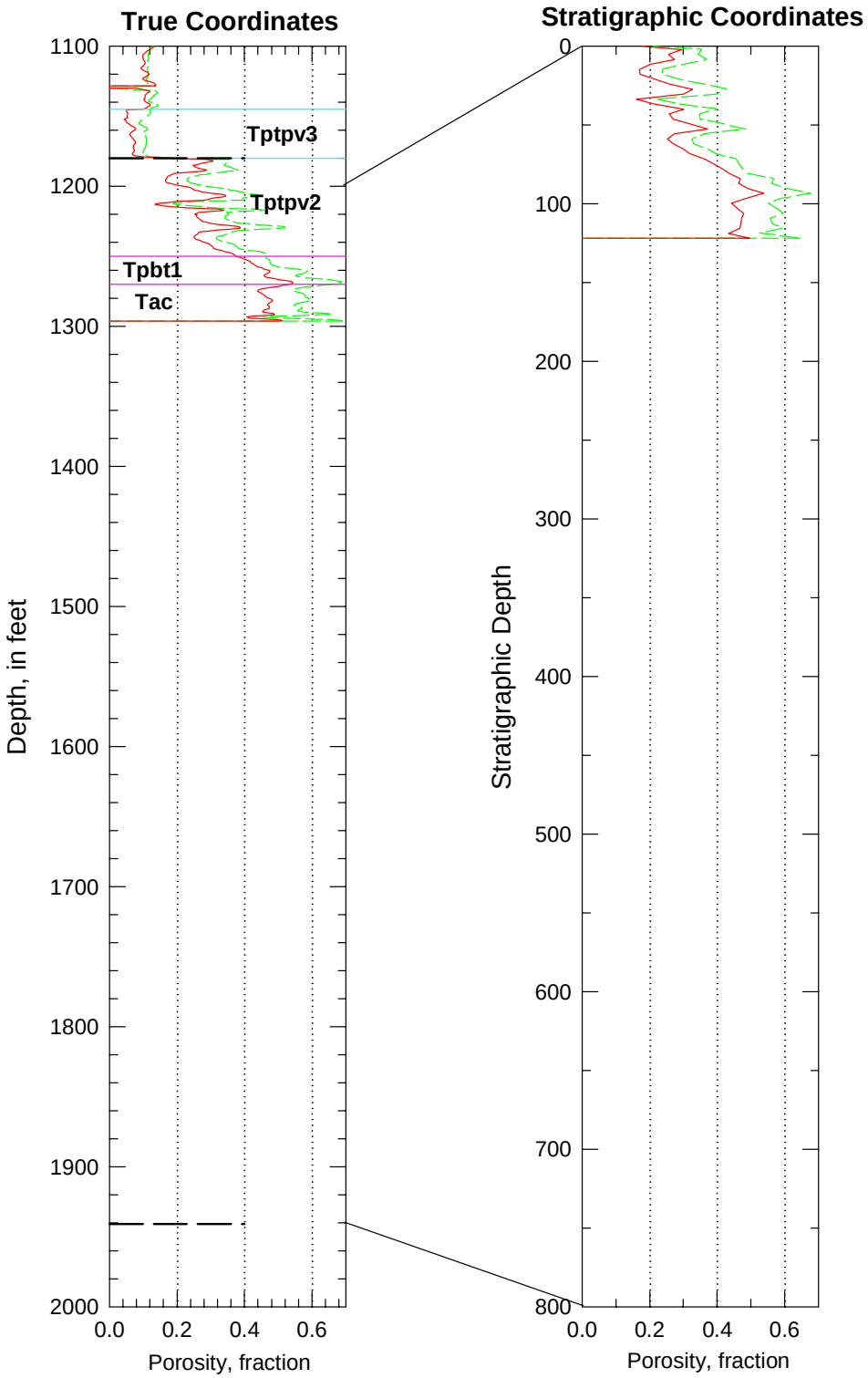

Figure B-111. Porosity data in real-world and in stratigraphic coordinates for the combined CH–PP model unit in drillhole WT-12.

Drillhole WT-12 (Modern Data)

Drillhole WT-12 is one of an older series of holes drilled to obtain hydrologic information principally from the saturated zone at Yucca Mountain. The hole was not cored, and the earliest geophysical logs belong the older suite of petrophysical data. The hole was relogged as part of site characterization efforts, and there is also a full suite of modern geophysical data. These data have been converted to values of total and water-filled porosity. The modern data were not used in the rock properties modeling activity.

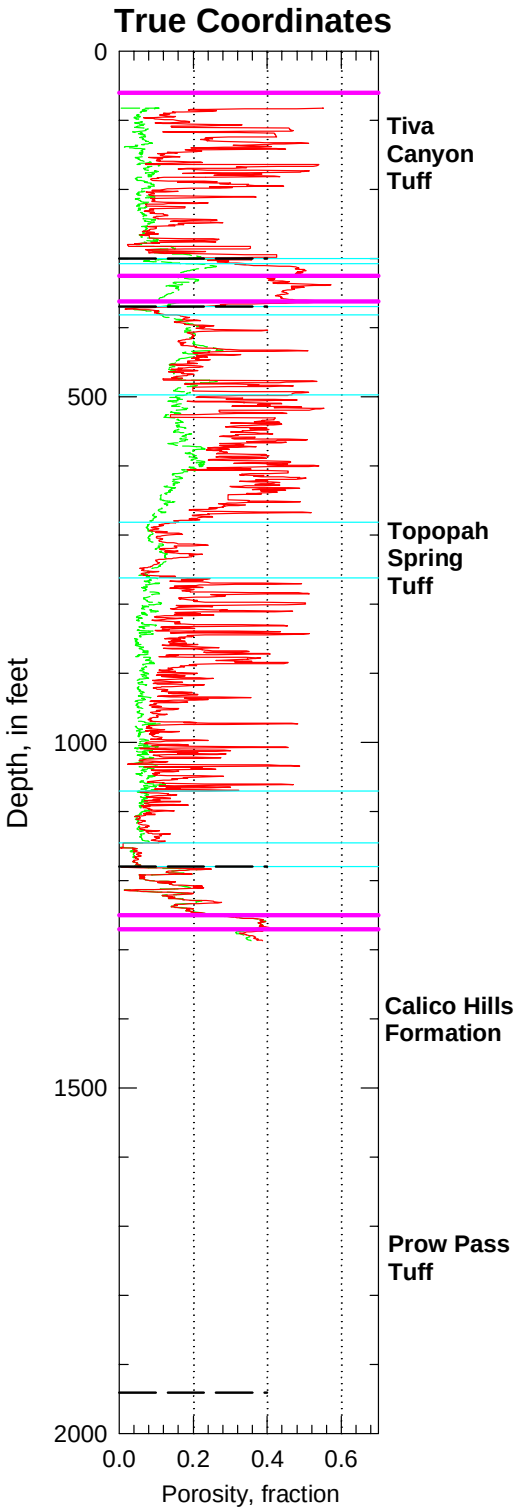

Figure B-112. Porosity data in true coordinates from drillhole WT-12 for the entire drillhole using petrophysical data from the modern data set.

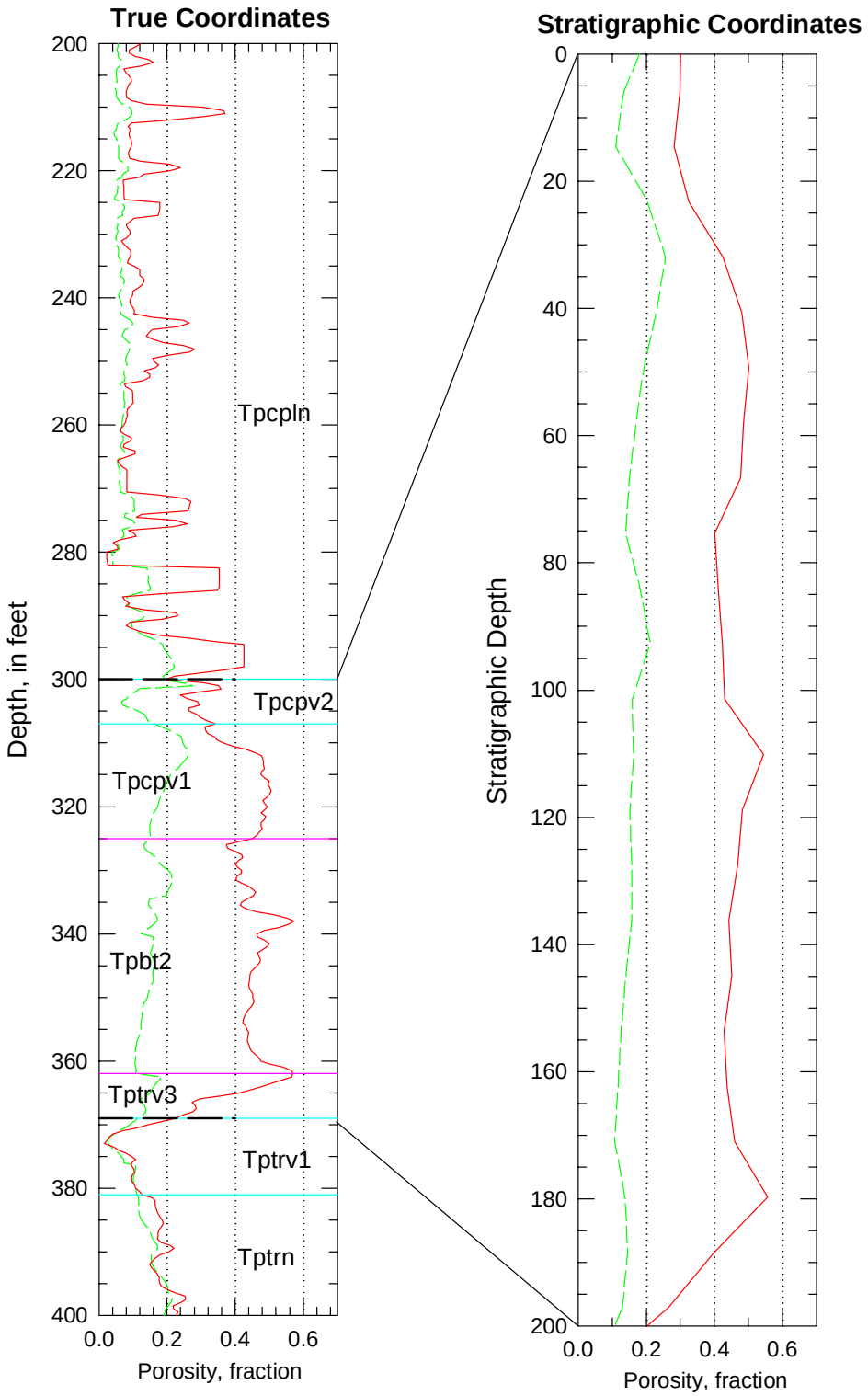

Figure B-113. Porosity data in real-world and in stratigraphic coordinates for the PTn model unit in drillhol WT-12 using petrophysical data from the modern data set.

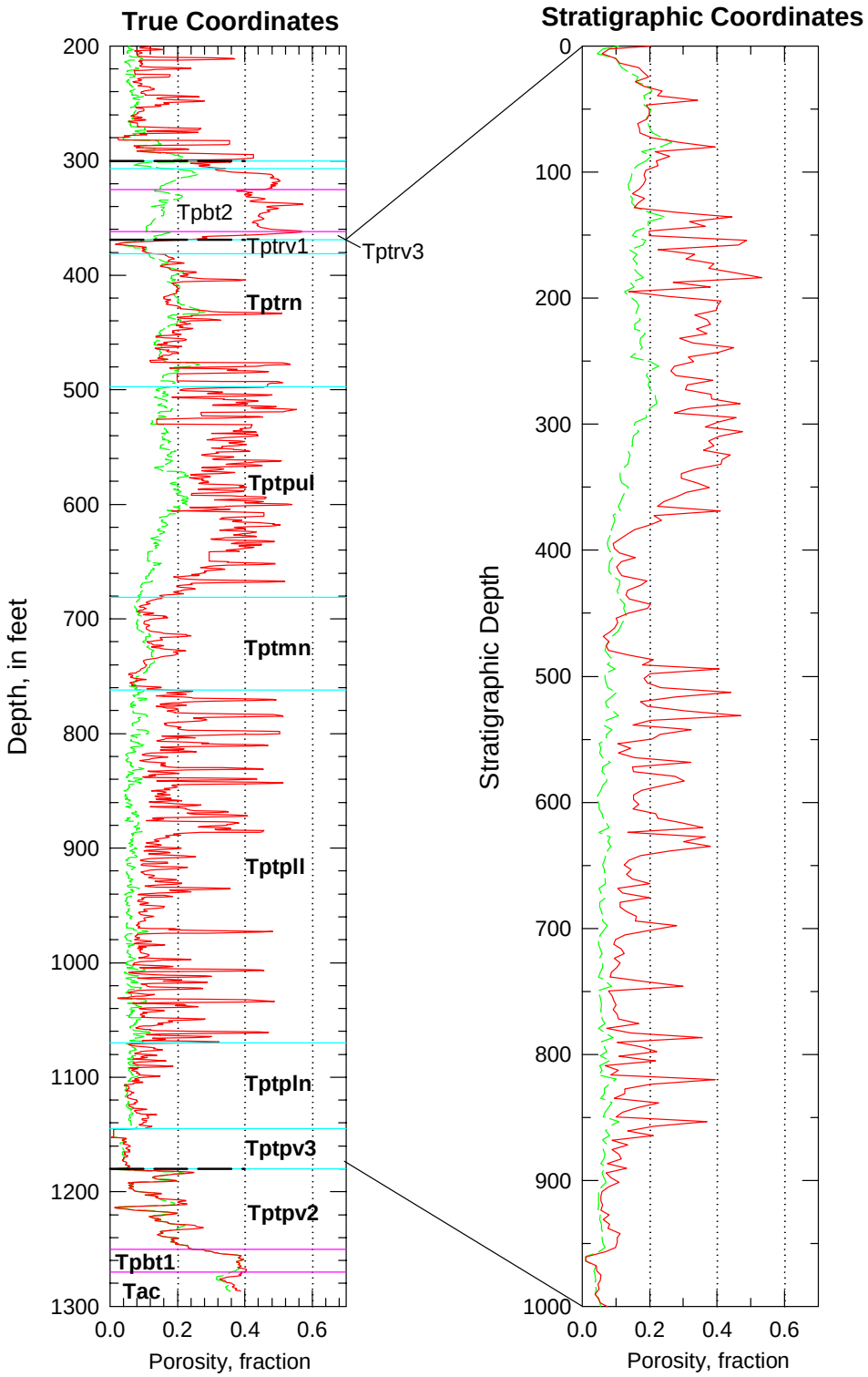

Figure B-114. Porosity data in real-world and in stratigraphic coordinates for the TSw model unit in drillhole WT-12 using petrophysical data from the modern data set.

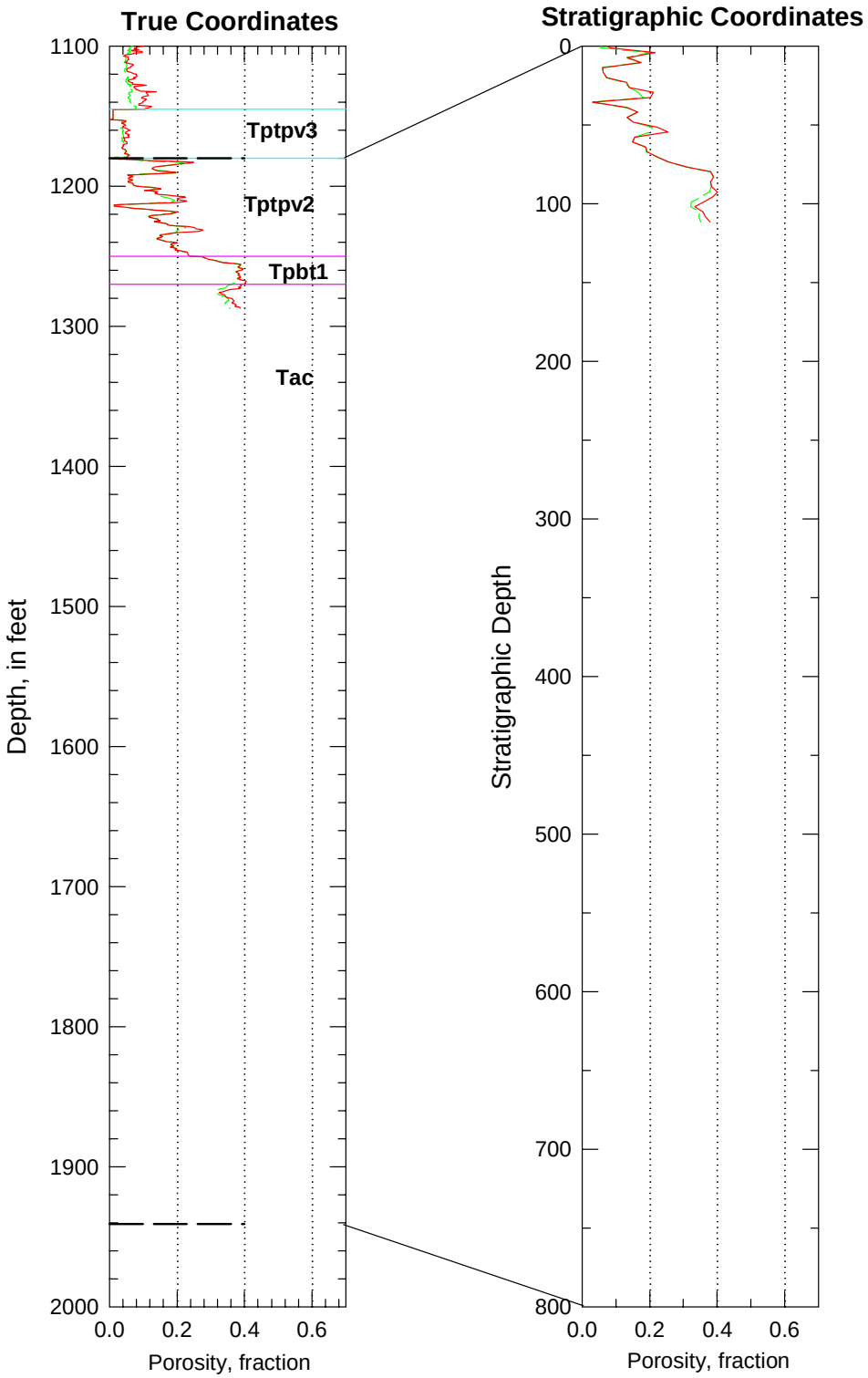

Figure B-115. Porosity data in real-world and in stratigraphic coordinates for the combined CH–PP model unit in drillhole WT-12 using petrophysical data from the modern data set.

Drillhole WT-13

Drillhole WT-13 is one of an older series of holes drilled to obtain hydrologic information principally from the saturated zone at Yucca Mountain. The hole was not cored, and the earliest geophysical logs belong the older suite of petrophysical data. These data have been converted to values of total and water-filled porosity.

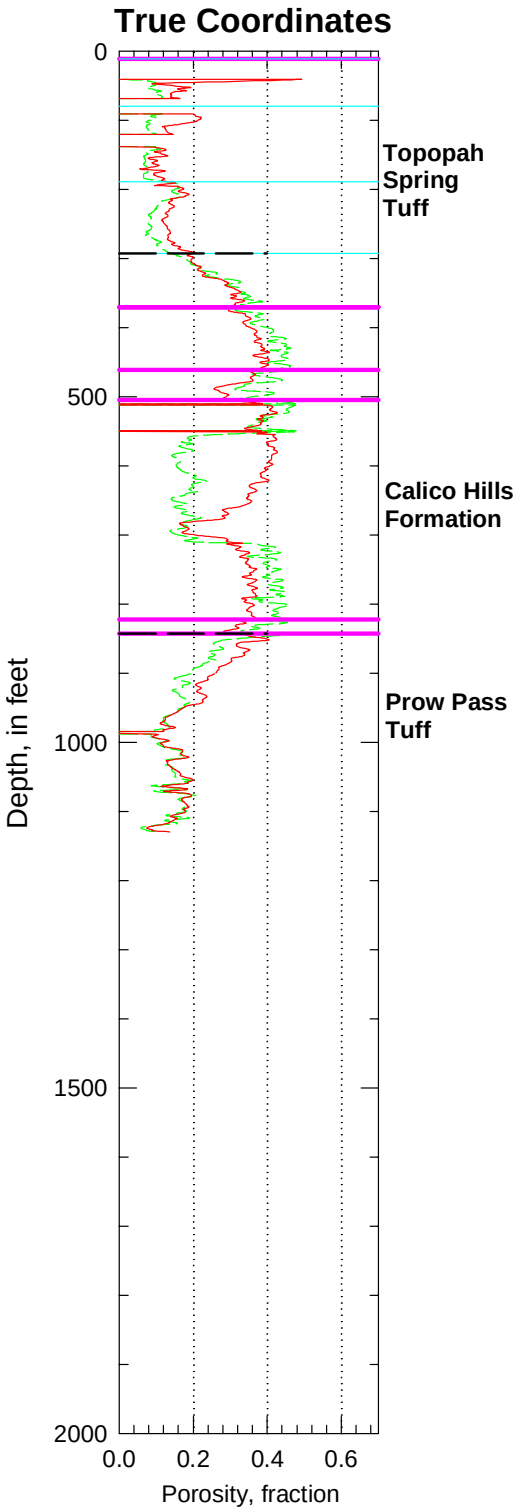

Figure B-116. Porosity data in true coordinates from drillhole WT-13 for the entire drillhole.

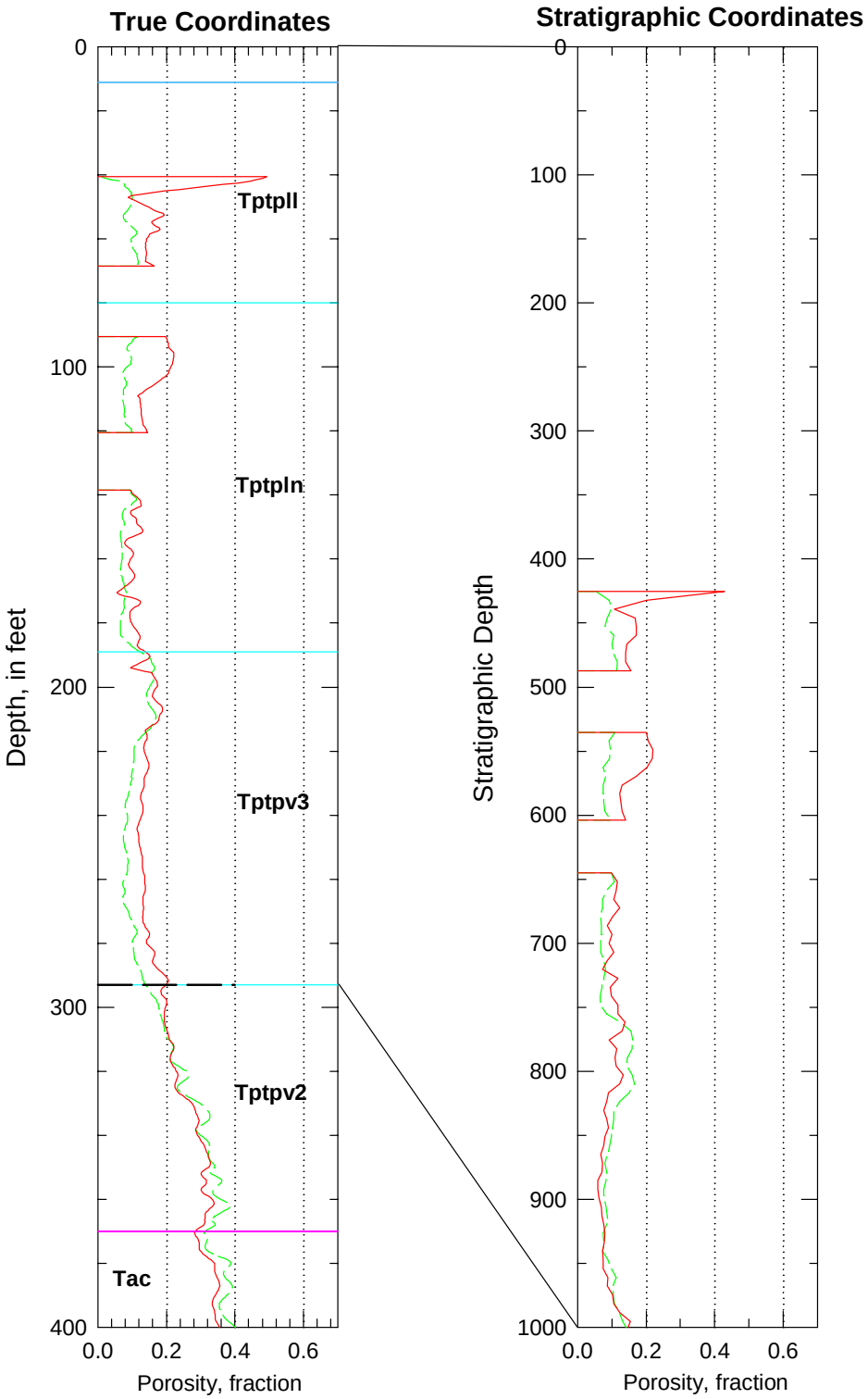

Figure B-117. Porosity data in real-world and in stratigraphic coordinates for the TSw model unit from drillhole WT-13.

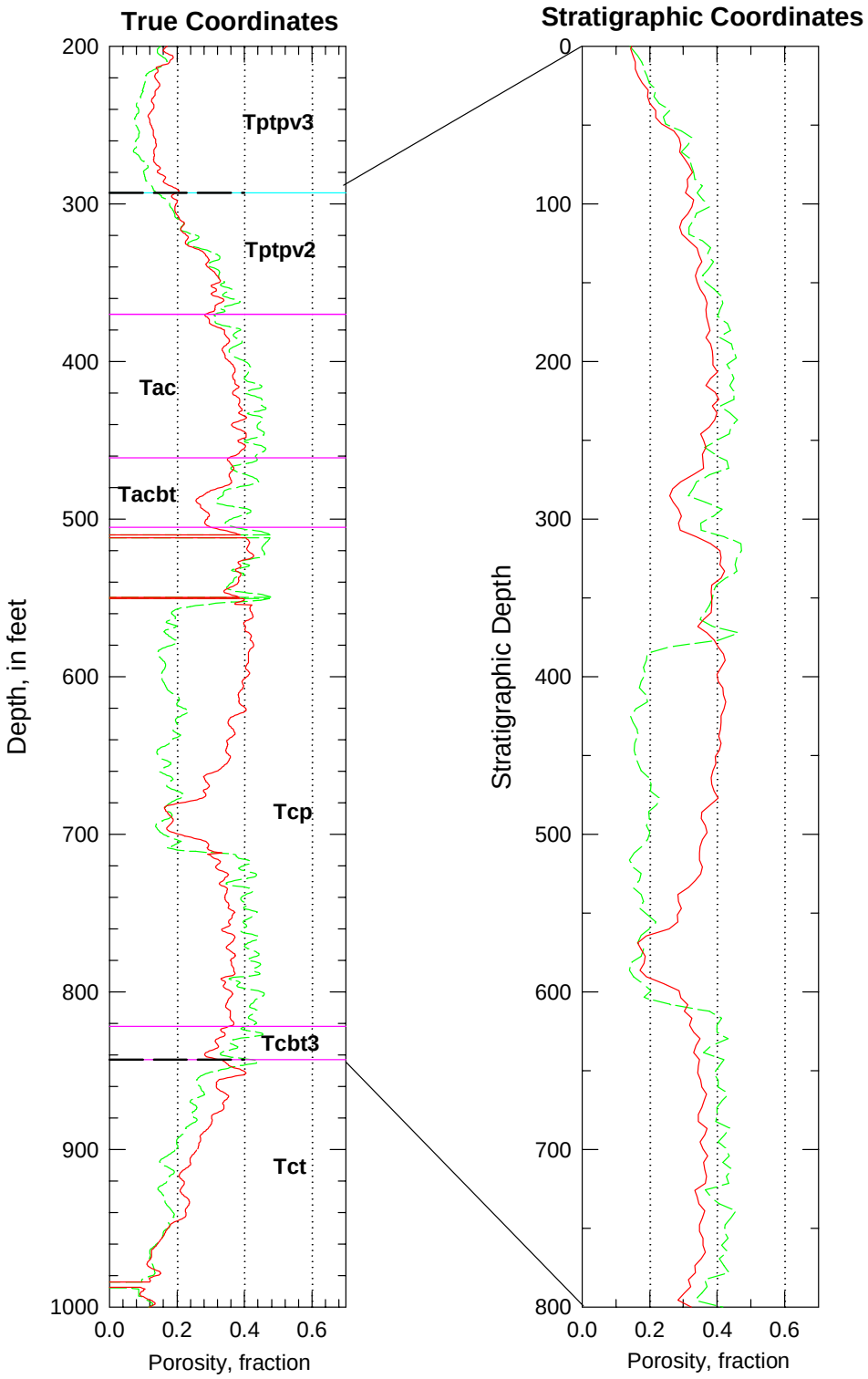

Figure B-118. Porosity data in real-world and in stratigraphic coordinates for the combined CH–PP model unit in drillhole WT-13.

Drillhole WT-14

Drillhole WT-14 is one of an older series of holes drilled to obtain hydrologic information principally from the saturated zone at Yucca Mountain. The hole was not cored, and the geophysical logs belong the older suite of petrophysical data. These data have been converted to values of total and water-filled porosity.

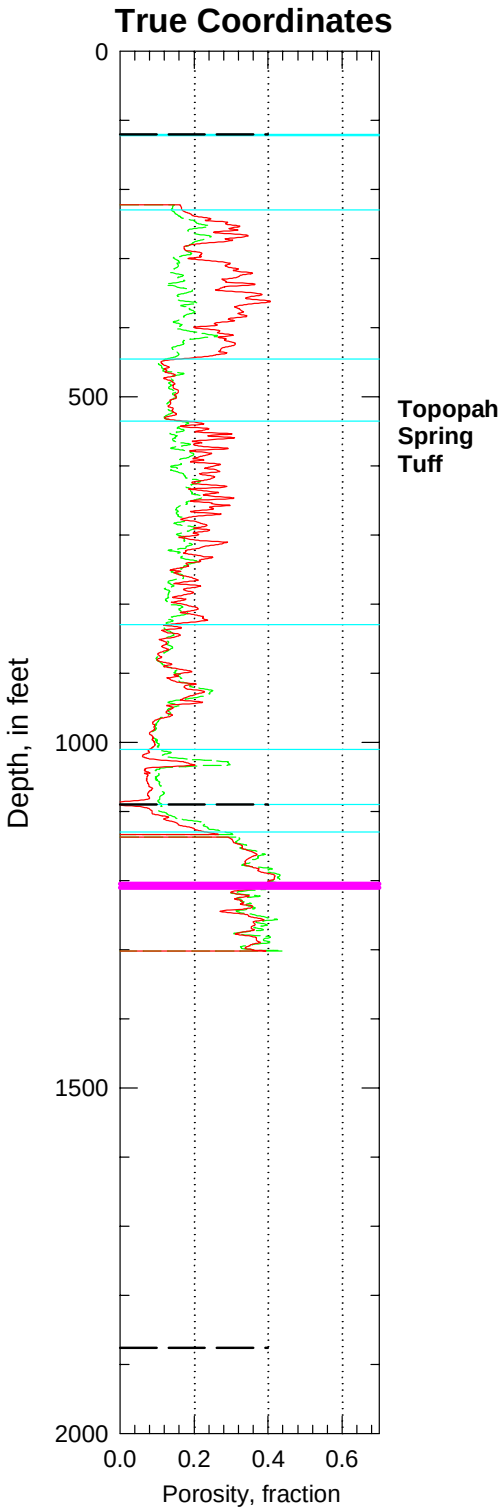

Figure B-119. Porosity data in true coordinates from drillhole WT-14 for the entire drillhole.

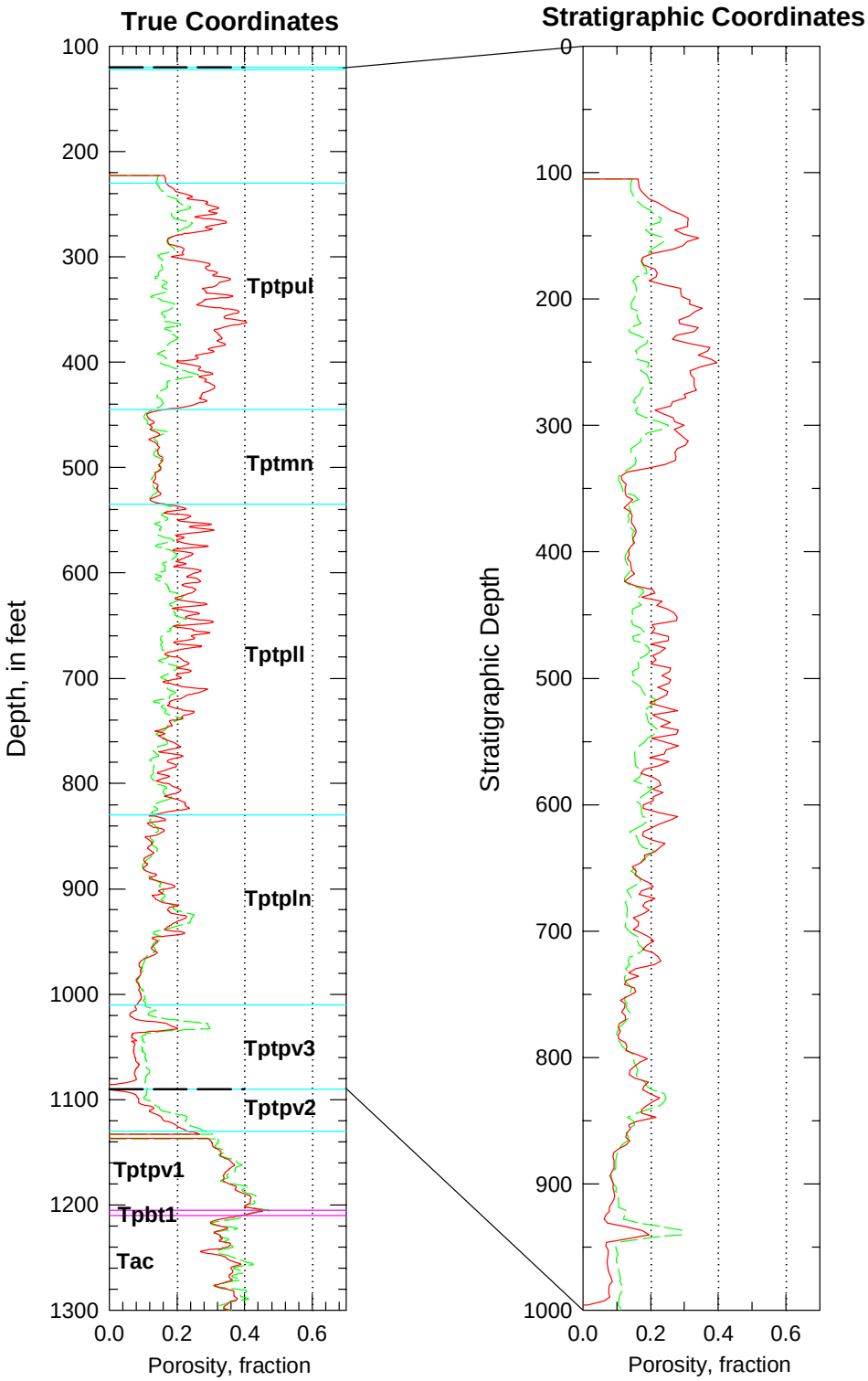

Figure B-120. Porosity data in real-world and in stratigraphic coordinates for the TSw model unit in drillhole WT-14.

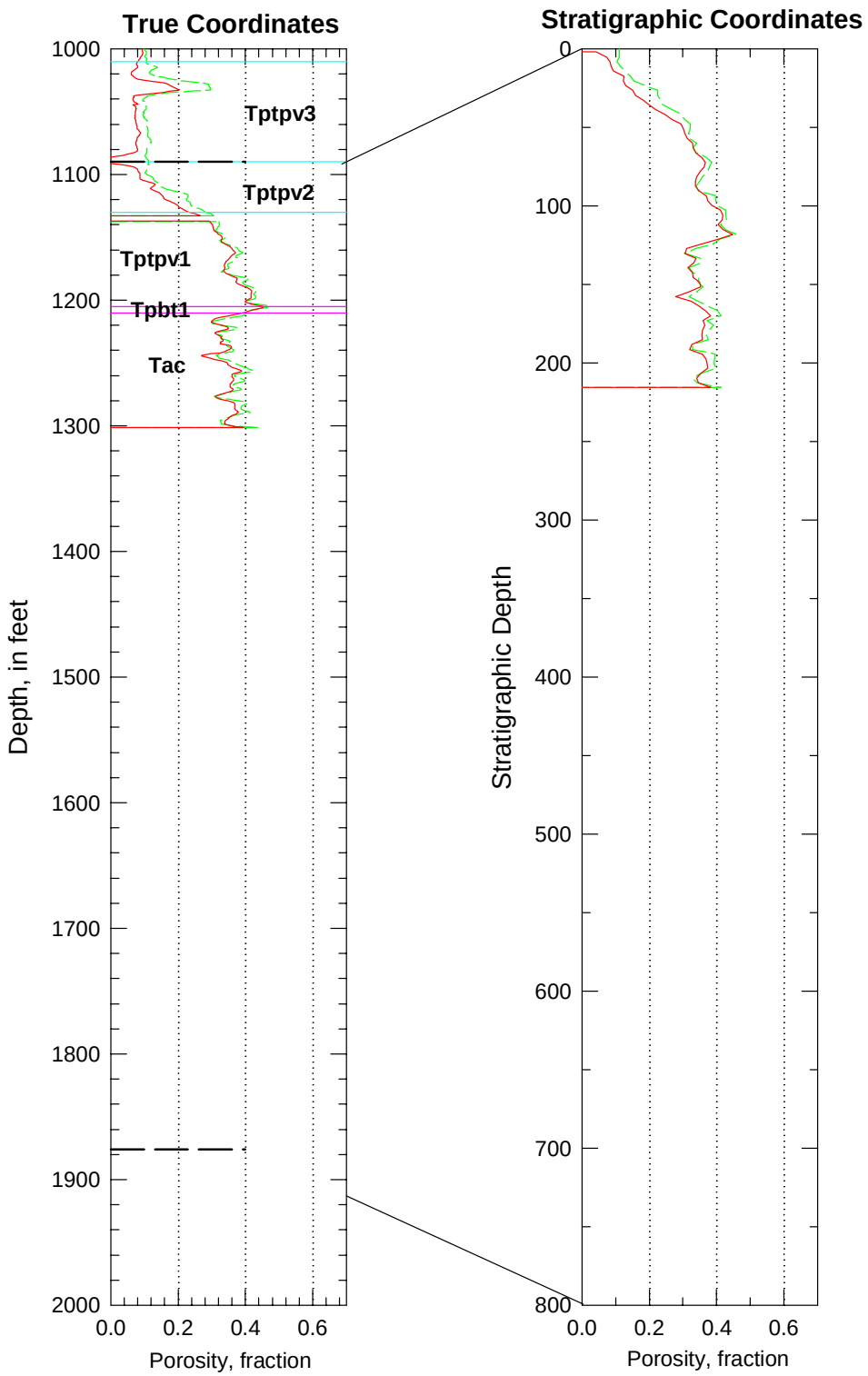

Figure B-121. Porosity data in real-world and in stratigraphic coordinates for the combined CH–PP model unit in drillhole WT-14.

Drillhole WT-15

Drillhole WT-15 is one of an older series of holes drilled to obtain hydrologic information principally from the saturated zone at Yucca Mountain. The hole was not cored, and the geophysical logs belong the older suite of petrophysical data. These data have been converted to values of total and water-filled porosity.

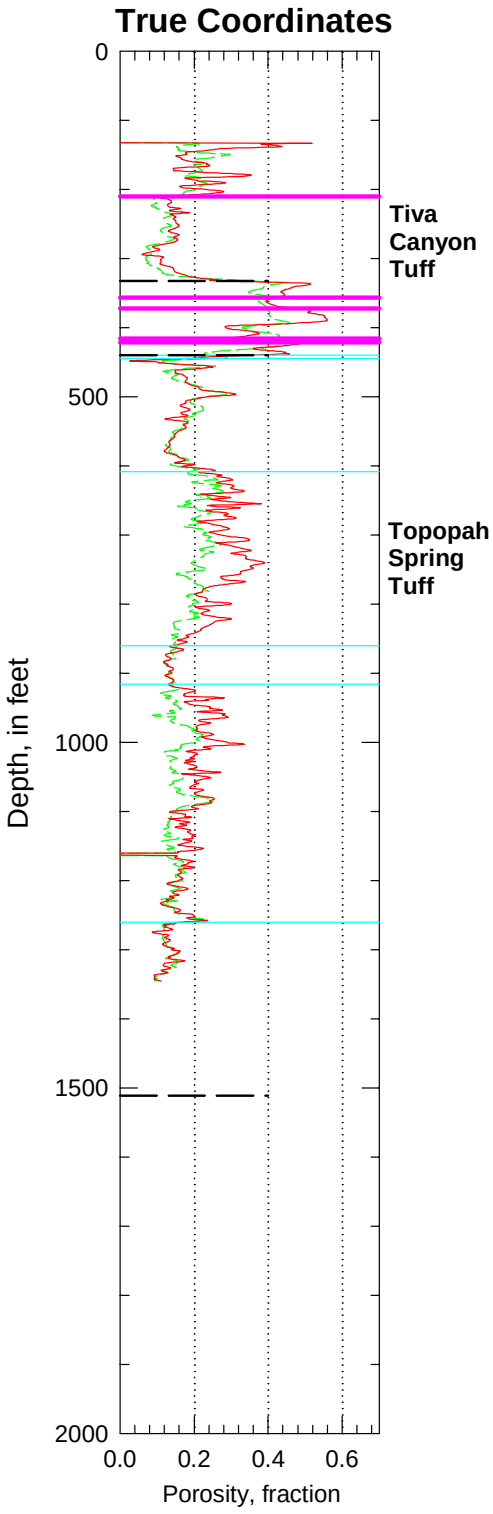

Figure B-122. Porosity data in true coordinates from drillhole WT-15 for the entire drillhole.

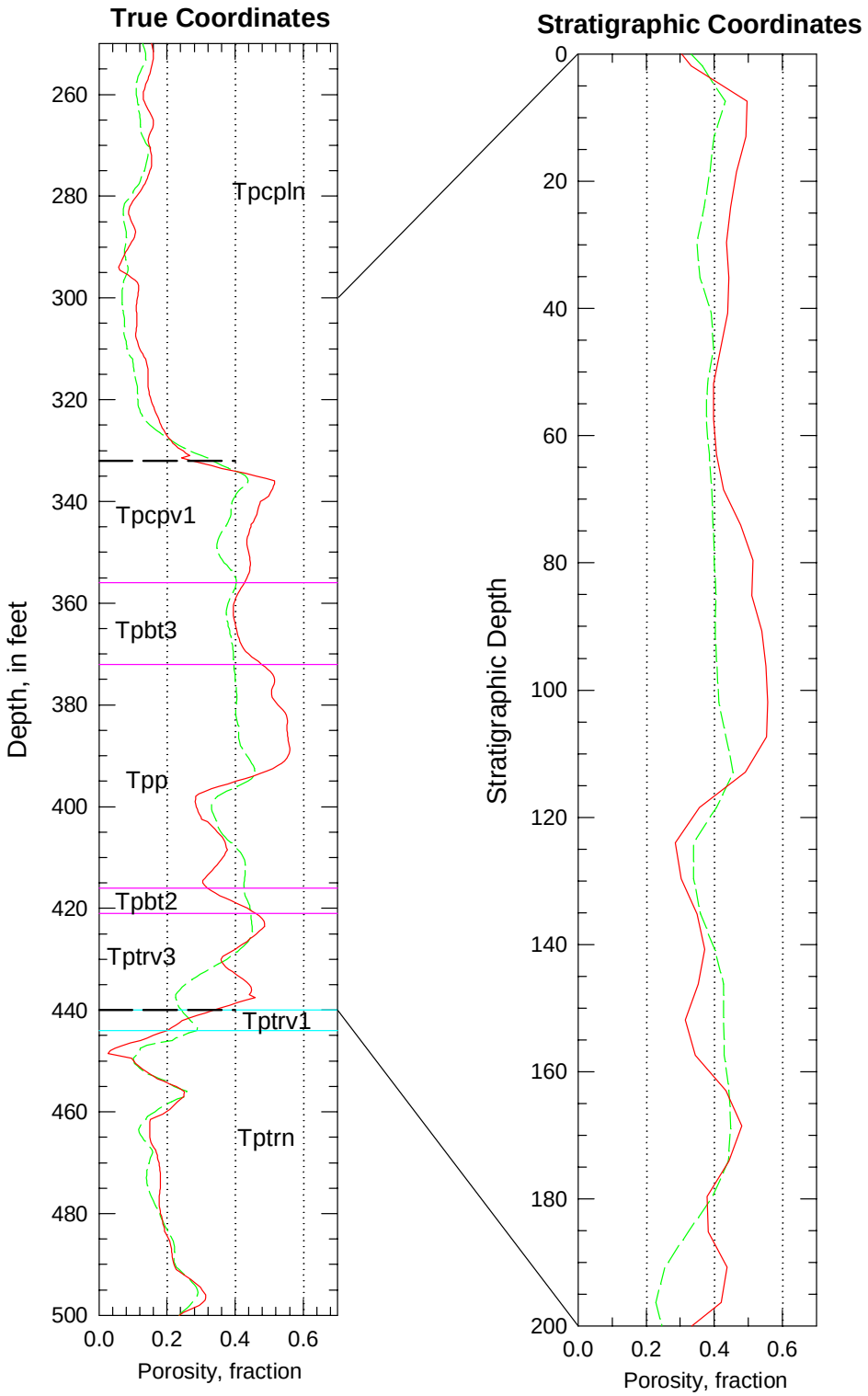

Figure B-123. Porosity data in real-world and in stratigraphic coordinates for the PTn model unit in drillhole WT-15.

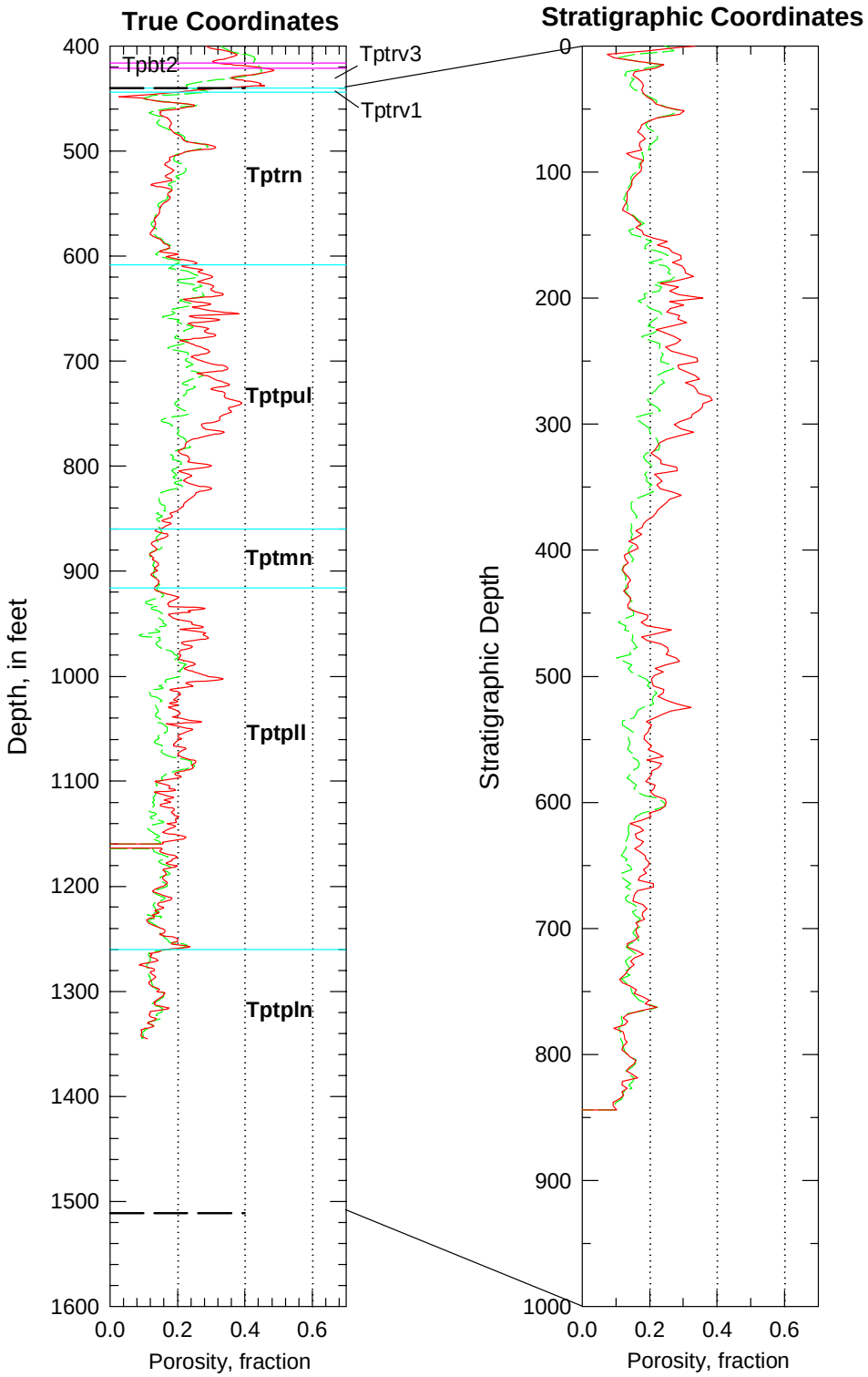

Figure B-124. Porosity data in real-world and in stratigraphic coordinates for the TSw model unit in drillhole WT-15.

Drillhole WT-16

Drillhole WT-16 is one of an older series of holes drilled to obtain hydrologic information principally from the saturated zone at Yucca Mountain. The hole was not cored, and the geophysical logs belong the older suite of petrophysical data. These data have been converted to values of total and water-filled porosity.

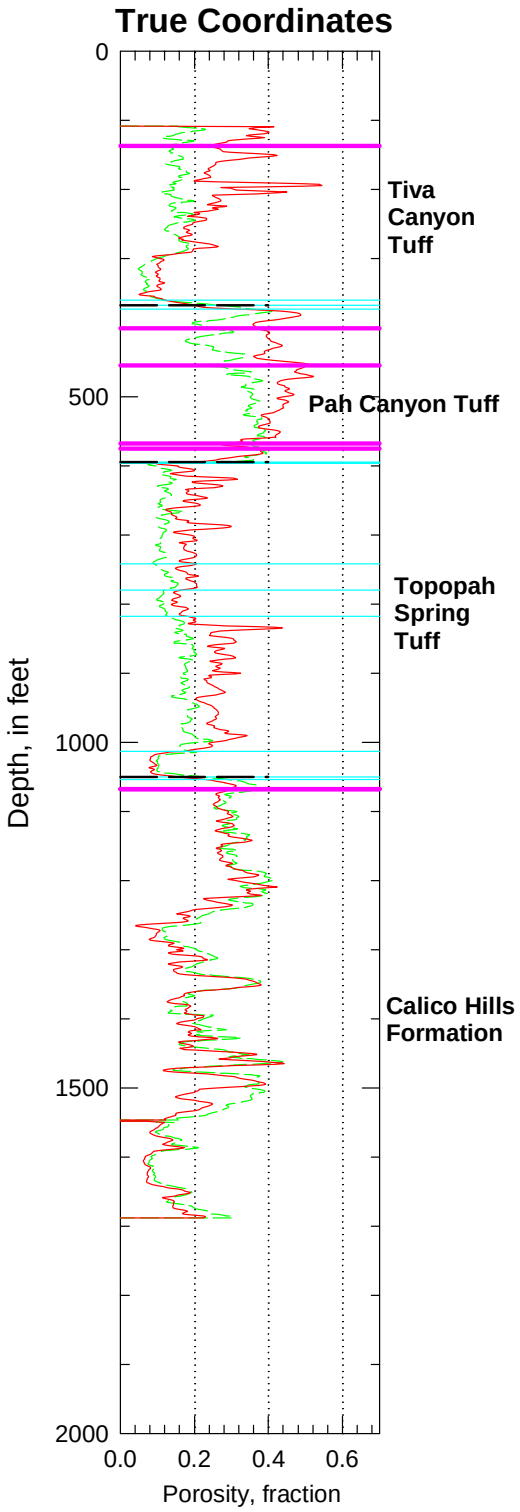

Figure B-125. Porosity data in true coordinates from drillhole WT-16 for the entire drillhole.

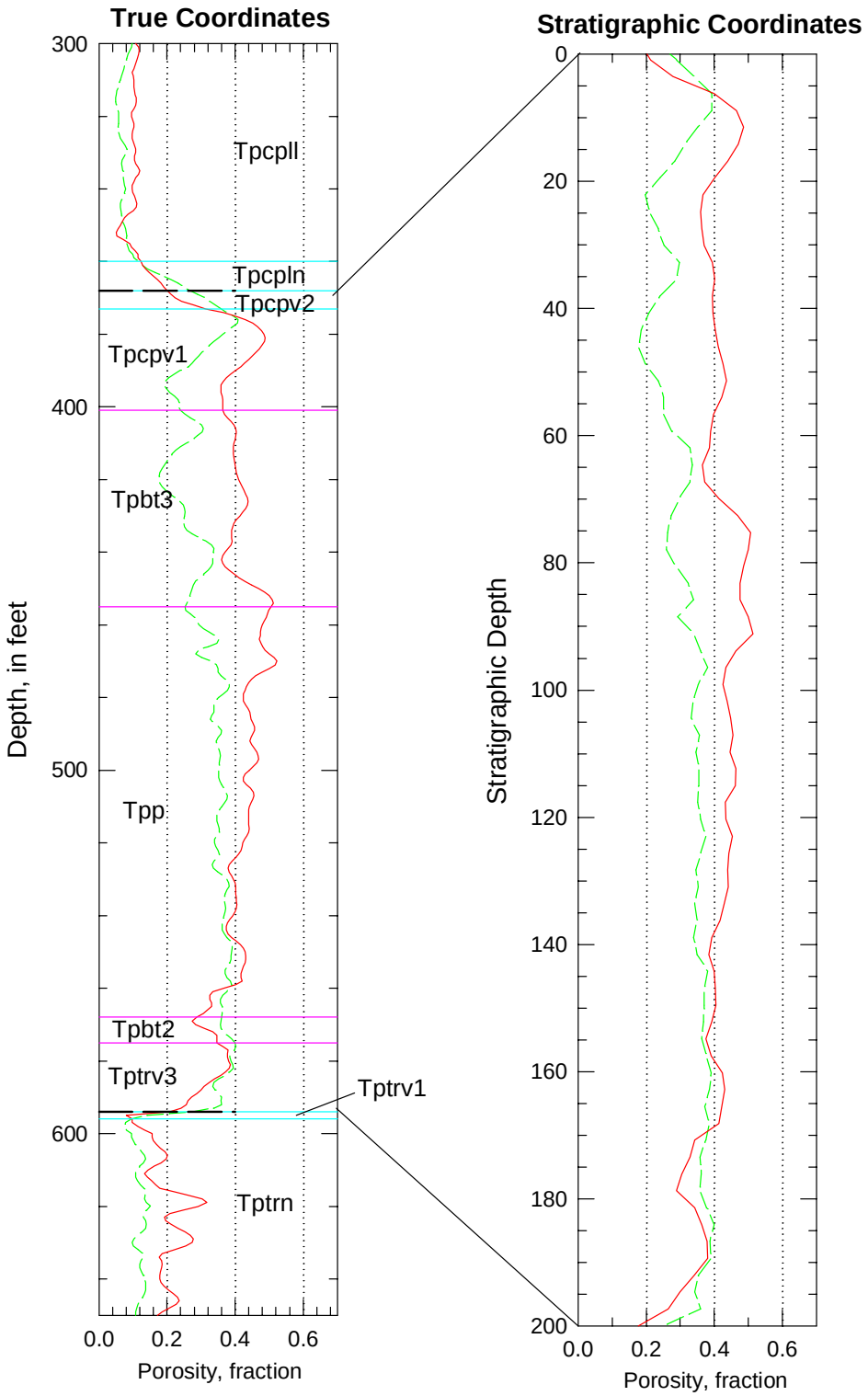

Figure B-126. Porosity data in real-world and in stratigraphic coordinates for the PTn model unit in drillhole WT-16.

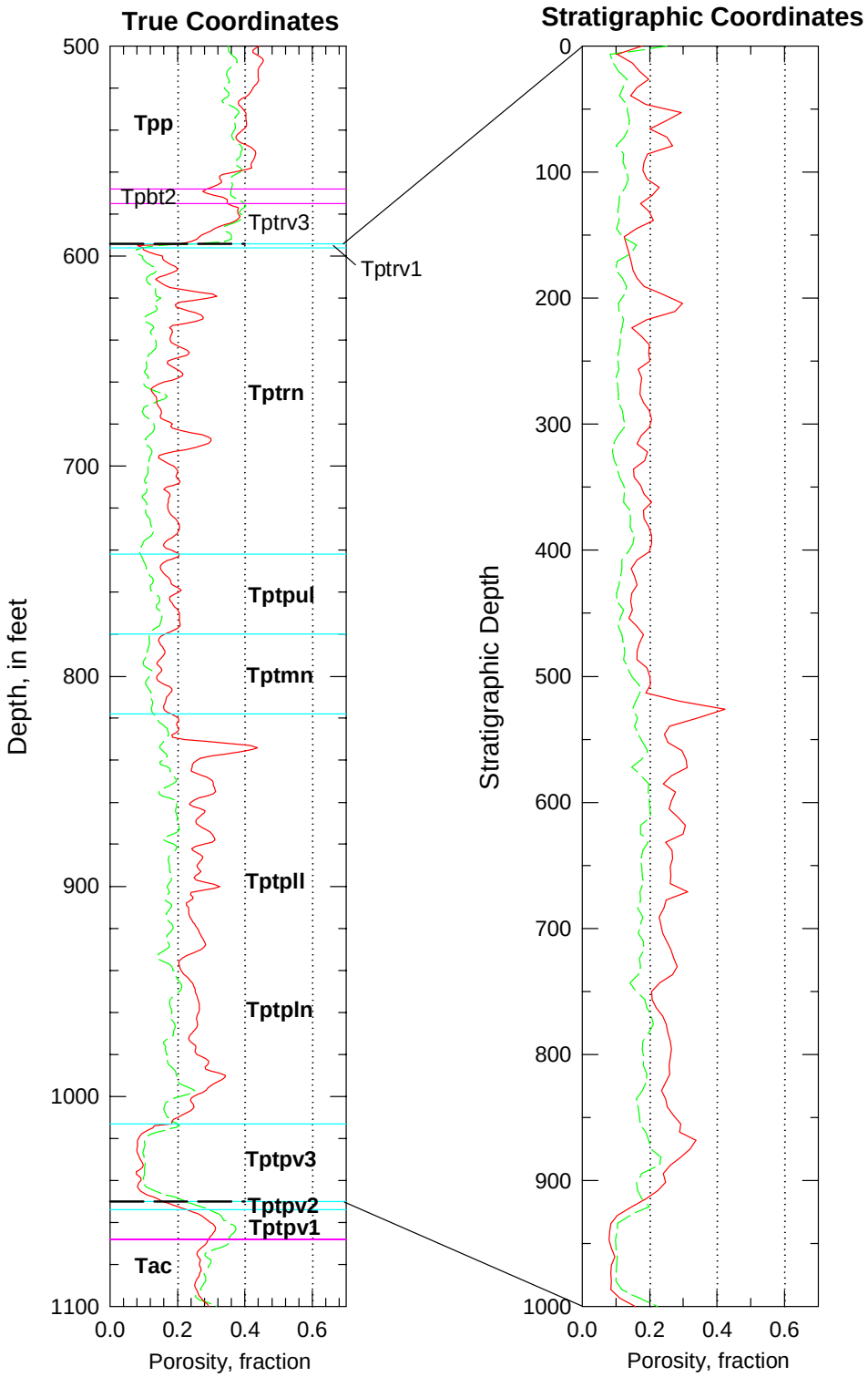

Figure B-127. Porosity data in real-world and in stratigraphic coordinates for the TSw model unit in drillhole WT-16.

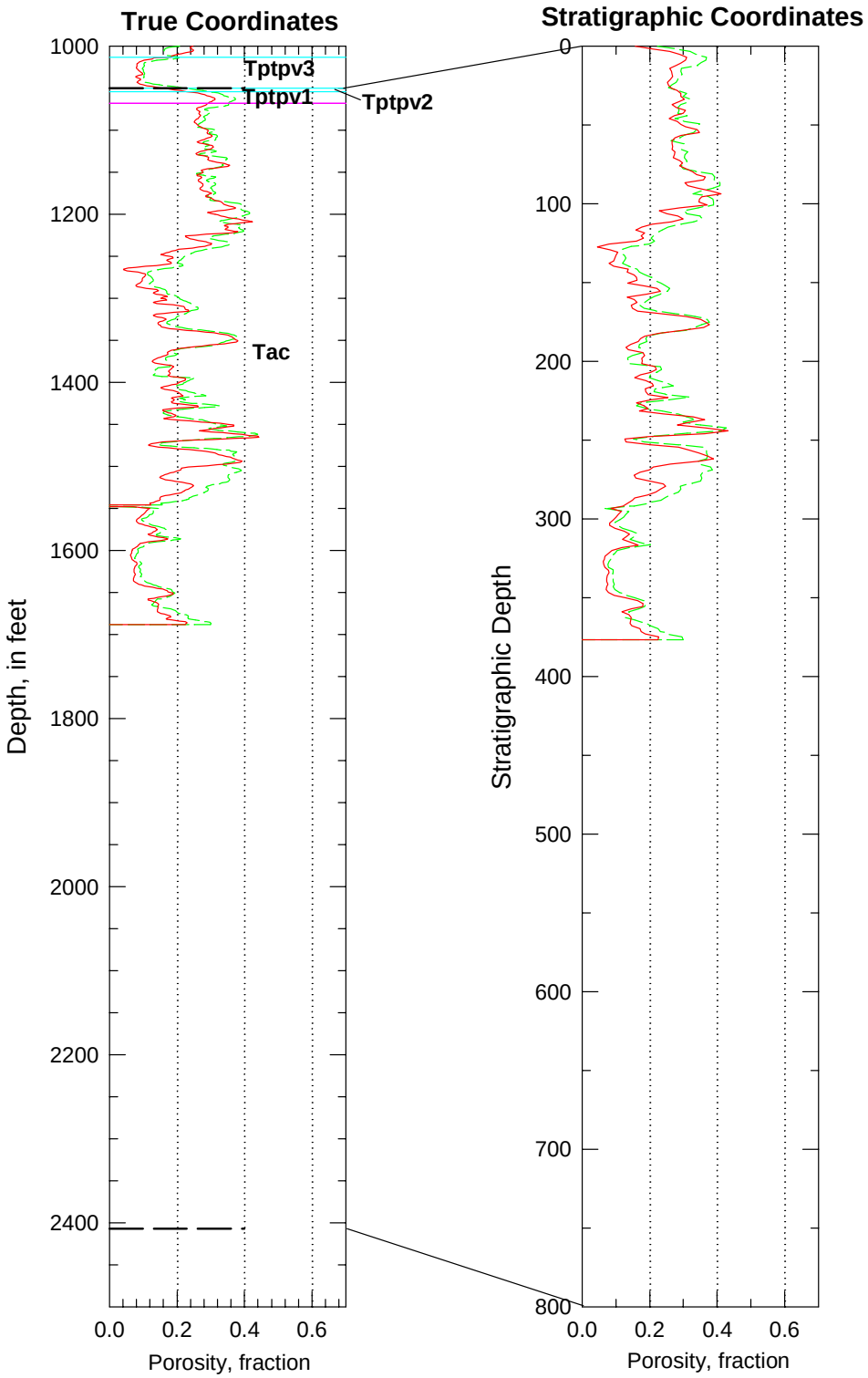

Figure B-128. Porosity data in real-world and in stratigraphic coordinates for the combined CH–PP model unit in drillhole WT-16.

Drillhole WT-17

Drillhole WT-17 is one of an older series of holes drilled to obtain hydrologic information principally from the saturated zone at Yucca Mountain. The hole was not cored, and the geophysical logs belong the older suite of petrophysical data. These data have been converted to values of total and water-filled porosity.

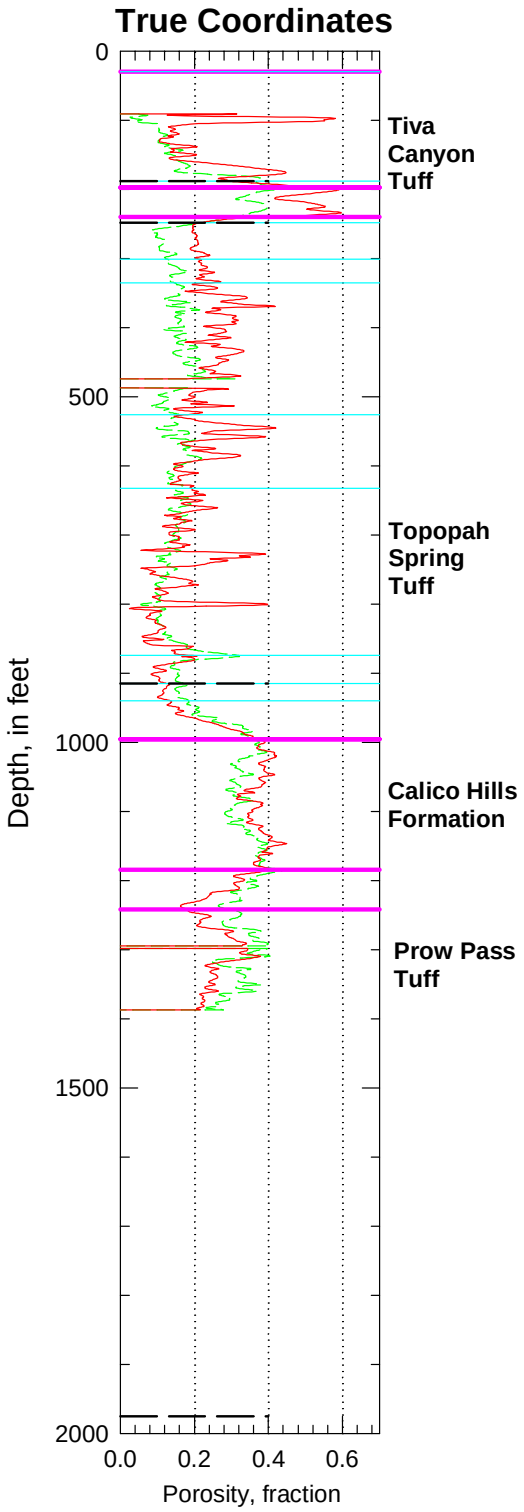

Figure B-129. Porosity data in true coordinates from drillhole WT-17 for the entire drillhole.

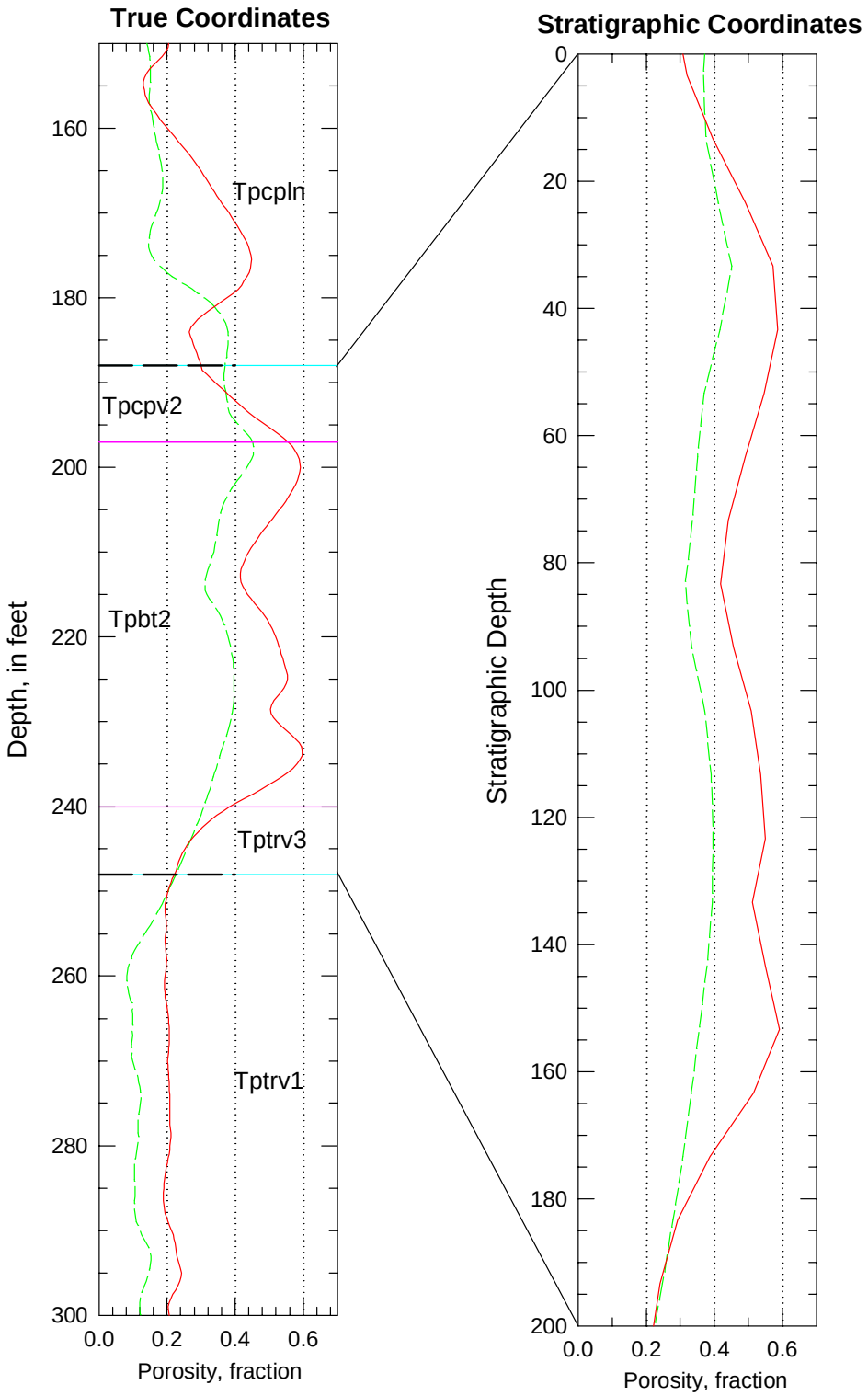

Figure B-130. Porosity data in real-world and in stratigraphic coordinates for the PTn model unit in drillhole WT-17.

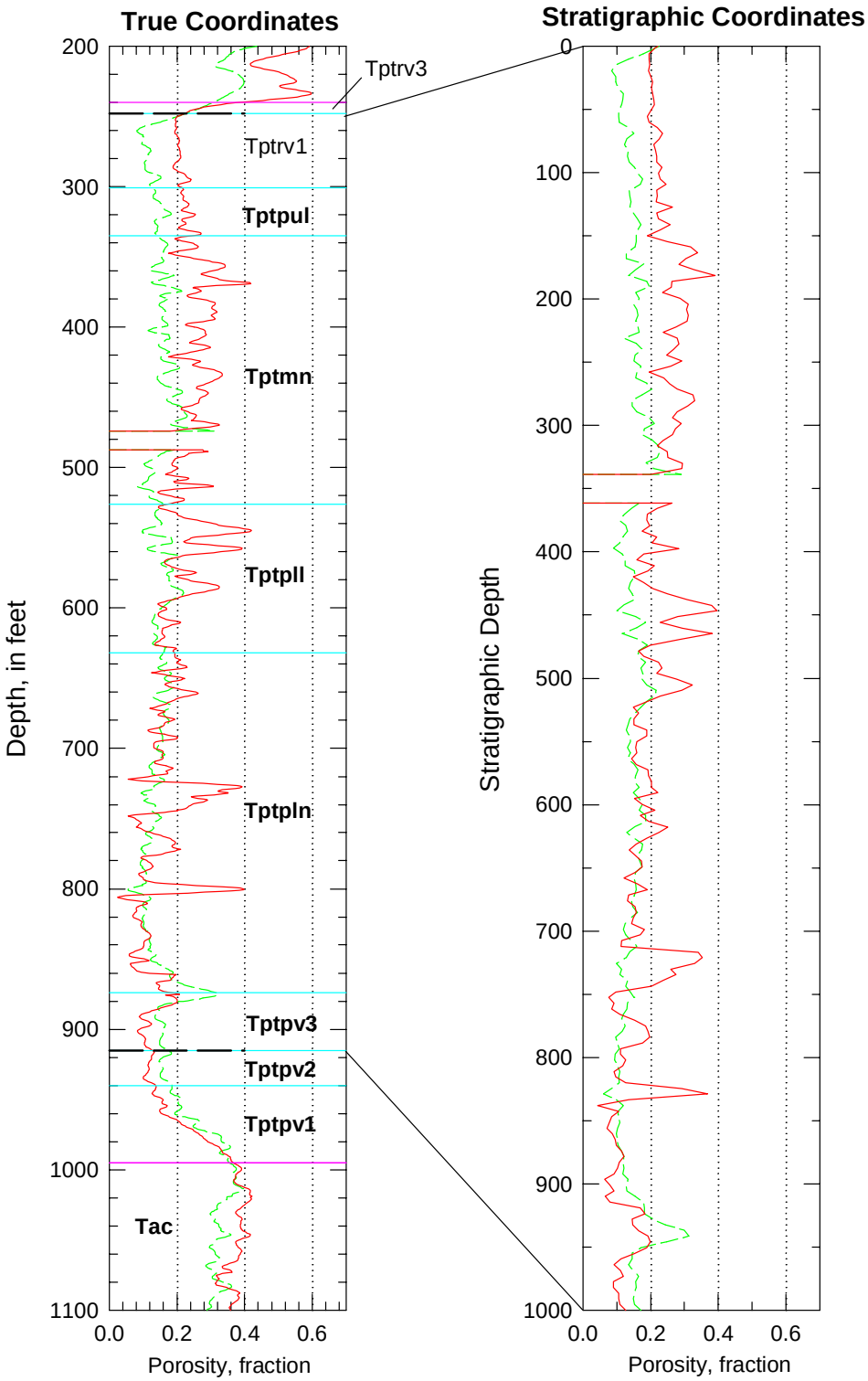

Figure B-131. Porosity data in real-world and in stratigraphic coordinates for the TSw model unit in drillhole WT-17.

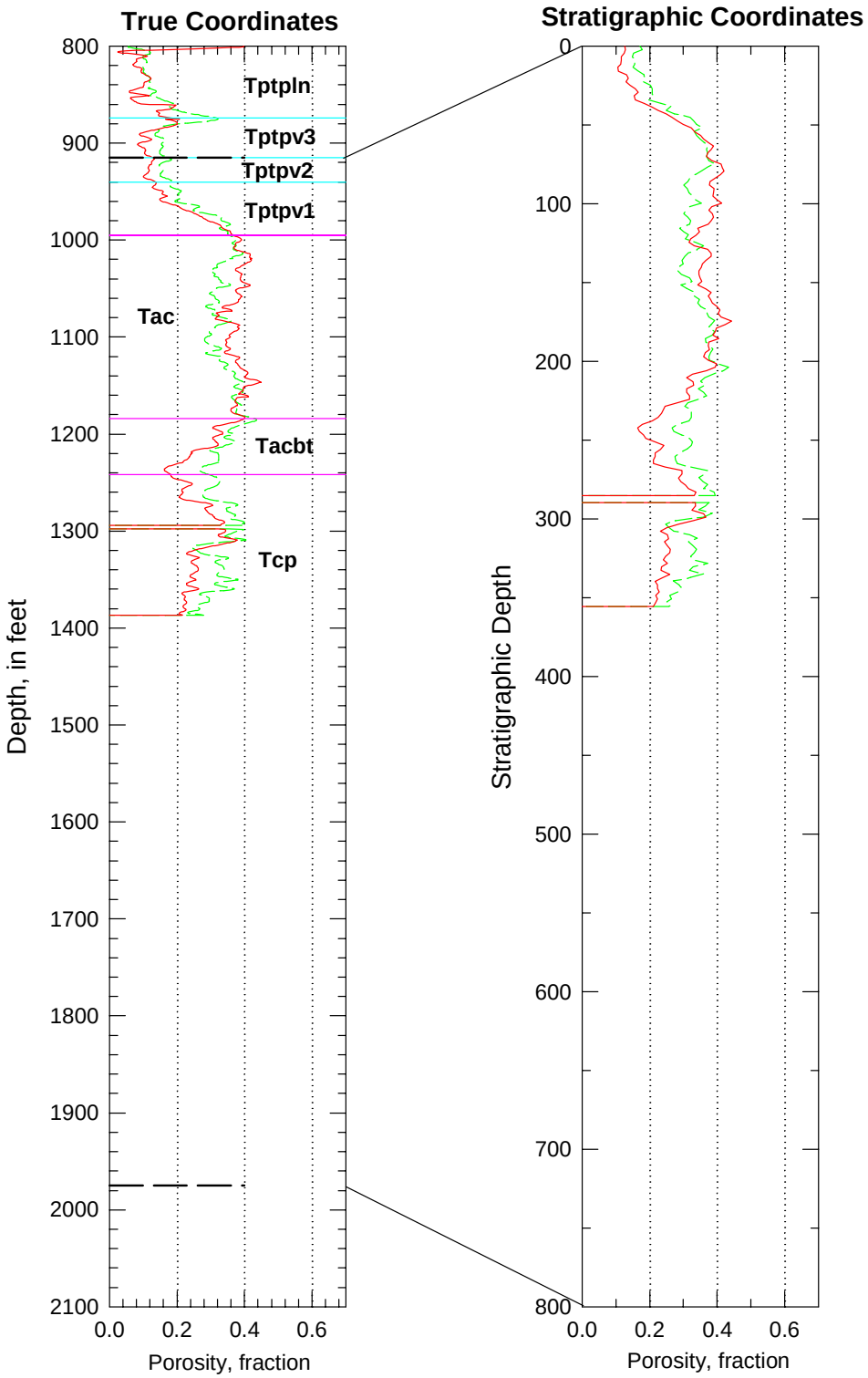

Figure B-132. Porosity data in real-world and in stratigraphic coordinates for the combined CH–PP model unit in drillhole WT-17.

Drillhole WT-18

Drillhole WT-18 is one of an older series of holes drilled to obtain hydrologic information principally from the saturated zone at Yucca Mountain. The hole was not cored, and the geophysical logs belong the older suite of petrophysical data. These data have been converted to values of total and water-filled porosity.

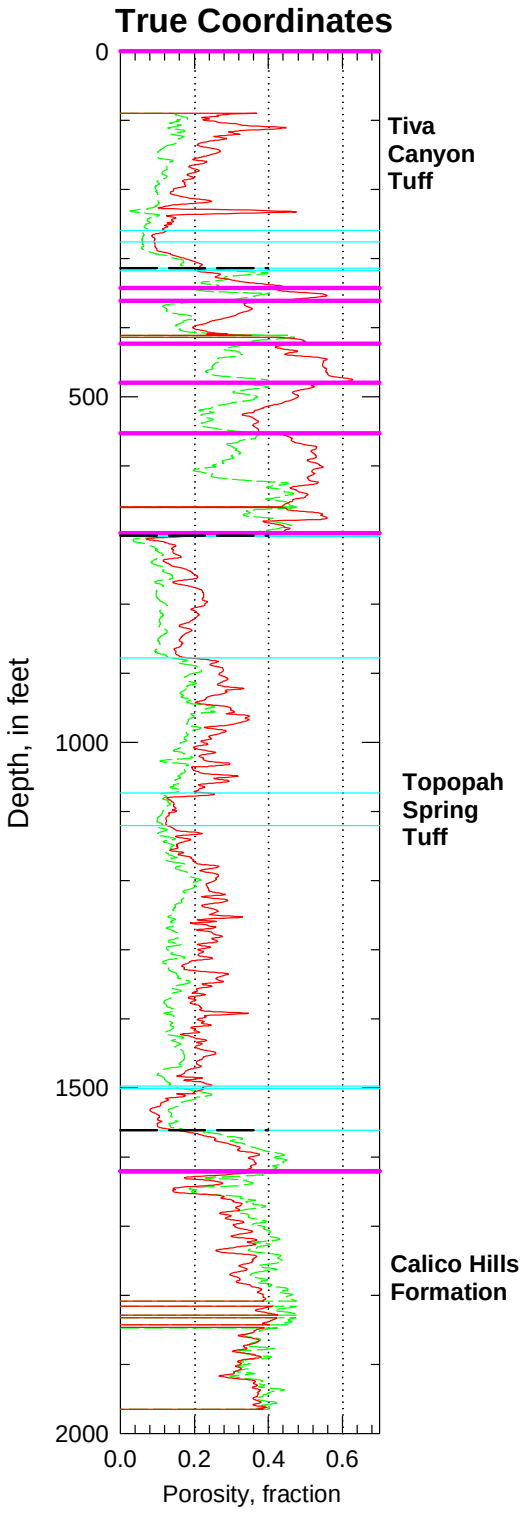

Figure B-133. Porosity data in true coordinates from drillhole WT-18 for the entire drillhole.

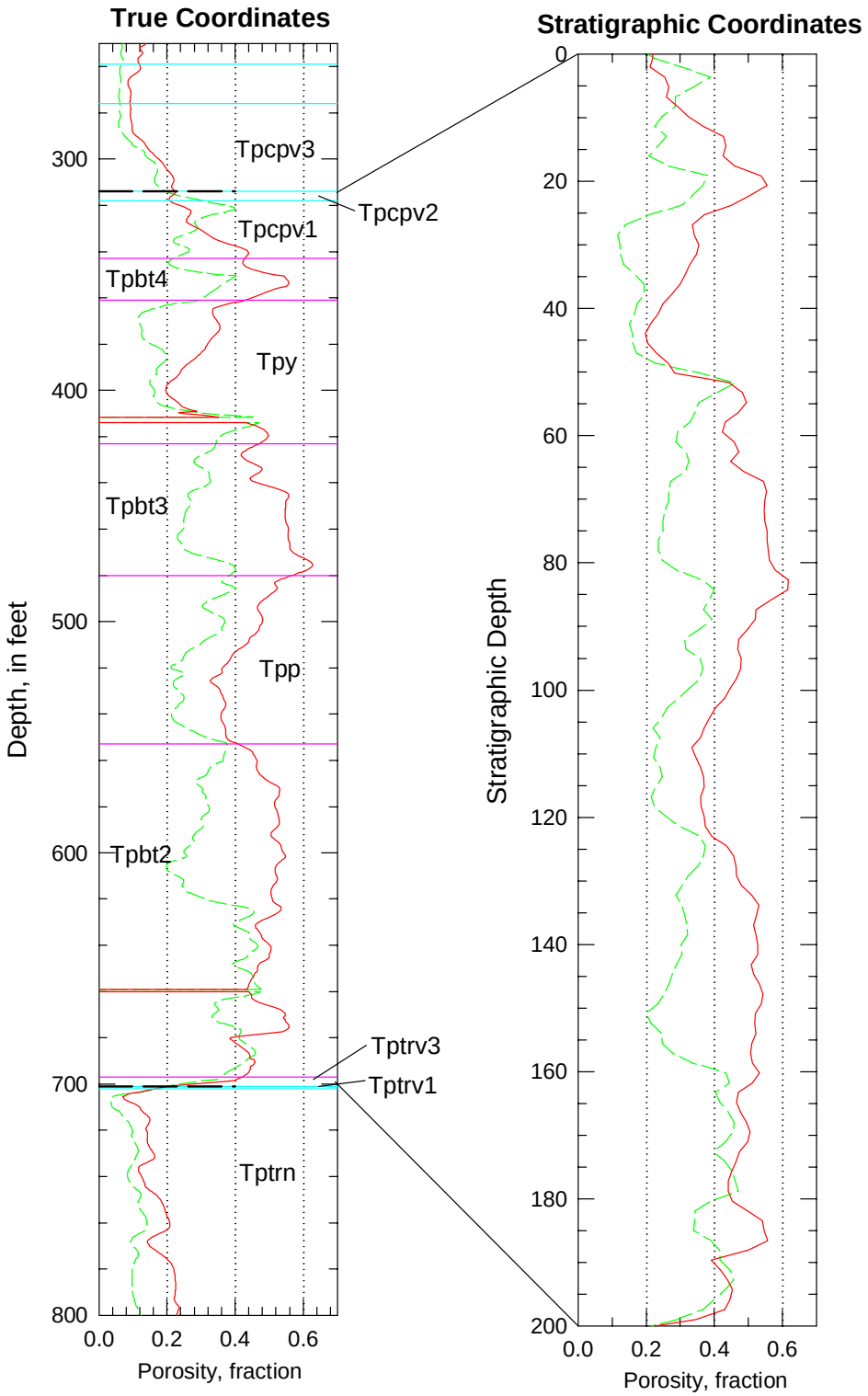

Figure B-134. Porosity data in real-world and in stratigraphic coordinates for the PTn model unit in drillhole WT-18.

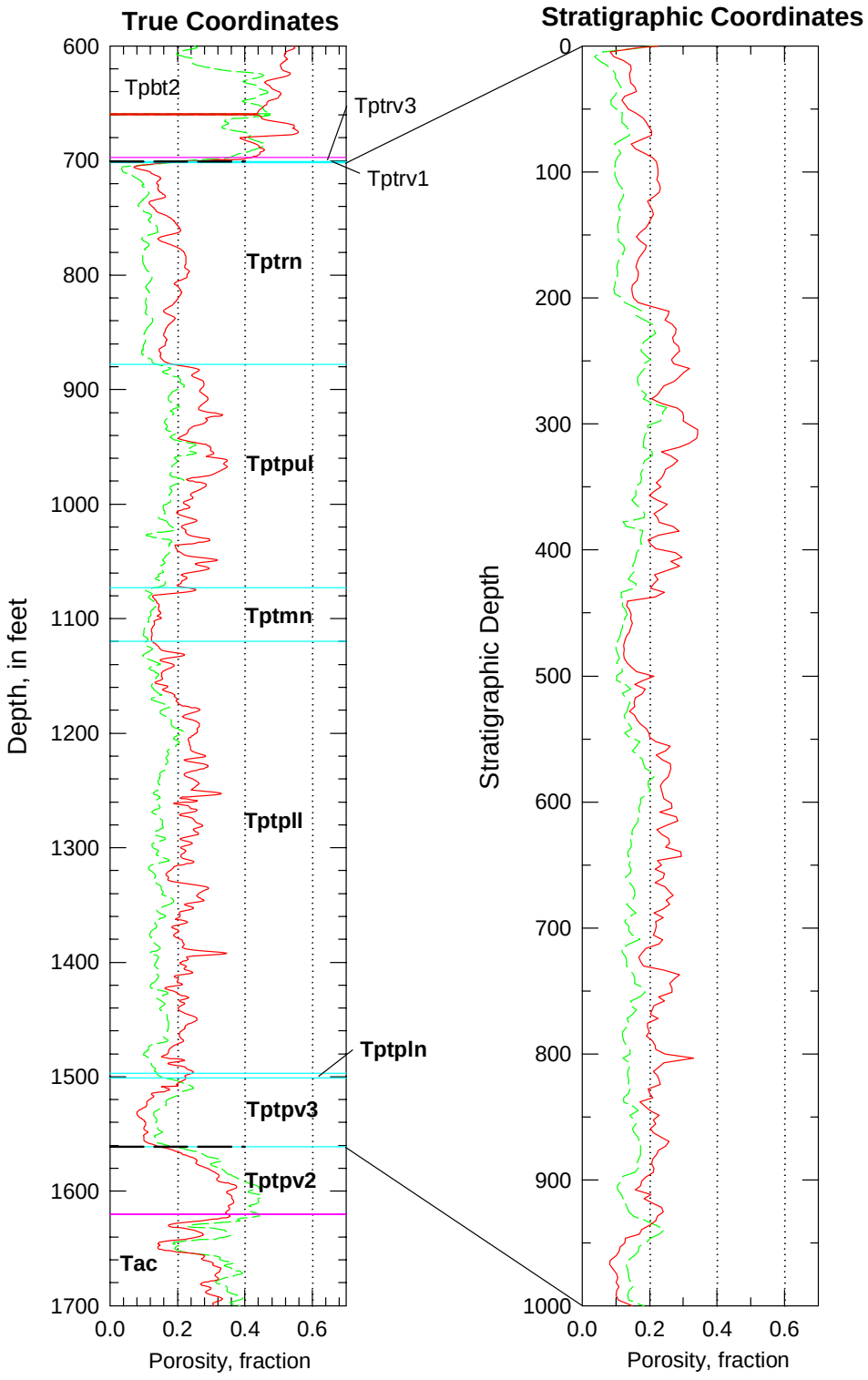

Figure B-135. Porosity data in real-world and in stratigraphic coordinates for the TSw model unit in drillhole WT-18.

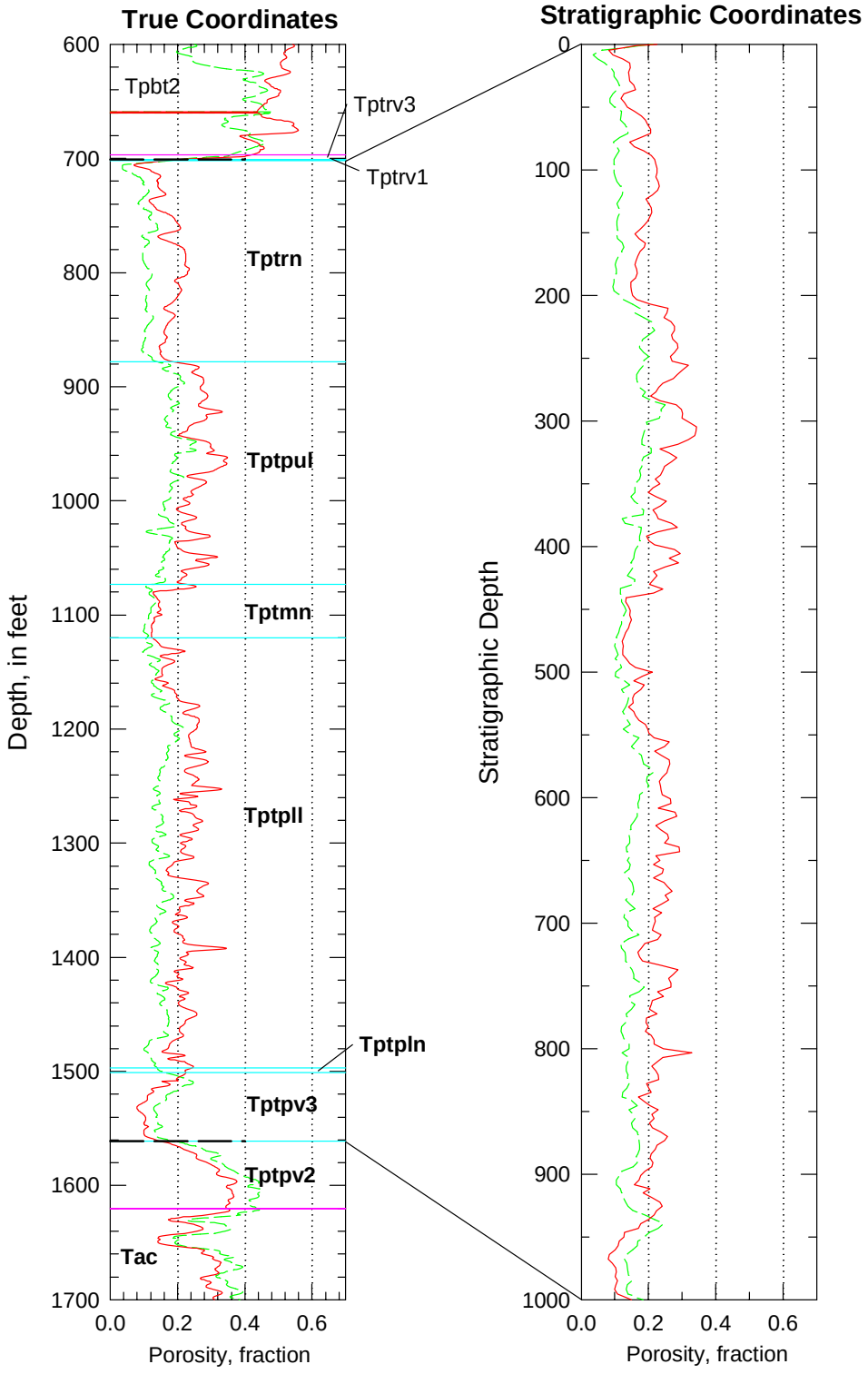

Figure B-136. Porosity data in real-world and in stratigraphic coordinates for the TSw model unit in drillhole WT-18.

The UZN Series of Drillholes

Drillholes with a prefix of “UZN-” are part of a series of neutron holes drilled to monitor near-surface moisture contents as a function of precipitation In general, the holes are quite shallow, typically less than 50 ft. However, a limited number of neutron holes were drilled to depths of approximately 250 ft, and these provide important information from the PTn and TSw model units. Only laboratory core measurements are available for these holes

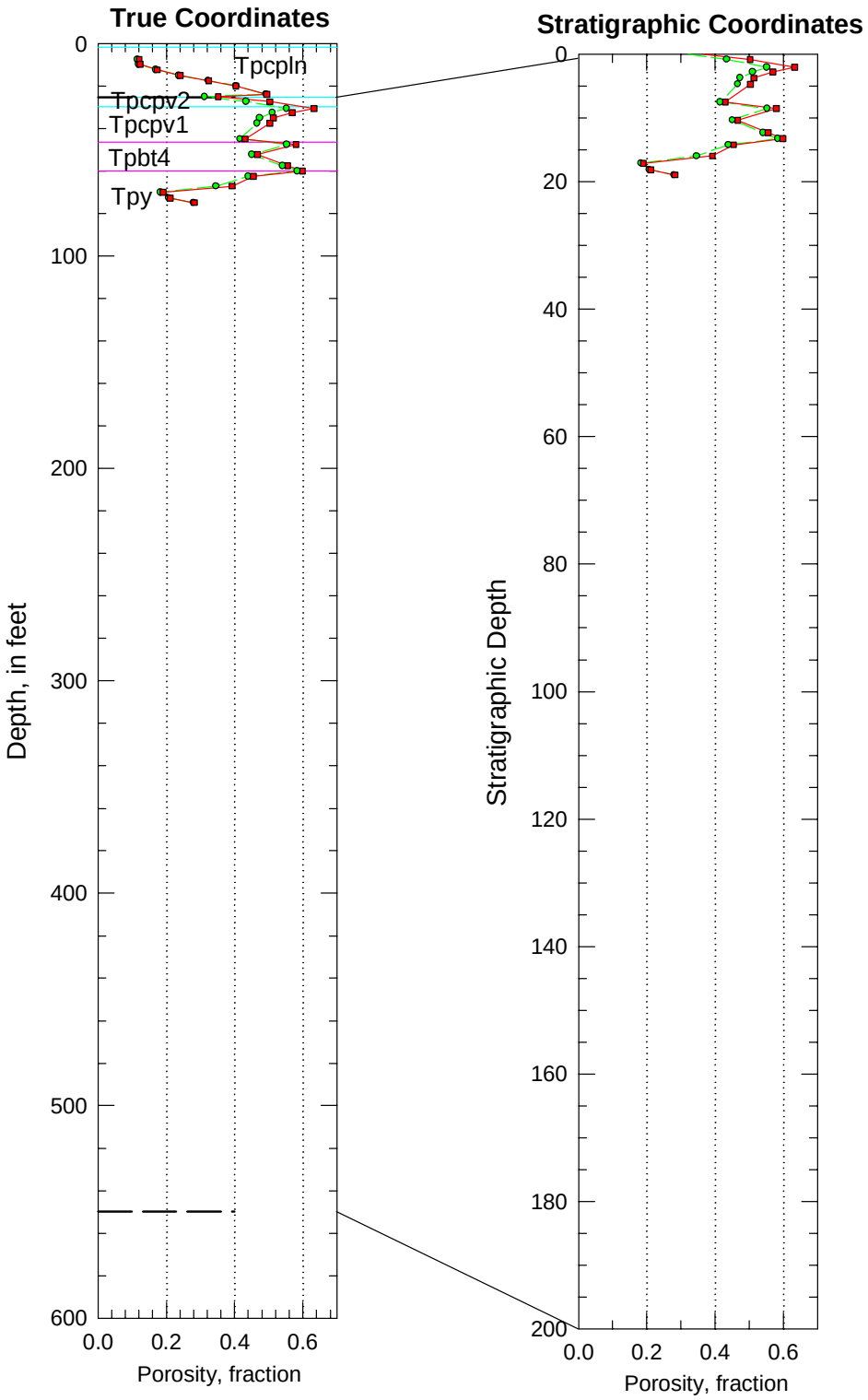

Figure B-137. Porosity data in real-world and in stratigraphic coordinates for the PTn model unit in drillhole UZN-11.

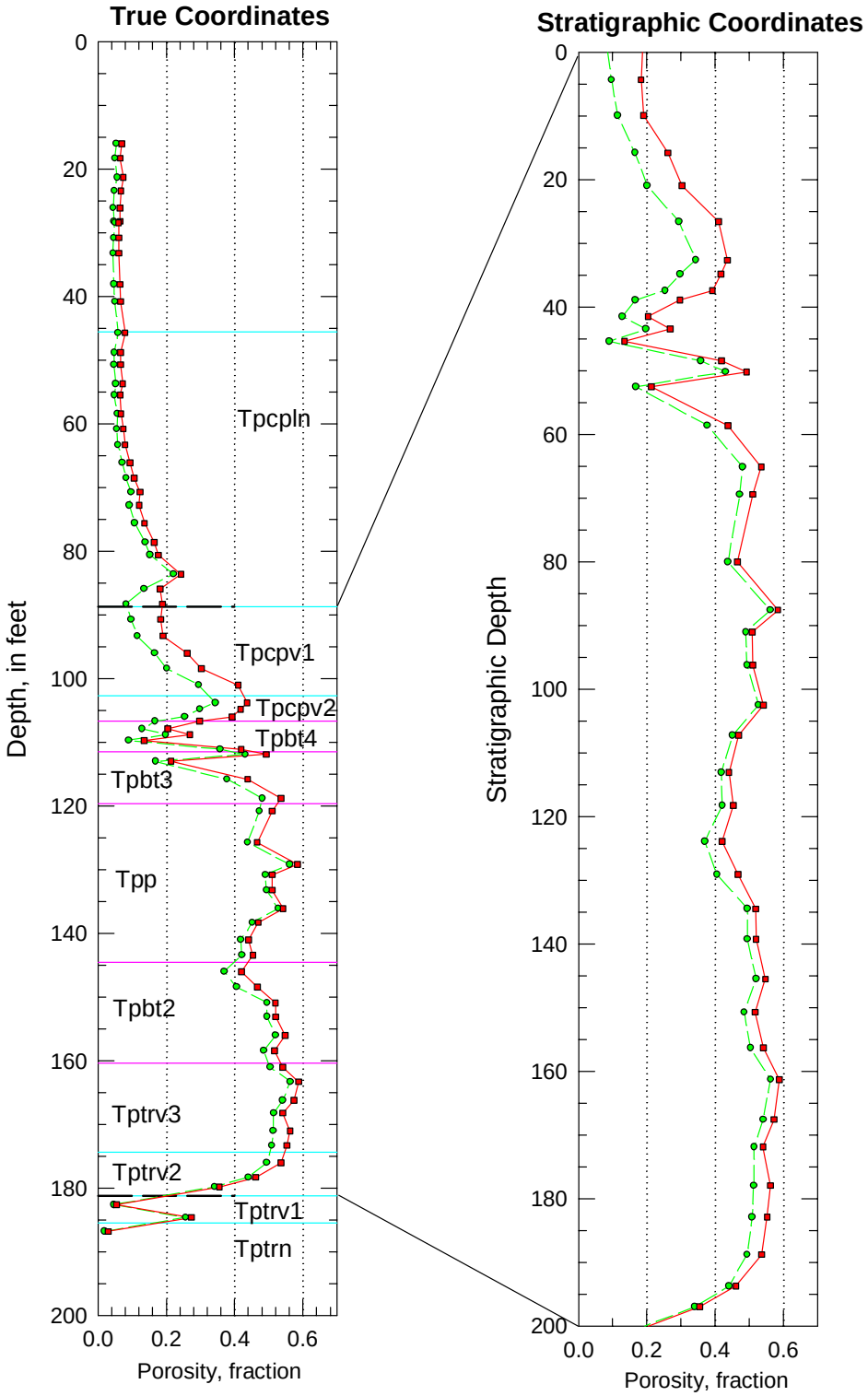

Figure B-138. Porosity data in real-world and in stratigraphic coordinates for the PTn model unit in drillhole UZN-31. Note: stratigraphic coordinates for samples of the TSw model unit not shown because there are so few values; however, these data were used in modeling.

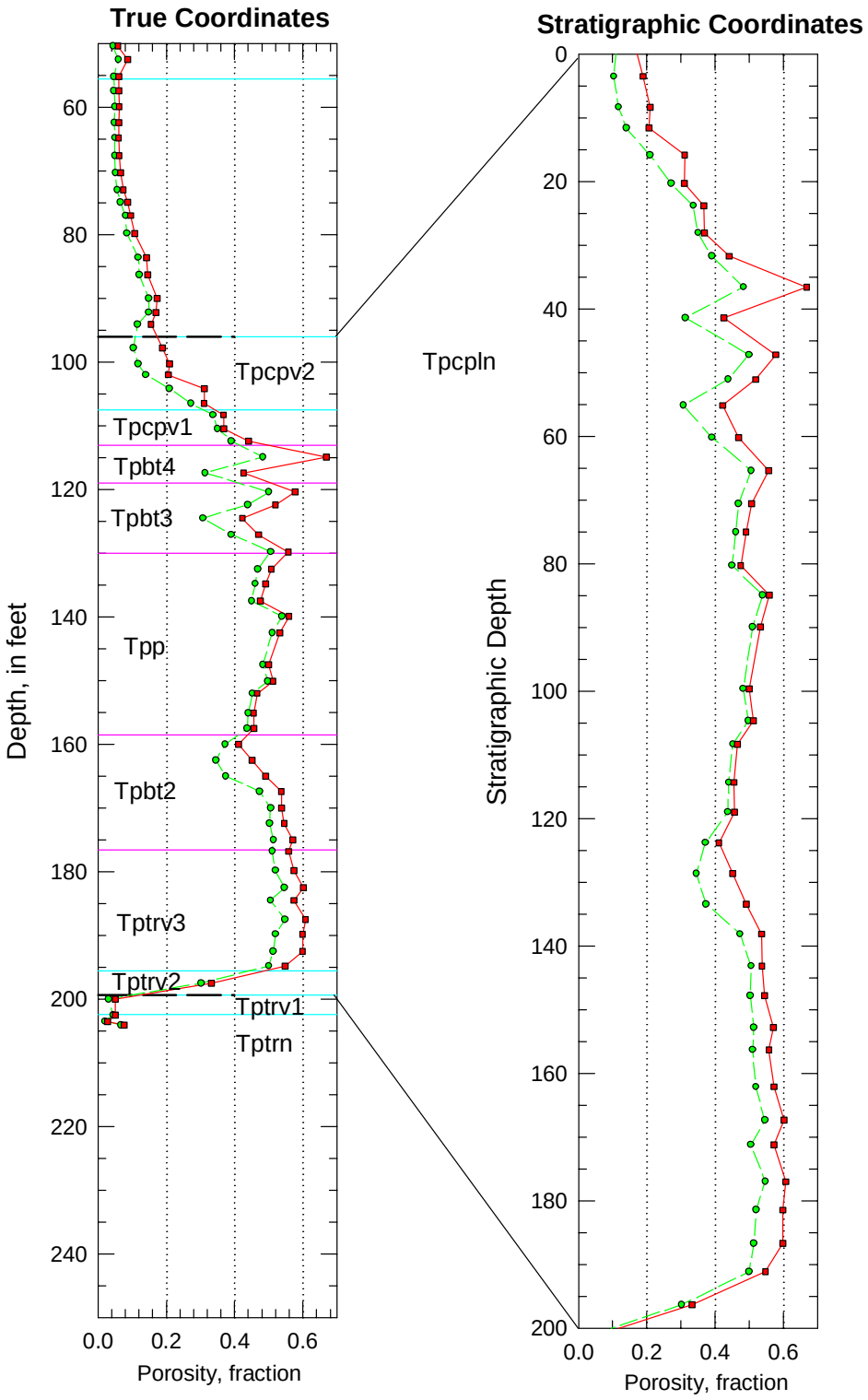

Figure B-139. Porosity data in real-world and in stratigraphic coordinates for the PTn model unit in drillhole UZN-32. Note: stratigraphic coordinates for samples of the TSw model unit not shown because there are so few values; however, these data were used in modeling.

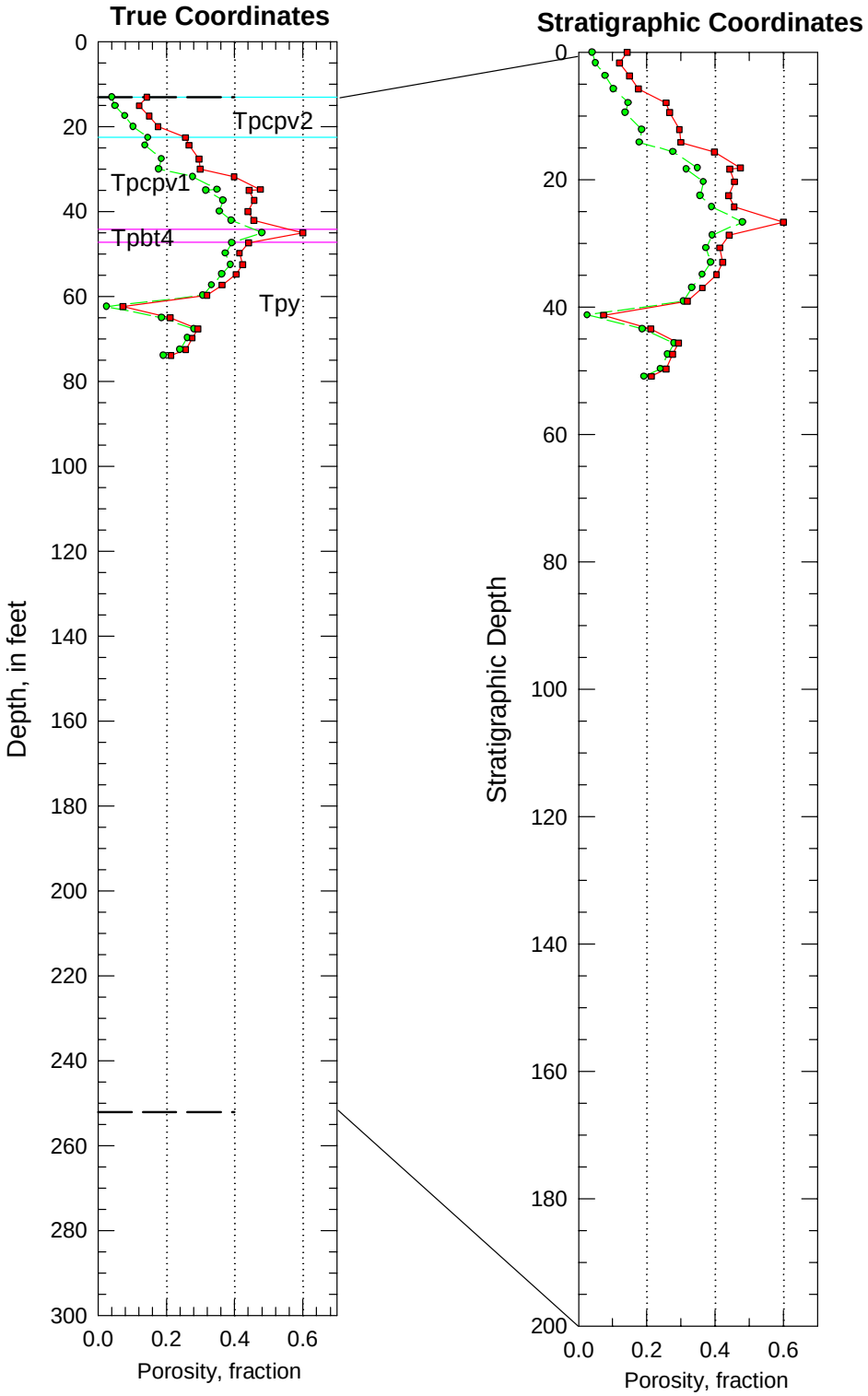

Figure B-140. Porosity data in real-world and in stratigraphic coordinates for the PTn model unit in drillhole UZN-33.

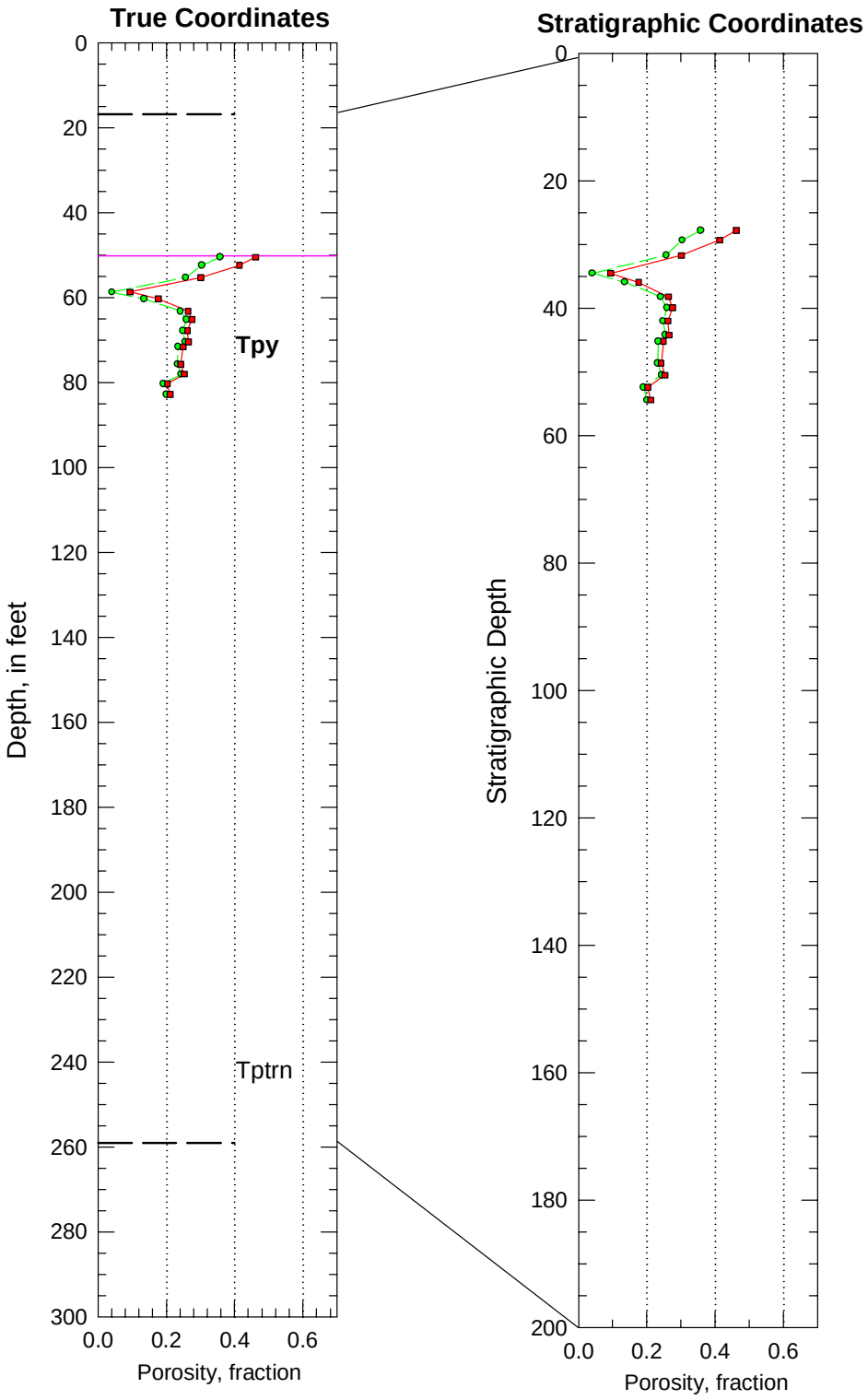

Figure B-141. Porosity data in real-world and in stratigraphic coordinates for the PTn model unit in drillhole UZN-34.

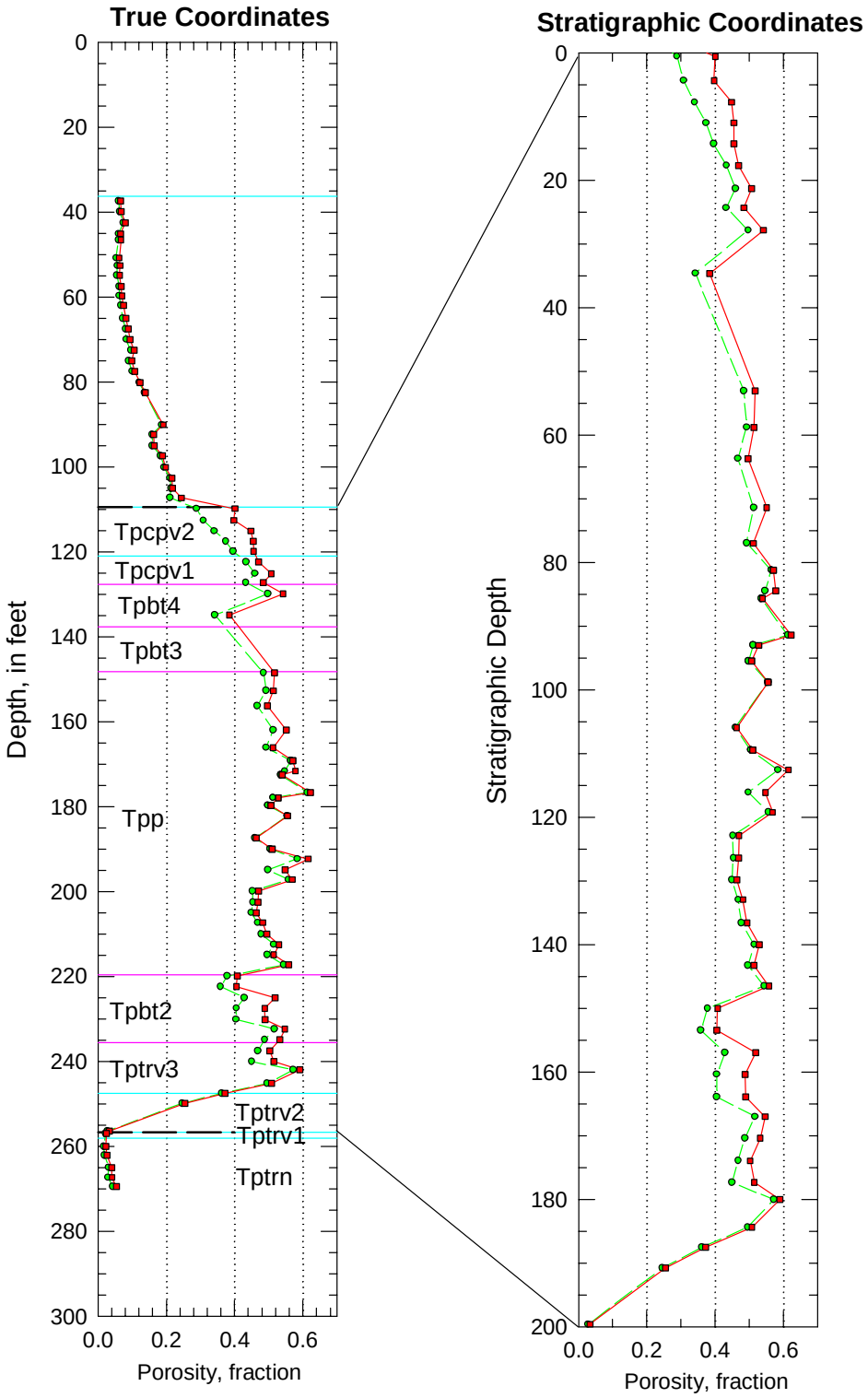

Figure B-142. Porosity data in real-world and in stratigraphic coordinates for the PTn model unit in drillhole UZN-37. Note: stratigraphic coordinates for samples of the TSw model unit not shown because there are so few values; however, these data were used in modeling.

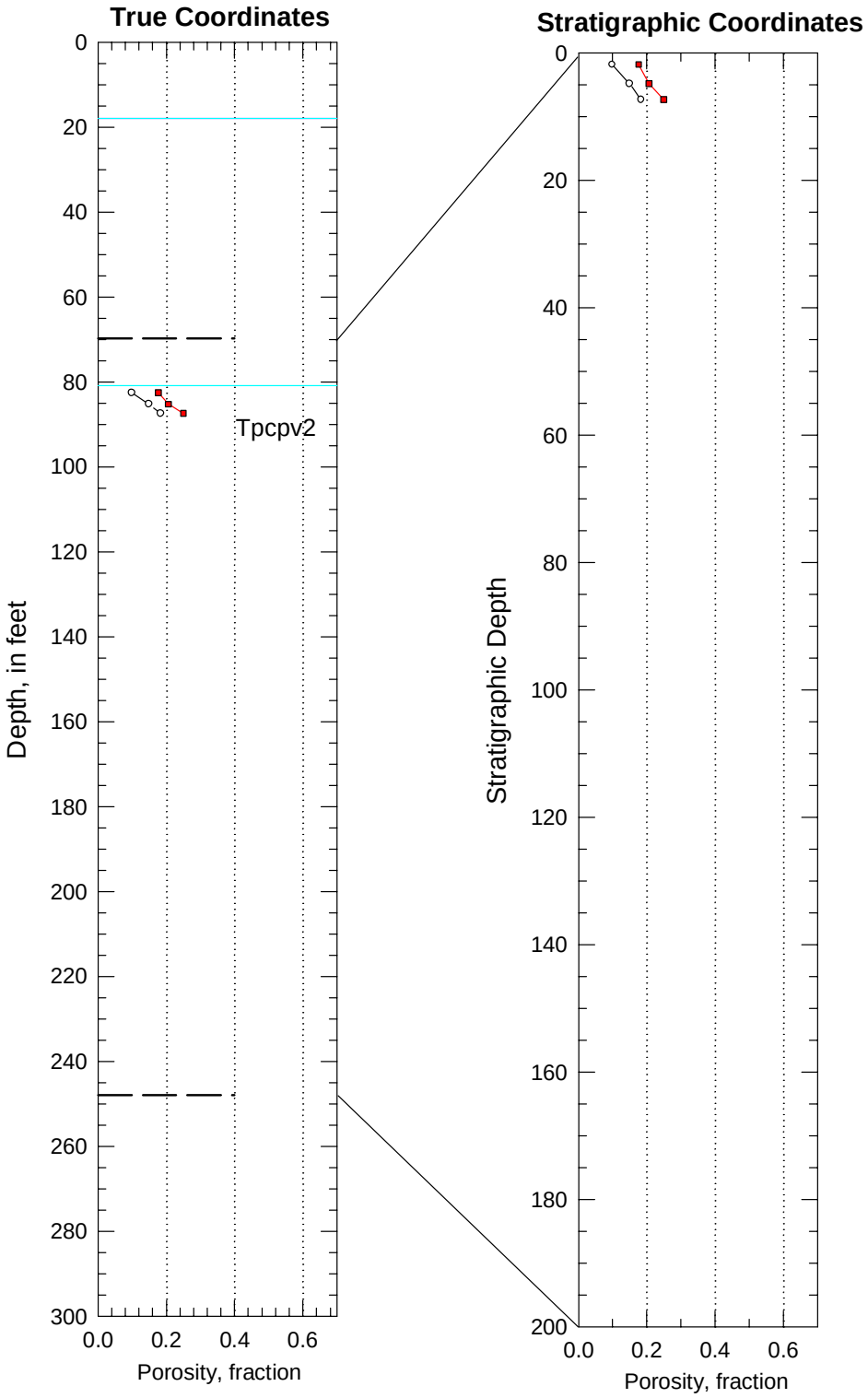

Figure B-143. Porosity data in real-world and in stratigraphic coordinates for the PTn model unit in drillhole UZN-38.

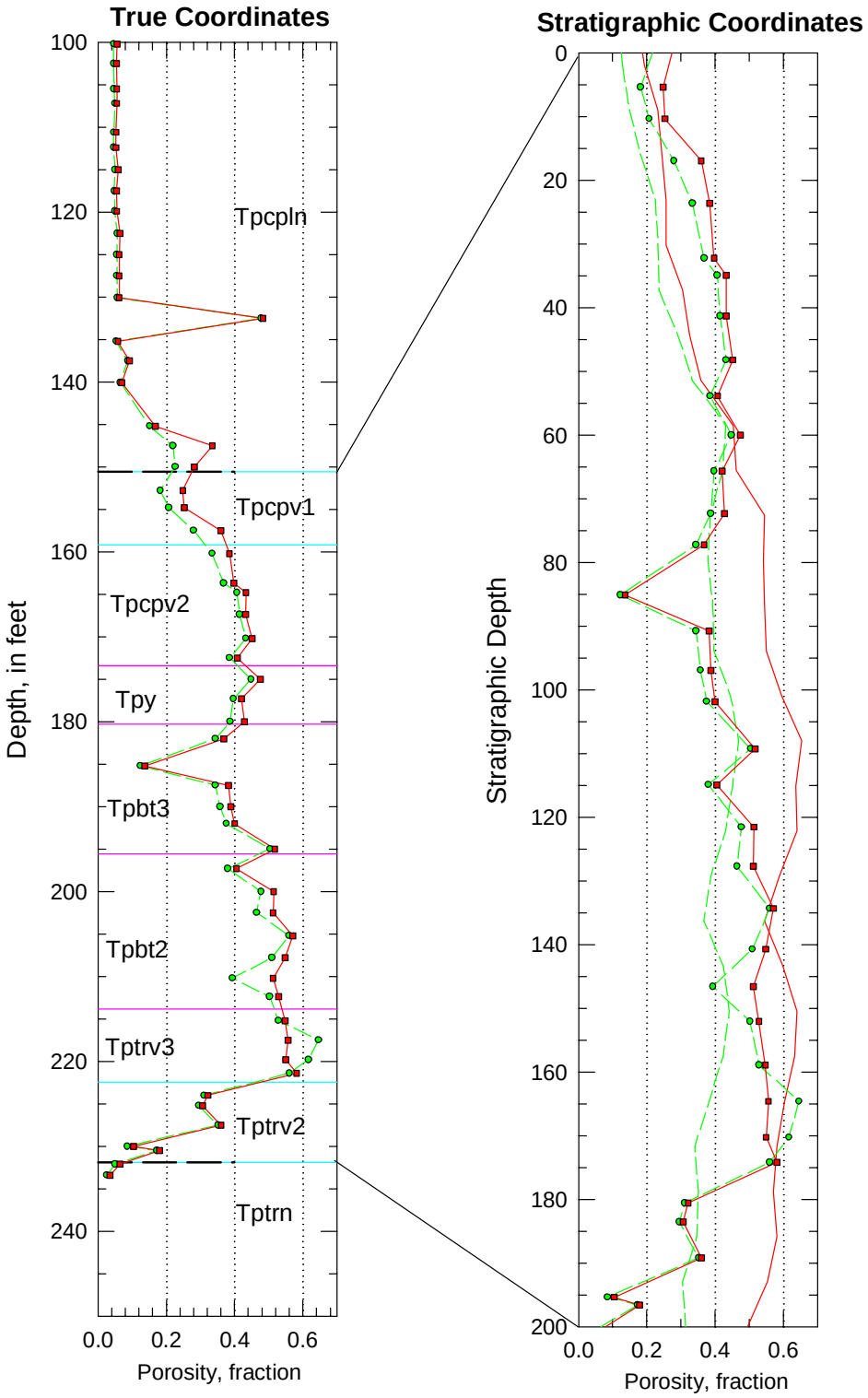

Figure B-144. Porosity data in real-world and in stratigraphic coordinates for the PTn model unit in drillhole UZN-53. Note: stratigraphic coordinates for samples of the TSw model unit not shown because there are so few values; however, these data were used in modeling.

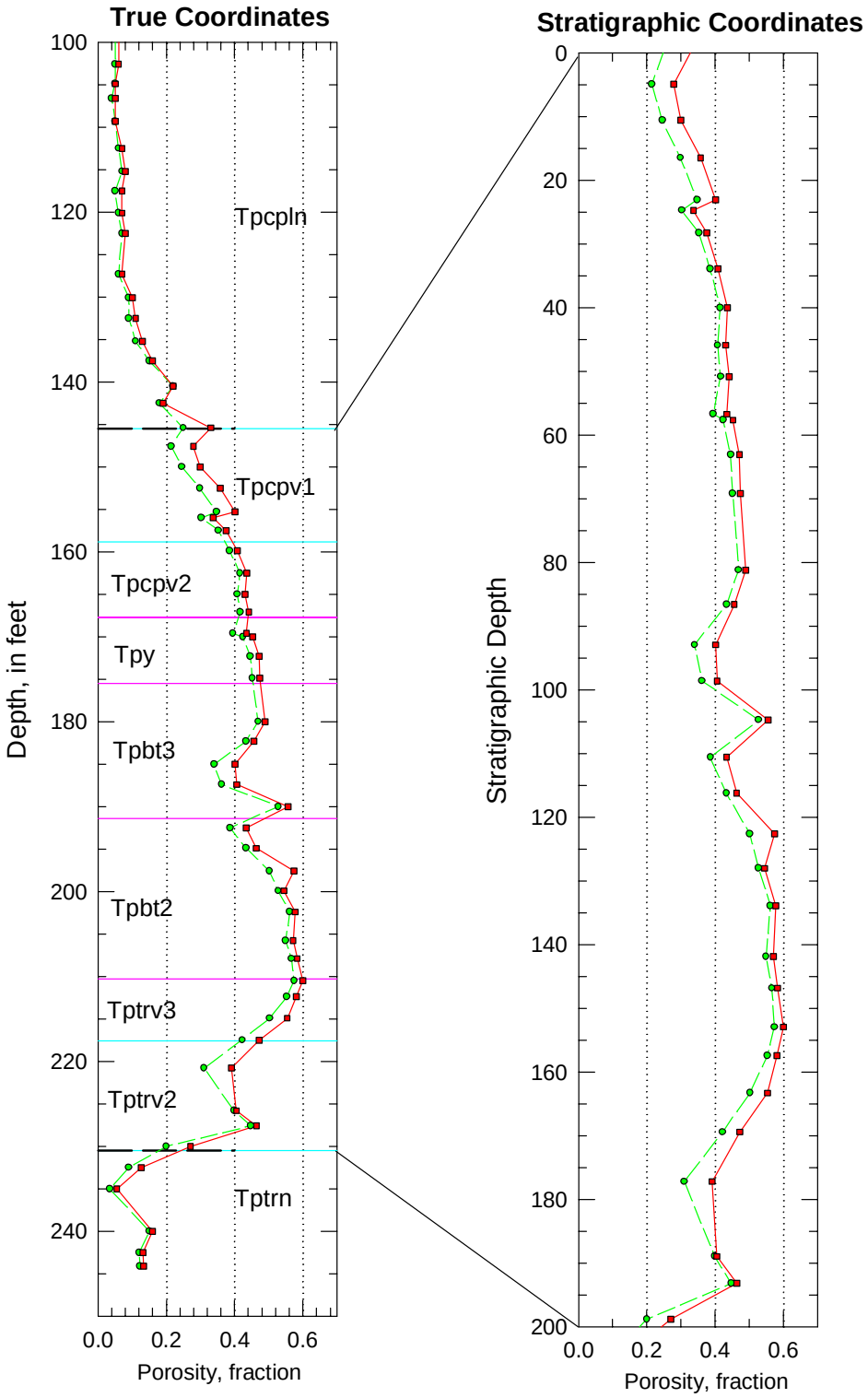

Figure B-145. Porosity data in real-world and in stratigraphic coordinates for the PTn model unit in drillhole UZN-54. Note: stratigraphic coordinates for samples of the TSw model unit not shown because there are so few values; however, these data were used in modeling.

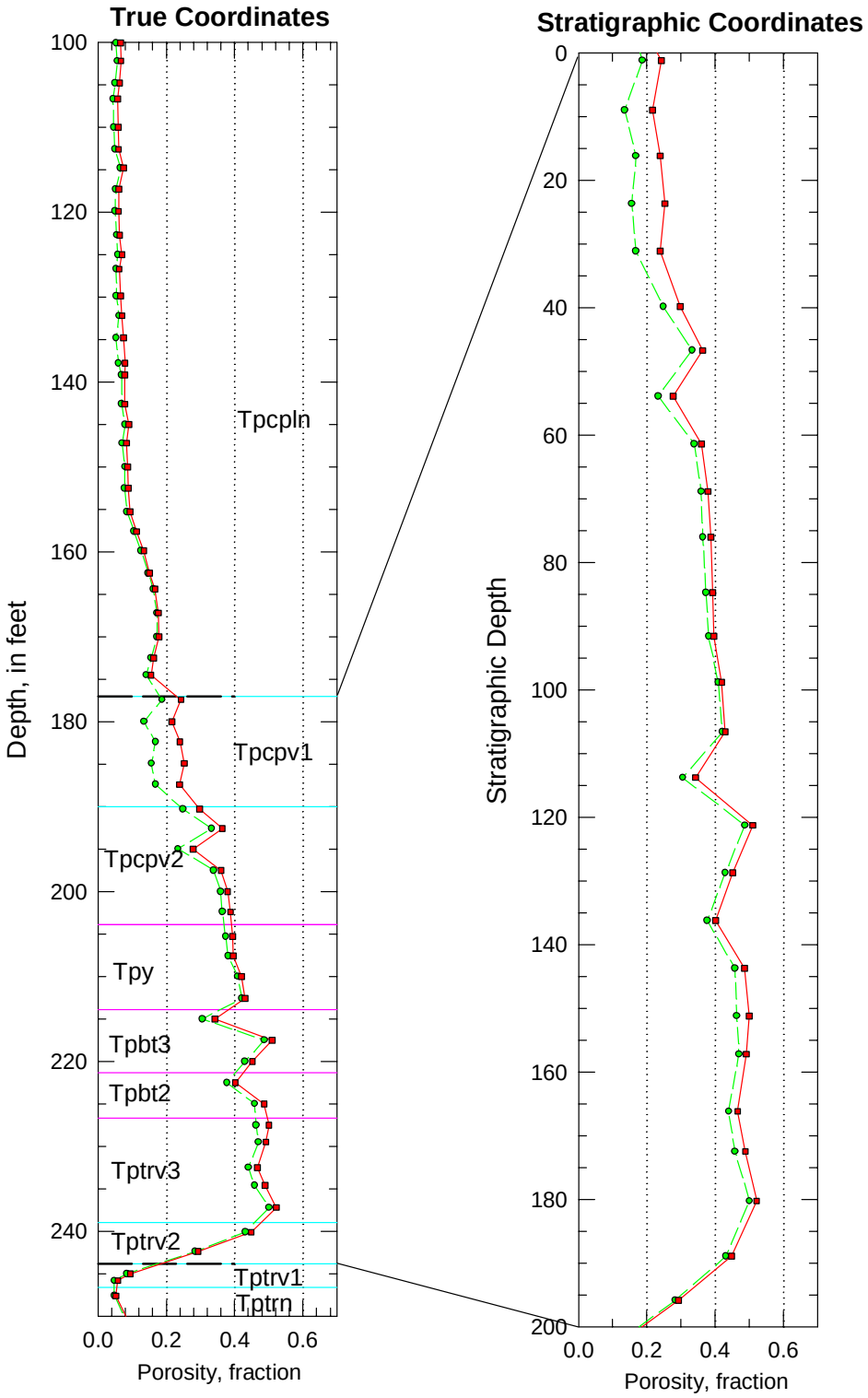

Figure B-146. Porosity data in real-world and in stratigraphic coordinates for the PTn model unit in drillhole UZN-55. Note: stratigraphic coordinates for samples of the TSw model unit not shown because there are so few values; however, these data were used in modeling.

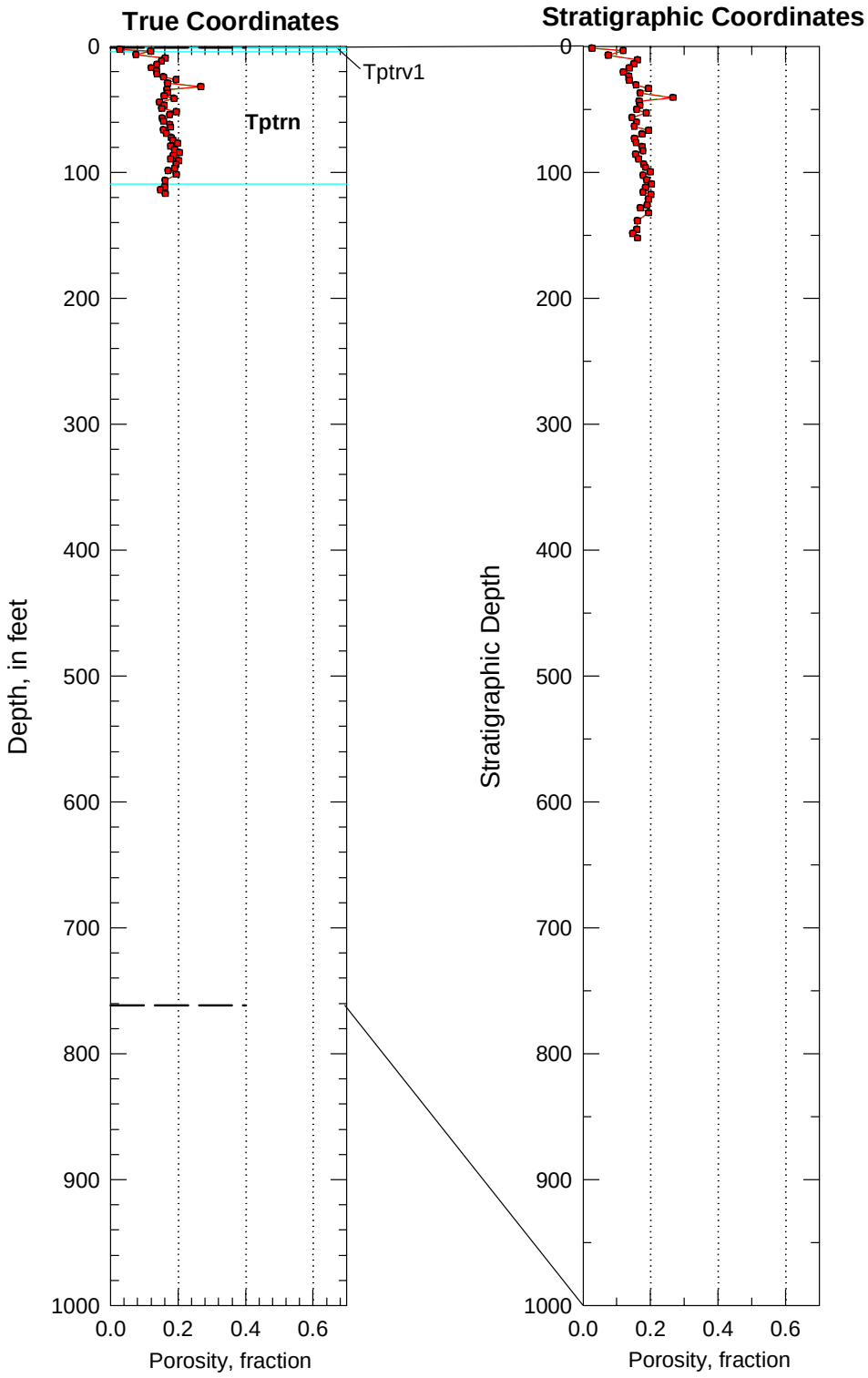

Figure B-147. Porosity data in real world and in stratigraphic coordinates for the TSw model unit in drillhole UZN-57.

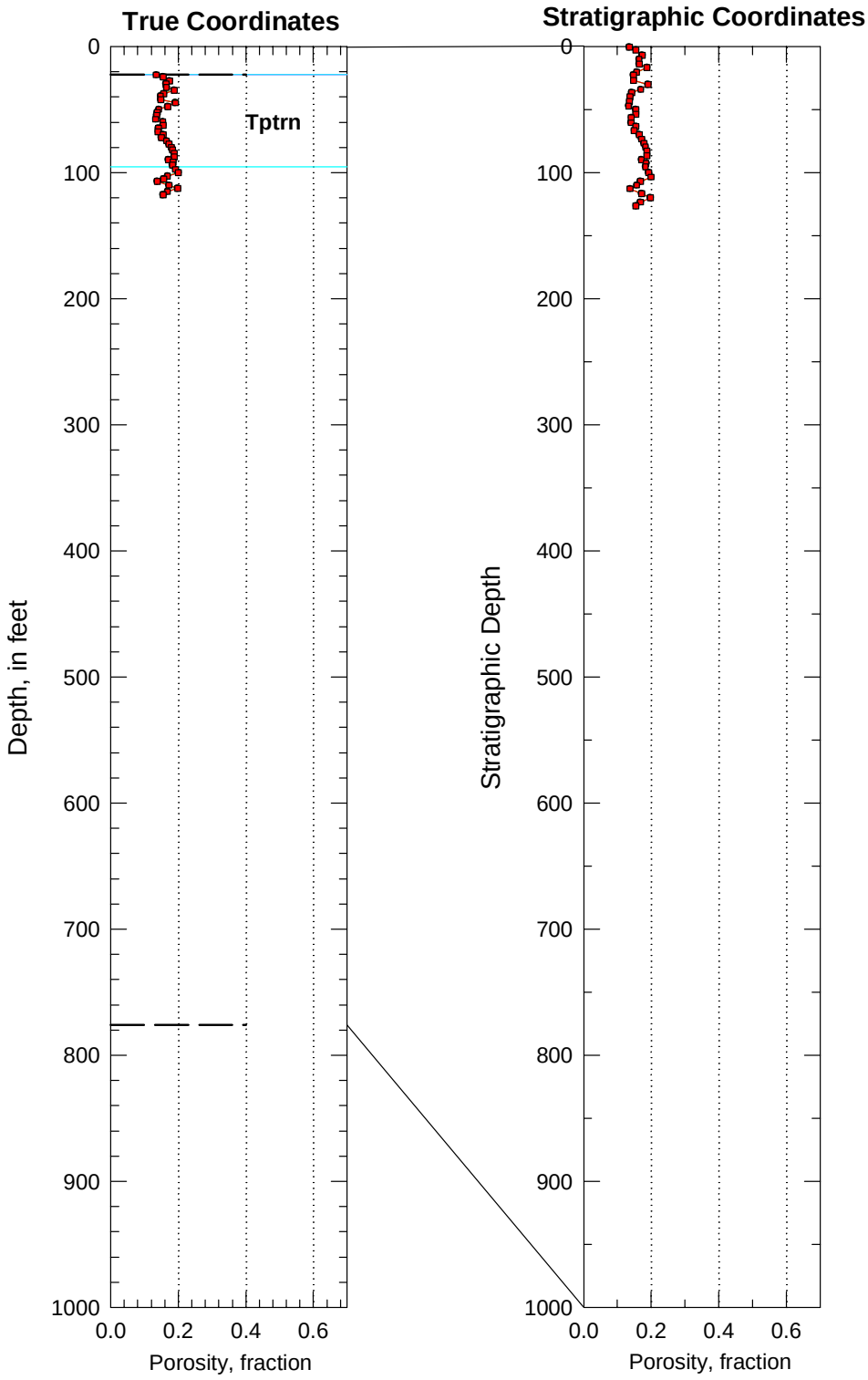

Figure B-148. Porosity data in real-world and in stratigraphic coordinates for the TSw model unit in drillhole UZN-58.

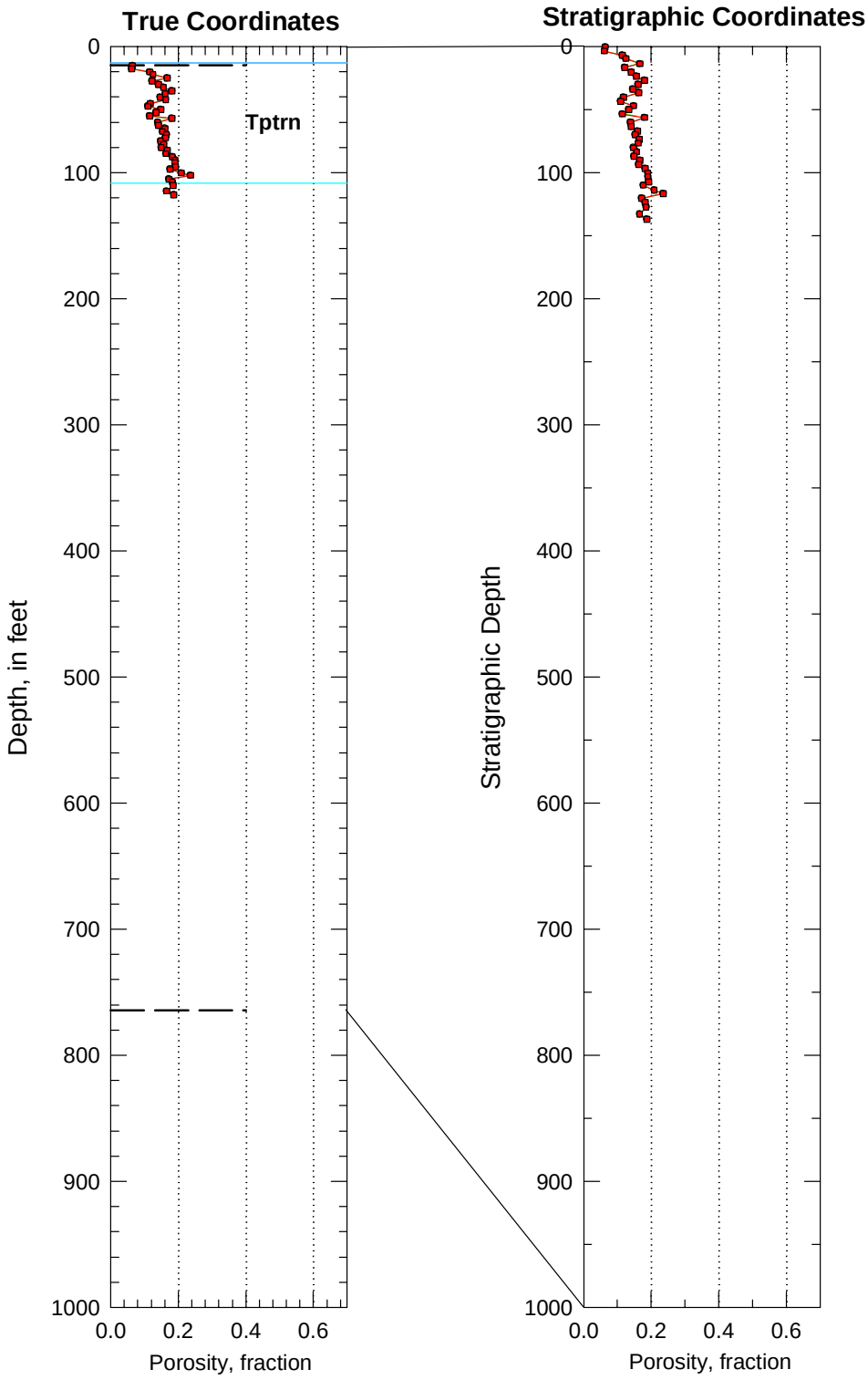

Figure B-149. Porosity data in real-world and in stratigraphic coordinates for the TSw model unit in drillhole UZN-59.

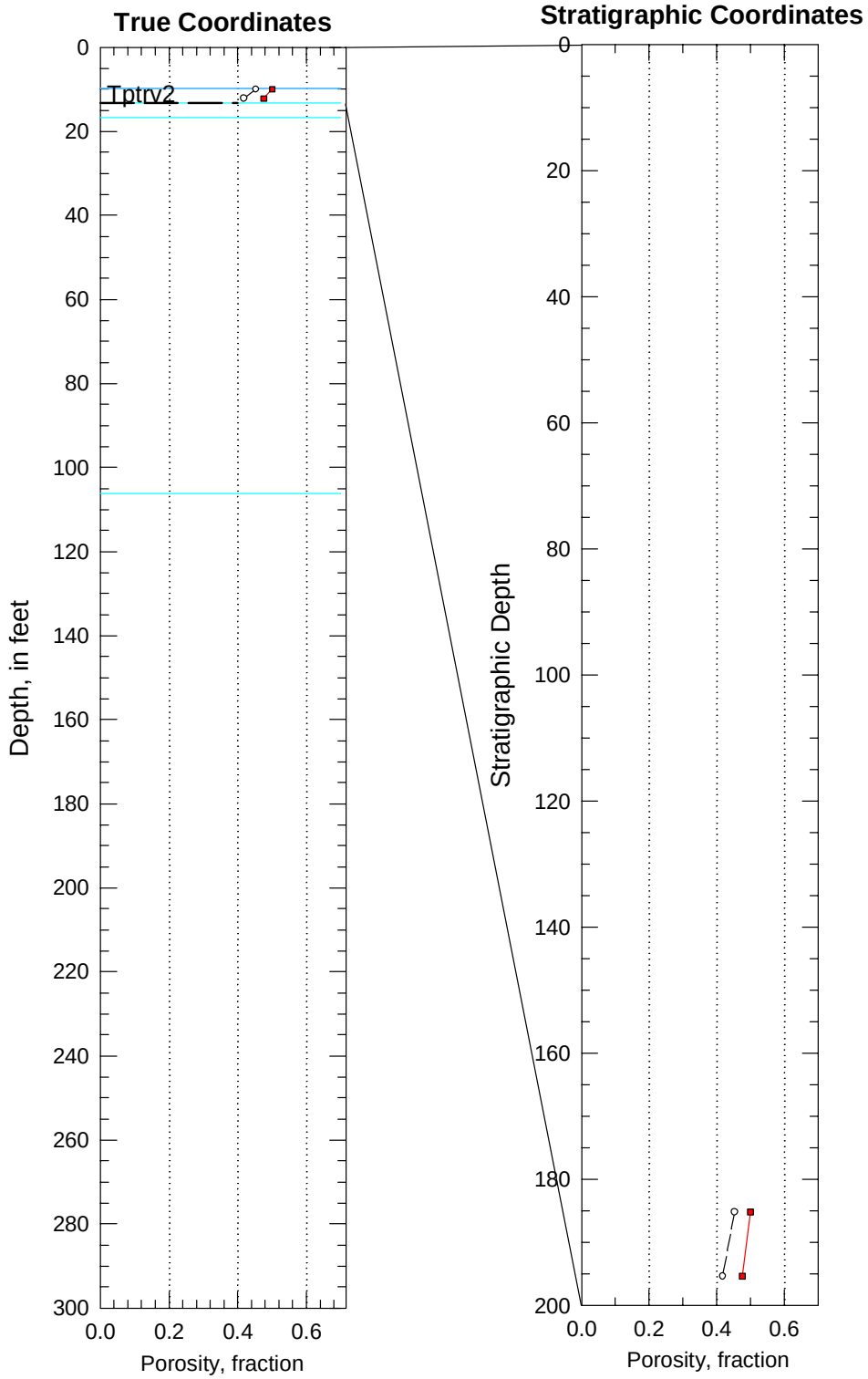

Figure B-150. Porosity data in real-world and in stratigraphic coordinates for the PTn model unit in drillhole UZN-61.

(This page intentionally left blank.)

Appendix C: LITHOPHYSAL ZONES

Introduction

One of the very distinctive features of the Paintbrush Group ash-flow tuff deposits is the presence of major lithophysal zones in both the Tiva Canyon and the Topopah Spring Tuffs (Lipman and others, 1966). Lithophysae are mesoscopic cavities that are formed by the escape of trapped air and volcanic gasses and the exsolution of volatiles still contained in the mass of hot glassy shards during cooling and crystallization of an emplaced ash-flow deposit (Ross and Smith, 1961; Cas and Wright, 1987). If the internal pressure of gas exceeds the lithostatic pressure of the overlying deposits, the trapped gas will inflate actual cavities ("bubbles") that may vary in size from a few millimeters to nearly a meter in diameter. The margins of such cavities are typically highly altered by the magmatic gasses, and the cavities may be lined by fibrous crystal aggregates indicating vapor-phase mineralization into open spaces. Buesch and others (1996; p. 12) present a detailed summary of the occurrence of lithophysal zones at Yucca Mountain.

It is clear that the formation of lithophysal cavities requires a delicate balance between the pressure of the inflating gas phase and that of the overlying material within what may be a still-accumulating pyroclastic deposit, combined with the rate of cooling and accompanying increase in mechanical strength of the deposit. In addition to the prototypical spherically shaped lithophysal cavity, lithophysae may be more elliptical in form, almost invariably with the long axis of the ellipse located roughly in the plane of flattening and welding of pumice clasts and relict shard structures. These ellipsoidal lithophysae appear to represent partially flattened (or incompletely inflated) gas pockets. Indeed, our experience at Yucca Mountain indicates that there is virtually a continuum of shapes between spheres, ellipsoids, flattened just-open partings, and solid veinlets of vapor-phase minerals surrounded by an altered border. Some exposures and drill holes at Yucca Mountain clearly indicate a bimodal distribution of sizes, with both mesoscopic (millimeters to a few centimeters) and megascopic (decimeter-plus) lithophysal cavities (*cavernous lithophysae* of Buesch and others, 1996), suggesting that conditions conducive to the formation of lithophysae may have occurred multiple times at a given location within the deposit. Cas and Wright (p. 84) make reference to broken lithophysae, which they interpret as evidence of additional flowage of a mostly solidified volcanic deposit after formation of the lithophysal cavities.

Given that lithophysae are early-formed lithologic features formed within an evolving and cooling ash-flow deposit, and that the requisite conditions for their formation may appear and disappear and reappear again at any particular location within that deposit, it is evident that lithophysae represent a type of early alteration, and are not truly a primary stratigraphic feature of volcanic rocks. Because an ash-flow tuff is typically a roughly tabular body with the "horizontal" dimensions many times the "vertical," it is also apparent that the pressure–temperature (P–T) gradients within such a deposit will be mostly vertical, with regions of roughly equivalent pressure and temperature aligned subparallel to the horizontal dimensions. It seems likely that lithophysal zones generally would be stratiform in nature, although not necessarily stratabound by primary depositional surfaces on the finer scale.

It is this alteration nature of lithophysae that leads us to treat "lithophysal porosity" as a material-property attribute, and not as a means of stratigraphically subdividing a rock mass into a number of layer-cake geological units. Figure C-2 presents porosity cross section from drillhole WT-18 on the north, through the repository block to drillhole WT-12 on the south (see fig. C-1 for locations). Each drillhole is represented by two curves: the total or lithophysal porosity curve from downhole petrophysical measurements (shown in red), and a matrix or water-filled porosity curve developed from either laboratory core measurements or downhole petrophysical measurements if there are no core data (shown in blue). In each case, the data are portrayed in stratigraphic-depth coordinates, scaled between zero and 1000 nominal feet. The contacts and correlations shown by the lighter weight lines are the formal lithostratigraphic unit boundaries obtained from the YMP Stratigraphic Compendium (Clayton, 1996) and based on the criteria of Buesch and others (1996).

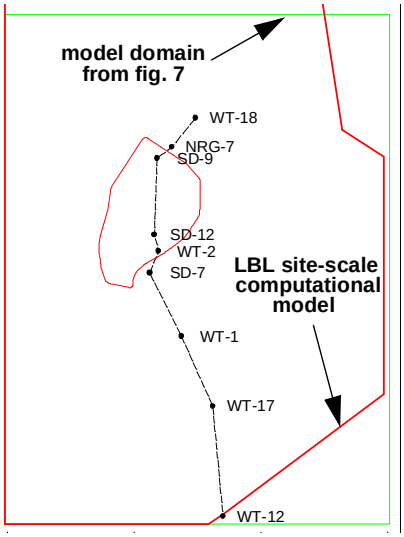

Figure C-1. Index map showing location and identity of holes used in creating the porosity cross section of Yucca Mountain.

Casual examination of figure C-2 indicates that there are intervals within each drill hole for which the two curves plot very close together or are virtually coincident, and intervals for which there is a distinct separation of the two types of data. Furthermore, it is relatively apparent that the interval correlated across the top half of the cross section (indicated as Tptrl and Tptpul on the figure, using nomenclature of Buesch and others, 1996) generally exhibits greater and more obviously continuous separation of the two porosity curves than does the interval correlated across the lower half of the figure (zone Tptpll). Indeed, the lower lithophysal zone in several drill holes appears to lack meaningful lithophysal porosity, as that term is defined in this report, with the lithophysal porosity data essentially plotting on top of the matrix/water-filled porosity data.

Note also, the heavy dotted correlation line that marks the boundary between the crystal-poor lower member of the Topopah Spring Tuff and the overlying crystal-rich member. This contact presumably is a true "stratigraphic" contact, originating from a change in the composition of the magma being erupted from high-silica rhyolite to lower-silica quartz latite in a compositionally zoned magma chamber (Lipman and others, 1966). In the vicinity of drillholes NRG-7, SD-9, and SD-12, the P–T conditions conducive to formation of lithophysal gas voids extended above this "depositional" contact, whereas at the other drillhole locations, they apparently did not.

In addition to the boundaries of the formally named lithophysal zones shown on figure C-2, we have indicated our interpretation of lithophysae-bearing intervals for which the increase in porosity is large enough to cause marked separation of the matrix and lithophysal porosity curves. These intervals are indicated by a heavy green bar on the left-hand side of a drill hole porosity plot. These interpreted intervals do not necessarily include all rocks that contain small lithophysae and/or "lithophysal-style alteration" typically expressed in core as small circular to elliptical spots of white vapor-phase alteration minerals. They simply reflect separations between the matrix and lithophysal porosity curves that are, in our opinion, large enough to suggest the presence of significant lithophysae.

Description of the Cross Section

Drillhole WT-18 — (Note: no core for this hole) The anticipated lithophysae-bearing intervals in drill hole WT-18 shown in figure C-2 as inferred from separation of the matrix and lithophysal porosity indicators from petrophysics correspond fairly closely to the formally named lithophysal zones. We classify the very bottom of the Tptpll zone (beginning at a depth of ~900 nominal feet) as potentially nonlithophysal because of the fairly abrupt decrease in the blue matrix porosity curve at this depth. Such shifts in matrix porosity can be characteristic of lithophysal intervals because of more intense vapor-phase alteration of the rock matrix; see for example the lower lithophysal interval of drillhole WT-1 and the shift in matrix porosity in WT-18. Note also that in drillhole WT-18, apparent lithophysae extend almost through the entire lower portion of the formation in marked contrast to the remaining holes shown on the figure.

Drillhole NRG-7 — (Note: partial core only for this hole) Our inferred lithophysae-bearing intervals correspond quite closely to the formally

named lithophysal zones; note that the upper lithophysae-bearing interval has been subdivided formally into crystal-rich and crystal-poor intervals. The top of the upper lithophysal interval is quite well defined by an abrupt increase in the amount of separation between the two petrophysical porosity curves. Note also, the shift of the matrix porosity curve toward higher values at this contact, presumably reflecting more intense vapor-phase alteration of the rock matrix exclusive of actual lithophysae. The middle nonlithophysal zone, formally identified between stratigraphic depths of 400 and 500 nominal feet, is marked by several separations of the two geophysical traces essentially equal to those observed in the upper and lower lithophysal zones. Although Buesch and others (1996) describe the occurrence of a "lithophysae-bearing subzone of the middle nonlithophysal zone," it is unclear what effect this subdivision has on the rock material properties through this middle part of the Topopah Spring Tuff in this drill hole. The lithophysal porosity curve indicates that porosities equal and exceed 20 percent in about half of the "nonlithophysal" zone, a porosity fraction that qualifies most of the lower lithophysal zone (Tptpll).

Drillhole SD-9 — (Cored hole) Our interpreted lithophysae-bearing intervals are definitely less extensive vertically than the formally named lithophysal zones. Note that Engstrom and Rautman (1996) describe a fairly pronounced change in character of the Tptpul zone at a depth of about 676 ft, which corresponds to the base of the upper green bar in figure C-2 at a stratigraphic depth of some 354 nominal feet. Above this depth, lithophysae are described as most open, whereas below this depth lithophysae are described as "closed." The lower lithophysal zone in this drillhole appears as a sequence of alternating lithophysae-bearing and non-lithophysae bearing intervals in the geologic log of Engstrom and Rautman; however, the existence of extensive intervals of lost or rubblized core through this interval makes interpretation difficult. Isolated large lithophysal cavities are described in the Tptpll zone from downhole video images. This interpretation is consistent with the erratic short intervals of curve separation that typifies the geophysical data traces below about 600 ft in stratigraphic coordinates.

Drillhole SD-12 — (Cored hole) Our inferred lithophysae-bearing interval in the upper part of drillhole SD-12 corresponds almost exactly to the formally named Tptrl and Tptpul zones. It appears that the lower lithophysae-bearing interval below a stratigraphic depth of about 480 nominal ft may be less continuous than the formally named lower lithophysal zone might imply. Similar to drillhole SD-9, the impression is one of alternating significant lithophysae-bearing intervals separated by intervals of less-significant large number of lithophysal cavities, potentially on the order of 10 nominal feet. This impression is confirmed by the detailed geologic log of Rautman and Engstrom (1996b).

Drillhole WT-2 — (Note: no core for this hole) The apparent lithophysae-bearing intervals in this hole seem to coincide fairly closely with the formally named lithophysal zones. We would extend the interpretation of the top of the upper lithophysal interval to a stratigraphic depth of approximately 100 nominal ft in order to coincide with the prominent increase in both the matrix and lithophysal porosity curves at this depth. The extent of the lower lithophysal interval appears to be somewhat less than the formally described depth of about 780 ft (in stratigraphic coordinates), as the two porosity curves merge at a depth of about 750 ft. Note, however, that both curves decrease again at the formal contact.

Drillhole SD-7 — (Cored hole) A fairly strong argument can be made for drillhole SD-7 that the intervals of significant lithophysae development extend for quite some distance above and below the formally named lithophysal zones. The published detailed geologic log for this hole (Rautman and Engstrom, 1996a) clearly indicates that lithophysae associated with the upper lithophysal interval extend to a stratigraphic depth of about 330 ft (true depth: 682.5 ft). The published log also indicates a sharp change in the lithophysal character of the rock associated with the lower lithophysae-bearing interval at a depth of 803.3 ft, which corresponds to the sharp separation of the two porosity curves at a stratigraphic depth of about 464 nominal ft. The extent of the lower lithophysae-bearing interval in hole SD-7 is less clearly indicated in the geologic log; however, the charac-

ter of the petrophysical traces suggests the presence of unidentified large cavities to a stratigraphic depth of nearly 780 nominal ft.

Drillhole WT-1 — (Note: no core for this hole) Without core or detailed downhole video descriptions, there is little that can be said regarding this particular drillhole. However, our choices of the depths for what we infer are the lithophysae-bearing intervals are strongly influenced by the distinct breaks in the character of the matrix porosity curve. Note that these inferred higher-matrix-porosity/vapor-phase alteration intervals extend above and below the formal limits of the Tptpul zone, yet coincide fairly closely with the same limits of the Tptpll zone.

Drillhole WT-17 — (Note: no core for this hole) Something is clearly amiss with the formal zonation of drillhole WT-17. In addition, it is not clear that the hole can be subdivided into two relatively discrete lithophysal zones, upper and lower. The formally named upper lithophysal zone, that part of the drill hole between 301 and 335 ft (stratigraphic depths of 79–130 nominal ft), while marked by separation of the lithophysal and matrix porosity curves, does not really exhibit the "anomalous" separation and ragged character of the other drill holes on the cross section. In contrast, the "middle nonlithophysal zone" identified between stratigraphic depths of 130 and 417 nominal feet (true depth: 335–526 ft) is marked by much greater separation between the two petrophysical porosity curves and exhibits much of the character of a lithophysae-bearing interval in, for example, drillhole SD-7 or WT-18. Only a part of the purported "lower lithophysal zone" between stratigraphic depths of 417–576 ft (true depth 526–632 ft) exhibits separation of the two porosity curves, and the anomalously thick "lower nonlithophysal zone" from 632 to 874 ft in the real world (576–938 ft in stratigraphic coordinates) contains at least three and possibly as many as five lithophysae-bearing intervals.

What appears to be happening is that to the south of the Yucca Mountain area, which is the more distal portion of the Topopah Spring Tuff outflow sheet, deposition by a modestly large number of separate pyroclastic flows produced favorable conditions for development of lithophysal cavities at a number of different times. In effect, we are most likely dealing with a composite cooling unit, that cooled overall from magmatic temperatures to ambient conditions as a package, but within which the separate individual ash-flow deposits near (?) their feather edges retained enough separate character to produce multiple lithophysal intervals within the Topopah Spring Tuff as a whole.

Drillhole WT-12 — (Note: no core for this hole) The southernmost drill hole plotted on the cross section of figure C-2 indicates a continuation of what should be, by now, a familiar pattern of separations between the matrix and lithophysal porosity curves. We infer a relatively massive upper lithophysae-bearing interval that extends above the top of the formally named upper lithophysal zone (Tptpul), and we have attempted to interpret a number of thinner, less-well developed lithophysae-bearing intervals within what is formally described as the lower lithophysal zone (Tptpll). The previously described pattern of higher matrix porosities associated with the inferred lithophysae-bearing intervals is weakly developed at the top and base of the formal middle nonlithophysal zone.

Concluding Remarks

Our examination of the material properties data, specifically for porosity, from the available drill holes at Yucca Mountain clearly indicates that intervals of markedly higher "lithophysal" porosity compared to the "matrix" porosity at a given depth, and which are therefore inferred to represent intervals of significant lithophysal cavity development, are not restricted to the formally named lithophysal zones identified by Clayton (1996, and references therein). Furthermore, not all formally named lithophysal zones exhibit any particularly pronounced evidence of "lithophysal porosity," identifiable by systematic separation of the petrophysical total porosity curve and the "matrix porosity" data consisting of either core measurements or "water-filled" porosity computed from petrophysics.

For purposes of constructing simulated models of porosity, per se, we have elected to abandon the use of such qualitatively and apparently ambig-

uously defined terms as “lithophysal zones,” and to work directly with the underlying material properties measurements. Assuming that the petrophysical logs and the computed porosity data developed by Nelson (1996) and Thompson and Rael (1996) have any validity as quantitative measures of the pore space present in the rock mass surrounding a drill hole, it appears that the so-called lithostratigraphic zonation of the Topopah Spring Tuff developed by Buesch and others is of limited value in assisting material properties modeling. Although the majority of the formally named lithophysal zones do exhibit higher porosities than the majority of the formally named nonlithophysal zones, the drillhole plots shown in figure C-2 clearly demonstrate that high porosity zones occur outside of the supposed lithophysal zones and that intervals of porosity typical of the nonlithophysal matrix are extensive within these same zones.

It appears that the mismatches between the lithostratigraphic designation and the actual porosity of the rock mass are much more common in the lower part of the Topopah Spring Tuff than in the upper part. This observation is consistent with the interpretation that lithophysae-bearing intervals are formed by inflation of gas “bubbles” and “pockets” within a cooling pyroclastic flow deposit under conditions when the pressure of the contained and escaping gas slightly exceeds the lithostatic pressure of the overlying deposit existing at one particular time. If the major outflow-sheet deposit of the caldera eruptive sequence continues to accumulate, it is highly likely that multiple lithophysal zones may form and be partially to completely collapsed and destroyed as time proceeds. It is thus very likely that mesoscopic evidence of one-time inflated lithophysal cavities may coexist with low-porosity, re-flattened welded tuff.

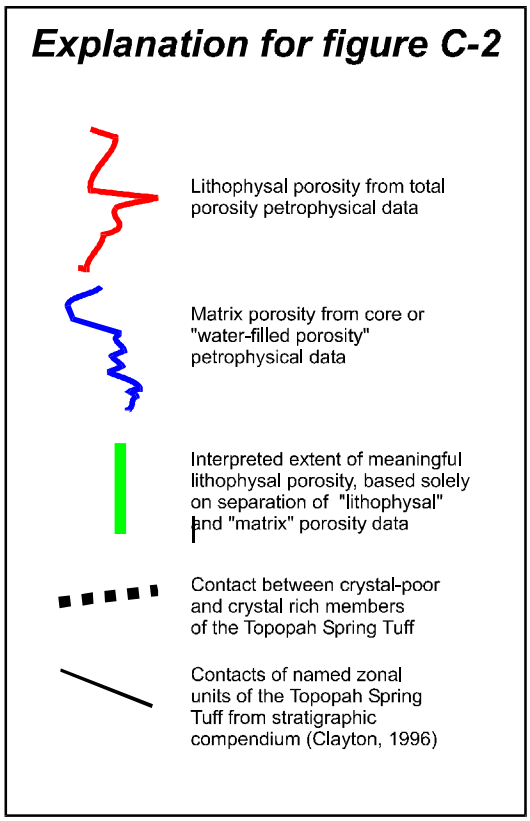

(Note: this page and the oversize plate that follows are single sided.)

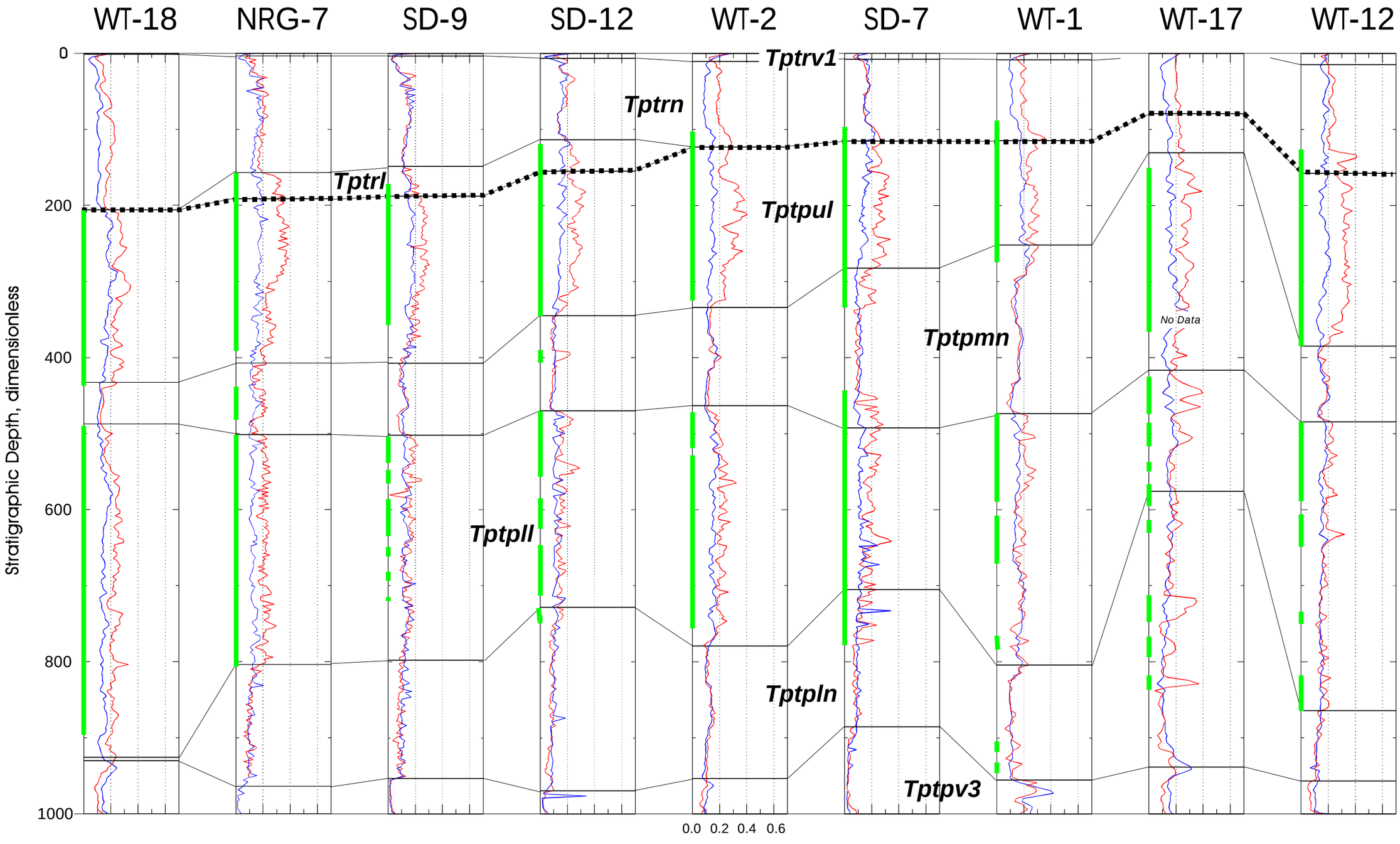

Figure C-2. Porosity cross section through Yucca Mountain from north to south. See separate explanation.

Appendix D: NOTES ON REPRODUCTION OF THE VARIOGRAM

Motivation

During technical review of this report considerable attention was directed to the fact that reproduction of the input-model variograms by the ensembles of simulated models appeared less than exact; see for example figures 52, 53, 61, 62, 65, 66, 79, 80, 83, and 84. As has been discussed in the text associated with these figures, as well as in the earlier descriptive sections of the report, the analysis of spatial correlation structure is frequently difficult for any number of reasons, and slavish reproduction of an input variogram is not necessarily the goal of geostatistical modeling.

For example, an experimental variogram is based upon a particular (finite) set of sample values at a given set of physical locations. Had the same number of samples been measured at slightly different locations, it is almost certain that the experimental variogram computed for these hypothetical alternative samples would be different in detail. Also, as noted on page 90, some of the variograms from the simulated porosity realizations do resemble the original sample variograms more closely than they do the modeled interpretation of those sample variogram. Nevertheless, spurred by the apparently consistent differences between the variograms of the simulated models and the input model variogram, we have pursued an investigation into the potential causes of these differences, as described in this appendix.

Influence of the Normal-Score Transformation

Variogram computation and modeling were conducted in "normal-score space" after transformation from the original porosity space by a quantile-preserving transform, such as that illustrated in figure 45. The modeled variograms then used as input to the sequential Gaussian simulation process thus describe the spatial continuity of normal-score values, and indeed the simulation algorithm actually generates a set of spatially correlated normal scores. These simulated random numbers are ultimately back-transformed using the same quantile-preserving inverse transform such that the output numbers represent porosity values.

It turns out that the standard **SGSIM** implementation of the sequential Gaussian simulation algorithm (Deutsch and Journel, 1992) will perform the translation (in both directions) automatically. The difficulty with this process is that in so doing, the normal-score values themselves are discarded after the back-transformation. The variograms of the simulated models included in the body of this report were, in fact, calculated in normal-score space, but as part of later post-processing. This post-processing used a second transformation step [a general univariate transformation algorithm, **TRANS** (Deutsch and Journel, 1992)] tied to the original normal-score transform table computed by program **NSCORE** (Deutsch and Journel, 1992) from the raw input porosity data. This re-conversion to normal score space prior to computing the check variograms induces "noise" in the normal-score values, noise that appears in the variograms as higher variability for a given separation distance.

The explanation of this induced noise is as follows. The standard-normal distribution of mean = zero and variance = 1 is monotonically increasing when graphed in cumulative distribution function format; see figure D-1. However, a large set of sample data measured with finite precision, such as the porosity data used in this study, are not necessarily *continuously* monotonically increasing in the same manner, in that there inevitably are multiple values of, say, 11.3-percent porosity (0.113). This problem will increase in severity as the number of sample data increase. Because the standard normal function does not allow such "identical" values, the transformation program (**NSCORE**) breaks "tied" input values in an arbitrary random manner, which results in a legitimate but *unique* standard-normally distributed cumulative function for use in generating a simulated model. Unfortunately, once the interim normal score simulated values are discarded upon back-transformation, any reconversion to normal score space will result in the identical spatial distribution of normal-score values only under extremely fortuitous conditions—functionally, never.

Figures D-2 through D-3 present the results of an experiment in which we have re-simulated the four specific simulations of lithophysal poros-

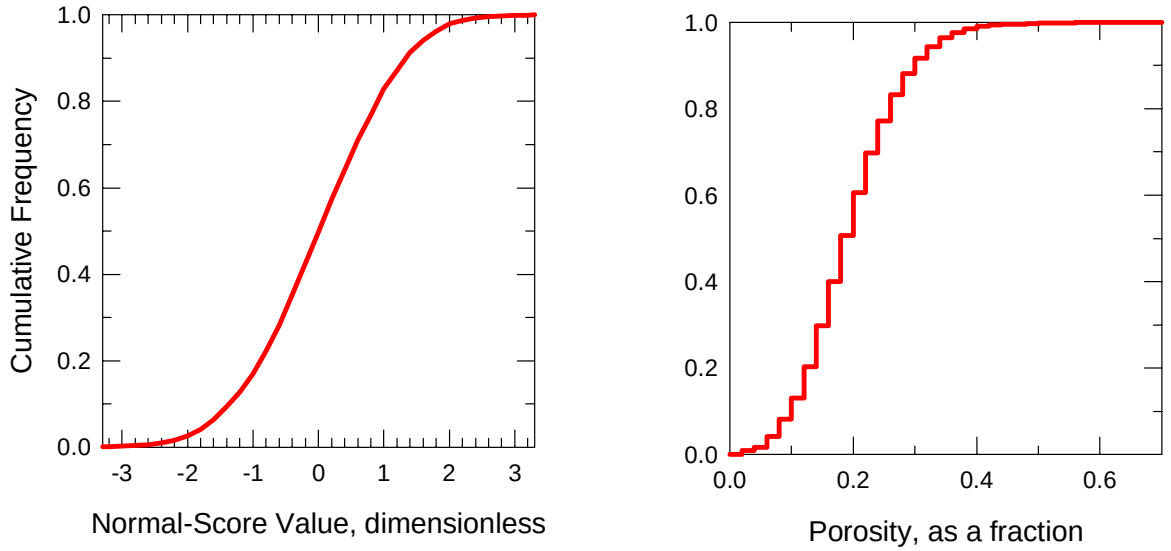

Figure D-1. (a) A standard-normal distribution in cumulative-distribution function format demonstrating the continuously monotonic increasing nature of this function. (b) A "real" porosity distribution in cumulative-distribution function format illustrating the effect of multiple "identical" (finite-precision) measurements,

ity shown in the validation diagrams of figures 58–62. Figure D-2 is identical to figure 62 of the text, and it represents the results of the multiple-transformation procedure described above. Figure D-3 shows the same variograms, only in this case the variograms plotted represent the normal-score values generated directly by program **SGSIM** (using the same random number seed) applied to directly to the normal-score transformed porosity data themselves. No back-transformation and re-transformation is required under these circumstances. Figure D-3 clearly indicates that the input model variogram is reproduced much more closely for the unback-transformed normal-score values. The departure of the simulated values from the model shown in part (a) of figure D-3 is attributed to the fact that the vertical search during the simulation process was restricted to a small fraction of the total vertical separation. Note, however, that the match between the four simulations and the input variogram model is much improved over that shown in part (a) of figure D-2.

Other Influences

Figure D-4 presents the results of two additional experiments involving re-simulation of simulation number 34 of lithophysal porosity in the TSw model unit. Case 1 involves doubling the size of the kriging matrix used during the estimation of the local expectation of the spatially distributed probability density function. In this case, the size of the kriging matrix was increased from 12 to 24 values. The minimum number of measured data values was kept at 2, and the estimation process would allow no more than 8 previously simulated grid nodes—double the previous value. The search criteria also used a maximum of 12 data nodes. Case 2 involved the maximum search distance used to search for nearby data. In this case the search distance was more than doubled to a maximum of 30,000 ft. The search was kept isotropic in the stratigraphically horizontal plane, and a constant vertical-to-horizontal anisotropy ratio was maintained as well.

Figure D-4 clearly indicates that the effect of using a larger kriging matrix and more data (or data plus previously simulated nodes) is the more significant in improving the match of the simulated models to the input variogram. That increasing the search radius did not appear to improve variogram reproduction is most likely attributable to the fact as the simulation proceeded, the maximum number

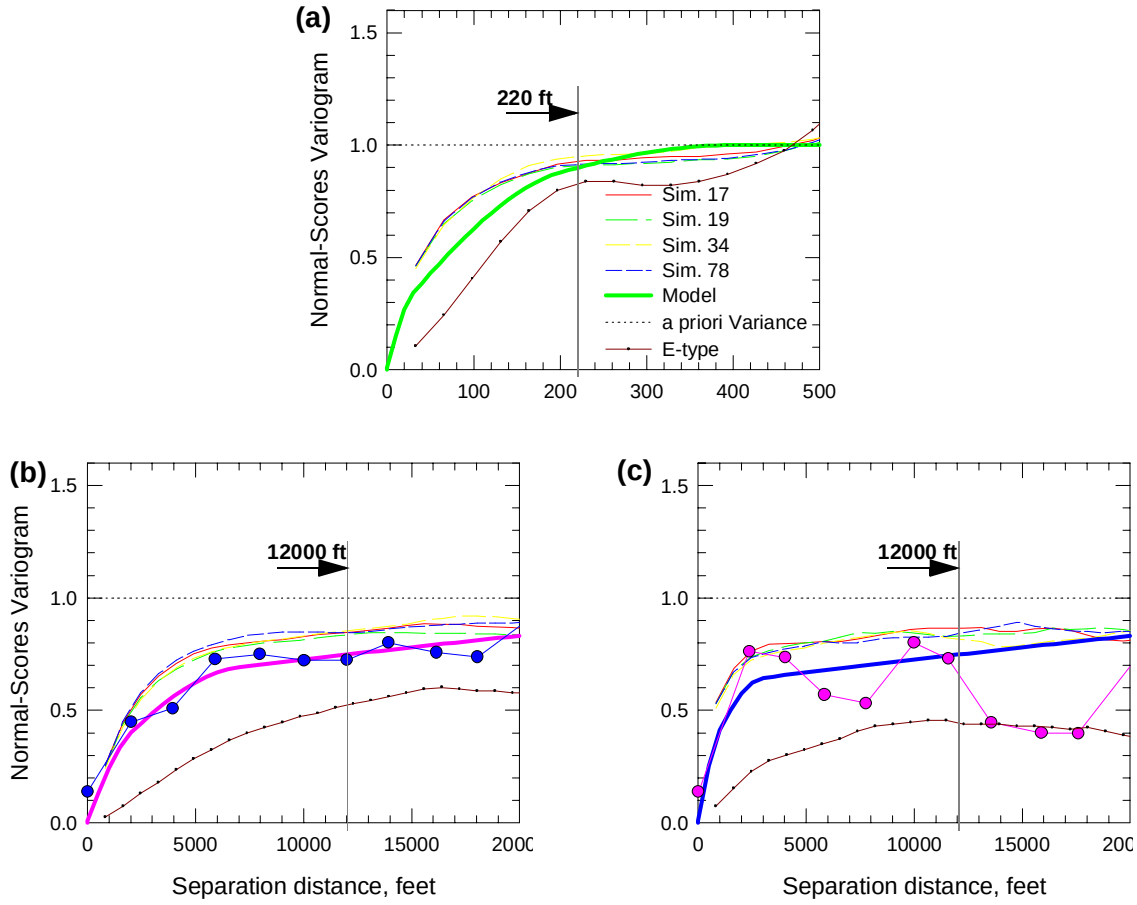

Figure D-2. Variogram from four simulated models of lithophysal porosity in the TSw model unit compared to input model and original data where simulated values have been re-transformed from porosity to standard-normal space prior to calculation of variogram. (a) Stratigraphic vertical; (b) stratigraphic horizontal, azimuth = 0°; (c) stratigraphic horizontal, azimuth = 90°. Original search limits shown; identical to figure 62; compare to figure D-3.

of data allowed could be located quite nearby, thus defeating the other benefits of the increased search distance.

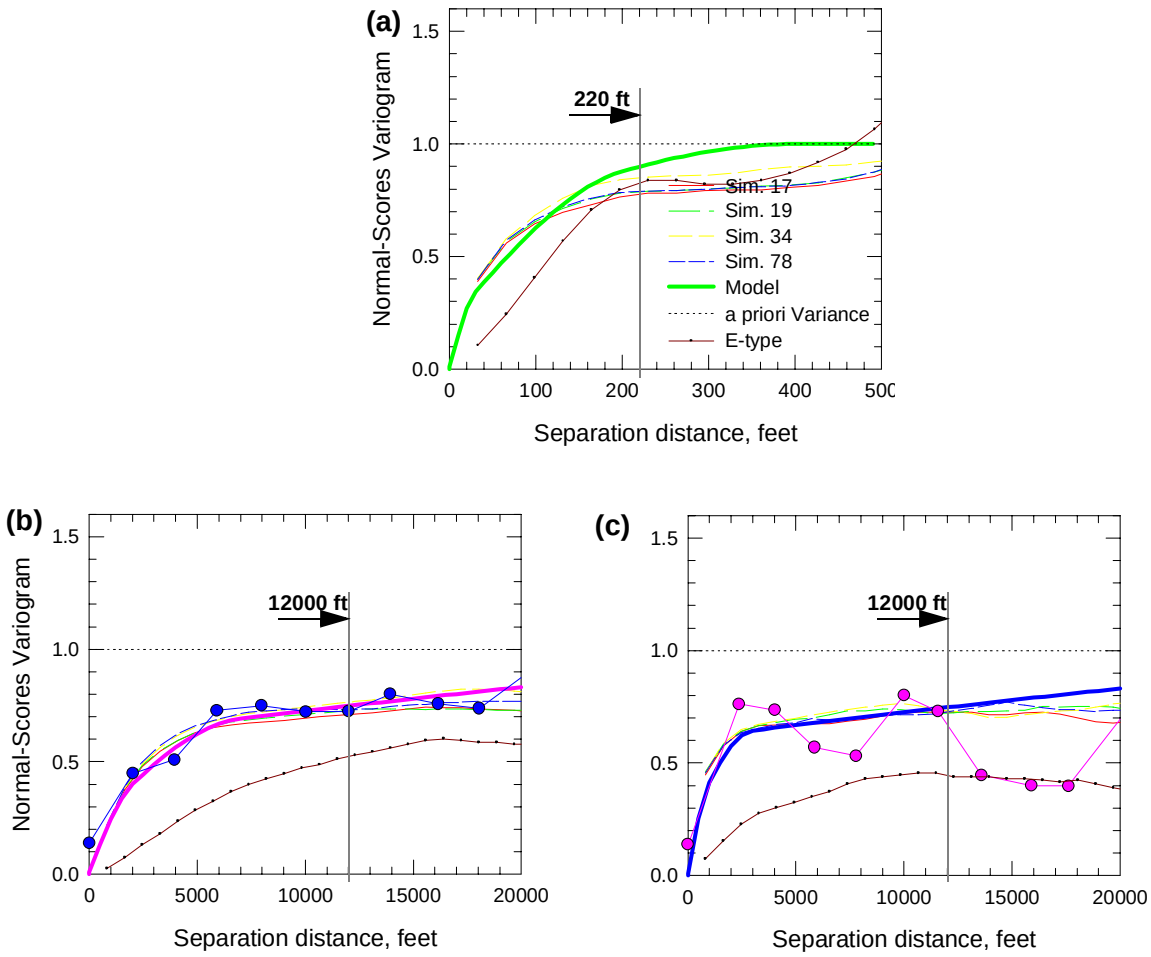

Figure D-3. Variogram from four simulated models of lithophysal porosity in the TSw model unit compared to input model and original data where simulated values have been kept in standard-normal space prior to calculation of variogram. (a) Stratigraphic vertical; (b) stratigraphic horizontal, azimuth = 0°; (c) stratigraphic horizontal, azimuth = 90°. Original search limits shown; compare to figure D-2

Summary Remarks

Because of the sequence in which the various suites of simulated models were generated and post-processed, it would appear that the poor reproduction of the input variogram, as described in the body of this report, is an artifact related to post-processing, and does not represent a problem with the simulations themselves. Specifically, the transformation of the measured porosity data to normal-score space and back-transformation of the simulated values for each simulation was conducted within an internally consistent framework. As demonstrated by figure D-3, the directly generated normal-score porosity values for a selected subset of the total simulations described in this report reproduce their input variogram models quite closely once freed of the confounding influence of multiple transformation steps. We believe that this increased exactitude is a general phenomenon, and that had the interim normal-score porosity values been retained, the variograms of the simulated models could be demonstrated to reproduce their input spatial continuity models as well. Because there is no way short of rerunning all simulations to recreate these interim values, we do not believe that the increased certainty of statistical validation warrants the required effort and delay.

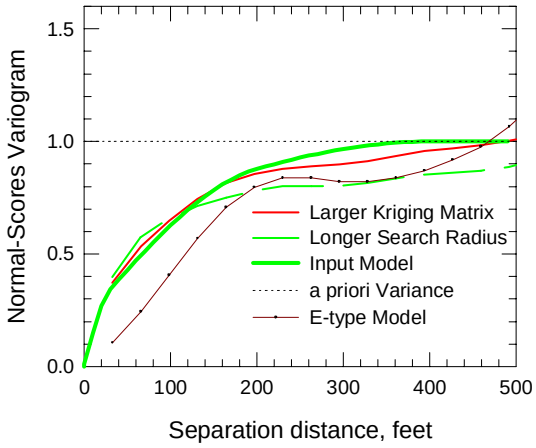

Figure D-4. Re-simulated normal-score models of lithophysal porosity showing influence of a larger kriging matrix and longer search radius during simulation. Vertical direction only; TSw model unit. Compare to parts (a) of figure D-2 and D-3.

YUCCA MOUNTAIN SITE CHARACTERIZATION PROJECT
SAND97-1730 - DISTRIBUTION LIST

1 D. A. Dreyfus (RW-1)
Director
OCRWM
US Department of Energy
1000 Independence Avenue SW
Washington, DC 20585

1 L. H. Barrett (RW-2)
Acting Deputy Director
OCRWM
US Department of Energy
1000 Independence Avenue SW
Washington, DC 20585

1 S. Rousso (RW-40)
Office of Storage and Transportation
OCRWM
US Department of Energy
1000 Independence Avenue SW
Washington, DC 20585

1 R. A. Milner (RW-30)
Office of Program Management
and Integration
OCRWM
US Department of Energy
1000 Independence Avenue SW
Washington, DC 20585

1 D. R. Elle, Director
Environmental Protection Division
DOE Nevada Field Office
US Department of Energy
P.O. Box 98518
Las Vegas, NV 89193-8518

1 T. Wood (RW-14)
Contract Management Division
OCRWM
US Department of Energy
1000 Independence Avenue SW
Washington, DC 20585

4 Victoria F. Reich, Librarian
Nuclear Waste Technical Review Board
1100 Wilson Blvd., Suite 910
Arlington, VA 22209

1 Wesley Barnes, Project Manager
Yucca Mountain Site Characterization
Office
US Department of Energy
P.O. Box 30307 MS 523
Las Vegas, NV 89036-0307

1 Director, Public Affairs Office
c/o Technical Information Resource Center
DOE Nevada Operations Office
US Department of Energy
P.O. Box 98518
Las Vegas, NV 89193-8518

8 Technical Information Officer
DOE Nevada Operations Office
US Department of Energy
P.O. Box 98518
Las Vegas, NV 89193-8518

1 J. R. Dyer, Deputy Project Manager
Yucca Mountain Site Characterization Office
US Department of Energy
P.O. Box 30307 MS 523
Las Vegas, NV 89036-0307

1 S. A. Orrell
Laboratory Lead for YMP
M&O/Sandia National Laboratories
1180 Town Center Dr.
Las Vegas, NV 89134

1 J. A. Canepa
Laboratory Lead for YMP
EES-13, Mail Stop J521
M&O/Los Alamos National Laboratory
P.O. Box 1663
Los Alamos, NM 87545

1 Repository Licensing & Quality
Assurance
Project Directorate
Division of Waste Management, MS T7J-9
US NRC
Washington, DC 20555

1 Senior Project Manager for Yucca
Mountain
Repository Project Branch
Division of Waste Management, MS T7J-9
US NRC
Washington, DC 20555

1 NRC Document Control Desk
Division of Waste Management, MS T7J-9
US NRC
Washington, DC 20555

1 Chad Glenn
NRC Site Representative
301 E Stewart Avenue, Room 203
Las Vegas, NV 89101

1 Center for Nuclear Waste
Regulatory Analyses
Southwest Research Institute
6220 Culebra Road
Drawer 28510
San Antonio, TX 78284

2 W. L. Clarke
Laboratory Lead for YMP
M&O/ Lawrence Livermore Nat'l Lab
P.O. Box 808 (L-51)
Livermore, CA 94550

1 Robert W. Craig
Technical Project Officer
US Geological Survey
1180 Town Center Dr.
Las Vegas, NV 89134

1 J. S. Stuckless,
Senior Science Advisor
MS 425
Yucca Mountain Project Branch
US Geological Survey
P.O. Box 25046
Denver, CO 80225

1 L. D. Foust, Asst. General Mgr.
Nevada Site
TRW Environmental Safety Systems
1180 Town Center Dr.
Las Vegas, NV 89134

1 A. L. Flint
U. S. Geological Survey
1180 Town Center Dr.
Las Vegas, NV 89134

1 Robert L. Strickler
Vice President & General Manager
TRW Environmental Safety Systems, Inc.
2650 Park Tower Dr.
Vienna, VA 22180

1 Jim Krulik, Technical Program Officer
US Bureau of Reclamation
Code D-8322
P.O. Box 25007
Denver, CO 80225-0007

1 B. T. Brady
Records Specialist
US Geological Survey
MS 421
P.O. Box 25046
Denver, CO 80225

1 M. D. Voegele
Deputy of Technical Operations
M&O/SAIC
1180 Town Center Dr.
Las Vegas, NV 89134

2 A. T. Tamura
Science and Technology Division
OSTI
US Department of Energy
P.O. Box 62
Oak Ridge, TN 37831

1 P. J. Weeden, Acting Director
Nuclear Radiation Assessment Div.
US EPA
Environmental Monitoring Sys. Lab
P.O. Box 93478
Las Vegas, NV 89193-3478

1 John Fordham, Deputy Director
Water Resources Center
Desert Research Institute
P.O. Box 60220
Reno, NV 89506

1 The Honorable Jim Regan
Chairman
Churchill County Board of
Commissioners
10 W. Williams Avenue
Fallon, NV 89406

1 R. R. Loux
Executive Director
Agency for Nuclear Projects
State of Nevada
Evergreen Center, Suite 252
1802 N. Carson Street
Carson City, NV 89710

1 Brad R. Mettam
Inyo County Yucca Mountain
Repository Assessment Office
P. O. Drawer L
Independence, CA 93526

1 Vernon E. Poe
Office of Nuclear Projects
Mineral County
P.O. Box 1600
Hawthorne, NV 89415

1 Les W. Bradshaw
Program Manager
Nye County Nuclear Waste Repository
Project Office
P.O. Box 1767
Tonopah, NV 89049

1 Florindo Mariani
White Pine County Coordinator
P. O. Box 135
Ely, NV 89301

1 Tammy Manzini
Lander County Yucca Mountain
Information Officer
P.O. Box 10
Austin, NV 89310

1 Jason Pitts
Lincoln County Nuclear Waste
Program Manager
P. O. Box 158
Pioche, NV 89043

1 Dennis Bechtel, Coordinator
Nuclear Waste Division
Clark County Dept. of Comprehensive
Planning
P.O. Box 55171
Las Vegas, NV 89155-1751

1 Juanita D. Hoffman
Nuclear Waste Repository
Oversight Program
Esmeralda County
P.O. Box 490
Goldfield, NV 89013

1 Sandy Green
Yucca Mountain Information Office
Eureka County
P.O. Box 714
Eureka, NV 89316

1 Economic Development Dept.
City of Las Vegas
400 E. Stewart Avenue
Las Vegas, NV 89101

1 Community Planning & Development
City of North Las Vegas
P.O. Box 4086
North Las Vegas, NV 89030

2 Librarian
YMP Research & Study Center
1180 Town Center Dr.
Las Vegas, NV 89134

1 Library Acquisitions
Argonne National Laboratory
Building 203, Room CE-111
9700 S. Cass Avenue
Argonne, IL 60439

1 Glenn Van Roekel
Manager, City of Caliente
P.O. Box 158
Caliente, NV 89008

1 G. S. Bodvarsson
Head, Nuclear Waste Department
Lawrence Berkeley National Laboratory
1 Cyclotron Road, MS 50E
Berkeley, CA 94720

1 Steve Hanauer (RW-2)
OCRWM
U. S. Department of Energy
1000 Independence Ave.
Washington, DC 20585

1 Lorraine E. Flint
USGS
Placer Hall
6000 J Street
Sacramento, CA 95818-6129

1 Mark C. Tynan
DOE/YMPSCO
1180 Town Center Drive / HL423
Las Vegas, NV 89134

1 Robert W. Andrews
INTERA
1180 Town Center Drive / MS 423
Las Vegas, NV 89134

1 Robert W. Clayton
M&O/ WCFS
1180 Town Center Drive / MS423
Las Vegas, NV 89134

1 Paul Dixon
M&O/LANL
1180 Town Center Drive / MS423
Las Vegas, NV 89134

1 Robert W. Elayer
M&O/ MK
1180 Town Center Drive / MS423
Las Vegas, NV 89134

1 Howard Rael
M&O/ SAIC
1180 Town Center Drive / MS 423
Las Vegas, NV 89134

1	David Vaniman Los Alamos National Laboratory P.O. Box 1663 Los Alamos, NM 87545	
	MS	
1	1324	C. K. Ho, 6115
1	1324	S. A. McKenna, 6115
1	1326	H. A. Dockery, 6851
1	1326	M. L. Wilson, 6851
7	1324	C. A. Rautman, 6115
2	1330	K. Hart, 6811 100/1.2.3.2.2.2.2/SAND97-1730
20	1330	WMT Library, 6752
1	9018	Central Technical Files, 8940-2
5	0899	Technical Library, 4916
2	0619	Review and Approval Desk, 12690, For DOE/OSTI